The formation of dense gas in low- and high-mass star forming regions

Lars Bonne

université de BORDEAUX

THÈSE PRÉSENTÉE

POUR OBTENIR LE GRADE DE

DOCTEUR DE

L'UNIVERSITÉ DE BORDEAUX

ÉCOLE DOCTORALE DES SCIENCES PHYSIQUES ET DE L'INGÉNIEUR

SPÉCIALITÉ ASTROPHYSIQUE, PLASMAS, NUCLÉAIRE

Par Lars BONNE

LA FORMATION DU GAZ DENSE À L'ORIGINE DES ÉTOILES DE FAIBLE ET DE HAUTE MASSE

THE FORMATION OF DENSE GAS IN LOW- AND HIGH-MASS STAR FORMING REGIONS

Sous la direction de : Sylvain BONTEMPS
co-directrice : Nicola SCHNEIDER

Soutenue le 02/10/2020
Membres du jury:

M. HERPIN, Fabrice	Astronome	LAB Bordeaux	Président
M. KLESSEN, Ralf	Professeur d'université	Université de Heidelberg	Rapporteur
M. BELLOCHE, Arnaud	Chargé de recherche	MPIfR Bonn	Rapporteur
Mme GRENIER, Isabelle	Professeur d'université	Université Paris Diderot	Examinatrice
Mme RISTORCELLI, Isabelle	Directrice de recherche	IRAP Toulouse	Examinatrice
M. BONTEMPS, Sylvain	Directeur de recherche	LAB Bordeaux	Directeur de thèse
Mme SCHNEIDER, Nicola	Chargée de recherche	Université de Cologne	Co-directrice de thèse

Abstract

To understand how stars can form in the interstellar medium (ISM), it has to be understood how cold ($\sim$ 10 K) and dense ($> 10^4$ cm^{-3}) gas can emerge during the evolution of the ISM. This thesis studies the physical processes responsible for cold and dense gas formation in the ISM in the context of the GENESIS project[1][2], which aims to improve our understanding of structure formation in the ISM.

The *Herschel* Space Telescope revealed that most of this dense star forming gas is organised in filamentary structures. To understand the origin of this dense filamentary gas, multiple CO transitions were observed towards the Musca filament, which can form low-mass stars, using the APEX telescope. These observations were complemented with [CII] and [OI] observations by the SOFIA telescope. The non-detection of [CII] shows that the Musca cloud is embedded in a weak FUV field (< 1 G$_0$). However, the observed ^{12}CO(4-3) line with APEX demonstrates the presence of warm (> 50 K) CO gas around the Musca filament which cannot be explained by radiative heating. A comparison of the observed ^{12}CO(4-3) emission with shock models shows that the emission can be the result of a low-velocity ($<$ 4 km s^{-1}) J-type shock that can be responsible for mass accretion on the filament. This suggests that low-velocity shocks as a result of continuous mass accretion might play a prominent role in the formation of cold and dense star forming gas.

The accretion scenario for Musca is further analysed with low-J CO observations from APEX and NANTEN2 to study the gas kinematics. These observations unveil a velocity gradient over the Musca filament crest which is correlated with the velocity field of the nearby ambient gas. This suggests that the velocity gradient is the result of mass accretion from the ambient cloud and fits with the proposed shock accretion scenario. Analysing the full Musca cloud reveals a spatial and kinematic asymmetry from low- to high-density gas. This asymmetry is seen as a V-shape in the position-velocity (PV) diagram perpendicular to the Musca filament. Including atomic hydrogen (HI) observations in the analysis first of all confirms that Musca is part of a larger HI cloud, the Chamaeleon-Musca complex. It also demonstrates that the kinematic asymmetry is seen from the HI cloud down to the filament crest. Furthermore, the CO-HI asymmetry is found for basically all dense regions (Cha I, Cha II, Cha III and Musca) of Chamaeleon-Musca, while HI shows indications of more than one velocity component. This asymmetric accretion scenario is predicted by magnetised cloud-cloud collision simulations, where the bending of the magnetic field is responsible for the observed asymmetric accretion scenario. The filament formation in Musca can thus be explained by two intersecting converging flows which are driven by the magnetic field bending due to a large-scale colliding HI flow that triggered the observed star formation in the full Chamaeleon-Musca complex.

To investigate dense filament formation in a different environment, in terms of star formation activity, density and ambient FUV field, the high-mass star forming DR21 ridge was selected for a similar study. This analysis shows a spatial and kinematic asymmetry similar to the one observed in Musca, which advocates that DR21 is formed by a giant molecular cloud (GMC) collision. However, in the DR21 cloud, gravity plays an important role on large scales (> 1 pc) while for the Musca filament gravity only starts to dominate locally (r $<$ 0.1-0.2 pc). Due to the high density in the DR21 cloud after the GMC collision, gravity will drive the evolution of this compressed high-mass star forming cloud.

[1] https://astro.uni-koeln.de/stutzki/research/genesis

[2] https://astrophy.u-bordeaux.fr/generation-and-evolution-of-structure-in-the-interstellar-medium/

Kinematic observations of the full Cygnus-X north region further show indications of two interacting velocity components over the entire region, which indicates that a high-velocity (> 10 km s^{-1}) GMC collision can result in the formation of an OB association similar to OB2. These OB stars then form in gravitationally collapsing hubs and ridges due to the compression by the GMC collision.
These results put forward that large-scale collisions can play a prominent role in the formation of dense filaments, which are dynamic structures at the intersection of persistent converging flows driven by gravity or the magnetic field depending on the region.

Résumé

Pour comprendre la formation des étoiles, il faut étudier les processus physiques qui forment le gaz froid et dense dans le milieu interstellaire. Le télescope spatial *Herschel* a récemment démontré que la majorité du gaz froid et dense est formée de structures filamentaires (des filaments). Dans cette thèse, les processus physiques qui forment le gaz dense sont étudiés dans le contexte du projet GENESIS qui envisage d'avancer la compréhension de la structuration dans le milieu interstellaire.
Plusieurs raies de CO ont été observées avec le télescope APEX autour du filament de Musca. Ces observations ont été complémentées par des observations [CII] et [OI] avec le télescope SOFIA. La non-détection de [CII] démontre que le nuage de Musca est situé dans un champ de radiation UV faible ($<$ 1 G_0). Par contre, les observations de ^{12}CO(4-3) avec APEX montrent qu'il y a du gaz CO chauffé ($>$ 50 K) autour du filament que l'irradiation UV ne peut pas expliquer. La comparaison avec des modèles de chocs indique que l'émission ^{12}CO(4-3) doit alors être le résultat d'un choc J à basse vitesse ($<$ 4 km s^{-1}). L'analyse du spectre ^{12}CO(4-3) montre aussi que l'émission venant du choc ressemble à une signature de choc d'accrétion. Cette observation suggère qu'un choc à basse vitesse, dû à une accrétion continue, est responsable de la formation du gaz dense et froid du filament de Musca.
Ce scénario d'accrétion du filament de Musca est de plus étudié à grandes échelles dans les raies CO(2-1) et CO(1-0) obtenues avec les télescopes APEX et NANTEN2. Ces observations montrent un gradient de vitesse sur la crête de Musca qui est correlé avec le champ de vitesse autour du filament. L'analyse globale des observations de Musca montre une asymétrie à la fois spatiale et cinématique. Cette asymétrie est vue comme une forme en V dans le diagramme position-vitesse perpendiculaire au filament. L'inclusion d'observations du gaz neutre HI dans l'analyse confirme que Musca fait partie d'un nuage HI plus grand, le complexe Chamaeleon-Musca. Le HI montre aussi que l'asymétrie cinématique est présente des grandes échelles du nuage HI jusqu'aux petites échelles de la crête du filament de Musca. En comparant le HI avec les vitesses CO de Cha I, Cha II et Cha III, on constate que l'asymétrie cinématique est présente pour toutes les régions denses du complexe de Chamaeleon-Musca. Ce scénario d'accrétion asymétrique, qui est observé, est reproduit dans des simulations d'une collision de nuages magnétisés. Dans ce scénario, c'est la déformation du champ magnétique qui est responsable de l'accrétion asymétrique. La formation du filament Musca serait ainsi due à la convergence de deux flots de matière guidée par la courbure du champ magnétique provoquée par la collision des nuages HI à grande échelle.
Dans la dernière partie, la cinématique du nuage massif DR21, qui forme des étoiles massives, est étudiée pour comparer la formation des étoiles massives à celle des étoiles de faible masse. Le nuage DR21 montre une asymétrie en V similaire à celle de Musca, ce qui indique que le nuage DR21 est aussi formé par une collision de nuages moléculaires mais avec une vitesse de collision plus importante que pour Musca. Les observations indiquent de plus que la formation des étoiles massives dans le nuage DR21 serait la conséquence directe de la prédominance de la gravité à grande échelle ($>$ 1 pc) du gaz dense en contraste avec Musca pour lequel la gravité ne dominerait qu'aux plus petites échelles ($<$ 0.1-0.2 pc). L'analyse cinématique globale de toute la région du Cygne montre que toute la région résulte de la même collision de nuages. Cette observation indique que c'est une collision de nuages à grande vitesse ($>$ 10 km s^{-1}) qui pourrait expliquer la formation d'une association d'étoiles OB de plusieurs milliers d'étoiles. Dans ce scénario, les étoiles massives (OB) se formeraient dans les structures denses et massives (hubs et ridges) formées aux convergences dues à la collision à grande vitesse de nuages, et

où la gravité à grande échelle domine la cinématique et l'évolution du gaz dense.

Acknowledgements

All corrections to the main body of the text are done! Time to start writing some of the first, and likely most read, pages of this thesis: the acknowledgements.
I will start with the people central to this thesis. A big thank you to Sylvain for preparing this thesis topic, getting the funding together, inviting me to a memorable interview and placing his trust in me for this project. I am also grateful for his continued involvement, leading to an entertaining three years with long and diverse discussions that even made me forget to eat (which is quite something). Another big thank you to Nicola for showing strong interest in my work from the beginning, inviting me to Cologne, and spending a large amount of time discussing and helping me progress, which resulted in the logical step to officially make her my co-director. I thus had a highly complementary team of supervisors that encouraged me to: always look at the bigger picture, think on future projects, be precise and at the same time keep my attention on the publication of results.
I also want to thank the jury for their interest in the manuscript below, the detailed evaluation and interesting questions and comments. Admittedly, seeing the substantial list of notes from Arnaud for the first time made me lose some of my appetite, but it turned out to be excellent food for thought.

During these three years I also had the privilege to meet many interesting people at some amazing places even though this was somewhat hampered in 2020 due to the corona pandemic.
I would first like to thank Hussein and Guillaume for their patience, explaining again and again the implications of their calculations that now start to produce interesting results. I also want to thank Hussein and Robert for their spontaneous encouraging words these last three years, Rolf and Friedrich for allowing access to several APEX PI instruments, and Seamus for his interesting perspective on the observational results. Then I would like to thank Antoine for his patience to keep answering my relentless questions about shocks and for his detailed comments on my first paper that did not need to be followed by an apology, and Andrew for his interesting ideas to constrain shock excitation. I am also grateful to Doris, first of all, for the successful organisation of the conference in Nagoya which brought me in touch with Kengo Tachihara who gave access to the NANTEN2 data, but also for the interesting discussions on how to exploit the NANTEN2 data set. Timea, thank you for helping me with the first reduction of the APEX observations and of course for the nice exchanges while driving to work.
In Nagoya, I had, among others, the pleasure to meet Slawa. Thank you for the warm welcome in Cologne afterwards and the great collaboration. In Cologne, I also had the pleasure to meet Martin who did meticulous work on the self-absorption modeling for my first paper. Then I want to thank Laure for looking into the spectral shift that affected some of my APEX observations and also for showing me around in Bonn. Carlos, thank you for offering the amazing opportunity to observe with the APEX telescope in Chile and making sure that I have eaten some of the best Belgian fries in the Atacama desert. Also a particular thank you to the APEX team, and of course Mathilda, for the warm welcome at the APEX basecamp, and Andreas for visiting ALMA with me which was truly impressive.
Lastly, I would like the to thank everyone at the LAB for the excellent atmosphere even though I was not always around. A particular shout out to Odile for the administrative work that was invaluable, and Arnaud for organising the Friday soccer matches that I will really miss.

The previous paragraphs should be a relatively fair summary with regard to the people who directly

had a role in the successful completion of this thesis. But there are also quite some people who played a role getting me here and making this thesis a memorable experience.
I would first like to thank Nicolas for offering me a postgraduate internship on star formation when I did not know what to do after finishing my studies. This internship convinced me to pursue a PhD related to star formation, but I also want to thank him for dedicating his time to introduce me to the field and making me aware of this thesis in Bordeaux. Let me rewind still further back: to high school, where likely most of my teacher would never believe their ears that I have written a thesis, and thank a person who unknowingly set me on this track. Therefore I would like to thank Jan for his presentation in sixth grade on special relativity which, because of the clarity, sparked my interest to study Physics and Astronomy. I would also like to thank him for the great years we spent together at the university, as well as my classmates who made the five years of studying Physics and Astronomy truly wonderful. Thank you Chris, Maude and Theo for providing unlimited access to your sofa in Bordeaux. Vincent, Loïs and Niko for welcoming me to Mérignac and of course for making me rediscover Age of Empires II. Jeroen, Alessandro, Elora and Bjorn, among others, to make a great effort trying to convince me that they were actually interested in what I did these last three years... We will see who of you will actually read this thesis. Berthe, Friedl, Bruce and Mia, thank you for the great and many distractions. Oma, opa, n. Monke and t. Mona for the nice moments together and their infinite support during these years. Last but not least of course my parents for their confidence in my decisions and support over these many years, even though they might have found some of my decisions questionable at best.

Then all what is left to me here, is to address you, the reader. I thank you for your interest in this manuscript and hope that you will enjoy reading it.

Résumé substantiel en Français

Les observations de la poussière interstellaire dans l'infrarouge lointain avec le télescope spatial *Herschel* ont démontré que la formation des étoiles dans le milieu interstellaire s'organise dans des structures filamentaires interstellaires (filaments) suffisamment denses et froides pour que la gravité y devienne dominante (voir par exemple André et al. 2014). Pour comprendre l'origine des étoiles et de leurs propriétés, il est donc vital de comprendre les processus physiques responsables de l'émergence de ces filaments denses dans le milieu interstellaire.

Dans ce but, le filament de Musca observable dans l'hémisphère sud apparaît comme le candidat idéal. En effet, c'est une région isolée dans le plan du ciel, ce qui évite la contamination d'autres nuages moléculaires. Musca est aussi un filament dans un stade évolutif peu avancé, reflétant ainsi parfaitement les conditions initiales de la formation d'étoiles, et évitant la présence de nombreuses jeunes étoiles et protoétoiles qui pourraient compliquer certaines interprétations, comme pour la recherche du gaz chauffé par des chocs à basse vitesse qui peuvent avoir une importance dans la formation des filaments. Le filament de Musca semble correspondre à un seul événement simple de formation de gaz dense filamentaire, sans sous-structure spatiale ou cinématique complexe qui pourrait compliquer l'analyse et l'interprétation des observations. Enfin, Musca est le filament pour lequel une étude récente tente de remettre en cause sa nature filamentaire, et selon laquelle Musca serait plutôt une nappe de gaz dense vue de côté. Il est vital de trancher cette dernière question car cela pourrait remettre en cause la nature de tous les filaments vus avec *Herschel* qui formeraient essentiellement toutes les étoiles. Pour étudier l'évolution du nuage moléculaire de Musca, des observations de nombreuses transitions rotationelles millimétriques du CO, ^{12}CO(2-1), ^{13}CO(2-1), C^{18}O(2-1), ^{12}CO(3-2), ^{13}CO(3-2) et ^{12}CO(4-3), ont été obtenues avec le télescope APEX selon deux cartes de quelques arcmin de côté chacune au travers de la crête du filament à deux endroits représentatifs le long du filament. Ces données permettent d'étudier la cinématique du gaz froid et dense en CO(2-1) et isotopologues et de chercher dans le même temps la présence de gaz plus chaud, et possiblement chauffé par des chocs à basse vitesse, grâce à la raie ^{12}CO(4-3) dont l'énergie du niveau haut J = 4 en unité de température est 55 K. Pour mieux contraindre l'excitation de cette dernière raie, des observations complémentaires ont été aussi obtenues dans la raie du carbone atomique [CI] à 491 GHz toujours avec le télescope APEX, et dans la raie du carbone ionisé [CII] à 1.9 THz observée en même temps que la raie de l'oxygène atomique [OI] à 4.7 THz (63 μm) avec SOFIA (l'avion-observatoire stratosphérique pour l'astronomie infrarouge de la NASA). Les observations en [CI] et [CII] permettent de contraindre le niveau local de rayonnement UV qui doit contribuer à chauffer le gaz, alors que la transition [OI] pourrait être préférentiellement excitée dans du gaz choqué. Une détection de [OI] vers Musca pourrait aussi montrer l'existence d'une forte abondance d'oxygène atomique dans le milieu interstellaire. La distribution d'oxygène dans le milieu interstellaire est une question clé, non résolue en astrochimie et physico-chimie des grains interstellaires.

Les raies [CII] et [OI] avec SOFIA vers le filament de Musca n'ont pas été détectées. Grâce à la bonne sensibilité des observations SOFIA, la non-détection de [CII], confirmée par l'émission faible mais bien détectée en [CI] avec APEX, nous a permis d'imposer de fortes contraintes sur le champ de rayonnement UV local (< 1 G$_0$) de Musca et par conséquent sur la température d'excitation maximale du CO (< 25 K) dans le nuage. Par contre, la non-détection de [OI] est apparue moins intéressante en

ne contraignant que très peu l'abondance d'oxygène atomique.

L'analyse des transitions CO et isotopologues indique la présence de trois composants de vitesse. Ces trois composantes de vitesse sont mises en évidence grâce à une discussion, un modèle avec transfert radiatif et l'ajustement des spectres en gaussiennes individuelles. L'inspection de la localisation spatiale des trois composantes montre qu'elles tracent des densités de colonne très différentes, et l'existence démontrée de ces composantes de vitesse indique une cinématique du nuage moléculaire plus complexe qu'anticipée.
Pour approcher et répondre à la question de la nature de Musca (un filament ou une feuille vue de côté), le code de transfer radiatif RADEX est utilisé pour montrer que le rapport d'intensité ^{13}CO(3-2)/^{13}CO(2-1) est un bon traceur de la densité quand on impose des températures cinétiques égales aux températures de poussières obtenues avec Herschel. Cette analyse de ^{13}CO(3-2)/^{13}CO(2-1) pointe vers une densité $n_{H_2} = 10^4$ cm^{-3} pour la crête du filament. Dans les alentours de la crête (r $\sim$ 0.2 pc) ce rapport des raies ^{13}CO indique des densités encore élevées, autour de $n_{H_2} = 2{\times}10^3$ cm^{-3}. Ces densités combinées avec les densités de colonne contraintes par *Herschel* permettent d'estimer la taille typique du gaz observé sur la ligne de visée. Cette estimation donne une taille typique pour la crête sur la ligne de visée de seulement $\sim$ 0.1 pc, identique à la taille mesurée en projection sur le ciel par un ajustement d'un profile Plummer sur la densité de colonne d'*Herschel*. Cette correspondance entre la taille dans le plan du ciel et la ligne de visée indique clairement que le filament de Musca est bien une vraie structure cylindrique, i.e. filamentaire.

Une des trois composantes de vitesse n'est vue qu'en ^{12}CO et permet de contraindre le gaz à faible densité de colonne. Cette composante est forte en ^{12}CO(4-3). Pour mieux comprendre l'origine de cette forte émission en ^{12}CO(4-3), les rapports ^{12}CO(4-3)/^{12}CO(3-2) et ^{12}CO(4-3)/^{12}CO(2-1) de cette composante sont étudiés avec des modèles de PDR (régions de photodissociation) et avec l'outil de transfer radiatif et d'excitation non-ETL RADEX. Cette analyse démontre que ces modèles ne peuvent pas expliquer l'intensité de ^{12}CO(4-3) par un seul chauffage par le rayonnement local UV. Une analyse directe d'excitation avec RADEX démontre que la raie ^{12}CO(4-3) est excitée dans une région à relativement haute température ($>$ 50 K) et de densité intermédiaire, $n_{H_2} \gtrsim 3{\times}10^3$ cm^{-3}, proche des densités des couches de gaz autour de la crête du filament. Ces caractéristiques sont attendues pour du gaz excité par un choc à basse vitesse. Une première comparaison avec des modèles de chocs démontre que la raie ^{12}CO(4-3) peut être excitée par un choc-J non-irradié avec une vitesse inférieure à 4 km s^{-1}. Une comparaison avec des observations synthétiques de simulations numériques montre que le spectre en ^{12}CO(4-3) ressemble fortement à la signature d'un choc d'accrétion sur le filament. Cela suggère que le ^{12}CO(4-3) observé trace l'accrétion d'un flux de matière convergent sur le filament par un choc, et que le gaz dense dans le filament de Musca se forme grâce à ce/ces chocs qui dissiperaient au moins une partie de l'énergie cinématique et/ou gravitationnelle.

La détection du choc d'accrétion autour du filament de Musca indique un scénario d'accrétion pour l'évolution du filament de Musca. Pour mieux comprendre la formation du filament, il est donc nécessaire d'aussi analyser la cinématique du filament et du nuage moléculaire autour du filament de Musca, et en particulier avec les isotopologues de CO qui démontrent l'existence de ces trois com-

posantes de vitesse dans le nuage. $C^{18}O$(2-1) est seulement détectée vers la crête du filament et montre une seule composante de vitesse. L'ajustement de cette raie dans les deux cartes montre des gradients de vitesse organisés perpendiculairement à la crête du filament. En plus les gradients sont dans des directions opposées entre les deux cartes suggérant que ces gradients ne sont pas le résultat d'une simple rotation du filament. L'analyse de ^{13}CO(2-1) démontre la présence d'une deuxième composante de vitesse qui trace les alentours directs de la crête. Dans les deux cartes, cette deuxième composante est décalée vers le bleu par rapport à la composante de la crête en $C^{18}O$. Cette deuxième composante est observée à l'est de la crête dans la première carte et à l'ouest de la crête dans la deuxième carte. La localisation de ces deuxièmes composantes dans chaque carte, décalées vers le bleu, semblent être directement reliée aux vitesses "bleues" des gradients de vitesse de la crête vu en $C^{18}O$. Cela suggère fortement que ces gradients de vitesse sont une signature d'accrétion des alentours directs sur la crête en déposant du moment angulaire dans les régions les plus denses. La troisième composante de vitesse est uniquement observé en ^{12}CO et correspond au gaz chaud chauffé par chocs. Dans les deux cartes, cette composante est décalée vers le bleu par rapport à l'émission tracée avec ^{13}CO et en $C^{18}O$. Cette observation indique que le gaz qui est le plus dense dans le nuage moléculaire/filament de Musca est systématiquement décalé vers le rouge. Pour vérifier cette asymétrie cinématique de Musca, une carte complète de la région de Musca en ^{12}CO(1-0) est analysée. Cette carte a été obtenue avec le télescope NANTEN2 (données d'archive obtenues auprès de l'équipe NANTEN à Nagoya, Japon) et démontre clairement pour tout le nuage que le gaz moléculaire plus diffus est aussi décalé vers le bleu par rapport à la crête du filament. Un diagramme position-vitesse (PV) perpendiculaire à la crête, moyen le long du filament, montre de plus une forme en V avec la vitesse de la crête à l'apex (vers le rouge) du V. Cette forme du diagramme PV suggère que l'accrétion est le résultat de la dynamique à grande échelle du nuage moléculaire qui est de façon surprenante asymétrique. Comme en plus aux alentours du filament, le gaz accrétant bleu est principalement localisé à l'est de la crête, l'asymétrie n'est pas que cinématique, elle est aussi spatiale en projection sur le ciel, donc nécessairement en 3D aussi.

Cette asymétrie est intrigante, et pousse à mieux comprendre la cinématique à grandes échelles. Pour cela, les observations CO de NANTEN2 ont été combinées avec les données du relevé GASS en HI dans l'hémisphère sud. La comparaison de l'émission HI avec l'émission des poussières observées avec Planck confime que Musca fait partie du complexe cohérent Chamaeleon-Musca avec une taille globale de l'ordre de 50 pc. La comparaison de l'émission HI avec le CO dans la région large autour de Musca montre que l'émission CO de façon globale est décalée vers le rouge par rapport au HI moyen comme si tout le réservoir local possible de gaz (HI et CO à basse densité) est bleu vers Musca. Il y aurait donc une asymétrie cinématique depuis le nuage HI (grandes échelles, basse densité) jusqu'à la crête de Musca (petites échelles, haute densité). Une comparaison identique du HI avec le CO vers les autres nuages moléculaires du complexe Chamaeleon-Musca indique de plus que cette asymétrie s'applique à l'ensemble de ces nuages comme si l'asymétrie cinématique est globale depuis les 50 pc du complexe jusqu'au gaz dense aux échelles typiques de 0.1 pc qui forme les étoiles. Les observations HI montrent aussi des indications de plusieurs composantes de vitesse qui pourraient interagir.
Un scénario qui arrive à expliquer naturellement cette asymétrie des grandes échelles jusqu'à la crête de Musca est une collision de nuages HI. Les simulations numériques du groupe de Nagoya (Inoue, Inutsuka et Fukui) ont permis à Inoue et coll. de proposer que la collision de nuages magnétisés avec des

sous-structures pré-existantes mène à la formation de filaments perpendiculaires au champ magnétique comme c'est systématiquement le cas. Lors de la collision, le champ magnétique est courbé autour des sur-densités pré-existantes et cette courbure guide, amplifie des flots de matière convergents qui concentrent efficacement les sur-densités en un filament dense. L'asymétrie émerge naturellement de la courbure du champ magnétique par l'onde de choc de la collision. Ces simulations numériques prédisent que cette accrétion/concentration par la courbure du champ magnétique entraine une forme V des diagrammes PV perpendiculaires au filament comme nous l'observons.

Pour aller au delà de Musca qui ne peut former que quelques étoiles de faible masse, et comprendre la formation du gaz dense qui pourrait former des centaines d'étoiles en amas et des étoiles massives, le ridge extrêment dense et massif de DR21 a été étudié grâce à des observations d'une variété de molécules obtenues avec le télescope 30m de l'IRAM. Le ridge de DR21 est une structure allongée, filamentaire très dense qui est de plus connecté à un réseau de filaments moins massifs qui semblent converger vers la structure centrale du ridge, située dans le nuage moléculaire géant du Cygne. Ce ridge contient plusieurs coeurs massifs (> 100 $M_\odot$) qui forment des étoiles massives. Comprendre la formation et lévolution de ce ridge est donc important pour comprendre dans quelles circonstances les étoiles massives peuvent se former. Les observations obtenues avec le télescope de 30m couvrent entre autres les raies ^{13}CO(1-0), C^{18}O(1-0), N_2H^+(2-1), HCO^+(1-0) et $H^{13}CO^+$(1-0). Ces raies tracent des régimes de densité différents dans les nuages moléculaires. L'ajustement d'un profil gaussien à ces spectres montre des gradients alternants dans le ridge qui étaient déjà observés dans l'étude de Schneider et al. (2010) et similaires à ceux vus dans Musca. Les raies qui tracent les filaments moins massifs autour du ridge montrent que tous ces filaments sont décalés vers le rouge par rapport au ridge. De nouveau il y a une asymétrie cinématique qui apparaît, similaire à Musca. En plus, le diagramme PV perpendiculaire au ridge montre aussi une forme V avec la vitesse du ridge à l'apex du V. Ces observations de DR21 pointent vers un scénario similaire à celui pour Musca. Par contre quand une analyse du viriel du nuage DR21 est menée, il devient clair que le potentiel gravitationnel domine actuellement l'effet potentiel de courbure du champ magnétique proposé pour Musca. La gravité serait actuellement responsable de l'accrétion de matière sur le ridge, mais la gravité n'arrive pas à expliquer l'asymétrie cinématique. L'analyse des spectres CO montre qu'en effet il y a deux composantes de vitesse vers le ridge DR21. Une inspection détaillée des spectres moyens et des diagrammes PVs des deux composantes de vitesse, montre que ces deux composantes sont connectées par des ponts de gaz CO. Ces ponts sont attendus en cas de collision de nuages déjà structurés et probablement au moins en partie déjà moléculaires. Ces observations indiquent qu'une collision de nuages est responsable de la formation du ridge et que la cinématique asymétrique des filaments autour du ridge est soit due à la courbure du champ magnétique qui initie ou a initié l'accrétion sur le ridge, ou soit à l'asymétrie des ponts de gaz due à la direction privilégiée entre les deux nuages déjà structurés en collision. Combinés ces résultats montrent que le ridge DR21 a été formé par une compression à grande échelle comme pour Musca. Par contre, la compression du nuage DR21 était beaucoup plus forte, du fait d'une collision de nuages plus denses et à une vitesse plus élevée, entrainant que la gravité soit devenue dominante dans le nuage DR21 et menant à une accrétion sur le ridge par la gravité plus que par le champ magnétique.

Avec l'information de vitesse et le nombre de filaments, il est possible de calculer le taux d'accrétion

sur le ridge de DR21. Cet calcul montre que l'accrétion par les filaments est insuffisante pour maintenir la présence du ridge. Il faut considérer une accrétion supplémentaire plus isotrope de gaz plus diffus pour maintenir la présence du ridge. Dès que les étoiles massives commencent à se former, leur effet en retour énergétique pourra arrêter l'accrétion de ce gaz diffus entrainant la disparition du ridge. Comme la masse du ridge est certainement critique pour maintenir l'accrétion globale et donc la formation d'étoiles massives, ces calculs pourraient indiquer que la formation d'étoiles massives n'est active que pendant une durée limitée dans l'évolution de la région globale de DR21. Ces observations suggèrent fortement que la gravité à grandes échelles joue un rôle important dans la formation des étoiles massives après la compression de la collision de nuages.
Les observations avec le télescope 30m montrent aussi la présence de SiO(2-1) partout le long du ridge avec une largeur de raie similaire à $H^{13}CO^+$(1-0). La présence de SiO dans la phase gazeuse est généralement un traceur de chocs à grande vitesse (> 10 km s^{-1}). Cette observation de SiO(2-1) dans le ridge pourrait ainsi être la conséquence de la collision des nuages.

Les deux composantes de vitesses vers DR21, responsables de la compression du nuage moléculaire, sont présentes sur toute la région nord du Cygne. Des observations de la raie ^{12}CO(3-2) avec le télescope JCMT vers toute cette région du Cygne, montrent à l'aide de spectres moyens et de diagrammes PV qu'il y a des ponts entre les deux composantes de vitesse sur toute la région. Cela indique que la formation d'étoiles massives qui est repartie sur toute la région est le résultat d'une collision de deux nuages moléculaires géants (GMCs) au delà de la région la plus active actuellement de DR21. Avec les données *Herschel*, la masse totale de gaz dense dans la région nord du Cygne est calculée. Cela permet d'estimer la masse stellaire totale que la région pourrait former durant les prochains quelques Myr: $\sim 1.5\times10^4$ $M_\odot$. Cette masse stellaire est très similaire à la masse de Cygne OB2, l'association d'étoiles OB bien étudiée, située au centre du complexe du Cygne, et indique que dans la région nord du Cygne on observe actuellement la formation d'une nouvelle association d'étoiles OB du fait de la collision de deux GMCs qui a certainement aussi formé Cygnus OB2 dans le passé (il y a 3 à 5 millions d'années). L'analyse des observations *Herschel* et JCMT démontre aussi que cette collision résulte dans la formation de sous-structures avec des tailles de 0.5 à 3 pc, comme pour DR21, et qui forment des étoiles massives. Les étoiles OB qui seront formées montreront donc des sous-structures spatiales et cinématiques de tailles similaires. Des observations récentes ont montré de la sous-structure cinématique et spatiale dans des associations d'étoiles OB avec une taille souvent autour de 0.5 pc. Cette similarité pourrait indiquer que toutes les associations d'étoiles OB sont formées par des collisions de GMCs (si on peut établir le lien entre la taille des sous-structures et la collision de GMCs). Enfin, une collision de GMCs à grande vitesse explique facilement pourquoi les observations indiquent que les associations d'étoiles OB ne sont pas liées et se dispersent dès que le gaz est dispersé par les effets de rétroaction de ces étoiles.

Dans la dernière partie de la thèse, les coeurs denses massifs qui forment des étoiles massives dans le Cygne sont analysés avec des observations, faites avec le télescope FCRAO et le GBT, dans les raies $C^{18}O$(1-0), CS(2-1), N_2H^+(2-1) et NH_3(1,1). Ces observations montrent que l'intérieur des coeurs, tracé avec N_2H^+ et NH_3, a une largeur de raie plus faible que l'extérieur du coeur tracé avec $C^{18}O$(1-0) et CS(2-1). Une analyse de la stabilité gravitationnelle montre que la masse des coeurs est largement supérieure à leur masse de Bonnor-Ebert suggérant un effondrement gravitationnel systématique de

ces coeurs. Ce résultat est aussi en accord avec les observations interférométriques qui montrent une certaine fragmentation à l'intérieur des coeurs massifs mais qui reste limitée.

Pour résumer, le filament de Musca accrète de la matière en continu venant d'un flux de matière convergent avec des chocs d'accrétion qui aident à dissiper l'énergie cinétique et forme ainsi le gaz dense du filament. Les observations à grandes échelles montrent que les collisions de nuages peuvent former des filaments qui sont eux même le lieu de formation des étoiles de haute et de faible masse. Pour les étoiles de faible masse, l'accrétion sur le filament est dominée par la courbure du champ magnétique du fait de la collision. Dans les régions de formation d'étoiles massives la densité après la compression est tellement forte que l'accrétion est dominée par la gravité locale du gaz dense. Une discussion a aussi été menée sur la question de savoir si les conditions observées de formation des structures denses permettent de proposer, favoriser un scénario de formation des étoiles massives où l'accrétion continue de matière permettrait de dépasser les masses typiques de l'instabilité gravitationnelle de Jeans ou de Bonnor-Ebert.

Contents

Chapter 1

Introduction

The formation of stars and their feedback are intimately linked with the dynamical and chemical evolution of the interstellar medium (ISM) of galaxies. On large scales, stars and star formation play an essential role in driving and probing galaxy evolution across cosmic time. On small scales star formation sets the initial conditions for the formation of planetary systems. Understanding the star formation process and the interplay with the ISM is thus a cornerstone of modern astrophysics (McKee & Ostriker, 2007).

1.1 The universal star formation outcome in galaxies

It is well established by now that stars form in the cold ($\sim$ 10 K) and dense ($n_{H_2} > 10^4$ cm^{-3}) gas of the interstellar medium, through the gravitational collapse of individual cores (Bergin & Tafalla, 2007). For this dense gas, a universally observed star formation outcome is found from individual star forming clouds to galactic scales over cosmic time. The universal star formation laws generally refer to the initial mass function (IMF; Salpeter, 1955; Kroupa, 2001; Chabrier, 2003), the correlation of the star formation rate (SFR) with the total (dense) gas mass (Schmidt, 1959; Kennicutt, 1998; Gao & Solomon, 2004b,a; Lada, Lombardi & Alves, 2010; Kennicutt & Evans, 2012; Shimajiri et al., 2017) and the fact that stars tend to form in clusters (Lada & Lada, 2003; Krumholz, McKee & Bland -Hawthorn, 2019).
The universal correlation between the star formation rate and the dense gas mass indicates that a given amount of (dense) gas in a star forming galaxy or cloud will always result in roughly the same amount of stellar mass formed per unit time. The universal IMF, which resembles the core mass function in the ISM (Motte, Andre & Neri, 1998), implies that the stellar content of newly born clusters of stars has a universal mass distribution. This universal outcome of star formation suggests that star formation in galaxies is regulated by the same physics, which implies that understanding the physics of dense gas formation in our own galaxy will allow to understand and trace star formation in galaxies over most of cosmic time.
While the fragmentation into cores that can form low-mass stars is reasonably well explained by the Jeans criterion for gravitational instability (Jeans, 1902), understanding the formation of cores that can form massive stars is particularly challenging for this theory. This seems to imply that the formation

of the massive stars is closely tied to the dynamic evolution of the ISM (Zinnecker & Yorke, 2007).
Understanding the physics of star formation in present-day galaxies over the full stellar mass range, in particular the formation of high-mass stars, is also of importance as a step to understand more extreme events such as the formation of the first stars in the primordial gas of the universe. This is, in particular, because the understanding of star formation in the local universe can serve as a reference to understand how the first stars formed, and how their formation affected the early evolution of the ISM (Bromm & Larson, 2004). In contrast to present-day star formation, the first star formation episode in the universe predominantly formed high-mass stars. Furthermore, it is expected that these first stars could have reached higher masses than the stars that are formed in the present-day galaxy.

Over the years, there has been a significant evolution in our understanding of how the evolution of the ISM leads to the presence of dense star forming gas. In the 70's, 80's and 90's the ISM was generally described by a quasi-static evolution of interstellar clouds which slowly condense in star forming cores where stars form by a gravitational collapse (Mouschovias, 1976; Shu, Adams & Lizano, 1987). However, the observed large velocity differences in molecular clouds posed significant problems for this quasi-static view (Elmegreen, 2000), which led to a more dynamic view where dense, gravitationally unstable, cores and filaments form as a result of turbulent motions in molecular clouds which can be driven by supernovae (Mac Low & Klessen, 2004). In this more dynamic view, it was also found that large scale colliding flows of diffuse gas could form dense filamentary clouds with large velocity dispersions (Koyama & Inutsuka, 2000; Audit & Hennebelle, 2005). In this emerging dynamic view of the ISM, it was proposed that a gravitational instability at the scale of molecular clouds, instead of individual cores, could be essential to form the stars at the high-mass end of the IMF as a result of strong mass provision (Motte, Bontemps & Louvet, 2018).
Recently, it has been observed with the *Herschel* Space Telescope that the dense star forming gas is quite universally located in filamentary structures (André et al., 2014; Schisano et al., 2014). In order to understand how dense gas is generally formed in the ISM, observational studies thus have to put a significant focus on understanding the mechanism that leads to this dense filamentary gas.

1.2 Objectives

The goal of this thesis is to progress in our understanding, summarised in Chapter 3, of the physical processes responsible for dense gas formation from low- to high-mass star forming regions. Once these main physical mechanisms are identified, the aim is to better constrain the initial conditions of star and cluster formation to provide a perspective on the origin of the universal star formation laws, the highest mass stars and rich cluster formation.
To work towards these ambitious goal, the immediate objectives are:
• To understand the formation of typical low-mass filaments such as Musca using extensive molecular line observations (Chapter 4).
• To investigate the kinematics and equilibrium of the most active young region of high-mass star formation within 1.5 kpc, i.e. the DR21 ridge in Cygnus-X (Chapter 5).
• To compare these two extreme regions to obtain a global picture of the dense gas formation process.
• To discuss the consequences of dense gas formation on the initial conditions of low- and high-mass

star formation, with a particular emphasis on the massive dense cores in Cygnus-X (Chapter 6).

Chapter 2

Introduction (en français)

La formation des étoiles et leurs effets de rétroaction sont intimement liés à la dynamique et à l'évolution physico-chimique du milieu interstellaire (MIS) des galaxies. Aux grandes échelles, la formation des étoiles est un processus central et fondamental pour l'évolution des galaxies au cours des temps cosmologiques depuis la formation des premières étoiles il y a 13 milliards d'années. Aux petites échelles, c'est la formation des étoiles qui nous informe sur les conditions initiales de la formation des systèmes planétaires. Comprendre les processus qui gouvernent la formation des étoiles en lien avec le milieu interstellaire reste ainsi un challenge de première importance pour l'astrophysique actuelle (McKee & Ostriker, 2007).

2.1 Les lois universelles de la formation des étoiles dans les galaxies

Les étoiles se forment dans le gaz froid (10 K) et moléculaire par effondrement gravitationnel des coeurs les plus denses ($n_{H2} > 10^4\,cm^{-3}$) du MIS (Bergin & Tafalla, 2007). Le processus de formation de ces coeurs denses et de leurs effondrement montre une grande universalité au cours des temps cosmologiques avec une universalité forte de la fonction de masse initiale des étoiles (IMF; Salpeter, 1955; Kroupa, 2001; Chabrier, 2003), une corrélation serrée entre le taux de formation stellaire (SFR) et la masse totale de gaz (dense) présente (Schmidt, 1959; Kennicutt, 1998; Gao & Solomon, 2004b,a; Lada, Lombardi & Alves, 2010; Kennicutt & Evans, 2012; Shimajiri et al., 2017), et un fait établi que la plupart des étoiles se forme en amas (Lada & Lada, 2003; Krumholz, McKee & Bland -Hawthorn, 2019).

L'universalité du SFR (taux de formation d'étoiles) indique que pour une certaine masse de gaz (dense) dans une galaxie ou un complexe interstellaire on obtient toujours la même masse d'étoiles formées. L'universalité de l'IMF (fonction de masse des étoiles) dont la forme se retrouve dans la fonction de masse des coeurs denses (CMF; Motte, Andre & Neri, 1998) indique que la fraction d'étoiles de différentes masses reste toujours identique montrant que dès que du gaz (dense) est présent dans une galaxie, on peut prédire quelles étoiles vont se former, et en quelle quantité. Cette universalité est une indication extrêmement forte que la formation des étoiles des galaxies est régulée par la même physique depuis les premières étoiles, impliquant que la compréhension de cette physique dans le voisinage solaire de notre galaxie doit permettre de maitriser une grande partie de l'évolution des galaxies sur les

temps cosmologiques. Alors que la fragmentation du MIS en coeurs denses de masses typiques des étoiles (entre 0.1 et 1 Msun) est raisonnablement expliquable par l'instabilité de Jeans (Jeans, 1902), la compréhension de la formation de coeurs qui pourraient former des étoiles 10 à 100 fois plus massives que le Soleil reste un challenge pour les théories de formation stellaire. Il semble que la seule direction possible pour comprendre cette direction soit la maitrise des effets de la forte dynamique du MIS (Zinnecker & Yorke, 2007).

Comprendre la physique de la formation des étoiles dans les galaxies proches actuelles sur l'ensemble de la gamme des masses stellaires, et plus particulièrement des étoiles les plus massives, est aussi une étape essentielle et critique pour comprendre les cas de formation stellaire les plus extrêmes qu'a connu l'Univers comme la formation des premières étoiles et des trous noirs primordiaux qui n'ont pas suivi les lois universelles discutées ci-dessus. La compréhension profonde de la formation stellaire locale doit nous servir de référence pour comprendre la formation des premières étoiles et leur effet sur l'évolution précoce du MIS des galaxies (Bromm & Larson, 2004). Au contraire de la formation stellaire actuelle, les épisodes de formation des premières étoiles ont principalement formé des étoiles de très grandes masses, au delà des masses stellaires possibles actuellement.

Durant les dernières années, des progrès importants ont été obtenus sur notre compréhension de l'émergence des coeurs denses qui forment les étoiles dans le MIS. Au cours des années 70, 80 et 90 le MIS était vu comme un milieu en quasi équilibre où des coeurs pouvaient se concentrer progressivement jusqu'à l'instabilité gravitationnelle, notamment par une diffusion progressive du champ magnétique par diffusion ambipolaire (Mouschovias, 1976; Shu, Adams & Lizano, 1987). Les vitesses typiques du gaz montraient néanmoins des temps dynamiques courts non compatibles avec l'évolution quasi-statique (Elmegreen, 2000). Cela a amené à considérer des scénarii plus dynamiques basés sur l'importance de la turbulence comme moteur dominant en plus de la gravité pour la formation des structures denses, la turbulence étant souvent proposée comme étant due aux explosions de SNs (Mac Low & Klessen, 2004). Dans cette vue plus dynamique, les simulations numériques ont commencé à montrer que la collision de gaz diffus pourrait expliquer la formation des structures denses et aussi le niveau de turbulence observé dans le MIS (Koyama & Inutsuka, 2000; Audit & Hennebelle, 2005). Dans le même temps, il est aussi apparu que si le MIS moléculaire était globalement instable gravitationnellement, les dispersions de vitesses et lois de Larson seraient expliquées naturellement (Vázquez-Semadeni et al., 2019). Dans cette vue dynamique prédominante du MIS, il a aussi été proposé que les effondrements dits globaux au delà des coeurs denses individuels pourraient être un ingrédient essentiel pour former les amas d'étoiles et les étoiles les plus massives (Motte, Bontemps & Louvet, 2018).
Enfin, le satellite *Herschel* a clairement établi que l'une des étapes fondamentales pour former des étoiles est la formation de structures filamentaires, de filaments (André et al., 2014; Schisano et al., 2014). Pour comprendre comment le gaz dense qui forme les étoiles se condense et se forme, il apparaît vital de se focaliser sur la compréhension du processus qui mène à ces structures filamentaires dans le MIS.

2.2 Objectifs

Le but de la thèse est de progresser dans notre compréhension, résumée dans le Chapitre 3, des processus qui sont responsables de la formation du gaz dense des régions qui forment des étoiles de faible masse ainsi que des régions qui forment aussi des étoiles massives. Dès que ces mécanismes seront identifiés, le but sera de mieux contraindre les conditions initiales de la formation des étoiles et des amas d'étoiles pour maitriser entièrement l'origine des lois universelles de la formation d'étoiles, et l'origine des étoiles les plus massives et des amas stellaires riches.
Pour avancer dans cette direction ambitieuse, les objectifs immédiats de la thèse sont:
• Comprendre la formation d'un filament typique de faible masse tel que Musca grâce à de nouvelles observations moléculaires (Chapitre 4).
• Étudier la cinématique et l'équilibre de la région de formation stellaire massive la plus active à moins de 1.5 kpc, i.e. le ridge de DR21 dans le Cygne (Chapitre 5).
• Comparer ces deux régions (Musca et DR21) pour obtenir une vue globale de la formation de gaz dense dans le MIS de la Galaxie proche.
• Discuter les conséquences de notre nouvelle compréhension de la formation de gaz dense sur les conditions initiales de la formation stellaire de faible et haute masse, avec une attention particulière à la population de coeurs denses massifs du Cygne (Chapitre 6).

Chapter 3

Star formation and the evolution of the interstellar medium

3.1 The Milky Way

3.1.1 Star formation in the Milky Way

To understand the physics of star formation in interstellar clouds, studies almost exclusively focus on the Milky Way which is the host galaxy of the solar system. An artist impression of the Milky Way seen face-on is presented in Fig. 3.1. The Milky Way has a disk structure, seen as a band of extinction in the plane of the sky at optical and infrared wavelengths because of interstellar dust, and it is basically the only location where star formation, which occurs in molecular clouds, can be spatially resolved. Extensive work has been done to classify galaxy types in the nearby universe, e.g. with the Hubble classification diagram, and to explain how this classification is related to the evolution and history of these galaxies. Based on a first-order geometrical classification, not taking into account dwarf galaxies and special galaxy types, galaxies can be divided in elliptical galaxies and disk galaxies which entails the Milky Way. In contrast to elliptical galaxies, disk galaxies are in general still actively forming stars.

Molecular clouds are the relatively dense ($n_{H_2} \gtrsim 10^2$ cm^{-3}) and cold (10-20 K) regions of the ISM (Bergin & Tafalla, 2007). In these denser regions of the ISM, chemical reactions and shielding from ionising radiation can start the formation of molecules such as carbon monoxide (CO). Molecular hydrogen (H_2) is the most abundant molecule in these molecular clouds, and can form already in quite diffuse gas. The fact that the Milky Way is a disk, seen edge-on, complicates observations of molecular clouds as there can be multiple star forming regions at different distances in the line of sight. Furthermore, the velocity information from the cloud does not always allow to unambiguously determine the cloud distance based on the galaxy rotation profile.
Resolving star formation inside molecular clouds with current observational facilities generally requires studying regions within a distance < 10 kpc ($\sim 3.3{\cdot}10^4$ light year) which is only possible inside the Milky Way. However, it is also attempted now with the unprecedented resolution of the Atacama Large Millimeter Array (ALMA) to study star formation in molecular clouds in the Large Magelanic Cloud

(LMC) with a spatial resolution of ~ 0.1 pc (Fukui et al., 2019b). The LMC is located at a distance of ~ 50 kpc (Schaefer, 2008), and it is seen face-on (Balbinot et al., 2015) such that it generally avoids contamination from other star forming regions along the line of sight.

The Milky Way contains a large number of star forming molecular clouds distributed across the galactic plane. There are several ways to observe the presence of these star forming molecular clouds and characterise them. They can be observed as regions of strong extinction against the near- and mid-infrared background of the galactic plane, the so-called infrared dark clouds (IRDCs) (Perault et al., 1996; Egan et al., 1998; Hennebelle et al., 2001; Simon et al., 2006a; Peretto & Fuller, 2009; Ragan, Bergin & Gutermuth, 2009). This extinction is the result of the absorption of cold dust grains in the molecular clouds. The absorbing dust grains then re-emit the absorbed energy in the far-infrared and millimeter wavelength range. Observations of these IRDCs at far-infrared and millimeter wavelengths indeed find corresponding emission (Teyssier, Hennebelle & Pérault, 2002; Rathborne, Jackson & Simon, 2006; Peretto et al., 2016). Large scale surveys in the far-infrared and millimeter range of the galactic plane with the APEX and *Herschel* Space Telescope have further demonstrated the presence of a rich distribution of star forming clouds (Schuller et al., 2009; Molinari et al., 2010; Marsh et al., 2017). The presence of cold molecular gas distributed over the full galactic plane was also observed with surveys of typical molecular lines such as CO and NH_3, and it is found that the peak emission of these molecular lines are associated with the strong dust extinction regions (e.g. Burton et al., 1975; Scoville & Solomon, 1975; Dame, Hartmann & Thaddeus, 2001; Jackson et al., 2006; Simon et al., 2006b; Pillai et al., 2006; Ragan et al., 2006; Ragan, Bergin & Wilner, 2011; Rigby et al., 2016; Schuller et al., 2017). As already noted, molecular hydrogen is the most abundant molecule in molecular clouds, but it can not be used as a direct tracer of molecular clouds because it is a symmetric molecule with no permanent dipole moment, and therefore no transition that can be excited at the low temperature of star forming molecular clouds.

3.1.2 The interstellar medium in the Milky Way

The gas and dust that constitute galaxies is referred to as the interstellar medium. As already mentioned, a part of this ISM is found in the form of molecular clouds. However, these dense star forming molecular clouds only constitute a small fraction of the ISM which is inherently complex. The Milky Way and most disk galaxies have overdense spiral regions, which are shown in Fig. 3.1 for the Milky Way, where most star forming clouds are located (e.g. Reid et al., 2009, 2014, 2019; Pineda et al., 2013; Schuller et al., 2017). The large scale galactic motions of the spiral arms could significantly affect the star formation process (e.g. Dobbs & Bonnell, 2006; Bonnell, Dobbs & Smith, 2013; Duarte-Cabral & Dobbs, 2017; Smith et al., 2020). In combination with energy injection by supernovae of massive stars this plays an essential role in regulating the evolution of the ISM (e.g. Cox & Smith, 1974; McKee & Ostriker, 1977; Mac Low & Klessen, 2004; Kim & Ostriker, 2015; Walch et al., 2015).
The ISM consists of multiple phases. There is the ionised interstellar medium which is the result of heating by ionising radiation from massive stars, stellar winds and supernovae. It is generally defined as the part of the ISM where hydrogen is ionised, which requires an excitation energy above 13.6 eV. The ionised regions generally have temperatures $> 10^5$ K and hydrogen densities $n_H < 1$ cm^{-3}. These

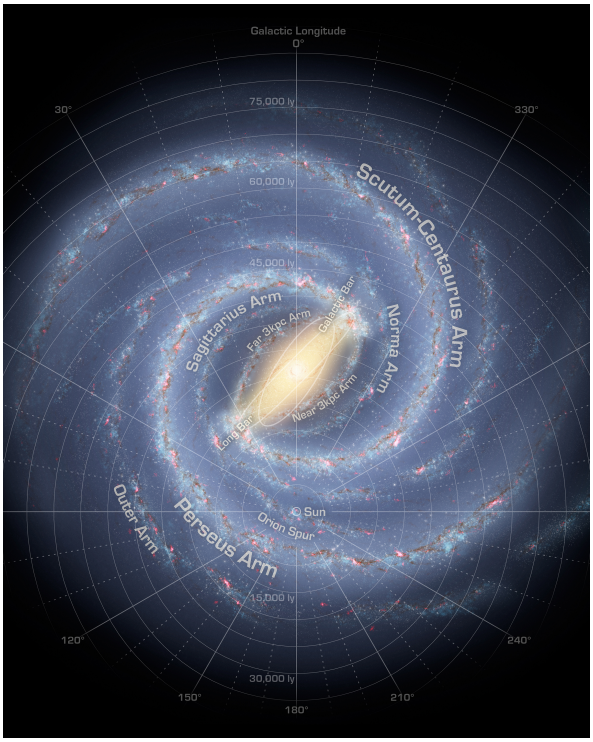

Figure 3.1: An artist impression of the Milky Way, seen face-on, with the currently identified spiral arms in studies of the Milky Way. It also indicates the expected location of the sun in our galaxy. This figure was adapted from NASA/JPL-Caltech/R. Hurt (SSC/Caltech).

regions give rise to continuum emission as a result of free-free interactions between charged particles such as electrons and protons, and synchrotron emission. This continuum emission can be easily observed at radio wavelengths. It is also possible to trace the kinematics of these ionised gas regions with e.g. hydrogen recombination lines, ionised oxygen lines and ionised nitrogen lines.
Regions that are sufficiently shielded from radiation above 13.6 eV form atomic hydrogen. These regions are referred to as the neutral medium which is turbulent (e.g. Mac Low & Klessen, 2004; Elmegreen & Scalo, 2004; Hennebelle & Falgarone, 2012). Observations and the calculation of heating and cooling functions for the neutral clouds indicate that the neutral medium is thermally bistable with the stability points found around a temperature of $\sim$ 100 K and $\sim$ 8000 K (Field, Goldsmith & Habing, 1969; Low et al., 1984; Kulkarni & Heiles, 1987; Boulanger & Perault, 1988; Wolfire et al., 1995, 2003). In these calculations, both heating by high-energy cosmic rays and ultraviolet radiation (UV) are taken into account. The gas at $\sim$ 8000 K is diffuse ($n_H \sim 1$ cm^{-3}) and referred to as the warm neutral medium (WNM), while the medium at T $<$ 200 K, which is mostly two orders of magnitude denser ($n_H \gtrsim 10^2$ cm^{-3}), is referred to as the cold neutral medium (CNM). This CNM is highly supersonic (e.g. Zuckerman & Evans, 1974; Elmegreen & Scalo, 2004). In addition, the entire interstellar medium is pervaded by a magnetic field (e.g. Ferrière, 2001; Stahler & Palla, 2005; Crutcher, 2012; Hennebelle & Inutsuka, 2019) and high-energy cosmic rays (e.g. Strong, Moskalenko & Ptuskin, 2007; Grenier, Black & Strong, 2015). Both the magnetic field and cosmic rays play a non-negligible role in the evolution of the ISM at the large scales (interstellar clouds) and small scales (individual star forming cores).

3.2 Star formation in individual molecular clouds

3.2.1 The Gould Belt

Most molecular clouds are located close to the galactic plane between a galactic latitude of -1° and 1°, but there is also a prominent region called the Gould Belt which contains extended extinction structures such as Taurus, Ophiuchus, Perseus, Orion,... (Barnard, 1919). In later work it was shown that these regions of extinction in the Gould Belt are associated with star formation (e.g. Bok, 1948). It is now known that these regions are associated with the most nearby star forming molecular clouds and that they have a distance smaller than 500 pc from the sun (e.g. Vergely et al., 2010; Lallement et al., 2014; Schlafly et al., 2014; Zucker et al., 2019). The Gould Belt is a region in the sky with an arc-like structure of stars containing many OB stars, which are the hot massive stars in the Milky Way with high surface temperatures $> 10^4$ K (Vacca, Garmany & Shull, 1996; Fitzpatrick & Massa, 2005; Pecaut & Mamajek, 2013). However, analysis of the data from the GAIA survey (Gaia Collaboration et al., 2016, 2018) recently unveiled the 3D structure of the nearby Milky Way. From this, it was found that the nearby clouds are distributed over a kpc wave-like structure, which puts into question the ring structure often associated with the Gould-Belt (Alves et al., 2020).

The Gould Belt clouds were covered in a large variety of millimeter continuum observations and molecular line observations. They were also extensively covered with the *Herschel* Gould Belt survey[1] (HGBS), which is a dedicted far-infrared dust continuum survey program at wavelengths between 70 μm and 500

[1] http://www.herschel.fr/cea/gouldbelt/en/Phocea/Vie_des_labos/Ast/ast_visu.php?id_ast=66

μm with the *Herschel* Space Telescope (André et al., 2010) to map the well known nearby (< 500 pc) star forming clouds. The molecular clouds in the Gould Belt survey are all mainly associated with active low- to intermediate mass star formation. High-mass star formation involves the formation of stars with a mass higher than typically 8 solar masses ($M_\odot$) and requires the observation of different regions at larger distances (> 1 kpc) close to the galactic plane (Zinnecker & Yorke, 2007; Motte, Bontemps & Louvet, 2018). The high-mass star formation process and its open questions will be presented in more detail after a description of the low-mass star formation process in the following sections.

3.2.2 Star formation from pre- and protostellar cores

It has long been known that molecular clouds have further density substructure in the form of clumps, cores and filaments. In the densest regions of the molecular clouds, which are found in the form of cores, stars can form as a result of gravitational collapse (Shu, Adams & Lizano, 1987). These cores that will form one or more stars are separated into pre- and protostellar cores. A prestellar core is a gravitationally bound core that is stabilised against collapse by thermal, turbulent and magnetic pressure (Shu, Adams & Lizano, 1987; Andre, Ward-Thompson & Barsony, 2000; di Francesco et al., 2007; Ward-Thompson et al., 2007). A protostellar core is a gravitationally collapsing core containing a protostar. Several mechanisms have been proposed to initiate the gravitational collapse to form a star: Ambipolar diffusion (e.g. Mouschovias, 1991), the dissipation of turbulent support (e.g. Nakano, 1998; Myers, 1998) or an external trigger such as mass inflow (e.g. Bonnell et al., 1997; Ballesteros-Paredes, Klessen & Vázquez-Semadeni, 2003). By the gravitational collapse of a prestellar core, a protostar can form in the core. This transition from pre- to protostellar core is generally considered to occur as a result of a couple of consecutive steps (Larson, 1969; Stahler, Shu & Taam, 1980; Shu, Adams & Lizano, 1987; Masunaga, Miyama & Inutsuka, 1998; Masunaga & Inutsuka, 2000). When a prestellar core is gravitationally collapsing it manages to maintain its low temperature and continue the gravitational collapse at the center because radiation can escape from the prestellar core and thus radiate away the energy. However, as the collapse progresses, the central density increases, leading to an increasing opacity for the radiation. Because of this increasing opacity in the prestellar core, radiation gets trapped at the center resulting in the formation of a first hydrostatic core (also called the first Larson core). Because radiation can no longer escape, this leads to an increasing temperature and an adiabatic contraction of the core while gas from larger scales is still gravitationally falling in on the central core, leading to an accretion shock which either radiates away the infalling energy away or deposits this energy in the adiabatic core (Winkler & Newman, 1980; Commerçon et al., 2011; Vaytet et al., 2012). During the adiabatic contraction of the core, the temperature rises until a temperature of 2000 K is reached which dissociates molecular hydrogen. This dissociation process absorbs energy (it is endothermic) such that it removes the internal support leading to a short gravitational collapse of the first core. Once all H_2 has been dissociated, the gravitational collapse is halted again, leading to the formation a second significantly more compact core (Larson, 1969; Stamatellos et al., 2007; Tomida et al., 2013; Vaytet et al., 2013). This second, protostellar, core continues further adiabatic contraction while the surrounding gas is falling in onto the core. At this moment we talk of a protostellar core.
The protostellar accretion results in observed high-velocity (> 10 km s^{-1}) mass outflow from protostellar cores (Bally & Lada, 1983; Lada, 1985; Bachiller, 1996; Bontemps et al., 1996; Arce et al., 2007; Frank et al., 2014). This mass ejection from the protostellar core is broadly found in the form of a

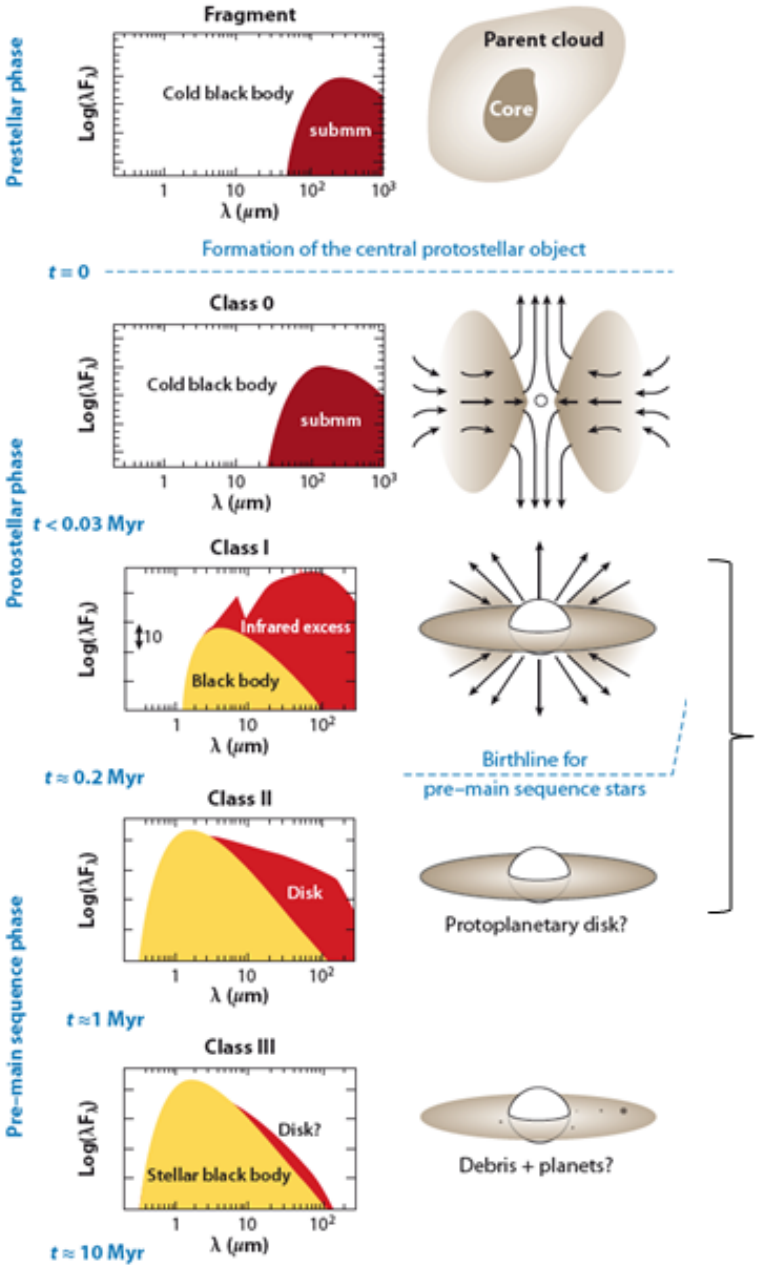

Figure 3.2: A schematic display of the different stages from a prestellar core to the formation of a main-sequence star based on the classification from André & Montmerle (1994).

jet that entrains surrounding material (e.g. Raga & Cabrit, 1993; Masson & Chernin, 1993; Gueth & Guilloteau, 1999). There is only a limited knowledge on how the mass/momentum is exactly ejected in the form of a jet (e.g. Bacciotti et al., 2002; Ferreira, Dougados & Cabrit, 2006; Louvet et al., 2016a, 2018; Lee et al., 2017; Tabone et al., 2017), but it is evident that this jet can remove excess angular momentum from the accreting protostellar core. This removal of angular momentum is essential because the angular momentum of the stars that are formed is only a fraction ($< 1\%$) of the initial angular momentum of the gas from which they form (Stahler & Palla, 2005).

The road from a formed protostar to a main sequence star is generally divided into 4 stages of young stellar objects (YSOs) which are schematically shown in Fig. 3.2. These stages are referred to as: class 0, class I, class II and class III (Lada, 1987; André, Ward-Thompson & Barsony, 1993). The youngest stage is class 0 which evolves through class I and II to class III just before it becomes a main sequence star. A main sequence star is defined as a star obtaining its thermal energy from a hydrogen burning core. Such a star is located on the main sequence in the Hertzsprung-Russel (HR) diagram, which displays the relation between the colour (temperature) and magnitude (luminosity) for observed stars. This main sequence is highly populated in the HR diagrams (e.g. Perryman et al., 1995; Gaia Collaboration et al., 2018).
In the case of class 0 and I, we talk of a protostar embedded in a core, and in the case of Class II (also referred to as a T-Tauri star) and III (post T-Tauri star) we talk of pre-main sequence stars that have a circumstellar disk but no longer have an embedding core (André & Montmerle, 1994). Class I to class III YSOs are detected at 2 μm and can be subdivided into the different classes based on the slope of their spectral energy distribution (SED) between 2 μm and 25 μm (Lada & Wilking, 1984; Wilking, Lada & Young, 1989). The slope of the SEDs are defined as $\alpha_{\rm IR} = \frac{{\rm dlog}(\lambda {\rm F}_\lambda)}{{\rm dlog}\lambda}$ with F_λ the flux at wavelength λ. Class I is then defined by $\alpha_{\rm IR} > 0$, class II is defined by -1.5 $< \alpha_{\rm IR} <$ 0 and class III is defined by $\alpha_{\rm IR} <$ -1.5 (Andre, Ward-Thompson & Barsony, 2000). In Beckwith et al. (1990) and André & Montmerle (1994) it was found that the transition between class II and class III is associated with a transition in disk opacity at 10 μm. It was also found that class I protostars are surrounded by both a disk and a diffuse core (e.g. Whitney & Hartmann, 1993; Kenyon, Calvet & Hartmann, 1993) while class 0 protostars dominantly have an embedding core (André, Ward-Thompson & Barsony, 1993).
With observations by several space telescopes (ISO, Spitzer, WISE and Herschel) and the 2 Micron All Sky Survery (2MASS, Skrutskie et al., 2006) it was possible to construct the SEDs and calculate the luminosity for large sets of YSOs (e.g. Nordh et al., 1996; Persi et al., 2000, 2003; Bontemps et al., 2001, 2010a; Kaas et al., 2004; Dunham et al., 2008, 2015; Evans et al., 2009; Gutermuth et al., 2009; Rebull et al., 2010; Beerer et al., 2010; Maury et al., 2011; Megeath et al., 2012). These observed SEDs can then be analysed with dedicated models to constrain the evolution of these YSOs (e.g. Adams, Lada & Shu, 1987; Kenyon & Hartmann, 1987, 1995; Robitaille et al., 2007; Zhang, Tan & Hosokawa, 2014; Robitaille, 2017; Zhang & Tan, 2018).

The study of large samples of prestellar cores and YSOs has allowed to obtain estimates for the lifetime of prestellar cores and each stage of a YSO. For the prestellar stage, the estimated ages are typically of the order of 0.1-0.5 Myr based on a comparison of the number of prestellar cores compared to protostellar cores (Onishi et al., 2002; Kirk, Ward-Thompson & André, 2005; Enoch et al., 2008; Maury et al.,

class	$\alpha_{\rm IR}$	τ (Myr)
class 0		0.03-0.2
class I	> 0	0.3-0.5
class II	[-1.5,0]	~ 2
class III	$<$ -1.5	~ 10

Table 3.1: The values for the SED slope between 2 μm and 25 μm that can be used to differentiate between the different classes of YSOs, and the generally estimated lifetimes for each class.

2011). With Spitzer observations of nearby clouds, the class 0 and class I lifetimes were estimated to be 0.16 Myr and 0.54 Myr (Evans et al., 2009). This was estimated based on the comparison of the number of class 0, class I and class II YSOs and combining it with the estimated age of class II YSOs, 2±1 Myr (Spezzi et al., 2008), which remains uncertain. Recently, it was indicated in Simon et al. (2019a) that class II YSOs might be a factor 3-5 older than currently assumed when including the magnetic field in their evolution. It should be noted that there are significant differences and that several studies have indicated different lifetimes for class 0 and class I YSOs (e.g. André & Montmerle, 1994; Greene et al., 1994; Andre, Ward-Thompson & Barsony, 2000; Visser, Richer & Chandler, 2002; Hatchell et al., 2007; Brünken et al., 2014) which are generally considered to be between 0.01 and 1 Myr.

3.2.3 The core mass function

With large scale millimeter and far-infrared continuum mapping, in particular of nearby clouds, it was possible to obtain a census of prestellar cores and their mass. This census became increasingly complete with increasing sensitivity. Already from the first studies it became evident that there is a striking similarity between the prestellar core mass function (CMF) and the observed initial mass function (IMF) of stars. Furthermore, the CMF is shifted by roughly a factor 3 to higher masses with respect to the IMF (Motte, Andre & Neri, 1998; Testi & Sargent, 1998; Johnstone et al., 2000). The IMF is the mass probability distribution for stars reaching the main sequence (Offner et al., 2014). The currently constrained IMF can be more or less described by a lognormal function with a peak near 0.3 $M_\odot$, followed by a power law described by $dN/dm \propto m^{-\alpha}$ with α = 2.-2.5, see Fig. 3.3. There are ongoing discussions whether the initial mass function is truly universal, but this will not be adressed in more detail here as it is out of the scope of the current work (e.g. van Dokkum & Conroy, 2010; Cappellari et al., 2012).
The similarity between the CMF and IMF was further confirmed in later studies with millimeter continuum emission (Nutter & Ward-Thompson, 2007; Enoch et al., 2008), extinction maps (Alves, Lombardi & Lada, 2007) and most recently with the results from the *Herschel* Gould Belt survey (André et al., 2010; Könyves et al., 2010, 2015, 2020; Marsh et al., 2016; Benedettini et al., 2018; Bresnahan et al., 2018; Ladjelate et al., 2020). The results from *Herschel* for the Aquila cloud are shown in Fig. 3.3. The observed resemblance of the CMF and IMF can nicely fit with a scenario where the observed prestellar cores form stars from the mass contained inside each prestellar core with a star formation efficiency around 30-40%. As a result, the CMF that emerges from the ISM evolution would be responsible for the observed IMF (Padoan & Nordlund, 2002; Hennebelle & Chabrier, 2008; Hopkins, 2012; Hennebelle,

Lee & Chabrier, 2019). An opposing view argues that the IMF is not directly related to the CMF, but rather the result of accretion in a dynamic environment (Bonnell et al., 2001b; Bate, Bonnell & Bromm, 2003; Clark, Klessen & Bonnell, 2007). In the recent review by Offner et al. (2014) it was emphasised that the origin of the IMF is still not understood because of the interplay of complex physical processes, but it was indicated that an intermediate scenario might be applicable. In any case, these proposed scenarios demonstrate that understanding the formation of dense star forming gas is important to understand the origin of the IMF.

3.2.4 Challenges of high-mass star formation

Up to this point, the generally considered framework for the formation of low- and intermediate mass stars was discussed. However, there are also massive stars in the ISM with masses higher than 8 $M_\odot$. Understanding the formation of these high-mass stars has been extremely challenging.

First of all, observational studies of high-mass star formation are complicated because the formation of high-mass stars occurs in very dense, high column density regions. As a result of this high column density, the formation sites are highly obscured. Furthermore, the rapid evolution and immediate impact of feedback from high-mass stars makes it challenging to obtain reliable information on the initial conditions. There is also a lack of nearby (< 1 kpc) high-mass star formation sites which makes it more difficult to resolve individual star forming cores than for low-mass stars (Zinnecker & Yorke, 2007).
From theoretical considerations it also became clear that a classical scenario for low-mass star formation by the gravitational collapse of an isothermal core that overcomes thermal pressure, as described in Shu (1977), could not apply for high-mass star formation. Namely, the masses of high-mass stars are far above the typical Jeans masses of cold and dense cores in the ISM. The resulting mass accretion rate on a protostar at the typical low temperatures in dense cores is predicted by this model to be $\sim 10^{-6}$ $M_\odot$ yr^{-1} which is sufficient to form low-mass stars. However, for high-mass star formation this is insufficient and leads to formation times that are significantly longer than 10^6 year (Stahler, Palla & Ho, 2000). However, from the observed protostellar outflows (e.g. Behrend & Maeder, 2001; Beuther et al., 2002b; Duarte-Cabral et al., 2013; Tan et al., 2016) and SED observations of massive hot cores (Osorio, Lizano & D'Alessio, 1999; Nakano et al., 2000) it was found that higher mass accretion rates are required, resulting in a formation timescale for massive stars that has to be significantly shorter than 1 Myr.
Another important problem to form high-mass stars following the Shu (1977) model is the strong feedback from massive stars. The short Kelvin-Helmholtz contraction time of massive stars compared to their accretion timescale implies that massive stars will start to burn hydrogen in their core before accretion has ended. As a result, the strong luminosity can stop the spherical low mass accretion rate and thus puts a hard upper limit on the mass of a star that is below the observed mass of several stars (Larson & Starrfield, 1971; Wolfire & Cassinelli, 1987).
From observational studies an extra problem started to emerge. Observations found a complete lack of, or at least extremely short lifetimes of, massive prestellar cores (Motte et al., 2007). This search for high-mass prestellar cores became a hot topic in particular with the *Herschel*, Plateau de Bure/NOEMA and ALMA telescopes (Motte et al., 2010; Tan et al., 2013; Duarte-Cabral et al., 2013; Tan et al., 2016; Tigé et al., 2017; Motte, Bontemps & Louvet, 2018; Louvet et al., 2019). Yet, to this point there are

only a couple, unconfirmed, high-mass prestellar candidates (Duarte-Cabral et al., 2013; Cyganowski et al., 2014; Wang et al., 2014; Kong et al., 2017; Nony et al., 2018; Molet et al., 2019) which may even indicate that there is no high-mass equivalent of a prestellar core.

Consequently, several ideas have been proposed to explain the formation of massive stars. An early proposed idea was that stellar mergers at the center of dense clusters might form massive stars (Bonnell, Bate & Zinnecker, 1998; Bonnell & Bate, 2002), yet stellar mergers are expected to be rare (Zinnecker & Yorke, 2007).
Bondi-Hoyle competitive accretion by low-mass protostellar cores from the high mass reservoir in dense molecular clumps was also proposed to circumvent the possible problems associated with high-mass star formation (Bonnell et al., 2001a; Bonnell & Bate, 2006; Murray & Chang, 2012).
In strong contrast to competitive accretion, the turbulent core model was described by McKee & Tan (2002, 2003) where high-mass stars form through the collapse of a massive prestellar core that was maintained in a stable state with an increased effective Jeans mass against further fragmentation because of important turbulent and/or magnetic support. The resulting collapse of such a high-mass prestellar core could then provide sufficiently large accretion rates for massive star formation. However, an exact application of this model has problems with the later established difficulty to find high-mass prestellar cores.
On the other hand, the idea of a scenario with an important role for the large-scale dynamics has also increasingly gained attention outside of the Bondi-Hoyle scenario. In particular, high mass star formation as a result of the gravitational collapse of a clump has been proposed (Smith, Longmore & Bonnell, 2009; Wang et al., 2010; Hartmann, Ballesteros-Paredes & Heitsch, 2012) e.g. in the form of the global hierarchical collapse scenario where collapsing substructures on different size scales in a molecular cloud provide continuous mass towards smaller scales. This large scale gravitational collapse replinishing smaller substructures will then eventually lead to massive star formation in the hubs of filamentary structures (Vázquez-Semadeni et al., 2009; Vázquez-Semadeni, González-Samaniego & Colín, 2017; Vázquez-Semadeni et al., 2019). Another dynamic scenario based on gravitational inflow is the fragmentation-induced starvation scenario. In this scenario, gravitational inflow along filaments leads to massive star formation at the center of the gravitationally collapsing clump. The magnetic field inhibits strong fragmentation, provides local support and brakes rotational motion which increases the gravitational inflow, while fragmentation and resulting star formation in the inflowing filaments limit the mass accretion onto the central massive star forming cores (Peters et al., 2010, 2011; Girichidis et al., 2012). There is also a more recently proposed dynamic scenario based on inertial converging flows in supersonic turbulence which provide continuous inflow responsible for increasing the mass of massive star forming cores over time (Padoan et al., 2019).
In order to overcome the issue related to radiation pressure preventing high-mass star formation, it was proposed that disk accretion plays an important role. It was found that the high opacity in the disk can lead to an anisotropic radiation pressure such that accretion from the disk can overcome the radiation pressure barrier (e.g. Yorke & Bodenheimer, 1999; Yorke & Sonnhalter, 2002; Krumholz, McKee & Klein, 2005; Kuiper et al., 2010, 2011).

From an observational point of view, significant progress has been made to understand the forma-

tion of massive stars thanks to Spitzer, *Herschel*, ALMA and NOEMA/the Plateau de Bure (PdB) interferometer to name a few telescopes. It was pointed out before that these telescopes have demonstrated the lack of massive prestellar cores and thus point to a more dynamic massive star formation scenario. In particular ALMA and NOEMA/PdB have allowed to investigate the fragmentation of massive dense cores (Motte et al., 2007). Massive dense cores (MDCs) are the locations of high-mass star formation, and are generally defined as ~ 0.1 pc cores with a mass above 40 $M_\odot$ (Motte, Bontemps & Louvet, 2018). In these MDCs, further fragmentation was observed (Bontemps et al., 2010b; Palau et al., 2013, 2014; Beuther et al., 2015a, 2018; Csengeri et al., 2017). The subfragmentation shows quite some variation depending on the source, but generally the fragmentation is higher than expected for the turbulent core model but also lower than expected for competitive accretion.
Both low- and high-resolution kinematic studies of high-mass star forming regions and MDCs provide interesting information. Several observations have put forward that the observed large scale kinematics of massive molecular clouds tend to support a more dynamic scenario. It was in particular proposed that large scale gravitational collapse and the resulting inflow of filaments drive the formation of massive stars (Peretto, André & Belloche, 2006; Galván-Madrid et al., 2010; Schneider et al., 2010; Wyrowski et al., 2012, 2016; Peretto et al., 2013, 2014; Beuther et al., 2013; Henshaw et al., 2014; Hacar et al., 2017; Williams et al., 2018; Traficante et al., 2018, 2020; Montillaud et al., 2019). Focusing on the kinematics inside the massive dense cores it is found that this large scale inflow might result in small scale converging flows and shears that are responsible for high mass star formation (Csengeri et al., 2011a,b; Beuther et al., 2015a). This idea that intersecting small scale velocity coherent flows are responsible for high-mass star formation was also proposed in the framework of the so-called fibers for Orion (Hacar et al., 2018). The concept of fibers will be discussed in more detail in Sec. 3.3.1. The formation of high-mass stars at the intersection of inflowing filaments, and possibly by the collapse of an entire molecular cloud, fits with the observations of the *Herschel* telescope that high-mass protostars are located at the intersection of multiple filaments (Schneider et al., 2012).

When studying higher mass regions with ALMA, it was recently shown that the core mass function in these regions is flatter than the IMF (Motte et al., 2018; Liu et al., 2018). As there are no, or very little high-mass prestellar cores, these CMFs are made of all extracted, mostly class 0, dense cores. The physical reason for this departure from the IMF slope is still an open question, but the result suggests that the IMF is not inherited from the CMF at high masses (> 10 $M_\odot$). This is not necessarily surprising since it was already mentioned that high-mass stars are increasingly considered to form in a more dynamic scenario. However, recently it was suggested by Sadaghiani et al. (2020) that this apparent flatter CMF slope could be a simple temperature effect.

3.3 The filamentary structure of the ISM

Molecular clouds are found to have further dense substructure and contain elongated filamentary structures, which has been noticed early-on in observations of what later turned out to be molecular clouds (Barnard, 1907). This presence of filaments in molecular clouds was further observed in a large variety of studies (Bergin & Tafalla, 2007) and the presence of filament hubs, which are locations where filament intersect, was found in e.g. Spitzer images (Myers, 2009). This led to several theoretical studies

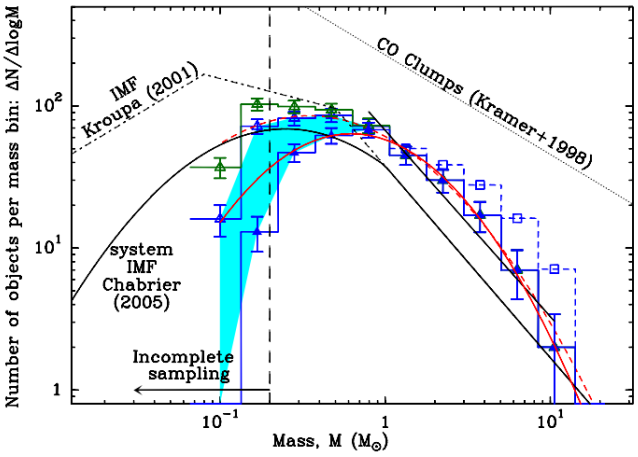

Figure 3.3: The black curves indicate the observed IMF descriptions in several studies (Salpeter, 1955; Kroupa, 2001; Chabrier, 2005) and the mass distribution of CO clumps (Kramer et al., 1998). The green histogram shows the CMF for starless cores (which are not necessarily bound), and the blue histograms show the CMF for prestellar cores in the Aquila molecular cloud as seen with *Herschel*. The lowest blue histogram contains only robust prestellar cores. A prestellar core was considered robust if $\alpha_{\rm vir} = {\rm M_{vir}/M_{obs}} \leq 2$ (Bertoldi & McKee, 1992). The vertical line indicates the completeness limit of the CMF, and the red curve indicates the fit to the CMF of robust (full line) and candidate (dashed line) prestellar cores. This image was adapted from Könyves et al. (2015).

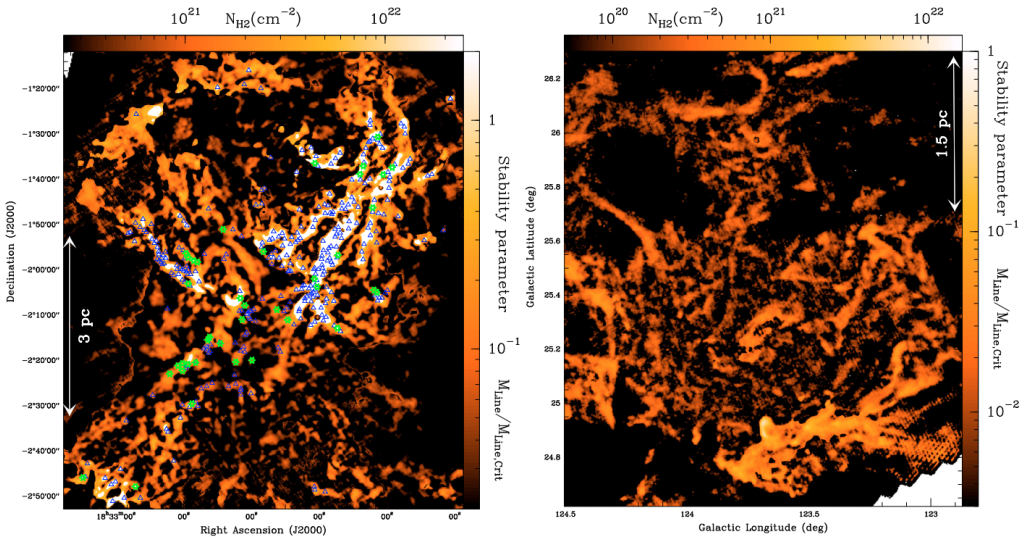

Figure 3.4: The *Herschel* images of Aquila (left; Könyves et al., 2010; Bontemps et al., 2010b) and Polaris (right; Men'shchikov et al., 2010; Miville-Deschênes et al., 2010) which are processed by a curvelet transform to enhance the filamentary structures. The green and blue triangles indicate the candidate class 0 protostars and prestellar cores, respectively. This figure was adapted from André et al. (2010).

of filaments in equilibrium with the surrounding ISM to understand their fragmentation and role in cluster formation (e.g. Ostriker, 1964; Inutsuka & Miyama, 1992; Nakamura, Hanawa & Nakano, 1993; Inutsuka & Miyama, 1997; Fiege & Pudritz, 2000; Inutsuka, 2001). These theoretical studies have put forward that there is a critical mass per unit length for filaments around 16 $M_\odot$ pc^{-1}, above which an isothermal filament is no longer stable against perturbations. A perturbation in a filament above the critical mass per unit length will lead to rapid gravitational fragmentation of the filament. Numerical simulations also addressed the formation scenario of the interstellar filaments. It was proposed that turbulent compression could give rise to filamentary structures (e.g. Padoan et al., 2001; Mac Low & Klessen, 2004; Jappsen et al., 2005), and it was also observed that numerical simulations of large scale converging flows give rise to filamentary clouds (Ballesteros-Paredes, Hartmann & Vázquez-Semadeni, 1999; Vázquez-Semadeni et al., 2007; Heitsch et al., 2008; Banerjee et al., 2009).

Though filaments in the ISM were known since long, it was the unprecedented sensitivity of the *Herschel* telescope that highlighted the ubiquitous filamentary nature of the dense ISM in multiple large programs (*Herschel* Gould Belt survey, HiGAL, HOBYS, EPoS) dedicated to map the dust continuum emission of galactic clouds (André et al., 2010; Molinari et al., 2010; Motte et al., 2010; Henning et al., 2010). In Fig. 3.4, the filamentary structure of the Aquila and Polaris clouds, observed as part of the *Herschel* Gould Belt survey, are presented. Further studies of these Herschel filaments, in particular with regard to the location of the pre- and protostellar cores, have shown that the majority of stars form in filaments (Men'shchikov et al., 2010; Polychroni et al., 2013; Könyves et al., 2015; Marsh et al., 2016; Rayner et al., 2017). This has led to a proposed filamentary paradigm for star formation where filamentary properties regulate the outcome of star formation (André et al., 2014; Shimajiri et al., 2017; André et al., 2019a). This paradigm is in particular based on the proposed universal 0.1 pc radial width of *Herschel* filaments in the Gould Belt molecular clouds (Arzoumanian et al., 2011, 2019; Koch & Rosolowsky, 2015). However, the filamentary origin for the IMF proposed in André et al. (2019a), where gravitational fragmentation of filaments (and their statistics) sets the CMF and as a result the IMF, for example does not consider the substructure found in *Herschel* filaments (e.g. Hacar et al., 2013). Furthermore, the proposed universal 0.1 pc filament width is still highly debated. Several observational and numerical studies have questioned the validity of this universal 0.1 pc filament width based on a variety of arguments (e.g. Panopoulou et al., 2014, 2017; Smith, Glover & Klessen, 2014; Ntormousi et al., 2016; Seifried et al., 2017; Hacar et al., 2018; Ossenkopf-Okada & Stepanov, 2019). From an observational point of view it was argued, among others, that averaging over the filament significantly affects the results (Panopoulou et al., 2017), and that taking into account further filamentary substructure also affects the results (Hacar et al., 2018). It was also argued that using a single temperature in the line of sight to construct the column density profile affects the obtained filament width (Howard et al., 2019).

Filamentary structures are also ubiquitous in high-mass star forming regions where the massive stars form in filament hubs and ridges (Hill et al., 2011; Schneider et al., 2012; Hennemann et al., 2012; Ragan et al., 2012, 2015; Peretto et al., 2013, 2014). A hub was already defined as a location where filaments intersect (Myers, 2009). A ridge is a high column density ($N_{H_2} > 10^{23}$ cm^{-2}) elongated structure/filament where massive stars can form (Hartmann & Burkert, 2007; Hill et al., 2011; Hennemann et al., 2012). Generally, lower density filaments are also connected to a ridge, such that it could be seen

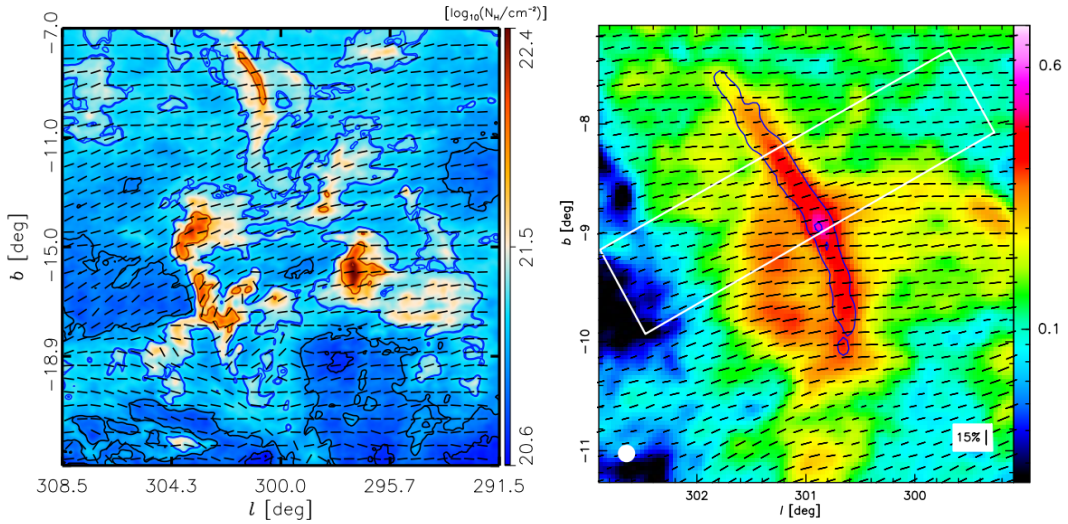

Figure 3.5: **Left:** The magnetic field orientation from the Planck telescope overlayed on the column density map of the Chamaeleon-Musca cloud. The filamentary orientation is generally perpendicular to the densest structures. This figure is adapted from (Planck Collaboration et al., 2016b). **Right:** A zoom into the magnetic field orientation near the Musca filament. This demonstrates a highly organised magnetic field in the Musca cloud. This figure was adapted from (Planck Collaboration et al., 2016c).

as an elongated filament hub. This filamentary structure in massive star forming regions can provide compact inflow towards the MDCs in hubs and ridges. The relatively small cross section associated with filamentary inflow could limit the mass accretion rate, but possibly this can be overcome by a global inflow off the filaments towards the hubs and ridges (Schneider et al., 2010; Peretto et al., 2013). Once the feedback from massive stars becomes important, this can halt global inflow. In this case, filaments might provide a continued inflow towards MDCs because they are better shielded from feedback through their high density and compactness.

Observations of the galactic plane with Spitzer and *Herschel* also demonstrated the presence of filaments with lengths up to 100 pc and high column densities, which are in some cases associated to the galactic spiral arms. These filamentary structures are often referred to as giant molecular filaments, giant *Herschel* filaments and galactic bones, and can be the location of significant high-mass star formation (Jackson et al., 2010; Ragan et al., 2014; Goodman et al., 2014; Schisano et al., 2014, 2020; Zucker, Battersby & Goodman, 2015; Wang et al., 2015, 2016; Abreu-Vicente et al., 2016; Mattern et al., 2018a,b). Recently, efforts were made to classify these different large scale filaments based on their velocity substructure, association with spiral arms and aspect ratio (Zucker, Battersby & Goodman, 2018).

3.3.1 Observational constraints on nearby interstellar filaments

In the last decade, a significant effort has been started to better understand physical properties of the resolved star forming filaments, in particular in the Gould Belt. It was found that their density profile obtained with *Herschel* can be fitted reasonably well with a Plummer profile (Arzoumanian et al., 2011, 2019). The Plummer density profile is given by

$$\rho(\mathrm{r}) = \frac{\rho_\mathrm{c}}{[1 + (\mathrm{r}/\mathrm{R}_\mathrm{flat})^2]^{p/2}} \tag{3.1}$$

with ρ_c the central density, R_{flat} the inner flat radius of the density profile, and p the power law of the density profile. With *Herschel* these values can be deduced by fitting the column density profile using

$$\Sigma(\mathrm{r}) = \mathrm{A_p} \frac{\rho_\mathrm{c} \mathrm{R}_\mathrm{flat}}{[1 + (\mathrm{r}/\mathrm{R}_\mathrm{flat})^2]^{\frac{p-1}{2}}} \tag{3.2}$$

with A_p given by

$$A_p = \frac{1}{\cos\theta} \int_{-\infty}^{\infty} \frac{\mathrm{du}}{(1 + \mathrm{u}^2)^{\mathrm{p}/2}} \tag{3.3}$$

with θ the inclination angle with respect to the plane of the sky.
Fitting the column density profiles of filaments it is typically found that their power law can be described with p $\sim$ 2, and that the typical width of the filaments is around 0.1 pc (Arzoumanian et al., 2011, 2019; Peretto et al., 2012; Palmeirim et al., 2013; Koch & Rosolowsky, 2015; Cox et al., 2016). However, it was already pointed out that this proposed universality is questioned by several studies. Furthermore, it was proposed by Tritsis & Tassis (2018) that some of the observed filaments that are not yet forming stars are in fact sheets that are seen edge-on.
Observations with the Planck telescope that are shown in Fig. 3.5, reveal that the orientation of interstellar filaments is closely coupled to the local magnetic field orientation. Star forming filamentary structures are generally perpendicular to the magnetic field orientation (Planck Collaboration et al., 2016c,b; Malinen et al., 2016). Indications of this behaviour were already found with polarisation measurements of dust extinction and millimeter dust emission (e.g. Vrba, Strom & Strom, 1976; Vrba, Coyne & Tapia, 1981; Heyer et al., 1987, 2008; Pereyra & Magalhães, 2004; Vallée & Fiege, 2006; Chapman et al., 2011; Koch et al., 2014).
Looking into lower density and even HI regions, large filamentary structures (> 10 pc) (e.g. Miville-Deschênes et al., 2003; McClure-Griffiths et al., 2006; Begum et al., 2010) as well as smaller scale ($\sim$ 1 pc) filamentary structures are observed. These smaller scale low-density filaments are often referred to as striations (Goldsmith et al., 2008; Heyer et al., 2016; Cox et al., 2016). These lower density filaments in the ISM are generally aligned with the magnetic field orientation (McClure-Griffiths et al., 2006; Clark, Peek & Putman, 2014; Planck Collaboration et al., 2016b,a; Cox et al., 2016; Kalberla et al., 2016; Clark et al., 2019). There thus appears to be a transition from filament alignment with the magnetic field to filaments being perpendicular to the magnetic field. The transition has been suggested to occur near a typical column density $\mathrm{N}_H \sim 5{\times}10^{21}$ cm^{-2} based on observations (Planck Collaboration et al., 2016b; Malinen et al., 2016; Fissel et al., 2016; Soler et al., 2017), which poses an important contraint on models of filament formation. It has been suggested that this transition point could be

related to a transition from a regime in the ISM that is dominated by the magnetic field to a regime that is dominated by gravity (e.g. Soler & Hennebelle, 2017; Fissel et al., 2019).

Observations of line transitions from different molecules that trace high density gas in filaments (e.g. $C^{18}O$, N_2H^+, NH_3,...) unveil the kinematics in the line of sight for star forming filaments. One of the first results when studying filament kinematics, was the presence of filamentary velocity coherent substructure, so-called fibers (Hacar et al., 2013, 2018; Hacar, Tafalla & Alves, 2017; Dhabal et al., 2018; Shimajiri et al., 2019a). These fibers are identified in the three dimensional position-position-velocity (PPV) space. The two spatial axes identify the plane of the sky and the velocity axis provides information on the velocity in the line of sight. In PPV space, spectra can contain multiple velocity components at a specific location in the plane of the sky. Separating these individual velocity components at each location shows that they form filamentary structures in the plane of the sky, which are the fibers. Evaluating the properties of fibers it was suggested that they can have a significant diversity, even in a single filament. For example, indications of large density differences have been presented for fibers inside a single dust continuum filament (Hacar et al., 2013). Elaborating on these results, it was proposed that these fibers are spatially (in 3D) individual structures where prestellar cores form as a result of fiber fragmentation instead of fragmentation by the dust continuum filament (Tafalla & Hacar, 2015). It was also suggested that these fibers have no characteristic filament width of 0.1 pc (Hacar et al., 2018).
Studying the molecular linewidth of fibers and filaments that are established with dust continuum emission, it was observed that filaments below their critical line mass have a relatively universal sub-/transonic velocity dispersion of $\sigma_{NT}/c_s \sim 0.5$-1 (where c_s is the sound speed and σ_{NT} is the non-thermal contribution to the linewidth) while higher column density filaments and fibers have a growing spectral linewidth with increasing column density (Arzoumanian et al., 2013; Hacar et al., 2018; Mattern et al., 2018b). When studying the increase of the spectral linewidth for filaments that are established with dust continuum emission, it should be taken into account that this spectral linewidth can be the result of several individual velocity components. It should also be noted that there are dust continuum filaments without or with limited further velocity substructure (Hacar et al., 2016).
Fitting spectral line observations not only provides information on the linewidth in the filament, but also provides information on the velocity field of filaments. Studying the resulting velocity fields demonstrated velocity gradients aligned with the dust continuum filament axes (Kirk et al., 2013; Peretto et al., 2014; Jiménez-Serra et al., 2014), as well as velocity gradients perpendicular to the filament orientation (Olmi & Testi, 2002; Schneider et al., 2010; Fernández-López et al., 2014; Beuther et al., 2015b; Dhabal et al., 2018). The gradients aligned with the filament axes have generally been interpreted as inflow to a hub of these filaments, though this interpretation is debated (Fernández-López et al., 2014), while the gradients perpendicular to the filaments have generally been considered as evidence of mass inflow to the filament (e.g. Smith et al., 2016; Chen et al., 2020). From the large scale kinematics of molecular clouds around star forming filaments this idea of large scale inflow, aligned with the magnetic field, to star forming filaments was also proposed to be the result of the gravitational potential of the filament (Palmeirim et al., 2013; Shimajiri et al., 2019b). This could provide an explanation for the observed correlation between filament orientation and magnetic field orientation. A possible scenario emerges where the low mass filamentary structures are flowing along the magnetic field to provide mass accretion

on the dense star forming filaments that are consequently oriented perpendicular to the magnetic field. Since the *Herschel* observations there has thus been a significant effort to establish the properties of filaments, but there obviously is still strong debate on their properties and the origin of these filament properties.

3.3.2 Cloud formation and the ubiquitous filamentary structure of the ISM

Now, it is well established that dense star forming gas emerges in the ISM in the form of filamentary structures, and even that lower density gas in the ISM is highly filamentary. Consequently, it is important to study the physics of filamentary gas in the ISM since it sets the conditions of star formation.

In early work on the evolution of the ISM, it was proposed that clouds and dense core formation is governed by slow, quasi-static contraction that might be driven by ambipolar diffusion (e.g Mouschovias, 1976; Shu, Adams & Lizano, 1987). However, it was pointed out that the observed small crossing times of molecular clouds (e.g. Zuckerman & Evans, 1974; Larson, 1981; Solomon et al., 1987) prevent the molecular cloud from reaching such a quasi-static behaviour (e.g. Ballesteros-Paredes, Hartmann & Vázquez-Semadeni, 1999; Elmegreen, 2000; Hartmann, Ballesteros-Paredes & Bergin, 2001). This led to the so-called gravo-turbulent view where dense gravitationally unstable cores and filaments emerge from turbulent motions in the molecular clouds (e.g. Klessen, Heitsch & Mac Low, 2000; Padoan & Nordlund, 2002) which can be driven by energy injection from supernovae (McKee & Ostriker, 1977; Mac Low & Klessen, 2004). Simulations also showed that supersonic molecular clouds can be formed by a converging flow in the WNM. In this converging flow scenario, the collision triggers the thermal instability such that cold supersonic filamentary clouds can be formed (e.g. Hennebelle & Pérault, 1999; Koyama & Inutsuka, 2000, 2002; Audit & Hennebelle, 2005; Banerjee et al., 2009). In more recent work, it was proposed by Inutsuka et al. (2015) that the dynamics of such converging flows can be driven by expanding shells around OB stars and supernovae. In this scenario of converging flows, it was more recently also considered that cloud-cloud collisions, i.e. converging flows that already contain dense molecular gas, can also result in the creation of (massive) star forming clouds (e.g. Inoue & Fukui, 2013; Wu et al., 2015, 2017; Inoue et al., 2018). It was also found that cold supersonic filamentary clouds can form during the hierarchical gravitational collapse of a cloud (e.g. Vázquez-Semadeni et al., 2009; Gómez & Vázquez-Semadeni, 2014).

In simulations that aim to describe the ISM with different initial conditions and physical processes, it is thus almost universally observed that dense filamentary structures are formed. This indicates that basically all processes that play a role in the ISM in some way lead to or increase the presence of filamentary structures: gravity (e.g. Nagai, Inutsuka & Miyama, 1998; Gómez & Vázquez-Semadeni, 2014), turbulence (e.g. Padoan et al., 2001; Jappsen et al., 2005; Smith, Glover & Klessen, 2014; Federrath, 2016), the magnetic field (e.g. Hennebelle, 2013; Auddy, Basu & Kudoh, 2016; Tritsis & Tassis, 2016; Inoue et al., 2018) and galactic shear (e.g. Smith et al., 2014; Duarte-Cabral & Dobbs, 2016). This universal tendency to form filaments is intriguing and strongly suggests that different processes will be responsible for the diverse filamentary structures observed in the galaxy (Gould Belt filaments, striations, ridges, galactic bones,...). However, it is thus required to find observational signatures of the filament formation process for each type of filament. For filaments in the Gould Belt, this implies

e.g. searching for low-velocity shocks which can form dense filamentary gas through compression (e.g. Padoan et al., 2001; Pudritz & Kevlahan, 2013; Federrath, 2016; Clarke et al., 2018), quantifying velocity gradients in the filament (Chen et al., 2020), mapping the large scale kinematics (e.g. Nagai, Inutsuka & Miyama, 1998; Inoue et al., 2018) and probing the magnetic field orientation (e.g. Soler & Hennebelle, 2017; Seifried et al., 2020).
Furthermore, simulations do not necessarily point to a complete filament paradigm as proposed by André et al. (2014); Shimajiri et al. (2017); André et al. (2019a) where the filaments form first and their properties then set the outcome of star formation and the star formation efficiency. Simulations rather indicate that star forming gas emerges in filametary structures, but that e.g. the star formation rate and initial mass function are set by the turbulent properties and the magnetic field of the molecular clouds (e.g. Padoan et al., 2014; Krumholz, 2014; Hennebelle, Lee & Chabrier, 2019).

Numerical studies have also tried to reproduce the proposed universal 0.1 pc filament width, which is generally not found in simulations of the ISM. The reason(s) for this is currently unclear, but multiple explanations have been proposed: filament selection differences (Ntormousi et al., 2016), possibly missing physics of filament formation (Ntormousi et al., 2016; Federrath, 2016), the fitting procedure (Smith, Glover & Klessen, 2014), optical depth effects (Seifried et al., 2017) and the assumption of an isothermal filament (Seifried et al., 2017). Even though most simulations tend not to produce 0.1 pc width filaments, Federrath (2016) managed to reproduce a universal filament width in turbulent box simulations including gravity, turbulence, the magnetic field and feedback from protostellar outflow jets. It was suggested that the inclusion of all these physical processes was essential for this result.
The fibers in dust continuum filaments have also received considerable attention in numerical simulations, since turbulent simulations naturally produce filamentary substructure (Moeckel & Burkert, 2015). Based on simulations, two main scenarios of fiber formation have been proposed. Smith, Glover & Klessen (2014); Smith et al. (2016) put forward that fibers are produced by shock compression in the turbulent ISM. After their formation, the fibers are gathered in large dust continuum filaments. On the other hand, fibers can form inside dust continuum filaments as a result of vorticity in the filament due to an inhomogeneous accretion flow (Clarke et al., 2017). Simulations also indicated that care has to be taken with fiber-based star formation theories since coherent velocity structures are not necessarily independent spatial structures (Moeckel & Burkert, 2015; Zamora-Avilés, Ballesteros-Paredes & Hartmann, 2017; Clarke et al., 2018).

3.3.3 Low-velocity shocks and dense gas formation in the ISM

Because of supersonic turbulent motions in a molecular cloud, the supersonic energy will be dissipated by shocks. The shocks that dissipate this supersonic motion are often referred to as low-velocity shocks. The presence of low-velocity shocks in molecular clouds is intriguing because they can strongly enhance the gas density which can result in star formation (e.g. Vazquez-Semadeni, 1994; Klessen, Heitsch & Mac Low, 2000; Padoan et al., 2001). Since dense gas is often formed in filamentary structures, low-velocity shocks may play an important role during the formation process of the observed filaments. In particular, it was pointed out by Federrath (2016) that shock compression in a converging flow can provide an explanation for the observed $\rho \propto \mathrm{r}^{-2}$ density profile of filaments. If gas encounters a shock front, it is heated directly behind the shock front such that it excites higher atomic and molecular en-

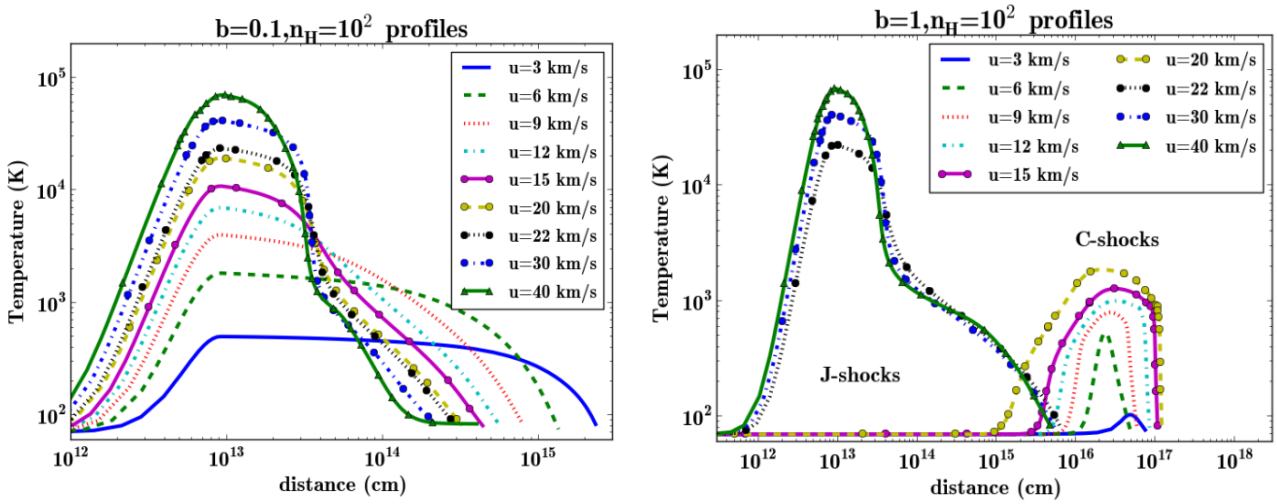

Figure 3.6: **Left:** The temperature profile for J-type shocks with a preshock density $n_H = 10^2$ cm^{-3}, presented in Lesaffre et al. (2013). **Right:** The same for C-type shocks, where it can be noted that above a specific velocity ($\sim$ 20 km s^{-1} for the presented models) C-type shocks can not occur. It also becomes obvious that J-type shocks lead to a higher peak temperature.

ergy levels. Based on predictions by low-velocity shock models and photo-dissociation models, it is then possible to detect the presence of low-velocity shocks. The densification by these low-velocity shocks can also play an important role in the cooling of the dense ISM thanks to the CO molecule (Goldsmith & Langer, 1978; Whitworth & Jaffa, 2018). With *Herschel* spectroscopic observations, some indications of possible shock excitation have been reported with relatively bright high-J (≥ 5) CO lines in a couple of molecular clouds (Pon et al., 2014, 2015; Larson et al., 2015). In these papers, the observed high-J CO lines were then attributed to the dissipation of generic turbulent motions in the molecular cloud, but it was not possible to study the association with dense gas formation.

Shock morphology is quite generally distributed in two classes: J-type shocks (e.g. Shull & McKee, 1979; Hollenbach & McKee, 1989) and C-type shocks (e.g. Mullan, 1971; Draine, 1980; Draine, Roberge & Dalgarno, 1983; Kaufman & Neufeld, 1996a,b; Flower & Pineau des Forêts, 2003; Pon, Johnstone & Kaufman, 2012; Lesaffre et al., 2013). Model results from Lesaffre et al. (2013) for both shock types are presented in Fig. 3.6. A J-type shock stands for a sudden jump in physical conditions. This leads to adiabatic compression, consequent heating and radiative cooling over a small distance which is $\sim 10^{14}$ - 10^{15} cm for low-velocity shocks (e.g. Lesaffre et al., 2013). The adiabatic phase is described by Rankine-Hugoniot jump conditions

$$\begin{aligned} \rho_1 v_1 &= \rho_2 v_2 \\ \rho_1 v_1^2 + p_1 &= \rho_2 v_2^2 + p_2 \\ \frac{1}{2}\rho_1 v_1^2 + h_1 &= \frac{1}{2}\rho_2 v_2^2 + h_2 \end{aligned} \tag{3.4}$$

with ρ the densities, v the velocities, p the pressure and h the specific enthalpy at both sides of the shock discontinuity. In the radiative cooling phase, the temperature drops while the density increase continues to maintain the pressure balance.
A C-type shock stands for a continuous shock and can occur in a magnetised medium where the dissipation continuously happens through ion-neutral friction over a relatively large distance compared to J-type shocks. This also results in a significantly lower temperature of the shock heated gas. However, a C-type shock can only exist up to a maximal velocity that corresponds to the magnetosonic velocity of the charged fluid. Above this upper velocity for signal propagation, the magnetic field can no longer smooth the shock excitation which will result in a J-type shock.

3.4 Far infrared and submillimeter observations of the ISM

3.4.1 Atmospheric absorption

The dust continuum emission and a variety of atomic and molecular lines that trace the star forming ISM are emitted at far infrared and (sub)millimeter wavelengths. However, at ground level, the atmosphere is completely opaque for wavelengths from $\sim$ 20 μm down to 1 mm, see Fig. 3.7, because of different molecules in the atmosphere. The most important ones are O_3 (ozone), H_2O (water) and CO_2 (carbon dioxide).

1) The largest fraction of ozone is located at an altitude between 15 and 35 km, in the so-called ozone layer. Ozone mostly absorbes UV light and shorter wavelengths, but plays no role for far infrared and submillimeter emission.

2) Water is the most important absorber for longer wavelengths. Specifically between 5.5 μm and 7.0 μm, and at wavelengths $>$ 27 μm.

3) Carbon dioxide mainly absorbs in the mid- and far-infrared, but it's contribution is not as important as water.

Water is the most constraining molecule to perform observations in the infrared and millimeter. Unfortunately, 99 % of the water vapour is located in the troposphere which has an average altitude of $\sim$ 13 km. For observations in the infrared, it is thus recommended to observe from space or at least from the stratosphere to avoid most water vapor in the atmosphere. Infrared observations will thus be carried out from space (e.g. Spitzer Space Telescope, *Herschel* Space Telescope), from a stratospheric airplane (SOFIA) or from instruments on high-altitude balloons (e.g. BLAST). At submillimeter wavelengths, water vapor becomes less disturbing. Consequently, it is possible to observe in important spectral windows between 0.5 and 1 mm from dry places at high altitude. Studies have been carried out to determine dry places with low water vapor based on satellite data of the atmosphere. One of the primary locations with low water vapor over most of the year is around the Chajnantor plateau in the Atacama desert (Tremblin et al., 2012). This is why several telescopes are located there or under construction such as the Atacama Large Millimeter Array (ALMA), the Atacama Pathfinder Experiment (APEX), the NANTEN2 observatory and the Cerro Chajnantor Atacama Telescope (CCAT-p).

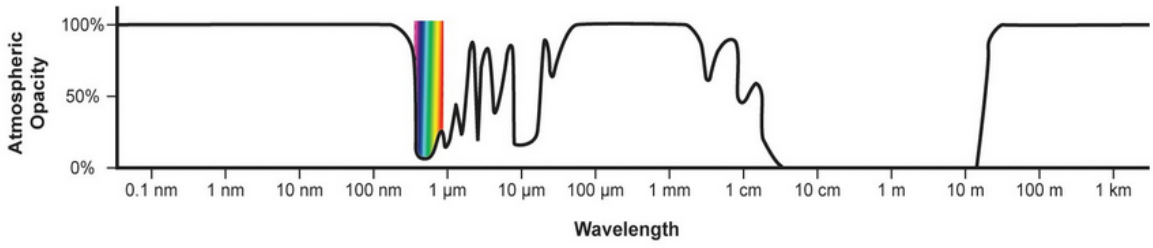

Figure 3.7: The absorption percentage by the earth atmosphere at sea level as a function of wavelength. Strong absorption happens for long radio wavelengths ($>$ 10 m), in the infrared, and for ultraviolet, X-ray and gamma ray radiation. This figure was adapted from Wikipedia.

3.4.2 Single dish observations

Both refracting and reflecting telescopes can be used for astronomical observations. The refracting telescope makes use of a lens system and was for a long time a primary instrument for optical observations. However, in modern astronomy the refracting telescope has been replaced by the reflecting telescope which allows for a much larger light collecting area to observe fainter objects. In a reflecting telescope, the primary mirror is a large dish that collects the incident radiation and sends it to the secondary mirror. This secondary mirror focusses the collected light to the focal plane where the receiver is located, see Fig. 3.8. For a circular reflecting telescope, the maximal resolution is a function of the reflector/dish size and the observed wavelength because of the diffraction of light. The resulting maximal resolution is given by

$$\mathrm{R} = 1.22\frac{\lambda}{\mathrm{D}} \tag{3.5}$$

With D the diameter of the dish, and λ the observed wavelength.
There is a vast diversity of reflecting telescope types. It is not aimed to be comprehensive here, but the major types of reflecting telescopes are presented in Fig. 3.8:
- A Newtonian telescope consists of a primary mirror and a flat secondary mirror which reflects the light to a focal plane near the top of the telescope.
- A Gregorian telescope has a primary mirror with a hole at its center. This hole is the location where the concave secondary mirror focusses the observed emission.
- A Cassegrain telescope also contains a hole at the center of the primary mirror. The incoming light is focussed in this hole by the hyperbolic secondary mirror. This designs allows to increase the focal length of the telescope.
- The Nasmyth telescope resembles the Cassegrain telescope, but has a third mirror which reflects the light to the side of the telescope.

To perform observations with a reflecting dish, the dish needs to have the smallest possible defects, because the gain of the telescope (G) is related to the rms of the dish imperfections (ϵ) and the observed

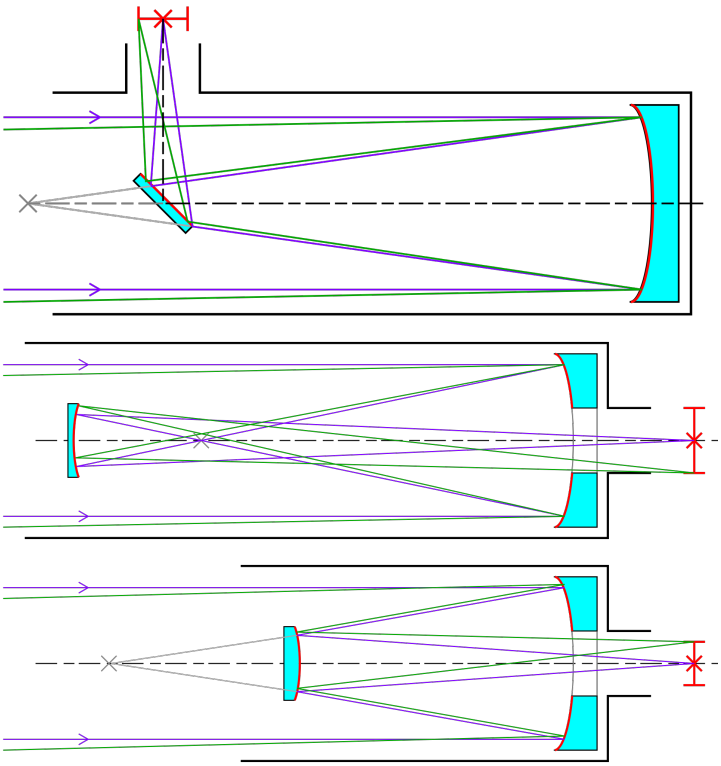

Figure 3.8: **Top:** A sketch of a Newtonian type reflecting telescope. **Middle:** The same for a Gregorian telescope. **Bottom:** The same for a Cassegrain telescope. These figures were adapted from Wikipedia.

wavelength (λ) as was demonstrated by Ruze (1952). This relation is given by

$$G(\epsilon) = G_0 e^{-(\frac{4\pi\epsilon}{\lambda})^2} \tag{3.6}$$

with G_0 the gain of the antenna in the absence of imperfections. When observing longer wavelengths, a larger surface error rms is allowed to maintain a good antenna gain. This dependence of the gain, the so-called Ruze factor, on the observed wavelength and surface imperfections at the wavelengths covered by the APEX telescope (Güsten et al., 2006) is demonstrated in Fig. 3.9.

Heterodyne observations

Ground based spectral observations in the radio and (sub)millimeter domains are generally carried out with heterodyne receivers such as PI230 and FLASH$^+$ (Klein et al., 2014) on APEX, because it allows a high spectral resolution (< 0.1 km s^{-1} at (sub)mm wavelengths). This technology uses frequency mixing of the received signal with a second signal provided by a local oscillator (LO) to convert the received signal to an intermediate frequency (IF) which makes the later signal processing easier.
A consequence of the heterodyne technology is the generation of the image frequency ($f_{\rm im}$), which is a

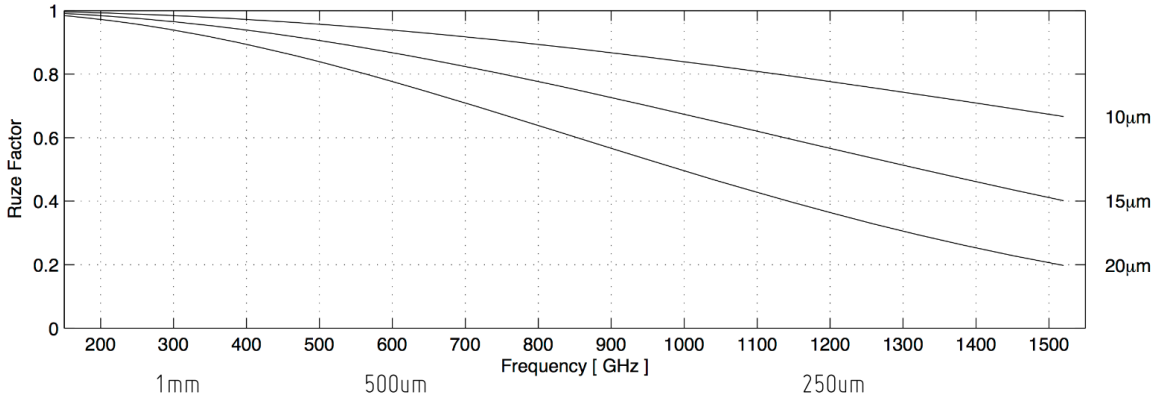

Figure 3.9: The Ruze factor ($e^{-(\frac{4\pi\epsilon}{\lambda})^2}$) as a function of frequency for three surface rms values (10, 15 and 20 μm) for the submillimeter and far-infrared wavelengths covered by the APEX telescope. This figure was adapted from Parra (2018).

signal at plus or minus twice the IF

$$f_{\rm im} = \begin{cases} \mathrm{f+2f_{IF}}, & \text{if } f_{\rm LO} > f \\ \mathrm{f-2f_{IF}}, & \text{if } f_{\rm LO} < f \end{cases} \tag{3.7}$$

If the signal at the image frequency can be suppressed, it is possible to simultaneously observe the original incoming radiation at the image frequency as well. However, when observing bright lines it should always be checked if there is the presence of emission in the image band because of insufficient attenuation of the generated image signal.

Bolometer observations

If spectral resolution is not important, e.g. to study the dust continuum emission, bolometer observations can be used in the submm and far infrared wavelength ranges. Examples of bolometers are the PACS (Poglitsch et al., 2010) and SPIRE (Griffin et al., 2010) receivers on the *Herschel* Space Telescope (Pilbratt et al., 2010). A bolometer uses a material with a varying resistance as a function of the temperature, which allows to measure the incident radiation. A bolometer is thus essentially a thermometer. Because of this it has to be cooled to extremely low temperatures ($\ll$ 1 K) to avoid contamination of the observations.

Antenna and main beam temperatures

The observed part of the sky emits energy that results in a flux (S_ν) that will be collected by the telescope receiver. The flux of a source is obtained by integrating its specific intensity (I_ν) over the solid angle (Ω) of the source. This specific intensity is expressed in W m^{-2} Hz^{-1} sr^{-1}, and is used in particular when the source is resolved. The flux of a source in the sky is generally very weak in radio-

and (sub)millimeter astronomy. Because of this, the flux is expressed in the Jansky unit (Jy) which corresponds to 10^{-26} W m^{-2} Hz^{-1}. The specific intensity at a location in the sky can be related to the radiation temperature in Kelvin (K), which is the unit that is generally used for observations in the radio and (sub)mm domain. Under local thermal equilibrium (LTE), the specific intensity for a temperature T at frequency ν is given by

$$\mathrm{B}_\nu(\mathrm{T}) = I_\nu = \frac{2\mathrm{h}\nu^3}{\mathrm{c}^2}\frac{1}{\mathrm{e}^{\mathrm{h}\nu/\mathrm{kT}} - 1} \tag{3.8}$$

with h the Planck constant, k the Boltzmann constant and c the speed of light. When considering long wavelengths with respect to the temperature (i.e. $\mathrm{h}\nu \ll \mathrm{kT}$), one can work under the Rayleigh-Jeans approximation, which is given by Taylor expansion of the factor $e^{h\nu/kT}$ ($\approx 1 + \mathrm{h}\nu/\mathrm{kT} + ...$)

$$\mathrm{B}_\nu(\mathrm{T}) \approx \frac{2\mathrm{h}\nu^3}{\mathrm{c}^2}\frac{1}{(1 + \mathrm{h}\nu/\mathrm{kT}) - 1} = \frac{2\nu^2\mathrm{kT}}{\mathrm{c}^2} \tag{3.9}$$

Under the Rayleigh-Jeans limit there is a direct relation between the radiation temperature and the specific intensity. Converting the expression above to wavelength, the following relation for the radiation temperature is obtained

$$\mathrm{T_b} = \frac{\lambda^2}{2\mathrm{k}}\mathrm{I}_\nu \tag{3.10}$$

The observational output of a telescope is given by the antenna temperature ($\mathrm{T_A^*}$) and can be converted to the main beam temperature ($\mathrm{T_{mb}}$), by $\mathrm{T_{mb}} = \eta_{\mathrm{for}}/\eta_{\mathrm{mb}}\mathrm{T_A^*}$. With η_{for} the forward efficiency, and η_{mb} the main beam efficiency of the telescope. To calibrate the main beam efficiency in the (sub)millimeter domain, observations of solar system planets (e.g. Mars and Uranus) are compared with models of their brightness, which usually have uncertainties smaller than 5%[2]. In the case of the APEX telescope, Mars and Uranus are representative calibrators for the point source main beam efficiency in the covered frequency range because they have a typical source size (θ_s) of $4''$. Jupiter on the other hand, with $\theta_\mathrm{s} \sim$ 30-40$''$, is a better calibrator for extended sources. While performing astronomical observations, one also has to verify the focus and pointing accuracy of the telescope using a reference source to make sure that the observations are trustworthy. Regularly calibrating the focus is in particular important when there are rapid temperature variations as this can have an effect on the reflector.

Receiver noise and calibration

Radio and (sub)mm sources are extremely weak, which is why the incoming signal has to be amplified. To calibrate the receiver noise, the relation between the increase in noise temperature and the increase in receiver output has to measured. This is done with the so-called $'$hot-cold$'$ load, where the receiver output is measured for input by two resistive loads at fixed temperatures $\mathrm{T_H}$ (hot) and $\mathrm{T_C}$ (cold). Generally $\mathrm{T_H}$ works at the ambient temperature ($\sim$ 293 K) and $\mathrm{T_C}$ at the temperature of liquid nitrogen ($\sim$ 78 K). If the receiver output is $'z'$, this allows to determine the receiver noise as follows

$$\begin{aligned} z_\mathrm{H} &= (T_\mathrm{H} + T_\mathrm{rx})G \\ z_\mathrm{C} &= (T_\mathrm{C} + T_\mathrm{rx})G \end{aligned} \tag{3.11}$$

[2]http://www.apex-telescope.org/telescope/efficiency/index.php

with T_{rx} the receiver noise temperature and G the gain. Then using ($y = z_H/z_C$), the receiver temperature can be calculated with

$$T_{rx} = \frac{T_H - yT_C}{y - 1} \tag{3.12}$$

The receiver noise is generally one of the most important noise contributors together with noise from the atmosphere. All the noise contributions can be added together resulting in

$$T_{sys} = \Sigma_i T_i \tag{3.13}$$

where T_i are the individual noise contributions. From this sum of noise contributors, the root mean square (RMS) noise can be calculated for the observation time τ within a fixed frequency interval ($\Delta\nu$) with the following equation

$$\Delta T_{RMS} = \frac{T_{sys}}{\sqrt{\tau \Delta\nu}} \tag{3.14}$$

Depending on the necessary RMS of the observations, this allows to estimate the required observation time.

Interferometers

Increasing the reflector size of a telescope becomes increasingly difficult, which limits the angular resolution of single dish telescopes. In order to increase the angular resolution one can make use of interferometers such as ALMA, the Very Large Array (VLA) or the Square Kilometre Array (SKA) which is under construction. An interferometer consists of multiple mirrors whose received signals are combined. The distance between each pair of mirrors in an interferometer is called a baseline. The maximal angular resolution of an interferometer is related to its maximal baseline. Interferometry can increase the angular resolution of observations by increasing the maximal baseline, but it also filters out extended emission. The maximal angular size of the extended emission that can be recovered is related to the minimal baseline of the interferometer. However, interferometric observations are not used in this thesis, such that this type of telescopes will not be discussed in more detail.

3.4.3 Radiation in the ISM

For telescopes to observe emission from interstellar gas, radiation eventually has to escape from a specific region in our direction. This is not necessarily a trivial problem, and requires an understanding of radiative transfer in interstellar clouds. First of all, the observed emission from an interstellar cloud can be separated into continuum and spectral line emission.
Continuum emission in the (sub)mm and far infrared is coming from dust emission. However, at longer wavelengths the free-free emission from the interaction between charged particles and synchotron emission from the interaction of charged particles with the magnetic field also contribute to the continuum emission.
To produce spectral line emission, atoms and molecules have to populate their different energy levels. When an electron makes the transition to a lower energy level, this is accompanied by the emission of a photon that carries the transition energy. Because of Doppler broadening due to thermal and turbulent motions of the atoms and molecules, the observed spectral line for each transition will show

line broadening. The population of different energy levels in atoms and molecules can happen through radiative and collisional excitation.

Spectral line excitation conditions

Because the ISM is not in thermal equilibrium, there are two situations to describe the excitation conditions of molecules and atoms in the ISM. Namely local thermal equilibrium (LTE) and non-local thermal equilibrium (non-LTE).

LTE is the situation where thermal equilibrium is not valid for the full system but only at a local level. This implies that the molecules are mainly excited by collisional excitation. The collisional partner of molecules in the ISM is generally molecular hydrogen, while molecular hydrogen, atomic hydrogen and sometimes electrons are the main collisional partners for atoms. LTE description of an observed transition thus requires that the molecule is excited in a region with a sufficiently high density. The required density for LTE depends on the observed molecule, transition and temperature. Specifically, the density must be above the critical density (n_c) which is defined by

$$n_c = \frac{A_{ul}}{\gamma_{ul}} \tag{3.15}$$

where A_{ul} is the coefficient which gives the rate of spontaneous light emission by an atom or molecule, and $n \times \gamma_{ul}$ gives the collisional rate out of level u to level l. γ_{ul} will be described in more detail later on.
When the atomic or molecular transition happens at a density below n_c, the non-LTE regime applies. The methods to analyse observations in the non-LTE regime will be addressed in a later section.

Radiative transfer equations

When describing the radiative transfer in the ISM, we can start from the specific intensity (I_ν) which is defined by the energy (dE) per unit time (dt) per unit frequency ($d\nu$) from a solid angle ($d\Omega$) passing through a surface area (dA). In an equation this is described by

$$I_\nu = \frac{dE}{dt\ dA\ d\nu\ d\Omega} \tag{3.16}$$

In this equation, the solid angle specifies the propagation direction of the radiation. As already mentioned in section 3.4.2, the specific intensity is often expressed in W m^{-2} Hz^{-1} sr^{-1} (or Jy sr^{-1}).
First, the situation sketched in Fig. 3.10 will be considered where there is no emission and absorption on the path of the light from a surface dA1 to dA2 over a path length R between the two surfaces. Because there is no emission and absorption, $dE_1 = dE_2$. This implies

$$I_{\nu,1}\ dA_1\ d\nu_1\ d\Omega_1\ dt = I_{\nu,2}\ dA_2\ d\nu_2\ d\Omega_2\ dt \tag{3.17}$$

Here, $d\Omega_1$ is the solid angle of dA_2 at dA_1, so $d\Omega_1 = dA_2/R^2$. Similarly we get $d\Omega_2 = dA_1/R^2$. Taking into account that there is no change in frequency, we get that the specific intensity is a conserved

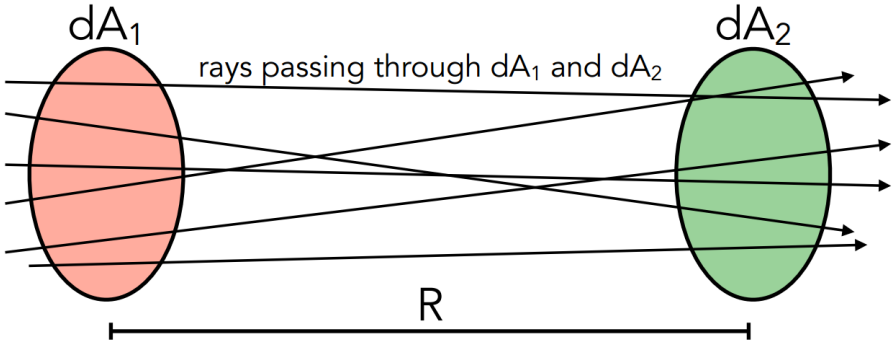

Figure 3.10: A sketch, to illustrate Eq. 3.17, of light ray propagation from a surface dA_1 to dA_2 over a distance R in a medium without emission or absorption.

quantity ($I_{\nu,1} = I_{\nu,2}$) over distance R.

Now consider that propagating radiation encounters a gas layer in the ISM with a path length ds and an optical depth $d\tau$, see Fig. 3.11. The incident specific intensity is given by I_ν, and the specific intensity at the other side of the layer is given by $I_\nu + dI_\nu$. Then, one can describe the change in specific intensity as follows

$$dI_\nu = -I_\nu \kappa_\nu ds + j_\nu ds = -I_\nu d\tau_\nu + j_\nu ds \tag{3.18}$$

With κ_ν the attenuation coefficient at the frequency ν, and j_ν the local emissivity. Defining the specific intensity of the gas parcel as $S_\nu = j_\nu/\kappa_\nu$, we get

$$\frac{dI_\nu}{d\tau_\nu} = -I_\nu + S_\nu \tag{3.19}$$

Integrating the equation up to a distance s, gives

$$I_\nu(s) = I_\nu(0)e^{-\tau_\nu} + \int_0^s S_\nu e^{-\tau_\nu} \kappa_\nu ds \tag{3.20}$$

In the case where S_ν is a constant $S_{\nu,0}$, we get the following solution

$$I_\nu(s) = I_\nu(0)e^{-\tau_\nu} + S_{\nu,0}(1 - e^{-\tau_\nu}) \tag{3.21}$$

When $\tau_\nu \ll 1$, we are in the optically thin case where $I_\nu(s) \approx I_\nu(0) + \tau S_\nu$. If $\tau_\nu \gg 1$, we are in the optically thick case where $I_\nu(s) \approx S_\nu$

Line radiative transfer simulations

To investigate the observed emission, codes that model the radiative transfer in the ISM can provide valuable information on the excitation conditions. Here, we will focus on non-LTE line radiative transfer.

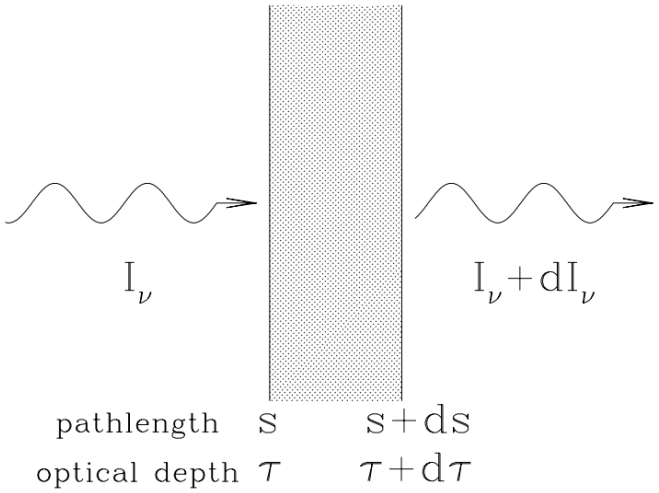

Figure 3.11: A sketch of incident radiation (I_ν) propagating through an emitting and absorbing gas layer.

There is a variety of non-LTE codes that take into account collisional data such as RADEX (van der Tak et al., 2007), the code used in Keto et al. (2004), RATRAN (Hogerheijde & van der Tak, 2000), Simline (Ossenkopf, Trojan & Stutzki, 2001), LIME (Brinch & Hogerheijde, 2010) or PYRATE (Tritsis, Yorke & Tassis, 2018). We will not go into the details of all codes, and rather focus on the RADEX code (van der Tak et al., 2007) which will be used in this thesis. RADEX is easy to use and allows to constrain important quantities such as the kinetic temperature, density and column density based on the observation of multiple lines. RADEX uses the information on atomic and molecular excitation from the Leiden Atomic and Molecular Database (LAMBDA) (Schöier et al., 2005) to predict the observed line brightness for specific excitation conditions. For these calculations, it starts from a uniform gas distribution which is either a spherical one or a layer. The input for the program consists of the background temperature (which is generally fixed at the cosmic microwave background of 2.73 K), the kinetic temperature, the H_2 density, the column density of the molecule and the linewidth.
RADEX works based on the following formalism as described in van der Tak et al. (2007). A molecule or atom is considered with multiple energy levels. The spontaneous emission rate from the upper level (u) to a lower level (l) is denoted by A_{ul}, the Einstein coefficients for the stimulated transitions are given by B_{ul} and B_{lu}, and the collisional rate is denoted as C_{ul} and C_{lu} and defined by

$$C_{ul} = n_{col}\gamma_{ul} \tag{3.22}$$

with n_{col} the number density (in cm^{-3}) of the collisional particles which are generally H_2. γ_{ul} is the collisional rate coefficient, which is described by the average of the collisional cross section times the collision velocity distribution of the particles (described by the Maxwell-Boltzmann distribution)

$$\gamma_{ul} = \left(\frac{8kT_{kin}}{\pi\mu}\right)^{-1/2} (kT_{kin})^{-2} \int \sigma E e^{-E/kT_{kin}} dE \tag{3.23}$$

Here, σ is the collisional cross section, E the collision energy, T_{kin} the kinetic temperature and μ the reduced mass. Consequently, the upward collisional rates are given by

$$\gamma_{lu} = \gamma_{ul} \frac{g_u}{g_l} e^{-h\nu/kT_{kin}} \tag{3.24}$$

with g the statistical weight of each energy level.
The local emissivity in Eq. 3.18 is defined by

$$j_\nu = \frac{h\nu n_u}{4\pi} A_{ul} \phi_\nu \tag{3.25}$$

with n_u the number density of the molecule (or atom) in this energy level, and ϕ_ν the line profile which is described by a gaussian.
The absorption coefficient α_ν is described by

$$\alpha_\nu = \frac{h\nu}{4\pi} \left(n_l B_{lu} \psi_\nu - n_u B_{ul} \chi_\nu \right) \tag{3.26}$$

where ψ_ν and χ_ν are the line profiles associated with absorption and stimulated emission, but RADEX works on the assumption that $\phi_\nu = \psi_\nu = \chi_\nu$ which implies full angular emission of the photons. ϕ_ν is given by

$$\phi_\nu = \frac{1}{\nu_D \sqrt{\pi}} \exp \left[- \left(\nu - \nu_{ul} - \mathbf{v} \cdot \mathbf{n} \frac{\nu_{ul}}{c} \right)^2 / \nu_D^2 \right] \tag{3.27}$$

with ν_D the width, $\mathbf{v}$ the velocity of the gas responsible for the scattering and $\mathbf{n}$ the propagation direction of the radiation. From this profile the full width at half maximum (Δv) is then defined. Working under this assumption ($\phi_\nu = \psi_\nu = \chi_\nu$) gives the following result

$$S_\nu = \frac{n_u A_{ul}}{n_l B_{lu} - n_u B_{ul}} \tag{3.28}$$

Then using $B_{ul} g_u = B_{lu} g_l$ and $A_{ul}/B_{ul} = \frac{2h\nu^3}{c^2}$ we get

$$S_\nu = \frac{2h\nu^3}{c^2} \left(\frac{g_u n_l}{g_l n_u} - 1 \right)^{-1} \tag{3.29}$$

To be able to describe the specific intensity from the source (S_ν) by the specific intensity of a blackbody $B_\nu(T_{ex})$ at an excitation temperature T_{ex}, the excitation temperature is defined by

$$\frac{n_u}{n_l} = \frac{g_u}{g_l} e^{-(E_u - E_l)/kT_{ex}} \tag{3.30}$$

When describing regions where LTE is not applicable, statistical equilibrium (SE) is often applicable. SE is used in RADEX, and is described by

$$\frac{dn_i}{dt} = 0 = \sum_{j \neq i}^{N} n_j P_{ji} - n_i \sum_{j \neq i}^{N} P_{ij} \tag{3.31}$$

with P_{ij} described by

$$\begin{aligned} P_{ij} &= A_{ij} + B_{ij}J_\nu + C_{ij} \quad (j < i) \\ P_{ij} &= B_{ij}J_\nu + C_{ij} \quad (i < j) \end{aligned} \tag{3.32}$$

with J_ν the specific intensity integrated over a solid angle.
From the populations of the different energy levels one can work to calculate the observed brightness. For this, the escape of photons from the observed gas has to be calculated, where one needs to consider the interplay of the population in each energy level and the radiation in the gas. Solving this requires an iterative approach, which is however simplified for RADEX because the code only considers homogeneous structures with a simple geometry. Because of this, the escape probability β of a photon can be introduced, which is related to the optical depth τ. In a spherical geometry, the relation between β and τ is given by (Osterbrock & Ferland, 2006)

$$\beta = \frac{1.5}{\tau}\left(1 - \frac{2}{\tau^2} + \left(\frac{2}{\tau} + \frac{2}{\tau^2}\right)e^{-\tau}\right) \tag{3.33}$$

Combining the above equations in this section, we get the following expression for the opacity

$$\tau = \frac{c^3}{8\pi\nu^3}\frac{A_{ul}N}{1.064\Delta V}\left(x_l\frac{g_u}{g_l} - x_u\right) \tag{3.34}$$

where N is the column density of the molecule or atom under study, and x_u and x_l the fraction of molecules that is in the specific energy level. In RADEX, the calculation of the statistical equilibrium is done iteratively starting from the optically thin case and gives the radiation temperature in the Rayleigh-Jeans limit.

Chapter 4

Dense gas formation in the Musca cloud

4.1 Low-velocity shocks as indicators for mass accretion in Musca

4.1.1 The Musca cloud

To understand how low-mass star forming filaments form, and how they interact with the ambient cloud, the studied clouds should be free from feedback associated with the star formation process. This is particularly important when investigating whether low-velocity shocks play a role in the dense gas formation process, because other heating processes such as FUV radiation and protostellar outflows make it increasingly difficult to confidently establish the heating source (Pon et al., 2016).
An interesting molecular cloud that is not yet affected by (proto)stellar feedback, is the Musca cloud in the Chamaeleon-Musca complex, see Fig. 4.1. The Musca cloud is expected to be at an early evolutionary stage with only one young stellar object that is located in the far north of the prominent Musca filament (e.g. Vilas-Boas, Myers & Fuller, 1994; Kainulainen et al., 2016). This early stage of evolution is also supported by indications that the filament is just starting to fragment in prestellar cores (Kainulainen et al., 2016; Machaieie et al., 2017). Furthermore, the cloud has no nearby ionising massive stars. This lack of stellar feedback makes Musca an ideal molecular cloud to study the presence of low-velocity shocks in the ISM because there is no other evident heating mechanism in the cloud. The prominent Musca filament also has a large aspect ratio which makes it a prototypical dense filament without further velocity substructure (Hacar et al., 2016; Cox et al., 2016). It is thus an interesting and relatively simple target to study the possible role of low-velocity shocks in the formation of dense star forming filaments.
The Musca cloud is a relatively isolated part of the nearby (140-180 pc) Chamaeleon-Musca complex (e.g. Franco, 1991; Whittet et al., 1997; Mizuno et al., 2001; Planck Collaboration et al., 2015; Liszt, Gerin & Grenier, 2019; Zucker et al., 2019), such that it basically has no contamination in the line of sight. Musca is one of the four prominent dense regions of the Chamaeleon-Musca complex: Chamaeleon I (Cha I), Chamaeleon II (Cha II), Chamaeleon III (Cha III) and Musca. In this complex, Cha III and Musca are two clouds with little or no indication of active star formation (e.g. Persi et al., 2003; Luhman, 2008; Kainulainen et al., 2009; Belloche et al., 2011a), while Cha I and Cha II are actively forming stars (e.g. Mattila, Liljeström & Toriseva, 1989; Persi et al., 2003; Luhman & Muench, 2008). The Cha I cloud was even proposed to be near the end of its star formation activity (Belloche et al.,

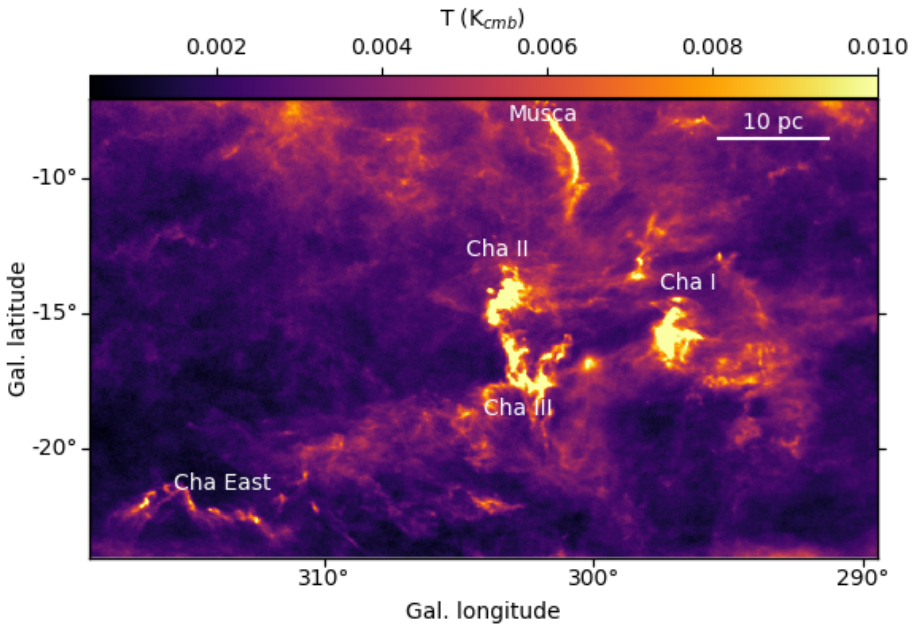

Figure 4.1: The Chamaeleon-Musca complex seen at 353 GHz with the Planck telescope. The location of the dense regions of this complex (Cha I, Cha II, Cha III, Musca and Cha East) are indicated with their name.

2011b). In the east of Chameaeleon-Musca there is a less prominent region (Cha East) which also contains molecular gas that is detected with CO (Mizuno et al., 2001).

4.1.2 Low-velocity shocks in molecular clouds

To investigate the presence of low-velocity shocks in the ISM ($v_{shock} < 4$ km s^{-1}), it is generally proposed by theoretical models to observe high-J CO lines ($J_{up} \geq 6$) for a straightforward analysis (e.g. Pon, Johnstone & Kaufman, 2012; Lehmann & Wardle, 2016). The warm and dense gas layer produced by a low-velocity shock will increase the intensity of these higher-J CO lines. This increased intensity of the high-J CO lines will be observed as an excess, based on the expected results from heating by the FUV field, when comparing with the intensity of the lower-J CO lines ($J \leq 3$). Comparing the observed intensity of several mid- and high-J lines with shock models can then help to constrain the physical properties of the shock (Pon et al., 2016). Some low-velocity shock models also take into account an important cooling contribution from the atomic oxygen [OI] transitions (Draine, Roberge & Dalgarno, 1983) since it is currently not clear where most of the oxygen is located in the ISM.

Often, low-velocity shocks are subdivided in J- and C-shocks. A J-shock is dissipated by a sudden velocity and density transition (e.g. Hollenbach & McKee, 1989), while C-shocks, which are generally modelled with shock propagation perpendicular to the magnetic field, are continuously dissipated by ion-neutral friction (e.g. Draine, 1980). However, when considering the more general situation where

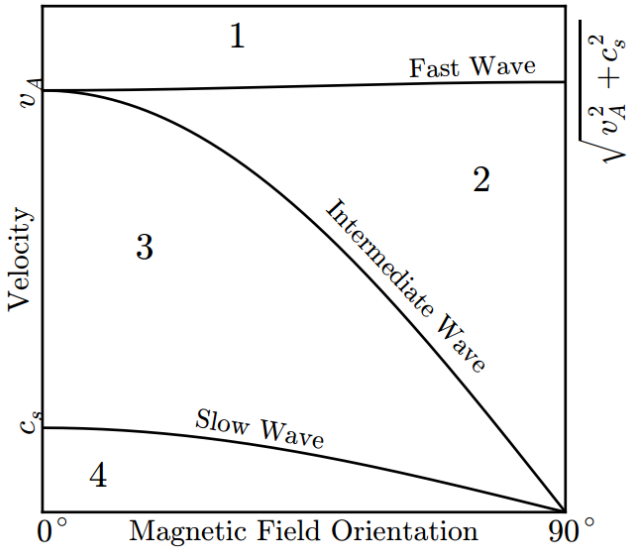

Figure 4.2: The three supported phase velocity curves as a function of the angle between the propagation direction and the magnetic field orientation. These curves separate the velocity space in 4 regions indicated with the numbers 1-4. This figure was adapted from Lehmann & Wardle (2016).

the magnetic field is not necessarily perpendicular to the shock front propagation, one can differentiate three types of shocks in the magnetised ISM. The slow, intermediate and fast type shocks (de Hoffmann & Teller, 1950; Kennel, Blandford & Coppi, 1989; Lehmann & Wardle, 2016). This is related to the fact that preshock gas with a velocity v_{shock} in ideal MHD will experience a transition to a velocity below one of the three supported linear wave phase velocities (fast, intermediate and slow)

$$\begin{aligned} v_f &= \left(\frac{v_A^2 + c_s^2}{2} + 0.5\sqrt{(v_A^2 + c_s^2)^2 - 4v_A^2 c_s^2 \cos^2\theta} \right)^{1/2} \\ v_i &= v_A \cos\theta \\ v_s &= \left(\frac{v_A^2 + c_s^2}{2} - 0.5\sqrt{(v_A^2 + c_s^2)^2 - 4v_A^2 c_s^2 \cos^2\theta} \right)^{1/2} \end{aligned} \tag{4.1}$$

with $\mathrm{v}_A = \frac{B}{4\pi\rho}$ the Alfvén speed, $\mathrm{c}_s = \sqrt{\frac{k_B T}{m}}$ the sound speed and θ the angle between the propagation direction of the wave and the magnetic field. Figure 4.2 shows that these three supported phase velocities separate the velocity space in 4 regions (indicated by 1, 2, 3 and 4 in the figure). This results in 6 possible velocity transitions that allow to separate fast, intermediate and slow type shocks. When the transition only passes the fast wave velocity (1→2) we talk of a fast shock. An intermediate shock crosses the intermediate wave velocity (1→3, 1→4, 2→3 and 2→4), while a slow shock only crosses the slow shock velocity (3→4). Consequently, a fast type shock needs a preshock velocity higher than the Alfvén speed, while a slow type shock has a preshock velocity below the Alfvén speed. In the case of

a fast shock, the heating can be controlled by ion-neutral friction leading to the formation of C-type shocks. However, when the velocity of a fast type shock is higher than the magnetosonic sound speed of the charged gas, the ion-neutral friction can no longer smooth the shock such that it will resemble a J-shock. In the case of a slow type shock, the shock evolution is driven by the neutral gas pressure such that it resembles a J-shock.
It is important to be aware of these different types of shocks, since a focus on these different shock types with simulations of the ISM has indicated that a combination of slow and fast magnetised shocks can play a role in the evolution of the magnetised molecular clouds (Lehmann, Federrath & Wardle, 2016; Park & Ryu, 2019; Lesaffre et al., 2020).

With the HIFI spectrometer (de Graauw et al., 2010) on the *Herschel* Space Telescope, some early studies have been performed to search for mid- and high-J CO excess emission that could be associated with low-velocity shocks in the ISM. Evidence of excess emission in molecular clouds has been found towards Perseus (Pon et al., 2014), Taurus (Larson et al., 2015), and two infrared dark clouds (G028.37+00.07 and G034.43+00.07) (Pon et al., 2015). This excess emission was interpreted as a result of shock dissipation of generic turbulent motions. In Pon et al. (2016), the observed high-J CO lines towards the infrared dark clouds were directly compared with predictions from low-velocity C-shock models from Pon, Johnstone & Kaufman (2012). This suggested shocks with a high preshock density ($n \sim 10^{4.5}$ cm^{-3}), but it was noted in Pon et al. (2016) that it was difficult to exclude that this excess is the result of protostellar feedback.

Inspecting shock models (Pon, Johnstone & Kaufman, 2012; Lehmann & Wardle, 2016) it is found that analysing the ratio of mid-J CO lines starting at ^{12}CO(4-3) over low-J CO lines could be sufficient to differentiate shock excitation from heating by a FUV field. This is because of the relatively high energy of the upper level (55 K) of this line and the possibly strong heating in the ISM by very low-velocity shocks. With current telescopes, ^{12}CO(4-3) is most easily accessible for a pilot study that does not require too much time to search for possible shock excitation. This is why ^{12}CO(4-3), ^{12}CO(3-2) and ^{12}CO(2-1) observations were carried out with the APEX telescope towards two locations in the Musca cloud, complemented with [CII] (158 μm) and [OI] (63 μm) observations by the SOFIA telescope. The observation of the [CII] line is particularly important to constrain heating by the FUV field. If the [OI] line would be detected, the observations would indicate the presence of strong heating by a shock and a large atomic oxygen reservoir in the ISM because both [OI] lines (at 146 μm and 63 μm) are particularly difficult to excite in molecular clouds.

4.1.3 Article: Dense gas formation in the Musca filament due to the dissipation of a supersonic converging flow (Paper-MS)

A&A 641, A17 (2020)
https://doi.org/10.1051/0004-6361/201937104

Astronomy & Astrophysics

Dense gas formation in the Musca filament due to the dissipation of a supersonic converging flow⋆

L. Bonne[1], N. Schneider[2], S. Bontemps[1], S. D. Clarke[2], A. Gusdorf[3,4], A. Lehmann[3], M. Steinke[2], T. Csengeri[1,5], S. Kabanovic[2], R. Simon[2], C. Buchbender[2], and R. Güsten[5]

[1] Laboratoire d'Astrophysique de Bordeaux, Université de Bordeaux, CNRS, B18N, allée Geoffrey Saint-Hilaire, 33615 Pessac, France
e-mail: lars.bonne@u-bordeaux.fr
[2] I. Physikalisches Institut, Universität zu Köln, Zülpicher Str. 77, 50937 Köln, Germany
[3] Laboratoire de Physique de l'École Normale Supérieure, ENS, Université PSL, CNRS Sorbonne Université de Paris, Paris, France
[4] Observatoire de Paris, PSL University, Sorbonne Université, LERMA, 75014 Paris, France
[5] Max-Planck-Institut für Radioastronomie, Auf dem Hügel 69, 53121 Bonn, Germany

Received 13 November 2019 / Accepted 22 June 2020

ABSTRACT

Observations with the *Herschel* Space Telescope have established that most star forming gas is organised in filaments, a finding that is supported by numerical simulations of the supersonic interstellar medium (ISM) where dense filamentary structures are ubiquitous. We aim to understand the formation of these dense structures by performing observations covering the ^{12}CO(4→3), ^{12}CO(3→2), and various CO(2–1) isotopologue lines of the Musca filament, using the APEX telescope. The observed CO intensities and line ratios cannot be explained by PDR (photodissociation region) emission because of the low ambient far-UV field that is strongly constrained by the non-detections of the [C II] line at 158 μm and the [O I] line at 63 μm, observed with the upGREAT receiver on SOFIA, as well as a weak [C I] 609 μm line detected with APEX. We propose that the observations are consistent with a scenario in which shock excitation gives rise to warm and dense gas close to the highest column density regions in the Musca filament. Using shock models, we find that the CO observations can be consistent with excitation by J-type low-velocity shocks. A qualitative comparison of the observed CO spectra with synthetic observations of dynamic filament formation simulations shows a good agreement with the signature of a filament accretion shock that forms a cold and dense filament from a converging flow. The Musca filament is thus found to be dense molecular post-shock gas. Filament accretion shocks that dissipate the supersonic kinetic energy of converging flows in the ISM may thus play a prominent role in the evolution of cold and dense filamentary structures.

Key words. ISM: individual objects: Musca – evolution – ISM: kinematics and dynamics – shock waves – turbulence – stars: formation

1. Introduction

Observations with the *Herschel* Space Telescope have revealed that filamentary structures are ubiquitous in the supersonic interstellar medium (ISM; e.g. André et al. 2010; Molinari et al. 2010; Henning et al. 2010; Arzoumanian et al. 2011; Schneider et al. 2012). However, there is an ongoing discussion regarding the nature and diversity of the filaments, namely, whether they are sheets viewed edge-on or, rather, dense gas cylinders. It is also considered whether we observe a full range of filament classes: from cross-sections of sheets to dense, star-forming cylindrical structures. In any case, understanding the nature, formation and evolution of filaments is essential as they are the sites of star formation. This was demonstrated by a number of recent studies which showed that pre- and protostellar cores are mostly located in filaments (e.g. Polychroni et al. 2013; André et al. 2014; Schisano et al. 2014; Könyves et al. 2015; Marsh et al. 2016; Rayner et al. 2017). In numerical simulations of the ISM, filaments are omnipresent and can form in various ways: through shocks in (magnetic) supersonic turbulent colliding flows (e.g. Padoan et al. 2001; Jappsen et al. 2005; Smith et al. 2016; Federrath 2016; Clarke et al. 2017; Inoue et al. 2018), during the global gravitational collapse of a cloud (Gómez & Vázquez-Semadeni 2014; Vázquez-Semadeni et al. 2019), through velocity shear in a magnetised medium (Hennebelle 2013), or via the gravitational instability of a sheet (Nagai et al. 1998).

However, it is challenging to find observational signatures that reveal how a filament is formed. In the view of large-scale colliding flows, filament formation is associated with the generation of warm gas from low-velocity shocks. An observational signature of these shocks are anomalously bright mid- and high-J CO lines, that is, line integrated intensities that are higher than expected considering only heating from the far-ultraviolet (FUV) field (e.g. Pon et al. 2012). Spectroscopic *Herschel* observations of such lines towards the Perseus and Taurus clouds detected this excess emission (Pon et al. 2014; Larson et al. 2015), where it was proposed to be the result of low-velocity shocks ($v_{\rm shock}$ < 4 km s^{-1}), dissipating the overall, generic supersonic turbulence of a molecular cloud.

In this paper, we report on the excess emission seen in mid-J ^{12}CO lines observed around the Musca filament and propose that in low- to moderate density regions, exposed to a very weak

⋆ The reduced datacubes and images are only available at the CDS via anonymous ftp to cdsarc.u-strasbg.fr (130.79.128.5) or via http://cdsarc.u-strasbg.fr/viz-bin/cat/J/A+A/641/A17

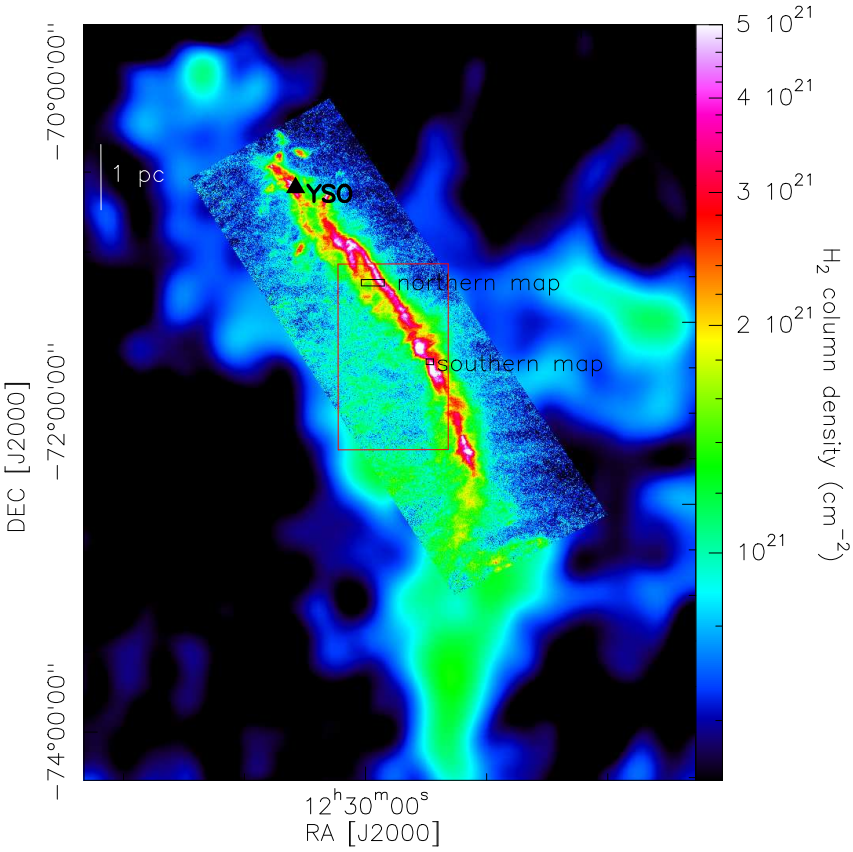

Fig. 1. *Herschel* column density map of the Musca filament (Cox et al. 2016) inserted into the extinction map of the Musca cloud (Schneider et al. 2011), which is scaled to the *Herschel* column density map. The filament crest is defined as $N > 3 \times 10^{21}$ cm^{-2} (purple and white). The region outlined by a red rectangle is the zoom displayed in Fig. 2. The ambient cloud is displayed in green and blue. The northern and southern areas mapped with FLASH+ on the APEX telescope are indicated in black. The triangle indicates the location of the only YSO in the Musca filament.

FUV field, these lines may also serve as a tracer for low-velocity shocks. The Musca filament is located at a distance of 140 pc (Franco 1991). We adopt the nomenclature from Cox et al. (2016) for the different features of the Musca filament and we indicate them in Fig. 2 (see also Fig. 2 in Cox et al. 2016). First, there is the high column density filament crest with $N > 3 \times 10^{21}$ cm^{-2} (similar value to the one used by Cox et al. (2016) which is $N > 2.7 \times 10^{21}$ cm^{-2}). In addition, C^{18}O(2–1) emission basically disappears below this column density value. Attached to the filament crest are intermediate column density ($N \sim 2 \times 10^{21}$ cm^{-2}) hair-like structures called strands, with a size of ~0.2–0.4 pc. Even further outwards at larger distances, narrow straight structures of up to a few parsec lengths, called striations (Goldsmith et al. 2008; Palmeirim et al. 2013; Alves de Oliveira et al. 2014; Heyer et al. 2016; Cox et al. 2016; Malinen et al. 2016) are seen. They are mostly orthogonal to the crest and located in the ambient cloud. The ambient cloud then refers to the environmental gas, traced by the extinction map in Fig. 1, embedding the denser Musca filament crest and strands. The filament crest is velocity-coherent (Hacar et al. 2016) and has only one young stellar object (YSO) located at the northern end (e.g. Vilas-Boas et al. 1994, Fig. 1). It was recently proposed that Musca is a sheet seen edge-on (Tritsis & Tassis 2018). However, one of the main results of a companion paper (Bonne et al., in prep., hereafter Paper I), is that the Musca filament crest is more consistent with a cylindrical geometry at a density of $n_{\mathrm{H_2}} \sim 10^4$ cm^{-3}. Because other authors (Cox et al. 2016; Kainulainen et al. 2016; Hacar et al. 2016) also support this cylindrical geometry, we adopt this view as a working hypothesis.

In Paper I, the large scale kinematics and physical conditions in the Musca filament and cloud are studied with the main

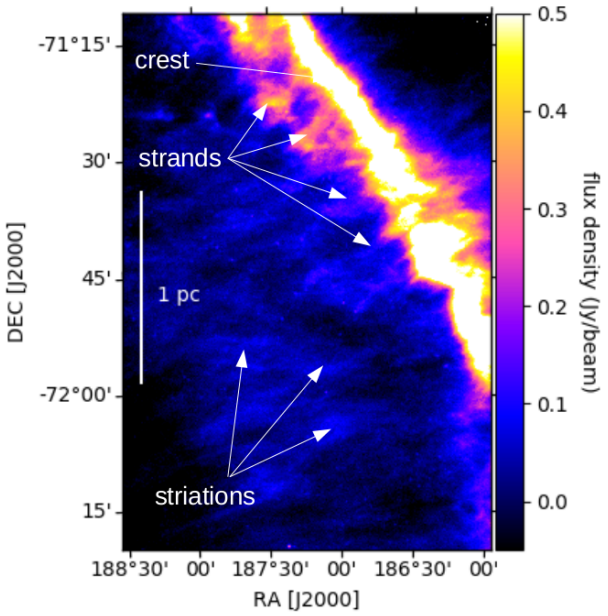

Fig. 2. Zoom (red box in Fig. 1) into the *Herschel* 250 μm map of Musca, indicating the striations, strands and the filament crest (Cox et al. 2016).

CO(2–1) isotopologues, as well as the relation between Musca and the Chamaeleon-Musca complex. In this paper, we present ^{12}CO(4–3) and ^{12}CO(3–2) lines and argue for the presence of

a blueshifted excess velocity component best visible towards the filament crest and strands. A detailed analysis of this 'blueshifted component' is the objective of this paper.

Here, we present a non-LTE CO excitation analysis of the blueshifted component, as well as complementary observations of the far-infrared fine structure transitions of carbon ([C I]), oxygen ([O I]) and ionised carbon ([C II]), which reveals a warm gas component around the filament. We show that the excitation of this warm gas can be explained by a filament accretion shock, that is, a low-velocity shock due to mass accretion on a filament from a converging flow in an interstellar cloud.

2. Observations

2.1. APEX

We used the FLASH460 receiver on the APEX telescope (Güsten et al. 2006; Klein et al. 2014), and obtained a single pointing in [C I] $^3P_1$-$^3P_0$ at 609 μm towards the Musca filament at α_{2000} = 12^{h}28^{m}55^s and δ_{2000} = −71°16′55″, using the OFF position α_{2000} = 12^{h}41^{m}38^s and δ_{2000} = −71°11′00″ (Hacar et al. 2016). The beamsize is 13″ and the spectral resolution is ∼0.05 km s^{-1}. The data reduction was done with the CLASS software[1]. A main beam efficiency[2] η_{mb} = 0.49 was applied for [C I], a baseline of order one was removed, and a correction for a 490 kHz shift in the FLASH460 instrument was performed (see Paper I, F. Wyrowski, priv. comm.). Fitting the [C I] single pointing (Fig. 3) with a Gaussian profile provides a peak temperature brightness T_{mb} = 3.5 K and $FWHM$ = 0.8 km s^{-1} (or 3.4×10^{-7} erg s^{-1} cm^{-2} sr^{-1}).

The CO observations with APEX are presented in more detail in Paper I, but here we shortly summarise the most important facts. All data was obtained in 2017 and 2018, using FLASH345 and FLASH460 for the ^{12}CO(3–2) and ^{12}CO(4–3) mapping of the northern and southern regions (Fig. 1). The FLASH345 (FLASH460) observations have a spectral resolution of 0.033 (0.05) km s^{-1} and an angular resolution of 18″ (14″). Main beam efficiencies of η_{mb} = 0.65 (0.49) were applied to the antenna temperatures. We here use data sampled to 0.1 km s^{-1} and smoothed to a resolution of 28″. This allows a better comparison to the CO(2–1) APEX data which were taken with the PI230 receiver. The spectral resolution for CO(2–1) is 0.08 km s^{-1} at an angular resolution of 28″. Here, we applied a main beam efficiency of η_{mb} = 0.68. The center (0,0) position of the maps is α_{2000} = 12^{h}28^{m}58^s, δ_{2000} = −71°16′55″ for the northern map and α_{2000} = 12^{h}24^{m}46^s, δ_{2000} = −71°47′20″ for the southern map.

2.2. SOFIA

In June 2018, the upGREAT instrument (Risacher et al. 2018) on the Stratopsheric Observatory for Far-Infrared Astronomy (SOFIA) was used for a 70 min single pointing of the 7 pixel array covering the atomic oxygen [O I] $^3P_1$-$^3P_2$ fine structure line at 63 μm and the ionised carbon [C II] $^2P_{3/2}$-$^2P_{1/2}$ fine structure line at 158 μm towards the southern APEX map at α_{2000} = 12^{h}24^{m}41^s.6, δ_{2000} = −71°46′41″.0. These observations were performed in the single beam switching mode with a chop amplitude of 150″ towards a location with weak or no emission in all *Herschel* far-infrared bands (70–500 μm). This was done to obtain a good baseline for such sensitive observations. Mars was used as a calibrator to determine the main beam efficiencies of the individual pixels. The fitted water vapor column was typically around 10 μm. All the intensities reported here are on the main beam temperature scale. The [O I] and [C II] observations have a main beam size of 6.3″ and 14.1″, respectively, and both data sets were smoothed to a spectral resolution of 0.3 km s^{-1}.

There is no detection of the [C II] and [O I] lines (Appendix A) in the individual pixels (Fig. A.1) or in the array-averaged spectra (Fig. 3). The 3σ upper limits for the two lines are 0.11 and 0.19 K, equivalent to 7.5×10^{-7} erg s^{-1} cm^{-2} sr^{-1} and 2.1×10^{-5} erg s^{-1} cm^{-2} sr^{-1} when assuming a FWHM of 1 km s^{-1}, for [C II] and [O I], respectively.

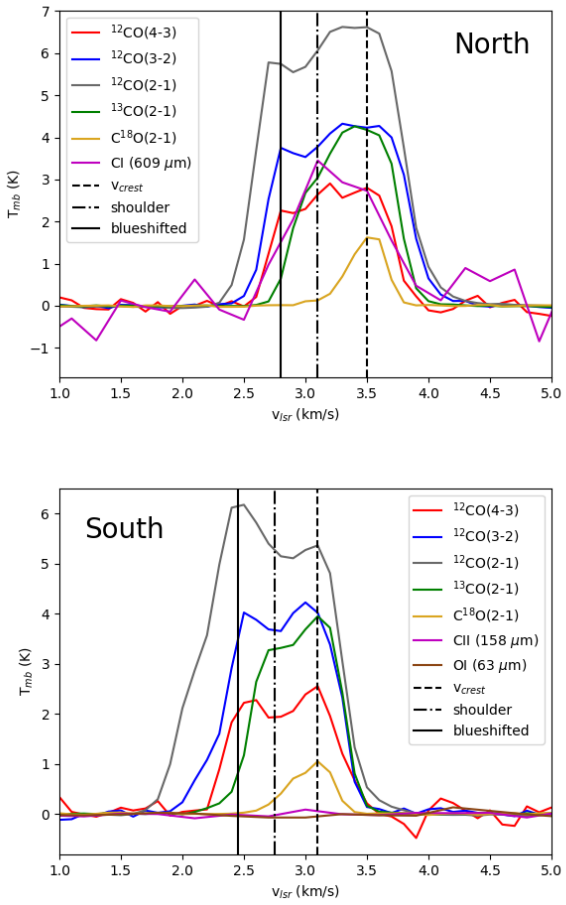

Fig. 3. *Top*: APEX CO and [C I] spectra in the northern map, averaged over the filament crest ($N > 3 \times 10^{21}$cm^{-2}). *Bottom*: APEX CO spectra averaged over the southern map and the 7-pixel averaged SOFIA [C II] and [O I] lines that are not detected above the 3σ level. We note the prominent blueshifted velocity component around 2.8 km s^{-1} in the north and at 2.5 km s^{-1} in the south, only visible in the ^{12}CO lines.

3. Results and analysis

3.1. The ambient FUV field from a census of nearby stars

We estimated the FUV field upper limit in Musca using a census of nearby ionising stars (e.g. Schneider et al. 2016). For that, we employed the SIMBAD[3] database (Wenger et al. 2000) and

[1] http://www.iram.fr/IRAMFR/GILDAS
[2] http://www.apex-telescope.org/telescope/efficiency/
[3] http://simbad.u-strasbg.fr/simbad/sim-fsam

imposed a search for B3 and earlier type stars within a radius of 40° (100 pc), centered on the Musca filament, and a maximal distance of 250 pc. This provided a census of 59 ionising stars including two dominant O9-type stars. Knowing the spectral type of these ionising stars, we estimated the contribution of the FUV emission using model atmospheres[4] of Kurucz (1979) with solar abundances (Grevesse & Sauval 1998) and log(g) ~4.0 (g is the surface gravity). The temperature of the different spectral types was obtained from Fitzpatrick & Massa (2005) and Pecaut & Mamajek (2013). The distance information and the location on the sky of both Musca and the stars then allows to calculate their relative distances. We assumed a r^{-2} decrease of the flux and projected all stars in the plane of the sky, and obtained in this way an ambient FUV field of 3.4 G_0 (Habing 1968) for the Musca cloud as an upper limit. The real field is lower because we did not take into account any extinction, that is, attenuation by diffuse gas and blocking by molecular clumps.

3.2. Limits on FUV heating from CI & CII

As a second method to constrain the ambient FUV field, we used the SOFIA [C II] upper limit and the APEX [C I] brightness observed in Musca. [C II] is an excellent tracer of the FUV field at low densities as it is a direct result of the ionising radiation (e.g. Tielens & Hollenbach 1985) and its non-detection points towards a low value for the ambient FUV field. [C I] is not a direct product of FUV ionisation, but PDR models demonstrate that its brightness is also sensitive to the FUV field (e.g. Hollenbach & Tielens 1997; Röllig et al. 2007). In this section, we compare the observed line brightness with predictions from PDR models using the 2006 models of the PDR toolbox[5] (Kaufman et al. 2006; Pound & Wolfire 2008). These plots are expressed in molecular hydrogen density n_{H_2}, where we assume that all hydrogen atoms are locked in molecular hydrogen.

The [C II] upper limit restricts the FUV field to values <1G_0 for densities $n_{H_2} \leq 10^4$ cm^{-3}. This is consistent with the intensity of the [C I] line which is so weak that it is below the minimum value in the PDR toolbox. Even with a beam filling value of 30% for [C I], which would be low around the Musca filament, the FUV field remains below 1 G_0 for typical densities of the Musca ambient cloud. Using the Meudon PDR code[6] (Le Petit et al. 2006; Le Bourlot et al. 2012; Bron et al. 2014) for the same lines, confirms that the upper limit on the [C II] intensity can only be the result of a FUV field strength <1 G_0. With these observational upper limits for the ambient FUV field, the Kaufman et al. (2006) PDR models restrict the maximal surface temperature of the cloud to 25 K. This temperature upper limit for gas embedded in such a weak FUV field is also found in other theoretical models where heating by the FUV field is taken into account (e.g. Godard et al. 2019), and consistent with the maximal CO temperature in numerical simulations of molecular clouds evolving in a FUV field ≤ 1.7 G_0 (Glover & Smith 2016; Clark et al. 2019).

3.3. CO spectra in Musca

3.3.1. Three CO velocity components

Figure 3 shows spectra averaged across the northern (top panel) and southern (bottom panel) filament for *Herschel* column densities N > 3 × 10^{21} cm^{-2}.

The spectra of the CO isotopologues unveil three velocity components that show small velocity variations in the north and south. First, there is a single component in C^{18}O(2–1) at 3.5 km s^{-1} (north) and 3.1 km s^{-1} (south) that traces the Musca filament crest (Hacar et al. 2016). In ^{13}CO(2–1) one observes a blueshifted shoulder to the velocity component of the filament crest, which is a velocity component related to the strands, namely, the dense interface region between the filament crest and the ambient cloud. It has a typical velocity of 3.1 km s^{-1} in the north and 2.7 km s^{-1} in the south and is not detected in C^{18}O with current data. In ^{12}CO a third velocity component is observed, without any clearly detected counterpart in ^{13}CO or C^{18}O, which is further blueshifted so that we call it the "blueshifted component". The brightness peak of the blueshifted component in the northern map occurs at 2.8 km s^{-1} and in the southern map at 2.5 km s^{-1}. This blueshifted component is the focus of this paper.

The individual ^{12}CO(4–3) spectra in the northern map are presented in Fig. 4, overlaid on the *Herschel* column density and temperature map in the top panels and together with individual spectra in other CO isotopologues at selected positions in the bottom panel. Inspecting the ^{12}CO(3–2) and ^{12}CO(4–3) spectra, we find that these lines are clearly detected towards the lower column density regions and that this blueshifted component is present over the entire map, see Fig. 4.

Because our assumption is that the Musca filament is cylindrical, the observed CO emission in direction of the crest and strands also contains gas from the ambient cloud along the line-of-sight. In particular, the ^{12}CO(2–1) blueshifted line can have a more significant component arising from this gas phase. We can thus not fully exclude effects of high optical depth and self-absorption, so we run tests using a two-layer gas model for the CO(2–1) isotopologue lines in order to calculate a possible impact of foreground absorption and present the results in Appendix B. For that, we assumed only 2 CO line components, i.e. the crest component and a shoulder+blueshifted one that it self-absorbed and only apparently shows separate components. However, the result of this modelling is that it is not possible to reproduce the observed CO line profiles with only two components, so that we are confident in our approach to use 3 separate lines. The best fitting model for the blueshifted component of all CO lines in the northern and southern map is the one with the parameters given in Table 1. We note from the Table that the fitted ^{12}CO(2–1) linewidth of the blueshifted component in the south is higher than the linewidth obtained for ^{12}CO(3–2) and ^{12}CO(4–3), which have a similar width. It is thus possible that there, the low-J ^{12}CO(2–1) line traces more material along the line-of-sight from the ambient cloud. Inspecting the spectra, see Fig. 3, confirms that ^{12}CO(3–2) and ^{12}CO(4–3) only show up at higher velocities and have a smaller linewidth. This difference, and the irregular ^{12}CO(2–1) shape in the southern map, suggests that ^{12}CO(2–1) traces the ambient cloud down to lower velocities than the detected ^{12}CO(4–3) and (3–2) emission. We also determined from the averaged ^{12}CO(2–1) and ^{13}CO(2–1) spectra that the ^{12}CO(2–1)/^{13}CO(2–1) line ratio in the blueshifted component in the northern and southern map are between 15 and 60, which are expected values for optically thin emission. Note that fractionation (see Appendix B) can cause observed values for the ^{12}CO/^{13}CO ratio significantly below 60. This is in agreement with early indications for Musca of significant CO isotopologue abundace variations (Hacar et al. 2016) which we further confirm in Paper I.

[4] http://www.oact.inaf.it/castelli/castelli/grids.html
[5] http://dustem.astro.umd.edu/
[6] http://ismdb.obspm.fr/

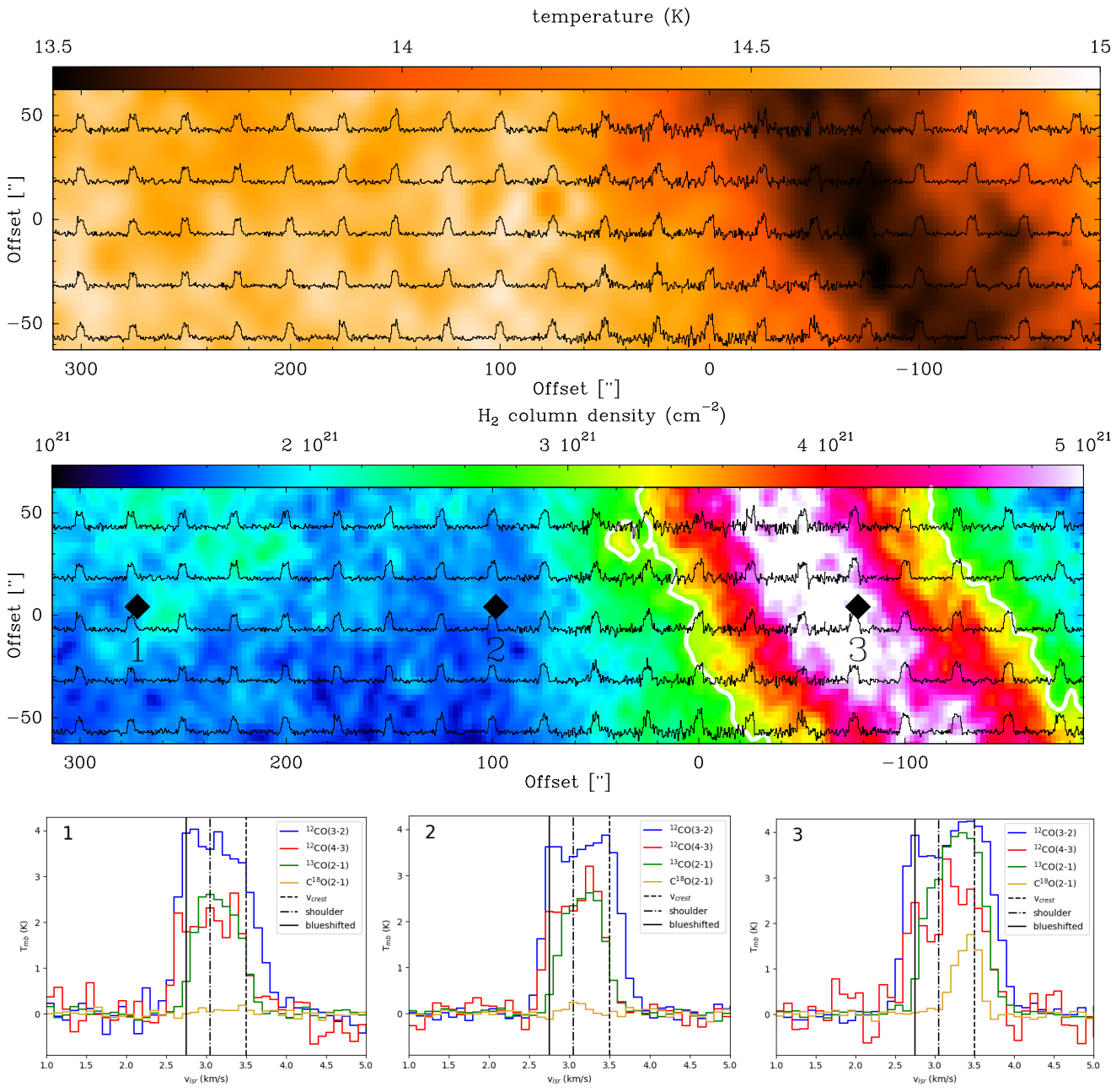

Fig. 4. *Top:* ^{12}CO(4–3) spectra overlaid on the *Herschel* dust temperature map. The (0,0) position of the map is α_{2000} = 12^{h}28^{m}58^{s}, δ_{2000} = −71°16′55″ *Middle:* ^{12}CO(4–3) spectra overlaid on the northern *Herschel* column density map. The white contours indicate Musca filament crest ($N > 3 \times 10^{21}$ cm^{-2}). The black squares indicate the locations of the spectra displayed below. *Below*: zoom into spectra at selected positions in the map. This shows that there is ^{12}CO(4–3) and ^{12}CO(3–2) emission at the velocity of the blueshifted component over the full map.

3.3.2. Density for the blueshifted component

From the sections before, we learned that the blueshifted component is an individual feature towards the crest and strand regions, and that the ^{12}CO(2–1) line has contributions from the ambient cloud along the line-of-sight. Here, we estimate the typical density and upper limit for this ambient cloud close to the filament. For that we use the density of the fitted Plummer profile at the outer radius of the filament. With the values from Cox et al. (2016), correcting for a distance of 140 pc for the Musca filament, this gives $n_{H_2} = 4.0 \times 10^2$ cm^{-3} at $r = 0.2$ pc. An approach to estimate the density upper limit is to combine the maximal column density associated with the ambient cloud, which is $N \sim 10^{21}$ cm^{-2} (Cox et al. 2016), with the minimal possible size of the ambient cloud. As it is unlikely that the ambient cloud has a smaller size along the line of sight than the filament, this gives a minimal size of 0.4 pc. Using a minimal size of 0.4 pc along the line of sight gives an upper limit of $n_{H_2} = 8 \times 10^2$ cm^{-3} for the ambient cloud.

The [C I] emission at the velocity of the blueshifted component in Fig. 3 is weak, ∼1–1.5 K, but it is difficult to constrain this because of the noise. This indicates that [C I] can trace the

Table 1. Linewidth, integrated brightness and velocity for the average ^{12}CO blueshifted component in the northern and southern map after fitting 3 gaussians to the spectrum.

line	$FWHM$ (km s^{-1})	$\int T\,dv$ (K km s^{-1})	$v_{\rm blue}$ (km s^{-1})
	North		
^{12}CO(2–1)	0.35	2.0	2.7
^{12}CO(3–2)	0.31	0.98	2.8
^{12}CO(4–3)	0.42	0.73	2.9
	South		
^{12}CO(2–1)	0.71	4.6	2.5
^{12}CO(3–2)	0.35	1.7	2.5
^{12}CO(4–3)	0.33	0.63	2.5

ambient cloud down to at least $n_{\rm H_2} \sim 4 \times 10^2$ cm^{-3} in a weak FUV-field. More extensive [C I] observations will be required to better understand the physical conditions traced by [C I] in the ISM. This is particularly important for comparison with simulations since the physical conditions traced by [C I] remain uncertain in simulations (e.g. Glover et al. 2015; Franeck et al. 2018; Clark et al. 2019).

3.4. ^{12}CO(4–3) excess emission in the blueshifted velocity component

The ^{12}CO(3–2) and ^{12}CO(4–3) transitions have relatively high excitation temperatures (33 and 55 K respectively; Müller et al. 2005). This allows us to investigate the presence of warm gas in the Musca cloud. We focus on the blueshifted component for which ^{12}CO(4–3) is observed over the full map. This could be an indication of quite uniform heating by e.g. a FUV field, though there are indications of spatial variations in the data. However, because of the noise in the spatially resolved map, we will not focus on these possible spatial variations in this paper. To further investigate the heating that leads to the ^{12}CO(4–3) emission, we study the ^{12}CO(4–3)/^{12}CO(2–1) and ^{12}CO(4–3)/^{12}CO(3–2) brightness temperature ratios. In the previous section, we noted that it is important to take care comparing the integrated brightness of ^{12}CO(2–1) with ^{12}CO(3–2) and ^{12}CO(4–3) in the blueshifted component because of their difference in linewidth. Furthermore, the noise in the ^{12}CO(3–2) and ^{12}CO(4–3) spectra makes it impossible to confidently fit a spectrum for every pixel in the map, even when spatially smoothing the data. Because of this, we will approach this section by focusing on the peak brightness temperatures.

The peak brightness of the blueshifted component occurs near 2.8 km s^{-1} in the northern map and near 2.5 km s^{-1} in the southern map. At these velocities, we determined the brightness temperature ratios for every pixel in the maps. In Fig. 5, the distribution of the ^{12}CO(4–3)/^{12}CO(2–1) and ^{12}CO(4–3)/^{12}CO(3–2) peak brightness ratios for the northern map are displayed. We determined the average and median values for the various ratios in both maps which are summarized in Table 2. Overall, there is no large difference between average and median values. For the ^{12}CO(4–3)/^{12}CO(2–1) and ^{12}CO(4–3)/^{12}CO(3–2) ratio in the northern map, we obtain a median value of 0.38 and 0.61 at 2.8 km s^{-1}, respectively. In the southern map, the noise of both the ^{12}CO(4–3) and ^{12}CO(3–2) transition is higher as it was observed under poorer weather conditions. The median

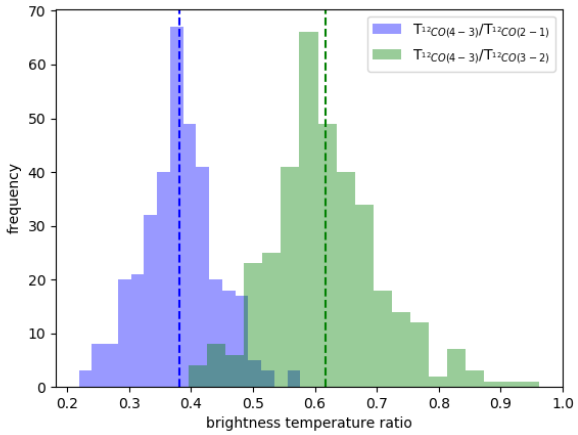

Fig. 5. Histograms of the ^{12}CO(4–3)/^{12}CO(2–1) (blue) and ^{12}CO(4–3)/^{12}CO(3–2) (green) main beam brightness ratio for the pixels in the northern map with a ^{12}CO(4–3) rms < 0.2 K. The dashed blue line indicates the average ^{12}CO(4–3)/^{12}CO(2–1) ratio for all pixels, and the dashed green line indicates the average ^{12}CO(4–3)/^{12}CO(3–2) ratio.

Table 2. Mean and median main beam brightness ratios for ^{12}CO(4–3)/^{12}CO(2–1) and ^{12}CO(4–3)/^{12}CO(3–2) in the blueshifted component for the northern and southern map.

	^{12}CO(4–3)/^{12}CO(2–1)		^{12}CO(3–2)/^{12}CO(2–1)	
	Mean	Median	Mean	Median
north (2.8 km s^{-1})	0.38 ± 0.06	0.38	0.62 ± 0.09	0.61
south (2.5 km s^{-1})	0.39 ± 0.13	0.38	0.55 ± 0.19	0.53

^{12}CO(4–3)/^{12}CO(2–1) ratio is 0.38 at 2.5 km s^{-1} and the respective value for the ^{12}CO(4–3)/^{12}CO(3–2) ratio is 0.53.

3.4.1. Modeling with the PDR Toolbox

We compared the observed ^{12}CO(4–3)/^{12}CO(2–1) and ^{12}CO(4–3)/^{12}CO(3–2) brightness temperature ratios in the blueshifted component with predictions using the PDR toolbox in the allowed density range of the ambient cloud in Musca, see Sect. 3.3.2. Figure 6 shows that for a FUV field strength <1 G_0, the predicted ^{12}CO(4–3)/^{12}CO(2–1) brightness temperature ratio is smaller than 0.05, which is more than a factor 5 lower than observed in Musca. The same is found for the ^{12}CO(4–3)/^{12}CO(3–2) brightness temperature ratio, with predicted ratios of ∼0.1, which is again more than a factor 5 lower than observed. It is thus impossible to obtain the observed ratios for the densities and FUV field strength in the ambient Musca cloud that are allowed by [C II], [C I], [O I], and the calculated upper limit from the nearby census of OB stars. This strongly suggests that the ^{12}CO(4–3) emission in the low-column density blueshifted component cannot be explained as a result of FUV heating.

3.4.2. Modeling with RADEX

We further investigate whether the ^{12}CO(4–3)/^{12}CO(2–1) and ^{12}CO(4–3)/^{12}CO(3–2) brightness temperature ratios in the blueshifted component can be reproduced with the non-LTE RADEX code (van der Tak et al. 2007). We use a non-LTE

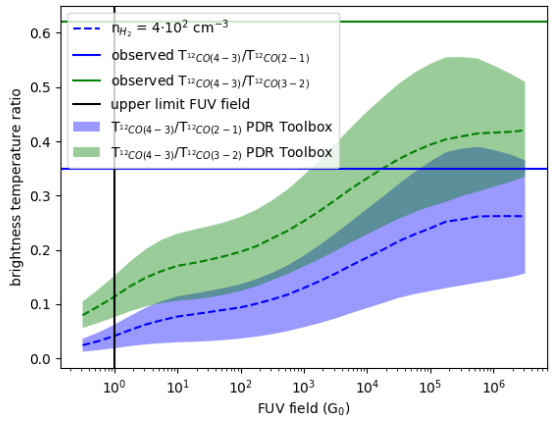

Fig. 6. Observed ^{12}CO(4–3)/^{12}CO(2–1) and ^{12}CO(4–3)/^{12}CO(3–2) ratios compared with predictions by the PDR Toolbox. The shaded areas, constructed by logarithmic interpolation between the points in the PDR Toolbox density grid, show the evolution of the ^{12}CO(4–3)/^{12}CO(2–1) and ^{12}CO(4–3)/^{12}CO(3–2) brightness temperature ratio as a function of the FUV field in the allowed density range of the Musca cloud. At a typical density $n_{H_2} = 4 \times 10^2$ cm^{-3} of the ambient cloud (dashed line) for the allowed FUV field strength (<1 G_0), the predicted line ratios are only a fraction of the observed ones in the blueshifted component.

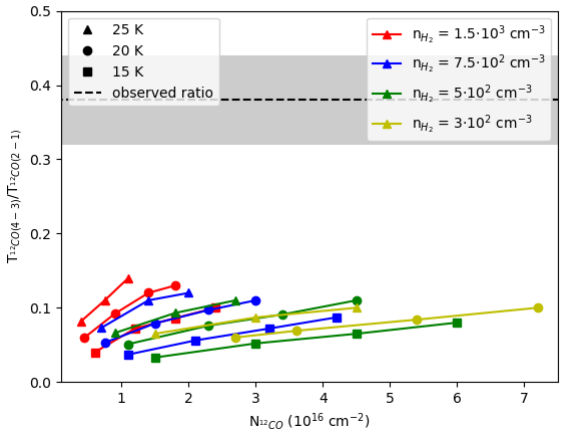

Fig. 7. ^{12}CO(4–3)/^{12}CO(2–1) brightness temperature ratios predicted with RADEX for the plausible range of physical conditions in the ambient cloud of the Musca filament. The lines connect the RADEX models with identical density and temperature for varying ^{12}CO column densities. The predicted ratios with RADEX show a huge discrepancy with the observed ^{12}CO(4–3)/^{12}CO(2–1) ratio towards the Musca cloud (indicated by the dashed line). The standard deviation of the observed values from the average is indicated by the grey area. The same is observed for the ^{12}CO(4–3)/^{12}CO(3–2) brightness temperature ratio.

approach because the high critical density ($n_{H_2} > 5 \times 10^4$ cm^{-3}) of ^{12}CO(3–2) and ^{12}CO(4–3) implies that these lines are subthermally excited. For RADEX analysis we use a FWHM of 0.4 km s^{-1}, temperatures between 15 and 25 K, and representative densities for the ambient cloud: $n_{H_2} = 3 \times 10^2$, 5×10^2, 7.5×10^2 and 1.5×10^3 cm^{-3}.

For each RADEX model, we also need an upper limit on the ^{12}CO column density of the blueshifted component. This can be done by calculating with RADEX the ^{13}CO column density from the ^{13}CO(2–1) brightness (~0.6 K, see Fig. 3) for every density and temperature. In a weak FUV field the [^{12}CO]/[^{13}CO] abundance ratio is ≤60 (Visser et al. 2009; Röllig & Ossenkopf 2013), which puts an upper limit on the ^{12}CO column density and opacity. For further analysis, we use RADEX models with a predicted ^{12}CO(2–1) brightness up to 50% brighter than observed towards Musca to take into account some uncertainties such as possible opacity broadening of ^{12}CO(2–1) compared to ^{12}CO(4–3), a non unity beam filling or different line calibration (uncertainty in η_{mb}).

Studying the ^{12}CO(4–3)/^{12}CO(2–1) and ^{12}CO(4–3)/^{12}CO(3–2) brightness temperature ratios within these limits, we find that the ratio increases with increasing density, column density or temperature, see Fig. 7. However, no model is capable to reproduce more than 40% of the observed ^{12}CO(4–3)/^{12}CO(2–1) and ^{12}CO(4–3)/^{12}CO(3–2) ratios towards the Musca ambient cloud, see Fig. 7 for the ^{12}CO(4–3)/^{12}CO(2–1) ratio.

Taking higher densities for the ambient cloud than put forward in Sect. 3.3.2, does not offer a solution for bringing calculations in agreement with observations. Though this can increase the predicted ratio for a fixed temperature and ^{12}CO column density, this also strongly increases the line brightness temperature. Consequently, one either has to reduce the temperature or ^{12}CO column density to keep line brightnesses that are not too far off from the observed values. This effort again forces brightness temperature ratios to values found in Fig. 7.

From both approaches, it thus appears impossible to reproduce the observed ^{12}CO(4–3)/^{12}CO(2–1) and ^{12}CO(4–3)/^{12}CO(3–2) brightness temperature ratios assuming that there is only collisional and radiative heating.

3.5. A warm and dense gas component

3.5.1. The CO line ratio with RADEX

In order to increase the ^{12}CO(4–3)/^{12}CO(2–1) and ^{12}CO(4–3)/^{12}CO(3–2) brightness temperature ratio while keeping the brightness of both lines low enough, one needs to consider a small layer embedded in the diffuse gas that can increase the ^{12}CO(4–3) brightness without significantly increasing the ^{12}CO(2–1) and ^{12}CO(3–2) emission. Based on the ^{12}CO(4–3) excitation conditions, the layer should contain warm gas (>50 K). In fact, this "layer" can be clumpy, that is, pockets of warm gas that are embedded in more tenuous interclump gas. However, modelling such a scenario is not possible with RADEX and out of the scope of this paper. Our objective here is to show the existence of a warm gas component. We thus investigated with RADEX the impact of a warm gas layer by running models with a FWHM of 0.4 km s^{-1} as an overall average, and temperatures between 10 and 150 K at different densities. Note that a temperature of 150 K would result in a thermal FWHM of 0.5 km s^{-1}. This is higher than the observed typical FWHM of 0.4 km s^{-1}, but we anticipate that there is also uncertainty on the FWHM so that we work with a kinetic temperature upper limit of 150 K. We additionally restrain ourself to models that manage to reproduce the observed ^{12}CO(4–3) brightness temperature in Musca[7]. Figures 8 and 9 show the results for different densities. Both the ^{12}CO(4–3)/^{12}CO(2–1) and ^{12}CO(4–3)/^{12}CO(3–2) ratios indicate that a temperature >50 K as well as relatively high

[7] Using brightness temperatures for modelling is less convenient because of the unknown beam filling factors of CO emission which are eliminated to first order using line ratios. We nevertheless use the ^{12}CO(4–3) line as an additional – though weak – indicator for the best fitting model.

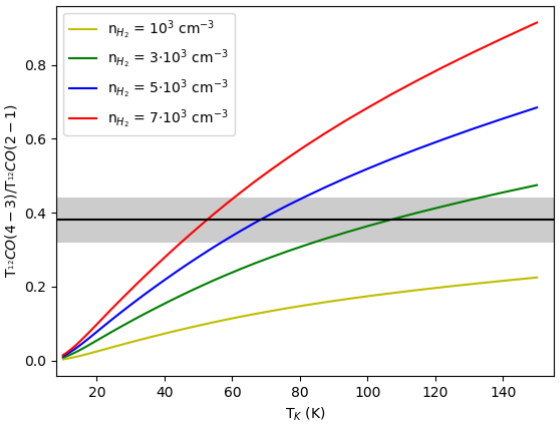

Fig. 8. Predicted brightness temperature ratio of ^{12}CO(4–3)/^{12}CO(2–1) by RADEX as a function of temperature for different densities. This demonstrates the need for a warm and dense CO layer to at least reach the observed brightness ratios in the blueshifted component. For each density we plot the ratio for a column density such that the predicted brightness of ^{12}CO(4–3) by RADEX is roughly similar to the observed brightness towards Musca (T_{mb} = 1.5–3 K) at the temperatures that obtain sufficiently high brightness ratios. The lowest three densities (n_{H_2} = 10^3, 3 × 10^3 and 5 × 10^3 cm^{-3}) use $N_{^{12}CO}$ = 1.1 × 10^{15} cm^{-2}, and n_{H_2} = 7 × 10^3 cm^{-3} uses $N_{^{12}CO}$ = 9 × 10^{14} cm^{-2}. The black horizontal line indicates the average observed ratio towards Musca, and the grey area indicates the standard deviation.

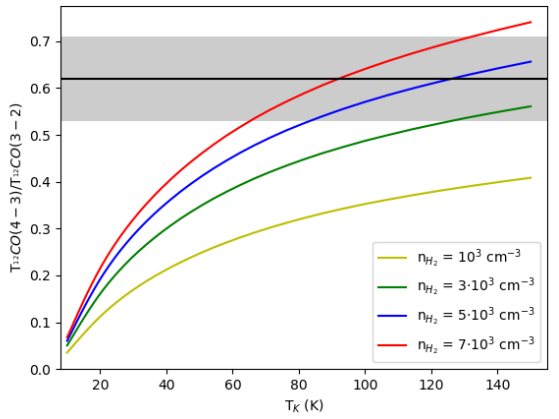

Fig. 9. Predicted brightness temperature ratio of ^{12}CO(4–3)/^{12}CO(3–2) by RADEX for the same models that are presented in Fig. 8. It confirms the need for high temperatures (>50 K) and densities (5–7 × 10^3 cm^{-3}) to reach the observed excitation of ^{12}CO(4–3). The black horizontal line indicates the average observed ratio towards Musca, and the grey area indicates the standard deviation.

densities are required to reach the observed ratios. The ^{12}CO(4–3)/^{12}CO(3–2) ratio, in particular, points to high densities and temperature, see Fig. 9, in order to reach the observed ratios.

Though the RADEX analysis demonstrates the need for warm and dense gas to obtain the observed ^{12}CO(4–3) brightness in the blueshifted component, we can not narrow down more precisely the temperature and density range because there are no higher-J CO observations at the moment. This warm and dense gas exactly fits with the predictions for gas heated by low-velocity shocks (Pon et al. 2012; Lesaffre et al. 2013), and so-called slow-type (with regard to their phase velocity) magnetised shocks with v_s = 1–3 km s^{-1} can easily reach temperatures as high as 100 K (Lehmann & Wardle 2016). These slow-type

Table 3. Predicted [C I] brightness temperatures (4), calculated with RADEX for various temperatures (1) and densities (2) for the blueshifted velocity component.

T (K) (1)	n_{H_2} (cm^{-3}) (2)	N$_{CI}$ (cm^{-2}) (3)	T_{mb} (K) (4)
Ambient cloud			
20	5 × 10^2	10^{16}	1.0
20	7.5 × 10^2	10^{16}	1.2
Warm gas layer			
60	7 × 10^3	9 × 10^{14}	0.16
90	7 × 10^3	9 × 10^{14}	0.15

Notes. This indicates a [C I] column density (3) of ∼10^{16} cm^{-2} for the ambient cloud, while the contribution from the warm gas layer to the observed [C I] emission is negligible.

shock models predict a physical size of the warm gas layer around 10^{15} cm, which fits with the estimated physical sizes for the RADEX models. The estimated size, that is the layer thickness, of the models that manage to reach the observed brightness temperature ratios in Figs. 8 and 9 are 1.3 × 10^{15} cm and 2.2 × 10^{15} cm, respectively at n_{H_2} = 7 × 10^3 cm^{-3} (with N$_{^{12}CO}$ = 9 × 10^{14} cm^{-2}) and 5 × 10^3 cm^{-3} (with N$_{^{12}CO}$ = 1.1 × 10^{15} cm^{-2}). To calculate the physical size of the RADEX models an abundance of [H$_2$]/[^{12}CO] = 10^4 was used, which is a typical value for weakly irradiated molecular gas.

Lastly, we note that this warm gas is observed in both maps and thus likely universally present around the Musca filament.

3.5.2. CI column density in the blueshifted component

We noted in Fig. 3 the presence of [C I] emission in the blueshifted component with a brightness temperature of the order of 1–1.5 K. From this weak [C I] emission we here estimate the [C I] column density. We use a $FWHM$= 0.4 km s^{-1}, a temperature of 20 K, and typical densities n_{H_2} = 5–7.5 × 10^2 cm^{-3} for the ambient Musca cloud with RADEX. This points to N$_{CI}$ ∼ 10^{16} cm^{-2}, see Table 3. Comparing this with the same models for ^{12}CO emission from the ambient cloud in Sect. 3.4, we find that at least 20% and possibly up to 50% of carbon is still found in its atomic form.

On the other hand, it is observed from Table 3 that the warm and dense gas layer, necessary to explain the bright ^{12}CO(4–3) emission, provides a negligible contribution to the [C I] emission.

We thus emphasise again that the blueshifted component has two contributions:

– the ambient cloud which gives rise to [C I] and low-J CO emission;

– a warm gas layer (or pockets of warm gas) with little [C I] emission that is responsible for the bright CO(4-3) line.

3.6. Shock models

For an in-depth comparison with shock models, it would be preferable to have additional observations of mid-to high-J (J_{up} > 4) CO lines (e.g. Pon et al. 2012; Lehmann & Wardle 2016) since ^{12}CO(2–1), and possibly some ^{12}CO(3–2), emission in the blueshifted component also comes from non-shocked

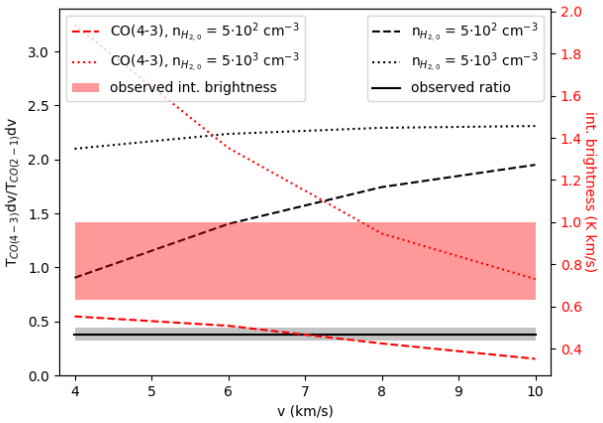

Fig. 10. ^{12}CO(4–3)/^{12}CO(2–1) integrated brightness ratio (black) for J-type shock models from the Paris-Durham code. The ratio at a shock velocity of 4 km s^{-1} is higher than observed in Musca. This is expected because the ratio decreases towards lower velocities and the ^{12}CO(2–1) emission in Musca also comes from non shocked gas, such that the observed ratio is a lower limit for the shock models. In red, we show the integrated brightness of ^{12}CO(4–3) for the same shock models, together with the ^{12}CO(4–3) integrated brightness interval of the blueshifted component in Musca. The observed values in Musca show a relatively good agreement with the predicted ^{12}CO(4–3) integrated brightness for a pre-shock density of $n_{\mathrm{H}_{2,0}} \sim 5 \times 10^2$ cm^{-3}.

gas (as it is found in synthetic observations of simulations; see Fig. 13).

Because observational studies so far focussed on the higher-J CO lines observed with *Herschel* (Pon et al. 2014; Larson et al. 2015), it is not well investigated to which extent mid-J CO lines, in particular the ^{12}CO(4–3) transition, contribute as a cooling line for shocks. We thus compared our observations to results of the Paris-Durham shock code (Flower & Pineau des Forêts 2003; Lesaffre et al. 2013; Godard et al. 2019) that are available for both non-irradiated C- and J-type shocks.

Looking into computed model grids, we find that non-irradiated C-type shocks with a pre-shock density $n_{\mathrm{H}_{2,0}} \sim 5 \times 10^2$ cm^{-3} do not manage to reproduce the observations. Both the integrated intensity of ^{12}CO(4–3) and the predicted ratios are below the observed values in Musca. However, J-type shocks, which are good first order models for slow-type shocks (Lehmann & Wardle 2016), with a pre-shock density $n_{\mathrm{H}_{2,0}} \sim 5 \times 10^2$ cm^{-3} fit with the ^{12}CO observations, see Fig. 10. The predictions by these models for the [C II], [O I], and [C I] brightnesses are also in agreement with the observations of Musca (see Appendix A). J-type shocks as a proxy for slow-type low-velocity shocks are justified since the dynamics of these slow-type shocks are driven by the gas pressure. Note that we used published shock models from the Paris-Durham code for this first comparison which have shock velocities of 4 km s^{-1} and higher, while in Musca the shock velocity can be lower. A comparison with shock models at lower velocities is work in progress, and will be addressed in a forthcoming paper.

The nondimensional parameter $b = (\mathrm{B}/1\mu\mathrm{G})/\sqrt{n\ \mathrm{cm}^{-3}} = 0.1$ in the shock models, with B the component of the magnetic field that is perpendicular to the direction of shock propogation, is used to model J-type shocks, and $b = 1$ is used to model C-type shocks (Lesaffre et al. 2013).

To perform a first estimate of the shock velocity, we have to take into account that there is an orientation angle for the shock propagation with respect to the plane of the sky (POS). We will assume shock propagation along the magnetic field. In this scenario, one can estimate the true shock velocity when the angle between the magnetic field and the POS is known, using

$$v_{\mathrm{shock}} = v_{\mathrm{los}} / \sin(\gamma), \quad (1)$$

where γ is the angle between the magnetic field and the POS, and v_{los} is the observed shock velocity along the line of sight for which we take 0.4 km s^{-1}. In Planck Collaboration Int. XXXIII (2016), a value around 25° is put forward for the angle between the magnetic field and the POS. This results in a shock velocity around 0.9 km s^{-1}. This fits nicely with the proposed presence of slow-type low-velocity shocks, which need to have velocities between the sound speed (c_{s}) and $v_{\mathrm{A}}\cos(\theta)$. With v_{A} the alfvén speed and θ the angle between the magnetic field and the propagation direction of the shock (Lehmann & Wardle 2016). The expected alfvén speed towards the ambient cloud in Musca is of the order of 2.2 km s^{-1}, assuming a 33μG magnetic field strength at $n_{\mathrm{H}_2} \sim 4 \times 10^2$ cm^{-3} (Crutcher 2012). We thus find that the estimated shock velocity fits with the conditions that allow a slow-type shock. An angle <10° between the magnetic field and the plane of the sky is required for a shock velocity >2.2 km s^{-1}.

Summarising, the CO brightness temperature ratios that we observe in Musca are consistent with the predictions from low-velocity shock models (e.g. Pon et al. 2012; Lehmann & Wardle 2016). Low- to mid-J CO lines may thus indeed be used to detect low-velocity shocks but more observational studies are required to better understand the quantitative contribution from shock excitation.

Since SiO transitions can be used as a tracer of certain shocks (e.g. Schilke et al. 1997; Gusdorf et al. 2008a,b), it is worth noting the SiO(5–4) line was not detected towards the Musca filament. With RADEX this allows to put a 3σ upper limit on the SiO column density of $\sim 10^{14}$ cm^{-2} at the filament crest, assuming $n_{\mathrm{H}_2} = 10^4$ cm^{-3}. This implies that less than 0.06% of Si is in the form of SiO at the Musca filament crest (see Appendix C for more information). Taking that all the gas-phase silicon is found in the form of SiO at the crest (Louvet et al. 2016), suggests that all Si is locked in the grains of the Musca cloud at an early stage of evolution. To explain the presence of SiO in the gas phase, as is found in regions like W43 (Louvet et al. 2016), implies that there is the need for an important dynamical or radiative history in such clouds to release Si from the grains in the gas phase.

4. A filament accretion shock signature in simulations

From the analysis of the observations, we found the presence a of warm gas layer around the dense gas (filament crest and strands) in the Musca cloud. These findings are here compared with synthetic observations from a converging flow simulation of filament formation (Clarke et al. 2018). We emphasize that this is a qualitative comparison to investigate the role of low-velocity shocks in filament formation, because the simulation was set up for simulating slightly denser features such as the filaments in Taurus. Nevertheless, we find in the simulations some generic features related to filament accretion that are observed in Musca. In these simulations a radially convergent flow forms dense filaments with $n_{\mathrm{H}_2} \gtrsim 10^4$ cm^{-3}, see Figs. 11 and 13. The filamentary structure, that continuously accretes mass from this converging flow, has a size of 3–4 pc. Turbulence in the flow leads to structure formation in the converging flow, causing inhomogeneities in the accretion and subsequent substructure in the

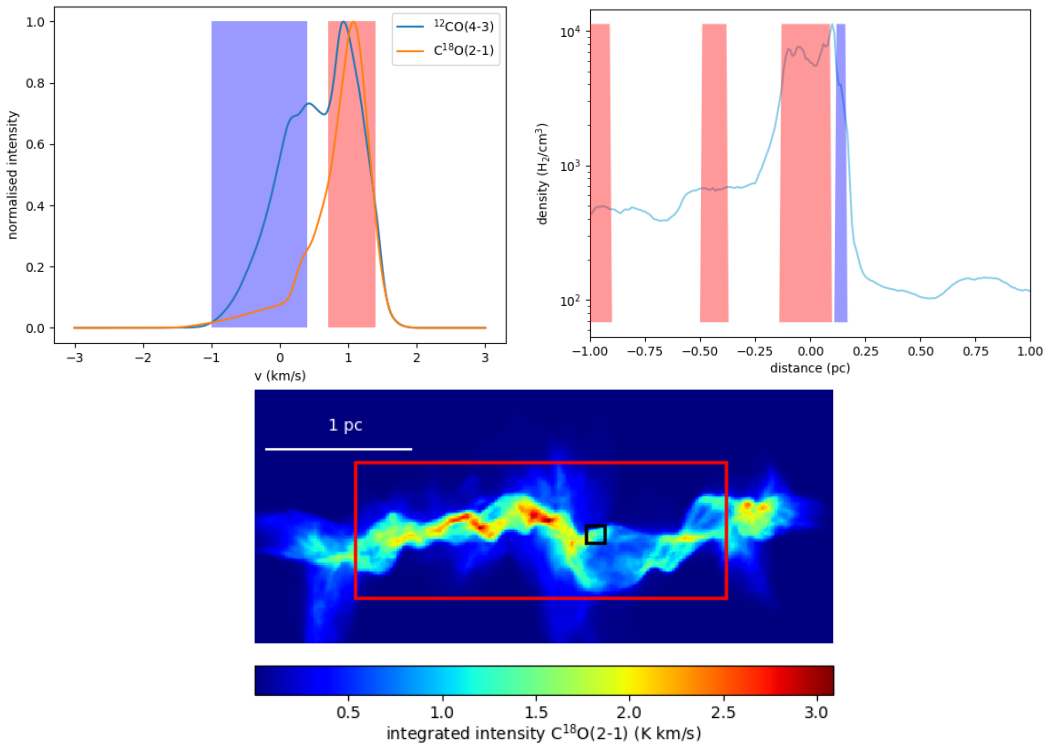

Fig. 11. *Bottom*: C^{18}O(2–1) integrated intensity map of the simulation (Clarke et al. 2018), with the black square indicating the region that is studied in this figure. The red box indicates the region displayed in Fig. 12. *Left*: ^{12}CO(4–3) and C^{18}O(2–1) spectra extracted from the square which show a blueshifted ^{12}CO(4–3) component (blue) in addition to the component related to the bulk emission of the filament crest (red). The two velocity intervals used for the plot on the right are indicated in blue and red. *Right*: physical location along the line of sight of the gas in the velocity intervals, showing that the larger blueshifted velocity interval covers a small region compared to the filament and that it is located at the border of this filament where the density strongly increases because of a filament accretion shock.

filament. The simulation includes hydrodynamics, self-gravity, and heating and cooling coupled with non-equilibrium chemistry. From this self-consistent CO formation in the simulations, synthetic observations are produced.

The filament edge is defined by filament accretion shocks, see for example Fig. 11, which is a low-velocity shock due to mass accretion on an interstellar filament from a converging flow in a molecular cloud. For more information on these simulations and synthetic observations, we refer to Clarke et al. (2017, 2018).

No magnetic field is included in the simulations, which could have an impact on the shock properties (e.g. Draine et al. 1983; Lesaffre et al. 2013). For a shock propagating perpendicular to the magnetic field, this makes the shock wider and decreases the peak temperature. However, slow-type shocks, which can fit the observed emission, tend to resemble non-magnetised shocks because the dynamics is driven by gas pressure (Lehmann & Wardle 2016). In the simulations the warm post-shock layer is not resolved, as post-shock cooling of a low-velocity J-type shock occurs over small distances (e.g. Lesaffre et al. 2013; Whitworth & Jaffa 2018), implying that the gas heated by the shocks is smeared out. Consequently, the temperature of the heated gas is underestimated. Nonetheless, it is generally observed in the simulations that the 3D dense filamentary structure is confined by a gas layer that shows an increase in temperature as a result of filament accretion shocks. Figure 12 shows a temperature map, cut out of the simulation, that illustrates this temperature increase at the border of the filament, followed by a temperature drop into the filament.

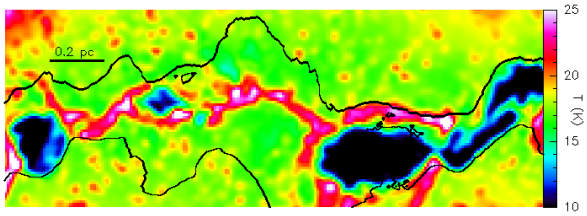

Fig. 12. Smoothed (σ = 1.3 pix) cut at z = 0.05 pc through the temperature cube of the simulation, with the black contours ($N = 5 \times 10^{21}$ cm^{-2}) roughly indicating the high column density filament. Note the local increase in temperature at the sub-filament border due to the accretion shocks and the temperature drop in the sub-filaments after the shock compared to the inflowing mass reservoir. Because of smoothing, the temperature peaks of the shocked gas in the map have decreased. The area of the simulation that is covered by this figure is indicated in Fig. 11.

The good correspondence with synthetic spectra derived from the simulation is remarkable, see Fig. 11. We observe the bulk emission of the filament with the C^{18}O(2–1) line and, more importantly, a bright blueshifted component in ^{12}CO(4–3) with no C^{18}O emission that connects the velocity of the inflowing cloud and the dense gas. This is similar to what is found in the Musca filament. In the simulations, this ^{12}CO(4–3) component corresponds to a strong velocity transition and density increase from a filament accretion shock of the inflowing mass reservoir, see Fig. 11. This accretion shock is responsible for the

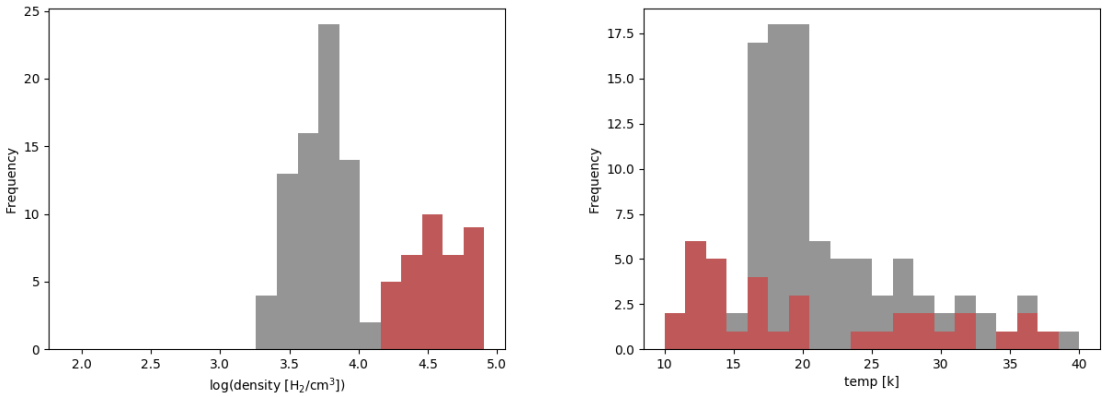

Fig. 13. *Left*: density distribution of the gas with a sufficient CO abundance to be observable in a ^{12}CO(4–3) excess component. CO is considered detectable if more than half of the carbon is locked in CO. Note that the density distribution is relatively bimodal, with the densest already shocked gas highlighted in red. *Right*: temperature distribution of all the CO gas in grey, with in red the temperature of the high density gas highlighted on the left. We find for the dense gas that almost all gas at T = 15–25 K has disappeared, leaving only the cold (<15 K) and warm gas (>25 K). This demonstrates that post-shock gas is either warm or cooled behind the shocked gas layer compared to the temperature of the inflowing mass reservoir.

observed blueshifted ^{12}CO(4–3) component. It can be wondered how the slightly lower temperatures in the simulation compare to the estimated values for Musca give rise to the same signature. But as mentioned before, the simulations were designed for somewhat higher densities than Musca, which increases the ^{12}CO(4–3) emission and thus compensates for the slightly lower temperatures.

Since the dense filaments in the simulation are confined by an accretion shock, it is not surprising that the ^{12}CO(4–3) excess is found at both observed locations in Musca as it likely confines the entire filament. Figure 12 displays that behind the heated gas layer by the filament accretion shock there is also a sharp decrease in temperature from ∼15 to ∼10 K. This creation of cold and dense gas through a filament accretion shock can also be observed in the temperature histograms of the simulations where the dense gas, created by an accretion shock, is either warmer (>25 K) or significantly colder (∼10 K) than the inflowing cloud (∼15–17 K), see Fig. 13. This demonstrates that accretion shocks from a continuously inflowing cloud, as observed in Musca, play an essential role in the cooling of the dense star forming ISM. This cooling is related to the increased shielding of the dense gas and the increased cooling rate by CO due to the higher density, since CO is an important coolant of molecular clouds (e.g. Goldsmith & Langer 1978; Whitworth & Jaffa 2018).

5. Filament formation due to the dissipation of MHD flows

We have put forward that the ^{12}CO(4–3)/^{12}CO(2–1) and ^{12}CO(4–3)/^{12}CO(3–2) excess in the blueshifted component can be explained by the presence of warm, dense gas that has properties predicted by low-velocity shock models. In particular the observed emission can fit with slow-type shocks, while simulations show that these slow-type shocks typically occur at relatively low velocities of v_s < 3 km s^{-1} found in Musca (Lehmann et al. 2016; Park & Ryu 2019). Furthermore, as the flow near the filament is expected to be well aligned with the magnetic field (Cox et al. 2016), the shock velocity upper limit for slow-type shocks ($v_A \cos\theta$) reaches a maximum. This increases the possibility for slow-type shocks to occur. A small, but significant, change in orientation of the magnetic field takes place from the mass reservoir to the filament in Musca (Planck Collaboration Int. XXXIII 2016) which could be the result of low-velocity shocks (Fogerty et al. 2017). Lastly, the observed warm and dense gas layer connects the velocity of the ambient cloud and dense gas in Musca, which indicates that the accretion shock dissipates the kinetic energy of the supersonic converging flow and increases the cooling rate to form a (trans-)sonic dense and cold filament.

If the Musca filament is indeed confined by the accretion shocks, we can do a first check whether the current results give a reasonable estimated mass accretion rate. The mass accretion rate through this low-velocity shock is estimated in Appendix D, giving a mass accretion rate $\gtrsim 20\ M_\odot$ pc^{-1} Myr^{-1}. This is similar to the typical values reported for mass inflow towards filaments that will form low-mass stars (e.g. Palmeirim et al. 2013), and would imply that Musca can accrete its current mass in 1 Myr.

6. Summary

In this paper we present observations of [C II] and [O I] with SOFIA, and observations of ^{12}CO(4–3), ^{12}CO(3–2) and [C I] with APEX towards the Musca filament. Studying these important cooling lines, we find that Musca has an extremely weak FUV field (<1 G_0), confirmed by determining the FUV field with a census of ionising stars. We further estimated a density $n_{H_2} \sim 5 \times 10^2$ cm^{-3} for the ambient gas near the Musca filament, and found that 20 to 50% of carbon in the ambient cloud is still in atomic form. In the interface region between the ambient cloud and dense gas in the crest and strands, blueshifted excess emission was found with the ^{12}CO(4–3), (3–2), and (2–1) lines.

A non-LTE radiative transfer study with RADEX points to the existence of a small warm (≳50 K) gas layer at relatively high density ($n_{H_2} \geq 3 \times 10^3$ cm^{-3}). This "layer" can actually be clumpy with pockets of warm gas embedded in a cooler interclump phase. This excess emission fits with predictions for non-irradiated slow-type low-velocity shock models with a pre-shock density $n_{H_{2,0}} \sim 5 \times 10^2$ cm^{-3}. The estimated shock velocity also fits with the shock velocity interval for slow-type shocks.

Comparing the location of the shock emission in the spectra with synthetic observations in simulations of filament formation, we obtain a scenario where the dense Musca filament is formed

by low-velocity filament accretion shocks in a colliding flow. These low-velocity MHD filament accretion shocks dissipate the supersonic kinetic energy of the colliding flow, creating a (trans-)sonic dense filament. Because of increased shielding and efficient CO cooling in the dense post-shock gas, these accretion shocks play an important role in cooling the dense filamentary ISM that can form stars in the near future.

Acknowledgements. We thank the anonymous referee for a critical review of the paper and providing useful comments that improved the quality and clarity of this paper. This work was supported by the Agence National de Recherche (ANR/France) and the Deutsche Forschungsgemeinschaft (DFG/Germany) through the project GENESIS (ANR-16-CE92-0035-01/DFG1591/2-1). L.B. also acknowledges support from the Région Nouvelle-Aquitaine. N.S. acknowledges support from the BMBF, Projekt Number 50OR1714 (MOBS-MOdellierung von Beobachtungsdaten SOFIA). We also appreciate support by the German Deutsche Forschungsgemeinschaft, DFG project number SFB 956. We thank M. Röllig, V. Ossenkopf-Okada and J. Stutzki for fruitful discussions on PDR and shock excitation, and self-absorption effects. We also thank F. Wyrowski for providing information to correct the frequency shift in the APEX FLASH observations. This work is based on observations made with the NASA/DLR Stratospheric Observatory for Infrared Astronomy (SOFIA). SOFIA is jointly operated by the Universities Space Research Association, Inc. (DSI) under DLR contract 50 OK 0901 to the University of Stuttgart. This publication is based on data acquired with the Atacama Pathfinder Experiment (APEX) under programme IDs 0100.C-0825(A), 0101.F-9511(A) and 0102.F-9503(A). APEX is a collaboration between the Max-Planck-Institut fur Radioastronomie, the European Southern Observatory, and the Onsala Space Observatory. This research has made use of the SIMBAD database, operated at CDS, Strasbourg, France.

References

Alves de Oliveira, C., Schneider, N., Merín, B., et al. 2014, A&A, 568, A98
André, P., Men'shchikov, A., Bontemps, S., et al. 2010, A&A, 518, L102
André, P., Di Francesco, J., Ward-Thompson, D., et al. 2014, Protostars and Planets VI (Tucson, AZ: University of Arizona Press), 27
Arzoumanian, D., André, P., Didelon, P., et al. 2011, A&A, 529, L6
Bisbas, T. G., Tanaka, K. E. I., Tan, J. C., Wu, B., & Nakamura, F. 2017, ApJ, 850, 23
Bron, E., Le Bourlot, J., & Le Petit F. 2014, A&A, 569, A100
Cartledge, S. I. B., Lauroesch, J. T., Meyer, D. M., & Sofia, U. J. 2004, ApJ, 613, 1037
Clark, P. C., Glover, S. C. O., Ragan, S. E., & Duarte-Cabral, A. 2019, MNRAS, 486, 4622
Clarke, S. D., Whitworth, A. P., Duarte-Cabral, A., & Hubber, D. A. 2017, MNRAS, 468, 2489
Clarke, S. D., Whitworth, A. P., Spowage, R. L., et al. 2018, MNRAS, 479, 1722
Cox, N. L. J., Arzoumanian, D., André, P., et al. 2016, A&A, 590, A110
Crutcher, R. M. 2012, ARA&A, 50, 29
Csengeri, T., Leurini, S., Wyrowski, F., et al. 2016, A&A, 586, A149
Draine, B. T., Roberge, W. G., & Dalgarno, A. 1983, ApJ, 264, 485
Duarte-Cabral, A., Bontemps, S., Motte, F., et al. 2014, A&A, 570, A1
Federrath, C. 2016, MNRAS, 457, 375
Fitzpatrick, E. L., & Massa, D. 2005, AJ, 129, 1642
Flower, D. R., & Pineau des Forêts, G. 2003, MNRAS, 343, 390
Flower, D. R., & Pineau Des Forêts, G. 2010, MNRAS, 406, 1745
Fogerty, E., Carroll-Nellenback, J., Frank, A., Heitsch, F., & Pon, A. 2017, MNRAS, 470, 2938
Franco, G. A. P. 1991, A&A, 251, 581
Franeck, A., Walch, S., Seifried, D., et al. 2018, MNRAS, 481, 4277
Glover, S. C. O., & Smith, R. J. 2016, MNRAS, 462, 3011
Glover, S. C. O., Clark, P. C., Micic, M., & Molina, F. 2015, MNRAS, 448, 1607
Godard, B., Pineau des Forêts, G., Lesaffre, P., et al. 2019, A&A, 622, A100
Goldsmith, P. F. 2001, ApJ, 557, 736
Goldsmith, P. F., & Langer, W. D. 1978, ApJ, 222, 881
Goldsmith, P. F., & Langer, W. D. 1999, ApJ, 517, 209
Goldsmith, P. F., Heyer, M., Narayanan, G., et al. 2008, ApJ, 680, 428
Gómez, G. C., & Vázquez-Semadeni, E. 2014, ApJ, 791, 124
Grevesse, N., & Sauval, A. J. 1998, Space Sci. Rev., 85, 161
Guevara, C., Stutzki, J., Ossenkopf-Okada, V., et al. 2020, A&A, 636, A16
Güsten, R., Nyman, L. Å., Schilke, P., et al. 2006, A&A, 454, L13
Gusdorf, A., Cabrit, S., Flower, D. R., & Pineau Des Forêts, G. 2008a, A&A, 482, 809
Gusdorf, A., Pineau Des Forêts, G., Cabrit, S., & Flower, D. R. 2008b, A&A, 490, 695
Gusdorf, A., Anderl, S., Lefloch, B., et al. 2017, A&A, 602, A8
Habing, H. J. 1968, Bull. Astron. Inst. Netherlands, 19, 421
Hacar, A., Kainulainen, J., Tafalla, M., Beuther, H., & Alves, J. 2016, A&A, 587, A97
Hennebelle, P. 2013, A&A, 556, A153
Henning, T., Linz, H., Krause, O., et al. 2010, A&A, 518, L95
Heyer, M., Goldsmith, P. F., Yıldız, U. A., et al. 2016, MNRAS, 461, 3918
Hincelin, U., Wakelam, V., Hersant, F., et al. 2011, A&A, 530, A61
Hollenbach, D., & McKee, C. F. 1989, ApJ, 342, 306
Hollenbach, D. J., & Tielens, A. G. G. M. 1997, ARA&A, 35, 179
Inoue, T., Hennebelle, P., Fukui, Y., et al. 2018, PASJ, 70, S53
Ivlev, A. V., Silsbee, K., Sipilä, O., & Caselli, P. 2019, ApJ, 884, 176
Jappsen, A. K., Klessen, R. S., Larson, R. B., Li, Y., & Mac Low, M. M. 2005, A&A, 435, 611
Jenkins, E. B. 2009, ApJ, 700, 1299
Jiménez-Serra, I., Caselli, P., Tan, J. C., et al. 2010, MNRAS, 406, 187
Kainulainen, J., Hacar, A., Alves, J., et al. 2016, A&A, 586, A27
Kaufman, M. J., Wolfire, M. G., & Hollenbach, D. J. 2006, ApJ, 644, 283
Klein, T., Ciechanowicz, M., Leinz, C., et al. 2014, IEEE Trans.Terahertz Sci. Technol., 4, 588
Könyves, V., André, P., Men'shchikov, A., et al. 2015, A&A, 584, A91
Kurucz, R. L. 1979, ApJS, 40, 1
Larson, R. L., Evans Neal J., I., Green, J. D., & Yang, Y.-L. 2015, ApJ, 806, 70
Le Bourlot, J., Le Petit, F., Pinto, C., Roueff, E., & Roy, F. 2012, A&A, 541, A76
Le Petit, F., Nehmé, C., Le Bourlot, J., & Roueff, E. 2006, ApJS, 164, 506
Lehmann, A., & Wardle, M. 2016, MNRAS, 455, 2066
Lehmann, A., Federrath, C., & Wardle, M. 2016, MNRAS, 463, 1026
Lesaffre, P., Pineau des Forêts, G., Godard, B., et al. 2013, A&A, 550, A106
Liszt, H. S. 2017, ApJ, 835, 138
Liszt, H. S., & Ziurys, L. M. 2012, ApJ, 747, 55
Liszt, H. S., Lucas, R., & Pety, J. 2006, A&A, 448, 253
Louvet, F., Motte, F., Gusdorf, A., et al. 2016, A&A, 595, A122
Malinen, J., Montier, L., Montillaud, J., et al. 2016, MNRAS, 460, 1934
Marsh, K. A., Kirk, J. M., André, P., et al. 2016, MNRAS, 459, 342
Meyer, D. M., Jura, M., & Cardelli, J. A. 1998, ApJ, 493, 222
Molinari, S., Swinyard, B., Bally, J., et al. 2010, A&A, 518, L100
Müller, H. S. P., Schlöder, F., Stutzki, J., & Winnewisser, G. 2005, J. Mol. Struct., 742, 215
Nagai, T., Inutsuka, S.-i., & Miyama, S. M. 1998, ApJ, 506, 306
Nguyen-Lu'o'ng, Q., Motte, F., Carlhoff, P., et al. 2013, ApJ, 775, 88
Padoan, P., Juvela, M., Goodman, A. A., & Nordlund, Å. 2001, ApJ, 553, 227
Palmeirim, P., André, P., Kirk, J., et al. 2013, A&A, 550, A38
Park, J., & Ryu, D. 2019, ApJ, 875, 2
Pecaut, M. J., & Mamajek, E. E. 2013, ApJS, 208, 9
Planck Collaboration Int., XXXIII. 2016, A&A, 586, A136
Polychroni, D., Schisano, E., Elia, D., et al. 2013, ApJ, 777, L33
Pon, A., Johnstone, D., & Kaufman, M. J. 2012, ApJ, 748, 25
Pon, A., Johnstone, D., Kaufman, M. J., Caselli, P., & Plume, R. 2014, MNRAS, 445, 1508
Pound, M. W., & Wolfire, M. G. 2008, ASP Conf. Ser., 394, 654
Rayner, T. S. M., Griffin, M. J., Schneider, N., et al. 2017, A&A, 607, A22
Risacher, C., Güsten, R., Stutzki, J., et al. 2018, J. Astron. Instrum., 7, 1840014
Röllig, M., & Ossenkopf, V. 2013, A&A, 550, A56
Röllig, M., Abel, N. P., Bell, T., et al. 2007, A&A, 467, 187
Schilke, P., Walmsley, C. M., Pineau des Forets, G., & Flower, D. R. 1997, A&A, 321, 293
Schisano, E., Rygl, K. L. J., Molinari, S., et al. 2014, ApJ, 791, 27
Schneider, N., Bontemps, S., Simon, R., et al. 2011, A&A, 529, A1
Schneider, N., Csengeri, T., Hennemann, M., et al. 2012, A&A, 540, L11
Schneider, N., Bontemps, S., Motte, F., et al. 2016, A&A, 591, A40
Smith, R. J., Glover, S. C. O., Klessen, R. S., & Fuller, G. A. 2016, MNRAS, 455, 3640
Szűcs, L., Glover, S. C. O., & Klessen, R. S. 2014, MNRAS, 445, 4055
Tielens, A. G. G. M., & Hollenbach, D. 1985, ApJ, 291, 722
Tritsis, A., & Tassis, K. 2018, Science, 360, 635
van der Tak, F. F. S., Black, J. H., Schöier, F. L., Jansen, D. J., & van Dishoeck, E. F. 2007, A&A, 468, 627
Vázquez-Semadeni, E., Palau, A., Ballesteros-Paredes, J., Gómez, G. C., & Zamora-Avilés, M. 2019, MNRAS, 490, 3061
Vilas-Boas, J. W. S., Myers, P. C., & Fuller, G. A. 1994, ApJ, 433, 96
Visser, R., van Dishoeck, E. F., & Black, J. H. 2009, A&A, 503, 323
Wenger, M., Ochsenbein, F., Egret, D., et al. 2000, A&AS, 143, 9
Whitworth, A. P., & Jaffa, S. E. 2018, A&A, 611, A20

Appendix A: SOFIA [O I] and [C II] observations

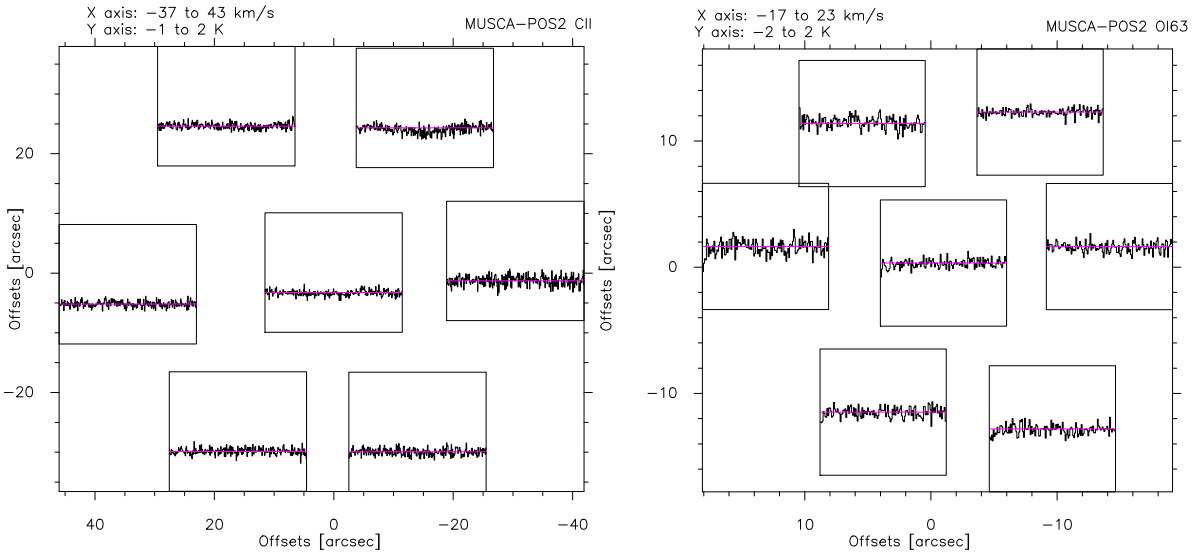

Fig. A.1. *Left*: observed pixels for the [C II] 158 μm line with the SOFIA telescope with a spectral resolution of 0.3 km s^{-1}. *Right*: observed pixels for the [O I] 63 μm line.

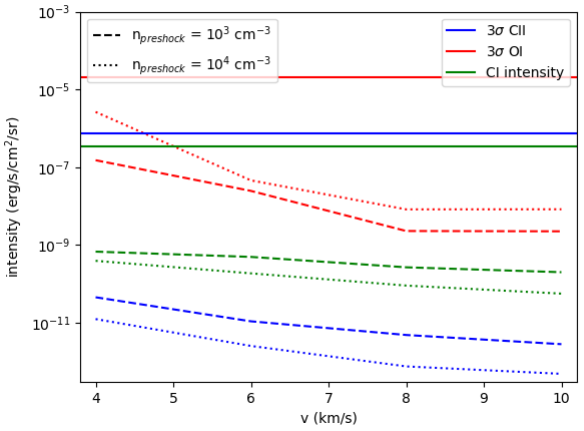

Fig. A.2. Intensity of [C II] (blue), [O I] (red), and [C I] (green) predicted for J-type shock models with a preshock density of $n = 10^3$ cm^{-3} and $n = 10^4$ cm^{-3} by the Paris-Durham code. The horizontal lines indicate the observed [C I] intensity and 3 σ upper limits for [C II] and [O I]. This shows that the [C II] and [O I] non-detections in Musca are consistent with shocks and that the [C I] brightness from the shock is not brighter than the total observed [C I] brightness in Musca.

The individual pixels of the upGREAT LFA and HFA, covering the [C II] 158 μm line and the [O I] 63 μm line, respectively, are displayed in Fig. A.1. Both lines, [C II] and [O I] are not detected above an rms (depending on the pixel) of 0.06 and 0.13 K for the LFA, and 0.11 and 0.21 K for the HFA.

[O I] is a possible shock tracer, but its non detection does not argue against a possible shock excitation, see Fig. A.2, because of the difficulty to excite [O I] emission. It either needs high-velocity shocks (Hollenbach & McKee 1989), an irradiated lower velocity shock (Lesaffre et al. 2013; Godard et al. 2019) or dense J/CJ-type shocks (Flower & Pineau Des Forêts 2010; Gusdorf et al. 2017). Simulations of massive molecular cloud formation through colliding flows predict an [O I] brightness around 0.01–0.05 K km s^{-1} (Bisbas et al. 2017). Yet, such predicted brightnesses are highly uncertain because of the unconstrained atomic oxygen abundance in the ISM (e.g. Meyer et al. 1998; Cartledge et al. 2004; Jenkins 2009; Hincelin et al. 2011).

Appendix B: A two layer multi-component model

To investigate possible effects of self-absorption, we apply a multi-component dual layer model (Guevara et al. 2020) to the observations of the CO(2–1) isotopologues. This LTE model fits the radiative transfer equations for multiple components distributed in two layers. The assumption of LTE for low-J CO lines is a justified approximation, as discussed in for example Goldsmith & Langer (1999); Liszt et al. (2006). van der Tak et al. (2007) also show that the LTE model is mostly valid for the ground state CO(1–0) transition and deviations from this approximation increase with the quantum number of the upper level. Here, we only use the CO(2–1) isotologue transitions. The fitted radiative transfer equation is given by

$$T_{\rm mb}(\mathrm{v}) = \left[\sum_{i_{\rm bg}} \mathcal{J}_\nu(T_{{\rm ex},i_{\rm bg}}) \left(1 - \mathrm{e}^{-\tau_{i_{\rm bg}}(\mathrm{v})}\right)\right] \mathrm{e}^{-\sum_{i_{\rm fg}} \tau_{i_{\rm fg}}(\mathrm{v})} + \sum_{i_{\rm fg}} \mathcal{J}_\nu(T_{{\rm ex},i_{\rm fg}}) \left(1 - \mathrm{e}^{-\tau_{i_{\rm fg}}(\mathrm{v})}\right), \quad \text{(B.1)}$$

with $\mathcal{J}_\nu(T_{\rm ex})$ the equivalent brightness temperature of blackbody emission at a temperature $T_{\rm ex}$:

$$\mathcal{J}_\nu(T_{\rm ex}) = \frac{h\nu}{k_{\rm B}} \frac{1}{\mathrm{e}^{T_0/T_{\rm ex}} - 1}, \quad \text{(B.2)}$$

with the equivalent temperature of the excited level $T_0 = h\nu/k_{\rm B}$ and ν the transition frequency. The single components of the model are represented by Gaussian profiles, thus the velocity dependent optical depth of every component is given by:

$$\tau(v) = \tau_0 \mathrm{e}^{-4\ln 2 \left(\frac{\mathrm{v}-\mathrm{v}_0}{w}\right)^2}, \quad \text{(B.3)}$$

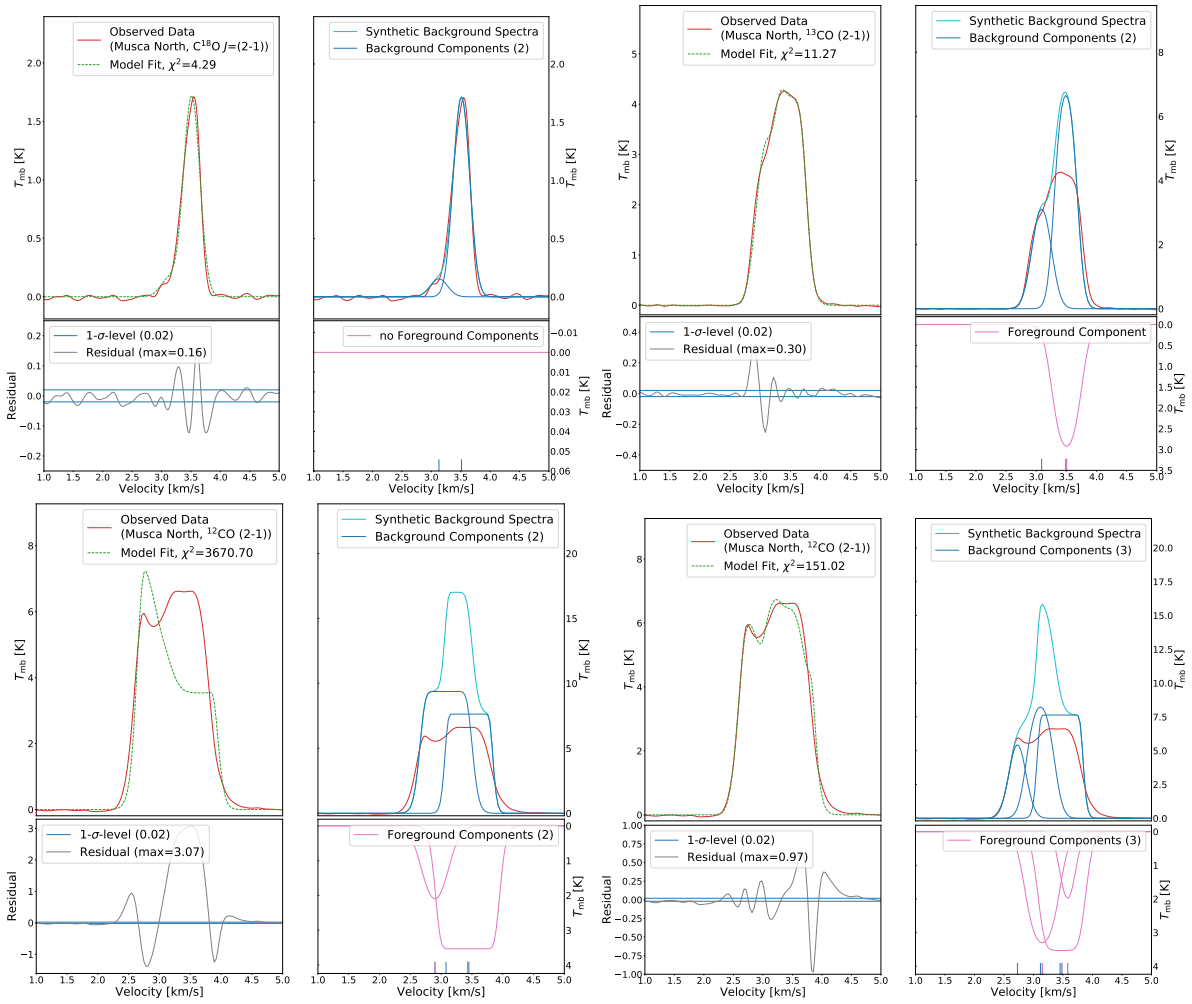

Fig. B.1. Results from a two-layer, multi-component fit to the observed CO(2–1) isotopes at the northern Musca position. *Upper two panels and the lower left panel*: fit with two velocity components derived from the optically thin $C^{18}O$(2–1) emission line, *lower right panel*: best model fit for the observed ^{12}CO(2–1) line. In each panel, *upper left sub-panel*: observed data as a red line and the model fit as a green dashed line. *Upper right sub-panel*: individual components, *lower left sub-panel*: residuals and *lower right sub-panel*: information on the number and contribution of the foreground. It becomes obvious that two components can be fitted for $C^{18}O$(2–1) and ^{13}CO(2–1), but are insufficient for the ^{12}CO(2–1) line.

with v_0 the central (LSR) velocity of the component and w the line width (FWHM).

Each of our components (background and foreground alike) are characterized by four quantities: excitation temperature, optical depth, position (LSR velocity), and width (FWHM). For a given number of components the model fit converges towards the best values for each parameter in a given range. The line position and its width are confined by the observed line profile, thus the excitation temperature and optical depth remain free parameter. The combination of T_{ex} and τ is degenerate, that is, higher excitation temperatures go together with lower optical depths and vice versa (and then give a similar fit). However, we can to first order constrain the gas temperature using the *Herschel* dust temperature T_d.

The Musca filament (in particular in the crest), is most likely heated by cosmic rays because neither thermal (low densities) nor radiative heating (low FUV field) dominates. The main cooling of the gas is happening via the low-J CO lines. Because of the low densities, freeze-out of CO is probably not so significant as it is for high densities. Standard dust models (Goldsmith 2001) predict a difference between gas and dust temperature (with $T_g > T_d$), while recent studies (Ivlev et al. 2019), considering also the grain size distribution, anticipate a less strong difference between gas and dust temperatures. We thus use as a starting value the dust temperatures derived from *Herschel* shown in Fig. 4 and apply a gas excitation temperature in the range of 10 to 13 K for the filament crest component and of T > 13 K for the shoulder+blueshifted component. Therefore, only the optical depth remains as a free parameter.

The two layer multi-component model is applied to the northern position (the results for the southern position are similar) iteratively for the three transition lines: $C^{18}O$(2–1), ^{13}CO(2–1) and ^{12}CO(2–1), as shown in Fig. B.1.

We start with the $C^{18}O$(2–1) line where we expect no absorption due to the foreground. This way we determine the background components, detected with this line, which are simply scaled up by the natural abundance ratio for the two remaining

Table B.1. Model results for the two layer multi-component fit.

Fit parameter	Background				Foreground			
Units	T_{ex} (K)	τ	v (km s^{-1})	Δv (km s^{-1})	T_{ex} (K)	τ	v (km s^{-1})	Δv (km s^{-1})
$C^{18}O$ component 1	12.50	0.24	3.51	0.31	–	–	–	–
$C^{18}O$ component 2	14.00	0.02	3.13	0.34	–	–	–	–
^{13}CO component 1	12.70	1.70	3.49	0.31	7.69	1.70	3.50	0.39
^{13}CO component 2	13.80	0.41	3.09	0.35	–	–	–	–
^{12}CO component 1	12.35	90.00	3.45	0.30	7.80	7.90	3.48	0.44
^{12}CO component 2	14.80	1.75	3.12	0.37	8.13	2.00	3.15	0.45
^{12}CO component 3	69.00	0.09	2.73	0.34	10.00	0.45	3.58	0.28

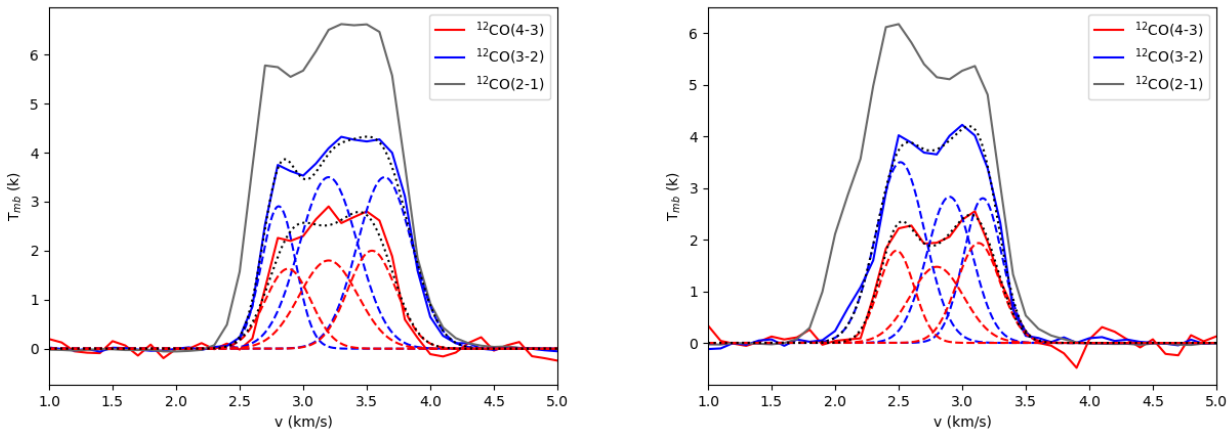

Fig. B.2. Results of a fit of three Gaussian profiles to the $^{12}CO(3–2)$ and $^{12}CO(4–3)$ lines towards the crest in the northern map (*left*) and southern map (*right*). The solid lines are the observed data, the long-dashed lines the fit with three individual components, and the short-dashed lines the resulting spectrum.

molecular carbon lines. The physical parameter of each component obtained from the model fit are summarized in Table B.1 and plotted in the upper left panel of Fig. B.1. This fit constrains the position and optical depth of the background component.

We then continue to model the $^{13}CO(2–1)$ line profile. Because the background components are here constrained by the $C^{18}O(2–1)$ fit, we scale up the background components by the $^{13}CO/C^{18}O \sim 7$ ratio. We do not strictly fix the parameter obtained from the $C^{18}O(2–1)$ model fit, but allow the model to find the best fit in a small range around the given parameter.

The scaled up background emission overshoots the observed line at $v \sim 3.5$ km s^{-1}. To model the observed line intensities, we add a cold foreground layer with $T < 10$. The foreground component absorbs the overshooting emission, see the upper right panel of Fig. B.1. Note, however, that it is unlikely that we have a cooler layer that "wraps around" the filament (which we consider a cylinder) because the *Herschel* temperature map clearly shows an increasing temperature when going outwards from the crest, see Fig. 4. The only possible way that one could have cool foreground emission that can absorb emission, is by considering a clumpy medium that is unresolved by the *Herschel* beam. In this unresolved clumpy medium, located in the foreground of the line of sight, one then would need mixed relatively cold (<10 K) and warm gas (>15 K) which gives rise to a steadily increasing average temperature in the *Herschel* beam when moving outwards from the filament crest.

The second blueshifted component only matches the observed emission with an increased $^{13}CO/C^{18}O$ abundance ratio, see Table B.1. The abundance ratio between the molecules is not a very well defined value. The processes of selective photodissociation and carbon isotopic fractionation can modify the relative abundances of CO isotopologues (e.g. Visser et al. 2009; Liszt 2017). In particular in more diffuse regions, the fractionation via the exchange reaction between $^{13}C^+$ and ^{12}CO leads to an enhancement of the ^{13}CO abundance (e.g. Liszt & Ziurys 2012; Röllig & Ossenkopf 2013; Szűcs et al. 2014). In addition - though probably less important for Musca because of the low FUV field - the more abundant ^{12}CO and ^{13}CO isotopologues shield themselves from the destructive effect of FUV photons more efficiently than the less abundant $C^{18}O$ isotopologue because the photodissociation of CO is governed by line absorption. In this context we note that Hacar et al. (2016) found indications of strong fractionation leading to a significant increase of the $^{13}CO/C^{18}O$ abundance ratio above the standard value of 7 at $A_V < 3$. Further analysis of this abundance ratio in our companion paper on the Musca filament confirms this result presented in Hacar et al. (2016).

In the previous two model fits, we determined the background and foreground components which we now scale up by the abundance ratio $^{12}CO/^{13}CO \sim 60$. Note that this value can be significantly lower because of fractionation (see above). The resulting fit is shown in the left lower panel of Fig. B.1.

Due to the large optical depths, we observe flat-topped spectra in the background and foreground layer. Since the observed intensities do not fit the natural carbon abundance ratio for the second component we only fix the first component and allowed the model to vary over a range of values in the second component to find the best possible solution. In addition we included a foreground component, which would only be observable in the ^{12}CO isotope, to remove the emission excess in the blueshifted wing and possibly reproduce the bump located in the blueshifted part of the observed ^{12}CO spectrum. The resulting spectra show a flat spectrum at velocities with bright C^{18}O(2–1) emission, followed by an emission peak at the blue-shifted wing. Thus, the model results do not manage to represent the line shape, the observed bump in particular, and intensity by taking self- or foreground absorption effects of the scaled up background components derived from the isotopes, see lower left panel of Fig. B.1.

Since two background components do not represent the observed spectrum, we include an additional component to the model, which is only visible in the ^{12}CO spectrum but vanishes in the noise for the weaker isotopes, see lower right panel of Fig. B.1. To meet this criteria we need to include a background component with low optical depth, which results in an increased temperature since a low optical depth requires an increase in temperature to produce the same amount of emission. This third background component is located at v = 2.8 km s^{-1}, see Table B.1. In addition we allow cold optically thin components in order to correct for the emission excess in the central and red-shifted part of the spectrum. As in the previous model fit we do not fix the central second component by the carbon abundance ratio, but allow it to vary in a wide range to find the best model fit to the observed data. We thus manage to represent the spectrum well, only with three background components.

Appendix C: SiO non-detection

The observations with the PI230 instrument on APEX towards the Musca cloud presented in Paper I covered the SiO(5–4) line. We have presented the detection of warm gas heated by low-velocity shocks, which makes the observation of SiO(5–4) interesting since some molecular clouds display extended SiO emission with relatively narrow linewidths (Jiménez-Serra et al. 2010; Nguyen-Lu'o'ng et al. 2013; Duarte-Cabral et al. 2014). This suggests that this is not SiO sputtered from the grains by protostellar outflows (e.g. Schilke et al. 1997; Gusdorf et al. 2008a). To explain this extended SiO emission in W43, it was considered that 1–10% of Si was not locked in the grains in the preshock gas (Louvet et al. 2016).

In Musca, because of the low-velocity shocks, sputtering of SiO from the grains seems improbable (Gusdorf et al. 2008b; Louvet et al. 2016). Upon analysing the data after averaging over the filament crest ($N > 3\times10^{21}$ cm^{-2}), no SiO emission is detected with an rms of 0.0134 K.

Since SiO has a high critical density (>10^6 cm^{-3}) it requires a non-LTE approach (Csengeri et al. 2016) to study the maximal SiO abundance in the gas phase. Therefore, we use RADEX to search for an upper limit on the SiO column density. This is done for two densities 10^3 and 10^4 cm^{-3}, assuming a minimal temperature of 10 K and a FWHM of 0.5 km s^{-1} (similar to the C^{18}O linewidth). The resulting 3σ SiO column density upper limits are ~10^{14} and 10^{15} cm^{-2} for densities of 10^4 and 10^3 cm^{-3} respectively.

This upper limit is observed toward the filament crest, which has a *Herschel* dust column density of ~4×10^{21} cm^{-2}, such that the upper limit obtained at a density of 10^4 cm^{-3} should hold, see Paper I. Assuming all hydrogen is in molecular form, using [Si]/[H] = 2×10^{-5} and taking that all Si is found in the form of SiO (Louvet et al. 2016). This poses an upper limit of 0.06 % on the Si abundance in the gas phase (0.6 % when assuming n_{H_2} = 10^3 cm^{-3}).

This indicates that in a molecular cloud at an early stage of evolution basically all Si is locked in the grains and that one needs environments with a radiative or dynamic history like W43 or protostellar outflows to release SiO in the gas phase.

Appendix D: Mass accretion rate

As we have presented the detection of a filament accretion shock, it is possible to estimate the mass accretion rate as a result of this shock using $2\pi R\cdot\Sigma_{\rm shock}\cdot t_{\rm psc}^{-1}$. Where R is the radius that encompasses most dense gas (≈0.2 pc), $\Sigma_{\rm shock}$ is the column density of the shock layer, and $t_{\rm psc}$ is the post-shock cooling time for which we use the expression in Whitworth & Jaffa (2018)

$$t_{\rm psc} \lesssim 1.2{\rm Myr}\left(\frac{X_{\rm CO}}{3\cdot10^{-4}}\right)^{-1}\left(\frac{n_{\rm H_2,O}}{\rm cm^{-3}}\right)^{-1}\left(\frac{\rm v_s}{\rm kms^{-1}}\right)^{-1}, \quad \text{(D.1)}$$

with $n_{H_2,0}$ the pre-shock density and v_s the shock velocity.

To calculate $\Sigma_{\rm shock}$ we start from the $\Sigma_{^{12}CO}$ column density of the RADEX models that manage to reach the observed ratios in Sect. 3.5, which is 9×10^{14} cm^{-2}. $\Sigma_{\rm shock}$ is then given by $\Sigma_{^{12}CO}/X_{CO}$. This X_{CO} cancels out with the same term in Eq. (D.1).

In Eq. (D.1), we use an estimated preshock density $n_{H_2,0}$ = 4×10^2 cm^{-3}, v_s = 0.9 km s^{-1} and assume that the equality in Eq. (D.1) roughly holds. This implies that our mass accretion rate estimate here will be a lower limit. Putting all this together results in an estimated minimal mass accretion rate of 20 $M_\odot$ pc^{-1} Myr^{-1}.

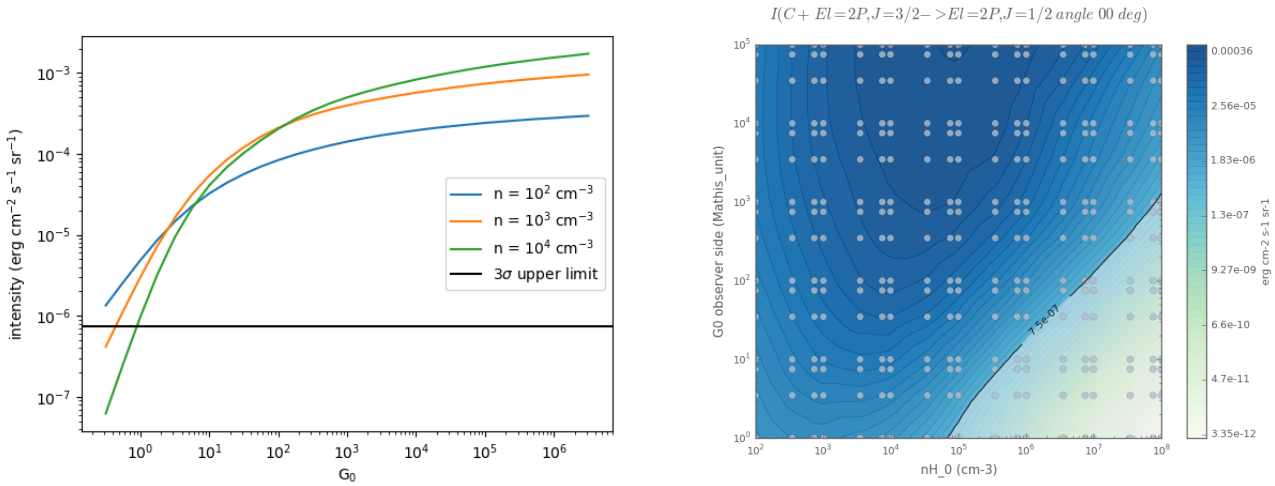

Figure 4.3: **Left:** The predicted [CII] intensity by the PDR Toolbox as a function of the FUV field strength for different densities. The horizontal line indicates the 3σ upper limit in Musca as obtained from the SOFIA observation. **Right:** The predicted [CII] intensity by the MEUDON PDR code on a grid of density and FUV field strength. The black curve indicates the observed [CII] 3σ upper limit. Both figures show that for acceptable densities in Musca ($n < 10^4$ cm^{-3}) the FUV field strength has to be significantly below 1 G_0.

4.1.4 Additional discussion of Paper-MS

The upper limit on the FUV field

The SOFIA observations indicate that the 3σ [CII] intensity upper limit is 7.5×10^{-7} erg cm^{-2} s^{-1} sr^{-1}. In Fig. 4.3 it is shown with the PDR Toolbox (Pound & Wolfire, 2008) that this upper limit requires an FUV field strength below 1 G_0 for acceptable densities ($n_H < 10^4$ cm^{-3}) in the Musca cloud. However, [CII] generally traces densities that are significantly below $n_H = 10^4$ cm^{-3} at the photodissociation surface of molecular clouds such as Musca (e.g. Tielens & Hollenbach, 1985; Beuther et al., 2014; Bertram et al., 2016; Franeck et al., 2018; Clark et al., 2019). Photodissociation codes have certain differences since the coupling between interstellar gas and radiation is a complex problem, which results in significant variations of the predicted results (Röllig et al., 2007). It is thus recommended to verify that a result is confirmed by another PDR code. This is why the implications of the [CII] upper limit on the FUV field strength were verified with the MEUDON code (Le Petit et al., 2006; Le Bourlot et al., 2012; Bron, Le Bourlot & Le Petit, 2014). Inspecting Fig. 4.3 shows that the [CII] intensity upper limit restricts the FUV field to values below 1 G_0 for $n_H < 10^5$ cm^{-3} with the MEUDON code. Two different photo-dissociation models thus consistently constrain the FUV field strength based on the [CII] observations with the SOFIA telescope.

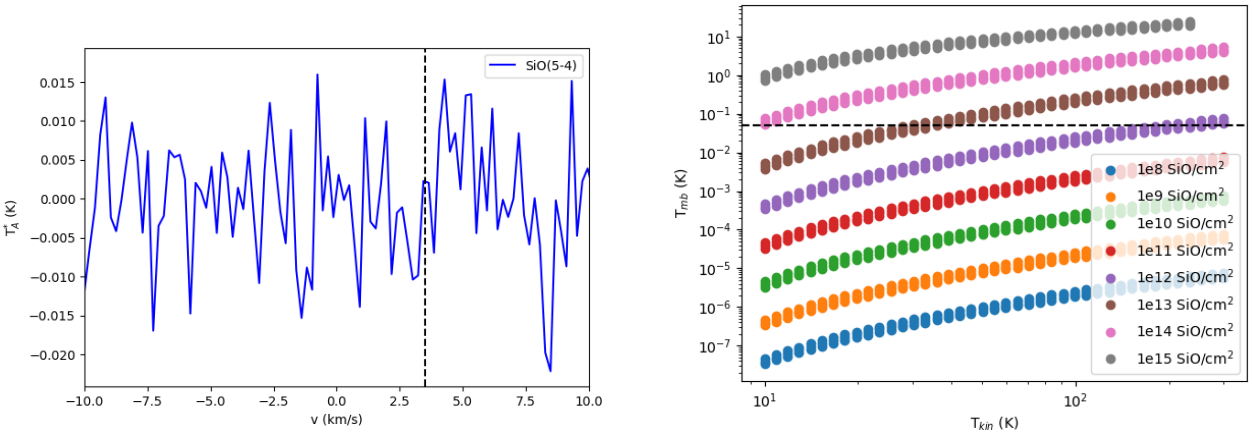

Figure 4.4: **Left:** The observed SiO(5-4) spectrum towards the Musca filament crest in the north with a baseline noise rms of 0.0134 K. The dashed vertical line indicates the rest velocity of the Musca filament crest in the north (3.5 km s^{-1}). **Right:** The predicted SiO(5-4) brightness with RADEX as a function of the kinetic temperature for different SiO column densities in the gas phase, assuming a density of $n_{H_2} = 10^4$ cm^{-3} in the filament crest. The dashed horizontal line indicates the 3σ noise rms.

The SiO(5-4) non-detection

The SiO(5-4) non-detection towards the Musca filament crest (N $> 3{\times}10^{21}$ cm^{-2}) mentioned before is shown in Fig. 4.4 for the northern map. The RADEX calculations that were used to determine the abundance upper limit are presented in the same figure. These RADEX calculations assume a FWHM of 0.5 km s^{-1} for SiO(5-4), which is roughly the linewidth found for the filament crest with C^{18}O(2-1), and $n_{H_2} = 10^4$ cm^{-3}. Figure 4.4 shows that a SiO column density of 10^{14} cm^{-2} and a temperature of 10 K correspond to the 3σ upper limit for the SiO(5-4) emission. This implies, as discussed in Paper-MS, that less than 0.06 % of the Si abundance is found in the gas phase for the Musca filament, and that an important dynamic and radiative history might be important to release Si in the gas phase in clouds such as W43 (Nguyen-Lu'o'ng et al., 2013; Louvet et al., 2016b).

The filament formation simulations

Simulations and synthetic observations from Clarke et al. (2017, 2018) were used to compare generic (shock) accretion signatures in filament formation simulations with the observations towards the Musca filament. These simulations were performed with the moving-mesh AREPO code (Springel, 2010a). This moving-mesh code makes use of a Voronoi tesselation[1]. Because a Voronoi tesselation divides space based on the distance between nearby particles, this tesselation naturally adapts the local resolution in the simulation to the local density. This makes it in a sense an intermediate solution between the more classical grid-based mesh (Teyssier, 2015) and smoothed particle hydrodynamics (SPH, Springel,

[1]For more information on Voronoi tesselations, see e.g. https://en.wikipedia.org/wiki/Voronoi_diagram

2010b) simulations.
The simulations start from a cylindrical converging flow, described by an initial density and velocity profile

$$\begin{aligned} n_H &= 6300\,\mathrm{cm^{-3}}\,R_0\,(r/pc)^{-1} \quad (\text{for } r < 3\,\mathrm{pc} \text{ and } \|z\| < 1.5\,\mathrm{pc}) \\ &= 0.063\,\mathrm{cm^{-3}} \quad (\text{elsewhere}) \end{aligned} \tag{4.2}$$

$$\begin{aligned} \mathbf{v} &= -0.75\mathbf{r}\,\mathrm{km\,s^{-1}} + \mathbf{v}_{\mathrm{turb}} \quad (\text{for } r < 3\,\mathrm{pc} \text{ and } \|z\| < 1.5\,\mathrm{pc}) \\ &= 0\,\mathrm{km\,s^{-1}} \quad (\text{elsewhere}) \end{aligned} \tag{4.3}$$

with $R_0 = 0.1$ pc, $\mathbf{r}$ the vector in the radial direction away from the filament center and $\mathbf{v}_{turb}$ the turbulent velocity field. This inflow velocity and density profile were constructed in order to be roughly representative of the B211/3 filament in Taurus (Palmeirim et al., 2013). The turbulent velocity field is generated assuming a power spectrum that is described by $P_k \sim k^{-4}$ with $k_{min} = 4.2$ pc^{-1}. The velocity field consists of solenoidal and compressive modes, and assumes a linewidth of 1 km s^{-1} (Clarke et al., 2018).
In order to produce synthetic observations with the RADMC-3D code (Dullemond et al., 2012), the simulations rely on a chemical network that is responsible for self-consistent CO formation. The chemical network in the simulations is the one presented in Glover & Clark (2012) which contains the simple CO network from Nelson & Langer (1997) that does not include fractionation of the CO isotopologues, and the hydrogen chemical network from Glover & Mac Low (2007a,b). The fact that the chemical network does not include fractionation effects is in contrast to the indications of fractionation effects in Musca (Hacar et al., 2016). Because the aim is to compare the observed spectra in Musca with generic kinematic signatures of filament accretion, this lack of fractionation in the simulations should, to first order, not have a major impact on the conclusions. It has however to be kept in mind that the comparison between observations and simulations has limitations.
To heat the gas in the simulations, an external interstellar radiation field of 1.7 G_0 and a cosmic ray ionisation rate of 10^{-17} s^{-1} were assumed. The radiation at UV wavelengths was adopted from Draine (1978) while the radiation at longer wavelengths was adopted from Black (1994). Such a weak embedding FUV field is a relatively good approximation for the Musca cloud.

Atomic oxygen in the ISM

With the SOFIA observations it was also attempted to detect the [OI] $^3P_0$ - $^3P_1$ line at 63 μm excited by the low-velocity shock, because a detection would have indicated that a large fraction of oxygen is found in atomic form in the ISM. It is critical to constrain the atomic oxygen abundance in the ISM because it is an important unknown in the oxygen chemistry of the ISM and thus the formation of life sustaining molecules (e.g. Wakelam, Herbst & Selsis, 2006). At the moment, the distribution of oxygen that is not locked in CO remains unknown. Particulary important in this search for the oxygen reservoir is the extensive search for O_2 with balloon-borne telescopes (Olofsson et al., 1998), the SWAS telescope (Goldsmith et al., 2000) and the Odin telescope (Pagani et al., 2003; Larsson et al., 2007). Only Larsson et al. (2007) presented a detection with a resulting O_2 abundance of $5{\cdot}10^{-8}$ compared to H_2.

The detection of [OI] would also have shown that atomic oxygen plays an important role as a coolant in the ISM. At the moment, the role of [OI] cooling remains uncertain which has led to some shock models taking into account cooling by [OI] (Draine, Roberge & Dalgarno, 1983), while other models (Kaufman & Neufeld, 1996a; Pon, Johnstone & Kaufman, 2012) do not focus on a possible role of [OI]. The [OI] line is extremely difficult to detect, e.g. because of its high energy of the upper level, such that the current observations do not put a really significant constraint on the atomic oxygen reservoir in the ISM. This can be demonstrated using RADEX and the detected shock layer in CO. For the excitation conditions that manage to reproduce the CO observations in Fig. 8 and 9 of Paper-MS, Tab. 4.1 shows that the predicted [OI] brightness is far below the 3σ upper limit of the performed SOFIA when assuming [O] = [CO] in the shocked layer. Furthermore, Table 4.1 even shows that, assuming T_{kin} = 100 K, [O] = 50×[CO] would have been necessary to detect the [OI] line with the current SOFIA observations. It will thus be necessary to wait for the facilities offered by SPICA or the Origins Space Telescope to detect [OI] for reasonable atomic oxygen abundances.
Table 4.1 also shows the predicted [OI] $^3P_1$ - $^3P_2$ transition at 146 μm has a similar predicted line brightness as the transition at 63 μm. It will thus be particularly challenging to detect either of the [OI] transitions.

Inspecting predictions by low-velocity shock models of the Paris-Durham code in Fig. 4.5, it is found that both for J- and C-type shocks it is difficult to detect [OI]. However, increasing the preshock density has an important impact on the predicted [OI] brightness, such that a preshock density of $n_H \sim 10^5$ cm^{-3} should be sufficient to detect [OI] from low-velocity shocks. For these preshock densities, massive star forming regions such as DR21 have to be considered where the inflowing filaments on the massive star forming ridge are expected to roughly have this density (Hennemann et al., 2012). However, in such regions the observations are highly contaminated by radiative and mechanical feedback from massive stars that form in these clouds.
In Fig. 4.6, the initial conditions for the oxygen chemistry of the Paris-Durham shock models is presented in more detail, showing the fractional abundance of H_2 and the most important oxygen-bearing molecules. The models shown in Fig. 4.6, are C-type shocks with a preshock density of $n_H = 10^3$ cm^{-3} and a velocity of 4 km s^{-1}. The first presented shock model is not irradiated by FUV photons, while the second model is irradiated by an FUV field of 1 G_0. Since the purpose of the analysis here is to study the initial oxygen abundances in the Paris-Durham code, it is not of importance whether a C- or J-type shock is studied.
Analysing the results, it can be noted that basically all hydrogen is found in molecular form in both the irradiated and non-irradiated case. Inspecting the oxygen-bearing molecules for the non-irradiated case, it is found that the sum of the fractional abundances of oxygen-bearing molecules do not reach the total oxygen abundance fraction in the ISM which is around 3.16×10^{-4}. Apart from CO, it is observed that a significant fraction of molecular oxygen is locked in O_2 which is above the observed abundances in molecular clouds (Larsson et al., 2007). However, this lack of molecular oxygen is a persistent difficulty for astrochemical models (e.g. Wakelam et al., 2019). Analysing the irradiated shock model, it is found that basically all oxygen (a fractional abundance of 3×10^{-4}) is in atomic gas form for the Paris-Durham shock code. The predicted difficulty to detect [OI] in a non-irradiated shock is thus also due to the lack of atomic oxygen in the model. As a final note, the observed lack of molecular oxygen

T_{kin} (K)	[OI] $^3P_1$ - $^3P_2$ (146 μm)	[OI] $^3P_0$ - $^3P_1$ (63 μm)
$N_O = 9{\cdot}10^{14}$ cm^{-2}, FWHM = 0.4 km s^{-1}, $n_{H_2} = 7{\cdot}10^3$ cm^{-3}		
50 K	$2.4{\cdot}10^{-4}$ K	$9.5{\cdot}10^{-5}$ K
75 K	$1.4{\cdot}10^{-3}$ K	$9.0{\cdot}10^{-4}$ K
100 K	$3.5{\cdot}10^{-3}$ K	$2.9{\cdot}10^{-3}$ K
$N_O = 5{\cdot}10^{16}$ cm^{-2}, FWHM = 0.4 km s^{-1}, $n_{H_2} = 7{\cdot}10^3$ cm^{-3}		
100 K	0.18 K	0.16 K

Table 4.1: The predicted brightness of the [OI] $^3P_1$ - $^3P_2$ and [OI] $^3P_0$ - $^3P_1$ transitions for the excitation conditions of the shocked gas detected with ^{12}CO(4-3). The estimated CO column density for the shocked (gas $N_{^{12}CO}$) is $\sim 9{\cdot}10^{14}$ cm^{-2}. For [OI], it is found than a column density N_O of at least $5{\cdot}10^{16}$ cm^{-2} is required for detection with SOFIA.

does not necessarily imply a large atomic oxygen fraction in the ISM. For example, Wakelam et al. (2019) reported that atomic oxygen could deplete on the dust grains over the full evolution from the diffuse ISM to dense star forming gas, which might be able to explain the observed lack of molecular oxygen.

4.1.5 Prospective: The relation between shocks, mass accretion and fiber formation

The results presented for the Musca filament indicate the importance of filament accretion shocks in the formation of dense filamentary gas. A next step is to search for signatures of filament accretion shocks in other filaments forming low-mass stars, and thus establish whether dense star forming filaments are post-shock gas. This can be an important constraint on the origin of the highly debated characteristic filament width (Arzoumanian et al., 2011, 2019; Koch & Rosolowsky, 2015). A study of filament accretion shocks could simultaneously provide indications on the formation of the so-called fibers (Hacar et al., 2013). There are several proposed scenarios for fiber formation. The first proposed scenario is often referred to as ′fray & gather′ (Smith, Glover & Klessen, 2014; Smith et al., 2016), where velocity coherent filamentary structures are formed in the supersonic turbulent ISM by compression from low-velocity shocks. After their formation, the fibers are gathered in a *Herschel* dust continuum filament by large scale motions in the cloud. This will lead e.g. to an evolution of the number of fibers in a filament over time. A second proposed scenario for fiber formation is called ′fray & fragment′ (Moeckel & Burkert, 2015; Tafalla & Hacar, 2015; Clarke et al., 2017). Here, a collision of two converging flows produce a dust continuum filament that consists of several intertwined fibers as a result of residual turbulent motions and gravity. Some of these fibers manage to accrete a sufficient amount of mass to become gravitationally unstable and fragment into prestellar cores. A last scenario has been proposed that aims to position itself between the two previous scenarios, which is called ′compress, accrete, fragment′ (Shimajiri et al., 2019a). In this scenario, dense filaments are formed from multiple episodes of compression. These filaments then accrete mass from gravitationally driven inflow in sheet-like structures. This gravitational energy of the inflow is then converted into turbulent energy and flows (Klessen & Hennebelle, 2010; Arzoumanian et al., 2013) which are responsible for the observed fibers.

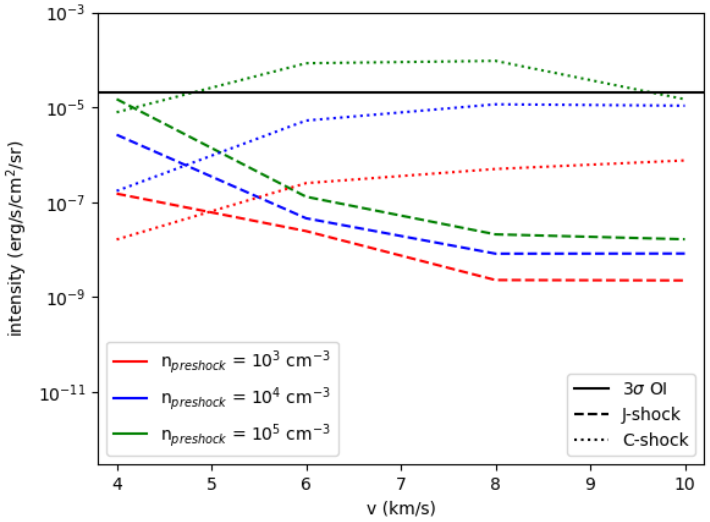

Figure 4.5: Predictions for the [OI] intensity as a function of velocity for different non-irradiated shock models in the Paris-Durham code (Flower & Pineau des Forêts, 2003; Lesaffre et al., 2013; Godard et al., 2019). It shows both the evolution of J-shocks (dashed lines) and C-shocks (dotted lines) for preshock densities ranging between $n_{H,preshock} = 10^3$ cm^{-3} and $n_{H,preshock} = 10^5$ cm^{-3}. The horizontal line indicates the observed 3σ upper limit of the [OI] intensity. This suggests that high preshock densities are required to detect the [OI] line.

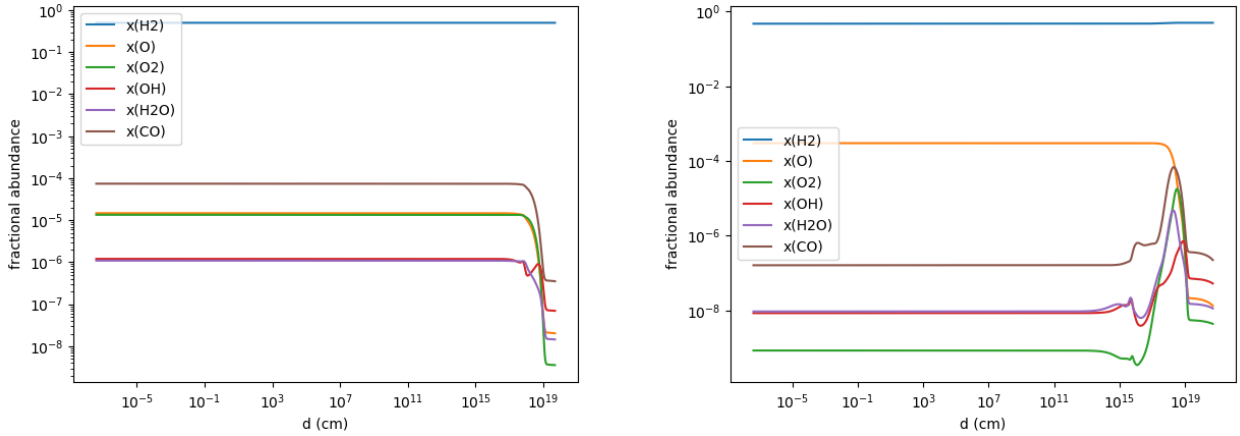

Figure 4.6: **Left:** The evolution of the fractional molecular abundance of H_2 and several oxygen-bearing molecules as a function of the distance for a non-irradiated C-type shock (v_{shock} = 4 km s^{-1}, $n_{H,preshock}$ = 10^3) with the Paris-Durham shock code. **Right:** The same shock model irradiated by a FUV field of 1 G_0.

In this scenario, it is proposed that non-fragmenting fibers are in fact accretion flows on the filament and fragmenting fibers are the imprint of the accretion driven turbulence.
Lastly, when studying fibers it was cautioned in particular by Zamora-Avilés, Ballesteros-Paredes & Hartmann (2017) and Clarke et al. (2018) that coherent structures in velocity space are not necessarily always individual structures in physical space.

In order to test these scenarios, observations of low-velocity accretion shocks can provide interesting constraints. It can be studied whether filament accretion shocks are associated with the fibers in a filament. This would indicate that fibers are directly accreting from an ambient converging flow. If fibers are not directly associated with accretion shocks, this would suggest that there is no direct relation between the ambient cloud and fibers in the filament. To determine whether an accretion shock is associated with a fiber or not, comparison with synthetic observations from simulations will be necessary. To avoid increasing complexity as a result of multiple velocity components, pilot studies would also ideally observe relatively isolated fibers. To attempt and provide the first constraints on these models, a proposal was submitted (Bonne et al. 2019) and accepted for the APEX telescope. Specifically, to observe ^{12}CO(4-3) and ^{12}CO(2-1) with a spectral resolution of 0.1 km s^{-1} towards the B211/3 filament in Taurus, which is the prototypical fibrous filament (Hacar et al., 2013). The ^{12}CO(4-3)/^{12}CO(2-1) ratio can constrain whether there is shock excitation near the filament, while the spectral resolution should be able to investigate whether the low-velocity shocks are directly associated to the fibers. Ideally, these APEX observations would be complemented with SOFIA observations of the [CII] line similar to the observations presented in Paper-MS, because it allows to constrain the FUV field and thus be more confident about the presence of shock excitation. It should be noted that the predictions for observed accretion signatures by the different fiber formation models are still highly qualitative and

not always specified in great detail. Ideally, the various proposed scenarios would provide predictions how one can differentiate the different scenarios. The proposed observations and their results can thus provide an incentive to study concrete predictions by the different models in more detail with regard to the presence of filament accretion shocks.

4.2 Dense gas formation in Chamaeleon-Musca by a cloud-cloud collision

4.2.1 The physics of the filamentary ISM

In the previous section, it was put forward that filament accretion shocks from a converging flow are responsible for continuous dense gas provision to the Musca filament. This finding suggests an accretion scenario for dense gas formation in the Musca filament. However, this study did not address the physical process that drives this converging flow.

The physical processes that are responsible for the observed filamentary structure of the ISM are still highly debated, in particular because filamentary structures are ubiquitous in a large variety of numerical simulations. Magnetohydrodynamic simulations with and without gravity naturally produce a filamentary ISM (e.g. Mac Low & Klessen, 2004; Federrath, 2016). The converging flows that compress the gas to form filaments can be the result of purely turbulent motions (e.g. Padoan et al., 2001; Jappsen et al., 2005; Pudritz & Kevlahan, 2013), but inflow can also be driven by a gravitational collapse (e.g. Nagai, Inutsuka & Miyama, 1998; Klessen & Burkert, 2000; Hartmann & Burkert, 2007; Van Loo, Keto & Zhang, 2014; Gómez & Vázquez-Semadeni, 2014). It was further shown that a filamentary cloud can also form from a large-scale HI converging flow (e.g. Ballesteros-Paredes, Hartmann & Vázquez-Semadeni, 1999; Koyama & Inutsuka, 2002; Audit & Hennebelle, 2005; van Loo et al., 2007; Banerjee et al., 2009), or as a result of a cloud-cloud collision (e.g. Anathpindika, 2009, 2010; Inoue et al., 2018; Iwasaki et al., 2019). When including the magnetic field in numerical simulations, it is found that the filamentary structure becomes even more evident (Hennebelle, 2013). The produced filamentary structures in Hennebelle (2013) form as a result of turbulent strain that is maintained by the magnetic field.

In order to address the processes responsible for filament formation in the ISM, observations of interstellar clouds are required that trace the physical properties and gas kinematics at different densities. First, we focus here on the Musca filament and ambient cloud, which are studied with several low-J ($\leq$ 3) CO isotopologues. These observations will be complemented with archival HI data and observations of the magnetic field orientation. From the presence of the filament accretion shocks, it was derived that there is dense gas near the Musca filament, but it did not truly address whether the Musca filament is a cylindrical structure. Since the cylindrical geometry was recently questioned by Tritsis & Tassis (2018), the paper below also particularly focusses on the geometry of the Musca filament.

4.2.2 Article: Formation of the Musca filament: evidence for asymmetries in the accretion flow due to a cloud-cloud collision (Paper-MC, in revision)

A&A 644, A27 (2020)
https://doi.org/10.1051/0004-6361/202038281

Astronomy & Astrophysics

Formation of the Musca filament: evidence for asymmetries in the accretion flow due to a cloud–cloud collision*

L. Bonne[1], S. Bontemps[1], N. Schneider[2], S. D. Clarke[2], D. Arzoumanian[3], Y. Fukui[4], K. Tachihara[4], T. Csengeri[5,1], R. Guesten[5], A. Ohama[4], R. Okamoto[4], R. Simon[2], H. Yahia[6], and H. Yamamoto[4]

[1] Laboratoire d'Astrophysique de Bordeaux, Université de Bordeaux, CNRS, B18N, allée Geoffrey Saint-Hilaire, 33615 Pessac, France
e-mail: lars.bonne@u-bordeaux.fr
[2] I. Physikalisches Institut, Universität zu Köln, Zülpicher Str. 77, 50937 Köln, Germany
[3] Instituto de Astrofisica e Ciencias do Espaco, Universidade do Porto, CAUP, Rua das Estrelas, 4150-762 Porto, Portugal
[4] Department of Physics, Nagoya University, Chikusa-ku, Nagoya 464-8602, Japan
[5] Max-Planck-Institut für Radioastronomie, Auf dem Hügel 69, 53121 Bonn, Germany
[6] INRIA Bordeaux Sud-Ouest, 33405 Talence, France

Received 28 April 2020 / Accepted 9 October 2020

ABSTRACT

Context. Dense molecular filaments are ubiquituous in the interstellar medium, yet their internal physical conditions and the role of gravity, turbulence, the magnetic field, radiation, and the ambient cloud during their evolution remain debated.
Aims. We study the kinematics and physical conditions in the Musca filament, the ambient cloud, and the Chamaeleon-Musca complex to constrain the physics of filament formation.
Methods. We produced CO(2–1) isotopologue maps with the APEX telescope that cut through the Musca filament. We further study a NANTEN2 ^{12}CO(1–0) map of the full Musca cloud, H I emission of the Chamaeleon-Musca complex, a *Planck* polarisation map, line radiative transfer models, *Gaia* data, and synthetic observations from filament formation simulations.
Results. The Musca cloud, with a size of ~3–6 pc, contains multiple velocity components. Radiative transfer modelling of the CO emission indicates that the Musca filament consists of a cold (~10 K), dense ($n_{H_2} \sim 10^4$ cm^{-3}) crest, which is best described with a cylindrical geometry. Connected to the crest, a separate gas component at $T \sim 15$ K and $n_{H_2} \sim 10^3$ cm^{-3} is found, the so-called strands. The velocity-coherent filament crest has an organised transverse velocity gradient that is linked to the kinematics of the nearby ambient cloud. This velocity gradient has an angle ≥30° with respect to the local magnetic field orientation derived from *Planck*, and the magnitude of the velocity gradient is similar to the transonic linewidth of the filament crest. Studying the large scale kinematics, we find coherence of the asymmetric kinematics from the 50 pc H I cloud down to the Musca filament. We also report a strong [C^{18}O]/[^{13}CO] abundance drop by an order of magnitude from the filament crest to the strands over a distance <0.2 pc in a weak ambient far-ultraviolet (FUV) field.
Conclusions. The dense Musca filament crest is a long-lived (several crossing times), dynamic structure that can form stars in the near future because of continuous mass accretion replenishing the filament. This mass accretion on the filament appears to be triggered by a H I cloud–cloud collision, which bends the magnetic field around dense filaments. This bending of the magnetic field is then responsible for the observed asymmetric accretion scenario of the Musca filament, which is, for instance, seen as a V-shape in the position–velocity (PV) diagram.

Key words. ISM: structure – ISM: kinematics and dynamics – ISM: individual objects: Musca – stars: formation – evolution

1. Introduction

The complexity of the interstellar medium (ISM) has been revealed in numerous continuum and molecular line studies, but it is only since the unprecedented far-infrared sensitivity of the *Herschel* Space Telescope (Pilbratt et al. 2010) that the ubiquity of dense filamentary structures in the ISM has been revealed and their integral role in the star formation process has been established. It was shown that almost all pre-stellar and protostellar cores are located in filaments or at a filament junction (e.g. André et al. 2010, 2014; Molinari et al. 2010; Bontemps et al. 2010; Könyves et al. 2010, 2015; Arzoumanian et al. 2011; Hill et al. 2011; Schneider et al. 2012; Rygl et al. 2013; Polychroni et al. 2013; Marsh et al. 2016). Spectral line observations of filamentary structures have shown that many dust continuum filaments contain several velocity-coherent sub-filaments, the so-called fibers (e.g. Hacar et al. 2013; Tafalla & Hacar 2015; Dhabal et al. 2018). However, recently some theoretical studies have indicated that coherent structures in velocity space are not necessarily coherent in three-dimensional space (Zamora-Avilés et al. 2017; Clarke et al. 2018). Massive filamentary structures in more distant regions, such as massive ridges (e.g. Schneider et al. 2010; Hennemann et al. 2012) and hub-filament systems (e.g. Myers 2009; Schneider et al. 2012; Peretto et al. 2013, 2014; Henshaw et al. 2017; Williams et al. 2018), are proposed to be the dominant way to form rich clusters of stars (e.g. Motte et al. 2018), and thus the bulk of star formation in our galaxy. It is therefore critical to unveil the precise physical processes at work to explain the formation of filaments of all types.

While early theoretical studies described filaments as structures confined by isotropic pressure equilibrium (Ostriker 1964;

* The reduced datacubes are only available at the CDS via anonymous ftp to cdsarc.u-strasbg.fr (130.79.128.5) or via http://cdsarc.u-strasbg.fr/viz-bin/cat/J/A+A/644/A27

Inutsuka & Miyama 1992), simulations support the argument that filaments are a manifestation of structure development caused by the thermodynamic evolution of the ISM during molecular cloud formation. All (magneto)-hydrodynamic ISM simulations with turbulence, including and not including self-gravity and/or a magnetic field, naturally produce filaments (e.g. Audit & Hennebelle 2005; Heitsch et al. 2005; Hennebelle et al. 2008; Nakamura & Li 2008; Banerjee et al. 2009; Gómez & Vázquez-Semadeni 2014; Smith et al. 2014, 2016; Chen & Ostriker 2014; Seifried & Walch 2015; Federrath 2016; Duarte-Cabral & Dobbs 2017). In these simulations, filaments are argued to originate from the collision of shocked sheets in turbulent flows (Padoan et al. 2001), by instabilities in self-gravitating sheets (Nagai et al. 1998), or as the result of long-lived coherent flows in the turbulent ISM (Hennebelle 2013) which could be at least partly convergent. The magnetic field can only reinforce the presence of filaments, as it increases local axisymetries and as it may stabilise and drive turbulent flows aligned with the field (Hennebelle 2013). The case of magnetised H I colliding streams and cloud–cloud collisions (e.g. Ballesteros-Paredes et al. 1999; Koyama & Inutsuka 2002) is particularly interesting in this context as it naturally creates a significant level of turbulence and flows. It can also lead to bending of the magnetic field around pre-existing structures, which could then drive local convergent flows perpendicular to the dense filamentary structures (Inoue & Fukui 2013; Inoue et al. 2018). Such local convergent flows were indeed observed for massive dense cores by Csengeri et al. (2011), for instance. From an observational point of view, cloud-cloud collisions at a velocity of 10–20 km s^{-1} have been argued to form massive star-forming filaments (Fukui et al. 2020, and references therein).

Any scenario to form filaments has to account for the most critical properties of observed filaments. The so-called universal (Arzoumanian et al. 2011, 2019; Koch & Rosolowsky 2015), yet highly debated (e.g. Panopoulou et al. 2017; Seifried et al. 2017; Ossenkopf-Okada & Stepanov 2019), filament width of 0.1 pc in nearby molecular clouds is close to the sonic scale which could fit in a scenario where filaments are made of dense, post-shock gas of converging flows (Arzoumanian et al. 2011; Schneider et al. 2011; Federrath 2016). In the companion paper (Bonne et al. 2020), observational indications were found of warm gas from low-velocity shocks associated with mass accretion on the Musca filament. It has also led to some theoretical models considering gravitational inflow that might provide an explanation for this universal width (Heitsch 2013; Hennebelle & André 2013). Indications of an inflowing mass reservoir as a result of gravity were presented in Palmeirim et al. (2013) and Shimajiri et al. (2019). In the medium surrounding dense filaments, striations are often found which are well aligned with the magnetic field (Goldsmith et al. 2008; Palmeirim et al. 2013; Alves de Oliveira et al. 2014; Cox et al. 2016; Malinen et al. 2016). This has often led to the interpretation of gas streaming along the magnetic field lines. So far, there is no strong observational evidence for this and recently it was argued from a theoretical study that striations might result from MHD waves (Tritsis & Tassis 2016) in large pc-scale sheets. Similarly, the so-called fibers, seen as sub-structures of filaments, are found at different velocities as if they would originate from slightly different velocity flows inside the same global convergence of flows in the cloud. Several numerical simulations also observe fibers (e.g. Smith et al. 2014, 2016; Moeckel & Burkert 2015; Clarke et al. 2017; Zamora-Avilés et al. 2017), while in pressure equilibrium models filaments naturally tend to fragment rapidly into cores (Inutsuka & Miyama 1997).

In summary, these different views on the relation between filaments and the surrounding ambient cloud, in particular the understanding of the physical origin of star-forming filaments, require detailed observational studies and comparison with simulations. In this paper, we study the Musca filament which is probably at an early evolutionary state as its ambient cloud is not yet perturbed by star formation.

The following section introduces the Musca filament and why this filament is particulary interesting to study the relation with its ambient cloud. Section 3 describes the observations carried out with the APEX telescope and Sect. 4 presents the first results of the APEX and NANTEN2 observations. Section 5 provides a radiative transfer analysis of the observational data to constrain the physical conditions in the filament. In Sect. 6 the implications of these results on the formation of the Musca filament and its relation with the ambient cloud are discussed.

2. The Musca filament and Chamaeleon clouds

2.1. The Musca filament

We focus on the Musca filament which is seen on the sky as a 6 pc long filamentary structure in continuum, extinction and molecular lines (e.g. Mizuno et al. 2001; Kainulainen et al. 2009; Schneider et al. 2011; Hacar et al. 2016; Cox et al. 2016). This filament is located in the Chamaeleon-Musca complex, see Fig. 1, which is considered a single molecular complex with a size of ~70 pc on the plane of the sky if one includes Cham East (e.g. Corradi et al. 1997; Mizuno et al. 2001; Planck Collaboration Int XXVIII 2015; Liszt et al. 2019). Figure 2 presents the column density map of the Musca filament combining 2MASS and *Herschel* data which shows that this high column density filament with its ambient cloud is in relative isolation in the plane of the sky. The Musca filament hosts one protostellar core (Vilas-Boas et al. 1994; Juvela et al. 2012; Machaieie et al. 2017), and may contain a few prestellar cores (Kainulainen et al. 2016) with an average core separation that could fit with gravitational fragmentation inside a filamentary crest. The filament is thus likely at a relatively early evolutionary stage and has indeed a relatively low line mass compared to other more active star forming filaments like B211/3 in Taurus (Palmeirim et al. 2013; Cox et al. 2016; Kainulainen et al. 2016). As there is only one protostar which is located in the far north of the filament, the cloud is still unperturbed by protostellar feedback and is thus a very interesting location to study the formation of star forming gas and the role of the ambient cloud. The presence and structure of this ambient cloud was clearly established with high sensitivity dust continuum observations with *Herschel* and *Planck* (Cox et al. 2016; Planck Collaboration Int. XIII 2016), and will be described in more detail below.

For clarity in this paper, we distinguish four features of the Musca cloud based on the column density map and profile of dust emission, mostly following the nomenclature introduced by Cox et al. (2016).

Firstly, the (filament) crest is the high column density spine of the large filament in the Musca cloud with $N_{\mathrm{H_2}} > 3 \times 10^{21}$ cm^{-2} (Cox et al. 2016), see Fig. 3. From fitting a Plummer profile to the average column density profile of the full Musca filament, working with a distance of 140 pc, this suggest a radius of 0.056 pc for the filament crest (Cox et al. 2016).

Secondly, strands were defined in Cox et al. (2016) as the immediate surrounding of the filament crest where dust column density was found to be significant ($N_{\mathrm{H_2}} \sim 2 \times 10^{21}$ cm^{-2}) and inhomogeneous. For instance, there is a strong tendency to be

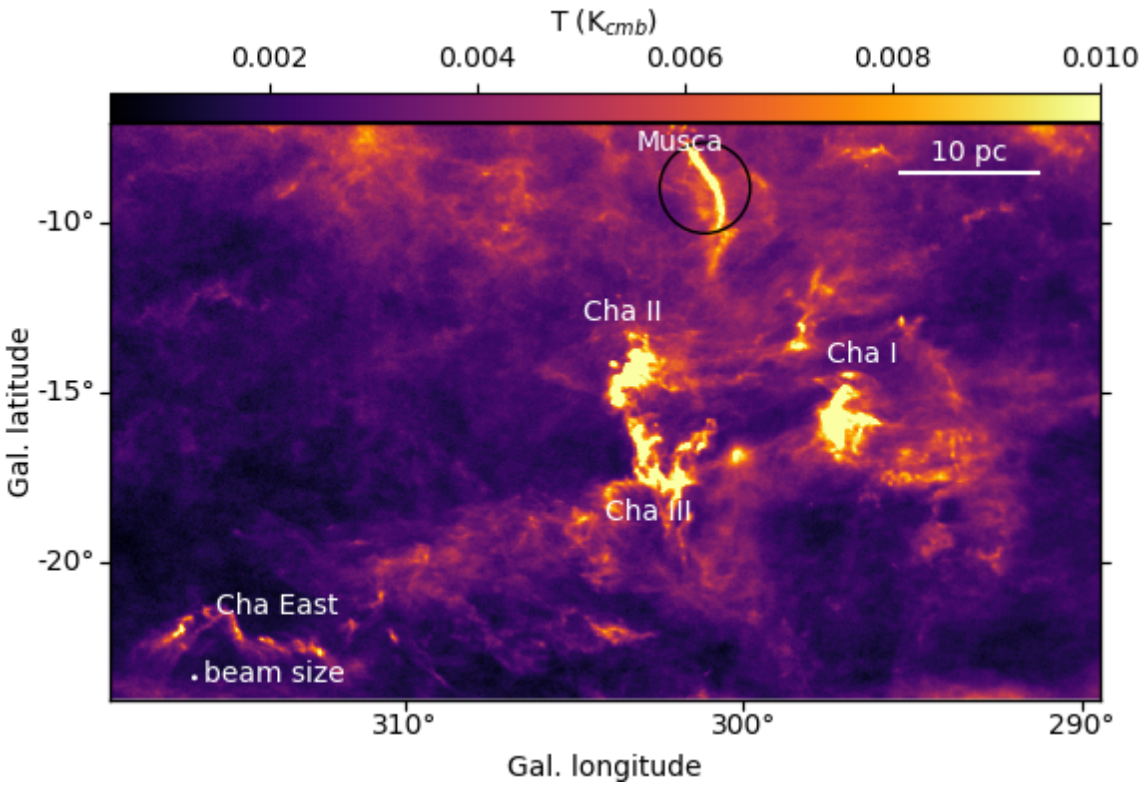

Fig. 1. *Planck* emission map at 353 GHz of the Chamealeon-Musca complex (Planck Collaboration I 2016). The names of the relatively dense regions in the complex are indicated in white. The black circle indicates the region where *Gaia* data were extracted to investigate the distance of the Musca filament and cloud. The *Planck* resolution at 353 GHz is 4.8′, which corresponds to a physical size of 0.25 pc at a distance of 180 pc (Zucker et al. 2019).

asymmetric with a brighter emission directly east of the filament crest, and the strands display a hair-like structure that is preferentially perpendicular to the filament crest (Cox et al. 2016), see Fig. 4. To go one step further we here propose that the strands could represent all column density in excess in Fig. 3 to the average Plummer profile fitted on the column density towards the crest. These strands might then contain the most nearby ambient gas of the filament crest and may represent a mass reservoir to be collected soon by the crest. In Fig. 3 and local cuts perpendicular to the filament axis, we found that the strands typically extend up to a distance of ∼0.4 pc from the filament crest. It is not straightforward to fit a function to the strands, but from Fig. 3 it can be observed that the column density excess to the Plummer fit typically extends up to a distance of 0.4 pc. The presence of the strands leads to an asymmetric column density profile for Musca. Other asymmetric column density profiles were already observed in the Pipe Nebula (Peretto et al. 2012).

The ambient Musca cloud then embeds the filament crest and strands, and has a typical average column density of $N_{\rm H_2} \sim 0.8 \times 10^{21}$ cm^{-2} within a typical distance of 3 pc from the filament crest, see Figs. 2 and 3.

Lastly, Striations are filamentary structures in the parsec scale ambient cloud and sub-parsec scale strands of the Musca filament, see Fig. 4. The striations are well aligned with the magnetic field on the plane of the sky (Cox et al. 2016). This magnetic field is roughly perpendicular to the Musca filament crest, as is also found for other dense filamentary structures (Planck Collaboration Int. XXXV 2016; Planck Collaboration Int. XIII 2016) and even at the centre of massive ridges like DR21 (Vallée & Fiege 2006; Schneider et al. 2010). Using C^{18}O observations it was proposed that the filament crest is a velocity-coherent structure (Hacar et al. 2016), or a single fiber following the nomenclature of Hacar et al. (2013), unlike well studied filaments such as B211/3 in Taurus and Serpens south (Hacar et al. 2013; Dhabal et al. 2018). This makes the Musca filament relatively simple in velocity space.

More recently, it was questioned whether the Musca filament can be described as truely cylindrical (in constrast to a sheet seen edge-on) by proposing that the striations pattern is reflecting magnetohydrodynamic vibrations which would require a large, pc-scale region of emission in contradiction to the 0.1 pc width of the crest. It would then suggest that the Musca cloud is a sheet that is seen edge-on and thus only appears filamentary due to projection (Tritsis & Tassis 2018). We use our new observations and an updated view of the global structure of the cloud to re-discuss this important issue. Meanwhile we continue to use the term "filament", at least for the crest, throughout the paper.

2.2. Distance of the Musca filament

In earlier studies, the distance of the Musca cloud was generally estimated to be 140–150 pc (e.g. Franco 1991; Knude & Hog 1998). Studying the reddening of stars in the *Gaia* DR2 data release (Gaia Collaboration 2018; Andrae et al. 2018) that are close to the Musca filament, with a method similar to Yan et al. (2019), shows indeed a noteworthy reddening increase at a distance of 140–150 pc, see Fig. 5. The region in the plane of the

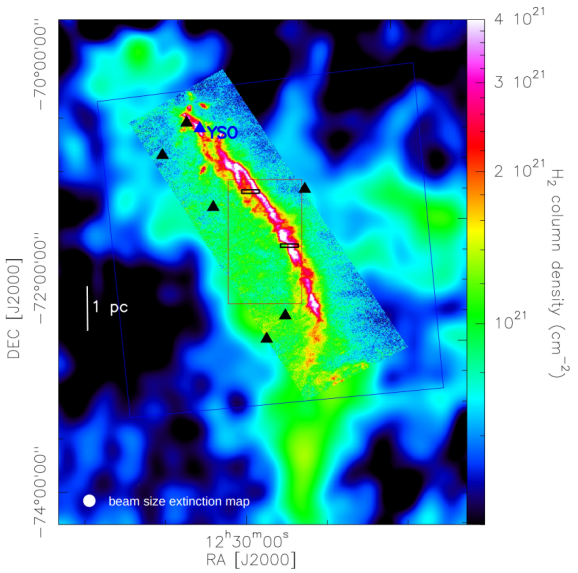

Fig. 2. Column density map of the Musca filament from the HGBS (André et al. 2010; Cox et al. 2016) embedded in the large scale 2MASS extinction map of Musca, scaled to the *Herschel* column density, that traces the ambient cloud. The extinction map was produced by the A_V mapping tool in Schneider et al. (2011). The black boxes indicate the maps made with the APEX telescope, the red box indicates the area displayed in Fig. 4, and the blue box indicates the area mapped with the NANTEN2 telescope. The black triangles show the locations of the stars with a distance smaller than 140 pc and a significant reddening (>0.3) in the *Gaia* catalogue. The blue triangle shows the location of the only young stellar object (YSO) in the Musca filament.

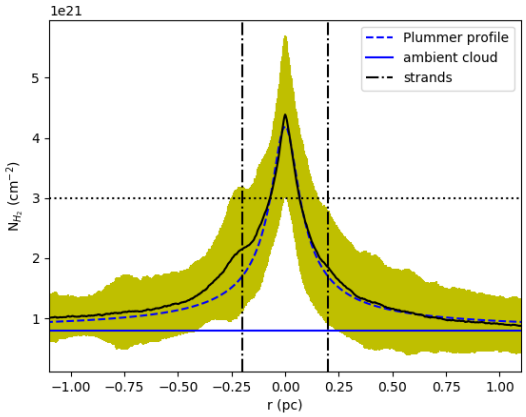

Fig. 3. Average column density profile of the Musca filament from the *Herschel* data (Cox et al. 2016), corrected to a distance of 140 pc. The blue horizontal line indicates the column density associated with the ambient cloud ($N_{H_2} \sim 0.8 \times 10^{21}$ cm^{-2}). The dashed blue line shows the fitted Plummer profile to the column density (excluding the strands). The vertical lines indicate the location of column density excess with respect to the Plummer fit close to the filament crest, the so-called strands. The dashed horizontal black line indicates $N_{H_2} = 3 \times 10^{21}$ cm^{-2}, which is the minimal column density used to define the filament crest.

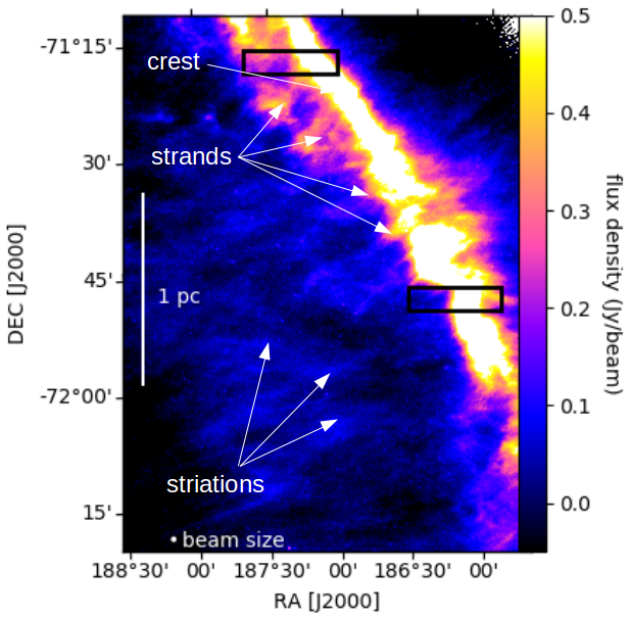

Fig. 4. Zoom (red box in Fig. 2) in the *Herschel* 250 μm map of the Musca cloud (Cox et al. 2016). The hair like structures perpendicular to the Musca filament, in the strands and ambient cloud, are indicated in white. The black boxes indicate the regions covered by the APEX maps.

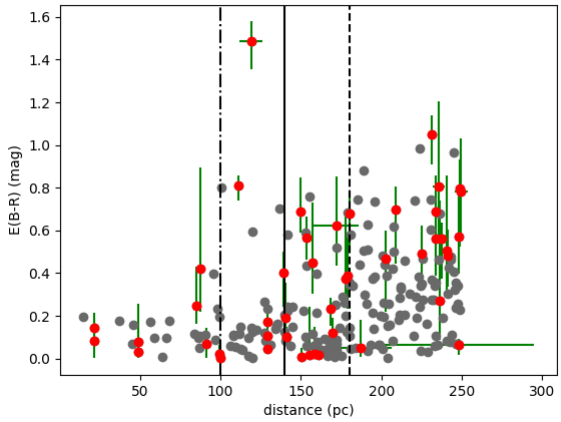

Fig. 5. Reddening obtained with the *Gaia* telescope as a function of distance for stars in the region of the Musca cloud. The coloured points are observed at locations where the *Planck* 353 GHz emission is above the threshold that was used to define the area covered by the Musca cloud, see Appendix A. This shows a general increase of the reddening at a distance of 140 pc, shown with the full vertical line, but there also appears to be some reddening starting at 90–100 pc, indicated with the dashdot vertical line. The dashed vertical line indicates the distance of the Chamaeleon I, II and III molecular clouds at 183 pc from Zucker et al. (2019).

sky studied with *Gaia* data is displayed in Fig. 1. For more information on the determination of the distance, see Appendix A. It can however be noted in Fig. 5 that there is already reddening for a couple of stars starting at 100 pc towards the Musca cloud. One should note that there are significant uncertainties on the reddening in the *Gaia* catalogue, but this behaviour can also be noted for two stars in Franco (1991). In the *Gaia* catalogue, the location of the stars with significant reddening at a distance <140 pc is spread over the full Musca cloud, see Fig. 2. This points to the fact that there might be some extended nearby gas at a distance of ~100 pc towards the Musca region. Since the Chamaeleon-Musca complex has a size of ~70 pc in the plane of the sky, it is not unlikely that the cloud has a similar size along the line of sight. This could possibly lead to extinction starting at 100 pc for some stars. However, the clearest jump in reddening

happens around 140 pc, which is consistent with several earlier studies (Franco 1991; Corradi et al. 1997; Whittet et al. 1997; Knude & Hog 1998) of the high column density Musca cloud. We thus assume a distance of 140 pc for the Musca filament in this paper. Note that this distance is smaller than the distance of 183 ± 3 ± 9 pc derived for the dense Chamaeleon clouds (Cha I, Cha II and Cha III) in Zucker et al. (2019). Inspecting the reddening as a function of distance with the *Gaia* data, we also found a distance of 180–190 pc for these dense Chamaeleon clouds, see Appendix A. This would indicate that Musca has a slightly more nearby location than the Chamaeleon clouds.

3. Observations

3.1. APEX: PI230 observations

In September 2018, we performed observations with the PI230 receiver which is installed on the APEX telescope (Güsten et al. 2006). The two bands of PI230, each with ∼8 GHz bandwidth, were tuned to a frequency to cover 213.7–221.4 GHz and 229.5–237.2 GHz such that the ^{12}CO(2–1), ^{13}CO(2–1), C^{18}O(2–1) and SiO(5–4) lines, respectively at 230.538, 220.399, 219.560 and 217.105 GHz, were observed simultaneously. The observations with PI230 were performed in the on-the-fly mode, creating two maps in all these lines with a size of 600″× 100″. These two maps cover the Musca filament crest and its nearby strands in two different regions, see Fig. 2. The northern map of the two is located towards a region that has a filamentary shape and the strands to the east, while the southern map is located in a region that shows signs of fragmentation with strands to the west. The OFF position used for the observations is located at $\alpha_{(2000)}$ = $12^{h}41^{m}38^{s}$; $\delta_{(2000)}$ = −71°11′00″, identical to the OFF position used for the observations presented in Hacar et al. (2016). This OFF position was checked using another OFF position that is located further away from the Musca filament, at $\alpha_{(2000)}$ = $12^{h}42^{m}21^{s}$; $\delta_{(2000)}$ = −72°27′31″, which was selected based on *Planck* maps. We found no contamination for any of the lines, for example, for ^{12}CO(2–1) the baseline rms was 2.8×10^{-2} K.

The spectral resolution of these observations is ∼0.08 km s^{-1}, which resolves the velocity-coherent filament crest component with $\sigma \sim 0.15$ km s^{-1} presented in Hacar et al. (2016). The spatial resolution of the observations is ∼28″, and inside a velocity interval of 0.1 km s^{-1}, the typical rms is ∼0.07 K. The main beam efficiency is η_{mb} = 0.68[1], and the forward efficiency used is 0.95. The data reduction was performed using the CLASS software[2].

3.2. APEX: FLASH^{+} observations

With FLASH^{+} (Klein et al. 2014) on the APEX telescope, the ^{12}CO(3–2), ^{12}CO(4–3) and ^{13}CO(3–2) lines at 345.796, 461.041 and 330.588 GHz, respectively were observed simultaneously. FLASH^{+} consists out of two receivers that can observe simultaneously: FLASH345 and FLASH460. Both receivers have two bands with a 4 GHz bandwidth. FLASH345 can observe in the 268–374 GHz range, while FLASH460 can observe in the 374–516 GHz range. These observations were performed towards the northern and southern map. Towards the northern area, the FLASH^{+} observations make a map of 500″× 100″ that covers an area including the filament crest and the eastern strands, and in the southern area the FLASH^{+} map only covers an area of 120″× 100″ which is centered on the filament crest. The observations towards the southern map were performed in a setup that did not cover the ^{13}CO(3–2) line. As a result this line is only available for the northern map. These observations with FLASH^{+} were spread over 3 observing periods: July 2017 (P100), from May to June 2018 (P101) and September 2018 (P102). All observations experienced certain complications requiring specific attention. The P100 ^{12}CO(3–2) observations have some contamination from the used OFF position (at $\alpha_{(2000)}$ = $12^{h}24^{m}05^{s}$; $\delta_{(2000)}$ = −71°23′45″). For ^{12}CO(3–2) a correction for the contamination from the OFF position was carried out by fitting a gaussian to the contamination in the OFF position and adding it to all spectra observed with this OFF position. This gaussian has T_{A}^{*} = 1.17 K, v = 3.05 km s^{-1} and a $FWHM$ = 0.418 km s^{-1}. For the ^{12}CO(4–3) observations, no contamination was found in this OFF position at a baseline rms of 0.09 K within 0.1 km s^{-1}. In P101, both the observations with FLASH345 and the FLASH460 instruments were shifted by respectively −230 and 490 kHz (F. Wyrowski, priv. comm.). In P102, the shift for the FLASH345 observations was solved, however the FLASH460 observations still had the same shift of 490 kHz (F. Wyrowski, priv. comm.). A correction was performed for these frequency shifts. The OFF position used in P101 and P102 is at $\alpha_{(2000)}$ = $12^{h}25^{m}15^{s}$ and $\delta_{(2000)}$ = −71°15′21″, which is free of ^{12}CO(3–2) emission with a baseline rms of T_{mb} = 0.04 K within 0.06 km s^{-1}.

The observations with FLASH345 have a spectral resolution of 0.033 km s^{-1} and an angular resolution of ∼18″. The FLASH460 observations have a spectral resolution of 0.05 km s^{-1} and an angular resolution of ∼14″. For further analysis, all the observations (both with PI230 and FLASH^{+}) were sampled at the same spectral resolution of 0.1 km s^{-1} since this is sufficient for Musca while it reduces the rms of CO(4–3) to ∼0.2 K and ∼0.5 K for the northern and southern map, respectively. This difference in data quality is due to different weather conditions with the water vapour varying between pwv = 0.4 and pwv = 1.0. Generally speaking, the observations for the northern map were carried out under better weather conditions. The main beam efficiencies[3] used for the FLASH345 and FLASH460 observations are η_{mb} = 0.65 and η_{mb} = 0.49, respectively. The results from the ^{12}CO(3–2) and ^{12}CO(4–3) transitions are presented in the companion paper (Bonne et al. 2020, hereafter Paper II), while the ^{13}CO(3–2) data will be discussed in this article.

3.3. NANTEN2: ^{12}CO(1–0) in Musca

To obtain a more general view of the Musca cloud, we use ^{12}CO(1–0) observations of the Musca cloud with the NANTEN2 telescope at Pampa la Bola in the Atacama desert. These observations were carried out with the single-beam SIS receiver on the telescope, developed by Nagoya University, with a 1 GHz bandwidth and a spectral resolution of 0.16 km s^{-1} at 115 GHz. The observations made several 30′ OTF maps, resulting in a full map size of 9 square degrees (7.3 pc × 7.3 pc at a distance of 140 pc) with an rms noise of 0.45 K within the spectral resolution of 0.16 km s^{-1}. This large map covers the Musca filament as well as the extended ambient cloud. The region of the Musca cloud covered by the NANTEN2 observations is indicated in Fig. 2. The main beam temperature scale was calibrated with Orion KL to be 52.6 K, such that the observations are consistent with the intensity of the CfA 1.2m telescope. The data was reduced with a linear baseline fit to the emission-free part of the spectrum.

[1] http://www.apex-telescope.org/telescope/efficiency/
[2] http://www.iram.fr/IRAMFR/GILDAS
[3] http://www.apex-telescope.org/telescope/efficiency/

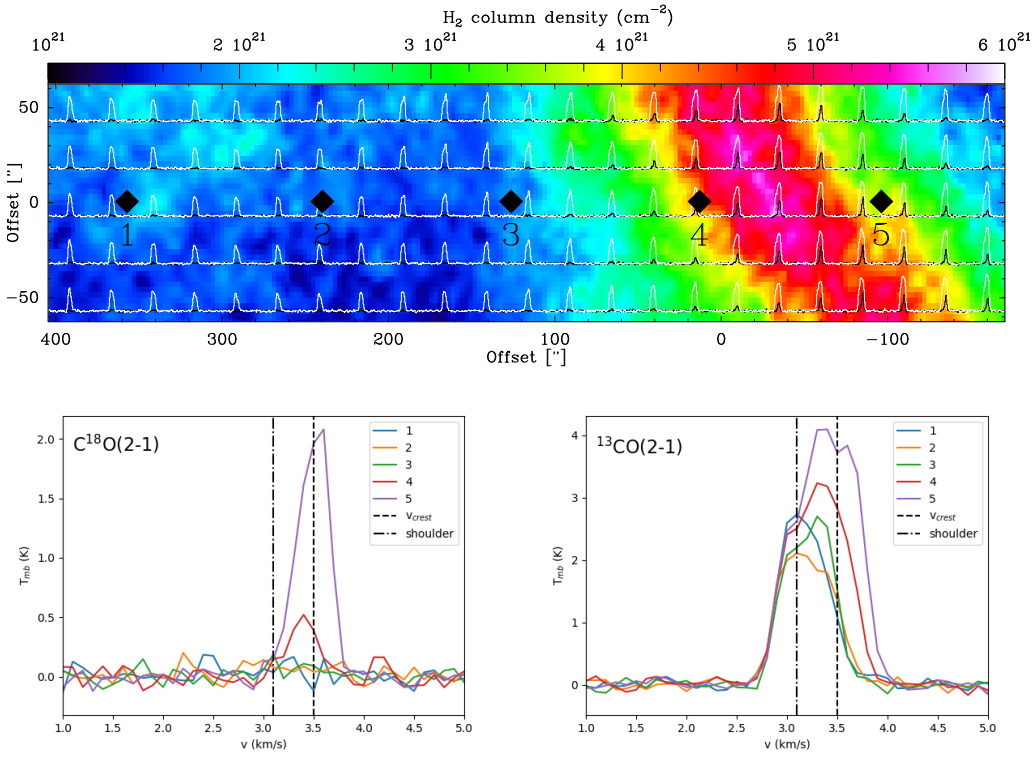

Fig. 6. *Top*: ^{13}CO(2–1) (in white) and C^{18}O(2–1) (in black) spectra overlayed on the *Herschel* column density map of Musca (Cox et al. 2016) for the northern position. The offset is centred on: $\alpha_{(2000)}$ = 12^{h}28^{m}58^{s} and $\delta_{(2000)}$ = –71°16′55″, and 100″ corresponds to ∼0.07 pc at a distance of 140 pc. C^{18}O emission is only detected at the crest (green-yellow-red), while ^{13}CO can be used to trace the strands (blue) as well. *Bottom right*: several ^{13}CO(2–1) spectra are displayed that were extracted at the indicated positions in the map above. This shows that ^{13}CO has two components towards the filament crest. *Bottom left*: same for C^{18}O(2–1), demonstrating it is only detected towards the filament crest.

3.4. Herschel and extinction maps

The column density and dust temperature profile close to the filament are provided by data from the *Herschel* Gould Belt Survey (HGBS)[4] (André et al. 2010; Cox et al. 2016). For a more extended view on the mass distribution in the Musca cloud, we derived an extinction map of the region using the code A_v*Map* (Schneider et al. 2011) which measures the average reddening of background stars in the 2MASS catalogue. The map was smoothed to a resolution of 5′ in order to improve the quality of the extinction map. In Fig. 2 the high resolution *Herschel* column density map (18.2″) is embedded in the extinction map. In order to combine the *Herschel* and large scale extinction data, a linear relation between the *Herschel* column density and extinction was fitted. A conversion $N_{H_2} = 0.83 \pm 0.02 \times 10^{21}$ A_v gave the best fit, which allowed to convert extinction to column density based on the information in the *Herschel* map. This conversion factor from extinction to column density for Musca is close to the canonical values reported for large samples in the galaxy (e.g. Bohlin et al. 1978; Güver & Özel 2009; Rachford et al. 2009).

4. Results

In this section, the first results from the CO(2–1) isotopologues are presented. The emission from these isotopologues in the northern and southern APEX map is presented in Figs. 6 and 7, while the average spectra towards the filament crest are presented in Fig. 8. The observations will be presented step by step, starting with C^{18}O, followed by ^{13}CO and in the end ^{12}CO, because it can be observed in the before mentioned figures that the spectra show increasing complexity from C^{18}O to ^{12}CO.

4.1. C^{18}O emission from the filament crest

Figures 6 and 7 show the ^{13}CO(2–1) and C^{18}O(2–1) spectra of the northern and southern map overlaid on the *Herschel* column density. In both maps, C^{18}O(2–1) is only detected at the crest of the Musca filament within a physical size of 0.1–0.15 pc, and the brightness of C^{18}O(2–1) quickly decreases when moving towards the strands around the filament crest. It suggests that C^{18}O is tracing only the highest column density regions of the filament (typically $N_{H_2} > 3 \times 10^{21}$ cm^{-3}).

Inspecting the spectra in both maps, we confirm that the filament crest has a single velocity component with a transonic linewidth of 0.15 km s^{-1}, going up to 0.2 km s^{-1}, as reported in Hacar et al. (2016). However, it should be noted that Fig. 8 shows that the C^{18}O emission in the southern map has a pronounced shoulder which might be the result of a second velocity component. Additionally, we note a slight and continuous shift of the central velocity across the crest. To further investigate this velocity structure, a gaussian line profile was fitted to the C^{18}O(2–1) spectra above the 3σ noise rms. The velocity field obtained from the fitting is presented in Figs. 9 and 10. These figures demonstrate organised velocity fields across the crest in both maps with a typical velocity interval of ∼0.2 km s^{-1}, which is similar to the spectral linewidth, suggesting a part of the linewidth might be due to these gradients. The velocity gradients were calculated

[4] http://gouldbelt-herschel.cea.fr/archives

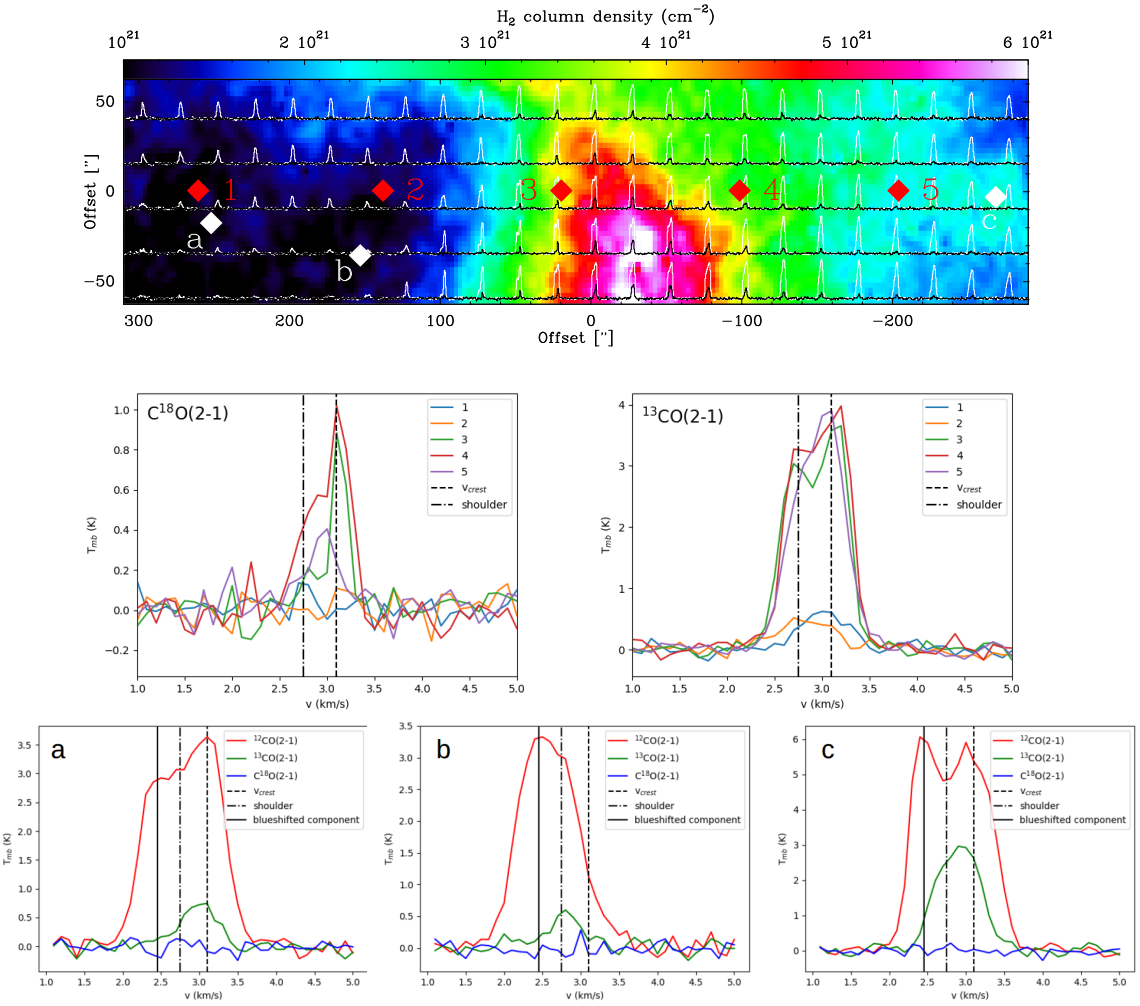

Fig. 7. *Top and middle*: same as Fig. 6, but for the southern position, where the offset is centered on: $\alpha_{(2000)}$ = $12^h24^m46^s$ and $\delta_{(2000)}$ = –71°47′20″. It can be noted that at the location where there are no strands ($N_{H_2} < 1.5 \times 10^{21}$ cm^{-2}) that the ^{13}CO emission also disappears. *Bottom*: ^{12}CO(2–1), ^{13}CO(2–1) and C^{18}O(2–1) emission at the indicated white positions (a, b, c) in the map above with the same beam size (28″) and spectral resolution (0.1 km s^{-1}). This indicates that in ^{12}CO(2–1) there is an extra blueshifted component that is barely detected in ^{13}CO(2–1). It also shows that C^{18}O(2–1) is not detected away from the filament crest with this data.

using the nearest neighbour values for every pixel. They have a magnitude of 1.6 and 2.4 km s^{-1} pc^{-1} and an angle of 77° and 45° compared to the local orientation of the filament crest for the northern and southern map, respectively. One should note that the southern map covers a part of the filament that is fragmenting which might have an impact on the observed velocity gradient (e.g Hacar & Tafalla 2011; Williams et al. 2018; Arzoumanian et al. 2018). We also find that the central velocity at the crest is ~3.5 km s^{-1} in the north and around 3.0–3.1 km s^{-1} in the south.

Since the velocity gradient is in the opposite direction in the south compared to the north, see Fig. 10, this does not lead to a straightforward analysis of the entire Musca filament crest as a simple rotating filament which is theoretically studied in Recchi et al. (2014).

4.2. ^{13}CO emission from the strands

In contrast to C^{18}O(2–1), the emission of ^{13}CO(2–1) is not confined to the filament crest alone, but is also high towards the strands of Musca, see Figs. 6, 7 and 11. At the locations where the strands are not bright in the *Herschel* dust column density map, the ^{13}CO emission also strongly decreases, see Figs. 7 and 11.

Inspecting the ^{13}CO(2–1) spectra of both maps in more detail, a component at the same velocity as the filament crest can be found, as well as a slightly blueshifted shoulder at $v_{los} \sim 3.1$ km s^{-1} in the northern map and $v_{los} \sim 2.7$–2.8 km s^{-1} in the southern map, see Fig. 8. The velocity component related to the filament crest disappears when moving away from the filament crest, while the emission from the shoulder remains present over the strands, see e.g. Figs. 6 and 11. This implies that the observed shoulder comes from slightly more blueshifted emission related to the strands. From this moment on, when talking about the shoulder we thus implicitly talk about the strands and vice versa.

The velocity field of C^{18}O(2–1) demonstrated internal motion in the filament crest. The ^{13}CO(2–1) spectra provide more information, namely that there are two velocity components: one related to the filament crest and a second component related to the strands.

At this point, we have presented the blueshifted shoulder that correlates well with the *Herschel* strands in both maps.

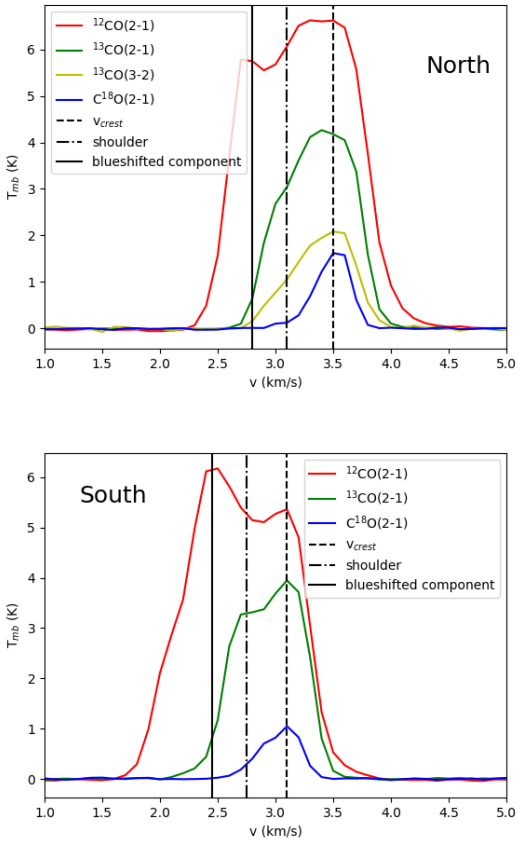

Fig. 8. *Top*: averaged CO(2–1) isotopologue spectra and the ^{13}CO(3–2) spectrum observed towards the filament crest ($N_{H_2} > 3 \times 10^{21}$ cm^{-2}) in the northern map, showing the presence of the three components. *Bottom*: same for the crest of the southern map.

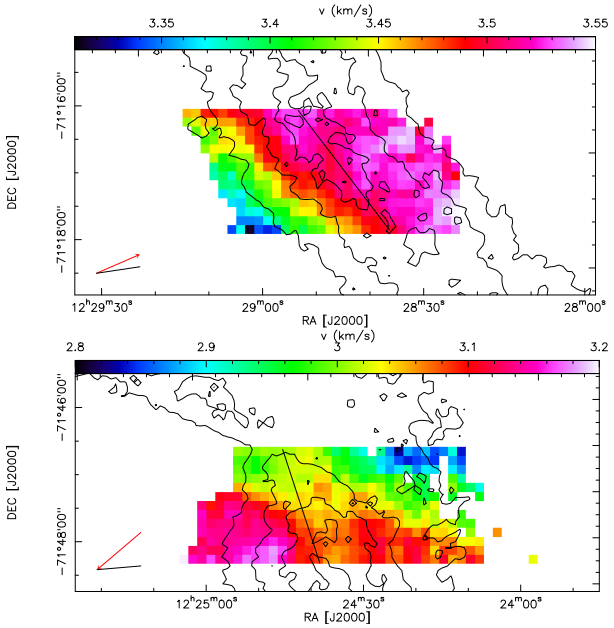

Fig. 9. Velocity field obtained over the Musca filament crest from the C^{18}O(2–1) line in the northern (*top*) and southern (*bottom*) map. The contours indicate the column density levels of the filament crest (N_{H_2} = 3–6 × 10^{21} cm^{-3}). The black line on the velocity field connects the maximal column density at the top and bottom of the map, indicating the local orientation of the filament axis. In the lower left corner, the red arrow indicates the orientation of the velocity gradient, while the black line indicates the orientation of the magnetic field.

This indicates that the strands around the filament crest are blueshifted compared to the filament crest. When inspecting the ^{13}CO(2–1) channel maps of the southern map in Fig. 11 in more detail, one finds that east of the filament crest there is some weak ^{13}CO(2–1) emission ($T_{mb} \lesssim 1$ K) away from the filament crest at more or less the same velocity as the filament crest, see Figs. 7 and 11. This emission suggests that at some locations there is also a small amount of "redshifted" gas near the filament crest that is roughly at the same velocity along the line of sight as the filament crest itself.

4.3. ^{12}CO: Blueshifted emission

Inspecting the APEX ^{12}CO(2–1) spectra, another velocity component shows up with little corresponding emission in ^{13}CO(2–1), see e.g. Figs. 7 and 8. This new velocity component, which is even more blueshifted than the shoulder, is observed both in the northern and southern map and also at the locations where the strands disappear (in the *Herschel* column density map), see Fig. 7. This suggests, as ^{13}CO(2–1) is only marginally detected at this velocity, that there is low column density gas present around the Musca filament with blueshifted velocities along the line of sight of 2.7 km s^{-1} in the north and 2.5 km s^{-1} in the south, see Fig. 8. We refer to it as "the blueshifted component" from now on.

These observations of the CO isotopologues thus indicate that the Musca cloud has two more velocity components on top of the already established velocity-coherent filament crest: the shoulder (detected in ^{13}CO) and the blueshifted velocity component (detected in ^{12}CO). These different velocities can also be seen as a continuous velocity structure from large scale blueshifted gas to the small scale crest which corresponds to the reddest CO emission of the region. This generally indicates that the kinematics in the Musca cloud is more complex than

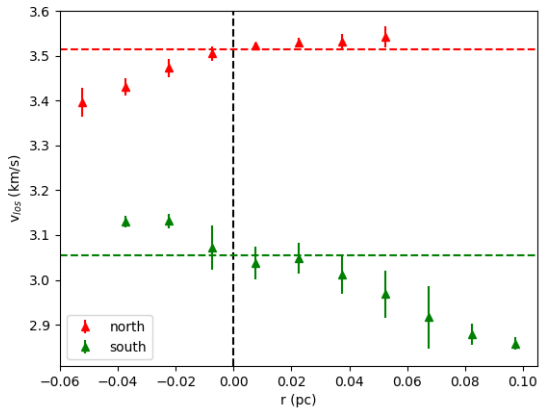

Fig. 10. Line-of sight velocity across the filament derived from C^{18}O(2–1) emission averaged along the filament as a function of the distance (r) for the northern (red) and southern (green) maps. The distance is always determined perpendicular to the local orientation of the filament crest center. The horizontal dashed lines indicate the velocity at the center of the filament crest, the vertical dashed line indicates the center of the crest, and the errorbars indicate the dispersion at each radius in the maps.

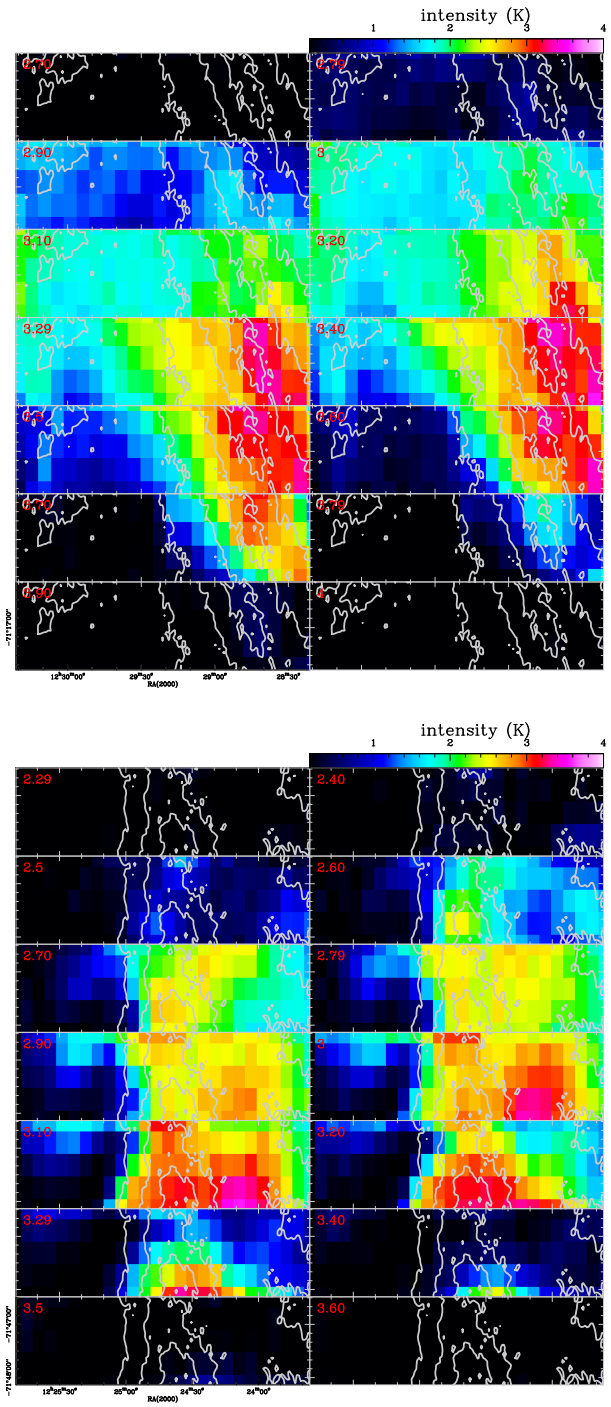

Fig. 11. *Top*: channel maps of the APEX ^{13}CO(2–1) observations in the northern map. The contours indicate the *Herschel* column densities $N_{H_2} = 2 \times 10^{21}$, 3.5×10^{21} and 5×10^{21} cm^{-2}. The velocity of the channel is indicated in red at the upper left corner of every channel. It can be seen that the velocities of the blueshifted shoulder trace the strands. *Bottom*: same for the southern map.

the single velocity component of the filament crest (Kainulainen et al. 2016; Hacar et al. 2016), and that large scale kinematics might play an important role in the filament formation and cloud evolution.

4.4. NANTEN2 ^{12}CO(1–0) data

The ^{12}CO(1–0) mapping performed by the NANTEN2 telescope provides a view on the large scale kinematics of the Musca filament and the ambient cloud. Figure 12 presents channel maps of this data set, which shows that the brightest ^{12}CO(1–0) gas is located at the crest and strands defined by the *Herschel* data.

In the channel maps with $v < 2.7$ km s^{-1}, there is also emission observed outside the filament contours. This is confirmed with the velocity field obtained from the NANTEN2 data in Fig. 13, which demonstrates that the blueshifted component traces a more diffuse and extended ambient cloud that is observed in dust continuum emission with *Herschel* and in the extinction map. At velocities between 2.7 and 4 km s^{-1}, corresponding to the velocity of the shoulder and crest, the emission is nicely constrained to the filament seen by *Herschel* as was already inferred from the APEX data, see Fig. 12.

The NANTEN2 observations confirm that the large scale, surrounding gas of the Musca filament is mostly blueshifted. It also confirms that smaller scale blueshifted strands can be found at both sides of the filament crest, as was already suggested from the APEX data. This indicates that there are local changes in the position of these blueshifted strands compared to the crest. The column density profile perpendicular to the filament crest in Fig. 14 also shows that the filament crest, both in the south and north, is not located at the center of the strands. It even shows that the crest has a direct border with the more diffuse ambient cloud at some locations, which results in locally asymmetric column density profiles.

Furthermore, NANTEN2 data shows that there is virtually no CO emission in the whole Musca region that is redshifted compared to the crest at 3.0–3.5 km s^{-1}. This confirms the tendency already noted at small scales with the APEX data in the two maps. In conclusion, the Musca filament and its possible gas reservoir have an interesting asymmetric distribution both spatially (crest concentrated in the west/north-west direction) and kinematically (redshifted crest and strands compared to the blueshifted large-scale ambient cloud).

4.5. Orientation of the velocity gradient and the magnetic field

An organised velocity gradient over the Musca filament crest was reported in Sect. 4.1 from C^{18}O observations. Here, the orientation of this velocity gradient is compared to the orientation of the local magnetic field. For the entire Musca filament, the magnetic field is nearly perpendicular to the filament crest (Pereyra & Magalhães 2004; Planck Collaboration Int. XIII 2016), with a typical angle between the filament crest and the magnetic field of 80° (Cox et al. 2016).

In order to further investigate a possible link between the plane of the sky magnetic field orientation and the velocity gradient in the filament crest, the magnetic field was constructed from the *Planck* 353 GHz data (Planck Collaboration I 2016). To reduce the noise in the magnetic field map, the I, Q and U maps were smoothed to a resolution of 10′ (or 0.4 pc for Musca at 140 pc) (Planck Collaboration Int. XXXV 2016; Planck Collaboration Int. XIII 2016). The orientation of the magnetic field was then calculated in the IAU convention using the formulas presented in Planck Collaboration Int. XXXV (2016) and Planck Collaboration Int. XIII (2016). In the area covered by the C^{18}O velocity maps, the magnetic field orientation (Planck Collaboration Int. XIII 2016) and the average velocity gradient were compared in Fig. 9, showing no clear correlation. In the northern map, the angle between the magnetic field orientation

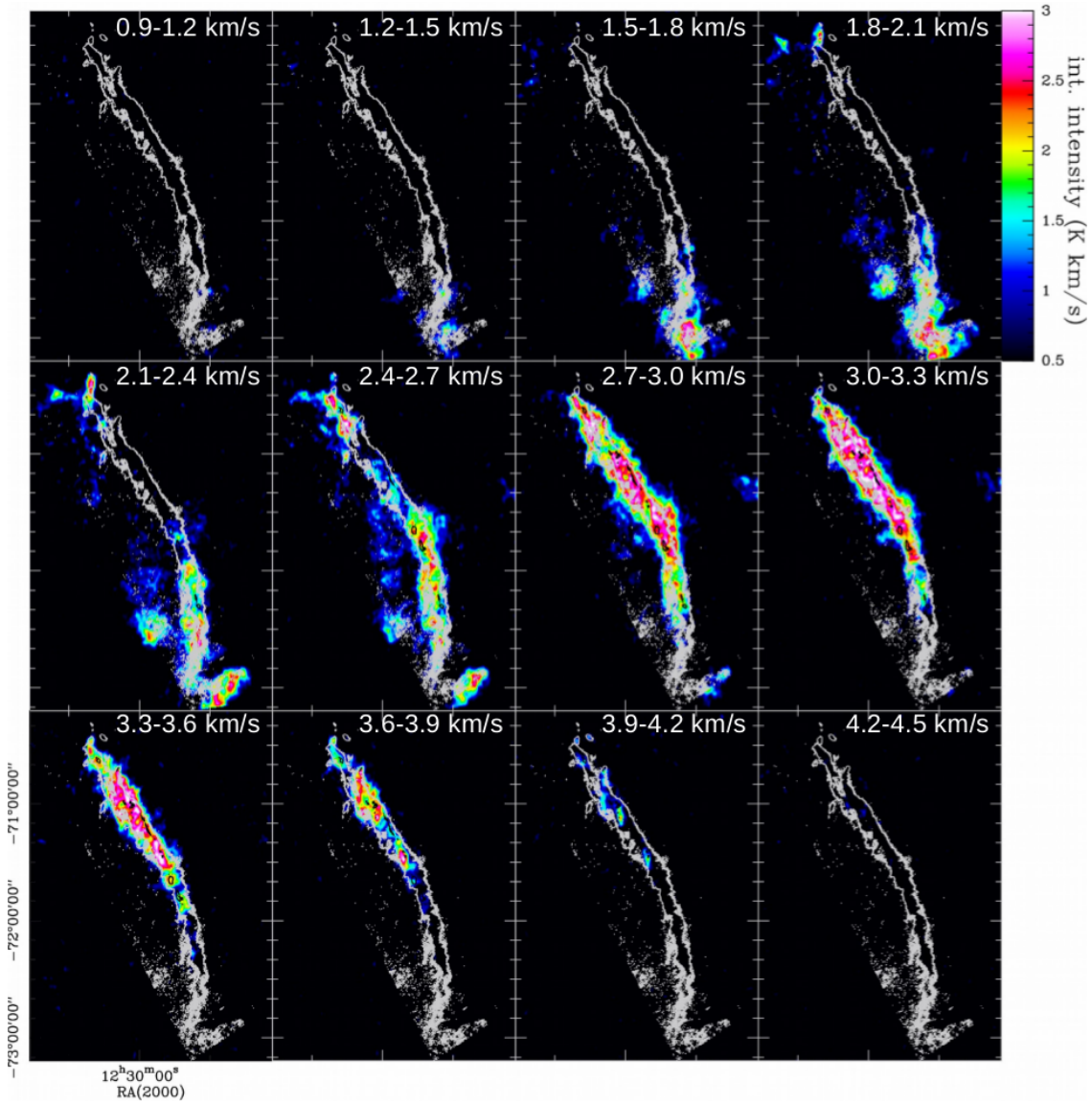

Fig. 12. Integrated intensity of NANTEN2 data over velocity intervals of 0.3 km s^{-1}. The black contours at $N_{H_2} = 5 \times 10^{21}$ cm^{-2} from the *Herschel* data indicate the center of the filemant crest. These black contours are best visible at velocities between 2.7 and 3.6 km s^{-1} when there is ^{12}CO(1–0) emission towards the crest. The grey contour, at $N_{H_2} = 2 \times 10^{21}$ cm^{-2}, indicates the area that encloses the strands. It can be observed that there is some extended emission east of the Musca filament and that the filament crest is not at the middle of the area containing the strands.

and the average velocity gradient is 28°. In the southern map the angle is 54°. A word of caution on this comparison: the velocity gradient is located over the filament crest, while the resolution of the *Planck* magnetic field orientation is significantly larger than the ∼0.1 pc size of the filament crest. It does however show that the velocity gradient over the filament crest has a significant offset compared to the large scale organised magnetic field in its close surroundings.

5. Line radiative transfer analysis

5.1. Density in Musca from radiative transfer of CO

With the non-LTE line radiative transfer code RADEX (van der Tak et al. 2007), which uses the LAMBDA database (Schöier et al. 2005), we investigate whether the CO isotopologue data can provide a consistent picture for the 3D geometry of the Musca filament. To do this, we begin with estimating the density profile across the Musca filament. In Fig. 15 it is shown that we can estimate the density with RADEX using the ^{13}CO(3–2)/^{13}CO(2–1) brightness ratio, after smoothing ^{13}CO(3–2) to the same resolution of ^{13}CO(2–1) (here 28″), because this ratio strongly depends on the density. In particular between 10^2 and 5×10^4 cm^{-3}, which covers the wide range of proposed densities at the Musca crest (Kainulainen et al. 2016; Tritsis & Tassis 2018), the ratio strongly depends on the density. We focus on the northern map since we only have ^{13}CO(3–2) and ^{13}CO(2–1) data for this location, which has a *Herschel* column density up to $N_{H_2} \sim 6 \times 10^{21}$ cm^{-2}, see Fig. 14.

In principle the line ratio does not depend on the abundance of ^{13}CO, but since both ^{13}CO lines become optically thick at the crest this is not completely true. However, in Appendix B it is

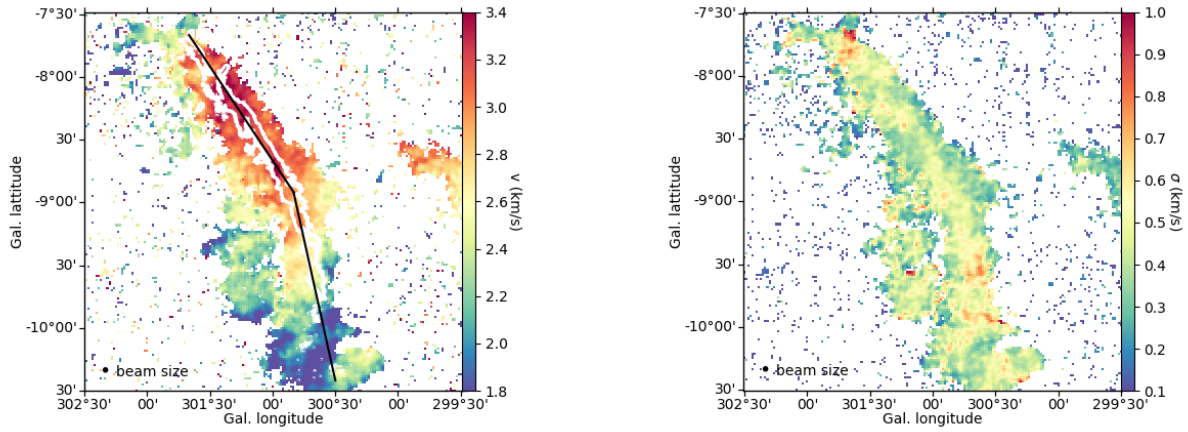

Fig. 13. *Left*: ^{12}CO(1–0) velocity field in the Musca cloud from fitting a single gaussian to the ^{12}CO(1–0) NANTEN2 data, showing an organised velocity field along the Musca filament. The black line indicates the central axis used to construct the PV diagram in Fig. 23 perpendicular to the Musca filament. The white contours show the high column density region ($N_{H_2} > 2 \times 10^{21}$ cm^{-2}) in Musca. *Right*: ^{12}CO(1–0) linewidth from the Gaussian fitting to the NANTEN2 data.

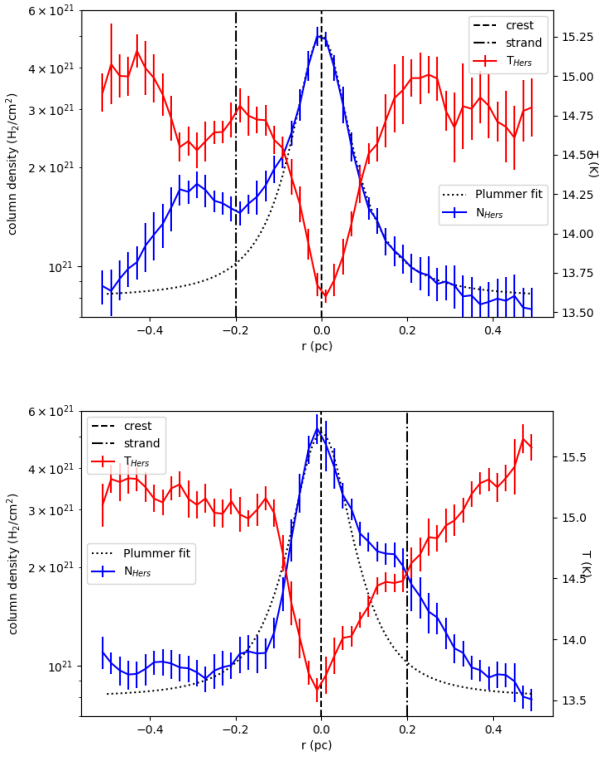

Fig. 14. *Top*: *Herschel* column density and temperature profile in the northern map. It demonstrates an asymmetry of the column density due to the strands. The fitted Plummer profile (excluding the strands) shows that the strand is a dense structure directly next to the filament crest. The standard deviation from the average value is also indicated at each radius. A negative radius was chosen to be located east of the filament crest. *Bottom*: same for the southern map, note that the strand has changed side.

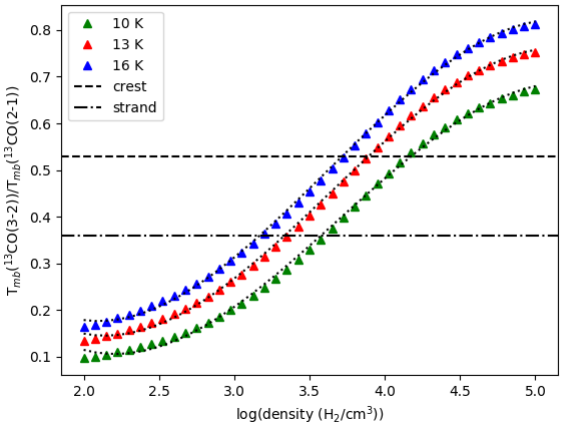

Fig. 15. Evolution of the ^{13}CO(3–2)/^{13}CO(2–1) brightness temperature ratio as a function of density for realistic temperatures of the Musca filament. The dotted curves are the functions fitted through the RADEX results to invert the observed ratio in Musca to a density. The horizontal lines indicate the average observed ratios for the strand and the crest in the northern map.

demonstrated that the varying optical depth related to the column density or abundance variations is not the main uncertainty for the ^{13}CO(3–2)/^{13}CO(2–1) ratio.

To construct the density profile, a RADEX grid of the ^{13}CO brightness temperature ratio was created with 40 points on a log scale between $n_{H_2} = 10^2$ and 10^5 cm^{-3} for three different kinetic temperatures: 10, 13, and 16 K. This covers the range of *Herschel* dust temperatures as well as kinetic gas temperatures put forward for Musca by Machaieie et al. (2017). The full width at half maximum (FWHM) and column density for ^{13}CO that are used in the RADEX calculations are 0.7 km s^{-1} and $N_{^{13}CO} = 1.1 \times 10^{16}$ cm^{-2}, respectively, which is obtained from $N_{H_2} = 6 \times 10^{21}$ cm^{-2} using $[H_2]/[^{13}CO] = 5.7 \times 10^5$ (from $[H_2]/[^{12}CO] \sim 10^4$ and $[^{12}CO]/[^{13}CO] \sim 57$ Langer & Penzias 1990). The calculated opacities by RADEX for these models vary between 3 and 6 for ^{13}CO(2–1) and 1 to 3 for ^{13}CO(3–2), which fits with the estimated opacities in Hacar et al. (2016).

To invert the observed ratios with APEX to a density profile, we work with the *Herschel* temperature profile in Fig. 14. The resulting density profile for the Musca filament is presented in Fig. 16.

This density profile predicts $n_{H_2} = 6.5 \pm 1.9 \times 10^3$ cm^{-3} at the filament crest that drops to $n_{H_2} \sim 1$–3×10^3 cm^{-3} for the strands,

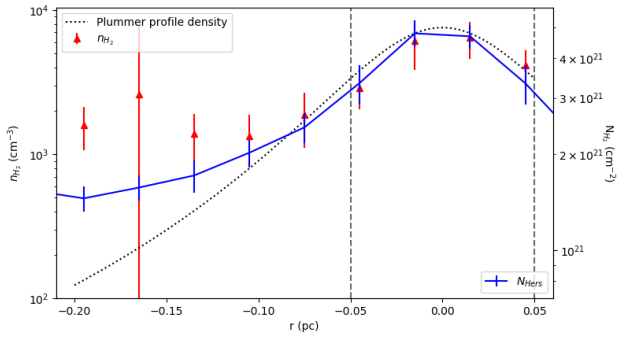

Fig. 16. Density profile and its standard deviation obtained from the ^{13}CO(3–2)/^{13}CO(2–1) ratio as a function of the distance from the filament crest for the northern map (in red). The vertical dashed lines indicate the extent of the filament crest. It should be noted that the *Herschel* temperature is too high for the filament crest such that the density will be slightly higher than the values shown in this figure, see Fig. 15. The dotted black line describes the Plummer density profile for the Musca filament as derived from the column density profile using Eq. (1) in Arzoumanian et al. (2011). This density profile fits with density predictions at the filament crest, but towards the strands the density is significantly higher than predicted from the Plummer profile. The *Herschel* column density profile, in blue, is plotted on the axis on the right. When comparing the density profile with the column density profile, one should take into account the different scales of the left and right axes.

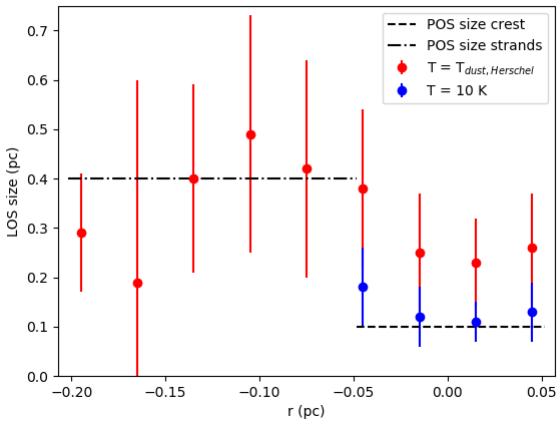

Fig. 17. Estimated characteristic size for the observed ^{13}CO emission in the line of sight as a function of the distance (r) from the center of the filament crest. The characteristic size is estimated combining the *Herschel* column density with the ^{13}CO(3–2)/^{13}CO(2–1) density estimate using the *Herschel* dust temperature (red) and a temperature of 10 K (blue). The horizontal lines indicate the characteristic sizes in the plane of the sky (POS) of the strands and the filament crest.

see Fig. 16. However, for the interior of the filament crest the 13 K temperature is certainly overestimated. It was shown by Nielbock et al. (2012) and Roy et al. (2014) that the temperature in the dense interior of different clouds is at least 3 K lower than the *Herschel* dust temperature on the sky. Using a temperature of 10 K, which is actually also suggested by the LTE study of ^{13}CO(1–0) and C^{18}O(1–0) by Machaieie et al. (2017) for the filament crest, one gets a more probable typical density in the crest of $n_{H_2} = 1.3 \pm 0.4 \times 10^4$ cm^{-3}.

Combining the obtained densities with the *Herschel* column densities, one can estimate the size of the dense gas along the line of sight as a function of the distance from the filament crest. This is shown in Fig. 17, demonstrating a typical size of 0.2–0.5 pc for the strands and a size of ~0.25 pc at the filament crest for the overestimated temperature of 13 K. For the most probable 10 K temperature of the crest, we get a size of ~0.1 pc for the crest. We thus get for both the filament crest and strands that their characteristic sizes along the lines of sight are roughly the same as their sizes in the plane of the sky, which implies a cylindrical geometry.

The density profile from the ^{13}CO(3–2)/^{13}CO(2–1) brightness ratio, is compared in Fig. 16 with the predicted density profile from fitting a Plummer profile to the filament crest in the northern APEX map (Cox et al. 2016). This shows that a Plummer profile provides an acceptable fit for the filament crest. In the strands we find that the density estimate from ^{13}CO(3–2)/^{13}CO(2–1) is significantly higher than the density predicted by the Plummer profile, similar to what is observed for the column density in Fig. 14. This suggests that the strands consist of denser gas than the surroundings, and it reinforces our earlier proposal that the strands are additional components on the top of the density (presumably plummer-like) profile of the filament crest.

We also verified the overall consistency of the obtained density results for the filament crest and strands by studying the observed brightness of the CO isotopologues, see Table 1. For the filament crest, we find that $n_{H_2} = 10^4$ cm^{-3} and T_k = 10 K reproduce the observed CO isotopologue brightnesses, even when taking into account a 30% uncertainty of the CO abundance as is shown in Table 1. For the strands, we reproduce the observed ^{13}CO brightness with $n_{H_2} = 10^3 - 3 \times 10^3$ cm^{-3} and T_k = 15–18 K, however it is not possible to reproduce the C^{18}O brightness of the strands with typical [^{13}CO]/[C^{18}O] ratios around 10. This will be addressed in more detail in the next section.

These results suggest that the kinetic temperature of the strands and the filament crest are similar to the *Herschel* dust temperature. Generally speaking it is found that $T_{dust} \leq T_k$ (e.g. Goldsmith 2001; Merello et al. 2019), but in the dense interior of the Musca cloud $T_{dust} \approx T_k$ can be expected (e.g. Goldsmith 2001; Galli et al. 2002; Ivlev et al. 2019). In the simulations by Seifried & Walch (2016), the dust is not yet fully coupled to the gas at the predicted densities inside the filament crest ($n_{H_2} \sim 10^4$ cm^{-3}), but in these simulations the dust temperature reaches values below 10 K.

5.2. C^{18}O abundance drop in the strands

Studying the CO isotopologue emission in the strands, a strong variation of the [^{13}CO]/[C^{18}O] abundance ratio is observed. As already noted, the C^{18}O(2–1) emission, with a typical rms of ~0.07 K, rapidly decreases in the strands until it is no longer clearly detected for a single beam in the strands. When studying the data in bins of 0.03 pc as a function of the distance from the center of the filament crest, we always obtain a >3σ detection of C^{18}O(2–1). This then allows to follow the rapid continuous increase of [^{13}CO]/[C^{18}O] in Fig. 18 as a function of the distance from the filament crest, showing that the ratio varies by an order of magnitude over less than 0.2 pc. Figure 18 displays the evolution of the integrated line brightness ratio as a function of the distance, which is a decent proxy for the [^{13}CO]/[C^{18}O] ratio because of the very similar excitation conditions for both lines. This strong increase of the [^{13}CO]/[C^{18}O] ratio agrees with a weak C^{18}O(2–1) detection at the velocity of the strands with a brightness of ~0.08 K when smoothing over the area covered by the strands, while the brightness of ^{13}CO(2–1) in the strands is still ~2.5 K, see Table 1.

Table 1. Results of several RADEX calculations for the filament crest using a FWHM of 0.5 km s^{-1}, and with varying column densities, temperatures and [H_2]/[^{13}CO] abundance ratios (top); RADEX calculations for the strands with varying abundances for ^{13}CO and C^{18}O. The [H_2]/[^{13}CO] abundance ratio is varied up to a factor 3, supported by theoretical models, and the [^{13}CO]/[C^{18}O] abundance ratio is varied to obtain results consistent with the observations (bottom).

Crest	N_{H_2} (cm^{-2})	T_{kin} (K)	n_{H_2} (cm^{-3})	[H_2]/[^{13}CO]	[^{13}CO]/[C^{18}O]	$T_{^{13}CO(2-1)}$ (K)	$T_{^{13}CO(3-2)}$ (K)	$T_{C^{18}O(2-1)}$ (K)
Observed values						4.2	2.1	1.6
RADEX	4×10^{21}	10	10^4	5.7×10^5	7.3	4.6	2.1	1.6
	6×10^{21}	10	10^4	5.7×10^5	7.3	4.9	2.6	2.3
	6×10^{21}	9	10^4	5.7×10^5	7.3	4.1	2.0	2.0
	4×10^{21}	11	10^4	8×10^5	7.3	4.8	2.2	1.5
	4×10^{21}	13	6.5×10^3	5.7×10^5	7.3	6.1	3.0	1.9
	3×10^{21}	10	10^4	5.7×10^5	7.3	4.3	1.8	1.3
Strand	N_{H_2} (cm^{-2})	T_{kin} (K)	n_{H_2} (cm^{-3})	[H_2]/[^{13}CO]	[^{13}CO]/[C^{18}O]	$T_{^{13}CO(2-1)}$ (K)	$T_{^{13}CO(3-2)}$ (K)	$T_{C^{18}O(2-1)}$ (K)
Observed values						2.4	0.8	0.085
RADEX	10^{21}	15	3×10^3	5.7×10^5	7.3	2.8	0.85	0.52
	10^{21}	15	2×10^3	5.7×10^5	7.3	2.3	0.59	0.42
	10^{21}	18	2×10^3	5.7×10^5	7.3	2.6	0.8	0.48
	10^{21}	15	3×10^3	3.8×10^5	7.3	3.7	1.2	0.78
	10^{21}	15	10^3	3.8×10^5	7.3	2.0	0.44	0.39
	10^{21}	15	10^3	2.9×10^5	7.3	2.4	0.59	0.52
	10^{21}	15	10^3	1.9×10^5	7.3	3.0	0.84	0.74
	10^{21}	15	3×10^3	5.7×10^5	40	2.8	0.85	0.10
	10^{21}	15	3×10^3	5.7×10^5	50	2.8	0.85	0.08

Notes. The predictions closely match the observed brightness towards Musca filament crest for n_{H_2} = 10^4 cm^{-3} and T_k = 10 K, in particular when working with $N_{H_2} = 4\times10^{21}$ cm^{-2} which is the column density that is associated with filament crest. The presented observed brightness is obtained from the average spectra at $N_{H_2} > 3\times10^{21}$ cm^{-2} (top). It demonstrates a high average [^{13}CO]/[C^{18}O] abundance ratio (~50) in the strands. The presented observed brightness is obtained from the average spectra at $N_{H_2} < 3\times10^{21}$ cm^{-2}. The observed brightness towards the strands generally matches predictions using n_{H_2} = 10^3–3×10^3 and T_K = 15–18 K (bottom).

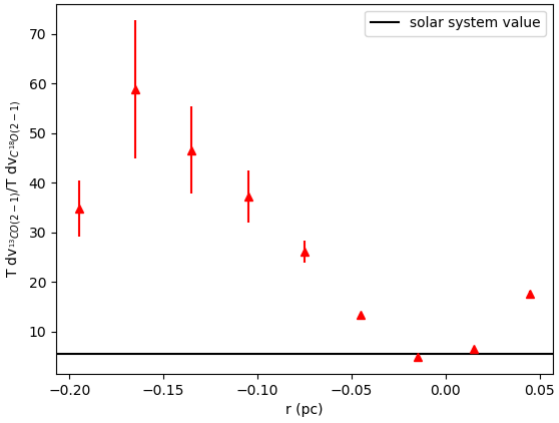

Fig. 18. Evolution of the ^{13}CO(2–1)/C^{18}O(2–1) integrated brightness ratio as a function of distance from the filament crest in the northern map, showing a rapid increase as a function of the distance. It shows the average ratio for the values in each distance bin of 0.03 pc with the uncertainty related to the noise.

It was shown by Zielinsky et al. (2000) that a FUV field can create a variation of [^{13}CO]/[C^{18}O] as a function of the column density due to fractionation (e.g. van Dishoeck & Black 1988). With theoretical studies of gas exposed to a weak FUV-field (~1 G_0), it was shown that carbon fractionation reactions can increase the ^{13}CO abundance up to a factor 2–3 and thus affect the CO isotopologue ratios, specifically at low A_V ~ 1 (e.g. Visser et al. 2009; Röllig & Ossenkopf 2013; Szűcs et al. 2014). For C^{18}O, the wavelengths of the dissociation lines can penetrate deeper into the interior of the molecular cloud because of its poor self-shielding (e.g. Glassgold et al. 1985). Furthermore, oxygen fractionation reactions can significantly decrease the C^{18}O abundance which can further increase the [^{13}CO]/[C^{18}O] ratio. However, to this point, oxygen fractionation reactions have received little attention (Loison et al. 2019).

The observations of Musca indicate that the weak FUV field in Musca (<1 G_0: see Paper II) might be able to significantly suppress the C^{18}O abundance in the strands to [^{13}CO]/[C^{18}O] = 40–50 on average, see Table 1. Inside the filament crest we find [^{13}CO]/[C^{18}O] $\lesssim$ 10. Significantly increasing [^{13}CO]/[C^{18}O] at the crest would drop the brightness of C^{18}O(2–1) below the observed value. This confirms that the [^{13}CO]/[C^{18}O] abundance ratio increases by roughly an order of magnitude over a small physical distance (≤0.2 pc in the plane of the sky) when going from the crest to the strands at lower A_V. In the study by Hacar et al. (2016) of the filament crest it was already noted that there were some indications of an increase of [^{13}CO]/[C^{18}O] towards lower A_V (<3) areas of the filament crest. Including the strands into the analysis, we now demonstrate that there is indeed a strong drop of C^{18}O abundance for low A_V gas in the Musca cloud. This observation indicates that even a weak FUV field can have a large impact on the molecular cloud chemistry of CO. The

formation of the dense filament crest is thus necessary for sufficient shielding such that $C^{18}O$ can form and implies that $C^{18}O$ is not a good column density tracer.

6. Discussion

6.1. A cylindrical geometry for the Musca filament crest and strands

In Sect. 5, from ^{13}CO line ratios, we derived estimates of the densities for the emitting CO gas in a section of the Musca filament to be n_{H_2} = 1−3 and 6−13 × 10^3 cm^{-3} in the strands and crest respectively. Using the *Herschel* total column densities towards the same directions (crest and strands), and assuming the standard CO abundance and gas/dust ratio, we then obtained the typical sizes on the line of sight for the crest and strands: 0.1−0.2 pc for the crest and 0.2−0.5 pc for the strands. This is very similar to their respective sizes projected on the sky. This clearly shows that both the strands and the crest are not more elongated along the line of sight than their transverse size in the plane of sky. Our CO observations therefore confirm that the Musca crest and strands correspond more to a filament, that is a cylindrical structure, than to a sheet seen edge-on as proposed in Tritsis & Tassis (2018). The 0.1−0.2 pc line of sight size of the crest is clearly in disagreement with the proposed 6 pc size in Tritsis & Tassis (2018) to explain the regular pattern of striations observed in the Musca cloud with MHD waves.

Looking carefully at the *Herschel* maps in Cox et al. (2016) we actually see that the striations are not necessary originating from the crest of the filament as assumed in Tritsis & Tassis (2018). The striations are indeed seen over an extended region of ∼2 × 4 pc around the crest (see Fig. 2 in Cox et al. 2016), that we here refer to as the ambient cloud. It could thus come from some extended, more diffuse gas around the filament.

For the immediate surroundings of the crest seen in our APEX maps, we also get a density from CO which points to sizes along the line of sight not larger than ∼0.5 pc only. This is still far from the 6 pc required to explain the striations with the magnetohydrodynamic waves. On the other hand our APEX CO study is limited to only the most nearby regions of the crest, of the order of ∼0.2 pc. At larger scale, the ambient cloud surrounding the filament could have a line of sight size up to 6 pc, and could then host the striation pattern. Using the typical observed column density of N_{H_2} = 1−3 × 10^{21} cm^{-2} in the direction of the strands, and assuming all this column density could be due to the surrounding ambient cloud, we would get for a line of sight length of 6 pc a typical density for this medium as low as ∼50−150 cm^{-3}. Such low densities might actually not be visible in CO and may correspond to some surrounding CO dark gas.

In conclusion, our CO observations clearly show that the densest region (crest and strands) of Musca is mostly a cylindrical filamentary structure. The striations are either not related to the proposed MHD vibrational modes of Tritsis & Tassis (2018) or these modes, if they require a depth of 6 pc, have developed in the extended ambient, probably CO-dark low density medium (∼50−150 cm^{-3}) surrounding the Musca filament.

6.2. Continuous mass accretion on the filament crest in Musca

The velocity structure of the Musca filament crest, displayed in Fig. 9 and that of the surrounding strands, traced with ^{13}CO(2–1), clearly indicates that in both APEX maps velocity gradients from blue-shifted extended gas to red-shifted dense gas are monotonic. These continuous gradients are a hint of slowing down of the large scale gas reaching the crest, and then point to accretion.

Interestingly enough these monotonic gradients have an opposite direction at both observed locations, see Fig. 9, similar to what was observed for instance in the massive DR21 ridge (Schneider et al. 2010). In DR21 this behaviour was proposed to be the result of a global collapse with inflowing subfilaments driving the velocity gradients.

Studying the location and velocity of the strands in the observed APEX maps, we found that the strands have changed side of the filament from our point of view, see Fig. 14, while at both locations the velocity of the strands are blueshifted, see e.g. Fig. 11. The blueshifted part of the filament crest velocity field, traced by $C^{18}O$(2–1), is always located at the side where the blueshifted strands connect with the filament crest, which strongly suggests a link between the velocity gradient over the filament crest and the immediate surrounding blueshifted strands. These observations point to a scenario where the strands are being accreted on the crest. As it is possible that this mass accretion is not exactly fixed on the filament axis, it can also deposit angular momentum inside the filament which could contribute to the $C^{18}O$(2–1) crest velocity field. This is schematically shown in Fig. 19.

Velocity gradients perpendicular to filaments have been found in other clouds as well, e.g.: DR21 (Schneider et al. 2010), IRDC 18223 (Beuther et al. 2015), Serpens (Dhabal et al. 2018; Chen et al. 2020) and SDC13 (Williams et al. 2018). In these studies, the observed velocity gradients have also been found to be possible indications of mass accretion by the filament from inflowing lower-density gas. However, the interpretation is often complicated by e.g. the presence of multiple velocity components (e.g Schneider et al. 2010; Beuther et al. 2015; Dhabal et al. 2018). In the southern map of Musca there is a hint of a second component in $C^{18}O$, but in the northern map the emission only shows a single velocity component which experiences the velocity gradient. This strongly suggests that the velocity gradient in Musca is indeed a mass accretion signature.

6.3. A potential H I cloud–cloud collision scenario to form the Chamaeleon-Musca complex

We obtain a scenario where the dense Musca filament is continuously accreting mass from large scale inflow, which fits with observed indications of filament accretion shocks towards the Musca filament in Paper II. Here we study the large-scale kinematics of the Chamaeleon-Musca complex to constrain the mechanism that drives the continuous mass accretion of the Musca filament and thus is responsible for the formation of the Musca filament.

6.3.1. A 50–100 pc coherent cloud complex in CO and H I

The results of the NANTEN CO survey of the Chamaeleon-Musca region in Mizuno et al. (2001) show the existence of a well-defined velocity (−1 to 6 km s^{-1}) and spatially coherent CO complex extending over roughly 20° × 24°, i.e. 35−40 pc at 90 pc to 70−80 pc at 190 pc while the analysis of *Gaia* data towards the CO clouds Cha I, II, III and Musca indicates walls of extinction ranging from 90 to 190 pc along the line of sight. This suggests that the global CO gas and the well known clouds Cha I, II, III and Musca are parts of a single complex of size 50 to 100 pc in projection and along the line of sight.

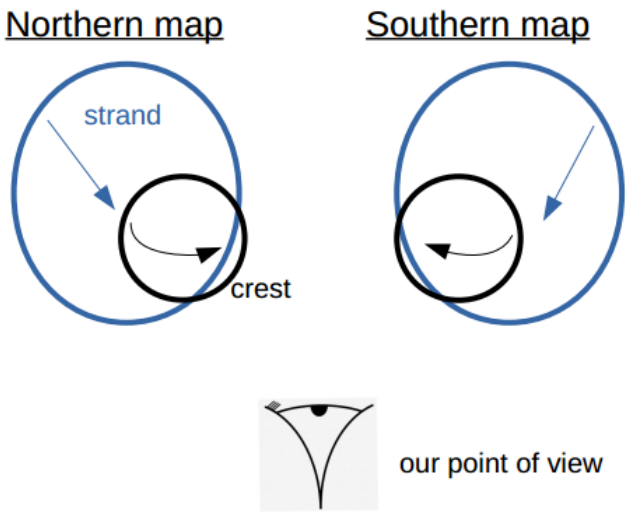

Fig. 19. Schematic illustration of the proposed accretion scenario responsible for the velocity gradient over the crest, possibly also related to some angular momentum deposition due to an accretion impact parameter, as seen from above the filament. The blue arrow indicates the motion of the strands compared to the crest from our point of view and the black arrows indicate the possible velocity field over the crest which is responsible for the observed velocity gradient.

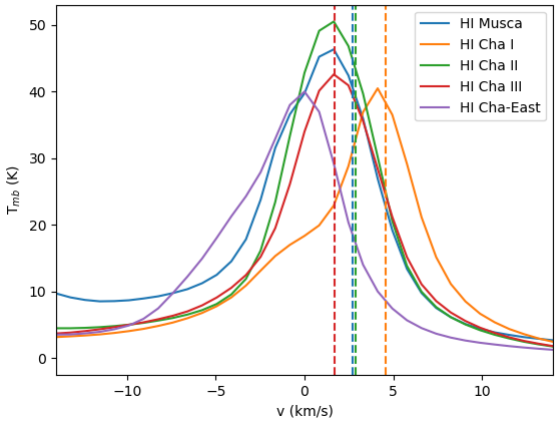

Fig. 20. H I spectra averaged towards Cha I, Cha II, Cha III, the eastern region of the Chamaeleon cloud and Musca. The dashed vertical lines give the ^{12}CO velocities of the dense regions Cha I, Cha II, Cha III and Musca (Mizuno et al. 2001). This shows that the dense gas traced by ^{12}CO for all regions is redshifted compared to their H I emission, identical to what is found for the filament crest of Musca when comparing ^{12}CO and C^{18}O.

To go one step further, we investigated the atomic hydrogen (H I) 21 cm line from the Galactic All Sky Survey (GASS) with the Parkes telescope (McClure-Griffiths et al. 2009; Kalberla et al. 2010; Kalberla & Haud 2015) towards the Chamaeleon-Musca region. The data has a spectral resolution of 0.8 km s^{-1} and a spatial resolution of 16′ (∼0.65 pc). This does not resolve CO clouds individually, but we find in Fig. 20 that the H I spectra have central velocities ranging from −2 to 5 km s^{-1} for the CO clouds. In Fig. 21 we show in the upper map the H I integrated emission between −10 and 10 km s^{-1} with contours of the *Planck* brightness at 353 GHz which indicates that there is a good spatial coincidence between H I and extended dust emission for the Chamaeleon-Musca complex. Fitting a gaussian to the H I spectra, we obtain a velocity field which is mapped in the lower map of Fig. 21. It shows that the whole complex displays a global velocity gradient from (slightly south) east at −2 km s^{-1} to (slightly north) west at +5 km s^{-1} which corresponds well to a similar ^{12}CO east-west gradient along a filamentary feature ∼15° long (i.e. 37 pc long in projection at 140 pc; Mizuno et al. 2001) which is also seen in *Planck* dust emission. We note that the magnitude of this gradient is similar to what was found for giant molecular clouds in M33 and M51, for which it had been proposed that it would be related to galactic pro- and retrograde rotational motion (Braine et al. 2018, 2020). The global velocity field in the Chamaeleon-Musca complex might thus also be linked to some galactic rotation. However, here it would then be retrograde motion unlike clouds in M33 and M51 which are mostly found to be prograde. While the velocity gradient in H I over the region is roughly identical to that of CO, the H I linewidths of ∼5–6 km s^{-1} are slightly larger than the linewidths in CO (2 to 2.8 km s^{-1} in Mizuno et al. 2001), as expected if the turbulent motions in H I are driving the CO motions as proposed for instance in numerical simulations of cloud formation by Koyama & Inutsuka (2002).

It is therefore clear that a coherent cloud complex exists connecting all known CO clouds of the region (Cha I, II, II and Musca) as well as a few additional more diffuse CO clouds such as Cha East and smaller CO clouds discussed for instance in Mizuno et al. (1998).

6.3.2. Dense gas mostly red-shifted in Chamaeleon/Musca

Studying the CO isotopologues towards Musca, we found that the dense filament crest, traced by C^{18}O, is at redshifted velocities compared to the molecular ambient cloud traced by ^{12}CO (Sect. 4.4). With H I, it is possible to study the kinematics of the even lower density and larger scale ambient gas. Inspecting the average H I spectrum towards the Musca cloud in Fig. 20, we found that the NANTEN2 ^{12}CO emission also appears redshifted compared to H I in the same way as C^{18}O compared to ^{12}CO at smaller scale in Fig. 8. This demonstrates that denser gas in the Musca cloud is systematically redshifted from low density, large scale atomic and molecular gas down to the Musca strands and filament crest.

In Fig. 21, we plot the individual H I spectra (in red) of the Chamaeleon/Musca clouds (Cha I, Cha II, Cha III, Cha East and Musca) together with their ^{12}CO velocities reported in Mizuno et al. (2001) (dashed lines) in comparison with the globally averaged H I spectrum (in blue). We see that while the individual H I spectra are equally present in the blue and red-shifted parts of the average H I spectrum, the CO gas tends to be mostly in the red-shifted part and is basically always red-shifted compared to the individual H I spectra towards each regions. This suggests that the velocity asymmetry of the dense gas, being mostly red-shifted, seen towards Musca is a general trend for the whole Chamaeleon-Musca cloud complex. Combining this with the identical redshifted asymmetry at small scales for Musca suggests a dynamical coherence in the complex, i.e. similar kinematic asymmetry, from the H I cloud with a size of ∼50−100 pc down to ∼0.1 pc around the Musca filament crest. This puts forward a scenario where the mass accretion of the dense (star forming) gas, which was in particular proposed based on the velocity gradients over the filament crest, in the complex is directly related to this large scale, and asymmetric H I /CO kinematics of the full complex.

We conclude that the local kinematic asymmetry observed towards Musca is observed for the whole complex and

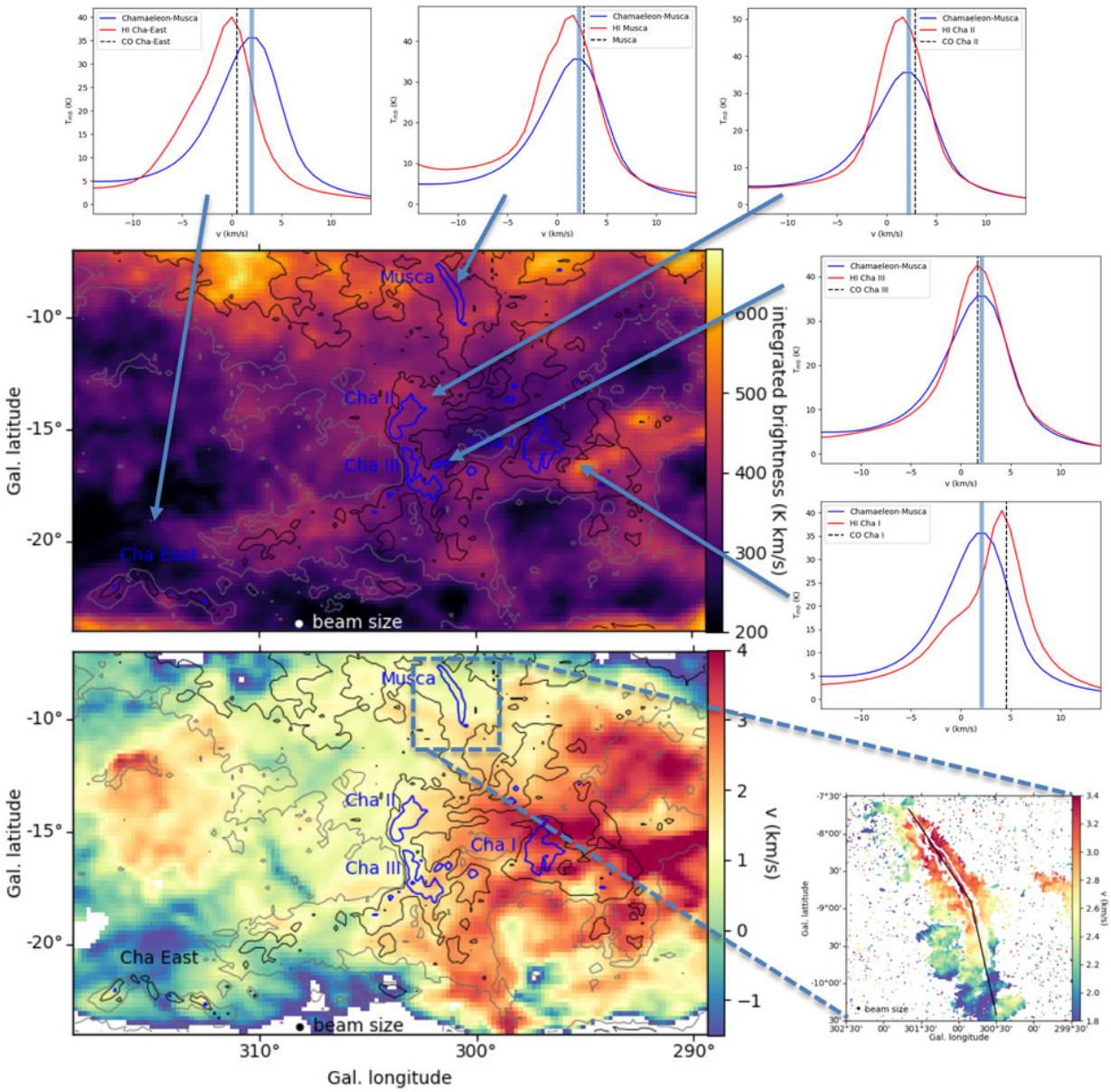

Fig. 21. Integrated H I map (*top*) and the velocity field (*below*) of the Chamaeleon-Musca complex from fitting a single gaussian to the H I spectra, with overplotted *Planck* brightness contours at 353 GHz. The blue contours highlight the dense Chamaeleon molecular clouds and the Musca filament, while the black and grey contours indicate the more extended continuum emission from *Planck*. Around the two maps, the average H I spectrum of the full complex and its peak emission (blue) is compared with the local H I spectrum (red) and velocity of the CO gas (black dashed line) (Mizuno et al. 2001) from the selected dense region (Cha I, Cha II, Cha III, Cha East and Musca). In the lower right figure, the ^{12}CO velocity field from the NANTEN2 data is shown.

individually for each CO cloud of the complex. This suggests that the region corresponds to a single event of cloud formation. We argue in the following subsection that a H I cloud-cloud collision event can explain the kinematic asymmetry, which can fit with the observed indications of more than one velocity component in several H I spectra.

6.4. Asymmetric inflow guided by the magnetic field in a H I cloud–cloud collision

The asymmetry in velocity between low and high density gas at all scales is difficult to explain with a classical view of an isotropic injection of turbulence at large scales. In this view, the velocity streams would be on average equally blue and red-shifted. In contrast, any scenario based on a (H I) cloud–cloud collision can easily introduce asymmetries if the two clouds in collision have different initial properties and substructure, which is actually expected and natural. In the case of a (H I) cloud–cloud collision with some primordial density substructure, numerical simulations show that such a collision is prone to concentrate the pre-existent structures (e.g. Inoue & Inutsuka 2012; Inoue & Fukui 2013; Inoue et al. 2018; Iwasaki et al. 2019). This concentration of matter can originate from a locally curved magnetic field leading to dense structures perpendicular to the

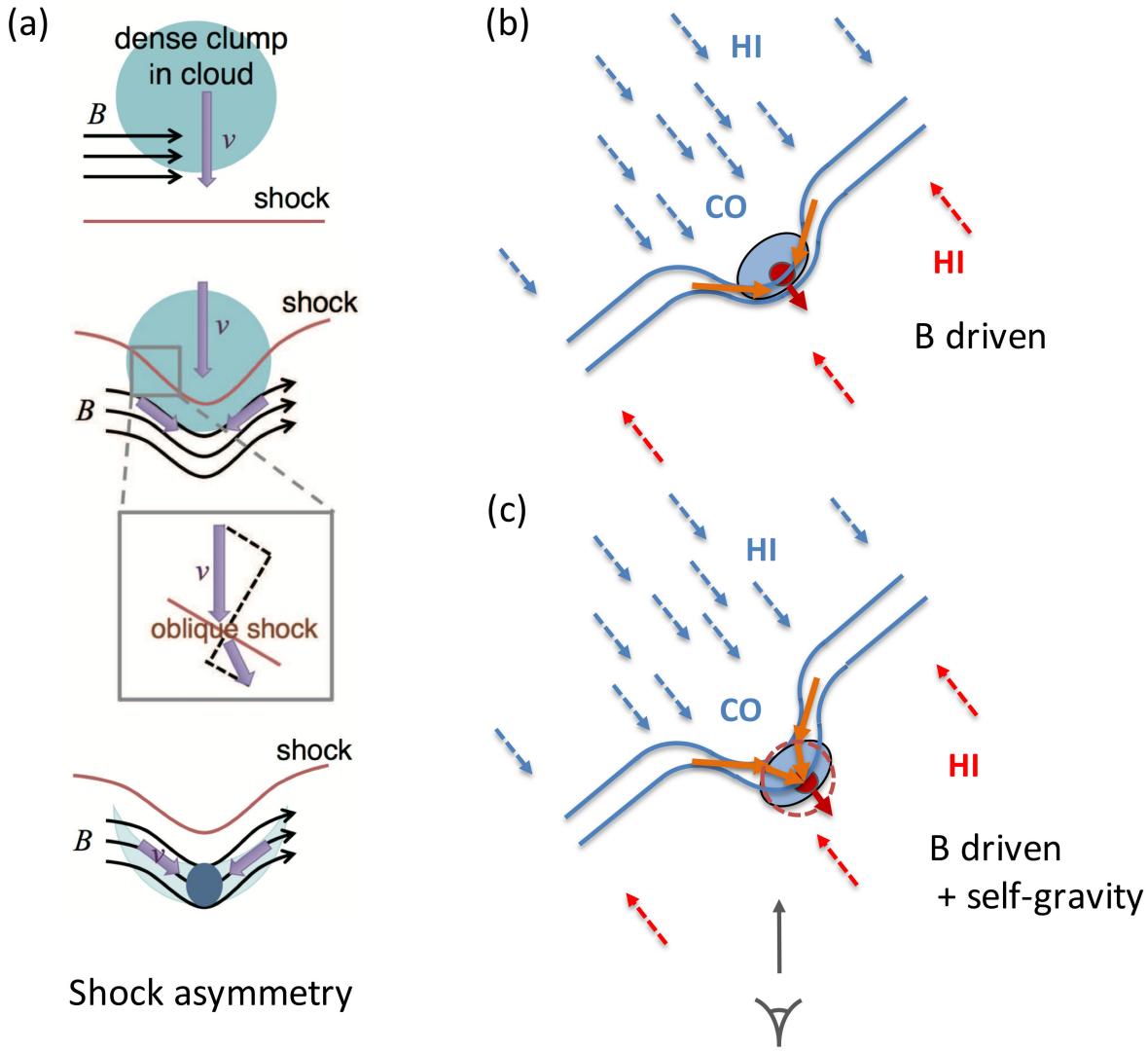

Fig. 22. Proposed sketch, observed from above the Musca filament, to explain the spatial and kinematic asymmetries of Musca originating from a H I cloud–cloud collision event (blue and red dashed arrows) following the Inoue scenario (see *panel a*, Inoue et al. 2018). The asymmetry between CO and H I could be due to the effect of compression of a clump in a cloud–cloud collision. The resulting bent of the magnetic field (blue lines) drives the gas towards the apex along the magnetic field, leading to a concentration of the mostly blue-shifted but slowed down (i.e. becoming red-shifted compared to the local mostly blue-shifted H I gas) CO gas (B driven concentration, *panel b*). Later on, the self-gravity of the strong concentration of matter (filament crest) can curve the concentration flows (see *panel c*) continuing the accretion onto the crest while magnetic field slowly drifts through the crest. The crest would then be in equilibrium between an asymmetric accretion and the tension of magnetic field. The progressive slowing down of the accretion flow, observed in the strands, from the bluest gas to the crest velocity could be partly due to magnetic pressure (the flows get less aligned with the magnetic field as self-gravity starts to take over) and perhaps some contribution from the turbulent pressure as it gets close to the crest (see Sect. 6.6). Seen from the side, the magnetic field would naturally appear perpendicular to the crest of the filament as observed.

magnetic field. This would fit with the generally accepted view that inflows towards the dense filaments are guided by the magnetic field (e.g. Banerjee et al. 2009; Soler et al. 2013), possibly in the form of striations (Palmeirim et al. 2013; Cox et al. 2016). This (Inoue) mechanism is based on the fact that when a shock wave impacts a slightly denser structure, the local magnetic field is bent around the structure and then channels the streams of gas (through an oblique shock; see Fig. 22a) towards the apex of the bent which is then rapidly the densest part of the original structure (Inoue & Fukui 2013; Vaidya et al. 2013).

Interestingly enough such a bent of the magnetic field by a shock in the Inoue mechanism naturally predicts a spatial and kinematic asymmetry of the dense structure with the densest region, the filament crest, being concentrated on the front side of the original structure. Figure 22 illustrates how such a scenario could explain the described kinematical asymmetry of Musca as well as the indicated spatial asymmetry in Sect. 4.4. The Musca filament/crest would trace this front side of the original structure which has been concentrated by favoured channelling parallel to the bent magnetic field (see the sketch in the right panels of Fig. 22). This dense structure is also the most slowed down gas by the opposite stream of gas from the red-shifted H I cloud (see panel b of Fig. 22). It would explain why all dense CO structures in the region appear red-shifted as they would be the most

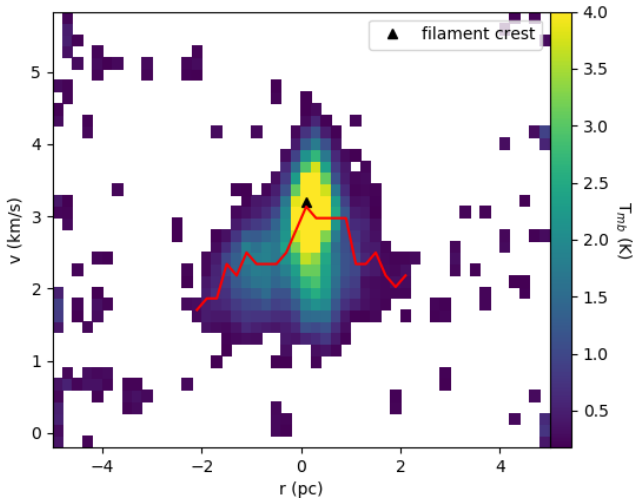

Fig. 23. PV diagram as a function of the distance from the center of the Musca filament for the ^{12}CO(1–0) emission from the NANTEN2 data. The red line follows the velocity with maximal brightness as a function of the distance from the filament crest. The PV diagram shows the expected V-shape from the Inoue scenario with respect to the velocity of the dense filament crest (Hacar et al. 2016) which is at the redshifted apex of the V-shape.

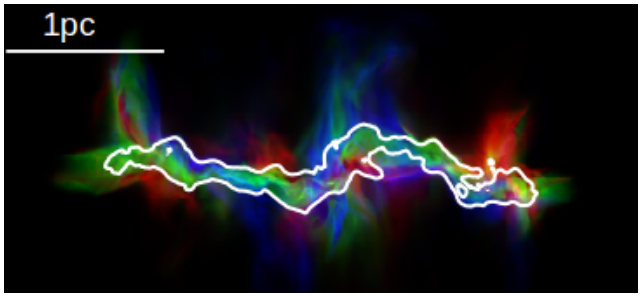

Fig. 24. RGB image using ^{12}CO(1–0) synthetic observations (red: 0.5–2 km s^{-1} & blue: −2 to −0.5 km s^{-1}) and ^{13}CO(1–0) synthetic observations (green: −0.5 to 0.5 km s^{-1}) of the simulations in Clarke et al. (2018). The white contour encloses the region with integrated C^{18}O(1–0) brightness >1 K km s^{-1}. This shows that close to the filament the direction of the velocity gradient can change, similar to what is observed in Musca, as a result of turbulent motions.

sensitive to the dragging force of the opposite flow of gas from the colliding red-shifted H I cloud. If globally H I is dominated by the blue-shifted H I gas, this would explain the tendency to have the H I spectrum slightly blue-shifted compared to the CO gas of all molecular clouds in the Cha/Musca region. In this scenario the magnetic field would channel the pre-existent mostly blue-shifted structure and its immediate surroundings, while slightly slowing down and becoming more red-shifted and therefore allowing for more accretion of faster blue-shifted gas from behind. The orientation of this organised inflow by two intersecting sheet-like structures could then explain why most CO emission is observed east of the filament. This scenario has the advantage to explain both the spatial and velocity asymmetries, and to explain the fact that the magnetic field is perpendicular to the filament/crest.

In particular, this bending of the magnetic field would lead to an observable signature in the PV diagram of the Musca cloud. This signature is displayed in Fig. 22 and in Fig. 16 from Arzoumanian et al. (2018). Specifically, the kinematic signature consists of a "V-shape" for the inflowing molecular cloud with the densest gas at the apex of this V-shape. A V-shape in the PV diagram was reported by Arzoumanian et al. (2018) for a filament in the Taurus molecular cloud. Figure 23 shows the PV diagram of the Musca cloud from the NANTEN2 data. This PV diagram shows exactly such a V-shape, with the C^{18}O velocity of the filament crest at the apex of this V-shape.

6.5. Inhomogeneities in the inflow driven by local gravity or large-scale dynamics

While the Inoue scenario may well explain the observed local asymmetries towards the Musca filament, the change of direction for the velocity gradient along the filament discussed in Sect. 6.2 might be more difficult to explain with this scenario alone. We note however that numerical simulations such as the ones presented in Clarke et al. (2017, 2018) reproduce very well this behaviour (see also simulations presented in Schneider et al. 2010 to explain similar features in the DR21 filament/ridge). These simulations consist of a cylindrical converging flow which produces an accreting dense filament. Turbulence in the flow leads to inhomogeneities in the accretion and substructures in the filament with accretion flows which are not always landing on the filament from the same side of the crest. The simulation includes hydrodynamics, self-gravity, a weak FUV-field (1.7 G_0), and heating and cooling coupled with non-equilibrium chemistry. This allows for the self-consistent formation of CO and thus the production of synthetic CO observations as shown in Fig. 24, which present an RGB image from the simulation that highlights the locations of the blue- and redshifted mass reservoir around the dense filament. These synthetic observations indicate that there is no clearly separated blue- and redshifted mass reservoir close to the filament crest, but rather that the location of the dominant inflowing mass reservoir alternates to each side of the filament as a consequence of the turbulence in the inflowing mass reservoir (Clarke et al. 2017, Fig. 24). The simulations demonstrate that in a cylindrical area close to the filament there can be large local position variations of the converging flows towards the filament. In Musca this relatively cylindrical area has a size of the order of 0.4 pc, covering the filament crest and strands.

We conclude that these inhomogeneities in the inflow can be expected at least in a non-magnetic case (the above discussed simulations do not include magnetic field). It is not clear though what is the main driver of these local variations of the converging flows in Musca. Including the possible role of magnetic field, it can either originate purely from the original kinematic fluctuations from large scales, forcing the magnetic field guidance or could be partly due to self-gravity close to the crest which could decouple the gas inflow from the guidance of magnetic field allowing for these variations along the filament.

6.6. A two step scenario: B driven followed by a gravity driven and B regulated accretion

As shown in the previous section thanks to numerical simulations, self-gravity of the filamentary structure may explain the changing direction of the velocity gradients along the crest of the filament. We may then have a situation as shown in panel c of Fig. 22 where there is a transition from the B (magnetic field) driven concentration to a gravity driven accretion regime close to the crest. This may correspond to the region of the strands

where we observe a smooth ^{13}CO velocity gradient from 3.1 to 3.5 km s^{-1} and from 2.7 to 3.1 km s^{-1} for the northern and southern APEX maps, respectively. The progressive slowing down of the blue-shifted gas to the velocity of the crest could then be due to the need to cross some magnetic field lines to reach the crest. Indeed, close to the crest where the self-gravity of the crest is maximal, the magnetic field should slowly drift through the filament crest in the Inoue scenario (Fig. 22) as it is dragged by the larger scale pressure from the red-shifted gas. So we would have a scenario where the gas is accelerated by gravity but slowed down by magnetic pressure to reach the up-stream crest.

Alternatively in Shimajiri et al. (2019) for the B211/3 filament in Taurus, gravity was claimed to accelerate gas from large to small scales, and with a slowing down of velocities close to the crest being due to a large turbulent pressure (up to an order of magnitude larger than the thermal pressure). To obtain a fit to the data, they had to assume that the whole CO linewidth would represent an effective turbulent pressure. In Musca in the APEX and NANTEN2 maps we see that the global velocity dispersion appears to be dominated by bulk motions with velocity gradients, and not by isotropic turbulence. We easily expect that at higher spatial resolution an even larger fraction of the linewidth is due to bulk motions rather than to isotropic turbulence. Also we note that the velocity dispersion (expressed in σ) is much smaller in Musca compared to B211/3. Instead of 0.9 km s^{-1} for B211/3, we obtain a maximal σ = 0.4–0.5 km s^{-1} over the whole region for Musca in the NANTEN2 ^{12}CO data (e.g. Fig. 13), and even down to $\sigma \sim 0.2$ km s^{-1} close to the crest in the ^{13}CO APEX data. The possible deceleration thanks to a possible contribution of the turbulent motions to pressure in the immediate surroundings of the crest is therefore reduced in Musca compared to B211. Since the gravitational acceleration in Musca is also reduced (lower mass filament) it is not possible to firmly reject some effect of the turbulent pressure effect, but we point out here that our scenario can explain the observed deceleration without heavily relying on an hypothetical full conversion of CO linewidth into effective sound speed such as in Shimajiri et al. (2019) for B211/3. Altogether we may actually have a mixture of magnetic and turbulent pressure to explain the deceleration of the accretion flow onto the crest.

We finally note that our scenario might also explain the geometry and velocity field of the B211/3 filament. This filament shows an asymmetry between the blue- and redshifted sides of the accretion flow, and also displays a V-like shape in the PV diagram (Shimajiri et al. 2019). The proposed angle of 130° between the two sheets in Shimajiri et al. (2019) could actually trace the bent of the magnetic field in the Inoue scenario.

6.7. The physical scale of dominant self-gravity

Here we compare the typical observed relative motions between the crest and the surrounding gas with the expected self-gravity velocities to discuss at which scale gravity may be responsible for the observed relative motions. In Chen et al. (2020) it is proposed to use the non-dimensional parameter C_ν to differentiate between gravity-driven mass inflow and other sources of motions (shock compression in Chen et al. 2020), with C_ν expressed as

$$C_\nu = \frac{\Delta v_{\rm h}^2}{G\, M(r)/L} \quad (1)$$

where $\Delta v_{\rm h}$ is half of the velocity difference over the filament and $M(r)/L$ the mass per unit length at the distance r from the center of the crest.

On large scales, the velocity difference between the filament and the CO gas reaches values of the order of 1 km s^{-1} at both sides of the filament crest, see Fig. 23. With a mass per unit length of 15.6 $M_\odot$ pc^{-1} (22.3 $M_\odot$ pc^{-1} corrected to d = 140 pc) for the Musca filament, this corresponds to C_ν = 15. At the pc scale, the kinematics are thus not dominated by the self-gravity of the filament. In other words the actual crossing time is clearly smaller than the free-fall time from the self-gravity of the filament. At the 0.4 pc scale of the strands, we still have a velocity difference of ~0.4 km s^{-1} leading to C_ν = 2.4. This suggests that self-gravity may start to play a role but is not dominant yet. At the scale of the filament crest with a velocity difference of 0.2 km s^{-1} we obtain C_ν = 1.1. We thus find that gravity may indeed take over from the large scale motions at sub-pc scales, reinforcing our proposed scenario in two steps with a B-driven followed by a gravity driven accretion when matter is reaching the crest of the filament at sub-pc scale.

When we apply the C_ν criterion to study the importance of self-gravity for the B211/3 filament, we similarly found large values of C_ν at the pc scale, and at the sub-pc scale close to the crest that C_ν could be approaching a value of 1. The velocities of the large scale flows in B211/3 are found to be typically 2–3 times larger than in Musca at the same distances from the crest while the M/L value is roughly 3 times larger (54 $M_\odot$ pc^{-1}). C_ν is therefore found to be typically 2–3 times larger in B211/3 at large scales.

6.8. Future star formation in the Musca filament

In this paper we proposed that a large scale colliding H I flow, forming the Chamaeleon-Musca complex, could be at the origin of the proposed mass accretion on the Musca filament crest. Here, we investigate whether such continuous mass accretion can eventually lead to star formation in the Musca filament.

In the NANTEN2 data, most molecular gas traced by ^{12}CO is present in the filament and in a structure east of the filament which has a relative velocity of −0.5 to −1 km s^{-1} compared to the velocity of the filament. Using simple assumptions, we now estimate a time scale for accretion of this gas on the filament. We assume a projected inflow velocity in the plane of the sky of 0.7 km s^{-1} towards the filament, while the distance perpendicular to the crest of this ^{12}CO emission is generally of the order of 0.5 to 1 pc. It would thus require roughly 0.7–1.4 Myr for the nearby ambient cloud within this radius to be accreted on the filament/strands. Then there are the strands at a velocity of −0.4 to −0.5 km s^{-1} along the line of sight compared to the filament crest. These strands are present from the edge of the filament crest up to a distance of ~0.4 pc. At this velocity, the accretion of these strands on the filament crest would take close to 1 Myr. The filament crest has a velocity gradient, with a maximal velocity difference of 0.15–0.2 km s^{-1}. This results in a similar crossing timescale for the filament crest of 0.7 Myr. However, one should note that this velocity gradient is not necessarily related to dispersion of the filament, and that the increasing role of gravity will confine the filament such that this timescale is a lower limit.

Similar to Palmeirim et al. (2013) we can estimate the mass accretion rate per unit length on the filament at R = 0.4 pc. For this we need a density estimate at R = 0.4 pc. Here we use the same approach as Palmeirim et al. (2013) by extracting the density from the fitted Plummer model to the averaged Musca filament (Cox et al. 2016). This results in a mass accretion estimate of 14 $M_\odot$ pc^{-1} Myr^{-1}. With this mass accretion rate it would roughly take 1 Myr to accrete the amount of mass already present in the Musca filament. Based on the estimated mass accretion

rates and time scales, we find that strands can be provided with sufficient mass from the more extend ambient cloud during the timescale of their accretion on the filament crest. This allows for a continuous mass accretion on the Musca filament.

Several theoretical studies have investigated the collapse timescales of non spherical structures (e.g. Burkert & Hartmann 2004; Toalá et al. 2012; Pon et al. 2012; Clarke & Whitworth 2015). To estimate the longitudinal collapse timescale of the Musca filament, we use the formula from Clarke & Whitworth (2015):

$$t_{\rm coll} = (0.49 + 0.26A_0)(Gn_{\rm H_2})^{-\frac{1}{2}}, \quad (2)$$

where A_0 is the initial aspect ratio, which is 54 using a half length of 3 pc and a radius of 0.056 pc for Musca (Cox et al. 2016, corrected to d = 140 pc), G is the gravitational constant, and for $n_{\rm H_2}$, the molecular hydrogen gas density, we use 10^4 cm^{-3}. This results in a timescale of 9.2 Myr, which is roughly an order of magnitude larger than the estimated accretion time scale for the large scale inflowing mass reservoir. This lifetime for longitudinal collapse is a lower limit because of possible magnetic field support.

We thus find a scenario where the Musca filament crest is a long-lived filament because it is a coherent structure with sufficient continuous mass accretion which is driven by the bending of the magnetic field due to the large scale colliding H I flow that forms the Chamaeleon-Musca complex. As this provides a sufficient amount of mass for Musca to become supercritical before it is dispersed, gravity starts playing a more important role in further confining the filament. The future continuous mass accretion, which might be increasingly driven by gravity, could further increase the density in the filament. This can lead to further fragmentation of the Musca filament, which has started in several regions of the filament (Kainulainen et al. 2016), to form pre-stellar and protostellar cores in a dynamic filamentary structure.

7. Conclusion

We have presented APEX observations of CO(2–1) isotopologues towards the Musca filament crest and the strands. This data was complemented with NANTEN2 observations of ^{12}CO(1–0) covering the full Musca cloud. We find that C^{18}O traces the filament crest, ^{13}CO the strands and ^{12}CO the more diffuse ambient molecular cloud. The main results of this study can be summarised as follows:

– *Gaia* star reddening data suggests a distance of 140 pc for Musca, but we note that there might already be some reddening at ∼100 pc.

– Modelling the CO lines with non-LTE line radiative transfer favours a scenario where Musca crest is a compact filament with a central density $n_{\rm H_2} \sim 10^4$ cm^{-3} at $T_{\rm K} \sim 10$ K, and where the strands are an independent feature, consisting of dense gas (with $n_{\rm H_2} \sim 10^3$–3×10^3 cm^{-3} at $T_{\rm K} \sim 15$ K) that is connected to the filament crest.

– We report a sharp increase of the [^{13}CO]/[C^{18}O] abundance ratio by roughly an order of magnitude over a small distance (<0.2 pc) at $A_{\rm V} < 3$. This occurs in a weak ambient FUV field (<1 G$_0$) and indicates C^{18}O is a limited column density tracer.

– We confirm that the filament crest is a velocity-coherent structure, and also demonstrate that there are transverse velocity gradients over the velocity-coherent filament crest with a magnitude similar to the transonic linewidth of the filament crest.

– The ambient cloud contains a significant amount of blueshifted gas along the line of sight with respect to the filament crest, while there is a lack of redshifted gas with respect to the filament crest.

– We observe a link between the transverse velocity gradient over the filament crest and the location of the blueshifted strands, indicating that the strands are accreted on the filament crest and that the velocity gradient is a signature of this accretion which possibly also deposits some angular momentum in the crest.

– We find a kinematically coherent asymmetry from the ∼50 pc H I cloud down to the Musca filament crest as well as an asymmetric column density profile for the Musca cloud, indicating that the large scale evolution of the Chamaeleon-Musca complex is directly related to the formation of the Musca filament and that the asymmetry contains essential information on the physical process responsible for dense gas formation in the region.

– The PV diagram of the Musca cloud traces a V-shape with the filament crest located at the redshifted apex of this V-shape.

Combining all data, we propose that the Musca filament crest is a long-lived dynamic filament because it is a coherent structure that is continuously replenished by inflowing gas. This mass accretion is driven by the colliding H I flow that forms the Chamaeleon-Musca complex and can eventually lead to the formation of protostellar cores embedded in this dynamic filament. This colliding flow in Chamaeleon-Musca is the result of a magnetised low-velocity H I cloud-cloud collision that produces the observed asymmetric accretion scenario, seen as a V-shape in the PV diagram, driven by the bending of the magnetic field.

Acknowledgements. The authors thank the anonymous referee for providing insightful input that improved the clarity and quality of this paper. L.B., N.S., R.S., and S.B. acknowledge support by the french ANR and the german DFG through the project "GENESIS" (ANR-16-CE92-0035-01/DFG1591/2-1). L.B. also acknowledges support from the Région Nouvelle-Aquitaine. N.S. acknowledges support from the BMBF, Projekt Number 50OR1714 (MOBS-MOdellierung von Beobachtungsdaten SOFIA). N.S. and R.S. are supported by the German Deutsche Forschungsgemeinschaft, DFG project number SFB 956. We thank F. Wyrowski for providing information to correct for the frequency shift in the APEX FLASH observations. We thank F. Boulanger for input on the production of the *Planck* polarisation maps. This research made use of Astropy (http://www.astropy.org), a community-developed core Python package for Astronomy (Astropy Collaboration 2013, 2018). Based on observations obtained with *Planck* (http://www.esa.int/Planck), an ESA science mission with instruments and contributions directly funded by ESA Member States, NASA, and Canada. This publication is based on data acquired with the Atacama Pathfinder Experiment (APEX) under programme IDs 0100.C-0825(A), 0101.F-9511(A) and 0102.F-9503(A). This research has made use of data from the *Herschel* Gould Belt survey project (http://gouldbelt-herschel.cea.fr). The HGBS is a *Herschel* Key Project jointly carried out by SPIRE Specialist Astronomy Group 3 (SAG3), scientists of several institutes in the PACS Consortium (CEA Saclay, INAF-IAPS Rome and INAF-Arcetri, KU Leuven, MPIA Heidelberg), and scientists of the *Herschel* Science Center (HSC).

References

Alves de Oliveira, C., Schneider, N., Merín, B., et al. 2014, A&A, 568, A98
Andrae, R., Fouesneau, M., Creevey, O., et al. 2018, A&A, 616 A8
André, P., Men'shchikov, A., Bontemps, S., et al. 2010, A&A, 518, L102
André, P., Di Francesco, J., Ward-Thompson, D., et al. 2014, Protostars and Planets VI (Tucson, AZ: University of Arizona Press), 27
Arzoumanian, D., André, P., Didelon, P., et al. 2011, A&A, 529, L6
Arzoumanian, D., Shimajiri, Y., Inutsuka, S.-i., Inoue, T., & Tachihara, K. 2018, PASJ, 70, 96
Arzoumanian, D., André, P., Könyves, V., et al. 2019, A&A, 621, A42
Astropy Collaboration (Robitaille, T. P., et al.) 2013, A&A, 558, A33
Astropy Collaboration (Price-Whelan, A. M., et al.) 2018, AJ, 156, 123
Audit, E., & Hennebelle, P. 2005, A&A, 433, 1

Ballesteros-Paredes, J., Hartmann, L., & Vázquez-Semadeni, E. 1999, ApJ, 527, 285
Banerjee, R., Vázquez-Semadeni, E., Hennebelle, P., & Klessen, R. S. 2009, MNRAS, 398, 1082
Beuther, H., Ragan, S. E., Johnston, K., et al. 2015, A&A, 584, A67
Bohlin, R. C., Savage, B. D., & Drake, J. F. 1978, ApJ, 224, 132
Bonne, L., Schneider, N., Bontemps, S., et al. 2020, A&A, 641, A17
Bontemps, S., André, P., Könyves, V., et al. 2010, A&A, 518, L85
Braine, J., Rosolowsky, E., Gratier, P., Corbelli, E., & Schuster, K.-F. 2018, A&A, 612, A51
Braine, J., Hughes, A., Rosolowsky, E., et al. 2020, A&A, 633, A17
Burkert, A., & Hartmann, L. 2004, ApJ, 616, 288
Chen, C.-Y., & Ostriker, E. C. 2014, ApJ, 785, 69
Chen, C.-Y., Mundy, L. G., Ostriker, E. C., Storm, S., & Dhabal, A. 2020, MNRAS, 494, 2675
Clarke, S. D., & Whitworth, A. P. 2015, MNRAS, 449, 1819
Clarke, S. D., Whitworth, A. P., Duarte-Cabral, A., & Hubber, D. A. 2017, MNRAS, 468, 2489
Clarke, S. D., Whitworth, A. P., Spowage, R. L., et al. 2018, MNRAS, 479, 1722
Corradi, W. J. B., Franco, G. A. P., & Knude, J. 1997, A&A, 326, 1215
Cox, N. L. J., Arzoumanian, D., André, P., et al. 2016, A&A, 590, A110
Csengeri, T., Bontemps, S., Schneider, N., Motte, F., & Dib, S. 2011, A&A, 527, A135
Dhabal, A., Mundy, L. G., Rizzo, M. J., Storm, S., & Teuben, P. 2018, ApJ, 853, 169
Duarte-Cabral, A., & Dobbs, C. L. 2017, MNRAS, 470, 4261
Federrath, C. 2016, MNRAS, 457, 375
Franco, G. A. P. 1991, A&A, 251, 581
Fukui, Y., Inoue, T., Hayakawa, T., & Torii, K. 2020, PASP, in press [arXiv:1909.08202]
Gaia Collaboration (Brown, A. G. A., et al.) 2018, A&A, 616, A1
Galli, D., Walmsley, M., & Gonçalves J. 2002, A&A, 394, 275
Glassgold, A. E., Huggins, P. J., & Langer, W. D. 1985, ApJ, 290, 615
Goldsmith, P. F. 2001, ApJ, 557, 736
Goldsmith, P. F., Heyer, M., Narayanan, G., et al. 2008, ApJ, 680, 428
Gómez, G. C., & Vázquez-Semadeni, E. 2014, ApJ, 791, 124
Güsten, R., Nyman, L. Å., Schilke, P., et al. 2006, A&A, 454, L13
Güver, T., & Özel, F. 2009, MNRAS, 400, 2050
Hacar, A., & Tafalla, M. 2011, A&A, 533, A34
Hacar, A., Tafalla, M., Kauffmann, J., & Kovács, A. 2013, A&A, 554, A55
Hacar, A., Kainulainen, J., Tafalla, M., Beuther, H., & Alves, J. 2016, A&A, 587, A97
Heitsch, F. 2013, ApJ, 769, 115
Heitsch, F., Burkert, A., Hartmann, L. W., Slyz, A. D., & Devriendt, J. E. G. 2005, ApJ, 633, L113
Hennebelle, P. 2013, A&A, 556, A153
Hennebelle, P., & André, P. 2013, A&A, 560, A68
Hennebelle, P., Banerjee, R., Vázquez-Semadeni, E., Klessen, R. S., & Audit, E. 2008, A&A, 486, L43
Hennemann, M., Motte, F., Schneider, N., et al. 2012, A&A, 543, L3
Henshaw, J. D., Jiménez-Serra, I., Longmore, S. N., et al. 2017, MNRAS, 464, L31
Hill, T., Motte, F., Didelon, P., et al. 2011, A&A, 533, A94
Inoue, T., & Fukui, Y. 2013, ApJ, 774, L31
Inoue, T., & Inutsuka, S.-i. 2012, ApJ, 759, 35
Inoue, T., Hennebelle, P., Fukui, Y., et al. 2018, PASJ, 70, S53
Inutsuka, S.-I., & Miyama, S. M. 1992, ApJ, 388, 392
Inutsuka, S.-i., & Miyama, S. M. 1997, ApJ, 480, 681
Ivlev, A. V., Silsbee, K., Sipilä, O., & Caselli, P. 2019, ApJ, 884, 176
Iwasaki, K., Tomida, K., Inoue, T., & Inutsuka, S.-i. 2019, ApJ, 873, 6
Juvela, M., Ristorcelli, I., Pagani, L., et al. 2012, A&A, 541, A12
Kainulainen, J., Beuther, H., Henning, T., & Plume, R. 2009, A&A, 508, L35
Kainulainen, J., Hacar, A., Alves, J., et al. 2016, A&A, 586, A27
Kalberla, P. M. W., & Haud, U. 2015, A&A, 578, A78
Kalberla, P. M. W., McClure-Griffiths, N. M., Pisano, D. J., et al. 2010, A&A, 521, A17
Klein, T., Ciechanowicz, M., Leinz, C., et al. 2014, IEEE Trans. Terahertz Sci. Technol., 4, 588
Knude, J., & Hog, E. 1998, A&A, 338, 897
Koch, E. W., & Rosolowsky, E. W. 2015, MNRAS, 452, 3435
Könyves, V., André, P., Men'shchikov, A., et al. 2010, A&A, 518, L106
Könyves, V., André, P., Men'shchikov, A., et al. 2015, A&A, 584, A91
Koyama, H., & Inutsuka, S.-i. 2002, ApJ, 564, L97
Langer, W. D., & Penzias, A. A. 1990, ApJ, 357, 477
Liszt, H., Gerin, M., & Grenier, I. 2019, A&A 627, A95
Loison, J.-C., Wakelam, V., Gratier, P., et al. 2019, MNRAS, 485, 5777
Machaieie, D. A., Vilas-Boas, J. W., Wuensche, C. A., et al. 2017, ApJ, 836, 19
Malinen, J., Montier, L., Montillaud, J., et al. 2016, MNRAS, 460, 1934
Marsh, K. A., Kirk, J. M., André, P., et al. 2016, MNRAS, 459, 342
McClure-Griffiths, N. M., Pisano, D. J., Calabretta, M. R., et al. 2009, ApJS, 181, 398
Merello, M., Molinari, S., Rygl, K. L. J., et al. 2019, MNRAS, 483, 5355
Mizuno, A., Hayakawa, T., Yamaguchi, N., et al. 1998, ApJ, 507, L83
Mizuno, A., Yamaguchi, R., Tachihara, K., et al. 2001, PASJ, 53, 1071
Moeckel, N., & Burkert, A. 2015, ApJ, 807, 67
Molinari, S., Swinyard, B., Bally, J., et al. 2010, A&A, 518, L100
Motte, F., Bontemps, S., & Louvet, F. 2018, ARA&A, 56, 41
Myers, P. C. 2009, ApJ, 700, 1609
Nagai, T., Inutsuka, S.-i., & Miyama, S. M. 1998, ApJ, 506, 306
Nakamura, F., & Li, Z.-Y. 2008, ApJ, 687, 354
Nielbock, M., Launhardt, R., Steinacker, J., et al. 2012, A&A, 547, A11
Ossenkopf-Okada, V., & Stepanov, R. 2019, A&A, 621, A5
Ostriker, J. 1964, ApJ, 140, 1056
Padoan, P., Juvela, M., Goodman, A. A., & Nordlund, Å. 2001, ApJ, 553, 227
Palmeirim, P., André, P., Kirk, J., et al. 2013, A&A, 550, A38
Panopoulou, G. V., Psaradaki, I., Skalidis, R., Tassis, K., & Andrews, J. J. 2017, MNRAS, 466, 2529
Peretto, N., André, P., Könyves, V., et al. 2012, A&A, 541, A63
Peretto, N., Fuller, G. A., Duarte-Cabral, A., et al. 2013, A&A, 555, A112
Peretto, N., Fuller, G. A., André, P., et al. 2014, A&A, 561, A83
Pereyra, A., & Magalhães, A. M. 2004, ApJ, 603, 584
Pilbratt, G. L., Riedinger, J. R., Passvogel, T., et al. 2010, A&A, 518, L1
Planck Collaboration I. 2016, A&A, 594, A1
Planck Collaboration Int. XXVIII. 2015, A&A, 582, A31
Planck Collaboration Int. XIII. 2016, A&A, 586, A136
Planck Collaboration Int. XXXV. 2016, A&A, 586, A138
Polychroni, D., Schisano, E., Elia, D., et al. 2013, ApJ, 777, L33
Pon, A., Toalá, J. A., Johnstone, D., et al. 2012, ApJ, 756, 145
Rachford, B. L., Snow, T. P., Destree, J. D., et al. 2009, ApJS, 180, 125
Recchi, S., Hacar, A., & Palestini, A. 2014, MNRAS, 444, 1775
Röllig, M., & Ossenkopf, V. 2013, A&A, 550, A56
Roy, A., André, P., Palmeirim, P., et al. 2014, A&A, 562, A138
Rygl, K. L. J., Benedettini, M., Schisano, E., et al. 2013, A&A, 549, L1
Schneider, N., Csengeri, T., Bontemps, S., et al. 2010, A&A, 520, A49
Schneider, N., Bontemps, S., Simon, R., et al. 2011, A&A, 529, A1
Schneider, N., Csengeri, T., Hennemann, M., et al. 2012, A&A, 540, L11
Schöier, F. L., van der Tak, F. F. S., van Dishoeck, E. F., & Black, J. H. 2005, A&A, 432, 369
Seifried, D., & Walch, S. 2015, MNRAS, 452, 2410
Seifried, D., & Walch, S. 2016, MNRAS, 459, L11
Seifried, D., Sánchez-Monge, Á., Suri, S., & Walch, S. 2017, MNRAS, 467, 4467
Shimajiri, Y., André, P., Palmeirim, P., et al. 2019, A&A, 623, A16
Smith, R. J., Glover, S. C. O., & Klessen, R. S. 2014, MNRAS, 445, 2900
Smith, R. J., Glover, S. C. O., Klessen, R. S., & Fuller, G. A. 2016, MNRAS, 455, 3640
Soler, J. D., Hennebelle, P., Martin, P. G., et al. 2013, ApJ, 774, 128
Szűcs, L., Glover, S. C. O., & Klessen, R. S. 2014, MNRAS, 445, 4055
Tafalla, M., & Hacar, A. 2015, A&A, 574, A104
Toalá, J. A., Vázquez-Semadeni, E., & Gómez, G. C. 2012, ApJ, 744, 190
Tritsis, A., & Tassis, K. 2016, MNRAS, 462, 3602
Tritsis, A., & Tassis, K. 2018, Science, 360, 635
Vaidya, B., Hartquist, T. W., & Falle, S. A. E. G. 2013, MNRAS, 433, 1258
Vallée, J. P., & Fiege, J. D. 2006, ApJ, 636, 332
van der Tak, F. F. S., Black, J. H., Schöier, F. L., Jansen, D. J., & van Dishoeck, E. F. 2007, A&A, 468, 627
van Dishoeck, E. F., & Black, J. H. 1988, ApJ, 334, 771
Vilas-Boas, J. W. S., Myers, P. C., & Fuller, G. A. 1994, ApJ, 433, 96
Visser, R., van Dishoeck, E. F., & Black, J. H. 2009, A&A, 503, 323
Whittet, D. C. B., Prusti, T., Franco, G. A. P., et al. 1997, A&A, 327, 1194
Williams, G. M., Peretto, N., Avison, A., Duarte-Cabral, A., & Fuller, G. A. 2018, A&A, 613, A11
Yan, Q.-Z., Zhang, B., Xu, Y., et al. 2019, A&A, 624, A6
Zamora-Avilés, M., Ballesteros-Paredes, J., & Hartmann, L. W. 2017, MNRAS, 472, 647
Zielinsky, M., Stutzki, J., & Störzer, H. 2000, A&A, 358, 723
Zucker, C., Speagle, J. S., Schlafly, E. F., et al. 2019, ApJ, 879, 125

Appendix A: Distance of the dense Musca-Chamaeleon clouds

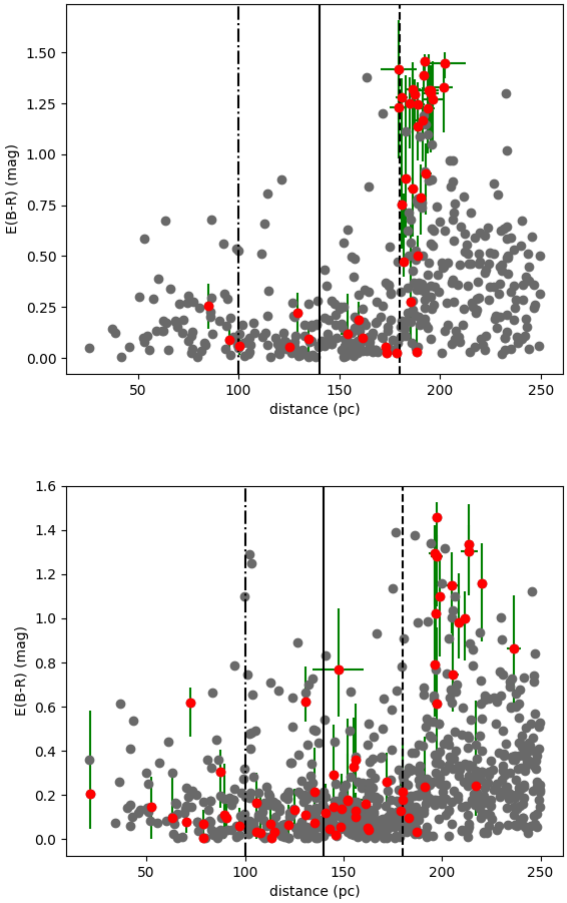

Fig. A.1. *Top*: reddening as a function of distance for stars in the area covered by Cha I. As in Fig. 5, the red points are located at the high density region of the cloud. This shows that the reddening experiences a strong jump around 180 pc as was found in Zucker et al. (2019). The other two vertical lines in the plots indicate a distance of 100 and 140 pc. *Bottom*: same for the region Cha II and Cha III together, showing a reddening jump at 190 pc.

With the recent *Gaia* DR2 (Gaia Collaboration 2018) data release, a vast amount of information on nearby stars in the Galaxy has become available. This makes it possible to estimate the distance of interstellar clouds by studying the reddening they cause on background stars of these clouds (e.g. Zucker et al. 2019; Yan et al. 2019). To estimate the distance of Musca, a region in the sky centered on the Musca filament with a radius of 80′ (∼3 pc at a distance of 150 pc) was selected in the *Gaia* catalogue, see Fig. 1. In this region, all stars with a calculated reddening (Andrae et al. 2018) and a distance <250 pc were selected. This results in a total of 223 stars found that can be used to estimate the distance of Musca. Because there can be foreground reddening we only select the stars that are located in the *Planck* 353 GHz map above a threshold (Yan et al. 2019). Inspecting the *Planck* map by eye, a threshold of 0.006 K_{cmb} was used. The idea behind the method is that the presence of the Musca cloud should give rise to a jump in reddening at a certain distance. The plot of the reddening as a function of the distance shows indication of such a jump at a distance of 140 pc, suggesting the presence of the Musca cloud. However, it can be noted that there already is reddening for a few stars before 140 pc. This generally starts at a distance of 90–100 pc and might indicate the presence of some gas that is more nearby than the Musca filament/cloud. Note that there generally is significant uncertainty about the reddening calculated in the *Gaia* catalogue (Andrae et al. 2018), such that this reddening effect before 140 pc might appear larger than it actually is. Figure 5 shows that the nearby stars (<140 pc) with high reddening are located all over the map. This could imply that this is not the result of nearby gas concentrated in a small region, but that such nearby gas might be present over a larger area which could be related to the Chamaeleon-Musca complex. The same approach was used for Cha I, Cha II and Cha III, suggesting a distance of 180-190 pc, see Fig. A.1, which is consistent with the results from Zucker et al. (2019).

Appendix B: The ^{13}CO(3–2)/^{13}CO(2–1) uncertainty

To estimate the average density along the line of sight in the Musca filament and make an evolution versus distance from the filament crest, we have studied the ratio of ^{13}CO(3–2)/^{13}CO(2–1). Here, we check the dependence of the density estimate on the width of the line and the column density of the line.

To study the impact of a change in width, the same setup as in Sect. 5.1 was run, but this time with a FWHM of 0.5 km s^{-1} (which is the minimal FWHM over the entire map). To study the impact of the column density, the setup from Sect. 5.1 was retaken but this time with $N_{H_2} = 4 \times 10^{21}$ cm^{-2} (or 33% less than the maximal column density used in Sect. 5.1). The impact of these changes are plotted in Fig. B.1. When one has a fixed ^{13}CO(3–2)/^{13}CO(2–1) ratio, for a lower column density this would result in a slightly higher density of the gas. The opposite is true for the FWHM: when the FWHM is lower for a fixed ^{13}CO(3–2)/^{13}CO(2–1) ratio, the density for this ratio will be slightly lower than for a higher FWHM. When comparing the variation of the ratio as a function of density for a different FWHM or column density with the variation related to a different temperature in Fig. B.1, it is found that the variation related to the temperature is larger than the variation related to the FWHM or column density. Furthermore, the FWHM and column density values used in Sect. 5.1 are both relatively high for the strands located around the filament such that for both parameters a lower value might be more accurate. But the above analysis indicates that the effect of lowering the FWHM and column density at the same time might roughly cancel out due to their opposite impact on the ratio. The estimated densities in the strands might thus be reasonable as well. This is confirmed when using the obtained estimates for the density in the strands and filament from the above model to characterise the gas in these components. The intensity of the observed lines towards Musca are reproduced for temperatures and column densities that can be expected from *Herschel*. This provides further confidence that the density estimates might be relatively good.

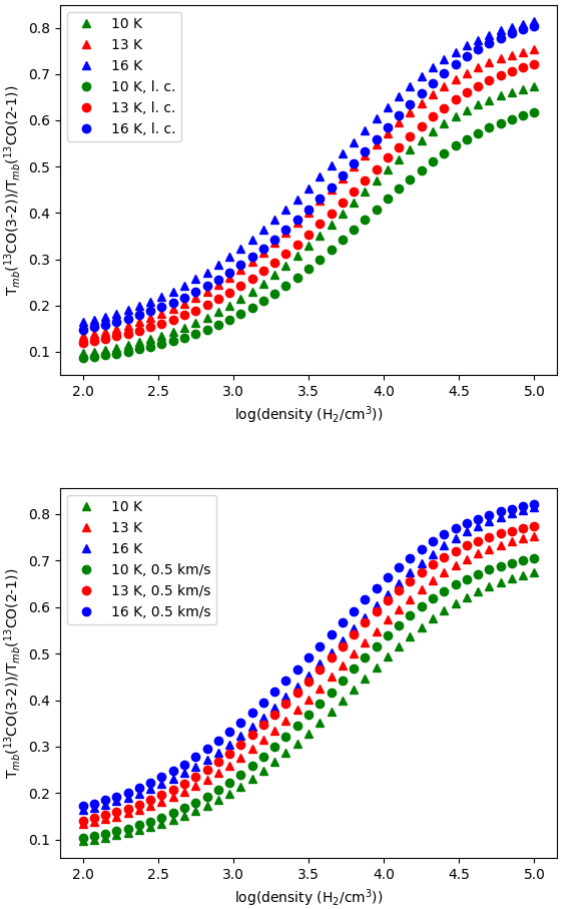

Fig. B.1. *Top*: impact of a lower column density, namely N_{H_2} = 4×10^{21} cm^{-2} (indicated with l. c.) instead of $N_{H_2} = 6 \times 10^{21}$ cm^{-2}, on the ^{13}CO(3–2)/^{13}CO(2–1) ratio as a function the density. *Bottom*: impact of a lower FWHM (0.5 km s^{-1} instead of 0.7 km s^{-1}) on the ^{13}CO(3–2)/^{13}CO(2–1) ratios as a function of the density. For both the width and the column density, their impact is plotted for 3 different temperatures: 10, 13 and 16 K. This shows that the impact of these two variables is smaller than the uncertainty related to the temperature.

crest	N_{H_2} (cm^{-2})	T_{kin} (K)	n_{H_2} (cm^{-3})	FWHM (km s^{-1})	$T_{^{13}CO(2-1)}$	$T_{^{13}CO(3-2)}$	$T_{C^{18}O(2-1)}$
RADEX	$4{\cdot}10^{21}$	20	$2{\cdot}10^{3}$	0.5	6.2 K	2.7 K	1.6 K
observed values					4.2 K	2.1 K	1.6 K

Table 4.2: The predicted brightness by RADEX for ^{13}CO and C^{18}O to test the robustness of the dense filamentary result, assuming an extreme value of 20 K for the filament crest. These calculations assume $[^{13}CO]/[C^{18}O] = 7.3$ and $[H_2]/[^{13}CO] = 5.7{\times}10^5$, and are compared to the observed values in the Musca filament. It is found that even an extreme case with $T_{kin} = 20$ K for the filament crest is still not able to represent the Musca filamentary structure as a 6 pc sheet that is seen edge-on.

4.2.3 Additional discussion of Paper-MC

The ^{13}CO emission: high densities in the filament crest

In order to test the robustness of our density modelling in the Musca filament, the effects of a varying column density and FWHM were presented in Paper-MC. For more certainty, we also considered the extreme case where the kinetic gas temperature would be somehow significantly higher than the *Herschel* dust temperature. This scenario could be justified when considering that the filament is in fact a sheet seen edge-on. In that case, a lower density in combination with a higher kinetic temperature might still be able to reproduce the observed ^{13}CO brightness ratios. Furthermore, in the case of the low densities predicted by a sheet seen edge-on ($n_{H_2} < 10^3$ cm^{-3}), the kinetic temperature is expected to be significantly higher than the dust temperature (e.g. Goldsmith, 2001; Seifried & Walch, 2016). When considering a kinetic gas temperature of 20 K at the filament crest, a density $n_{H_2} = 2.9{\pm}0.9{\cdot}10^3$ cm^{-3} is predicted by the observed ^{13}CO(3-2)/^{13}CO(2-1) ratio. This density is still a factor 3 higher than the maximal predicted densities for the 6 pc sheet in Tritsis & Tassis (2018). Furthermore, Tab. 4.2 shows that the predicted line brightness for this 20 K model is significantly off from the observed brightness.

^{13}CO and C^{18}O fractionation in a weak FUV-field

Following the brightness of ^{13}CO(2-1) and C^{18}O(2-1) in the Musca filament crest and strands, a very sharp evolution of their abundance ratio as a function of the column density was observed. Variations of the ^{13}CO/C^{18}O abundance ratio have been reported in a variety of dense molecular clouds (e.g. Lada et al., 1994; Shimajiri et al., 2014; Areal et al., 2018, 2019). At the moment, it remains difficult to quantitatively constrain the origin of this strong variation in Musca, but the possible processes will be discussed in more detail.

First, we focus on ^{13}CO with the most important fractionation reaction given by (Woods & Willacy, 2009; Röllig & Ossenkopf, 2013; Szűcs, Glover & Klessen, 2014)

$$^{13}C^+ + {}^{12}CO \rightleftharpoons {}^{12}C^+ + {}^{13}CO + \Delta E \tag{4.4}$$

with $\Delta E = 35$ K. The presence of this fractionation reaction was predicted by Watson, Anicich & Huntress (1976) and confirmed with laboratory experiments by Smith & Adams (1980). Further calculations were performed by Langer et al. (1984) and Lohr (1998) to evaluate the reaction rates in more

detail at different temperatures in the ISM. The reaction rate (k) for Eq. 4.4 is given by

$$k = 4.42 \times 10^{-10} \left(\frac{T}{300K} \right)^{-0.29} \tag{4.5}$$

where the returning reaction rate is reduced by the factor $e^{-\Delta E/T}$. Another reaction that can play a role in CO fractionation processes is

$$H^{12}CO^+ + {}^{13}CO \rightleftharpoons H^{13}CO^+ + {}^{12}CO + \Delta E \tag{4.6}$$

with $\Delta E = 9$ K.

Because $\Delta E = 35$ K in Eq. 4.4, this results in an increasing ^{13}CO abundance in weakly irradiated clouds. Observationally, such an abundance increase of $x(^{13}CO)/x(^{12}CO)$ was reported for diffuse molecular clouds (Keene et al., 1998; Liszt, 2007). In Röllig & Ossenkopf (2013) this fractionation in relatively high density gas ($n_{H_2} \sim 10^3$ - 10^6 cm^{-3}) was studied for a grid of core masses and FUV field strengths. When looking into the models with a mass of 1 $M_\odot$ displayed in Fig. 4.7, which can be qualitatively representative for the low-mass Musca filament, it is observed for a weak FUV field of 1.7 G_0 (Draine, 1978) that fractionation can lead to a significant increase of the ^{13}CO abundance (up to a factor 3-4) even relatively deep into the core. Fig. 4.7 also shows that this requires a relatively low density around $n_{H_2} = 10^3$ cm^{-3}, similar to what is found for the strands of the Musca filament.

^{13}CO fractionation most likely plays a role in the observed $^{13}CO/C^{18}O$ abundance evolution, but other processes might play a role as well. This can be noted when studying the evolution of the $C^{18}O$(2-1) brightness. From the *Herschel* data it was observed that the dust column density varies by a factor 3-4 from the filament crest to the strands. Studying the $C^{18}O$(2-1) brightness with RADEX, it is found that the decrease of the $C^{18}O$ column density is significantly larger. As indicated in Paper-MC and Tab. 4.3, the observed $C^{18}O$(2-1) brightness of the filament crest is reproduced for $N_{C^{18}O} \sim 9{\times}10^{14}$ cm^{-2}. When studying the expected brightness of the strands with a 4 times lower $C^{18}O$ column density, as expected based on *Herschel*, Tab. 4.3 shows that the predicted brightness by RADEX is a factor 5 higher than observed. This strongly suggests that the $C^{18}O$ abundance drops by roughly a factor 5 from the filament crest to the strands. One way to reduce the $C^{18}O$ abundance is selective photo-dissociation (Glassgold, Huggins & Langer, 1985) where UV radiation that dissociates $C^{18}O$ can penetrate deeper into the cloud. However, it seems unlikely that the weak embedding FUV field of Musca (< 1 G_0) can have this effect at $A_V = 2$-3 in the strands because of the strong FUV field attenuation at increasing A_V levels. On the other hand, one can look into oxygen fractionation reactions which have been poorly studied to this point (e.g. Langer et al., 1984; Lyons & Young, 2005; Loison et al., 2019). For a long time, only one oxygen fractionation reaction has been considered for astronomical studies (Langer et al., 1984)

$$HC^{16}O^+ + C^{18}O \rightleftharpoons HC^{18}O^+ + C^{16}O + \Delta E \tag{4.7}$$

with $\Delta E = 6$ K. Recently, in Loison et al. (2019) several other oxygen fractionation reactions were studied in the context of the ISM. However, the reaction that is given in Eq. 4.7, is the one related to $C^{18}O$. Comparing Eq. 4.7 with Eq. 4.4, shows that the evolution of the ^{13}CO and $C^{18}O$ abundance

	$N_{C^{18}O}$ (cm^{-2})	x(H_2)/x($C^{18}O$)	T_{kin} (K)	n_{H_2} cm^{-3}	FWHM (km s^{-1})	$T_{C^{18}O(2-1)}$ (K)
crest	$9{\cdot}10^{14}$	$4.4{\cdot}10^{6}$	10	10^{4}	0.5	1.6
strand	$2.3{\cdot}10^{14}$	$4.4{\cdot}10^{6}$	15	$3{\cdot}10^{3}$	0.5	0.47
strand	10^{14}	10^{7}	15	$3{\cdot}10^{3}$	0.5	0.21
strand	$5{\cdot}10^{13}$	$2{\cdot}10^{7}$	15	$3{\cdot}10^{3}$	0.5	0.11

Table 4.3: The predicted $C^{18}O$(2-1) temperature brightness with RADEX towards the filament crest and strands for different $C^{18}O$ column densities (and consequently different $H_2/C^{18}O$ abundance ratios). The observed $C^{18}O$(2-1) brightness with APEX is 1.6 K for the crest and 0.085 K for the strands.

in their fractionation reactions have opposite effects. Whether the fractionation of both molecules can explain the observed behaviour in Musca remains currently difficult to constrain due to the limited theoretical studies. Further theoretical studies of these fractionation reactions will be necessary to quantitatively understand the processes responsible for the observed behaviour in the strands of Musca.

Apart from possible carbon and oxygen fractionation, it should also be taken into account that there is a large amount of CO-dark molecular hydrogen in the Chamaeleon-Musca complex which dominates the mass budget up to $A_V \sim 0.9$ (Planck Collaboration et al., 2015; Liszt, Gerin & Grenier, 2018, 2019). This can fit with the observations in Paper-MS that a significant fraction of carbon in the Musca ambient cloud is in atomic form. It is thus not unlikely that there is an non-negligible amount of CO-dark gas in the strands. In that case the expected CO column density drop from the crest to the strands could be higher than the expected factor 3-4 based on the *Herschel* dust column density maps. The presence of possible CO-dark gas in the strands provides uncertainty on the exact amount of fractionation, but it can not explain the full $C^{18}O$(2-1) emission drop without $C^{18}O$ fractionation. If there would be no $C^{18}O$ fractionation, this would imply that only 20 % of the gas in the strands is traced by CO isotopologues. This would be extreme for a structure with a typical density $n_{H_2} \sim 3{\cdot}10^3$ cm^{-3}. Furthermore, this would imply that the entire $^{13}CO/C^{18}O$ abundance variation is the result of ^{13}CO fractionation, leading to an increase of the ^{13}CO abundance by a factor 10. This is above any prediction currently found in the literature (Röllig & Ossenkopf, 2013; Szűcs, Glover & Klessen, 2014).

4.2.4 Prospective: The density in the Musca filament with the ALMA Compact Array

In Paper-MC, a density profile was constructed for the Musca filament crest and the strands with ^{13}CO(3-2)/^{13}CO(2-1). In order to improve on this study for the filament crest, one would ideally work with an optically thin tracer of the filament crest. $C^{18}O$ transitions would be ideal for this. However, because the spectral band coverage of the 345 GHz CO isotopologue observations with FLASH+ can not simultaneously cover ^{12}CO(3-2) and $C^{18}O$(3-2), this study was not possible with $C^{18}O$ up to this point.
We worked on an ALMA Compact Array (ACA) proposal (PI: D. Arzoumanian) that has been accepted to map a significant part of the Musca filament crest in $C^{18}O$(2-1) and $C^{18}O$(1-0), see Fig. 4.8. The

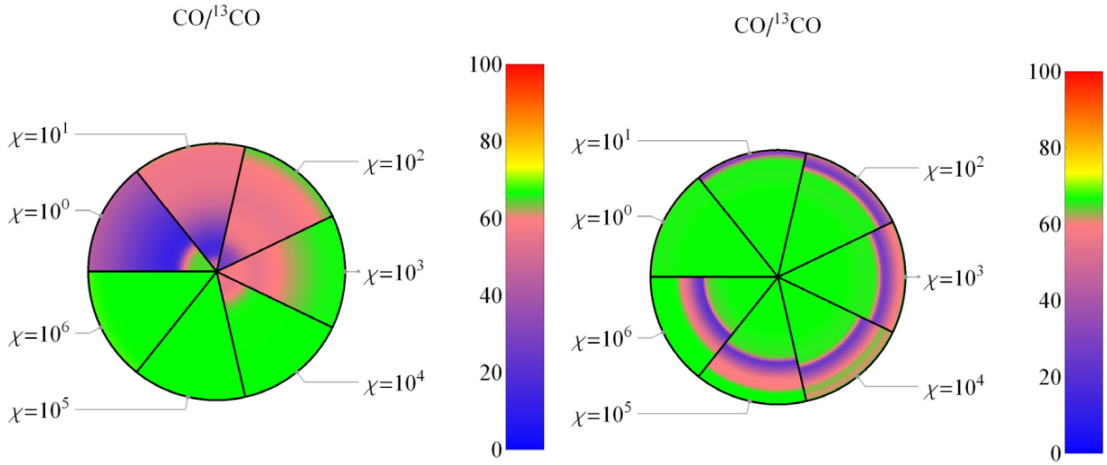

Figure 4.7: **Left**: The $^{12}CO/^{13}CO$ abundance ratio for a 1 $M_{\odot}$ core at a density n = 10^3 cm^{-3} for different FUV field strengths χ = 1 - 10^6 (Draine, 1978). For Musca, χ = 1 is most applicable. The radius of the core corresponds to 0.17 pc. This fractionation effect might thus play a role in the $^{13}CO/C^{18}O$ abundance increase in the strands of the Musca filament. **Right**: The same model with n = 10^5 cm^{-3}, resulting in a radius of 0.038 pc. This indicates that at higher densities, the fractionation effect is not observed in the weak FUV field of Musca. This figure is adapted from (Röllig & Ossenkopf, 2013).

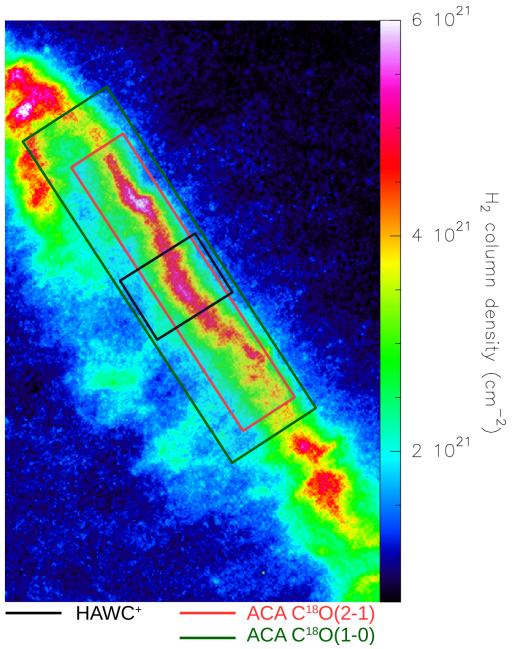

Figure 4.8: The *Herschel* column density map of the central part of the Musca filament (Cox et al., 2016). The red and green rectangles indicate the regions that will be mapped with the ALMA Compact Array (ACA) in $C^{18}O$(2-1) and $C^{18}O$(1-0), respectively. The black rectangle shows the region that was observed with the polarimetric HAWC$^+$ receiver on SOFIA (PI: J. Soler).

main goal of this proposal is to study the velocity and dust continuum power spectrum at high angular resolution. However, because the proposed setup covers both $C^{18}O$(2-1) and $C^{18}O$(1-0), it will not only be able to study the velocity field in the filament crest, but it will also be possible to study the density in the filament crest with a method similar to the one presented in Paper-MC. Performing some preliminary RADEX calculations with $C^{18}O$, it is found that the $C^{18}O$(2-1)/$C^{18}O$(1-0) temperature brightness ratio is strongly dependent on the density, see Fig. 4.9. These calculations were performed with $\sigma = 0.15$ km s^{-1} (Hacar et al., 2016) and $N_{C^{18}O} = 1.2{\times}10^{15}$ cm^{-2}, which corresponds to $N_{H_2} = 5{\times}10^{21}$ cm^{-2} using [H_2]/[^{12}CO] = 10^4 (Tielens, 2010), [^{12}CO]/[^{13}CO] = 57 (Langer & Penzias, 1990) and [^{13}CO]/[$C^{18}O$] = 7.3 (Wilson & Rood, 1994). Fig. 4.9 shows that the ratio becomes increasingly dependent on the temperature at high densities ($n_{H_2} > 10^4$ cm^{-3}). However, it is not expected that the Musca filament crest has a density significantly above $n_{H_2} = 10^4$ cm^{-3}, and CO molecules also start to deplete between $n_{H_2} = 10^4$ and 10^5 cm^{-3} (Caselli et al., 1999; Pagani et al., 2005). Lastly, the temperature in the filament crest is reasonably expected to be of the order of 10 K, which can help to further constrain the density (e.g. Kainulainen et al., 2016; Hacar et al., 2016; Machaieie et al., 2017).

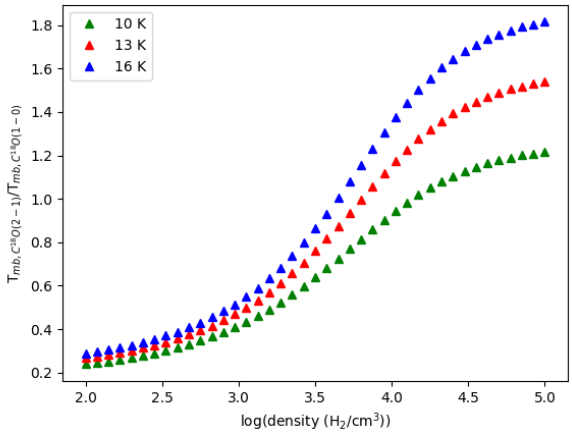

Figure 4.9: The predicted $C^{18}O(2\text{-}1)/C^{18}O(1\text{-}0)$ temperature brightness ratio with RADEX as a function of n_{H_2} for different temperatures (10 - 16 K). The predictions use $N_{C^{18}O} = 1.2{\times}10^{15}$ cm^{-2} and σ 0.15 km s^{-1}.

4.2.5 Prospective: The magnetic field in the Musca filament crest

If indeed the magnetic field guides inflow to the Musca filament, one would expect that the velocity gradient over the filament crest has a direction that is similar to the magnetic field orientation because it was proposed that this gradient is a mass accretion signature. However, there is a significant difference between the large scale magnetic field orientation, observed with the Planck telescope, and the velocity gradient over the filament crest. This suggests that either the inflow is not perfectly aligned with the magnetic field orientation or that some reorientation takes place from the ambient cloud to the filament crest. Indications of such magnetic field reorientation in the dense filament crest and strands towards Musca were in fact observed with Planck (Planck Collaboration et al., 2016c). The reorientation of the magnetic field in the filament can be a projection of the magnetic field bending, it can also occur in the presence of filament accretion shocks (Lehmann & Wardle, 2016; Fogerty et al., 2017), and it can change direction as a result of gravitational inflow when entering the filament (Gómez, Vázquez-Semadeni & Zamora-Avilés, 2018). However, due to the limited resolution of Planck ($\sim$ 0.4 pc at 140 pc) it was not possible to investigate this in more detail. It would thus be interesting to follow the magnetic field from the ambient cloud down to the filament crest. To do this in detail for the entire Musca filament, polarimetric sensitivity of future far infrared space telescopes such as SPICA will be required (André et al., 2019b).

It is however possible to obtain indications on the small-scale behaviour of the magnetic field orientation around the filament crest by combining the APEX velocity field and the Planck magnetic field orientation with polarimetric observations by the HAWC$^+$ instrument on SOFIA (Harper et al., 2018). Combining a HAWC$^+$ observation of the filament crest with the Planck magnetic field orientation on large scales will allow to quantify the magnetic field reorientation towards the densest areas in Musca.

Comparison of HAWC$^+$ observations with the APEX velocity field, which has the same angular resolution around 30″, allows to study the alignment of the velocity field and magnetic field orientation. In Fig. 4.8 it is shown that a recently observed HAWC$^+$ map (PI: J. D. Soler) overlaps with the APEX velocity map. This behaviour can thus be studied in the future.

4.3 Prospective: Future observations of cooling lines in the ISM

It was put forward that filament accretion shocks can play an important role in creating cold and dense star forming gas. It was also found that it is difficult to constrain the role of [OI] in the evolution of the ISM from the diffuse ISM (n $\sim$ 1 cm^{-3}) to the formation of star forming gas (n $>$ 10^4 cm^{-3}). In the following paragraphs, I will discuss some prospects with current and future telescopes to address these questions based on the here presented results while examining the possibility to study the evolution of nearby molecular clouds with [CI].

4.3.1 Higher-J CO lines to study low-velocity shocks

In section 4.1.5, it was already pointed out that the nFLASH receiver on the APEX telescope could be used to observe ^{12}CO(4-3) in order to detect the presence of filament accretion shocks in other filaments. The search for indications of filament accretion shocks is however not the only study that can be pursued with the APEX telescope. ^{12}CO(4-3) in combination with lower-J lines (^{12}CO(2-1) and ^{12}CO(3-2)) can establish the presence of low-velocity shocks, but it is not possible to significantly constrain the low-velocity shock properties. This requires the observation of higher-J CO lines (Pon, Johnstone & Kaufman, 2012), as well as the study of dedicated simulations of low-velocity shock models for a quantitative comparison.
Based on the RADEX models that manage to reproduce the observed ratios and ^{12}CO(4-3) brightness in Paper-MS, predictions were made for the expected brightness of higher-J CO lines. The results for different temperatures are shown in Tab. 4.4, and indicate that the observed brightness of higher-J CO lines are highly dependent on the temperature as well as the density. Observing multiple transitions can thus help constraining the temperature and density of the shocked gas layer. It will also allow to make rotational diagrams (Goldsmith & Langer, 1999), but their interpretation will not be straightforward because simple rotational diagram analysis by fitting a straight line assumes LTE conditions which is not applicable for high-J CO lines in Musca.
Comparing low-velocity shock models with observations of higher-J CO lines can constrain other parameters like the preshock density and the shock velocity. This can unveil information on the accreted gas from the ambient cloud and provide estimates for the mass accretion rate of the filament. The telescopes that can observe the required CO lines are described below.

- **The APEX telescope**

The SEPIA band 9 receiver can observe the ^{12}CO(6-5) line, for which a proposal has been submitted to observe this line towards the Musca filament. The detection of ^{12}CO(6-5) can clearly confirm the excess emission seen with ^{12}CO(4-3) by comparison with predictions of PDR models, see Fig. 4.10, and it can provide first constraints on the temperature and density of the shocked gas. Furthermore,

transition	50 K	75 K	100 K	telescope	detectable
^{12}CO(4-3)	1.5 K	2.3 K	2.9 K	APEX	yes
^{12}CO(5-4)	0.47 K	0.92 K	1.3 K	SOFIA	yes
^{12}CO(6-5)	0.11 K	0.30 K	0.51 K	APEX	yes
^{12}CO(7-6)	2.4×10^{-2} K	8.8×10^{-2} K	0.18 K	CCATp	yes
^{12}CO(8-7)	4.7×10^{-3} K	2.3×10^{-2} K	5.7×10^{-2} K	SOFIA	no

Table 4.4: The predicted brightness with RADEX for high-J CO lines for different kinetic temperatures of the warm and dense gas layer in Paper-MS. The input for RADEX was: $N_{^{12}CO} = 9\times10^{14}$ cm^{-2}, n_{H_2} = 7×10^{3} cm^{-3} and FWHM = 0.4 km s^{-1}. The telescope that covers each line is indicated, as well as the possibility for this telescope to detect the line.

^{12}CO(6-5) will be able to trace shock excitation over the full velocity range of CO emission in Musca, which was not possible for ^{12}CO(4-3) due to opacity effects. With ^{12}CO(4-3), the excess emission was only established in the most blueshifted velocity component.

• The SOFIA telescope
With the 4GREAT instrument on the SOFIA telescope, the ^{12}CO(5-4) and ^{12}CO(8-7) lines can be observed simultaneously. ^{12}CO(5-4) will be easily detected, requiring only 5 minutes per single pointing. However, the current 4GREAT sensitivity does not allow to detect the extremely weak ^{12}CO(8-7) emission.

• The CCAT-prime telescope
CCAT-prime is a telescope dedicated to performing surveys that is currently under construction at an altitude of 5600m at Cerro Chajnantor with expected first light in 2021. The CHAI receiver on this telescope will be able to simultaneously observe ^{12}CO(4-3) and ^{12}CO(7-6) with a good sensitivity (e.g. Schilke, 2018; Simon et al., 2019b). This will allow to make relatively large scale maps towards several filaments such as Musca to better understand the formation of dense star forming filaments. Specifically, the CHAI receiver is currently expected to reach an rms of 0.01 K (pwv = 0.36 mm) or 0.02 K (pwv = 0.6 mm) within a spectral bin of 0.2 km s^{-1} over a $1'\times1'$ map in 1.5 hours.
With this currently estimated sensitivity of the receiver, it was possible to perform some first estimates of what will be possible with the CCAT-prime telescope. Based on the ^{12}CO(7-6) predictions in Tab. 4.4 for the shock heated gas in Musca, it will be possible to make maps of ^{12}CO(4-3) and ^{12}CO(7-6) with $\theta_{beam} \sim 26''$ (smoothed to the resolution of ^{12}CO(4-3)) that cover $\sim$ 70 arcmin^2 in 100 hours.

4.3.2 The [CI] hyperfine transitions with CCAT-prime

The CHAI receiver on CCAT-prime does not only allow simultaneous coverage of the ^{12}CO(4-3) and ^{12}CO(7-6) transitions, but is also planned to be able to simultaneously observe the two [CI] hyperfine transitions. Namely [CI](1-0) at 492.16 GHz and [CI](2-1) at 809.34 GHz. This has several interesting applications.

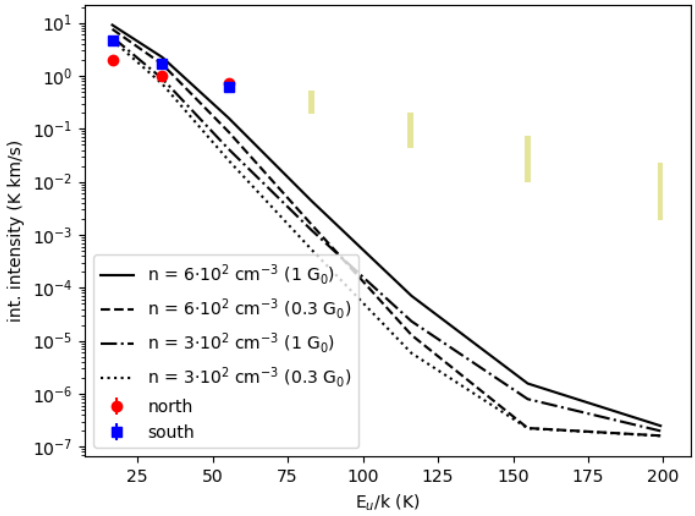

Figure 4.10: The observed intensities in Musca of ^{12}CO(2-1), ^{12}CO(3-2) and ^{12}CO(4-3) for the shocked gas emission in the northern (red) and southern (blue) map. The location on the x-axis of each transition is indicated by its energy level (E_u/k). The black curves show the predicted evolution as a function of the energy level from ^{12}CO(2-1) to ^{12}CO(8-7) by the PDR Toolbox for expected hydrogen densities in the ambient cloud of the Musca filament. This confirms that there is a significant excess of ^{12}CO(4-3) emission. The yellow bars indicate the expected line intensity from ^{12}CO(5-4) to ^{12}CO(8-7) for the shocked gas based on the RADEX models.

• The ambient cloud with [CI]

As indicated in Paper-MS, it is currently uncertain which density regime in interstellar clouds is traced by [CI] (Glover et al., 2015; Franeck et al., 2018; Clark et al., 2019). From the observations towards Musca presented in Paper-MS, it was proposed that [CI] might trace low to relatively high density ($n_{H_2} \sim 4{\times}10^2$ cm^{-3} up to 10^4 cm^{-3}). However, this is based on a single spectrum with a relatively high noise. To perform this analysis properly, large maps are required that cover both the dense filamentary gas and the ambient cloud. This will allow a comparison of the observed integrated intensity as a function of column density for these large maps with predictions from simulations. Knowledge of the density regime traced by [CI] will be interesting to better understand the kinematic evolution of interstellar clouds at different densities. In particular because it might trace gas densities that are not traced by ^{12}CO and because [CI] is quite generally optically thin (in contrast to ^{12}CO). If [CI] turns out to trace a significant amount of CO-dark gas, it could also be a good tracer of the total gas budget in the cloud.

• The FUV field strength with [CI]

When studying the thermodynamic evolution from the diffuse ISM to the dense star forming gas, the FUV photons originating from massive stars are particularly important since they dominate the heating of the neutral atomic gas in interstellar clouds (e.g. Tielens & Hollenbach, 1985; Sternberg & Dalgarno, 1989; Hollenbach & Tielens, 1999; Wolfire et al., 2003) and play an important role in the chemical evolution of the ISM (e.g. Sternberg & Dalgarno, 1995).

To study the impact of a relatively weak FUV field (< 10 G$_0$) on the evolution of interstellar clouds, observing both [CI] lines can be interesting. The PDR Toolbox models (Pound & Wolfire, 2008), show that the [CI](2-1)/[CI](1-0) temperature brightness ratio is mainly sensitive to the density in a FUV field stronger than 10 G$_0$, see Fig. 4.11. However, Fig. 4.11 also shows that in a weak FUV field the [CI](2-1)/[CI](1-0) temperature brightness ratio is strongly dependent on the FUV field strength. Studying the [CI](2-1)/[CI](1-0) brightness ratio can thus constrain the FUV field strength in low-mass star forming clouds such as Musca. Here, the time required to map clouds such as Musca in the [CI] lines with CCAT-prime will be estimated, knowing that the Musca cloud is an extreme case requiring sensitive observations on a large area.

• Time estimate for mapping the Musca cloud

With the FUV field upper limit in Musca from [CII] observations with SOFIA and the observed [CI](1-0) line with APEX it is possible to do some first estimates of what can be expected with CCAT-prime. As it can be noted from Fig. 4.12, the observed [CI](1-0) brightness in Musca is lower than the minimal predicted brightness by the PDR Toolbox. Following the curves from the PDR Toolbox, one can expect an FUV field strength of the order of 0.1 G$_0$ near the Musca filament. Now looking in Fig. 4.13 at the predicted intensity evolution for [CI](2-1) by the PDR Toolbox, one can get an idea of their expected intensity. This figure also shows that only a time of 0.013 to 0.05 h is required to make a resolved 1 arcmin^2 map of [CI](2-1) with a respective rms of 0.2 K and 0.1 K. This rms of 0.1 K to 0.2 K should result in a 5σ detection of [CI](2-1) per beam. To map the Musca cloud with an rms of 0.1 K for [CI](2-1), would require 225 to 450 hours to cover an area of $30' {\times} 2.5^o$ and $1^o {\times} 2.5^o$, respectively. The size of these maps is shown in Fig. 4.14, which indicates that the $1^o {\times} 2.5^o$ map would be preferable as

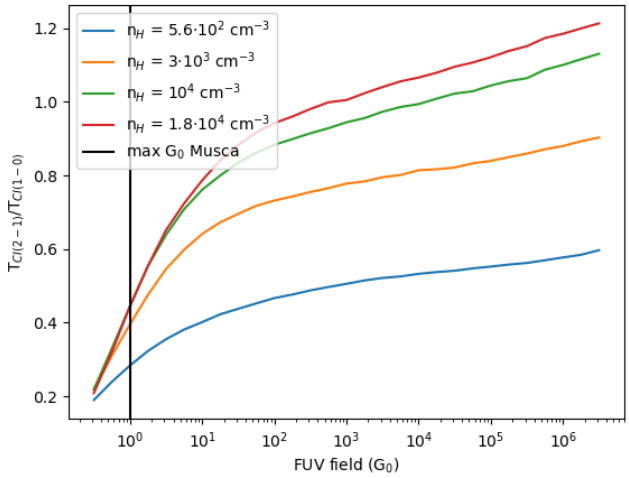

Figure 4.11: The [CI](2-1)/[CI](1-0) temperature brightness ratios from the PDR Toolbox for different densities as a function of the FUV field strength. It can be observed that in a strong FUV field the ratio is mainly dependent on the density, while in a weak FUV field the ratios increasingly depend on the field strength.

it covers both the filament and the ambient cloud. This is extremely time consuming. However, an rms of 0.2 K might be sufficient, resulting in a required 100 hours to cover the $1^o \times 2.5^o$ map. Furthermore, the [CI](2-1) observations with a beam size of $\sim 15''$ will have to be smoothed to the $26''$ resolution of the [CI](1-0) line which will further reduce the noise. This necessary spatial smoothing of [CI](2-1) will further reduce the observing time by a factor 3. It could thus be possible to get a full map of the Musca cloud in both [CI] lines in roughly 33 hours. It should be noted that Musca is most likely one of the weakest nearby clouds in [CI], such that CCAT-prime is extremely promising to make significant advances in the understanding of [CI] in some of the nearby Gould Belt clouds.

4.3.3 SPICA and the Origins Space Telescope

To study the cooling of the ISM in star forming regions, future (far) infrared space telescopes can make further significant steps. The two currently proposed telescopes are the Space Infrared Telescope for Cosmology and Astrophysics (SPICA; Roelfsema et al., 2018) and the Origins Space Telescope (Battersby et al., 2018). At the moment the SPICA telescope is in the most advanced stage, awaiting final selection by ESA in 2021 in competition with two other telescopes: Theseus and EnVision.
To study the cooling of the ISM, the SAFARI instrument (Roelfsema et al., 2012) has promising applications thanks to its unprecedented sensitivity in the (far) infrared between 34 and 230 μm. The grating based spectrometer limits the spectral resolution between R = 10 000 and R = 2000 depending on the wavelength, but allows to obtain spectra covering a large wavelength range that contains a vast range of important cooling lines. This will allow to study the cooling and abundances of the diffuse

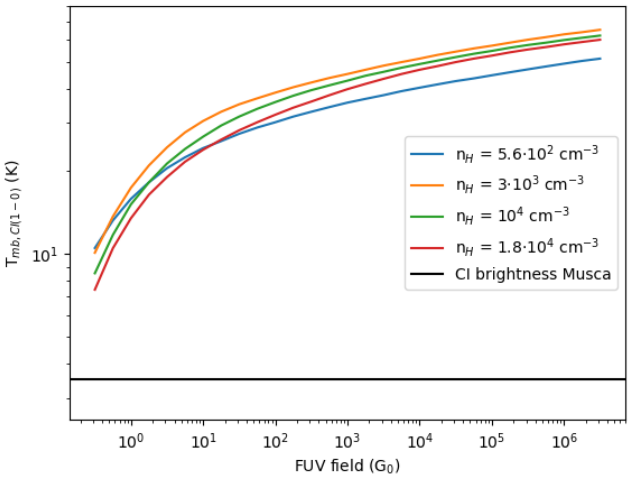

Figure 4.12: The curves display the predicted [CI](1-0) brightness as a function of the FUV field strength for different densities that can be found in the Musca cloud. The black horizontal line indicates the observed [CI] brightness in Musca, indicating an extremely weak FUV field.

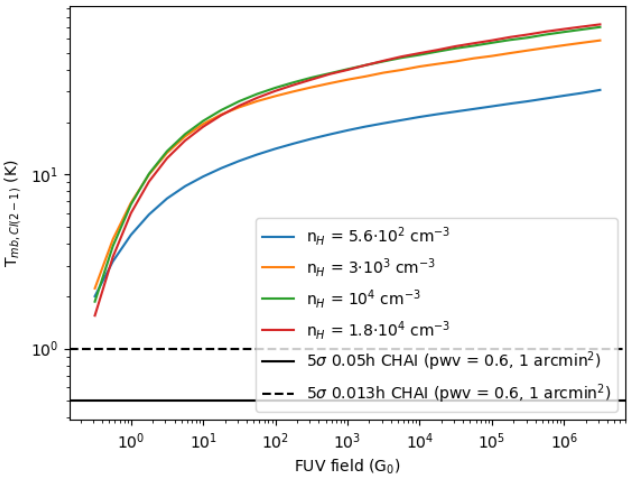

Figure 4.13: The curves display the predicted [CI](2-1) brightness as a function of the FUV field strength for different densities that can be found in the Musca cloud. The black horizontal lines indicate the 5σ levels that can be reached for a 1 arcmin^2 map within 0.2 km s^{-1} in the specified time with the CHAI receiver on CCAT-prime.

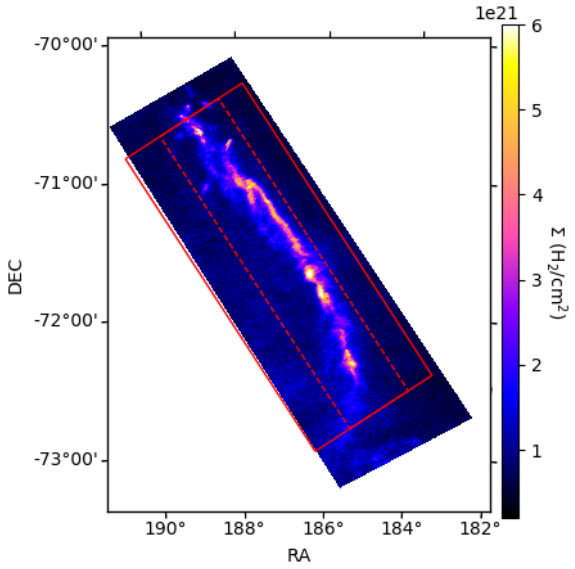

Figure 4.14: The size of the $30' \times 2.5^o$ map is outlined by the dashed red line on top of the *Herschel* column density map (Cox et al., 2016). The size of a $1^o \times 2.5^o$ map is outlined by the full red line.

ISM in great detail with different tracers. These tracers include the here discussed [CII] for cooling in weakly irradiated clouds and the two [OI] lines to study the dissipation of supersonic kinetic energy by low-velocity shocks. This could be combined with observations of the H_2 line at 17 μm covered by the MIRI receiver on JWST.
Also, the B-BOP polarimetric instrument on SPICA can further investigate the role of the magnetic field in the formation of dense interstellar filaments. B-BOP will be able to follow the magnetic field from the ambient cloud into the dense filamentary structures. It can thus provide further information on the physics of the magnetically driven inflow and the role of filament accretion shocks as it was proposed that low-velocity shocks can lead to strong magnetic field reorientation (Fogerty et al., 2017).

4.4 Prospective: Quantifying self-similarity in the ISM from singularity exponents

With a variety of studies, it was found that the ISM appears statistically self-similar from large to relatively small scales (e.g. Falgarone, Phillips & Walker, 1991; Elmegreen & Scalo, 2004; Mac Low & Klessen, 2004; Hennebelle & Falgarone, 2012). In particular, observed scaling relations that link the mass and size of a molecular cloud with its linewidth can be explained as a result of such a turbulent energy cascade (e.g. Larson, 1981). In the ISM, energy can be injected on several scales and cascade down to smaller scales which creates eddies that mix the gas in the cloud. This injection of energy can have multiple origins in the ISM: supernovae, extragalactic gas accretion, convergent flows, protostellar outflows, expanding HII regions,... (e.g. Matzner, 2002; Krumholz, Matzner & McKee, 2006; Vázquez-

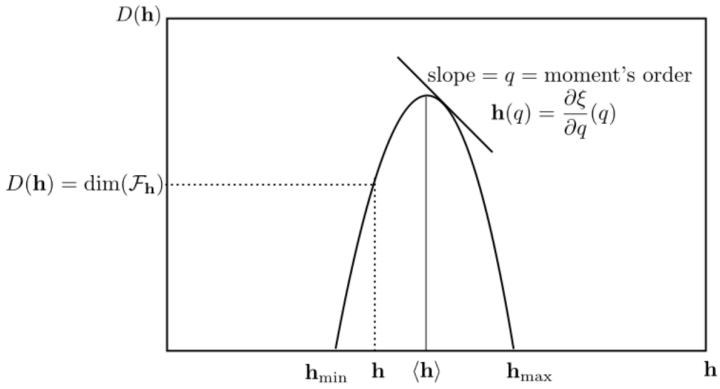

Figure 4.15: The typical concave form of a singularity spectrum.

Semadeni et al., 2007; Heitsch et al., 2008; Klessen & Hennebelle, 2010; Krumholz & Thompson, 2012; Padoan et al., 2019). It is thus important to further quantify this self-similarity of the ISM with statistical tools to investigate how it is associated with the physical processes that govern the evolution of the ISM and lead to the emergence of star forming filaments in the ISM.

The spatial structure of the turbulent ISM has been studied with several statistical tools, including among others: power spectra (e.g. Scalo, 1987; Miville-Deschênes et al., 2010), Delta-variance (e.g. Bensch, Stutzki & Ossenkopf, 2001; Ossenkopf & Mac Low, 2002; Ossenkopf, Krips & Stutzki, 2008a,b; Schneider et al., 2011) and fractal geometry (Stutzki et al., 1998). Another commonly used method to analyse the turbulent properties of the ISM are the probability density distributions of column density maps (N-PDFs) (e.g. Kainulainen et al., 2009; Froebrich & Rowles, 2010; Schneider et al., 2013, 2016b; Russeil et al., 2013; Stutz & Kainulainen, 2015), because a large variety of simulations have addressed the impact of physical processes in the ISM on the observed N-PDFs. In a basic description, isothermal turbulence leads to a log-normal N-PDF, while self-gravity develops a power-law tail (Vazquez-Semadeni, 1994; Padoan & Nordlund, 1999; Klessen, Heitsch & Mac Low, 2000; Padoan & Nordlund, 2002; Krumholz & McKee, 2005; Federrath, Klessen & Schmidt, 2008; Federrath et al., 2010; Kritsuk, Norman & Wagner, 2011). However, processes such as external pressure, radiative heating or the multiphase ISM can complicate the interpretation of N-PDFs (e.g. Vázquez-Semadeni, Gazol & Scalo, 2000; Gazol, Vázquez-Semadeni & Kim, 2005; Tremblin et al., 2014).
At small scales, self-similarity can break down when turbulence is dissipated. Several observational indications of this were found (e.g. Falgarone, Hily-Blant & Levrier, 2004; Falgarone, Pety & Hily-Blant, 2009; Schneider et al., 2011; Robitaille, Joncas & Miville-Deschênes, 2014; Robitaille et al., 2019).

In order to better understand the statistical properties of physical processes that govern the evolution of Musca and other molecular clouds, a collaboration has been developed during this thesis to analyse *Herschel* dust continuum observations with a microcanical multifractal approach (Yahia et al. in prep.). Multifractality is particularly useful to study the ISM since it was developed to quantify

self-similarity at different scales which is also observed in the ISM (e.g. Chappell & Scalo, 2001; Khalil et al., 2006; Elia et al., 2018).
Traditionally, multifractal analysis is carried out with a canonical approach which is based on statistical averages of multiple observations of the same system, so-called ensembles (Arneodo, Bacry & Muzy, 1995). This canonical approach is for example possible with simulations, because a simulation follows the evolution of the considered system. However, in observations of molecular clouds it is not possible to create such an ensemble because of the large timescales for molecular cloud evolution (several Myr). Observational multifractal analysis thus requires a microcanonical approach. Because of this, the box-counting method has been used for studies of the ISM (Chappell & Scalo, 2001; Elia et al., 2018). However, the box-counting method is imprecise, for example due to effects related to the sharp edge of the box (Arneodo, Bacry & Muzy, 1995). The method that will be applied in this project to the *Herschel* maps, is based on the evaluation of the individual states in a single observation as described in Turiel, Pérez-Vicente & Grazzini (2006); Turiel, Yahia & Pérez-Vicente (2007).

It is not the goal here to provide a full description of multifractality and the microcanonical approach, but rather to give a brief introduction on multifractality and provide a perspective on some work that is in progress.
In a multifractal system, the behaviour of a signal such as the column density can be described locally as $\Sigma(\mathbf{x} + \mathbf{r})$ - $\Sigma(\mathbf{x}) \sim \mathrm{r}^{\mathrm{h}(\mathbf{x})}$ for $\lim_{\mathbf{r}\to 0}$, with h the singularity exponent which is also referred to as the concentration strength in Chappell & Scalo (2001). This allows to define the set $\mathcal{F}_h$ of positions/points $\mathbf{x}$ for which $\mathbf{r}^h$ has a specific value for h. These sets of $\mathcal{F}_h$ have a complex geometry related to the turbulent statistics. The geometry of $\mathcal{F}_h$ can be quantified with the so-called Hausdorff fractal dimension $\mathrm{D(h)} = \dim_H(\mathcal{F}_h)$. The mapping of the singularity exponent h to the Hausdorff dimension D(h) is called the singularity spectrum of the signal, which contains essential information on the turbulence statistics. A typical concave shape of singularity spectra is presented in Fig. 4.15. However, the calculation of this singularity spectrum is a fundamental problem of multifractality. There are only a few specific processes for which an exact singularity spectrum can be computed (She & Leveque, 1994; Turiel, Pérez-Vicente & Grazzini, 2006).
When calculating the singularity spectrum in the microcanonical formalism, it is essential to precisely evaluate the singularity exponents. This is done with the method described in Pont, Turiel & Yahia (2011, 2013), which is based on formalism of Turiel, Yahia & Pérez-Vicente (2007). The resulting map of singularity exponents for Musca 250 μm emission is presented in Fig. 4.16, which shows that the strongest singularity exponents are located around the filament crest and in filamentary structures that are roughly perpendicular to the crest.
From this map of singularity exponents, it is possible to construct the singularity spectrum (Turiel, Yahia & Pérez-Vicente, 2007), which is shown in Fig. 4.17 for Musca. In order to create a trustworthy singularity spectrum, the noise of the signal should be removed because it will affect the constructed singularity spectrum. For the *Herschel* observations this background mainly includes background galaxies, the cosmic infrared background and the cosmic microwave background (Robitaille et al., 2019). Therefore, the effects of denoising the data on the resulting singularity spectrum will be examined. The goal of the denoising, is to eliminate the noise gradient while maintaining the coherent structures that emerge due to the physical processes that govern the cloud evolution. This denoising can be performed

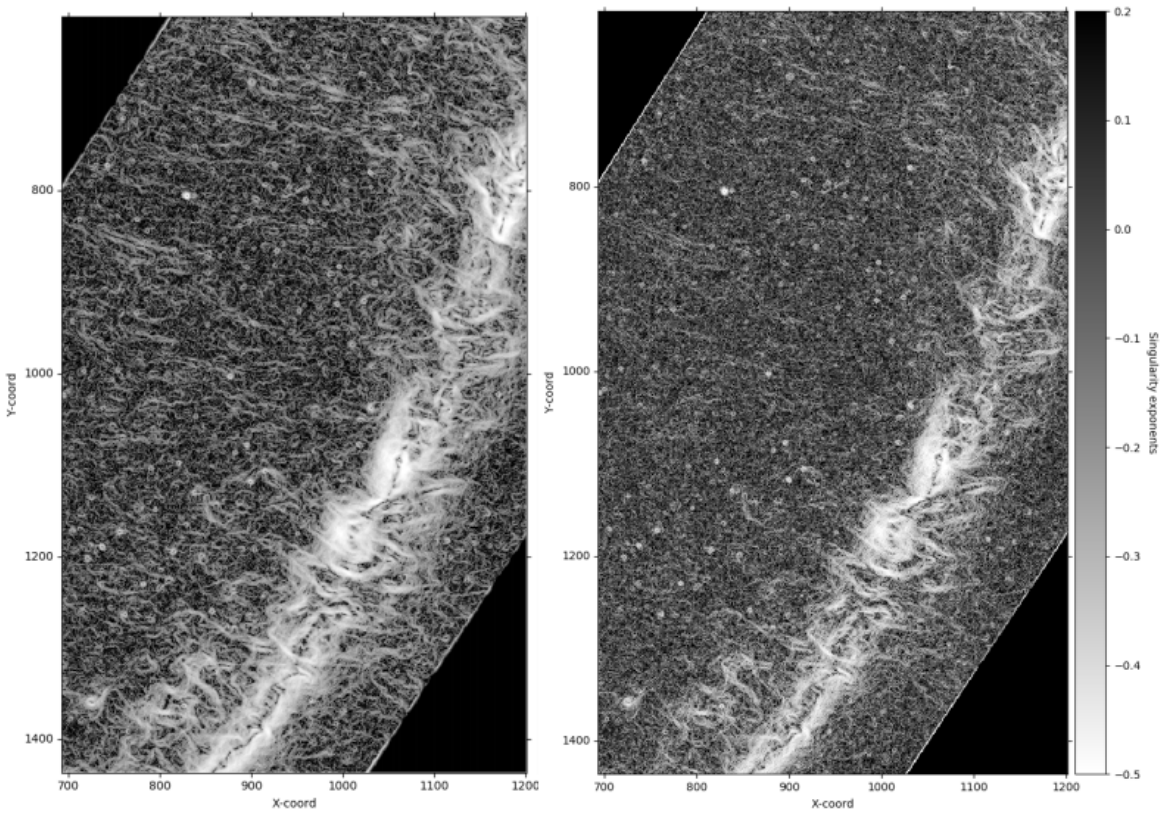

Figure 4.16: **Left:** A zoom into the singularity exponent map of Musca at 250 μm where the noise is filtered using $\lambda = 0.7$ in Eq. 4.8. **Right:** The same map without filtering the noise. Filtering noise has a significant impact on the obtained singularity map, in particular in the low column density region.

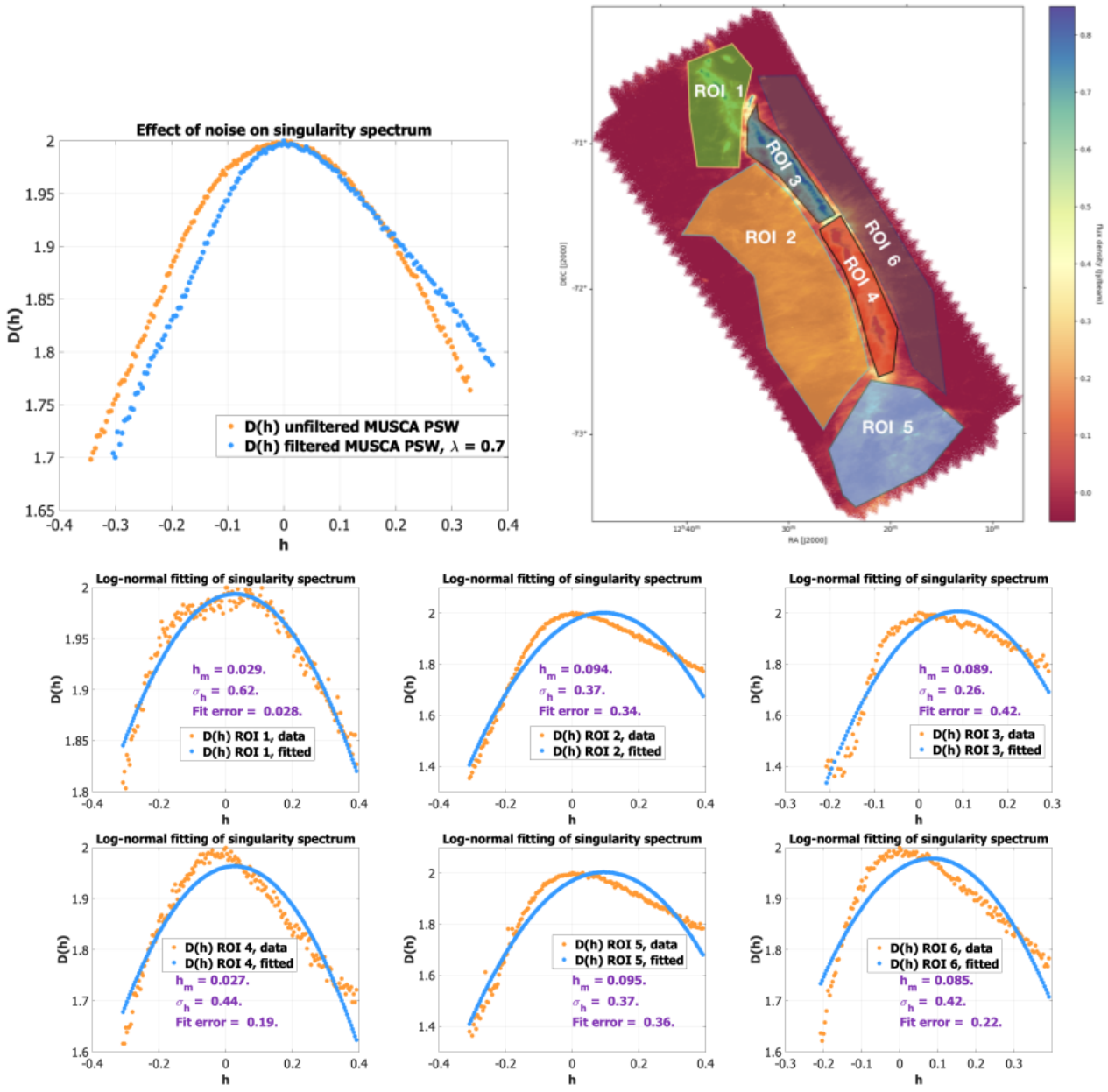

Figure 4.17: **Top left:** The singularity spectrum of the full Musca 250 μm map before (yellow) and after (blue) filtering the noise. Filtering the data has an important impact on the resulting singularity spectrum. **Top right:** The selected regions of interest (ROIs) in the Musca cloud to calculate the singularity spectrum. **Bottom:** The singularity spectra (yellow) with a fitted lognormal distribution (blue). Most singularity spectra are not lognormal, and strongly depend on the region of interest.

by computing

$$\mathrm{argmin}_{\mathrm{s_f}} \parallel \bigtriangledown s - \bigtriangledown s_f \parallel_1 + \lambda \parallel \bigtriangledown s_f \parallel_1 \tag{4.8}$$

with $\bigtriangledown$s the gradient of the original data, $\bigtriangledown \mathrm{s}_f$ the gradient of the filtered image and λ (> 0) a tuning parameter. $\parallel \bigtriangledown s - \bigtriangledown s_f \parallel_1$ makes sure that the final gradient is close to the original gradient, while $\lambda \parallel \bigtriangledown s_f \parallel_1$ favors the gradients of the coherent structures. The resulting singularity map for the filtered data using $\lambda = 0.7$ is presented in Fig. 4.16. This map better highlights the filamentary structures in the Musca cloud. The effect of denoising on the calculated singularity spectrum is presented in Fig. 4.17, demonstrating that the presence of noise tends to give the spectrum a log-normal distribution. When the noise is removed, the spectrum starts to show more substructure. Furthermore, since the microcanonical approach has to be employed, it is possible to study the singularity spectrum in specific regions of interest in the Musca cloud such as the filament crest and the ambient cloud. This study of several subregions of the cloud is presented in Fig. 4.17, and shows that the singularity spectrum significantly varies as a function of the region of interest. By comparing the observed singularity spectra with singularity spectra from simulations it should be possible to deduce information on the physical processes that govern the evolution in the Musca cloud and its subregions.

Chapter 5

Filament formation in low- and high-mass star forming regions

5.1 Cloud-cloud collisions from low- to high-mass star formation

From the results for the Musca cloud, it was proposed that the large scale evolution of the full Chamaeleon-Musca complex plays an important role for the emergence of star forming filaments. Interestingly, the proposed scenario of a cloud-cloud collision for the Chamaeleon-Musca complex has also received considerable attention in the context of massive star formation (e.g. Torii et al., 2011; Motte et al., 2014; Wu et al., 2015; Inoue et al., 2018; Fukui et al., 2019a). It was found that relatively high-velocity cloud collisions (≥ 10 km s^{-1}) can create very high density layers that are capable to form massive stars. A large number of cloud-cloud collision candidates have been put forward (Fukui et al., 2019a, and references therein), forming a range of isolated O stars up to clusters with OB stars. A well studied site of previous and continuing massive star formation is the Cygnus-X region (Reipurth & Schneider, 2008), presented in Fig. 5.1, with in particular the massive DR21 ridge (Schneider et al., 2010) which contains the most massive dense cores (MDCs) of Cygnus-X (Motte et al., 2007; Cao et al., 2019). For the DR21 ridge it was proposed in earlier work that a cloud-cloud interaction is responsible for its formation (Dickel, Dickel & Wilson, 1978). Studying the DR21 ridge and Cygnus-X region, and comparing the results with the study of the Chamaeleon-Musca complex, can thus provide an interesting opportunity to investigate the role of cloud-cloud collisions in the formation of dense filamentary structures in more detail.
It can unveil possible differences between low- and high mass star forming regions. For example, it can be expected that higher velocity cloud collisions are required for massive star formation as it leads to stronger compression. Studying the kinematics of the DR21 cloud at a distance of 1.4 kpc (Rygl et al., 2012), it can be investigated whether the inflow is guided by the bending of the magnetic field as proposed by Inoue et al. (2018) and put forward for Musca, or if another process drives the evolution of the DR21 cloud.

With the possible spatial and kinematic asymmetry in mind for dense gas formed by a cloud-cloud collision due to bending of the magnetic field (Inoue et al., 2018), a spatial asymmetry can be noted

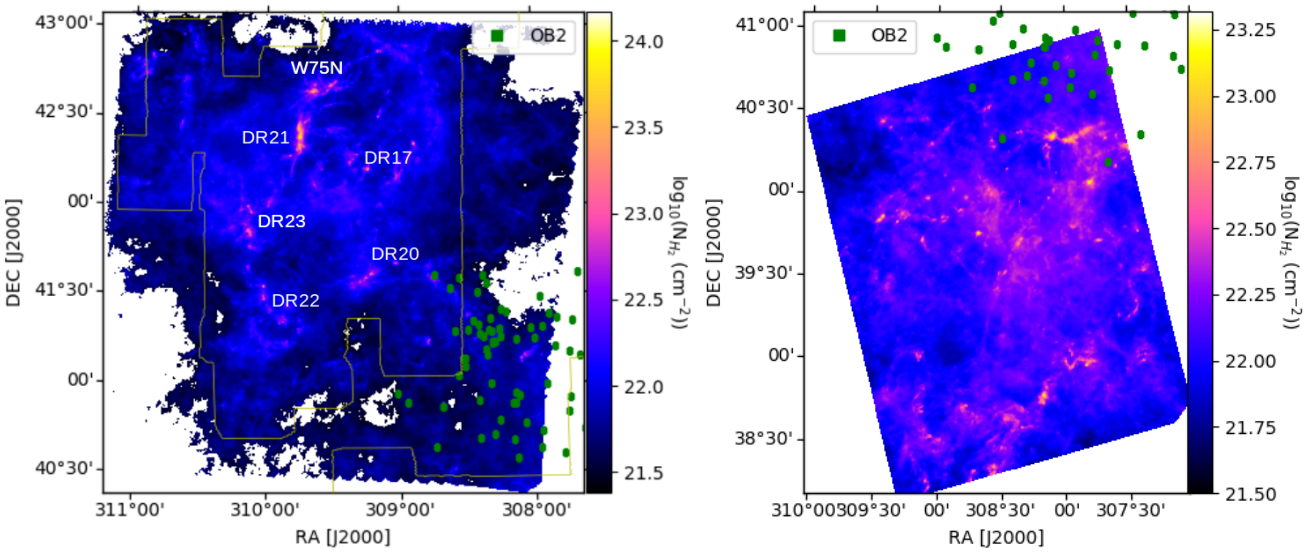

Figure 5.1: **Left:** The *Herschel* column density map of the Cygnus-X north region on a logscale. The green squares indicate the OB stars from the OB2 association that were found by Comerón & Pasquali (2012). Indicated in white are the names of the massive star forming regions in Cygnus-X north, which are often named, except for W75N, after the nearby radio continuum source listed in Downes & Rinehart (1966) **Right:** The same for Cygnus-X south.

for the DR21 ridge in the *Herschel* data from the HOBYS program (Motte et al., 2010). In Fig. 5.2 it is observed that inflowing subfilaments are located west of the DR21 ridge. This could be a result of the possible cloud-cloud collision that formed the DR21 ridge.

5.2 High-mass star formation in Cygnus-X north due to a giant molecular cloud collision

5.2.1 The DR21 ridge

In Fig. 5.2, the *Herschel* column density map of the DR21 ridge is presented. The DR21 ridge is the massive ($\sim 10^4$ $M_\odot$) filamentary structure that contains the bright DR21 radio continuum source (Downes & Rinehart, 1966) that is located in the southern part of the ridge. The ridge also consists of two massive clumps, namely DR21(OH) and the DR21 north (DR21-N), indicated in Fig. 5.2. Both clumps contain multiple MDCs with masses between 40 $M_\odot$ and 500 $M_\odot$. DR21(OH) contains the CygX-N44, -N38, -N48, -N41, -N36 and -N40 MDCs while DR21-N consists of CygX-N51, -N52, -N53, -N54, -N37 and -N43 MDCs (Motte et al., 2007; Schneider et al., 2010). These three sub-regions of the DR21 ridge [DR21, DR21(0H) and DR21-N] are at different stages of massive star formation.
DR21 is a bright HII region (e.g Cyganowski et al., 2003), that is possibly the result of strong stellar winds (Immer et al., 2014). This HII region is more evolved than DR21(OH) which shows the presence of multiple very compact radio continuum sources and CH_3OH, H_2O and OH maser sources (Woody

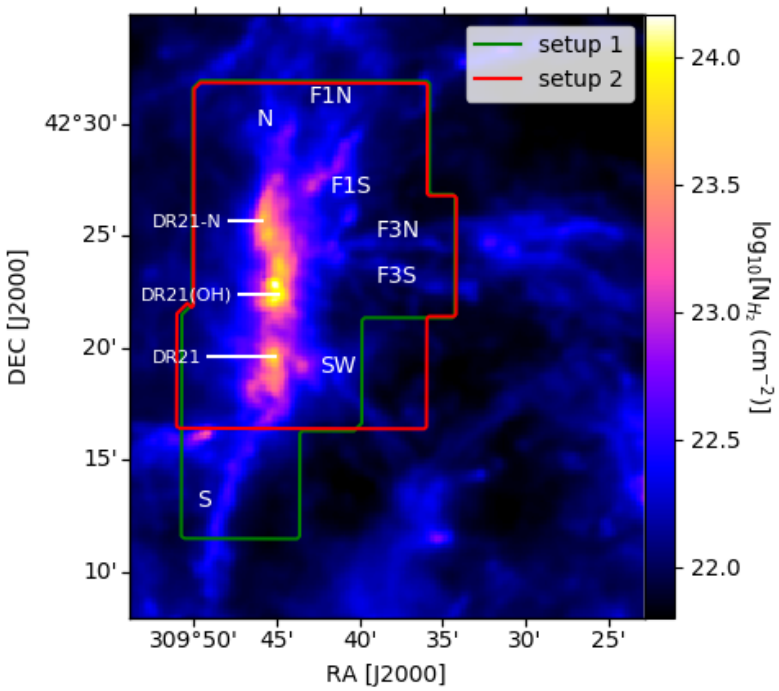

Figure 5.2: The *Herschel* column density map of the DR21 ridge and subfilaments. The location of DR21, DR21(OH) and DR21-N inside the DR21 ridge are indicated together with the names of the subfilaments (Schneider et al., 2010; Hennemann et al., 2012). The red and green contours outline the area of the cloud covered by the two spectral setups of the IRAM 30m observations.

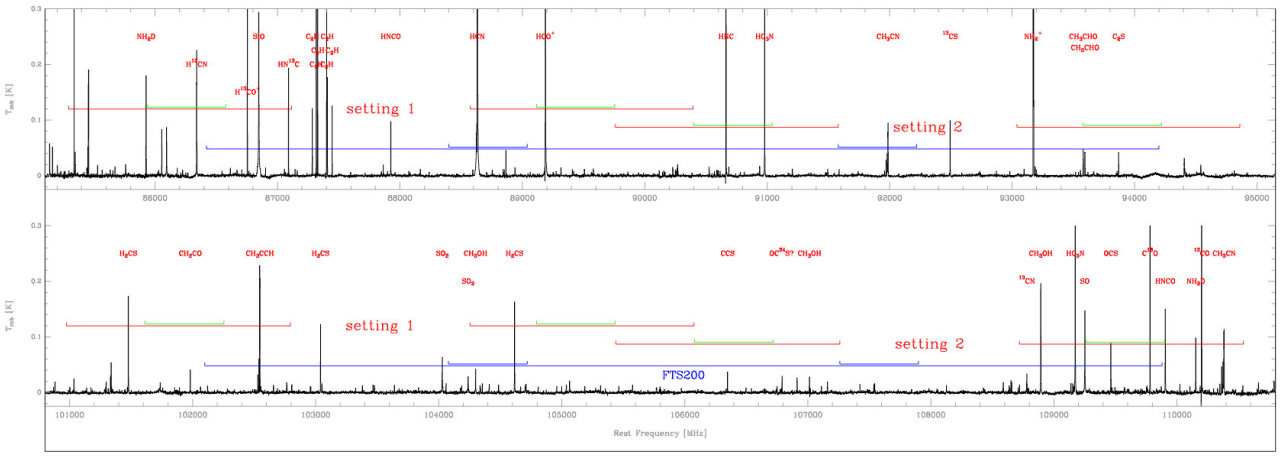

Figure 5.3: The two spectral setups (setting 1 and setting 2) of the IRAM 30m observations, indicated with the red intervals, overlaid on the observed spectrum of the CygX-N63 massive dense core (Fechtenbaum, 2015).

et al., 1989; Mangum, Wootten & Mundy, 1991; Araya et al., 2009). This fits with the observed presence of multiple dust continuum fragments that can form intermediate to high-mass stars (Bontemps et al., 2010b; Duarte-Cabral et al., 2013). It also contains a hot core with a temperature above 80 K (Mangum, Wootten & Mundy, 1992). Lastly, there is the DR21-N region which does not appear to contain any hot cores. This suggests that the northern region of the DR21 ridge only contains the early stages of high-mass star formation.
The DR21 ridge is also the location of an estimated young stellar population of 2900 stars, based on a combination of infrared excess and X-ray emission (Kuhn, Getman & Feigelson, 2015). Furthermore, the location of this young stellar population is associated with the DR21 and DR21(OH) clumps. This suggests, in combination with the large mass reservoir of the region, that the DR21 ridge is forming one or more OB star clusters.

In Schneider et al. (2010), it was proposed that the full DR21 ridge is undergoing a gravitational collapse. In order to better understand the velocity structure, density distribution and the chemical evolution of the DR21 cloud that is forming this OB star cluster, a dedicated observing program was carried out with the IRAM 30m telescope. The observations cover both the DR21 ridge and the surrounding filaments with two spectral setups which are shown in Fig. 5.3. These two spectral setups make sure that a variety of molecular lines is covered. This comprehensive observational approach is similar to the extensive study of the Orion B molecular cloud with the IRAM 30m telescope to reveal its anatomy (Pety et al., 2017).
The current status of the possibly detected lines with the IRAM 30m observations is summarized in Tab. 5.1. The detection is slightly rms dependent with a general rms in an 0.2 km s^{-1} velocity interval of 0.13-0.15 K for the observations around 90 GHz and an rms of 0.19-0.20 K for the observations around 110 GHz. The integrated intensity maps for the different molecular transitions are presented in App. A. In the integrated intensity maps, it is found that most complex molecules are found in DR21(OH) which contains at least one hot core (Mangum, Wootten & Mundy, 1992). This is in line with observed increasing molecular complexity in massive hot cores (e.g. Blake et al., 1987; Garay & Lizano, 1999; Kurtz et al., 2000; Herbst & van Dishoeck, 2009; Belloche et al., 2013). However, the vast amount of lines detected towards CygX-N63 by Fechtenbaum et al. (2015) in Fig. 5.3 is not found towards DR21(OH). This is not truly surprising since the unbiased spectral survey of the CygX-N63 core by Fechtenbaum et al. (2015) has a significantly better sensitivity, an rms of the order of 3 mK, than the maps that were made of the DR21 ridge.

5.2.2 Article: The formation of OB stars in the DR21 ridge by large-scale compression (Paper-DR21, in preparation)

Astronomy & Astrophysics manuscript no. output
December 17, 2020

The formation of OB stars in the DR21 ridge due to large-scale compression

L. Bonne et al.[1], S. Bontemps[1], N. Schneider[2], R. Simon[2], and F. Comeron[3] et al.

[1] Laboratoire d'Astrophysique de Bordeaux, Université de Bordeaux, CNRS, B18N, allée Geoffrey Saint-Hilaire, 33615 Pessac, France
e-mail: lars.bonne@u-bordeaux.fr
[2] I. Physikalisches Institut, Universität zu Köln, Zülpicher Str. 77, 50937 Köln, Germany
[3] European Southern Observatory, Karl-Schwarzschild-Str. 2, D-85748 Garching bei München, Germany

Draft of December 17, 2020

ABSTRACT

Context. The Cygnus-X region is a rich star forming region with several sites of high-mass star formation and well known OB associations. This makes it a primary region to understand the interplay of molecular cloud evolution and high-mass star formation.
Aims. We investigate the physics leading to high-mass star formation in the DR21 ridge and propose a scenario for the global evolution of the entire Cygnus-X region.
Methods. We present the first results from new ^{13}CO(1-0), C^{18}O(1-0), HCO$^+$(1-0), H^{13}CO$^+$(1-0) and SiO(2-1) maps of the massive DR21 ridge observed with the IRAM 30m telescope. These observations are complemented with ^{12}CO(3-2) observations by the JCMT telescope, ^{13}CO(1-0) observations by the FCRAO 14m telescope, Effelsberg 11 cm radio continuum observations and *Herschel* column density maps of the Cygnus-X region.
Results. With the IRAM observations we find that self-gravity drives the evolution of the massive DR21 ridge and the ∼3 pc ambient cloud, but we also observe that basically all inflowing subfilaments to the ridge are redshifted with respect to the massive DR21 ridge. This behaviour is also observed in the PV diagrams perpendicular to the DR21 ridge, which shows a V-like shape. At the location where the subfilaments are accreted on the ridge, there is a local but strong increase of the linewidth. The IRAM observations also unveil extended SiO(2-1) emission with a narrow linewidth over the entire DR21 ridge. From the *Herschel* maps of the full Cygnus-X region, we find that dense gas in Cygnus-X north is significantly more compact than Cygnus-X south. The *Herschel* column density map also indicates that the dense gas in Cygnus-X north can form a stellar mass of $1.6{\cdot}10^4$ M$_\odot$ over 5 Myr. A study of Cygnus-X north with FCRAO and JCMT unveils two velocity components, each with significant spatial substructure, that are connected by CO bridges over the full region. These CO bridges are also observed towards the DR21 cloud. However, Cygnus-X south shows no such substructure and bridging. Based on the age of OB stars in Cygnus-X from the literature and radio continuum maps, we also confirm an age gradient for massive star formation from the south-west to the north-east for the entire Cygnus-X region.
Conclusions. We propose that an OB association is currently in formation in Cygnus-X north because of a giant molecular cloud (GMC) collision with a 3D velocity of ∼ 17 km s^{-1}. Dense hubs and ridges, formed due to large scale compression by the GMC collision, then host high-mass star formation as a result of gravitational collapse that was initiated by the compression. This proposed formation of an OB association due to a GMC collision provides a natural explanation for several recently observed properties of OB associations.

Key words. ISM: individual objects: Cygnus-X – ISM: kinematics and dynamics – ISM: clouds – open clusters and associations: individual: OB2 and OB9 – stars: massive – stars: formation

1. Introduction

Massive stars can be found in OB associations, which are low-density groups of young OB stars (e.g. Ambartsumian 1947; Blaauw 1964; de Zeeuw et al. 1999). Because of this low number density, these associations can expand and disperse in the future (e.g. Blaauw 1964; Mel'nik & Dambis 2017). This observation, and the fact that a large fraction of stars are formed in clusters (e.g. Carpenter 2000; Lada & Lada 2003; Krumholz et al. 2019), has led to the idea that OB associations are the result of disrupted star clusters. This could be as a result of feedback (e.g. Hills 1980; Goodwin & Bastian 2006; Baumgardt & Kroupa 2007) or because of tidal disruption from a nearby giant molecular cloud (GMC) (e.g. Elmegreen & Hunter 2010; Kruijssen et al. 2011). An opposing view proposes that stars form hierarchically as a result of the structure formation in the star forming gas (e.g. Elmegreen 2002; Bastian et al. 2007; Bonnell et al. 2011; Wright et al. 2014). This could provide an explanation for the kinematic substructure that is observed with in depth studies of OB associations (e.g. Wright et al. 2016; Wright & Mamajek 2018).

Because they contain young and massive stars, the formation and evolution of OB associations has to be understood in relation with the process that is responsible for massive star formation. The formation of massive stars is still a matter of debate (e.g. Zinnecker & Yorke 2007; Motte et al. 2018a). Yet, the very short massive prestellar phase (e.g. Motte et al. 2007, 2010; Russeil et al. 2010; Csengeri et al. 2014; Tigé et al. 2017; Louvet et al. 2019), and indications of gravitational collapse of the ambient molecular clouds that form massive stars (e.g.

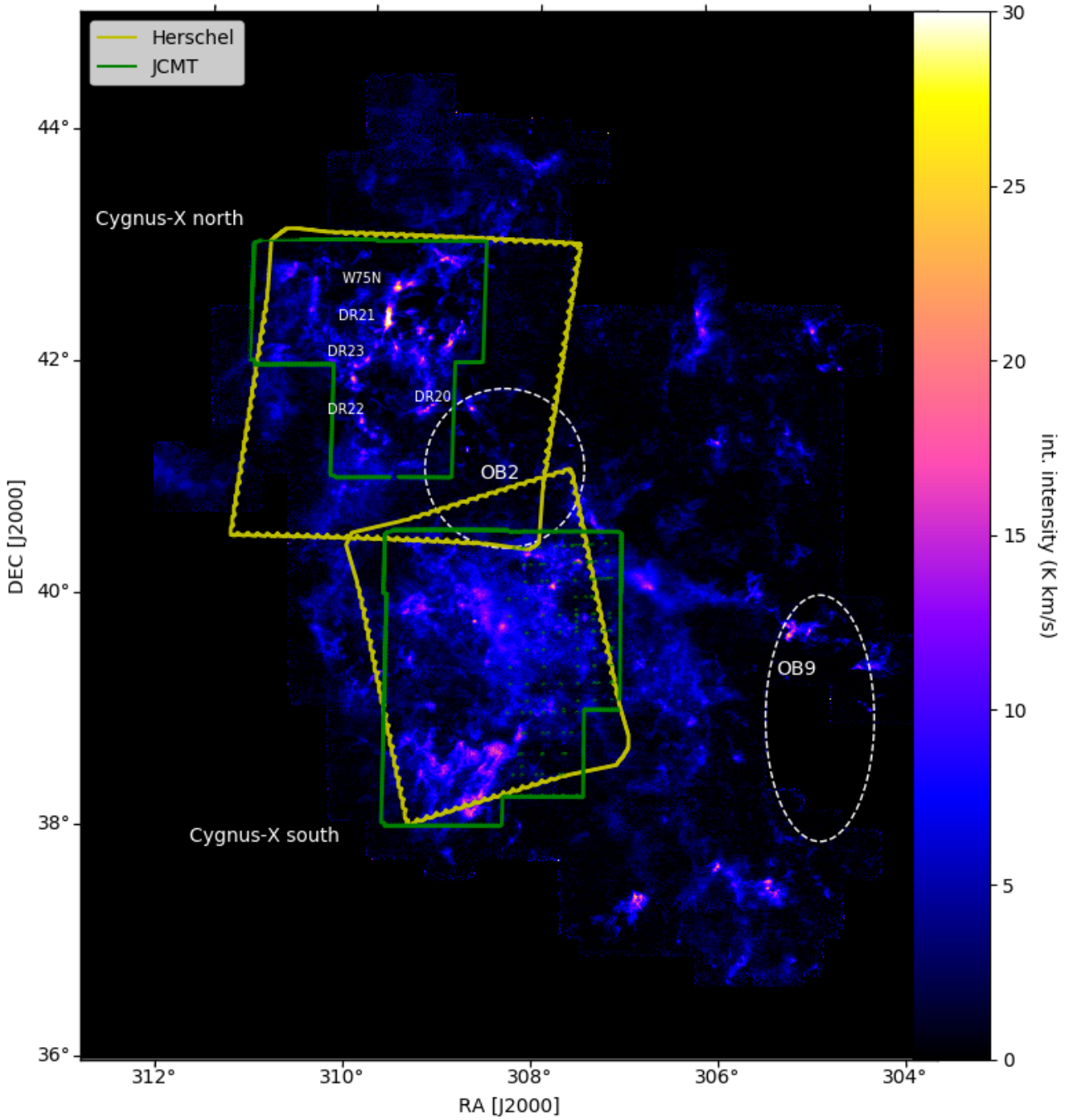

Fig. 1. The integrated ^{13}CO(1-0) FCRAO map of the Cygnus region (Simon et al. 2006; Schneider et al. 2006, 2007, 2016b). The dashed circle and ellipse indicate the location of OB2 and OB9. The DR20, DR21, DR22, DR23 and W75N molecular clouds in Cygnus-X north are indicated, which form the highest mass stars of the Cygnus-X complex. The yellow contours indicate the part of Cygnus-X north and south mapped with the *Herschel* telescope by the HOBYS program, while the green contours indicate the regions mapped in ^{12}CO(3-2) with the JCMT telescope.

Schneider et al. 2010, 2015; Galván-Madrid et al. 2010; Peretto et al. 2013, 2014; Beuther et al. 2015; Williams et al. 2018; Jackson et al. 2019) suggest that the formation of massive stars is intimately linked with the evolution of the molecular cloud. This is in tension with predications by the turbulent core collapse model (McKee & Tan 2002, 2003) which proposes that massive stars form from the collapse of massive prestellar cores. The link between massive star formation and the molecular cloud evolution is put forward by several theoretical models. In the competitive accretion model (Bonnell et al. 2001, 2004; Bonnell & Bate 2006; Wang et al. 2010), low-mass protostellar cores compete for mass from the ambient cloud. It was also proposed that global hierarchical collapse (Vázquez-Semadeni et al. 2009, 2017, 2019), with filamentary gravitational collapse on multiple scales is responsible for the formation of massive stars. In the fragmentation-induced starvation scenario, massive

stars form through gravitational fragmention at the center of dense filamentary accretion flows (Peters et al. 2010, 2011; Girichidis et al. 2012), where the fragmentation in the inflowing filaments limits the accretion on the most massive stars at the center of the accretion flow. From simulations it was also proposed that compression by the collision of molecular clouds with v > 10 km s^{-1} can form filamentary structures that are capable to host massive star formation (Inoue & Fukui 2013; Inoue et al. 2018), and that massive stars preferentially form in a cloud-cloud collision compared to a cloud evolving in isolation (Wu et al. 2015, 2017). Such cloud-cloud collisions could be the result of large scale motions in the ISM driven by supernova explosions and feedback from massive stars (Inutsuka et al. 2015).

From an observational point of view, the role of cloud-cloud collision in (massive) star formation has also been suggested for a wide variety of star forming regions based on the cloud kinematics from HI and CO (e.g. Dickel et al. 1978; Dobbs 2008; Furukawa et al. 2009; Duarte-Cabral et al. 2010, 2011; Motte et al. 2014; Fukui et al. 2016, 2019; Dobashi et al. 2019).

1.1. Cygnus-X

A well studied OB association is Cygnus OB2 (Münch & Morgan 1953; Johnson & Morgan 1954), which is located in the Cygnus-X molecular complex at a distance of 1.4 kpc (Rygl et al. 2012). Cygnus OB2 is an extremely rich association that contains over a hundred OB stars (Schulte 1958; Massey & Thompson 1991; Comerón et al. 2002; Hanson 2003; Kiminki et al. 2007; Comerón & Pasquali 2012), with a total stellar mass estimate between 10^4-10^5 $M_\odot$ (e.g. Knödlseder 2000; Drew et al. 2008; Wright et al. 2010). The most recent mass estimate for Cygnus OB2 gives a mass of 16 500^{+3800}_{-2800} $M_\odot$ (Wright et al. 2015). Estimating the age of the OB stars, demonstrated that Cygnus OB2 was formed by continuous star formation between roughly 1 and 10 Myr ago with a star formation peak around 3-6 Myrs ago (Comerón & Pasquali 2012; Wright et al. 2015).

Cygnus OB2 is located relatively central in the Cygnus-X region. This creates an expanding bubble (e.g. Schneider et al. 2006; Reipurth & Schneider 2008) in the complex, and is also responsible for the presence of a large amount of globules, pillars and proplyd-like structures as a result of the strong radiation field from OB2 (Wright et al. 2012; Schneider et al. 2012b, 2016a). Because of the relatively central location of Cygnus OB2, the Cygnus-X region is generally divided into Cygnus-X north and Cygnus-X south, see Fig. 1. Also associated with the Cygnus-X region is another agglomeration of OB stars, Cygnus OB9, in the western area of the region indicated in Fig. 1 (Comerón & Pasquali 2012). This association shows significant spatial substructure and it has been proposed that its outline needs to be revised (Mel'Nik & Efremov 1995; Schneider et al. 2007).

Studies of the molecular gas in the Cygnus-X region and *Herschel* data have demonstrated the presence of multiple velocity components (e.g. Cong 1977; Schneider et al. 2006) and that the dense gas is organised in massive structures, so-called ridges (Hartmann & Burkert 2007; Hill et al. 2011; Hennemann et al. 2012) and filament-hubs (Myers 2009; Schneider et al. 2012a; Peretto et al. 2013), such as DR21, W75N, DR23, DR22, see Fig. 1, which are often named after the name of their nearby HII regions in Downes & Rinehart (1966). More in depth kinematic studies of the DR21 ridge demonstrated that this massive ridge is experiencing large scale gravitational collapse (Schneider et al. 2010), that it contains subfilaments which are connected to the ridge, see Fig. 2, and that this ridge shows signs of a collision between two velocity components at ~ -3 km s^{-1} and ~ 9 km s^{-1} (Dickel et al. 1978; Dobashi et al. 2019). These hubs and ridges in Cygnus-X contain several massive dense cores (MDCs) (Motte et al. 2007; Cao et al. 2019). Follow-up studies of these MDCs demonstrated active high-mass star formation in the Cygnus-X region (Kumar et al. 2007; Bontemps et al. 2010; Beerer et al. 2010; Duarte-Cabral et al. 2013) as a result of small-scale converging flows (Csengeri et al. 2011a,b; Duarte-Cabral et al. 2014), making it a primary region to understand the processes associated with high-mass star formation.

In this paper we first present new IRAM 30m observations of the DR21 ridge. Starting from these results and complementing it with JCMT and FCRAO observation of the full Cygnus-X region, we will aim to understand the main driver of massive star formation in the full Cygnus-X region.

2. Observations

2.1. IRAM 30m observations

Observations with the IRAM 30m telescope of the DR21 ridge and the surrounding subfilaments were carried out in February 2015. These observations were performed with two different spectral setups using the FTS50 configuration of the EMIR receiver. Setup 1, which contains HCO^+(1-0) and $H^{13}CO^+$(1-0), covers the spectral ranges ~ 85.2 GHz - 87.2 GHz, 88.5 GHz - 90.5 GHz, 101.0 GHz - 102.8 GHz and 104.2 GHz - 106.0 GHz. Setup 2, which contains ^{13}CO(1-0) and $C^{18}O$(1-0), covers the spectral ranges ~ 89.6 GHz - 91.6 GHz, 93.0 GHz - 95.0 GHz, 105.4 GHz - 107.2 GHz and 108.8 GHz - 110.6 GHz. These two setups allow the coverage of a variety of possible molecular lines (e.g. $C^{18}O$(1-0), N_2H^+(1-0), HCN(1-0), HCO^+(1-0), NH_2D[1(1,1)0-1(0,1)0],...) which will allow to follow the kinematic and chemical evolution of the dense gas in the DR21 ridge and the connected subfilaments, similar to what was done for the Orion-B cloud with the data presented in Pety et al. (2017). The obtained antenna temperature (T_A^*) rms noise within a spectral resolution of 0.2 km s^{-1} varies between 0.13-0.15 K (around 90 GHz) and 0.19-0.2 K (around 110 GHz). A main beam efficiency of 0.81 for frequencies around 90 GHz and 0.78 for frequencies around 110 GHz was used (Kramer et al. 2013). The region on the sky that is covered by the two different setups is displayed in Fig. 2. The mapping was performed with OTF observations and has a spatial resolution between 23″ and 29″. The ^{13}CO(1-0) channel maps of these observations are displayed in Fig. 3. A full analysis of all the lines that are covered is in preparation and will be the topic of a future paper. Here, the first results from ^{13}CO(1-0), $C^{18}O$(1-0), HCO^+(1-0), $H^{13}CO^+$(1-0) and SiO(2-1) will be presented.

2.2. JCMT observations

With the JCMT telescope, a ^{12}CO(3-2) mapping of the Cygnus-X north and south data was performed. The area covered by this survey is shown in Fig. 1. The observations and reduction of this data is described in Gottschalk et al. (2012) for the pilot study. We here summarize the main characteristics of the data. The observations have a spatial resolution of 15″ and a spectral resolution of 0.423 km s^{-1}, with an noise rms of ~ 0.25 K.

2.3. FCRAO observations

The observations of the IRAM 30m telescope are complemented by ^{13}CO(1-0) observations that were carried out with the SE-

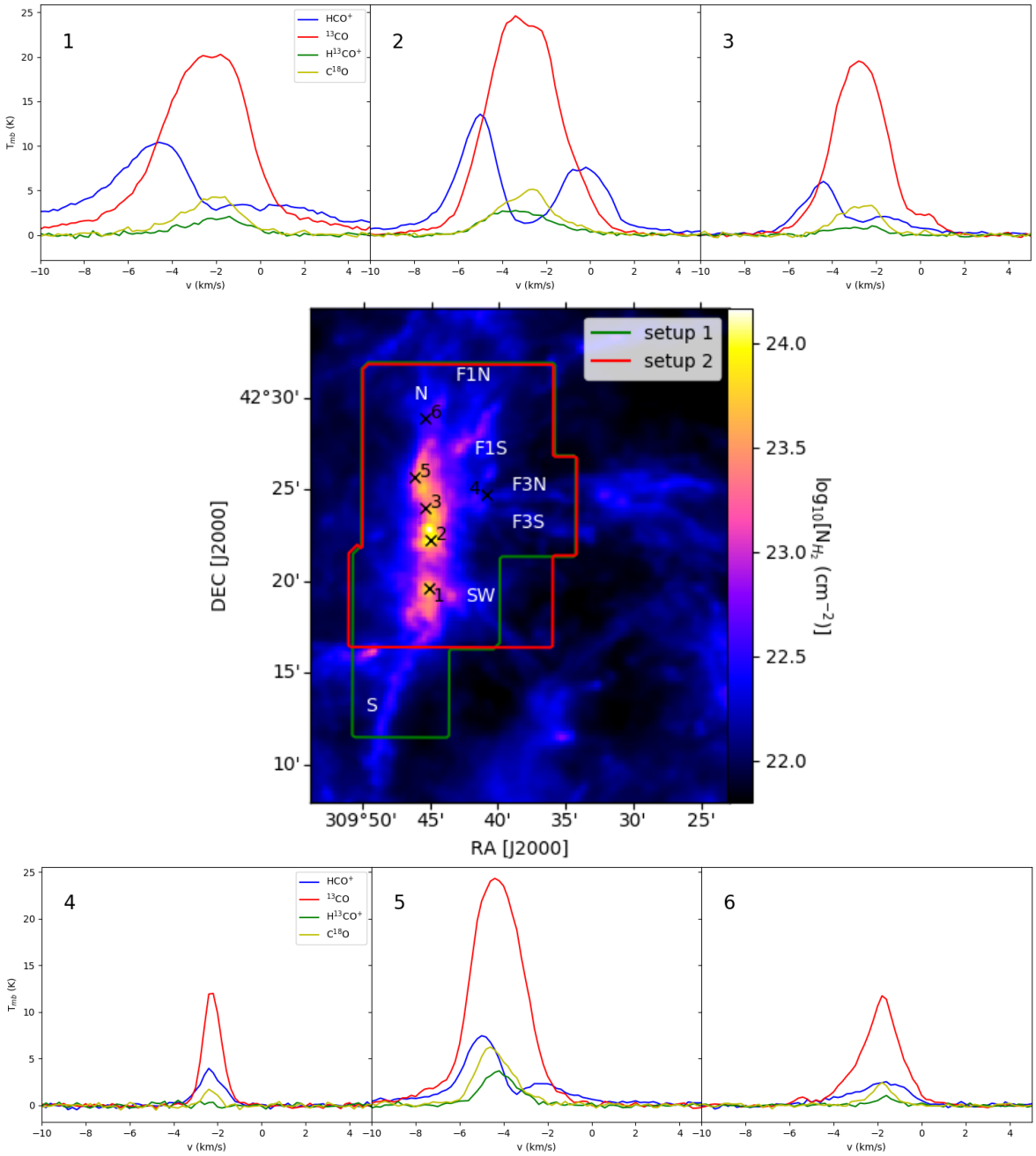

Fig. 2. The *Herschel* column density map of the DR21 ridge and its surrounding subfilaments on a log scale. The subfilaments are indicated by their name from Hennemann et al. (2012): N (north), F1N, F1S, F3N, F3S, SW (south-west), S (south). The contours indicate the area covered by the two different setups of the IRAM 30m observations. The southern subfilament is only covered by the first setup which contains HCO^+(1-0) and $H^{13}CO^+$(1-0). The crosses indicate the location of the displayed ^{13}CO(1-0), $C^{18}O$(1-0), HCO^+(1-0) and $H^{13}CO^+$(1-0) spectra.

QUOIA receiver on the FCRAO 14m telescope. This data is presented in Simon et al. (2006) and Schneider et al. (2006, 2007, 2010, 2016b). The data has an angular resolution of 45″ and a spectral resolution of 0.1 km s^{-1}. The rms noise of the spectra within this spectral resolution is around 0.4 K. The integrated ^{13}CO map is displayed in Fig. 1.

2.4. Herschel observations

We also use *Herschel* column density maps from the Cygnus-X north and south region (Schneider et al. 2016a). The observations of these regions were carried out as a part of the HOBYS program Motte et al. (2010), and the production of the column density maps is described in Hill et al. (2011, 2012). The observations of Cygnus-X south only cover a part of the full molecular cloud shown in Fig. 1.

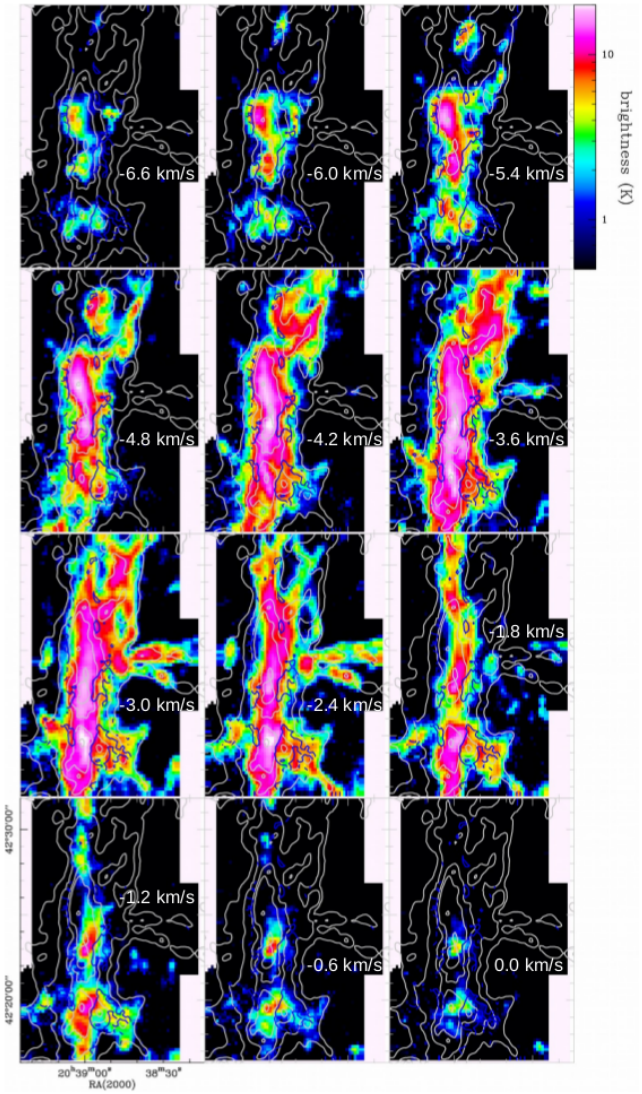

Fig. 3. The ^{13}CO(1-0) channel maps between -6.6 and 0 km s^{-1} of the IRAM 30m observations towards DR21. The grey contours trace the *Herschel* column density at N_{H_2} = 10^{22}, $2{\cdot}10^{22}$, $5{\cdot}10^{22}$, 10^{23} and $5{\cdot}10^{23}$ cm^{-2}. The blue contours indicate the location where the fitted C^{18}O(1-0) spectra have a FWHM above 2.5 km s^{-1}. One can notice that this occurs at the location where the subfilaments connect with the DR21 ridge.

3. The DR21 ridge

3.1. Integrated intensity and self-absorption

A variety of lines are detected with the IRAM 30m observations, but in this paper we will focus on the ^{13}CO(1-0), C^{18}O(1-0), HCO$^+$(1-0), H^{13}CO$^+$(1-0) and SiO(2-1) lines. A more in depth study of all the detected molecular lines will be presented in a future paper. ^{13}CO(1-0), C^{18}O(1-0), HCO$^+$(1-0) and H^{13}CO$^+$(1-0) will be analysed to study the large scale kinematics of the DR21 ridge and cloud. Inspecting the integrated intensity maps of these 4 lines, which are presented in Fig. 4, it is found that ^{13}CO(1-0) and HCO$^+$(1-0) are clearly detected in the ridge and subfilaments. This is also observed in the channel maps of ^{13}CO in Fig. 3. C^{18}O(1-0) and H^{13}CO$^+$(1-0) are also clearly detected in the ridge, but their detection, in particular for H^{13}CO$^+$(1-0), becomes increasingly difficult in the subfilaments. SiO(2-1) on the other hand is a well-known shock tracer (e.g Schilke et al. 1997; Gusdorf et al. 2008a,b). In Fig. 5, it can be observed that SiO(2-1) is detected over the full DR21 ridge. This presence of extended SiO emission was already noted by Duarte-Cabral et al. (2014) for MDCs over the Cygnus-X region. This is similar to what was found in e.g. the massive G035.39-00.33 infrared dark cloud (IRDC) (Jiménez-Serra et al. 2010; Nguyen Luong et al. 2011), the W43-MM1 ridge (Nguyen-Lu'o'ng et al. 2013; Louvet et al. 2016), the G028.23-00.19 IRDC (Sanhueza et al. 2013) as well as a large sample of massive clumps in the ATLASGAL survey (Csengeri et al. 2016). However, this is in contrast to the low-mass Musca filament where only an upper limit was found on the SiO abundance in the gas phase (Bonne et al. 2020).

Inspecting the ^{13}CO(1-0), C^{18}O(1-0), HCO$^+$(1-0) and H^{13}CO$^+$(1-0) spectra over the map in Fig. 2, we found that fitting a single velocity component can provide a reasonable global view of the DR21 cloud kinematics. However, note that the HCO$^+$ spectra can not be fitted with a gaussian in the ridge because of the strong self-absorption of this molecule (Schneider et al. 2010). This self-absorption is also seen in the spectra in Fig. 2. Furthermore, it is observed in Fig. 2 that HCO$^+$(1-0) has high-velocity wing emission towards DR21 and DR21(OH), tracing the strong protostellar outflow in these regions.

3.2. The velocity field of DR21

When fitting the spectra of the different molecular lines, a fit was accepted when the brightness was higher than 3 times the noise rms. The resulting velocity maps are presented in Fig. 6 for the different molecules, and show velocity gradients over the ridge similar to the gradients presented in Schneider et al. (2010) with N_2H^+(1-0). Inspecting the velocity field of the subfilaments, it can be directly noted that basically all subfilaments (N, F1N, F3N, F3S and SW) are redshifted with respect to the ridge. Only the F1S subfilament, which is roughly at the velocity of the DR21 ridge, is not clearly redshifted with respect to the ridge. Lastly, the southern subfilament appears slightly redshifted close to the ridge, but more to the south this filament becomes less reshifted with respect to the ridge. This observation of dominantly redshifted subfilaments and a complete lack of a truly blueshifted subfilament is also observed in the channel maps in Fig. 3.

3.3. Linewidth of the spectra

The gaussian fit also provides a map of the full width half maximum (FWHM), which is shown in Fig. 7 for C^{18}O(1-0) and H^{13}CO$^+$(1-0). In these maps it is observed that the subfilaments have a significantly lower FWHM than in the ridge. The FWHM in the subfilaments is generally $\lesssim$ 1 km s^{-1}, which makes them close to transonic. In the ridge, a FWHM between 1.5 and 2.5 km s^{-1} is observed. Noteworthy is the observed strong local increase of the FWHM up to 4-5 km s^{-1} at locations where the subfilaments are connected with the ridge, see Fig. 3. However, a single gaussian is generally not a good description at these locations where the subfilaments connect with the ridge. This resulting strong local increase is thus likely an accretion effect.

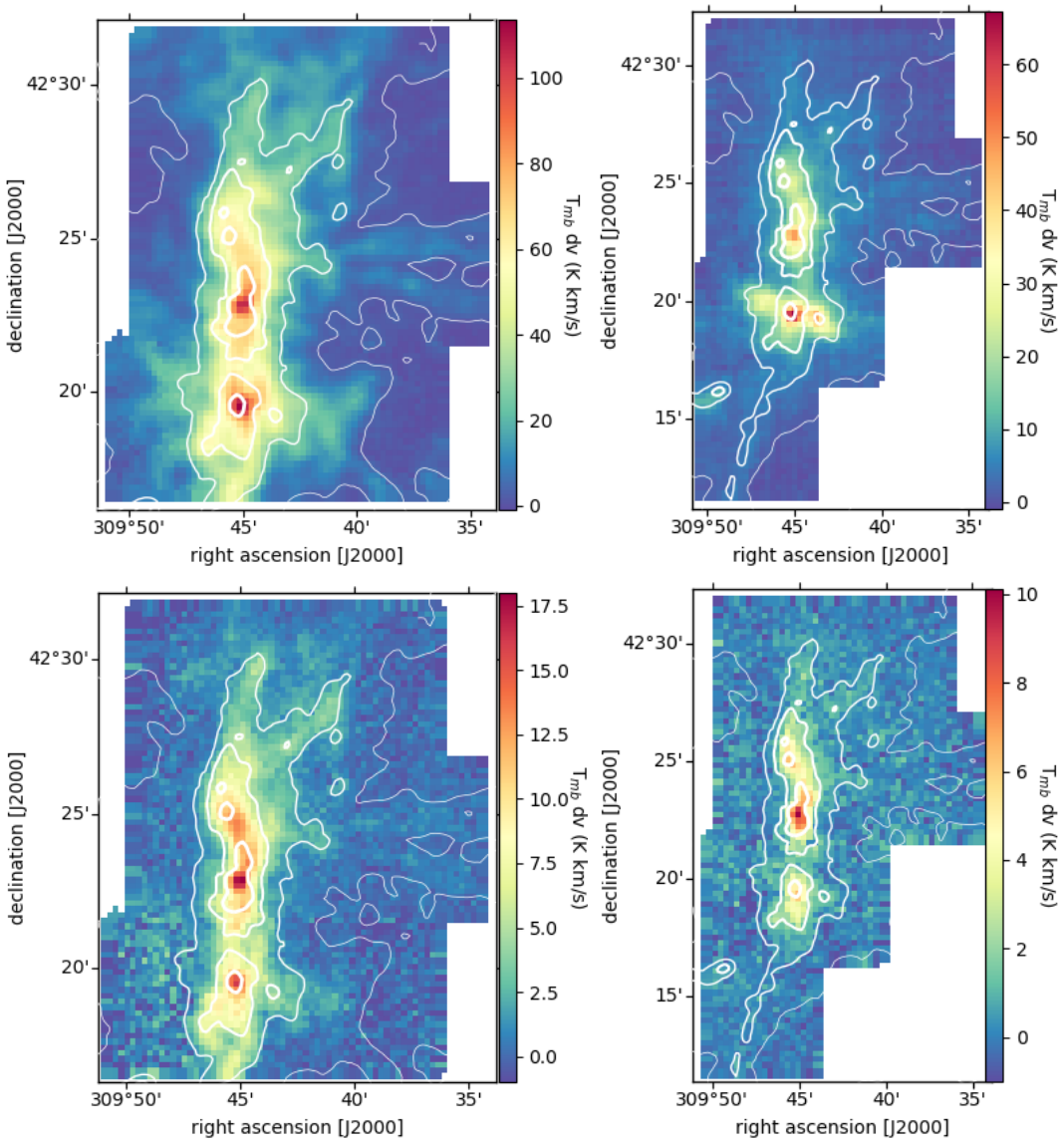

Fig. 4. Top left: The integrated brightness map of ^{13}CO(1-0) of the DR21 cloud. Overplotted on the map are the *Herschel* column density contours (in white) at N_{H_2} = 10^{22}, $3{\cdot}10^{22}$, 10^{23} and $4{\cdot}10^{23}$ cm^{-2} (with increasing contour width). **Top right:** The same for HCO$^+$(1-0). **Bottom left:** The same for C^{18}O(1-0). **Bottom right:** The same for H^{13}CO$^+$(1-0).

3.4. PV diagram of DR21

Looking into the PV diagram produced with the IRAM 30m and JCMT data of the DR21 ridge in Fig. 8, it is again observed that the subfilaments are indeed redshifted with respect the densest gas in the ridge. Interestingly, from these PV diagrams it can be noted that not only the subfilaments, which are all located to the west of the ridge, but also the ambient molecular gas east of the DR21 ridge is redshifted. This gives rise to a V-like shape in the PV diagram, similar to what was observed for a filament in the Taurus molecular cloud by Arzoumanian et al. (2018) and the Musca filament by Bonne et al. (2020b, submitted). Similar to these lower mass filaments, the densest gas of the region, which resides towards the center of the DR21 ridge, is located at the apex of this V-like shape. However, it is found that this V-like shape for DR21 is not as clear as observed in Musca. This can be related to the large linewidth in the DR21 ridge, while the Musca filament is transonic (Hacar et al. 2016).

3.5. Virial analysis of the DR21 cloud

It was proposed in Schneider et al. (2010) that the DR21 ridge is experiencing a gravitational collapse. With the new available data, covering a significantly larger area, we will investigate the stability of the cloud as a function of its radius. For this analysis, we will consider the gravitational energy, the turbulent support and magnetic support.

To calculate the gravitational potential and average density, we use the *Herschel* column density map of DR21. We subtract a fore-/background column density to calculate the mass in the cloud as a function of radius. For the background column density we work with a value of N_{H_2} = $5{\cdot}10^{21}$ cm^{-2}, based on an

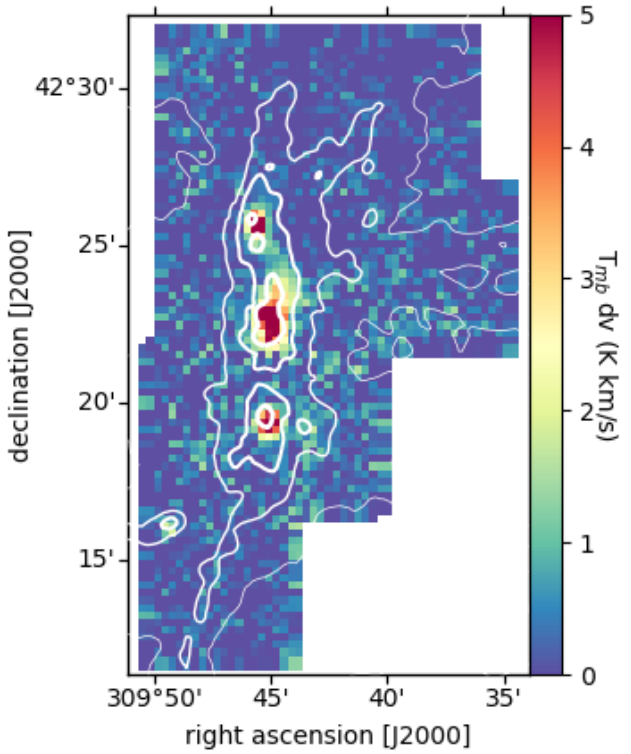

Fig. 5. The integrated SiO(2-1) map of the DR21 ridge, showing extended emission over the full ridge. The white contours indicate the *Herschel* column density at N_{H_2} = 10^{22}, $3{\cdot}10^{22}$, 10^{23} and $4{\cdot}10^{23}$ cm^{-2} (with increasing contour width).

inspection of the full map for Cygnus-X north (see also Schneider et al. 2020, in prep.). To study the possible internal support, we work with the assumption that the full linewidth is purely related to thermal and turbulent support. However, it should be noted that several studies suggest that the observed full linewidth is not necessarily a measure of the thermal and turbulent support (e.g. Ballesteros-Paredes et al. 2018; Traficante et al. 2018, 2020). This support will be studied with the ^{13}CO(1-0), C^{18}O(1-0) and H^{13}CO$^+$(1-0) lines. Lastly, for support by the magnetic field, we have no direct measurements. Therefore, this will be approximated with values from the literature. A first approach is to use the generic relation from Crutcher et al. (2010), which proposes that the magnetic field strength as a function of density is given by

$$B = \begin{cases} 0.01 \text{ mG} & (n_H < 300 \text{ cm}^{-3}) \\ 0.01 \, (\frac{n_H}{300})^{0.65} \text{ mG} & (n_H > 300 \text{ cm}^{-3}) \end{cases} \quad (1)$$

However, we can also work with earlier magnetic field orientation observations of the DR21 ridge (Vallée & Fiege 2006; Matthews et al. 2009; Girart et al. 2013; Zhang et al. 2014) from which it was proposed by Ching et al. (2017) that the magnetic field strength in the DR21 ridge is slightly below the Crutcher et al. (2010) relation, and that the magnetic field strength in the MDCs can be described by the relation $B \propto n_H^{0.54\pm0.30}$. Based on these results, we also use two other extrapolations for the magnetic support in the DR21 cloud as a function of density. In both cases, we start from the estimated magnetic field strength for the DR21 ridge (0.94 mG, Ching et al. 2017) and extrapolate the magnetic field strength using k=0.67 and k=0.5 (with $B \propto n_H^k$). These exponents represent two asymptotic cases: where k=0.67 is generally considered to describe the case where the magnetic field support is dominated by gravitational collapse, and k=0.5 the case where the magnetic field plays an important role in support against gravitational collapse (e.g. Basu 1997; Hennebelle et al. 2011).

To study which physical processes dominate the evolution of the DR21 cloud, the magnetic energy is calculated using

$$E_{mag} = \frac{1}{2} M V_A^2 \quad (2)$$

with M the mass in the region and V_A the Alfvén speed, which is given by $V_A = \frac{B}{\mu_0 \rho}$ with μ_0 the vacuum permeability.
The thermal and turbulent energy is calculated using

$$E_T = \frac{3}{2} M \sigma^2 \quad (3)$$

with σ the spectral linewidth of the region that is considered.
The gravitational energy is calculated with

$$E_G = -\frac{3}{5} \frac{GM^2}{R} \quad (4)$$

where G is the gravitational constant
In Fig. 9, the magnetic energy and the thermal + kinetic energy is compared with the gravitational energy as a function of the cloud radius. The thermal and turbulent support estimated from the linewidth is basically independent of the molecule that is used (^{13}CO(1-0), C^{18}O(1-0) and H^{13}CO$^+$(1-0)), with maximal values around 20% of the gravitational energy.
Fig. 9 also shows that the support by the magnetic field is highly dependent on its assumed evolution. Assuming k = 0.5 indicates that the cloud can experience significant support from the magnetic field on large scales (~ 3 pc), but gradually this magnetic support decreases leading to an increasing importance of gravitational collapse when approaching the ridge. Working with k = 0.67, the DR21 cloud evolution is strongly dominated by gravity. But when going to higher densities towards the ridge, the importance of the magnetic field increases because of the magnetic field concentration by this collapse.

3.6. Extended SiO emission in the DR21 ridge

It was already noted that the IRAM 30m observations in Fig. 5 show the presence of extended SiO(2-1) emission in the DR21 ridge. Here, we will examine the origin of this extended SiO(2-1) emission in more detail. It was already found by Duarte-Cabral et al. (2014) that there is SiO emission with a narrow linewidth towards observed MDCs with the PdB interferometer in Cygnus-X north. Three of these MDCs were located in the DR21 ridge. With the SiO observations that cover the full DR21 ridge, we now demonstrate that SiO is not only found in the MDCs but over the full DR21 ridge.
To study the origin of the detected SiO emission, the SiO(2-1) observations can be compared with the JCMT ^{12}CO(3-2) observations as they trace protostellar outflows. In Fig. 10, it is shown that there are locations in the DR21 ridge without detected protostellar outflows and only a narrow SiO(2-1) line emission that has the same linewidth as e.g. H^{13}CO$^+$(1-0) and C^{18}O(1-0). This narrow linewidth component is also present in spectra with protostellar outflows. This shows that there is a SiO(2-1) emission component over the full ridge with a typical FWHM of ~ 2-3 km s^{-1} along the line of sight.
Further inspecting the ^{12}CO(3-2) PV diagram along the DR21

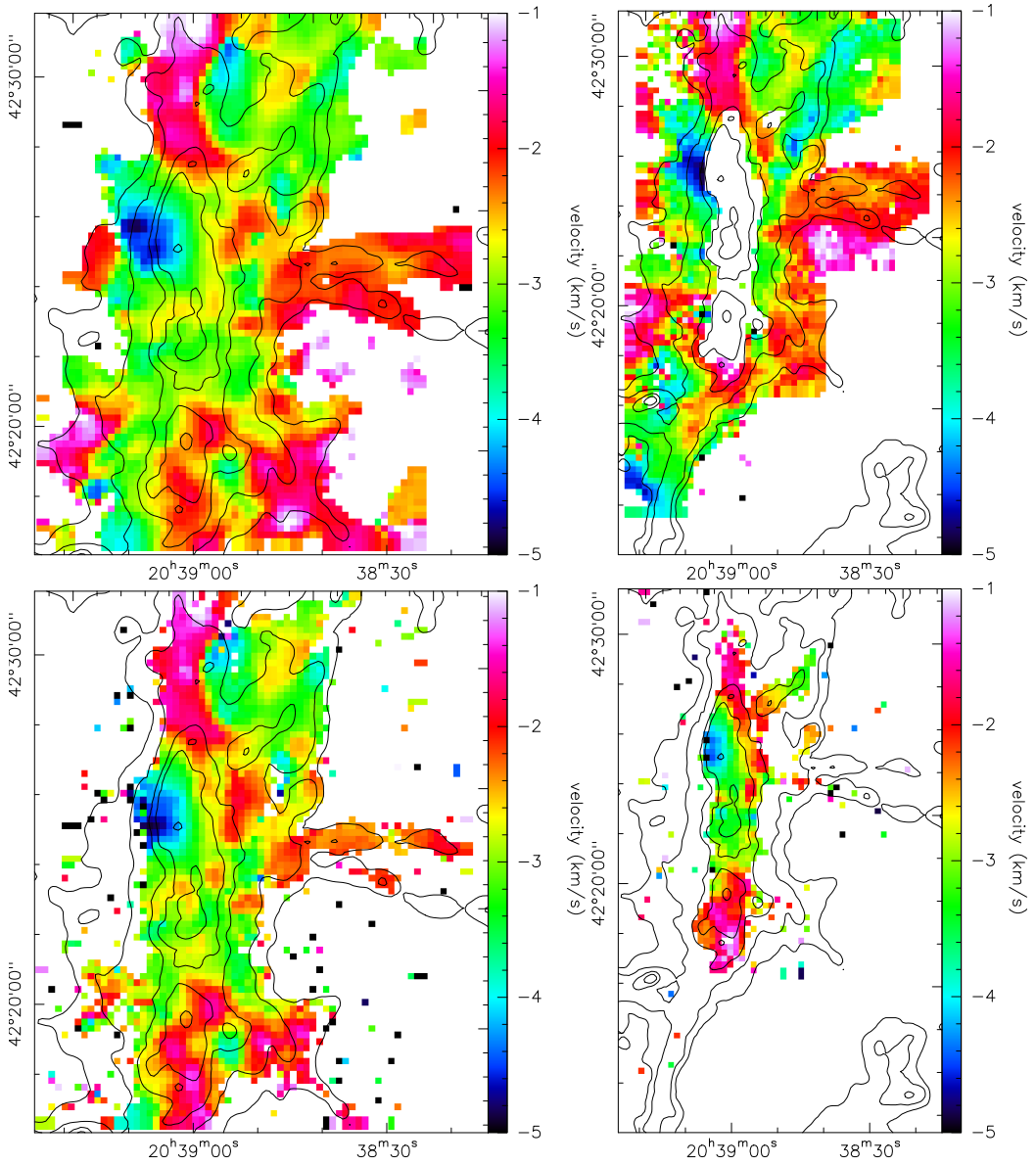

Fig. 6. Top left: The velocity map of ^{13}CO(1-0) over the DR21 ridge and subfilaments. Overplotted on the map, are the *Herschel* column density contours at N_{H_2} = 10^{22}, $2{\cdot}10^{22}$, $5{\cdot}10^{22}$, 10^{23} and $5{\cdot}10^{23}$ cm^{-2} which indicate the ridge as well as the surrounding subfilaments. **Top right:** The same for HCO$^+$(1-0), without fitting inside the DR21 ridge. **Bottom left:** The same for C^{18}O(1-0). **Bottom right:** The same for H^{13}CO$^+$.

ridge in Fig. 5, the kinematic asymmetry of the DR21 cloud is again confirmed. It is found that the brightest ^{12}CO emission is located at redshifted velocities compared to the DR21 ridge velocity at $\sim$ -3.5 km s^{-1}. The weaker emission at the velocity of the ridge can be explained as a result of self-absorption, but the lack of bright ^{12}CO(3-2) emission at blueshifted velocities compared to the ridge again strongly suggest an asymmetric accretion scenario.

4. Cygnus-X

The DR21 ridge is the most active high-mass star forming cloud in the Cygnus-X region. To discuss the evolution of the Cygnus-X region, the formation of this dense ridge and how this is related to the evolution of Cygnus-X, we will here study the structure and kinematics of the star forming gas in the Cygnus-X region.

4.1. Massive dense core distribution

From dust continuum mapping of the Cygnus-X region it was found that the Cygnus-X region contains a significant amount of massive dense cores (MDCs) (Motte et al. 2007), which was confirmed with higher sensitivity dust continuum mapping by the *Herschel* telescope (Cao et al. 2019, Bontemps et al. in prep.). In Fig. 11, the mass distribution of the MDCs from Motte et al. (2007) is presented for Cygnus-X north and south. Comparing the mass distribution in Cygnus-X north and south, demonstrates that the most massive cores are located in Cygnus-X north. This suggests that Cygnus-X north is the preferential location of mas-

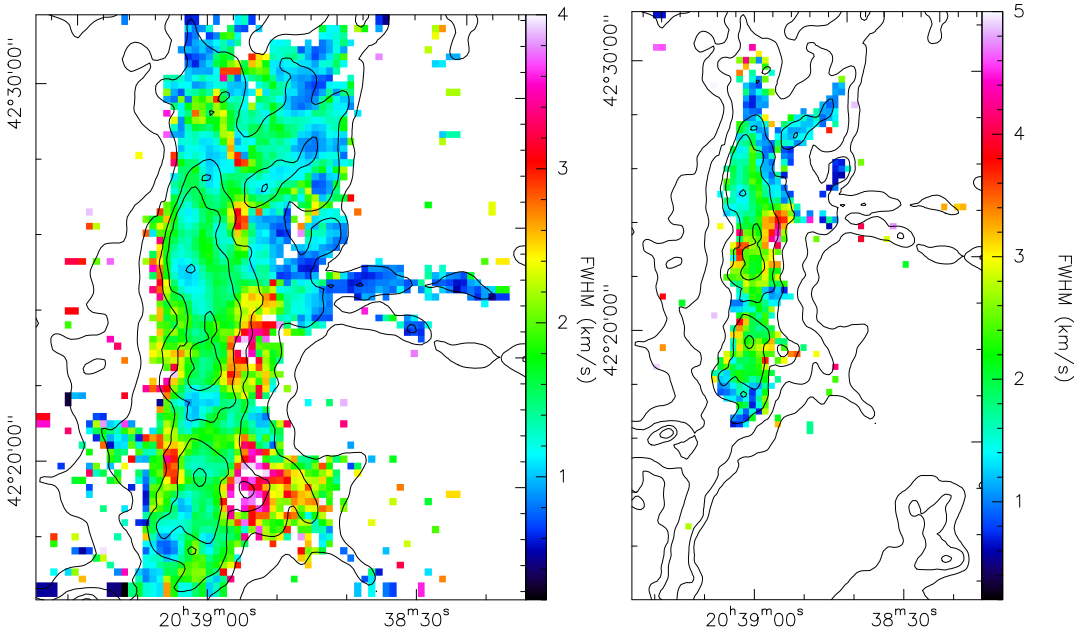

Fig. 7. Left: The FWHM map of $C^{18}O$(1-0) over the DR21 ridge and subfilaments. Overplotted on the map are the *Herschel* column density contours at N_{H_2} = 10^{22}, $2{\cdot}10^{22}$, $5{\cdot}10^{22}$, 10^{23} and $5{\cdot}10^{23}$ cm^{-2}. **Right:** The same for $H^{13}CO^+$(1-0).

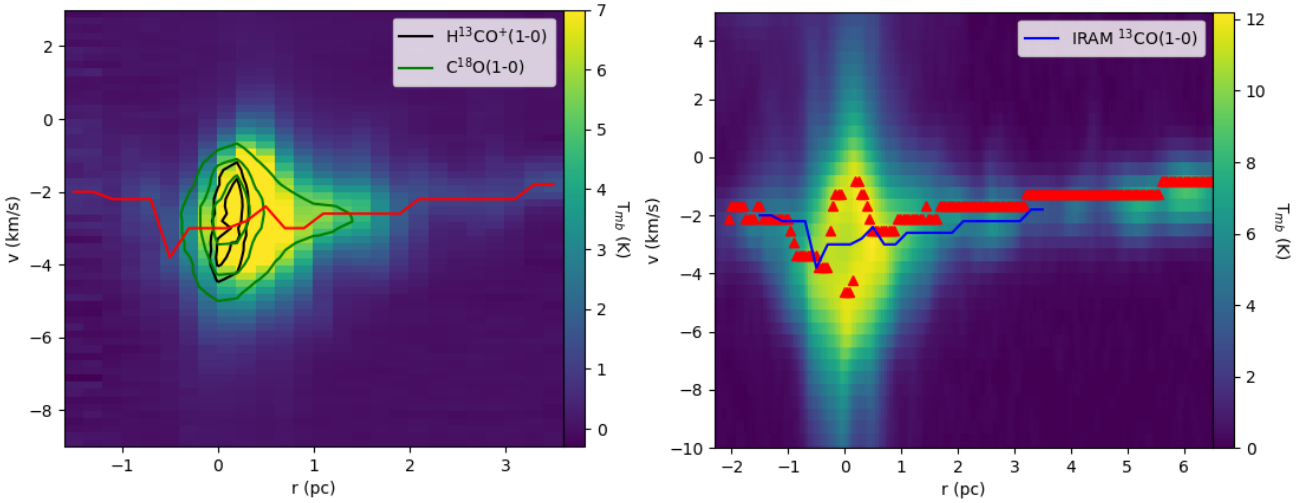

Fig. 8. Left: The ^{13}CO(1-0) PV diagram from the IRAM data, with the contours indicating the emission from $C^{18}O$(1-0) (green) and $H^{13}CO^+$(1-0) (black). The red line follows the velocity of the peak brightness as a function of the distance from the center of the ridge. This indicates that the gas surrounding the ridge is redshifted at both sides of the ridge. At the ridge, a large velocity dispersion is observed. **Right**: The PV diagram of DR21 from the JCMT ^{12}CO(3-2) data. The red triangles, indicating the velocity of the peak brightness, again show that the ambient gas is redshifted with respect to the ridge. The blue line indicates the peak brightness evolution from the IRAM ^{13}CO(1-0) data.

sive star formation, and that Cygnus-X south has limited massive star formation even though both regions appear to have a similar mass (e.g. Schneider et al. 2006).

4.2. Mass concentration in Cygnus-X North

In order to form stars, and specifically to form massive stars, dense gas is required. It is thus important to form dense, compact structures. Inspecting e.g. the integrated ^{13}CO(1-0) map in Fig. 1, it already appears that Cygnus-X north contains more compact structures than Cygnus-X south. However, it would be valuable to quantify this behaviour. Using the *Herschel* column density maps, we study the compactness in both Cygnus-X north and south for the gas with $N_{H_2} > 5{\cdot}10^{21}$ cm^{-2} to make sure that we only take into account mass associated with the Cygnus-X region. Specifically, we study the evolution of the fraction of the total mass as a function of the size of the area in which it is observed. This evolution for Cygnus-X north and south is displayed in Fig. 12, which shows that for Cygnus-X north a significantly larger fraction of the dense gas mass is located within a small region of the cloud (< 2-3 % of the total Cygnus-X north area) compared to Cygnus-X south. This demonstrates that somehow,

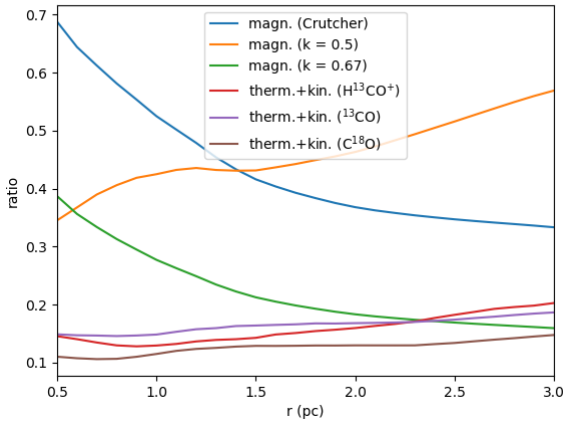

Fig. 9. The ratio of the magnetic and thermal + kinetic energy compared to the gravitational energy as a function of the radius in the DR21 cloud. The radius is centered on DR21(OH). For the thermal + kinetic energy, the linewidth of ^{13}CO(1-0), C^{18}O(1-0) and H^{13}CO$^+$(1-0) are used. This estimate does not vary strongly with regard to the line used, and is always a fraction of the gravitational energy. The three approaches to estimate the magnetic field support are also displayed. It shows, that the magnetic support is always smaller than the gravitational energy, but that its evolution highly depends on the assumptions for the magnetic field strength.

the north became significantly more compact than the south of Cygnus-X. This behaviour, found with the *Herschel* column density maps, is also confirmed with the FCRAO ^{13}CO integrated intensity map.

4.3. Velocity substructure of MDCs in Cygnus-X north

It was already shown in Schneider et al. (2006), based on the ^{13}CO FCRAO data, that one can define four velocity ranges in Cygnus-X north: -10 to 1 km s^{-1}, 1 to 6 km s^{-1}, 6 to 14 km s^{-1} and 14 to 20 km s^{-1}. The first velocity range roughly traces DR20-DR21-DR22-DR23. The second velocity range is not directly associated with any dense structures, and mainly traces rather diffuse gas. The last two ranges are associated with W75N-AFGL2620 and the DR17 pillars.
In Cygnus-X south, it was shown by Schneider et al. (2006) that there is a dominant velocity component from -10 to 3 km s^{-1}, covering a similar velocity interval as the first velocity range in Cygnus-X north. This velocity component is associated with basically all dense structures in Cygnus-X south. At slightly larger velocities of $\sim$ 5-10 km s^{-1} there is diffuse emission which might originate from the Cygnus-X rift (Schneider et al. 2006; Gottschalk et al. 2012) that appears as a coherent group of small clouds in the channel maps. This velocity structure of Cygnus-X north and south is also observed in the ^{12}CO(3-2) PV diagrams of both regions in Fig. 14.

From the *Herschel* data, dense cores were extracted in the Cygnus-X north region (Bontemps et al. in prep.). Using the FCRAO data it is possible to investigate the velocity distribution of the massive cores (i.e. with a mass above 30 M$_\odot$), and thus obtain an idea of the possible velocity distribution of the massive stars that will be formed in Cygnus-X north. The velocity for the cores with a mass above 30 M$_\odot$ was obtained by fitting the brightest C^{18}O(1-0) emission peak with a gaussian (Bonne et al. in prep.). For $\sim$90% of the cores above this mass threshold, the C^{18}O(1-0) line was detected.
Combining the velocity of all these massive dense cores, we indeed find in Fig. 13 indications of velocity substructure that is relatively independent of the minimal studied mass. Calculating the velocity dispersion in the line of sight for these MDCs, we get σ = 7.8 km s^{-1} which results in an estimated three dimensional velocity dispersion (σ_{3D}) of 14 km s^{-1}.
Inspecting the PV diagram of the ^{12}CO(3-2) JCMT data for both Cygnus-X north and south in Fig. 14, the presence of this velocity substructure for the MDCs in Cygnus-X north is confirmed. The PV diagram shows the presence of several dense substructures at different velocities between -5 to 15 km s^{-1}. Similar substructure is not observed for Cygnus-X south in Fig. 14, which indicates the presence of more diffuse ^{12}CO gas.

5. Discussion

5.1. DR21: Clump compression followed by gravitational collapse

Analysing the virial study of the DR21 cloud in Sec. 3.5 opens two asymptotic scenarios for the evolution of the DR21 cloud:
Either the magnetic field roughly follows B $\propto$ n$^{0.5}$ in the DR21 cloud. In that case the cloud evolution is significantly impacted by the magnetic field at large scales > 3 pc. The large amount of mass in the ridge then results in an increasing importance of gravitational collapse from the ridge to its MDCs. Note that such a collapse from the ridge to the MDCs can again start to increase the role of the magnetic field inside the MDCs.
The other possible scenario would more or less follow the scenario described in Hennebelle et al. (2011), where the large cloud roughly follows B $\propto$ n$^{0.67}$ and is experiencing an important gravitational collapse. This gravitational collapse then leads to an increasing role of the magnetic field, see also Fig. 9, such that the massive dense cores experience a significant magnetic support, which results in a behaviour of B $\propto$ n$^{0.5}$ for the MDCs.
A relatively important role of the magnetic field in a gravitational collapse of the MDCs can strongly limit their fragmentation and result in a high core formation efficiency (e.g Commerçon et al. 2011; Peters et al. 2011) which is observed for DR21 (Bontemps et al. 2010) and other massive star forming clumps (e.g. Palau et al. 2013; Csengeri et al. 2017).

In a simple scenario of gravitational collapse of the full DR21 cloud, it is not straightforward to explain why the vast majority of the inflowing subfilaments are redshifted with respect to the ridge. Furthermore, it is found that the subfilaments show a spatial asymmetry being dominantly located west of the ridge. We thus also have to consider the observed V-shape in the PV diagram of DR21 to understand what leads to massive star formation in DR21. A similar asymmetry and V-shape in the PV diagram was already noted for the low-mass Musca filament (Bonne et al. 2020b), where it was proposed to be the result of a cloud-cloud collision based on the simulations in Inoue & Fukui (2013); Inoue et al. (2018). A cloud-cloud collision, of the two velocity components at $\sim$ -3 km s^{-1} and $\sim$ 9 km s^{-1} in the line of sight, can thus lead to bending of the magnetic field, which gives rise to the observed asymmetric V-shape accretion scenario. In Inoue & Fukui (2013) and Bonne et al. (2020b), it is proposed that this bending of the magnetic field triggers the mass inflow towards the densest gas. The idea of a collision, resulting in the formation of the DR21 ridge, is not new. It has been proposed earlier that these two velocity components show indications of

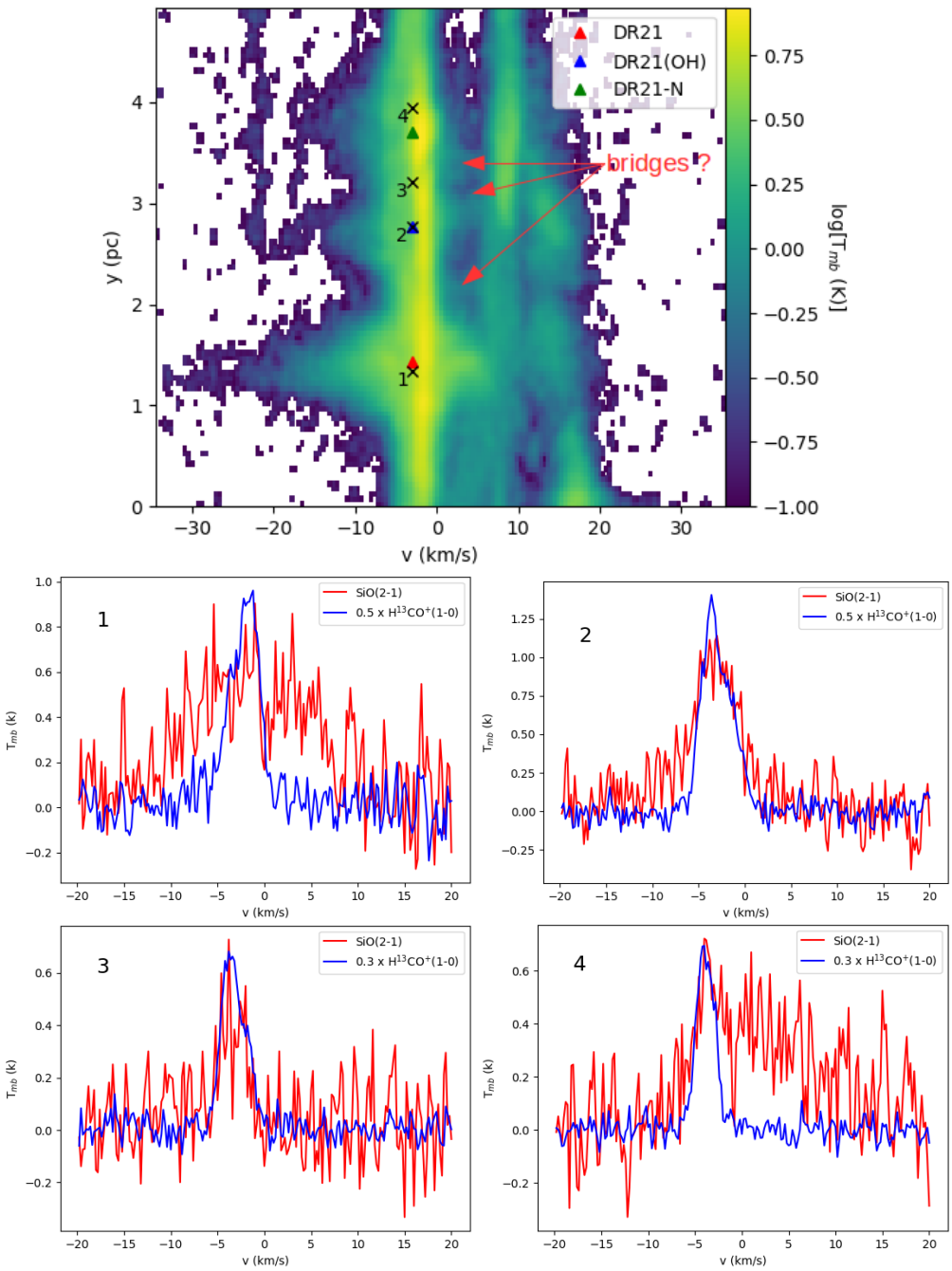

Fig. 10. Top: The ^{12}CO(3-2) PV diagram along the DR21 ridge, indicating the location of the DR21 radiocontinuum source, DR21(OH) and DR21-N (triangles) as well as the locations of the spectra shown below (crosses). This PV diagram shows the locations of protostellar outflows along the DR21 ridge. Protostellar outflows are seen as extended emission structures on the velocity axis and are located near DR21, DR21(OH) and DR21-N. However, there are also some locations along the DR21 ridge where we find no indications of a protostellar outflow (e.g. the location of spectrum 3) where possible bridges connect the two velocity components of Cygnus-X north. **Bottom**: The SiO(2-1) and $H^{13}CO^+$(2-1) spectra of the DR21 ridge at the indicated locations in the PV diagram above. These spectra show SiO emission in outflow wings as well as a narrow component. In particular spectrum 3 only shows SiO(2-1) emission in a narrow component without outflow wings.

interaction (Dickel et al. 1978; Dobashi et al. 2019).
Combining the velocity structure and virial analysis of the DR21 cloud, we thus get a two step scenario for DR21. First a cloud collision forms the massive DR21 cloud due to compression. In this compressed cloud, the bending of the magnetic field can then lead to mass accretion on the massive star forming ridge. However, because of the high density in the compressed cloud, gravity will also play an important role in guiding the inflow when the DR21 cloud has been compressed by the colliding flow. It still remains difficult to further constrain the exact

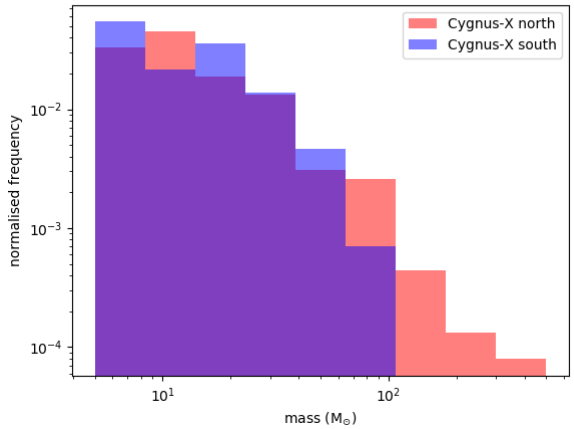

Fig. 11. The normalised core mass distribution of Cygnus-X north and south for the dense cores extracted in Motte et al. (2007).

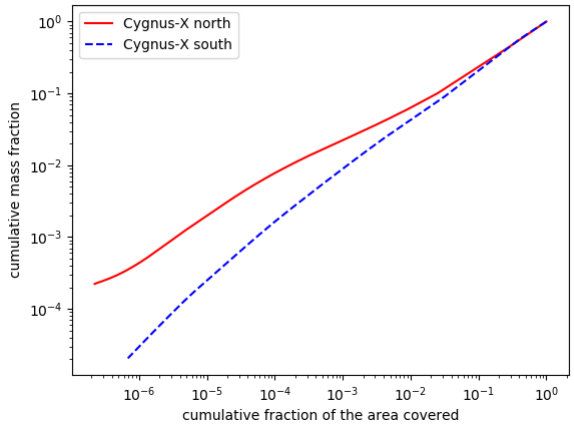

Fig. 12. The cumulative fraction of the cloud mass as a function of the fraction of the cloud area for the northern and southern region of Cygnus-X. The northern region clearly contains a larger mass fraction (up to an order of magnitude higher) in small regions ($\lesssim$ 2-3%) of the cloud. To study this compactness of the Cygnus-X regions, we use a background column density of $N_{H_2} = 5{\cdot}10^{21}$ cm^{-2}.

balance between gravity and magnetic field driven inflow with the current magnetic field information, but the observations suggest a mixed role for both processes. An important role of gravity close to the DR21 ridge could also explain the observed linewidth increase inside the DR21 ridge because of gravitationally driven accretion which is (partly) converted into turbulence (e.g. Klessen & Hennebelle 2010; Arzoumanian et al. 2013; Peretto et al. 2014). This strong gravitational acceleration near the DR21 ridge can then explain why the observed V-shape in the DR21 cloud is less pronounced than in the low-mass Musca filament.

5.2. Mass accretion on the DR21 ridge

The mass inflow towards the ridge guided by the subfilaments can be estimated using $\dot{M}_{acc} = N\pi R^2 v_{inf}\rho$ (Peretto et al. 2013), with N the number of inflowing filaments, R the radius, ρ the

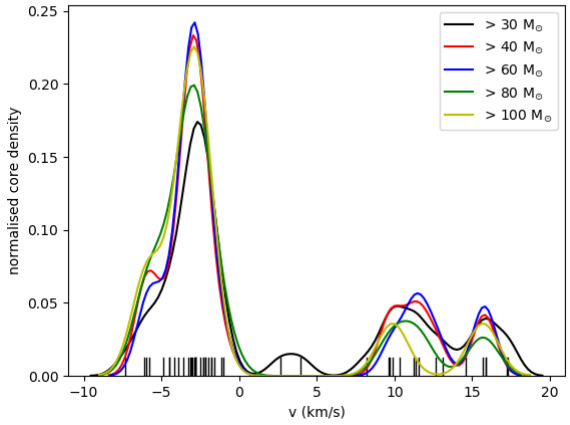

Fig. 13. The velocity distributions of the MDCs extracted by Bontemps et al. (in prep.) in Cygnus-X north, using different minimal masses to study the velocity distribution. This shows that the MDCs have velocity substructure which is relatively independent of the considered mass. The black vertical lines indicate the velocity of all dense cores more massive than 30 M$_\odot$.

density and v_{inf} the velocity of the infalling filaments. Working with 7 inflowing filaments with $n_{H_2} = 10^5$ cm^{-3}, R = 0.1 pc (Hennemann et al. 2012) and an inflow velocity of 1-2 km s^{-1}, we get an estimated mass provision rate of 1.3-2.6$\cdot 10^{-3}$ M$_\odot$ yr^{-1}. In Schneider et al. (2010), it was already shown that the F3 subfilaments continue their flow in the ridge towards DR21(OH). These subfilaments might thus directly flow towards multiple MDCs. Given their estimated mass inflow rate, this filamentary inflow can provide sufficient mass to MDCs to maintain the formation of a couple of massive stars. However, this mass inflow rate is roughly an order of magnitude lower than the required mass accretion rate ($\sim 10^{-2}$ M$_\odot$ yr^{-1}) to replenish the DR21 ridge in 1 Myr.

Considering that the mass inflow also happens off the subfilaments, we can calculate this contribution of mass inflow to the ridge. We consider inflow over the full surface of the ridge for which we assume a cylindrical geometry with R = 0.36 pc and L = 4.15 pc. For the inflow, we work with a velocity of $\sim$ 1-2 km s^{-1} and $n_{H_2} = 10^4$ cm^{-3}, which is justified by $N_{H_2} \sim 3{\cdot}10^{22}$ cm^{-2} within 1 pc of the ridge that is not directly associated with subfilaments. This results in an estimated mass accretion rate of 0.56-1.1$\cdot 10^{-2}$ M$_\odot$ yr^{-1}, which might be able in combination with the filamentary inflow to roughly replenish the DR21 ridge in 1-2 Myr. This is an expected lifetime for the DR21 ridge when taking the expression from Clarke & Whitworth (2015) for the timescale of a free-fall longitudinal collapse for a filament

$$\tau_{ff} = (0.49 + 0.26A)(Gn_{H_2})^{\frac{-1}{2}} \quad (5)$$

where A is the initial aspect ratio of the filament half length over the filament radius and n_{H_2} the average density. This results in a τ_{ff} of 0.38 Myr. Taking into account support from the magnetic field, which is roughly perpendicular to the DR21 ridge at its center (Vallée & Fiege 2006; Matthews et al. 2009), and possibly some turbulent support, 1-2 Myr is an appropriate time scale to replenish the DR21 ridge.
Note that in contrast to the subfilaments it is not expected that

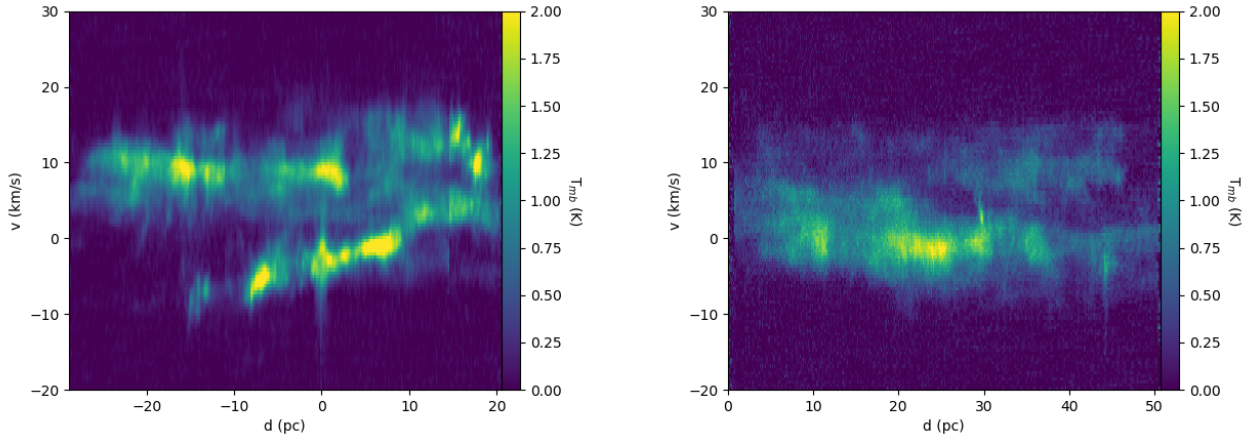

Fig. 14. Left: The PV diagram of Cygnus-X north along the celestial equator. The PV diagram is centered on the location of the DR21 ridge. This shows a significant amount of dense substructure between -5 and 15 km s^{-1} in Cygnus-X north. It is also found that elongated diffuse structures in velocity space connect the different velocity components. This so-called bridging is inherently predicted by cloud-cloud collision simulations. **Right**: The same for Cygnus-X south, showing there is way less dense substructure than in Cygnus-X north.

this off-filament inflow will directly provide mass to the MDCs. This inflow will rather encounter the DR21 ridge as a discontinuity, such that it will only provide mass accretion on the ridge. However, the gravitational collapse of the ridge, seen e.g. with HCO^+, will then provide more mass to the MDCs to maintain very active high-mass star formation over the full ridge. We thus propose a scenario where filamentary inflow directly provides mass to the MDCs in the ridge because of gravitational attraction by the mass of the ridge ($\sim 10^5$ $M_\odot$). However, once feedback from the formed high-mass stars prevents continuous low-density mass accretion on the ridge, the ridge will quickly disappear and consequently end the active high-mass star formation at this location. This scenario implies that high-mass star formation only happens over a short fraction of the total star formation time for a cloud. This shortly maintained phase of high-mass star formation by the ridge can fit with the observed shallow slope of the core mass function for high-mass protostars (Motte et al. 2018b; Liu et al. 2018) compared to the power law tail of the initial mass function, as well as the slightly shallower initial mass functions in young clusters (< 4 Myr) of Cygnus-X (Maia et al. 2016).

5.3. A GMC collision resulting in high-mass star formation in Cygnus-X north

In the previous section, observations were presented that indicate that the formation of the DR21 ridge is the result of a colliding flow which compresses the cloud and bends the magnetic field. Furthermore, it was noted that the two components that led to the formation of the DR21 ridge are present over the full Cygnus-X north region and that MDCs over the full region are associated with these two velocity components. This strongly suggests that the high-mass star formation activity is triggered by a GMC collision in Cygnus-X north. This also fits with observations of W75N, which is kinematically more complicated, but also shows spatial and kinematic asymmetries that are expected for the proposed GMC collision scenario (Bonne et al., in prep.).
The observed velocity substructure with the MDCs and in the PV diagram are also predicted by synthetic observations of cloud-cloud collision simulations (e.g. Haworth et al. 2015; Bisbas et al. 2017). Synthetic observations of cloud-cloud collisions also focus on gas bridging between the two velocity components in PV diagrams (Haworth et al. 2015; Bisbas et al. 2017). In Dobashi et al. (2019), indications of CO bridging between the two velocity components near DR21 were found in the presented average ^{12}CO(1-0) spectra. Inspecting Fig. 10, also indicates bridges of CO gas between the two velocity components towards DR21, but it is observed that one has to take care with confusion in the PV diagram from protostellar outflows. The same is valid for Fig. 14 where diffuse bridges can be seen over the full Cygnus-X north region, which look similar to synthetic observations presented in Haworth et al. (2015).

This GMC collision scenario might also provide an explanation for the observed SiO emission in the DR21 ridge as well as the other presented MDCs of Cygnus-X north in Duarte-Cabral et al. (2014). Because of the high-velocity (> 10 km s^{-1}) of the GMC collision this could release SiO into the gas phase (Gusdorf et al. 2008b). This high-velocity GMC collision releasing SiO into the gas phase would also explain, in combination with the significantly lower column density of the Musca filament, why SiO emission was not detected in the Musca filament.
It is however not possible to exclude that the observed narrow SiO emission in Cygnus-X originates from shocks related to accretion on the DR21 ridge and MDCs. Though these accretion shocks would be associated with significantly lower velocities which are not necessarily expected to sputter Si from the dust grains mantels.

5.4. Evolutionary stages in Cygnus-X

In order to discuss a full scenario for the evolution of Cygnus-X in the next section and how this results in massive star formation, we will here combine several results from this and other studies to propose a spatial sequence of evolutionary stages in Cygnus-X.
We start from the results in Comerón & Pasquali (2012) where it was proposed that OB9 is older than OB2 in Cygnus-X. Indeed, using the estimated stellar ages in Comerón & Pasquali (2012),

we obtain an average age of 5.9 ± 5.6 Myr for OB2 and 13.9 ± 9.0 Myr for OB9. In both OB associations, star formation happened over several Myrs which explains the large standard deviations on the average age. To go a step further, we also examine the radio continuum maps that have been made of Cygnus-X with the Effelsberg telescope at 11 cm (Furst et al. 1990; Reich et al. 1990) which mostly traces thermal HII gas that is ionised by massive (proto)stars in Cygnus-X (Xu et al. 2013). This radio continuum map is presented in Fig. 5.4 with overlaid contours of the FCRAO ^{13}CO emission. A first thing that can be noted is that Cygnus-X south contains way less continuum emission than the north, except for the surroundings of OB9 which is located in the west of Cygnus-X south. Examining Cygnus-X north in more detail, strong radio continuum emission is observed at certain locations which confirms that Cygnus-X north is actively forming or has recently formed massive stars. The bright large scale radio continuum emission is most notable in DR23, DR17, DR22 and DR20. However, in the most northern area of Cygnus-X, specifically the DR21 ridge and W75N, the radio continuum emission is way less dominant. Furthermore, classification of protostars in Cygnus-X north with Spitzer data in Beerer et al. (2010) showed that most class 0 and I protostars are located in the DR21 ridge and W75N. These are the locations of the most massive MDCs in the full Cygnus-X complex (Motte et al. 2007). This strongly suggests that these two most northern massive structures in Cygnus-X north are still at an earlier stage of massive star formation.
Combining the locations of MDCs, the age of OB stars and radio continuum, we get the following results: Cygnus-X south contains a limited amount of ionised gas and no strong indications of significant massive star formation in the direct future. On the other hand, we get a quite linear spatial evolutionary sequence from south-west to north(-east) for the formation of massive stars: starting at OB9, going over OB2 towards Cygnus-X north which is still at the earliest stages in the most northern area. This evolutionary sequence is indicated with an arrow in Fig. 5.4.

5.5. The origin of high-mass star formation in Cygnus-X

The age gradient of massive star formation and the fact that Cygnus-X south shows limited massive star formation, suggests that a mechanism is progressively triggering massive star formation in Cygnus-X. However, this mechanism is currently not affecting Cygnus-X south. In sec. 5.3 it was proposed for Cygnus-X north that the active high-mass star formation there was triggered by a GMC collision, which fits with Cygnus-X north being significantly more compact than the south. In numerical simulations it was shown that a cloud-cloud collision naturally leads to a rapid and strong compactification of the gas in filamentary structures (e.g. Inoue et al. 2018).

As there are multiple OB associations in Cygnus-X, this produces expanding shells which have been proposed to result in sequential high-mass star formation (Elmegreen & Lada 1977). In Inutsuka et al. (2015) it was further proposed that expanding shells as a result of radiation pressure or supernovae can lead to a GMC collision which triggers the high-mass star formation activity. It is thus a plausible scenario that the GMC collision observed in Cygnus-X north is triggered by expanding shells from OB2 and/or OB9. This scenario is schematically shown in Fig. 16. Furthermore, expanding shells from OB stars and associations tend to have velocities of the order of 10 km s^{-1} (e.g. Ferriere et al. 1991; Hosokawa & Inutsuka 2006; Pabst et al. 2019) which can provide an explanation for the collision velocity in Cygnus-X north.

Though this expanding shell scenario from OB2 and/or OB9 could provide an explanation for the observed scenario in Cygnus-X north, it also leaves a couple of questions that have no straightforward answer. First of all there is the fact that Cygnus-X south is significantly less compact and as a result not forming a lot of massive stars. It is somewhat surprising that the northern region experiences a completely different effect from the expanding shells than the southern region. Possibly this is purely the result of different conditions in the regions, where Cygnus-X north has the presence of a second GMC to create a GMC collision during the passage of an expanding shell as described in Inutsuka et al. (2015).
Another remarkable feature of the observed high-mass star formation history in Cygnus-X, is its spatial linearity in the plane of the sky from OB9 over OB2 to Cygnus-X north, see Fig. 5.4. Again, this is not necessarily a feature that remains unexplained by the expanding shell scenario, and can be a projection effect. However, it also led us to consider another scenario for the observed collision in Cygnus-X north, which is described below.

Instead of expanding shells from OB9 and OB2, we also consider that the observed collision in Cygnus-X north is the result of a much larger GMC collision in the Cygnus-X region. This is schematically shown in Fig. 16. It can be considered that the -3 km s^{-1} velocity component, observed over the 100 pc full Cygnus-X region, is colliding with another GMC at a velocity in the line of sight of $\sim$ 7 km s^{-1} and that this GMC collision first formed OB9, followed by OB2 and is now in the last part of the collision which results in the observed current high-mass star formation in Cygnus-X north. This 100 pc scale GMC collision provides a straightforward explanation for the linearity in the plane of the sky for the massive star formation history. Evidently, this 100 pc scale GMC collision does not necessarily hit the full cloud at -3 km s^{-1} which could explain the lack of high-mass star formation in Cygnus-X south. What could drive this 100 pc scale GMC collision is however not directly evident. It might be driven by large scale expanding shells. As Cygnus-X is a very complex region with a wide range of expanding structures, this scenario is not necessarily unrealistic. However, it should be noted that in this 100 pc scale GMC collision scenario the presence of expanding shells from OB2 and OB9 are not included. Possibly this could lead to a second wave of (high-mass) star formation which further increases the star formation complexity of the Cygnus-X region. Another possibility might be that the presence of the Sagittarius spiral arm plays a role in triggering such a large scale GMC collision (Dobbs et al. 2015; Duarte-Cabral & Dobbs 2016).

With the information from the two velocity components that are colliding in Cygnus-X north, we can check whether their velocity difference along the line of sight of $\sim$ 10 km s^{-1} can fit with the time scale of the evolutionary sequence found in the previous section. For this, we use the distance between OB9 and OB2, and OB2 and DR21 in the plane of the sky (which is $\sim$ 50 pc for both distances). We combine this with the estimated ages of the OB stars in OB9 and OB2, and the fact that DR21 has started the process of massive star formation. In terms of age for the OB stars this gives 13.9 Myr, 5.9 Myr and 0 Myr for OB9, OB2 and DR21, respectively. These results are presented in Tab. 1 and gives an estimated velocity of 6.4 km

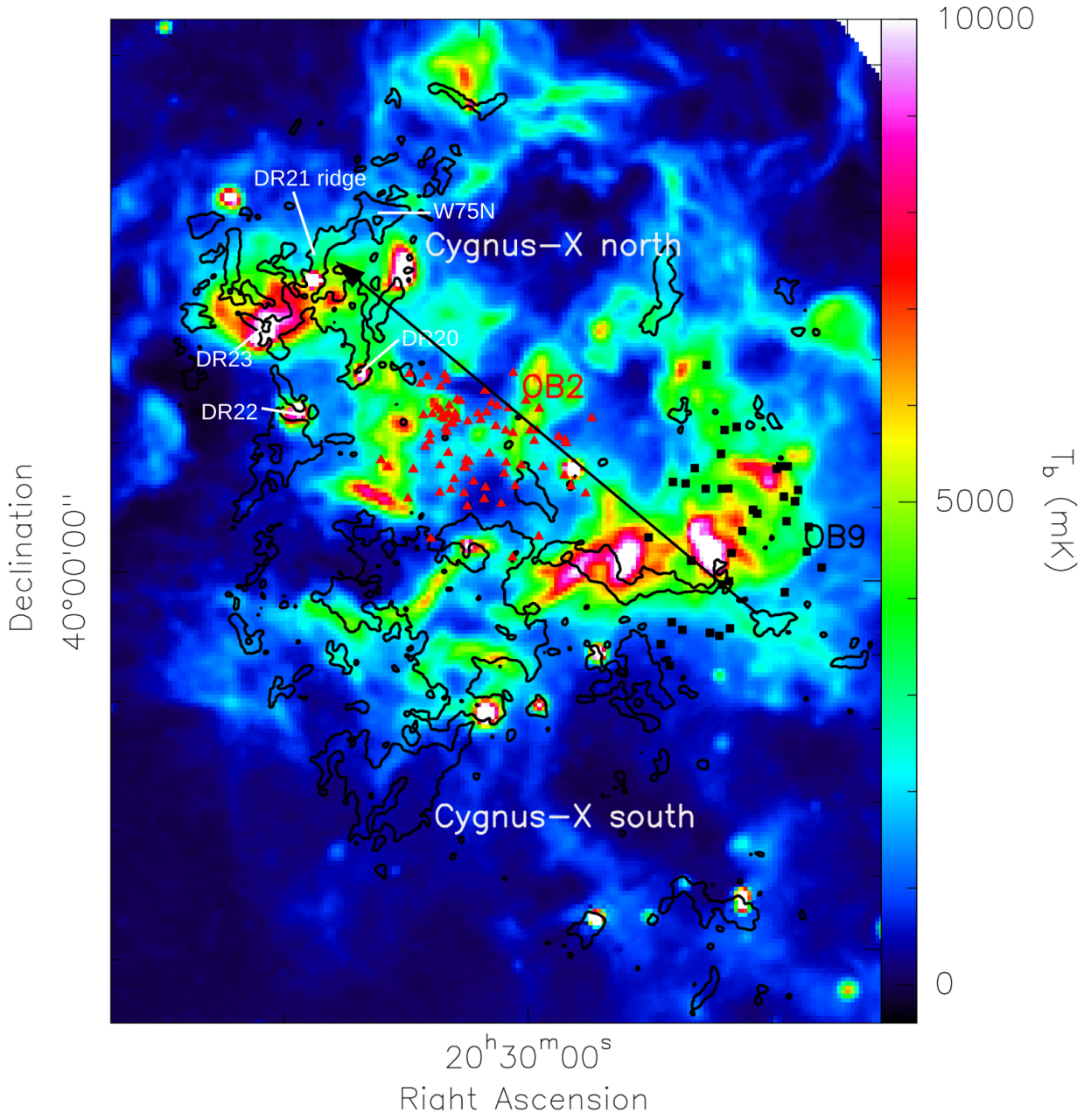

Fig. 15. The radio continuum emission at 11 cm, observed by the Effelsberg telescope (Furst et al. 1990; Reich et al. 1990). The overlaid contours indicate the locations where the integrated brightness of ^{13}CO(1-0), observed with the FCRAO telescope, is above 4 K km s^{-1}. The red triangles indicate the OB stars associated with OB2 and the black squares indicate the OB stars associated with OB9 (Comerón & Pasquali 2012). The black arrow indicates the proposed spatial time evolution for high-mass star formation from older to younger based on Comerón & Pasquali (2012).

s^{-1} between OB9 and OB2, and an estimated velocity of 8.6 km s^{-1} between OB2 and DR21. These characteristic velocities that describe the age gradient in Cygnus-X are similar to the velocity difference between the two velocity components in Cygnus-X north. This indicates that the age gradient in Cygnus-X could be associated with the observed two velocity components in Cygnus-X north, and thus that a 100 pc scale collision of these two velocity components could be responsible for the high-mass star formation observed in Cygnus-X. However, as the typical velocity of expanding shells is of the order of 10 km s^{-1} this progression speed of high-mass star formation can also fit with expanding shells from OB2 and OB9.

In conclusion, it does not appear possible with current observations to distinguish the possible triggers of the GMC collision in Cygnus-X north. Future dedicated observations will be necessary to unveil the mechanism responsible for this collision in Cygnus-X.

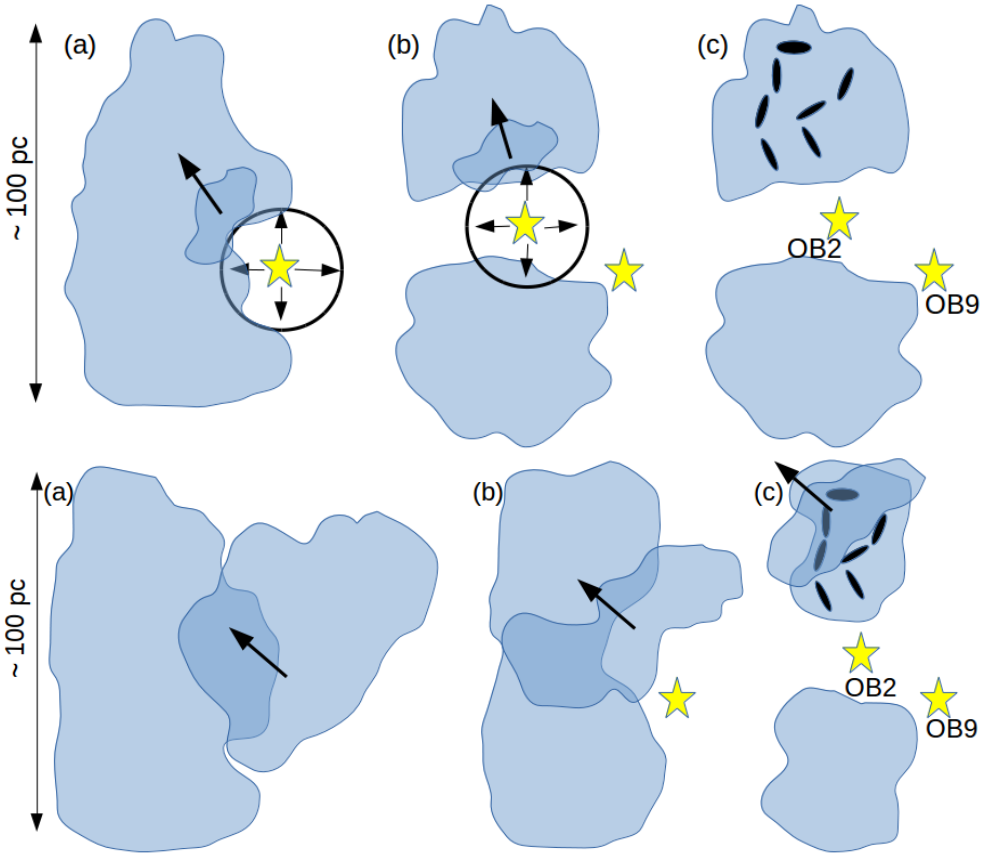

Fig. 16. Top: A possible scenario for the evolution of the Cygnus-X region, where expanding shells from previously formed OB associations result in a GMC collisions that form other OB associations. The clouds are represented by the blue regions. (a) The expanding shell driven by OB9 provokes a GMC collision which results in the formation of the OB2 association. (b) The expanding shell driven by OB2 (or OB9) provokes a GMC collision in Cygnus-X north. (c) This collision results in the observed massive ridges and filament hubs, indicated in black, which actively form high-mass stars. **Bottom:** An alternative scenario for the evolution of the Cygnus-X region. (a) A 100 pc scale GMC collides in Cygnus-X. This compresses the gas which results in the formation of OB9. Because of the relative velocity of the GMC collision, it will not hit Cygnus-X south. (b) The collision continues, compressing the central region between Cygnus-X north and south which results in OB2. (c) Now we witness the last phase of this GMC collision in Cygnus-X north, leading to its active high-mass star formation.

5.6. The formation of an OB association in Cygnus-X north from a GMC collision

Calculating the mass of Cygnus-X north from the *Herschel* data, using a background N_{H_2} = 5·10^{21} cm^{-2} (Schneider et al., in prep.), we get a total dense gas (A_V > 8) mass of 0.7·10^5 $M_\odot$ for Cygnus-X north. Based on the relatively universal star formation efficiency in molecular clouds (e.g. Lada et al. 2010; Shimajiri et al. 2017), this allows to estimate the stellar mass that can be formed in Cygnus-X north. Taking the total dense gas mass, we get a star formation rate around 3.2·10^{-3} $M_\odot$ yr^{-1}. Working under the assumption that star formation can go on for ~ 5 Myr, which is observed for OB2 and OB9, this suggests that Cygnus-X north is capable to form a total stellar mass of 1.6·10^4 $M_\odot$. This is of the same order as the estimated stellar mass of OB2 (Wright et al. 2015), and strongly suggests that Cygnus-X north is forming an OB association that might be very similar to OB2. That Cygnus-X north might be forming an OB association was already indicated by Comerón et al. (2008) based on the presence of early-type stars, associated with nearby HII regions, that do not yet have a detailed spectral classification in the near-infrared.

For OB2, spatial and velocity substructure was observed (Wright et al. 2014, 2016) with a typical size of ~ 0.5 pc (Arnold et al. 2020), while spatial substructure in OB9 was outlined in Schneider et al. (2007). In this scenario of one or more GMC collision(s) that form OB associations in Cygnus-X, the dense gravitationally collapsing hubs and ridges (e.g. DR21, DR22, W75N,...) contain the MDCs that can form OB stars. The GMC collision scenario in Cygnus-X north (as a result of expanding shells from OB9/OB2 or 100 pc scale GMC collision) also naturally leads to spatial and kinematic substructure in a young OB association, see Sec. 4.3, similar to other OB associations.

In Wright et al. (2016), it was found that OB2 has a three-dimensional velocity dispersion of 17.8 km s^{-1}, which is similar to the 14 km s^{-1} velocity dispersion of the MDCs in Cygnus-X north. On the other hand, the two velocity components that drive the high-mass star formation in Cygnus-X north have a velocity difference of ~ 10 km s^{-1} along the line of sight, which gives an estimated three-dimensional velocity difference of $\sqrt{3}$·10 km s^{-1} = 17 km s^{-1}. This suggests that the velocity of the GMC collision that triggers the formation of an OB association then provides an explanation for the observed velocity dispersion of the resulting OB association. In both scenarios, expanding shells

	OB9		OB2		DR21
d		50 pc		50 pc	
t	13.9 Myr		5.9 Myr		0 Myr
Δt		8 Myr		5.9 Myr	
v_{char}		6.4 km s^{-1}		8.6 km s^{-1}	

Table 1. The typical distance (d) between OB9, OB2 and DR21, the estimated age (t) and age difference (Δt) of the three regions, and the resulting characteristic velocity associated with the spatial progression of massive star formation.

with v $\sim$ 10-20 km s^{-1} or a 100 pc scale GMC collision, this proposed relation between the GMC collision velocity and the velocity dispersion of the OB association assumes that OB2 has not experienced strong gravitational relaxation yet which was concluded in Wright et al. (2014). Finally, if OB associations are indeed formed by GMC collisions, this naturally explains why an association might disperse in the future.

6. Conclusion

We have presented new IRAM 30m observations of the DR21 cloud, and combined the first results from this data with *Herschel*, JCMT and FCRAO data of the full Cygnus-X region.

We find that the DR21 ridge is accreting from a spatially and kinematically asymmetric inflow that is particularly visible with the subfilaments. In the PV diagram, this asymmetric inflow is seen as a V-like shape with the DR21 ridge at the blueshifted apex of the V-like shape. Furthermore, virial analysis of the DR21 cloud indicates that gravity plays a significant role in the evolution of the DR21 cloud. Combining the observed asymmetric inflow with the presence of two interacting velocity components near DR21, strongly suggests that a high-velocity ($\sim$ 17 km s^{-1}) colliding flow has formed the DR21 cloud. The initial bending of the magnetic field due to this collision then explains the observed asymmetric inflow in a gravity dominated cloud. Massive star formation in the DR21 ridge is thus the result of a high-velocity cloud compression followed by a gravitational collapse of the compressed cloud. It is found that off-filament inflow from the full cloud is necessary to replenish the DR21 ridge which is key for the active high-mass star formation. When this accretion on the ridge is halted by feedback, high-mass star formation will end in the DR21 cloud. High-mass star formation might thus be only a short phase of the star formation process of the DR21 cloud. The IRAM 30m observations also unveil extended SiO(2-1) emission in the ridge with a narrow linewidth similar to other optically thin tracers such as $H^{13}CO^+$(1-0).

Studying the kinematics of Cygnus-X north, we find evidence of a recent GMC collision which is responsible for the noteworthy compactness of Cygnus-X north compared to Cygnus-X south (which shows no signs of a recent GMC collision). The compression by the collision then explains why Cygnus-X north is actively forming a significant amount of high-mass stars while Cygnus-X south is not. This high-velocity GMC collision could also provide an explanation for the observed extended SiO(2-1) emission in the DR21 ridge. Studying the full Cygnus-X region, we find that the age gradient of massive star formation from OB9 over OB2 to Cygnus-X north fits with the velocity of the observed GMC collision in Cygnus-X north as well as the typical velocities of expanding shells. This opens two possible scenarios for the GMC collision in Cygnus-X north. Either the collision is driven by expanding shells from the OB2 and/or OB9 associations, or it is the result of a larger 100 pc scale GMC collision that already was responsible for the formation of OB2 and OB9. It is not possible with current observations to differentiate both scenarios.

We find that the massive star forming MDCs in Cygnus-X north have velocity substructure and a 3D velocity dispersion of 14 km s^{-1}, similar to the 3D velocity dispersion found for the OB stars of OB2 in a recent study. The $0.7{\cdot}10^5$ $M_\odot$ of dense gas in Cygnus-X north is capable to form a $1.6{\cdot}10^4$ $M_\odot$ stellar mass within 5 Myr. This is close to the stellar mass of OB2 and the formation time of OB2, suggesting that we are witnessing in Cygnus-X north the formation of an OB association that is similar to OB2. We thus obtain a scenario where OB associations in Cygnus-X form as a result of one or more GMC collisions. The formation of an OB association as the result of a GMC collision, which produces massive star forming ridges and hubs, naturally explains several of their observed properties such as their spatial and kinematic substructure and the fact that OB associations can disperse in the near future.

Acknowledgements.

References

Ambartsumian, V. A. 1947, The evolution of stars and astrophysics
Arnold, B., Goodwin, S. P., & Wright, N. J. 2020, MNRAS, 495, 3474
Arzoumanian, D., André, P., Peretto, N., & Könyves, V. 2013, A&A, 553, A119
Arzoumanian, D., Shimajiri, Y., Inutsuka, S.-i., Inoue, T., & Tachihara, K. 2018, PASJ, 70, 96
Ballesteros-Paredes, J., Vázquez-Semadeni, E., Palau, A., & Klessen, R. S. 2018, MNRAS, 479, 2112
Bastian, N., Ercolano, B., Gieles, M., et al. 2007, MNRAS, 379, 1302
Basu, S. 1997, ApJ, 485, 240
Baumgardt, H. & Kroupa, P. 2007, MNRAS, 380, 1589
Beerer, I. M., Koenig, X. P., Hora, J. L., et al. 2010, ApJ, 720, 679
Beuther, H., Henning, T., Linz, H., et al. 2015, A&A, 581, A119
Bisbas, T. G., Tanaka, K. E. I., Tan, J. C., Wu, B., & Nakamura, F. 2017, ApJ, 850, 23
Blaauw, A. 1964, ARA&A, 2, 213
Bonne, L., Schneider, N., Bontemps, S., et al. 2020, A&A, 641, A17
Bonnell, I. A. & Bate, M. R. 2006, MNRAS, 370, 488
Bonnell, I. A., Bate, M. R., Clarke, C. J., & Pringle, J. E. 2001, MNRAS, 323, 785
Bonnell, I. A., Smith, R. J., Clark, P. C., & Bate, M. R. 2011, MNRAS, 410, 2339
Bonnell, I. A., Vine, S. G., & Bate, M. R. 2004, MNRAS, 349, 735
Bontemps, S., Motte, F., Csengeri, T., & Schneider, N. 2010, A&A, 524, A18
Cao, Y., Qiu, K., Zhang, Q., et al. 2019, ApJS, 241, 1
Carpenter, J. M. 2000, AJ, 120, 3139
Ching, T.-C., Lai, S.-P., Zhang, Q., et al. 2017, ApJ, 838, 121
Clarke, S. D. & Whitworth, A. P. 2015, MNRAS, 449, 1819
Comerón, F. & Pasquali, A. 2012, A&A, 543, A101
Comerón, F., Pasquali, A., Figueras, F., & Torra, J. 2008, A&A, 486, 453
Comerón, F., Pasquali, A., Rodighiero, G., et al. 2002, A&A, 389, 874
Commerçon, B., Hennebelle, P., & Henning, T. 2011, ApJ, 742, L9
Cong, H. I. L. 1977, PhD thesis, Columbia University
Crutcher, R. M., Wandelt, B., Heiles, C., Falgarone, E., & Troland, T. H. 2010, ApJ, 725, 466
Csengeri, T., Bontemps, S., Schneider, N., Motte, F., & Dib, S. 2011a, A&A, 527, A135
Csengeri, T., Bontemps, S., Schneider, N., et al. 2011b, ApJ, 740, L5
Csengeri, T., Bontemps, S., Wyrowski, F., et al. 2017, A&A, 600, L10
Csengeri, T., Leurini, S., Wyrowski, F., et al. 2016, A&A, 586, A149
Csengeri, T., Urquhart, J. S., Schuller, F., et al. 2014, A&A, 565, A75
de Zeeuw, P. T., Hoogerwerf, R., de Bruijne, J. H. J., Brown, A. G. A., & Blaauw, A. 1999, AJ, 117, 354
Dickel, J. R., Dickel, H. R., & Wilson, W. J. 1978, ApJ, 223, 840
Dobashi, K., Shimoikura, T., Katakura, S., Nakamura, F., & Shimajiri, Y. 2019, PASJ, 71, S12
Dobbs, C. L. 2008, MNRAS, 391, 844
Dobbs, C. L., Pringle, J. E., & Duarte-Cabral, A. 2015, MNRAS, 446, 3608
Downes, D. & Rinehart, R. 1966, ApJ, 144, 937
Drew, J. E., Greimel, R., Irwin, M. J., & Sale, S. E. 2008, MNRAS, 386, 1761
Duarte-Cabral, A., Bontemps, S., Motte, F., et al. 2014, A&A, 570, A1
Duarte-Cabral, A., Bontemps, S., Motte, F., et al. 2013, A&A, 558, A125
Duarte-Cabral, A. & Dobbs, C. L. 2016, MNRAS, 458, 3667

Duarte-Cabral, A., Dobbs, C. L., Peretto, N., & Fuller, G. A. 2011, A&A, 528, A50
Duarte-Cabral, A., Fuller, G. A., Peretto, N., et al. 2010, A&A, 519, A27
Elmegreen, B. G. 2002, ApJ, 564, 773
Elmegreen, B. G. & Hunter, D. A. 2010, ApJ, 712, 604
Elmegreen, B. G. & Lada, C. J. 1977, ApJ, 214, 725
Ferriere, K. M., Mac Low, M.-M., & Zweibel, E. G. 1991, ApJ, 375, 239
Fukui, Y., Inoue, T., Hayakawa, T., & Torii, K. 2019, arXiv e-prints, arXiv:1909.08202
Fukui, Y., Torii, K., Ohama, A., et al. 2016, ApJ, 820, 26
Furst, E., Reich, W., Reich, P., & Reif, K. 1990, A&AS, 85, 691
Furukawa, N., Dawson, J. R., Ohama, A., et al. 2009, ApJ, 696, L115
Galván-Madrid, R., Zhang, Q., Keto, E., et al. 2010, ApJ, 725, 17
Girart, J. M., Frau, P., Zhang, Q., et al. 2013, ApJ, 772, 69
Girichidis, P., Federrath, C., Banerjee, R., & Klessen, R. S. 2012, MNRAS, 420, 613
Goodwin, S. P. & Bastian, N. 2006, MNRAS, 373, 752
Gottschalk, M., Kothes, R., Matthews, H. E., Land ecker, T. L., & Dent, W. R. F. 2012, A&A, 541, A79
Gusdorf, A., Cabrit, S., Flower, D. R., & Pineau Des Forêts, G. 2008a, A&A, 482, 809
Gusdorf, A., Pineau Des Forêts, G., Cabrit, S., & Flower, D. R. 2008b, A&A, 490, 695
Hacar, A., Kainulainen, J., Tafalla, M., Beuther, H., & Alves, J. 2016, A&A, 587, A97
Hanson, M. M. 2003, ApJ, 597, 957
Hartmann, L. & Burkert, A. 2007, ApJ, 654, 988
Haworth, T. J., Tasker, E. J., Fukui, Y., et al. 2015, MNRAS, 450, 10
Hennebelle, P., Commerçon, B., Joos, M., et al. 2011, A&A, 528, A72
Hennemann, M., Motte, F., Schneider, N., et al. 2012, A&A, 543, L3
Hill, T., Motte, F., Didelon, P., et al. 2011, A&A, 533, A94
Hill, T., Motte, F., Didelon, P., et al. 2012, A&A, 542, A114
Hills, J. G. 1980, ApJ, 235, 986
Hosokawa, T. & Inutsuka, S.-i. 2006, ApJ, 646, 240
Inoue, T. & Fukui, Y. 2013, ApJ, 774, L31
Inoue, T., Hennebelle, P., Fukui, Y., et al. 2018, PASJ, 70, S53
Inutsuka, S.-i., Inoue, T., Iwasaki, K., & Hosokawa, T. 2015, A&A, 580, A49
Jackson, J. M., Whitaker, J. S., Rathborne, J. M., et al. 2019, ApJ, 870, 5
Jiménez-Serra, I., Caselli, P., Tan, J. C., et al. 2010, MNRAS, 406, 187
Johnson, H. L. & Morgan, W. W. 1954, ApJ, 119, 344
Kiminki, D. C., Kobulnicky, H. A., Kinemuchi, K., et al. 2007, ApJ, 664, 1102
Klessen, R. S. & Hennebelle, P. 2010, A&A, 520, A17
Knödlseder, J. 2000, A&A, 360, 539
Kramer, C., Penalver, J., & Greve, A. 2013
Kruijssen, J. M. D., Pelupessy, F. I., Lamers, H. J. G. L. M., Portegies Zwart, S. F., & Icke, V. 2011, MNRAS, 414, 1339
Krumholz, M. R., McKee, C. F., & Bland -Hawthorn, J. 2019, ARA&A, 57, 227
Kumar, M. S. N., Davis, C. J., Grave, J. M. C., Ferreira, B., & Froebrich, D. 2007, MNRAS, 374, 54
Lada, C. J. & Lada, E. A. 2003, ARA&A, 41, 57
Lada, C. J., Lombardi, M., & Alves, J. F. 2010, ApJ, 724, 687
Liu, M., Tan, J. C., Cheng, Y., & Kong, S. 2018, ApJ, 862, 105
Louvet, F., Motte, F., Gusdorf, A., et al. 2016, A&A, 595, A122
Louvet, F., Neupane, S., Garay, G., et al. 2019, A&A, 622, A99
Maia, F. F. S., Moraux, E., & Joncour, I. 2016, MNRAS, 458, 3027
Massey, P. & Thompson, A. B. 1991, AJ, 101, 1408
Matthews, B. C., McPhee, C. A., Fissel, L. M., & Curran, R. L. 2009, ApJS, 182, 143
McKee, C. F. & Tan, J. C. 2002, Nature, 416, 59
McKee, C. F. & Tan, J. C. 2003, ApJ, 585, 850
Mel'nik, A. M. & Dambis, A. K. 2017, MNRAS, 472, 3887
Mel'Nik, A. M. & Efremov, Y. N. 1995, Astronomy Letters, 21, 10
Motte, F., Bontemps, S., & Louvet, F. 2018a, ARA&A, 56, 41
Motte, F., Bontemps, S., Schilke, P., et al. 2007, A&A, 476, 1243
Motte, F., Nguyên Luong, Q., Schneider, N., et al. 2014, A&A, 571, A32
Motte, F., Nony, T., Louvet, F., et al. 2018b, Nature Astronomy, 2, 478
Motte, F., Zavagno, A., Bontemps, S., et al. 2010, A&A, 518, L77
Münch, L. & Morgan, W. W. 1953, ApJ, 118, 161
Myers, P. C. 2009, ApJ, 700, 1609
Nguyen-Lu'o'ng, Q., Motte, F., Carlhoff, P., et al. 2013, ApJ, 775, 88
Nguyen Luong, Q., Motte, F., Hennemann, M., et al. 2011, A&A, 535, A76
Pabst, C., Higgins, R., Goicoechea, J. R., et al. 2019, Nature, 565, 618
Palau, A., Fuente, A., Girart, J. M., et al. 2013, ApJ, 762, 120
Peretto, N., Fuller, G. A., André, P., et al. 2014, A&A, 561, A83
Peretto, N., Fuller, G. A., Duarte-Cabral, A., et al. 2013, A&A, 555, A112
Peters, T., Banerjee, R., Klessen, R. S., & Mac Low, M.-M. 2011, ApJ, 729, 72
Peters, T., Klessen, R. S., Mac Low, M.-M., & Banerjee, R. 2010, ApJ, 725, 134
Pety, J., Guzmán, V. V., Orkisz, J. H., et al. 2017, A&A, 599, A98
Reich, W., Fuerst, E., Reich, P., & Reif, K. 1990, A&AS, 85, 633
Reipurth, B. & Schneider, N. 2008, Star Formation and Young Clusters in Cygnus, ed. B. Reipurth, Vol. 4, 36
Russeil, D., Zavagno, A., Motte, F., et al. 2010, A&A, 515, A55
Rygl, K. L. J., Brunthaler, A., Sanna, A., et al. 2012, A&A, 539, A79
Sanhueza, P., Jackson, J. M., Foster, J. B., et al. 2013, ApJ, 773, 123
Schilke, P., Walmsley, C. M., Pineau des Forets, G., & Flower, D. R. 1997, A&A, 321, 293
Schneider, N., Bontemps, S., Motte, F., et al. 2016a, A&A, 591, A40
Schneider, N., Bontemps, S., Motte, F., et al. 2016b, A&A, 587, A74
Schneider, N., Bontemps, S., Simon, R., et al. 2006, A&A, 458, 855
Schneider, N., Csengeri, T., Bontemps, S., et al. 2010, A&A, 520, A49
Schneider, N., Csengeri, T., Hennemann, M., et al. 2012a, A&A, 540, L11
Schneider, N., Csengeri, T., Klessen, R. S., et al. 2015, A&A, 578, A29
Schneider, N., Güsten, R., Tremblin, P., et al. 2012b, A&A, 542, L18
Schneider, N., Simon, R., Bontemps, S., Comerón, F., & Motte, F. 2007, A&A, 474, 873
Schulte, D. H. 1958, ApJ, 128, 41
Shimajiri, Y., André, P., Braine, J., et al. 2017, A&A, 604, A74
Simon, R., Schneider, N., Bontemps, S., Brunt, C., & Motte, F. 2006, in Astronomical Society of the Pacific Conference Series, Vol. 357, The Spitzer Space Telescope: New Views of the Cosmos, ed. L. Armus & W. T. Reach, 153
Tigé, J., Motte, F., Russeil, D., et al. 2017, A&A, 602, A77
Traficante, A., Duarte-Cabral, A., Elia, D., et al. 2018, MNRAS, 477, 2220
Traficante, A., Fuller, G. A., Duarte-Cabral, A., et al. 2020, MNRAS, 491, 4310
Vallée, J. P. & Fiege, J. D. 2006, ApJ, 636, 332
Vázquez-Semadeni, E., Gómez, G. C., Jappsen, A. K., Ballesteros-Paredes, J., & Klessen, R. S. 2009, ApJ, 707, 1023
Vázquez-Semadeni, E., González-Samaniego, A., & Colín, P. 2017, MNRAS, 467, 1313
Vázquez-Semadeni, E., Palau, A., Ballesteros-Paredes, J., Gómez, G. C., & Zamora-Avilés, M. 2019, MNRAS, 490, 3061
Wang, P., Li, Z.-Y., Abel, T., & Nakamura, F. 2010, ApJ, 709, 27
Williams, G. M., Peretto, N., Avison, A., Duarte-Cabral, A., & Fuller, G. A. 2018, A&A, 613, A11
Wright, N. J., Bouy, H., Drew, J. E., et al. 2016, MNRAS, 460, 2593
Wright, N. J., Drake, J. J., Drew, J. E., et al. 2012, ApJ, 746, L21
Wright, N. J., Drake, J. J., Drew, J. E., & Vink, J. S. 2010, ApJ, 713, 871
Wright, N. J., Drew, J. E., & Mohr-Smith, M. 2015, MNRAS, 449, 741
Wright, N. J. & Mamajek, E. E. 2018, MNRAS, 476, 381
Wright, N. J., Parker, R. J., Goodwin, S. P., & Drake, J. J. 2014, MNRAS, 438, 639
Wu, B., Tan, J. C., Christie, D., et al. 2017, ApJ, 841, 88
Wu, B., Van Loo, S., Tan, J. C., & Bruderer, S. 2015, ApJ, 811, 56
Xu, W. F., Gao, X. Y., Han, J. L., & Liu, F. S. 2013, A&A, 559, A81
Zhang, Q., Qiu, K., Girart, J. M., et al. 2014, ApJ, 792, 116
Zinnecker, H. & Yorke, H. W. 2007, ARA&A, 45, 481

transition	frequency (GHz)	location
Setup 1		
HCS^+(2-1)	85.348	DR21? + DR21(OH)
SO[2(2)-1(1)]	86.094	ridge
$H^{13}CN$(1-0)	86.342	ridge
$H^{13}CO^+$(1-0)	86.754	ridge + subfilaments
SiO(2-1)	86.847	ridge
HCN(1-0)	88.632	ridge + subfilaments
HCO^+(1-0)	89.189	ridge + subfilaments
H_2CO[6(1,5)-6(1,6)]	101.333	detected?
H_2CS[3(1,3)-2(1,2)]	101.478	DR21(OH)
CF^+(1-0)	102.587	detected?
Setup 2		
HNC(1-0)	90.664	ridge + subfilaments
HC_3N(10-9)	90.979	ridge
N_2H^+(1-0)	93.173	ridge + subfilaments
C_2S[7(8)-6(7)]	93.870	DR21 + DR21(OH)
SO[3(2)-2(1)]	109.252	ridge
OCS(9-8)	109.463	DR21(OH)
$C^{18}O$(1-0)	109.782	ridge + subfilaments
HNCO[5(0,5)-4(0,4)]	109.906	DR21 + DR21(OH)
NH_2D[1(1,1)0-1(0,1)0]	110.154	DR21(OH)? + DR21 north
^{13}CO(1-0)	110.201	ridge + subfilaments
CH_3CN[6(1)-5(1), F=7-6]	110.381	MDCs

Table 5.1: The molecular transitions that were detected with the IRAM 30m telescope, with the frequency of the transition and the location where the transition was detected. A question mark indicates uncertainty whether a transition was detected.

5.2.3 Additional discussion of Paper-DR21

Average spectra towards the DR21 ridge

As for Musca, an asymmetric accretion scenario was observed for the DR21 ridge with the subfilaments and in the PV diagrams. In the Musca cloud, this asymmetry was evident from the average spectra of the cloud and filament crest which trace gas at different densities (HI, ^{12}CO, ^{13}CO and C^{18}O). However, when studying the average spectra observed with the 30m telescope towards the DR21 cloud in Fig. 5.4, such an asymmetry is not observed. A possible explanation for this, is the strong emission coming from the DR21 ridge which is extremely bright compared to the rest of the DR21 cloud. Because of this, the asymmetric inflow is hidden in the average spectra as the ridge kinematics are dominated by its gravitational collapse which possibly drives a turbulent linewidth (Klessen & Hennebelle, 2010; Arzoumanian et al., 2013). This could then give rise to the observed relatively symmetric average spectrum. This is in contrast with the Musca cloud, where the filament crest is way less dominant compared to the strands and ambient cloud.
The transitions presented in Fig. 5.4, namely ^{13}CO(1-0), C^{18}O(1-0), H^{13}CO$^+$(1-0) and H^{13}CN(1-0), are also different from the transitions used to study the kinematic asymmetry in Musca. When studying the average ^{12}CO(3-2) transition of the DR21 cloud in Fig. 5.5, the kinematic asymmetry starts to show hints in the average spectrum. However, because of strong self-absorption at the velocity of the DR21 ridge, this still does not appear as clear as for the Musca cloud. Inspecting the velocity interval in Fig. 5.5 between the DR21 ridge velocity at -3 km s^{-1} and the 10 km s^{-1} component, it is found that there is significantly more ^{12}CO(3-2) emission than at velocities $<$ -7 km s^{-1}. This suggests that the interval between the two velocity components towards DR21 might also trace gas bridging the two velocity components on top of the emission from protostellar outflows.

Spitzer extinction maps and the velocity structure of DR21

Since the Cygnus-X (north) region is a rich nursery of high-mass stars, the GMC is permeated by a strong FUV-field $\gtrsim$ 100 G$_0$ (Schneider et al., 2016a). As a result, there are strong Spitzer 8 μm emission and absorption features toward the DR21 ridge. Combining these absorption and emission features with the molecular line observations from the IRAM 30m can provide an interesting perspective on the kinematics and geometry of the DR21 ridge. For this analysis, both the HNC(1-0) and the ^{13}CO(1-0) line are used since they trace different regimes in molecular clouds. HNC(1-0) is more representative for high-density gas ($n_{crit} \sim 10^5$ cm^{-3}) (Shirley, 2015), while ^{13}CO(1-0) is more representative for lower-density gas $n_{crit} \sim 10^3$ cm^{-3}. Inspecting the Spitzer 8 μm in Fig. 5.6 it becomes obvious that there is bright diffuse emission with significant extinction in a part of the DR21 ridge. Compact 8 μm sources are also observed in the ridge, which are associated with massive protostellar objects in DR21(OH) and the north of the ridge (Duarte-Cabral et al., 2013). The DR21 radio continuum source on the other hand shows much more extended 8 μm emission. Comparing the IRAM 30m molecular line emission for both tracers with the Spitzer emission in Fig. 5.6, it is observed that the blueshifted velocities of the ridge ($\sim$ -4.5 km s^{-1}) are mostly observed in the area of the ridge with bright Spitzer 8μm emission. On the other hand, the redshifted emission from the ridge ($\sim$ -1.5 km s^{-1}) is mainly observed in the 8 μm dark region of the ridge. The DR21 ridge and cloud are obviously a complex region, but the fact that the redshifted gas is located in the Spitzer dark region suggests that the gas at this velocity is in

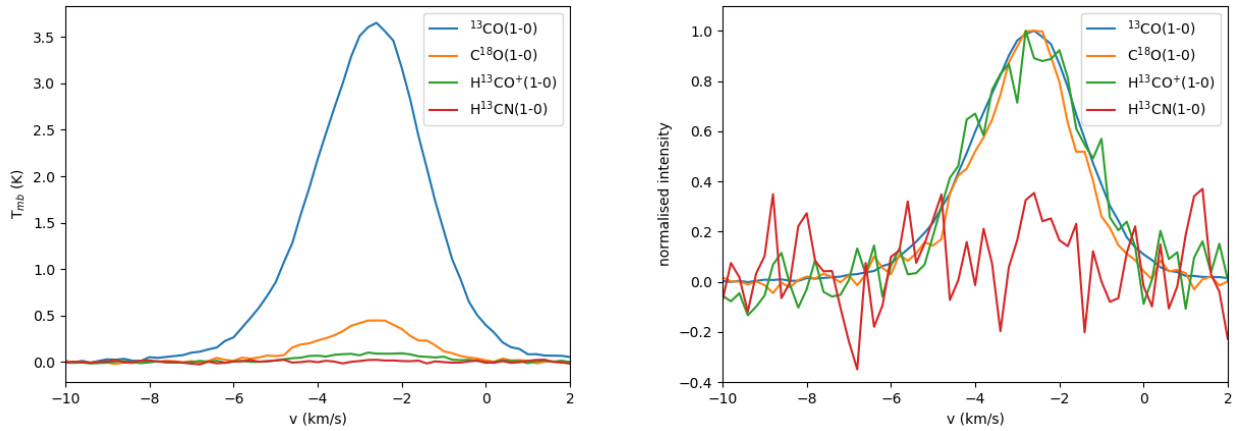

Figure 5.4: **Left**: The average spectra of ^{13}CO(1-0), C^{18}O(1-0), H^{13}CO$^+$(1-0) and H^{13}CN(1-0) towards the DR21 cloud mapped with the IRAM 30m telescope. It shows no direct indications of a kinematic asymmetry for slightly less dense gas traced by ^{13}CO(1-0). It is also observed that H^{13}CO$^+$(1-0) and H^{13}CN(1-0) are extremely weak over the full DR21 cloud. **Right**: The same spectra normalised to the maximal intensity to highlight the lack of asymmetry when comparing the spectra of the different tracers.

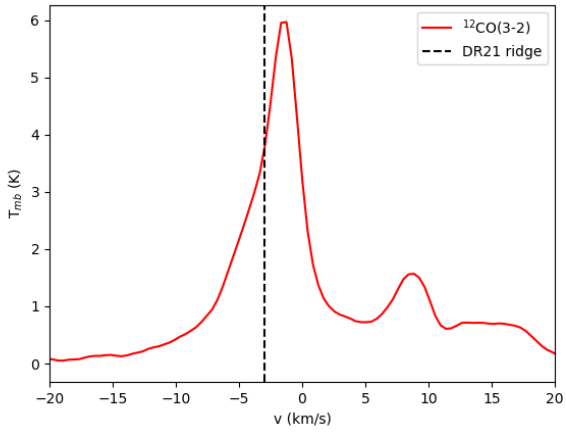

Figure 5.5: The average ^{12}CO(3-2) spectrum of the DR21 cloud from the JCMT data. The vertical dashed line indicates the velocity of the DR21 ridge with higher density tracers (-3.5 km s^{-1}).

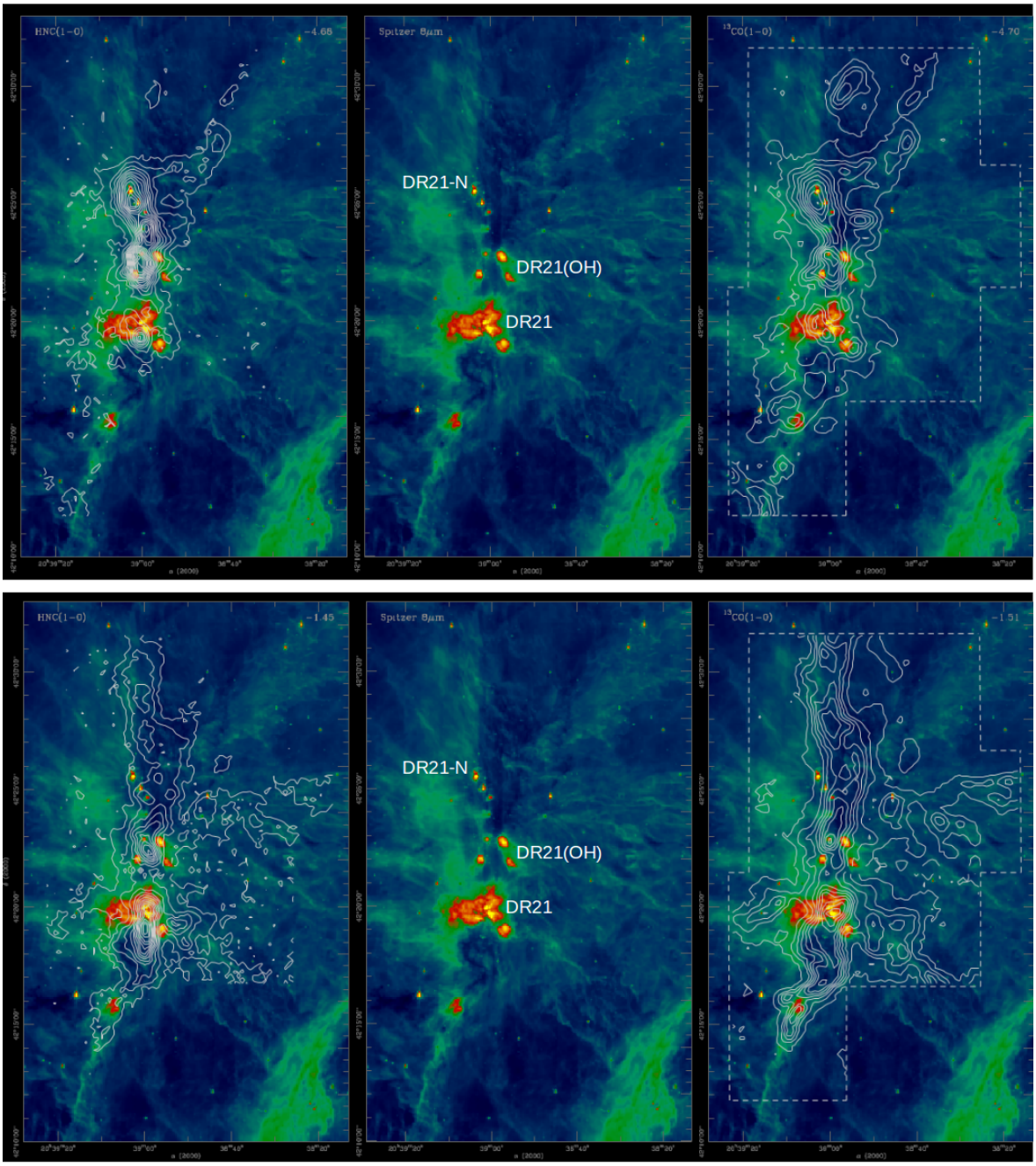

Figure 5.6: **Top:** The spitzer 8 μm map of the DR21 ridge. In the left map, the IRAM 30m HNC(1-0) emission contours at $\sim$ -4.5 km $^{-1}$ are overlaid on the Spitzer map. In the right map, the IRAM 30m ^{13}CO(1-0) emission contours at the same velocity are shown. **Bottom:** The same with emission contours at $\sim$ -1.5 km s^{-1}. It is observed that the gas at -4.5 km s^{-1} in the ridge is mostly located at strong extended spitzer emission, while the gas at -1.5 km s^{-1} nicely follows the extinction in the DR21 ridge.

the front area of the ridge. On the other hand, the fact that the blueshifted gas is observed in the area of bright Spitzer emission suggests that it is mainly located in the back of the ridge from our point of view. This relative location of the blue- and redshifted gas in the ridge fits with the scenario that the blue- and redshifted gas are moving towards one another and thus that the redshifted gas is being accreted on the ridge. Inspecting the Spitzer dark regions in detail, dark filamentary substructures are observed which appear to be connected to the subfilaments that connect to the ridge. This fits with the scenario that the redshifted subfilaments continue their flow into the ridge down to the MDCs (Schneider et al., 2010). However, the IRAM 30m observations do not manage to resolve these narrow filamentary structures in the ridge. Better understanding these filamentary extinction features will thus require comparison with interferometric NOEMA observations.

OB associations in Cygnus-X

An OB association is generally defined as a group of stars with ten to hundreds of OB stars, that are formed in a giant molecular cloud, which can disperse in the future as they are unbound. This poses the question how to define the OB associations in Cygnus-X. It was already put forward by Mel'Nik & Efremov (1995), Schneider et al. (2007) and Comerón & Pasquali (2012) that the OB9 association in Cygnus-X had to be redefined. In particular, that OB1, OB8 and OB9 could in fact be a single OB assocation with further spatial substructure. Spatial and kinematic substructure was further unveiled for the OB2 association (Wright et al., 2014, 2016; Winter, Clarke & Rosotti, 2019; Arnold, Goodwin & Wright, 2020).
Considering the proposed possible scenario that a 100 pc scale GMC collision in Cygnus-X could be the trigger of high-mass star formation, it should be examined whether the observed OB associations in Cygnus-X can be considered a single OB association with substructure on multiple scales. Cygnus-X north would then be the region of the OB association that is still in formation.
In Fig. 4 of Comerón & Pasquali (2012) and Fig. 15 of Paper-DR21, OB2 is a well defined structure in the Cygnus-X region. However, a possible 100 pc scale collision will lead to a hierarchical structure. In this scenario, it could be considered that OB2 is a large scale hierarchical structure in the forming OB assocation over the full Cygnus-X region. The spatial substructure of OB2 and OB9 could then be a lower level hierarchical structure as a result of the hubs and ridges that form the OB stars. Lastly, it was indicated earlier that e.g. DR21 has the potential to form a cluster on its own and that e.g. DR22 and DR23 have already formed clusters of stars. The observed OB associations in Cygnus-X might thus be associations of multiple clusters with OB stars where each cluster is formed by individual cloud compression events during the GMC collision.

5.2.4 The kinematics of W75N

The DR21 ridge is the most prominant massive star formation area in Cygnus-X north, but it is not the only location. Another important massive star formation region in Cygnus-X north, that is not yet perturbed by strong feedback from massive stars, is the W75N cloud. However, W75N has been significantly less studied than DR21 (e.g. Persi, Tapia & Smith, 2006), while it has an equally interesting spatial and kinematic structure.

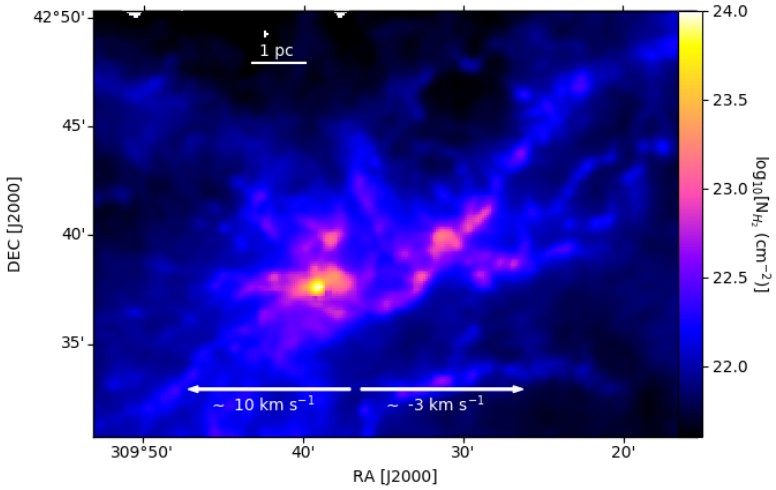

Figure 5.7: The *Herschel* column density map of the W75N massive star forming region in Cygnus-X north. In the column density maps it looks like a typical filament hub. The arrows indicate the part of W75N at a velocity of $\sim$ -3 km s^{-1} and 10 km s^{-1}.

Inspecting the *Herschel* column density map in Fig. 5.7, W75N looks like a relatively common filament hub structure. However, inspecting the FCRAO ^{13}CO(1-0) and JCMT ^{12}CO(3-2) PV diagrams of the cloud in Fig. 5.8, an interesting velocity substructure is seen. It is observed that the cloud is split in two velocities that are separated at the center of the column density hub. Furthermore, the filaments of the first hub at $\sim$ 10 km s^{-1} are located to the east, while the filaments of the second hub at $\sim$ -3 km s^{-1} are located to the west of the hub. The spatial asymmetry of both velocity components in W75N is particulary interesting, when comparing with DR21. For DR21, at -3 km s^{-1}, the lower density filaments are also located west of the dense hub/ridge.
If the observed spatial asymmetry of the DR21 ridge is indeed the result of bending by the magnetic field described in Inoue et al. (2018) due to a GMC collision in Cygnus-X north, it is expected that the -3 km s^{-1} component in W75N has the same spatial asymmetry as DR21. The fact that the filaments of the 10 km s^{-1} component of W75N are located to the east of the hub, is further consistent with the proposed scenario that the massive star forming gas in Cygnus-X north is the result of compression by a GMC collision. Inspecting Fig. 5.8 in detail, it is also observed that there are some bridging effects between both velocity components in W75N.
Looking in more detail into the ^{13}CO(1-0) kinematic structure in Fig. 5.8 of both velocity components in W75N, it is found that both structures also show indications of further kinematic asymmetry. For the $\sim$ 10 km s^{-1} component, the lower density filaments at r $<$ 0 pc show indications of more blueshifted emission. On the other hand for the $\sim$ -3 km s^{-1}, the emission at r $>$ 2 pc from the lower density filaments is mostly redshifted just as what was found for the DR21 ridge. However, the velocity gradient from high-density to low-density gas of the $\sim$ -3 km s^{-1} can also be part of a larger scale velocity

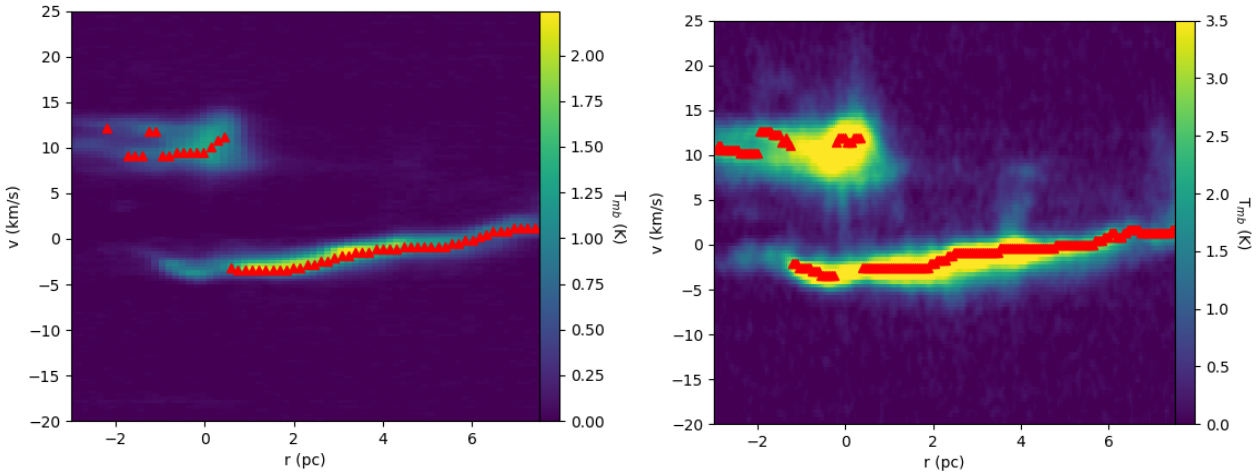

Figure 5.8: **Left**: The FCRAO ^{13}CO(1-0) PV diagram along the celestial equator for the W75N molecular cloud. The PV diagram is centered on the peak *Herschel* column density of the W75N cloud, presented in Fig. 5.7. The emission in the PV diagram up to 0.3 pc is dominated by $\sim$ 10 km s^{-1} velocity component, while at r $>$ 0.3 pc there is a sharp transition to emission at the $\sim$ -3 km s^{-1} component. Note that there is a bit of - 3 km s^{-1} emission at r $<$ 0.3 pc, which originates from confusion of the DR21 cloud. The red triangles indicate the peak intensity evolution. **Right**: The same for the JCMT ^{12}CO(3-2) data. In ^{12}CO(3-2), the -3 km s^{-1} emission at r $<$ 0.3 pc from the DR21 cloud provides more confusion to the PV diagram. Also note indications of gas bridging between both velocity components at e.g. r $\sim$ -2 pc, r $\sim$ 1 pc and r $\sim$ 4 pc.

gradient of this velocity component over the full Cygnus-X north region (Schneider et al., 2006). In any case, this suggests that both the W75N and DR21 massive star forming gas are indeed formed by a GMC collision in the scenario described by Inoue & Fukui (2013); Inoue et al. (2018).

5.3 Cloud and filament formation in the ISM

5.3.1 Dense gas formation by asymmetric inflow and low-velocity shocks

The observed V-shape, associated with asymmetric inflow, in the transverse PV diagrams of the Musca and DR21 clouds is an interesting observation as it puts important constraints on the formation of filamentary structures in the ISM. It was in particular noted that the bending of the magnetic field by a cloud-cloud collision, sketched in Fig. 5.9, is responsible for this asymmetric accretion as proposed by Inoue et al. (2018). Indications of this V-shape inflow were also found for a filament at an early evolutionary stage in the Taurus molecular cloud (Arzoumanian et al., 2018), and the PV diagram of the B211/3 filament also appears in the form of a V-like shape which is demonstrated in Fig. 5.10 (Shimajiri et al., 2019b). It thus appears that the mechanism responsible for the observed V-shape around these prototypical filaments might play a more universal role in the formation of star forming

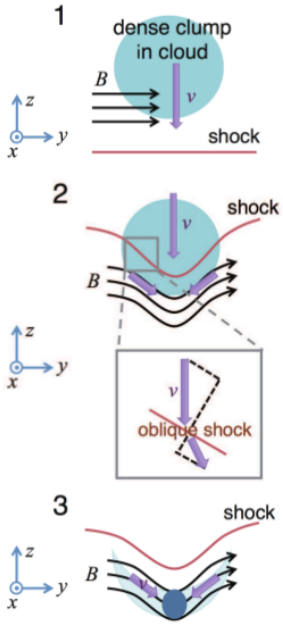

Figure 5.9: A schematic illustration of the inflow driven by the bending of the magnetic field in a cloud-cloud collision. This figure is adapted from Inoue et al. (2018).

filaments. The presence of organised V-shapes around filamentary structures in any case indicates that a large scale organised process plays an important role in the formation of star forming filaments. At the intersection of the created converging flows, mass can then be accreted as a result of filament accretion shocks for which indications were found towards the Musca cloud. It has been proposed that such filament accretion shocks could be an explanation for the proposed characteristic filament width (e.g. Arzoumanian et al., 2011; Federrath, 2016). However, the presented observation of low-velocity shocks does not necessarily confirm the proposed universal 0.1 pc width.

The observed asymmetric inflow towards Musca and DR21 provide an interesting starting point to further investigate dense gas formation. Extensive mapping at high spatial and spectral resolution of molecular clouds will also be essential to fully understand the origin of the observed velocity substructure in dust continuum filaments, which was not addressed in this thesis. This will e.g. require to address whether turbulence in the converging flows form fibers that are accreted on the filaments or if fibers are only formed in the dust continuum filaments. It might also provide more information on the properties of striations, which are observationally poorly characterised. Mapping the large scale cloud kinematics in different clouds will also address the frequency of V-like shapes in a variety of clouds. In particular, in clouds that are not dominated by a single filament or ridge such as Musca, B211/3 and DR21. If such a V-shape is also observed in clouds with a filamentary network such as Aquila or Perseus, the resulting point of convergence might have important implications to understand stellar cluster formation.

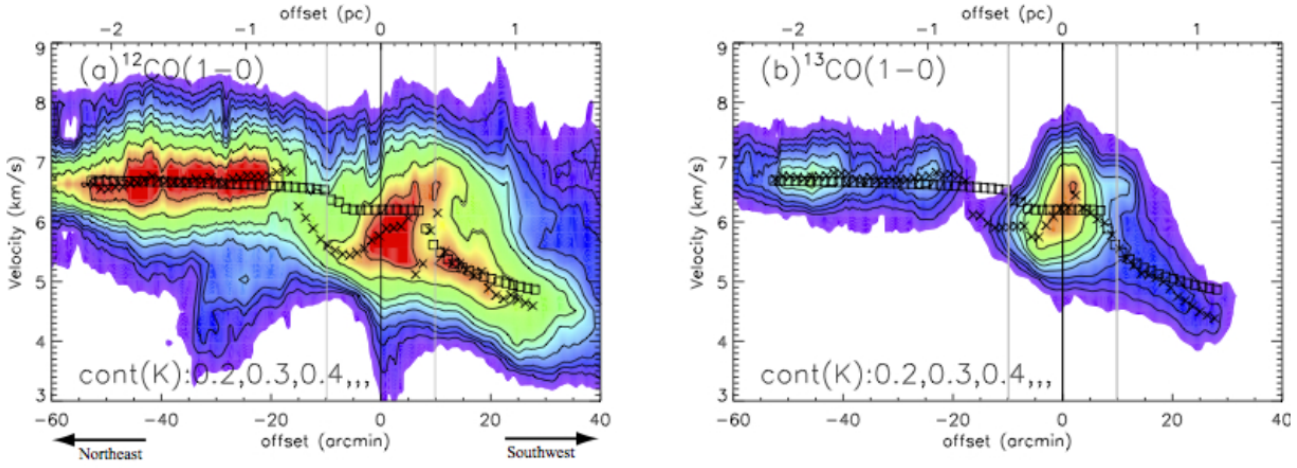

Figure 5.10: The PV diagrams of ^{12}CO(1-0) and ^{13}CO(1-0) perpendicular to the B211/3 filament in the Taurus molecular cloud. The black crosses indicate the velocity of the observed maximal intensity as a function of the distance from the filament. This figure was adapted from (Shimajiri et al., 2019b).

5.3.2 Bridging between velocity components in Chamaeleon-Musca

There have been several numerical studies that have studied the dynamics of cloud-cloud collisions. This has strongly focused on bridging signatures between two velocity components (Haworth et al., 2015a,b; Bisbas et al., 2017). Inspecting Fig. 14 in Paper-DR21 and Fig. 5.8, showing the JCMT ^{12}CO(3-2) PV diagram, signatures of bridging between the two components are observed. One should however be careful because strong protostellar outflows can also give rise to elongated velocity structures in PV diagrams (e.g. Arce et al., 2010; Bally, 2016; Nony et al., 2020).
Looking into the HI PV diagram of the Chamaeleon-Musca complex in Fig. 5.11, there are no evident bridging effects. This is not really surprising because HI traces extremely extended gas, while the synthetic observations in simulations mainly focus on CO, [CI] and [CII] emitting gas to observe bridging gas. Furthermore, the proposed cloud-cloud collision in Chamealeon-Musca has a low velocity, and in Haworth et al. (2015b) it was shown that for such a low-velocity cloud-cloud collision (3 km s^{-1} in their simulations) the bridging features are very difficult to extract because of the nearby velocity components. The HI PV diagram in Fig. 5.11 does however show a relatively sharp velocity evolution, near a galactic longitude of 300^o to 305^o, from a dominant velocity at $\sim$ 0 km s^{-1} to a dominant velocity at $\sim$ 5 km s^{-1}. This galactic longitude is where most dense star forming gas has formed in Chamaeleon-Musca. This velocity transition and associated star formation could thus indicate the main location where the two clouds collided. Furthermore, inspecting the CO(1-0) PV diagram of the Chamaeleon-Musca region in Fig. 5.12 (Mizuno et al., 2001), substructure and some hints of bridging can be observed. These indications are tentative, because of the limited sensitivity of the observations and small velocity difference, but hint at the presence of cloud-cloud collision signatures in Chamaeleon-Musca as well.

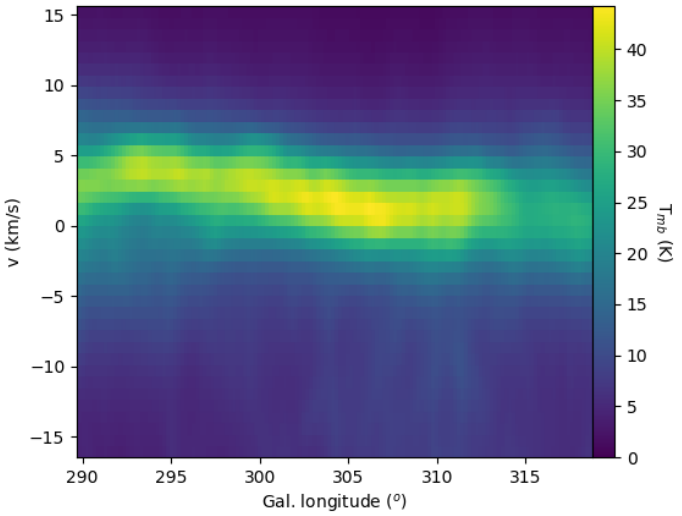

Figure 5.11: The PV diagram along the Galactic Longitude of the HI emission for the Chamaeleon-Musca complex. It indicates a significant transition for the brightest emission in velocity between a galactic longitude of 300^o and 305^o.

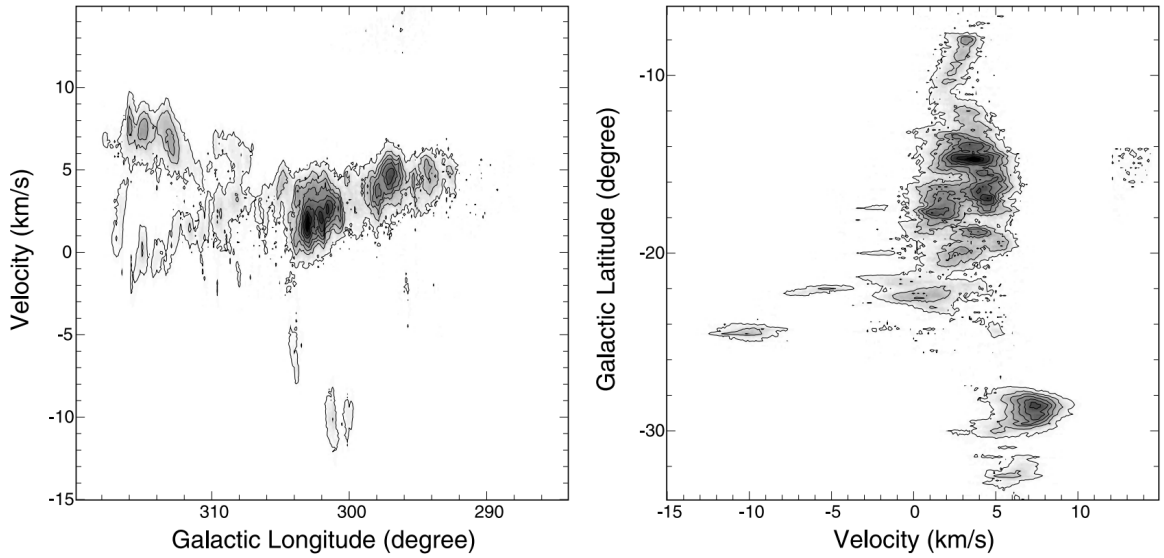

Figure 5.12: The ^{12}CO(1-0) PV diagram of the Chamaeleon-Musca complex along the Galactic Longitude (left) and the Galactic Latitude (right). These diagrams show some possible hints of two velocity components which might be interacting. There is e.g. a possible bridge near a Galactic Longitude of 318^o and 308^o. This figure was adapted from (Mizuno et al., 2001).

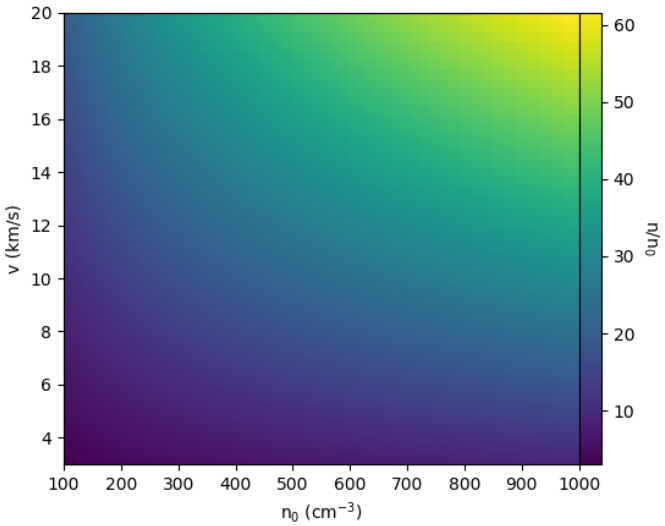

Figure 5.13: The compression rate of a magnetised cloud-cloud collision as a function of shock velocity and initial density for a magnetic field strength perpendicular to the shock front of 20 μG.

5.3.3 The difference between low- and high-mass star formation

From both the Musca cloud and DR21, we get a scenario where star forming filaments are a result of the cloud formation process. It also indicates that this mechanism might play a role in both low- and high-mass star formation. One can thus wonder what are the differences in physical processes and cloud properties that decide if a cloud forms low- or high mass stars. An obvious parameter is the velocity of the collision. A larger velocity leads to a larger mass provision rate and a stronger compression resulting in a higher density of the compressed gas. The compression ratio (r) for a magnetised collision is given by r $\simeq \sqrt{2}$M$_A$ (Inoue et al., 2018), where M$_A = \sqrt{4\pi\rho_0}$v$_0$/B$_{t,0}$ is the Alfvén Mach number. B$_{t,0}$ is the magnetic field component perpendicular to the shock normal, ρ_0 the preshock density and v$_0$ the collision velocity. It thus comes to no surprise that the collision velocity in Cygnus-X north is significantly higher than Musca. Another possible parameter is the pre-collision density of the clump that will be compressed. A higher preshock density will also lead to a higher density in the compressed cloud. In the compression ratio equation, the magnetic field component perpendicular to the shock normal also plays a role in determining the postshock density. Calculating the compression rate for typical velocities (3-20 km s^{-1}), preshock densities (n$_{H_2,0}$ = 10^2-10^3 cm^{-3}) and B$_{t,0}$ = 20 μG, shown in Fig. 5.13, gives compression rate values up to 60.
Inspecting the compression ratio in more detail it is found that the density in the compressed cloud is linearly proportional to the collision velocity. The preshock density, however, provides the starting value and also plays a role in the compression ratio. This results in a $\rho_0^{3/2}$ dependence for the postshock density, which suggests that the clump evolution before the collision is a very important parameter for

the resulting star formation. There is also the magnetic field component perpendicular to the shock normal which is inversely proportional to the compression. In conclusion, the formation of star forming filaments and the eventual stellar mass formed are the result of multiple parameters. From Fig. 5.13 it is also observed that both high velocities ($\geq$ 10 km s^{-1}) and high pre-shock densities ($n_0 \sim 10^3$ cm^{-3}) are required to trigger high-mass star formation as it is predicted in Inoue et al. (2018), because high-mass star formation requires high densities and thus important preshock densities and strong compression.

With a higher density in the compressed cloud, gravity becomes increasingly important on large scales as was indicated in Paper-DR21. In Inoue et al. (2018) it was proposed that the inflow due to the bending of the magnetic field can be sufficient to form massive stars without the need for gravitational collapse. However, gravity is present, so its role has to be taken into account.
In Paper-MC, it was found with the C_v ($= \frac{\Delta v_h}{GM(r)/L}$) parameter proposed in Chen et al. (2020) that gravity only starts playing a significant role within a small radius ($\sim$ 0.1-0.2 pc) around the center of the filament. In C_v, Δv_h is half the velocity difference over the filament/ridge and M(r)/L the mass per unit velocity. With the virial analysis for the DR21 cloud, it was found that gravity can dominate the entire cloud evolution on parsec scale, which fits with the observation of strong gravitational collapse in the DR21 ridge (Schneider et al., 2010). This gravitational dominance for the full cloud is confirmed with the C_v parameter. This parameter was calculated with an M(r)/L of 2.5×10^3 and 5×10^3 M$_\odot$ pc^{-1} for the DR21 ridge and cloud, respectively. These values are obtained assuming a length of 4 pc for the DR21 ridge and a mass of $\sim 10^4$ and $\sim 2\times10^4$ M$_\odot$ in the ridge and cloud, respectively. With Δv_h = 1 km s^{-1} near the ridge and 2 km s^{-1} on larger scales in the cloud perpendicular to the ridge, this results in $C_v = 0.09$ for the ridge and $C_v = 0.19$ for the cloud. In both cases C_v is significantly below 1, which again suggests that the gravitational potential is driving the accretion flow from parsec scale down to the ridge (Chen et al., 2020).
These results put forward a scenario where the compression and observed kinematic asymmetry of low- and high-mass star forming filaments can be the result of a cloud-cloud collision which bends the magnetic field. However, in the low-mass case of Musca the turbulent inflow is driven by this magnetic field bending, while the inflow responsible for the high-mass star formation in DR21 is mainly driven by gravity. Note that even for the gravitationally driven inflow in DR21, the bending of the magnetic field probably provides a relatively important counterbalance against the gravitational acceleration. This could explain the relatively smooth velocity gradient from the subfilaments to the ridge, seen in Fig. 8 of Paper-DR21, which is not expected for strong gravitational acceleration.

5.3.4 Prospective: Evolution of the ISM with the SOFIA Legacy Program FEEDBACK

The role of cloud-cloud collisions or large scale colliding flows in the context of star forming filaments brings forward the question of the large scale evolution of the more diffuse ISM. Generally, it is considered that the evolution of the ISM is driven by supernovae (e.g. Cox & Smith, 1974; McKee & Ostriker, 1977; Mac Low & Klessen, 2004; Kim & Ostriker, 2015; Walch et al., 2015; Girichidis et al., 2016; Padoan et al., 2019). In combination with radiative feedback, stellar winds and shear of galactic arms, this can disperse star forming clouds, set in motion large scale flows and inject turbulence into the ISM.

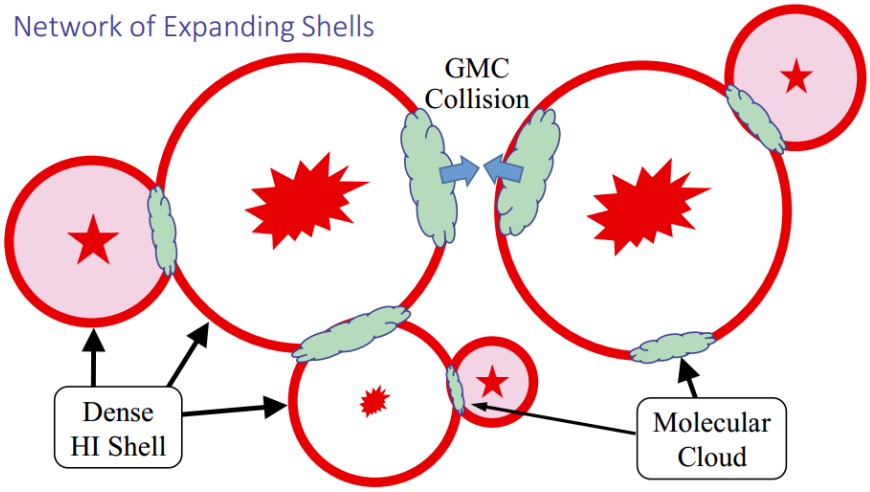

Figure 5.14: A schematic representation of the scenario described in Inutsuka et al. (2015). Molecular clouds generally form at the intersection of expanding bubbles, with a GMC collision leading to extremely active star formation as is observed for example in Cygnus-X north.

In terms of the observed filament formation in Musca and DR21, the description of the large scale ISM evolution by Inutsuka et al. (2015) is particularly interesting. It puts forward a scenario, shown in Fig. 5.14, where stellar feedback leads to multiple compressions as a result of large scale colliding flows/cloud-cloud collisions at the edges of expanding shells in the multiphase ISM. Such large scale colliding flows or cloud-cloud collisions can generate turbulent molecular gas layers with a filamentary structure (e.g. Hartmann, Ballesteros-Paredes & Bergin, 2001; Koyama & Inutsuka, 2002; Audit & Hennebelle, 2005; Heitsch et al., 2006; Vázquez-Semadeni et al., 2011; Inoue & Inutsuka, 2012). The ubiquitous presence of expanding shells in the ISM is observed in a wide variety of studies (e.g. Hartmann & Burton, 1997; Churchwell et al., 2006, 2009) and demonstrated in a 3D reconstruction of the nearby ISM by Lallement et al. (2019). In this evolution, the mechanism described in Inoue & Fukui (2013); Inoue et al. (2018) could be of primary importance in the formation of filamentary structures and generating inflow. It was however found with kinematic observations of [CII] with SOFIA that such bubbles might not have a simple spherical structure (Pabst et al., 2019). In order to fully understand the evolution of the ISM and how stars can form as a result, it is thus necessary to observe how stellar feedback impacts the ISM.
The FEEDBACK Legacy Program[1] with the SOFIA telescope (Schneider et al. 2020, in revision), in which I participate as a consortium member, can provide further insight into how the ISM spatially and kinematically evolves as a result of stellar feedback. It particularly focusses on the impact of UV radiation and stellar winds from OB stars in prominent star-forming regions, by mapping the [CII] and [OI] fine structure lines with the upGREAT receiver (Risacher et al., 2018). However, it could also unveil the large scale kinematics of CO-dark gas which should be traced by [CII] and [CI], even

[1]https://astro.uni-koeln.de/index.php?id=18130

though it is still a field of active research to understand the density regimes that are traced by each line (Bisbas, Papadopoulos & Viti, 2015; Glover et al., 2015; Glover & Smith, 2016; Franeck et al., 2018; Clark et al., 2019). This can be particularly interesting to detect signatures of a cloud-cloud collision (Bisbas et al., 2017, 2018). The FEEDBACK program is currently observing 11 regions in the galaxy that are experiencing an impact from OB stars, namely Cygnus-X north, M16, M17, NGC6334, NGC7538, RCW49, RCW79, RCW120, RCW36, W40 and W43. These regions consist of prototypical bubbles, massive star forming ridges and hubs, pillars and a star burst region.

• Cygnus-X with FEEDBACK

As of july 2020, $\sim$ 30% of the planned mapping for the Cygnus-X north region has been carried out, see Fig. 5.15. The planned map covers the DR21 ridge, the W75N hub, and DR17 which is also known as the Diamond Ring (Marston et al., 2004). In Fig. 5.15, it is shown that DR17 is seen as a bubble in Spitzer images (Marston et al., 2004; Beerer et al., 2010). DR17 is associated with radio continuum emission (Lockman, 1989; Furst et al., 1990), and Beerer et al. (2010) demonstrated the presence of a cluster of class II young stellar objects at the center of DR17 which could be responsible for the observed radio continuum emission. It was also shown with 2MASS data that the bright tip of DR17 (the diamond) is associated with a stellar cluster (Dutra & Bica, 2001) that contains 12 B stars (Le Duigou & Knödlseder, 2002).

These [CII] observations will unveil the kinematic structure of the diamond ring as well as the bright PDRs and low-density gas of this full northern region. A detailed study of the structure and kinematics of the low-density gas and bright PDRs in Cygnus-X north has not been performed so far because of the complexity of the Cygnus-X region and the associated self-absorption effects in HI. With the sensitivity and large map of the FEEDBACK observations this will be possible for the first time. A first important point to test with these observations is the GMC collision scenario. It was proposed by synthetic observations of cloud-cloud collision simulations by Bisbas et al. (2017) that [CII] and [CI] emission is better suited than ^{12}CO to establish a cloud-cloud collision, and in particular to confirm the gas bridging between two velocity components. One other advantage of [CII] is, that it does not suffer the same confusion from protostellar outflows.

As a GMC collision is associated with a high-velocity shock, the observation of shock excitation and tracers is important. It was already noted that the large scale presence of SiO in gaseous form in the DR21 ridge could be the result of this cloud-cloud collision. With FEEDBACK, the [OI] line at 63 μm is also covered. However, analysing predictions by the Paris-Durham shock code in Fig. 5.16 it is found that an [OI] detection due to the GMC collision is not necessarily expected. The 3σ [OI] detection limit with FEEDBACK will be of the order of 3×10^{-4} ergs s^{-1} cm^{-2} sr^{-1} while the predicted intensity by shock models is at least an order of magnitude lower, both for irradiated (1 G$_0$) and non-irradiated shock models at realistic preshock densities ($\sim 10^3$ cm^{-3}). Even spatial smoothing might thus be insufficient to detect the [OI] line emission. In this context it should be noted that the FUV field in Cygnus-X north might even be of the order of 100 G$_0$, such that further analysis with strongly irradiated shock models will be necessary.

5.3.5 Article: FEEDBACK: a SOFIA legacy program to study stellar feedback in regions of massive star formation (PASP, in revision, front page and abstract)

FEEDBACK: a SOFIA legacy program to study stellar feedback in regions of massive star formation

N. Schneider[1], R. Simon[1], C. Guevara[1], C. Buchbender[1], R.D. Higgins[1], Y. Okada[1], J. Stutzki[1], R. Güsten[2], L.D. Anderson[3], J. Bally[4], H. Beuther[5], L. Bonne[6], S. Bontemps[6], E. Chambers[7], T. Csengeri[6], U.U. Graf[1], A. Gusdorf[8], K. Jacobs[1], M. Justen[1], S. Kabanovic[1], R. Karim[9], M. Luisi[3], K. Menten[2], M. Mertens[1], B. Mookerjea[10], V. Ossenkopf-Okada[1], C. Pabst[11], M.W. Pound[9], H. Richter[12], N. Reyes[2], O. Ricken[2], M. Röllig[1], D. Russeil[13], Á. Sánchez-Monge[1], G. Sandell[14], M. Tiwari[9], H. Wiesemeyer[2], M. Wolfire[9], F. Wyrowski[2], A. Zavagno[13], A.G.G.M. Tielens[9,11]

E-mail: nschneid@ph1.uni-koeln.de

Abstract. FEEDBACK is a SOFIA (Stratospheric Observatory for Infrared Astronomy) legacy program dedicated to study the interaction of massive stars with their environment. It performs a survey of 11 galactic high mass star forming regions in the 158 μm (1.9 THz) line of [C II] and the 63 μm (4.7 THz) line of [O I]. We employ the 14 pixel Low Frequency Array (LFA) and 7 pixel High Frequency Array (HFA) upGREAT heterodyne instrument to spectrally resolve (0.24 MHz) these far-infrared fine structure lines. With a total observing time of 96h, we will cover ~6700 arcmin^2 at 14.1″ angular resolution for the [C II] line and 6.3″ for the [O I] line. The observations started in spring 2019 (Cycle 7). Our aim is to understand the dynamics in regions dominated by different feedback processes from massive stars such as stellar winds, thermal expansion, and radiation pressure, and to quantify the mechanical energy injection and radiative heating efficiency. This is an important science topic because feedback of massive stars on their environment regulates the physical conditions and sets the emission characteristics in the interstellar medium (ISM), influences the star formation activity through molecular cloud dissolution and compression processes, and drives the evolution of the ISM in galaxies. The [C II] line provides the kinematics of the gas and is one of the dominant cooling lines of gas for low to moderate densities and UV fields. The [O I] line traces warm and high-density gas, excited in photodissociations regions with a strong UV field or by shocks. The source sample spans a broad range in stellar characteristics from single OB stars, to small groups of O stars, to rich young stellar clusters, to ministarburst complexes. It contains well-known targets such as Aquila, the Cygnus X region, M16, M17, NGC7538, NGC6334, Vela, and W43 as well as a selection of H II region bubbles, namely RCW49, RCW79, and RCW120. These [C II] maps, together with the less explored [O I] 63 μm line, provide an outstanding data base for the community. They will be made publically available and will trigger further studies and follow-up observations.

[1]I. Physik. Institut, University of Cologne, Zülpicher Str. 77, 50937 Cologne, Germany
[2]Max-Planck Institut für Radioastronomie, Auf dem Hügel 69, 53121 Bonn, Germany
[3]Department of Physics and Astronomy, West Virginia University, Morgantown WV 26506
[4]Center for Astrophysics and Space Astronomy, University of Colorado, Colorado 80309, USA
[5]Max Planck Institute for Astronomy, Königstuhl 17, 69117 Heidelberg, Germany
[6]LAB, University of Bordeaux, CNRS, B18N, 33615 Pessac, France
[7]USRA/SOFIA, NASA Ames Research Center, Moffett Field, CA 94035-0001, USA
[8]LPENS, Université PSL, CNRS, Sorbonne Université, Université de Paris, Paris, France
[9]Department of Astronomy, University of Maryland, College Park, MD 20742, USA
[10]Tata Institute of Fundamental Research, Homi Bhabha Road, Mumbai 400005, India
[11]Leiden Observatory, Leiden University, PO Box 9513, 2300 RA Leiden, Netherlands
[12]Institute of Optical Sensor Systems, DLR, Rutherfordstr. 2, 12489 Berlin, Germany
[13]Aix Marseille Université, CNRS, CNES, LAM, Marseille, France
[14]Institute for Astronomy, University of Hawaii, 640 N. Aohoku Place, Hilo, HI 96720, USA

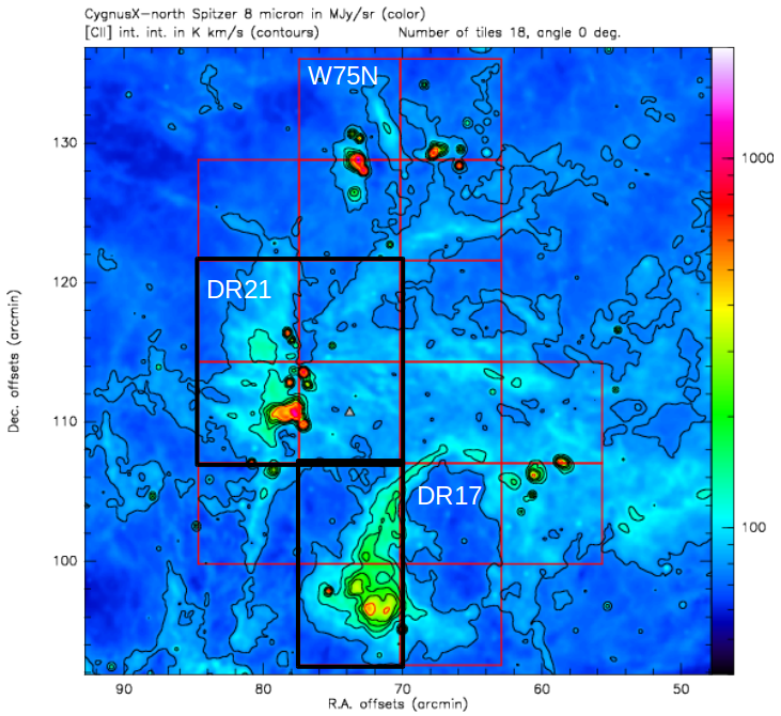

Figure 5.15: Figure adapted from Schneider et al. (2020), showing the Spitzer 8μm map of Cygnus-X north with the region that will be observed by FEEDBACK (outlined in red). The regions indicated in black have been currently mapped in the FEEDBACK program.

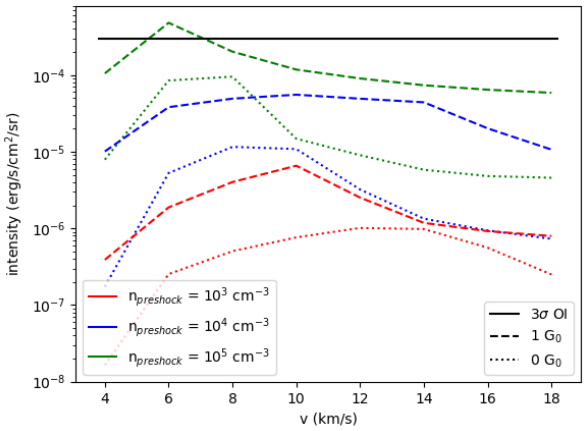

Figure 5.16: The predicted [OI] intensity at 63 μm for irradiated and non-irradiated C-type shocks as a function of the velocity. The horizontal line indicates the expected FEEDBACK detection limit.

5.4 Gravitational inflow to a filament decelerated by isotropic turbulent pressure

In Shimajiri et al. (2019b) a toy model was proposed to explain the mass accretion process on the B211/3 filament in the Taurus molecular cloud. This toy model works under the assumption that the filament is accreting mass from intersecting 100 pc scale sheets due to the self-gravity of the B211/3 filament (without taking the self-gravity of the sheet into account). In order to prevent strong gravitational acceleration, an isotropic turbulent pressure is invoked which was taken to be the full observed ^{12}CO linewidth over the filament (0.9 km s^{-1} in the sheet and 1.3 km s^{-1} in the filament). As explained in Paper-MC, a slightly different scenario for the formation of the Musca filament was proposed. First of all, it was observed for Musca that the full linewidth can not be used as an isotropic turbulent pressure that prevents gravitational collapse. But more importantly, we proposed that the converging flow that forms the Musca filament is not purely the result of self-gravity from a filament. It rather is the result of converging flows due to bending of the magnetic field by a HI cloud-cloud collision, where self-gravity of the filament only plays a role on the local scale. Furthermore, it was put forward in Paper-MC that the gravitational acceleration is not dominantly counteracted by a turbulent pressure but rather by the magnetic field.
For DR21, it was proposed that a cloud-cloud collision also plays an important role in the star formation process. In Inoue et al. (2018), it was suggested that the inflow driven by bending of the magnetic field would be sufficient to form massive stars. However, the study of the DR21 cloud showed that gravity most likely also plays an important role in guiding the inflow towards the massive star forming cores and fragments. Furthermore, the turbulent support in the DR21 cloud is very small with respect to the gravitational energy. It is thus proposed for the DR21 cloud that the bending of the magnetic field also plays an important role in preventing strong gravitational acceleration until the gas reaches the ridge.

To investigate the Shimajiri et al. (2019b) scenario in more detail, their toy model was applied to the Musca cloud and DR21 cloud. The toy model is described below and works with a Plummer model for the filament at the intersection of two sheets that each have an angle (θ) with the line of sight. A Plummer profile is given by

$$N = \frac{N_0}{\left[1 + \left(\frac{R}{R_{flat}}\right)^2\right]^{\frac{p-1}{2}}}, \qquad \rho = \frac{\rho_c}{\left[1 + \left(\frac{R}{R_{flat}}\right)^2\right]^{\frac{p}{2}}} \tag{5.1}$$

with μ the mean molecular mass, m_H the hydrogen mass, N_0 the central column density, R_{flat} the inner radius where the density profile is flat, p the density power law and ρ_c the central density.
To describe the gravitational potential of the filament in the toy model, the Plummer profile is approx-

imated by a broken power-law shown in Fig. 5.18

$$\begin{aligned}
\rho &= \rho_{flat} && (R' < R_{flat}) \\
\rho &= \rho_{flat}\left(\frac{R'}{R_{flat}}\right)^{-2} && (R_{flat} < R' < R_{out}) \\
\rho &= \rho_{flat}\left(\frac{R_{out}}{R_{flat}}\right)^{-2}\left(\frac{R'}{R_{out}}\right)^{-p} && (R_{out} < R' < R'_{init}) \\
\rho &= \rho_{flat}\left(\frac{R_{out}}{R_{flat}}\right)^{-2}\left(\frac{R'_{init}}{R_{out}}\right)^{-p} && (R'_{init} < R')
\end{aligned} \tag{5.2}$$

with p the exponent of the power law for the density distribution, R′ the distance corrected for the inclination along the line of sight (R′ = R/sin(θ)), ρ_{flat} the density for R′ < R_{flat}, R_{out} the outer radius of the filament and R'_{init} the initial radius for this toy model of turbulence counteracting gravitational acceleration. With this density profile, the gravitational potential can be described by (Hennebelle & André, 2013)

$$\begin{aligned}
\phi(R') &= G\rho_{flat}\pi R'^2 && (R' < R_{flat}) \\
\phi(R') &= GM_{line,flat}\left[1 + 2\ln\left(\frac{R'}{R_{flat}}\right) + 2\left(\ln\frac{R'}{R_{flat}}\right)^2\right] && (R_{flat} < R' \leq R_{out}) \\
\phi(R') &= GM_{line,flat}\left[1 + 2\ln\left(\frac{R_{out}}{R_{flat}}\right) + 2\left(\ln\frac{R_{out}}{R_{flat}}\right)^2\right] + 2GM_{line}\ln\left(\frac{R'}{R_{out}}\right) && (R_{out} < R')
\end{aligned} \tag{5.3}$$

where M_{line} and $M_{line,flat}$ are defined by

$$\begin{aligned}
M_{line,flat} &= \rho_{flat}\pi R_{flat}^2 \\
M_{line} &= \rho_{flat}\pi R_{flat}^2\left[1 + 2\ln\left(\frac{R_{out}}{R_{flat}}\right)\right]
\end{aligned} \tag{5.4}$$

With an assumed constant effective sound speed, the density profile in Eq. 5.2 is responsible for the pressure gradient to counteract gravity. The pressure gradient force and the conservation of energy then allow to follow the evolution of the velocity field starting from

$$\frac{1}{2}(V'^0_{init})^2 + \phi(R'_{init}) + C^2_{s,eff}\ln(\rho_{init}) = \frac{1}{2}V(R')^2 + \phi(R') + C^2_{s,eff}\ln(\rho(R')) \tag{5.5}$$

with V(R′) the velocity and $C_{s,eff}$ (= the linewidth of the average ^{12}CO(1-0) line) the effective sound speed which is assumed constant over the full cloud. Rewriting the above formula results in the following expression for the projected velocity field

$$V(R) = V_{fil} \pm \sqrt{2\left[\frac{1}{2}(V'^0_{init})^2 + \phi(R'_{init}) - \phi(R') + C^2_{s,eff}\ln\left(\frac{\rho_{init}}{\rho(R')}\right)\right]} \times \cos\theta \tag{5.6}$$

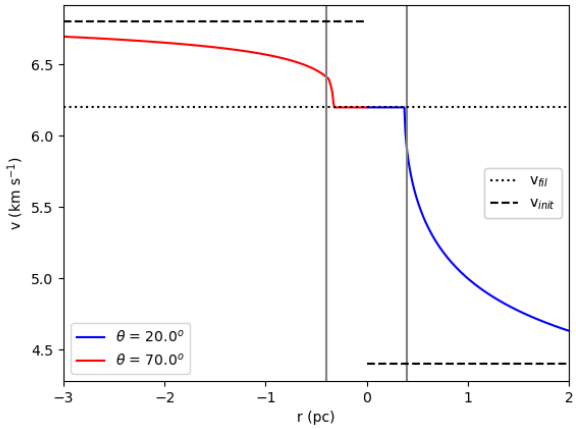

Figure 5.17: The velocity profile presented in Shimajiri et al. (2019b) for the B211/3 filament, which was reproduced with the code that will be used to analyse the Musca and DR21 cloud. The two angles (θ) are the inclination of the two inflowing sheets with respect to the line of sight as proposed in Shimajiri et al. (2019b).

with V_{fil} the velocity of the filament, and V'^{0}_{init}, R'_{init} and ρ_{init} the velocity corrected for the inclination, the distance corrected for the inclination and the density at the starting point for the model.
In the case of a strong isotropic turbulent pressure when approaching the filament, $C^2_{s,eff} \ln\left(\frac{\rho_{init}}{\rho(R')}\right)$ can become smaller than $\frac{1}{2}\left(V'^{0}_{init}\right)^2 + \phi(R'_{init})$ - $\phi(R')$. This leads to the square root of a negative value in Eq. 5.6. In this case, V(R) is set to V_{fil} in the model.

Before applying the mass accretion toy model described above to the Musca cloud, it has to be verified that the model works properly. This can be done by using the input values from Shimajiri et al. (2019b), which are given in Tab. 5.2, and verifying that the resulting velocity profile is exactly the same as the profile presented in the paper. The obtained velocity profile for B211/3 is presented in Fig. 5.17, and indeed looks exactly like the result in Fig. 6 of Shimajiri et al. (2019b). The code can thus be used to study the velocity field in Musca and DR21 as well.

5.4.1 Input parameters for Musca and DR21

The input parameters for Musca are not the same as for the B211/3 filament. For the initial radius of the model, a generally considered size of 6 pc for the Musca cloud is used (e.g. Kainulainen et al., 2016; Hacar et al., 2016; Tritsis & Tassis, 2018). For the central density the result from the RADEX calculations, namely $n_{H_2} = 10^4$ cm^{-3}, was used. For the filament velocity, 3.2 km s^{-1} from Hacar et al. (2016) is taken, and an initial velocity of 1.8 and 2.1 km s^{-1} is taken for the two sides of the filament. This choice is supported by the PV diagram that was derived from the NANTEN2 data. For

the effective turbulent sound speed, an upper limit of 0.4 km s^{-1} was found for the ambient cloud while observations towards the strand and crest have indicated an upper limit of 0.2 km s^{-1} there. The density power law index (p) of the ambient cloud is varied between 1 and 1.5 as in Shimajiri et al. (2019b), and for the filament a density power-law index of 2 is used which is consistent with the reported 2.2 $\pm$ 0.3 power-law index based on the *Herschel* observations for Musca (Cox et al., 2016). The resulting density profile for these input parameters is displayed in Fig. 5.18. Lastly, the inclination of the inflow with respect to the line of sight is varied between 20° and 80° to take into account the full range of possible orientations. All these input parameters are summarized in Tab. 5.2.

The input parameters for the DR21 models are also presented in Tab. 5.2. In this toy model for DR21 it is assumed that a Plummer profile with a relatively constant central density can describe the DR21 ridge. A first point of discussion is the central density. In Girart et al. (2013), an average density of $n_{H_2} = 2{\cdot}10^5$ cm^{-3} was proposed based on the data from Motte et al. (2007). This is however significantly lower than the central density of the DR21 ridge. Combining the column density at the center of the ridge, which easily reaches $N_{H_2} = 5{\cdot}10^{23}$ cm^{-2}, with an assumed central area of 0.1 pc, it is found that the central flat density of the DR21 ridge could reach $n_{H_2} \sim 2{\cdot}10^6$ cm^{-3}. This gives an order of magnitude difference with the average estimated density of the DR21 ridge. For the density power law decrease, p = 2 is assumed. For R_{flat}, a proposed typical value of 0.05 pc is used, and for the outer radius of the ridge a value of 0.4 pc is taken which is consistent with 0.34$\pm$0.12 pc in Hennemann et al. (2012). Based on the IRAM 30m information, the filament velocity is -3.5 km s^{-1} (Schneider et al., 2010), and the maximal possible effective sound speed is 1.4 km s^{-1} in all structures of the model. This value corresponds to the linewidth of the average spectrum over the full cloud, and thus assumes that the entire linewidth of the spectrum contributes to an isotropic turbulent pressure. As for the B211/3 filament in Taurus, this is a generous assumption. The two intersecting sheets are assumed to have V_{init} = -1.0 km s^{-1}, which can be expected from the PV diagram of the JCMT observations. Lastly, R'_{init} = 10 pc and p = 1-1.5 is used for the intersecting sheets in DR21 (as in B211/3). As for Musca, the inclination of the sheets with respect to the line of sight is varied between 20° and 80°.

5.4.2 The gravitational potential and effective pressure

In this study of the Shimajiri et al. (2019b) toy model to investigate if turbulent pressure can indeed slow down gravitational inflow towards the filament, multiple initial conditions (model 1, model 2,...) will be considered for Musca in the range of input parameters that are given in Tab. 5.2. In total, 6 models are considered which are summarized in Tab. 5.3. In each of these models, the angle of both sheets with respect to the line of sight is varied between 20°- 80°. In model 2, the scenario is considered where the filament ($R' < R_{out}$) has a lower turbulent pressure than the intersecting sheets. Lastly, in model 6, a scenario is considered that is not supported by the observations with $C_{s,eff}$ = 0.6 km s^{-1} to study the importance of the isotropic turbulent pressure.

Before studying the velocity profiles that are produced by the different models, the evolution of the gravitational potential and turbulent energy terms will be examined to better understand the results. When examining equation 5.6, it is found that the term $\phi(R'_{init})$ - $\phi(R')$ + $C^2_{s,eff}\ln\left(\frac{\rho_{init}}{\rho(R')}\right)$, expressing

component	parameter	Musca	B211/3	DR21
filament	$n^0_{H_2}$	10^4 cm^{-3}	4.5×10^4 cm^{-3}	$2\cdot10^5$-$2\cdot10^6$ cm^{-3}
	p	2	2	2
	R_{flat}	0.056 pc	0.03 pc	0.05 pc
	R_{out}	0.4 pc	0.4 pc	0.4 pc
	V_{fil}	3.2 km s^{-1}	6.2 km s^{-1}	-3.5 km s^{-1}
	$C_{s,eff}$	0.2-0.4 km s^{-1}	1.3 km s^{-1}	1.4 km s^{-1}
sheet 1	$V_{init,1}$	1.8 km s^{-1}	6.8 km s^{-1}	-1.0 km s^{-1}
	$R'_{init,1}$	6 pc	10 pc	10 pc
	θ_1	20° - 80°	70°	20° - 80°
	p_1	1-1.5	1	1.5
	$C_{s,eff}$	0.2-0.4 km s^{-1}	0.9 km s^{-1}	1.4 km s^{-1}
sheet 2	$V_{init,2}$	2.1 km s^{-1}	4.4 km s^{-1}	-1.0 km s^{-1}
	$R'_{init,2}$	6 pc	10 pc	10 pc
	θ_2	20° - 80°	20°	20° - 80°
	p_2	1-1.5	1.5	1
	$C_{s,eff}$	0.2-0.4 km s^{-1}	0.9 km s^{-1}	1.4 km s^{-1}

Table 5.2: The (range of) input parameters for the toy model from Shimajiri et al. (2019b) for Musca, DR21 and the B211/3 filament.

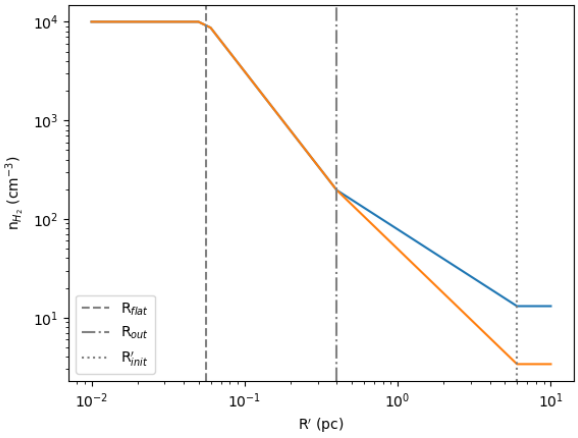

Figure 5.18: The density profiles used for Musca. The central area has a constant density ($n_{H_2} = 10^4$ cm^{-3}), followed by an R'^{-2} decrease up to the outer radius of the filament (R_{out}). Outside the filament, the density profile decreases following $R'^{-1.5}$ (orange) or R'^{-1} (blue) up to R'_{init}. After R'_{init}, a constant density is assumed.

parameter	model 1	model 2	model 3	model 4	model 5	model 6
p_1	1.	1.	1.	1.5	1.5	1.
p_2	1.	1.	1.	1.5	1.5	1.
θ_1	20°-80°	20°-80°	20°-80°	20°-80°	20°-80°	20°-80°
θ_2	20°-80°	20°-80°	20°-80°	20°-80°	20°-80°	20°-80°
$C_{s,eff}$	0.4 km s^{-1}	0.4 km s^{-1}	0.2 km s^{-1}	0.4 km s^{-1}	0.2 km s^{-1}	0.6 km s^{-1}
$C_{s,eff,filament}$	0.4 km s^{-1}	0.2 km s^{-1}	0.2 km s^{-1}	0.4 km s^{-1}	0.2 km s^{-1}	0.6 km s^{-1}

Table 5.3: The input values from Tab. 5.2 that were varied for the Shimajiri model of the Musca cloud. The angle of both sheets with respect to the line of sight are varied for each model between 20° and 80°.

the role of gravity and turbulent pressure, is essential to the evolution of the velocity profile.
Fig. 5.19 studies the evolution of $\phi(R'_{init})$ - $\phi(R')$ and $C^2_{s,eff}\ln\left(\frac{\rho_{init}}{\rho(R')}\right)$ as a function of the corrected distance (R′) from the center of the filament for the six models presented in Tab. 5.3. The evolution of the specific energy is shown for four different angles between 20° and 80° in each model.
Fig. 5.3 shows that the gravitational and turbulent specific energy in models with $C_{s,eff} = 0.4$ km s^{-1} (model 1, model 4) have a very similar evolution. Models with $C_{s,eff} = 0.2$ km s^{-1} (model 3, model 5) on the other hand, have a significantly lower turbulent specific energy than gravitational specific energy. In model 2, the changing effective sound speed when entering the filament leads to a sudden jump in the turbulent specific energy evolution, and demonstrates that the observed low turbulent linewidth in the filament crest is insufficient to provide significant support against gravitational acceleration. With the last model, model 6, it is found that a significant isotropic turbulent linewidth is necessary to truly counteract the gravitational potential. All these models also demonstrate that a higher density, assuming a constant effective sound speed, leads to an increasing importance of turbulent pressure with respect to gravity.

5.4.3 The predicted velocity profiles

Before starting an in depth study of the velocity profiles, it is first noted that the observed PV diagram of the Musca cloud requires a particular configuration for the intersecting sheets with respect to the filament crest. It requires that both intersecting sheets are coming from behind the filamentary structure from our point of view, as is illustrated in Fig. 20 of Paper-MC. The same requirement is valid for the DR21 cloud, only there the intersecting sheets are located in front of the ridge.
In Fig. 5.20, the velocity profiles predicted by the Shimajiri model are presented for the 6 considered initial conditions from Tab. 5.3. It is observed that with the relatively low upper limit of the effective turbulent sound speed (≤ 0.4 km s^{-1}), it is difficult to counteract the gravitational acceleration by the Musca filament. Only at a high turbulent effective sound speed above the observational constraints, described by model 6, it is possible to sufficiently reduce the gravitational acceleration. Furthermore, it is observed that none of the models manages to accurately follow the evolution of the velocity field as observed in the Musca cloud, in particular close to the filament, which suggests that different mechanisms are at work in the Musca cloud.

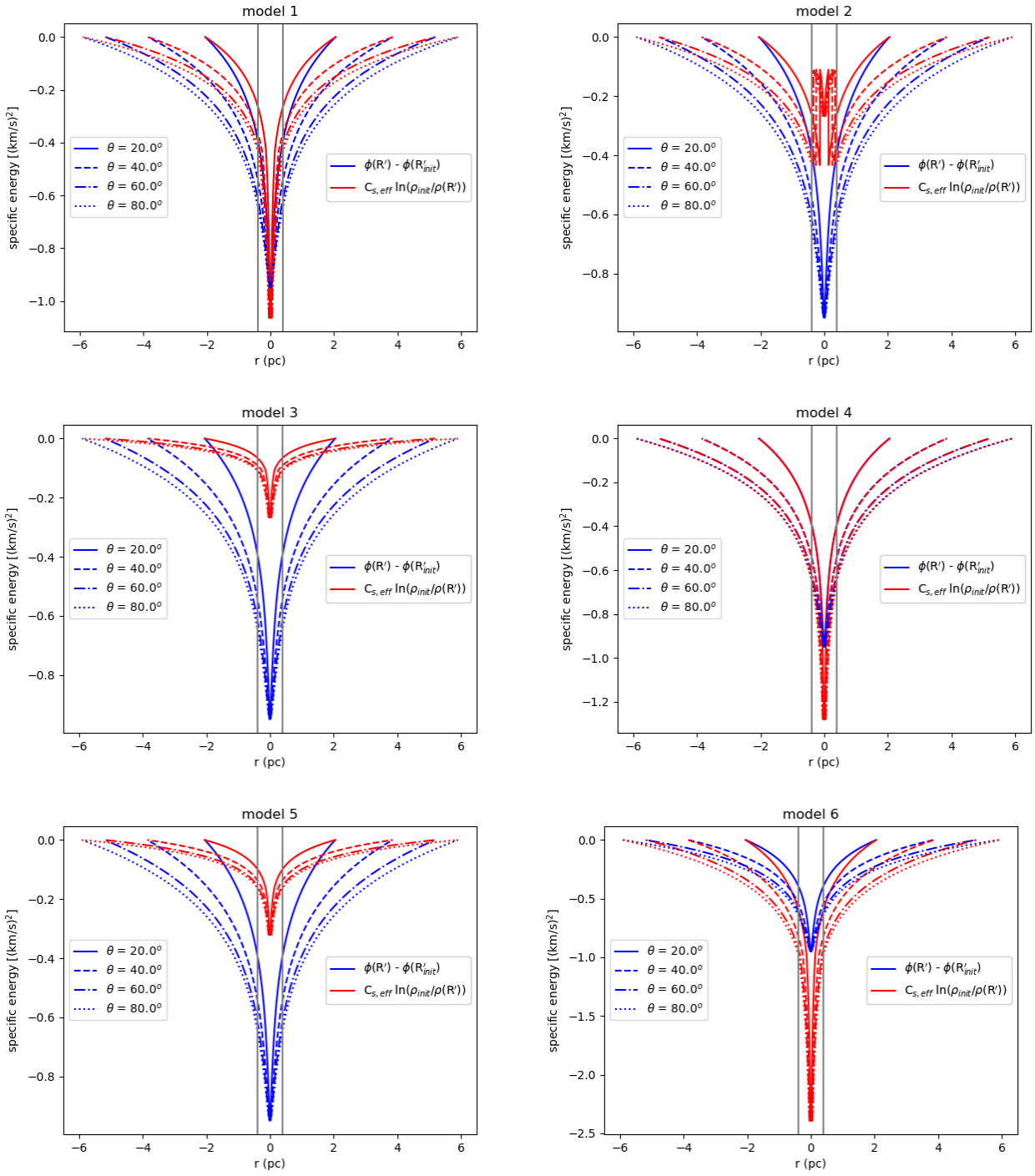

Figure 5.19: The evolution of the gravitational (blue) and turbulent (red) specific energy terms in the Shimajiri model as a function of the distance for the 6 different Musca models presented in Tab. 5.3. Each plot shows the evolution for different projection angles (θ) of the sheets at 20^o, 40^o, 60^o and 80^o. The grey vertical lines indicate r = 0.4 pc.

Most likely, the magnetic field plays an important role in the evolution of the velocity field in the Musca cloud, which would be expected based on the Inoue model. It should also be noted that the presence of low-velocity filament accretion shocks near the Musca filament can also provide an important contribution to the evolution of the velocity field in the vicinity of the Musca filament.
When closely inspecting the observed velocity profile of the B211/3 filament in Shimajiri et al. (2019b), see Fig. 5.10, it can be observed that close to the filament there are significant deviations of the velocity profile from the predictions by their toy model. This suggests that near the filament one must also take into account other physics than gravity and isotropic turbulent pressure. For example, low-velocity filament accretion shock might also play a role there.

For DR21, two models were run with the toy model. One using $n^0_{H_2} = 2{\cdot}10^5$ cm^{-3} and the other one using $n^0_{H_2} = 2{\cdot}10^6$ cm^{-3}. For both models, sheet 1 has a density power law decrease of p = 1.5 and sheet 2 has p = 1. This allows to study the dependence on the density profile for the possibly intersecting sheets. The resulting velocity profiles are presented in Fig. 5.21, demonstrating that the maximal possible isotropic turbulent pressure is insufficient to counteract the predicted gravitational acceleration by the model. For the considered initial conditions of DR21 it is thus found that the Shimajiri model does not manage to reproduce the observed velocity profile. In both cases, the predicted gravitational acceleration by the toy model is significantly higher than observed. This points, as for Musca, to an important role of the magnetic field in the DR21 cloud to maintain the smooth observed velocity profile. From the virial analysis, it was proposed that self-gravity of the cloud is relatively important, even on large scales. These results suggest that, though gravity can be the driver of the accretion, there is significant competition between gravity and the magnetic field in the DR21 cloud to maintain a smooth velocity profile.
Lastly, based on the problems of the Shimajiri toy model to reproduce the velocity fields of Musca and DR21, it is possible that the magnetic field is also the main force to counteract gravitational acceleration in B211/3. Furthermore, it was already indicated in Sec. 5.3.1 that the PV diagram of the cloud around B211/3 can be explained by the Inoue model.

5.5 The magnetic field in the ambient cloud and dense filament

5.5.1 The Planck magnetic field in the Musca and DR21 cloud

It was proposed for the Musca cloud that the magnetic field drives the inflow from the ambient cloud to the filament. This requires that the magnetic field is the dominant force in the ambient cloud of the Musca filament. At the moment, there are no direct measurements for the magnetic field strength in the Musca cloud. The polarised dust emission from Planck at 353 GHz however shows that the magnetic field is highly organised in the ambient cloud and perpendicular to the Musca filament (Planck Collaboration et al., 2016c; Cox et al., 2016). In e.g. Soler et al. (2013) and Seifried et al. (2020) it was shown that such an organised structure of the magnetic field in the ambient cloud indicates that the magnetic field is dominant in this region.
The Planck telescope covered the full sky. It is thus possible to study the magnetic field orientation of the Cygnus-X region and in particular the magnetic field around the DR21 ridge. The possibilities of this study with Planck are limited because of the poor spatial resolution of $4.8'$, which corresponds to a

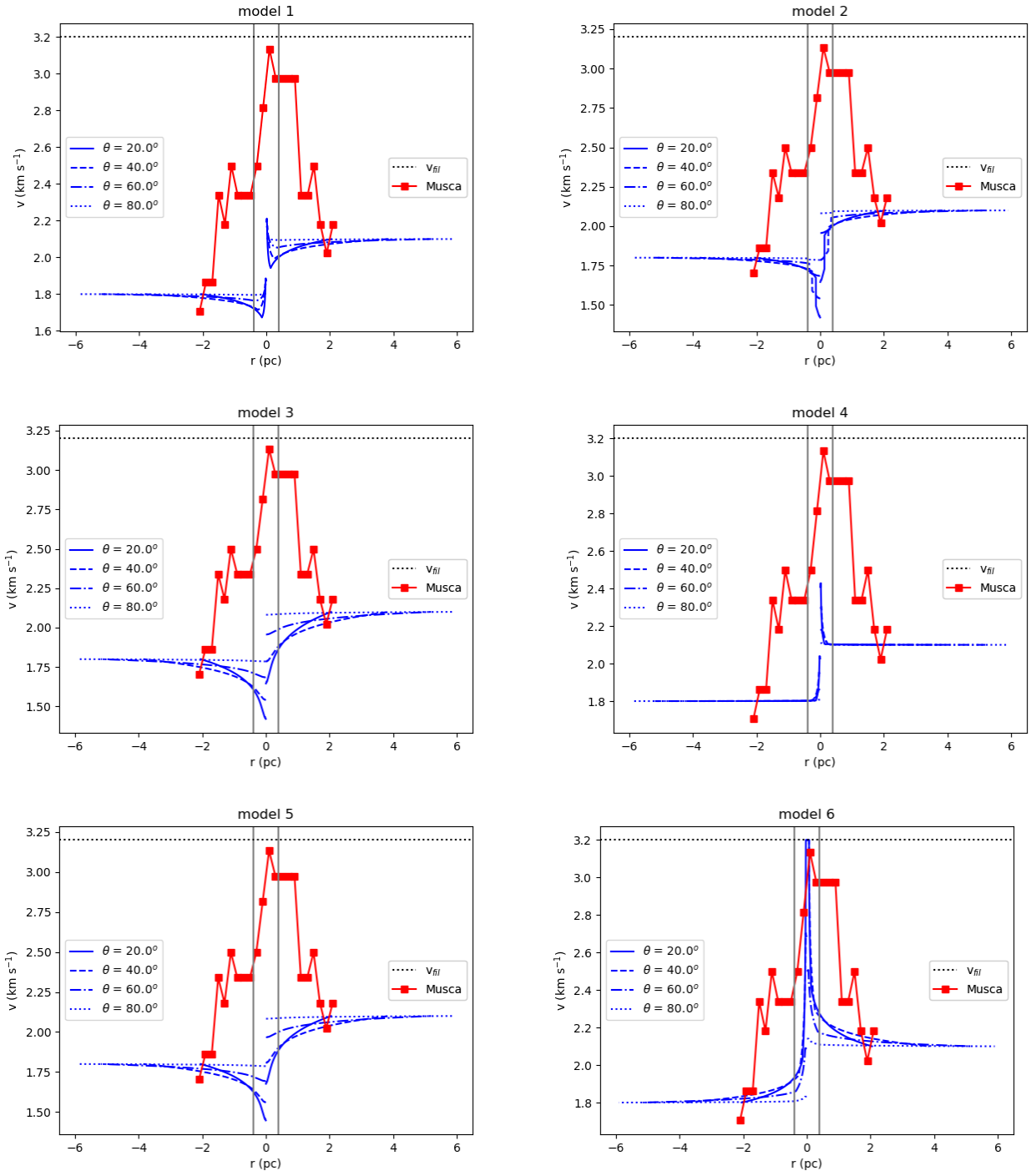

Figure 5.20: The predicted velocity profiles (blue) by the Shimajiri model from the 6 initial conditions (models) for Musca specified in Tab. 5.3. The velocity profile in red is the observed velocity profile of Musca in the PV diagram. With the presented models, it is difficult to reproduce the observed velocity profile.

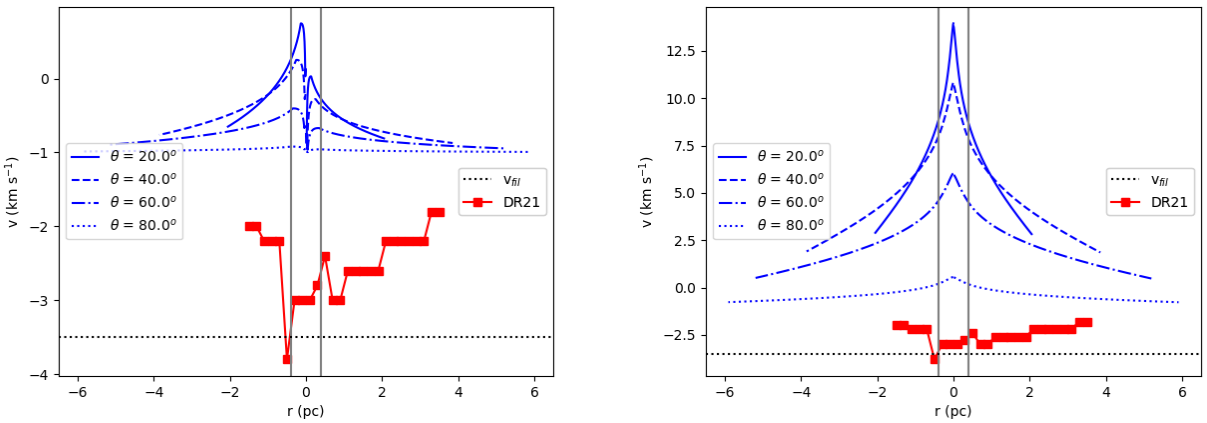

Figure 5.21: **Left**: The predicted velocity profiles (blue) by the Shimajiri model for DR21, assuming a central density $n^0_{H_2} = 2{\cdot}10^5$ cm^{-3}. The first sheet (r < 0), which reaches the highest peaking velocity, has p = 1.5. The sheet at the other side (r > 0) has p = 1. The observed velocity profile of the DR21 cloud in the PV diagram is shown in red. **Right**: The same, assuming a central density $n^0_{H_2} = 2{\cdot}10^6$ cm^{-3}. In this case, the gravitational dominance of the ridge is so large that the different power law exponent for the sheets has basically no effect on the predicted velocity field.

physical size of 2.0 pc in Cygnus-X. The map of the Planck magnetic field orientation for DR21 is shown in Fig. 5.22. This figure suggests a significantly more complex magnetic field than in the Musca cloud, shown in Fig. 3.5, where the orientation is nicely perpendicular to the ridge. The proposed large scale importance of gravity in DR21, in combination with the proposed magnetic field bending, might play an important role in the observed complex large-scale magnetic field. However, no typical hourglass shape for collapsing cores/clumps is observed either. The limited spatial resolution might play a role in this. Higher spatial resolution ($\sim 20''$) large scale mapping, which will be possible with the B-BOP receiver on the proposed SPICA telescope, will unveil the large scale structure of the magnetic field around massive star forming ridges in detail.

5.5.2 Prospective: Striations in Musca and subfilaments in DR21

Both in the Musca and DR21 clouds, it is observed that there is a main star forming filamentary structure with lower density filamentary structures in the ambient cloud. In Musca, these lower density structures are called striations which are closely aligned with the orientation of the magnetic field (Cox et al., 2016). Based on the column density contrast, it was proposed by Tritsis & Tassis (2016) that striations are the result of the coupling between density inhomogeneities and MHD waves. This is in contrast to the view proposed by Palmeirim et al. (2013) who suggests that striations are filamentary streams of gas along the magnetic field lines towards the star forming filament. In this 'streamer' point of view, it can be considered that the subfilaments that are flowing towards the DR21 ridge are simply a denser version of striations (Ballesteros-Paredes et al., 2020). In that case one would expect that

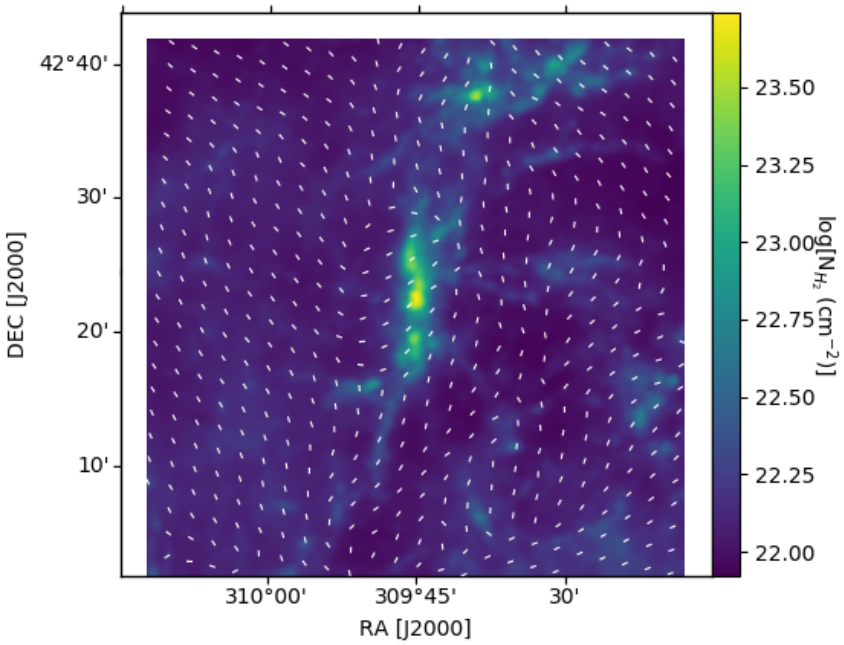

Figure 5.22: The magnetic field orientation towards the DR21 cloud and W75N from the Planck data at 353 GHz.

the magnetic field and the subfilaments of DR21 are roughly aligned. First of all, it should be noted that the subfilaments of DR21 are not all perfectly perpendicular to the ridge as is observed for the striations of Musca. But specifically, this would imply that the magnetic field orientation is aligned with the subfilaments of DR21. The resolution of the Planck observations is far from sufficient, but the obtained magnetic field orientation with the Planck observations does not appear to agree with this. In Fig. 5.22, it can be observed that the Planck magnetic field rather appears perpendicular to the subfilaments of DR21. This would suggest that the subfilaments of DR21 rather resemble star forming filaments than the striations of Musca. However, higher resolution magnetic field orientation observations will be required to address this question. Both the high sensitivity of the NIKA2 receiver on the IRAM 30m telescope and the HAWC$^+$ receiver on SOFIA could provide indications for this with the magnetic field orientation towards the subfilaments. However, for an in depth analysis of the subfilaments and ambient cloud, the sensitivity of B-BOP on SPICA will be required.

Chapter 6

Massive dense cores and the initial mass function

6.1 Massive dense cores in Cygnus-X North

In the previous sections, the physical processes were studied that play a role in the formation of dense filamentary gas in low- and high-mass star forming regions of the ISM. In this section, the focus will shift to dense cores and in particular massive dense cores (MDCs). The formation and stability of these MDCs will be investigated, to study how this could be related to dense gas gathering discussed in the previous sections and how this could affect the star formation process.

6.1.1 A lack of high-mass prestellar cores

The massive equivalent of dense cores, so-called massive dense cores (MDCs), are observed in high-mass star forming regions (e.g. Beuther et al., 2002a; Rathborne, Jackson & Simon, 2006; Motte et al., 2007, 2018; Butler & Tan, 2012; Tigé et al., 2017). However, unlike low-mass stars, evidence of massive prestellar cores, even for a short lifespan, remains scarce (e.g. Louvet et al., 2019; Peretto et al., 2020). Statistically studying the physical properties of massive dense cores thus allows to investigate under which conditions massive stars form, how this affects the IMF and why there possibly might not be massive prestellar cores. Simultaneously, it can be studied how the proposed role of large-scale gravitational inflow and the magnetic field are related to the observed conditions in the MDCs.
At the interface of the evolution of MDCs and how dense filamentary structures form, the question also arises on the difference between filament hubs, MDCs and ridges, and if this affects the process of (high-mass) star formation in these structures. To reiterate, filament hubs are intersections of inflowing filaments that can have a relatively spherical appearance (Myers, 2009; Schneider et al., 2012; Peretto et al., 2013) while ridges are high column density ($N_{H_2} \sim 10^{23}$ cm^{-2}) filaments (Hartmann & Burkert, 2007; Hill et al., 2011) which can have associated filaments that are connected to this ridge (also called subfilaments; Hennemann et al., 2012). MDCs on the other hand can be found in ridges and filament hubs, but Fig. 6.1 and Motte et al. (2007) show that some MDCs can be found in relative isolation. Higher resolution observations of several MDCs also show indications of possible filamentary gas in the

MDC vicinity $\sim$ 0.1 pc (Bontemps et al., 2010b; Fechtenbaum, 2015), which could suggest that MDCs in isolation are in fact small filament hubs.

6.1.2 The physical conditions in massive dense cores in Cygnus-X north

Recently, a census of MDCs has been extracted in the Cygnus-X regions from the *Herschel* data (Cao et al., 2019). These MDCs were extracted using the *getsources* code (Men'shchikov et al., 2012). In a simultaneous effort, MDCs are being extracted in the HOBYS maps with a different method. This core extraction code is based on the principles of CUTEX (Molinari et al., 2017) and works with second derivatives in the column density maps to identify a core (Bontemps et al., in prep.). A 2D gaussian is fitted to the core after subtraction of the background using interpolation. In contrast to the *getsources* code this source extraction gives more control and a clearer constraint on how an extracted core is defined (a gaussian fit on high curvature peaks). A comparison of these extracted cores with the extracted cores by the *getsources* code is work in progress by Bontemps et al. Here, a further analysis of the sample of MDCs with masses above 30 $M_\odot$ in Cygnus-X north will be presented. This sample contains a total of 54 cores with a mass above 30 $M_\odot$. The maximal mass of the MDCs in the sample is 497.6 $M_\odot$. Further analysis of these MDCs is based on complementary information for each core from Spitzer observations of the Cygnus-X region (Kraemer et al., 2010), NH_3 observations of the KEYSTONE program (Keown et al., 2019), and CS(2-1), N_2H^+(1-0) and $C^{18}O$(1-0) observations with the FCRAO telescope (Simon et al., 2006c; Schneider et al., 2007, 2010, 2016b).
Figure 6.1 shows the spatial distribution of the MDCs with the most massive cores ($>$ 60 $M_\odot$) highlighted in black. It is observed that the most massive cores are concentrated in the DR21 ridge and that W75N contains a second crowded region of MDCs. This suggests that most MDCs are located in the northern areas of Cygnus-X north. In the other regions (DR17, DR20, DR22 and DR23), the distribution of MDCs is less compact. Interestingly, these four regions are associated with well developed HII regions (e.g. Furst et al., 1990; Reich et al., 1990; Taylor et al., 2003). This could indicate that the observed MDCs in these regions trace the last evolving MDCs or a second wave of massive star formation as a result of compression by the feedback from massive stars that are in formation or have recently formed. This can fit with the observed presence of early-type stars in these regions by Comerón et al. (2008). The concentration of MDCs could then be an indicator to evaluate the evolutionary state of a massive star forming cloud. This idea of feedback, e.g. in the form of an expanding bubble, responsible for a second wave of MDC formation explains the distribution of MDCs on an arc-like structure in DR20, while in DR17 the MDCs have a circular distribution around a relatively low column density region with known radiocontinuum emission. This scenario would suggest that external compression is again the trigger of what will eventually lead to intermediate and possibly high-mass star formation.

Temperature and luminosity of the MDCs

In this section, some results obtained with the *Herschel* and Spitzer data will be presented before addressing the dynamics of the cores.
First of all, the contribution of submillimeter emission to the total luminosity of the cores can be studied. The submillimeter contribution is defined by $\lambda > 350$ μm (Andre, Ward-Thompson & Barsony, 2000). Similar to the result for NGC 6334 (Tigé et al., 2017), it is found in Fig. 6.2 that L_{submm}/L_{bol} is

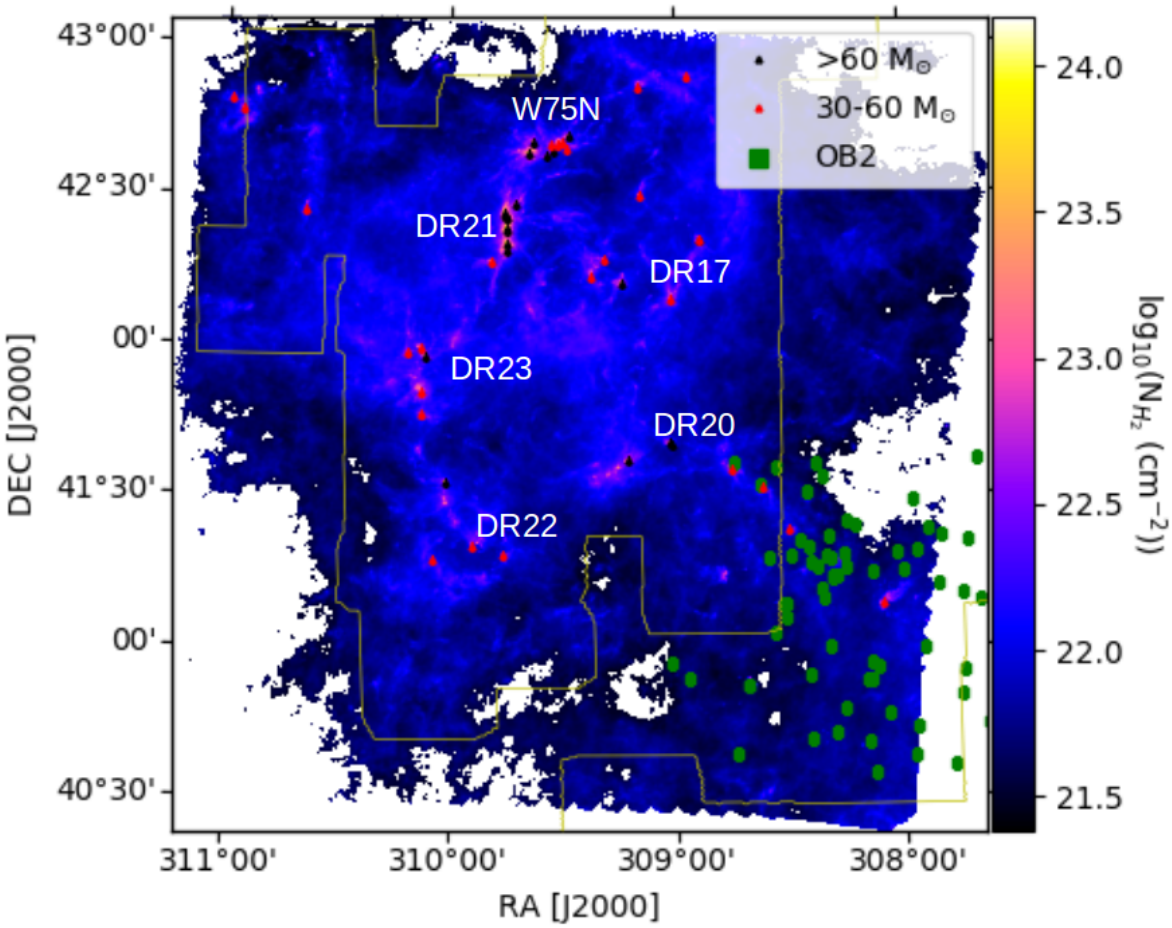

Figure 6.1: The *Herschel* column density map of Cygnus-X north on a log scale. The red and black triangles indicate the location of the MDCs extracted in the Cygnus-x north region (Bontemps et al. in prep). The green squares indicate the location of the OB stars in OB2 (Comerón & Pasquali, 2012). The yellow contours outline the area covered by the FCRAO observations.

generally larger than 1% for masses higher than 30 $M_\odot$. In the case of low-mass cores, this one percent threshold can be used to differentiate class 0 from class I protostars. Class 0 protostars were defined by $L_{submm}/L_{bol} > 1\%$. However, because of the significant differences between low- and high-mass star forming regions this threshold might not be directly applicable for MDCs (Hennemann et al., 2010; Tigé et al., 2017).
In Fig. 6.3, it is found that the bolometric luminosity increases with the core mass. This correlation could indicate an increasing mass for the MDCs over their lifetime as a result of mass accretion by the MDC from the surrounding clump. However, it should be noted in the evolutionary models of protostellar cores presented in Duarte-Cabral et al. (2013) that the start of protostellar evolution begins at a higher bolometric luminosity for high mass stars than low-mass stars, see Fig. 6.3. This higher start luminosity, which is also observed in luminosity models of clumps (Molinari et al., 2008, 2019), is related to the larger accretion rate for high-mass star forming cores, which leads to a higher accretion luminosity. The accretion luminosity is given by (Duarte-Cabral et al., 2013)

$$L_{acc}(t) = \frac{GM_\star(t)\dot{M}_{acc}}{R_\star(t)} \tag{6.1}$$

with $M_\star$ and $R_\star$ are the protostellar mass and radius which are obtained from protostellar evolution tracks for large accretion rates calculated by Hosokawa & Omukai (2009). More information on the evolutionary tracks and the intermittent accretion variation can be found in Duarte-Cabral et al. (2013). Comparing the starting point in the evolutionary diagram of Duarte-Cabral et al. (2013) with the observed bolometric luminosities in Fig. 6.3, it found that some MDCs over the full mass spectrum are located under the start luminosity of the evolutionary tracks. This is not necessarily an inconsistency because it was shown in Bontemps et al. (2010b) that protostars are located in subfragments of these MDCs which contain only a part of the total mass of the entire MDC. Furthermore, Duarte-Cabral et al. (2013) showed that these protostellar cores inside the MDCs are located on the evolutionary tracks. Inspecting Fig. 6.3 thus indicates that the increasing observed bolometric luminosity as a function of the core mass is no direct evidence of increasing core mass with increasing lifetime.

Fitting the SED of the MDCs also provides a dust temperature for each core. Fig. 6.4 presents the evolution of the dust temperature as a function of the core mass, showing that the MDC temperatures vary between 10 and 45 K. It also shows a tendency of increasing dust temperature with core mass. This could be an indication of:

• Possible gravitational inflow in MDCs, where part of the gravitational energy that is radiated away could increase the dust temperature because of the high opacity of these massive cores.

• Internal and external heating from compact objects in and around the more massive cores. This would imply that there are more, or warmer compact objects located in the most massive cores.

• Another possible heating mechanism would be shocks from converging flows in these MDCs. In Csengeri et al. (2011b), indications of such heating were found for several MDCs in Cygnus-X north.

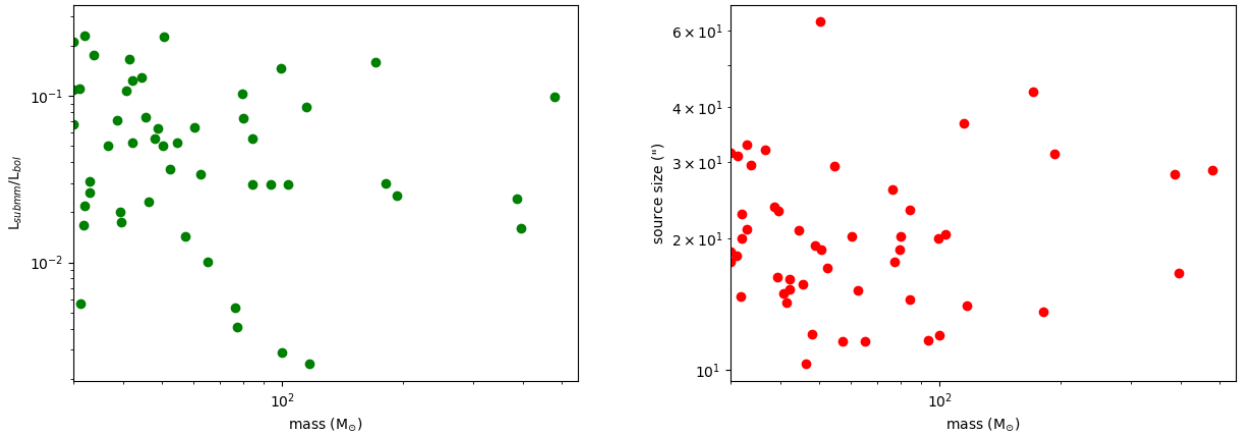

Figure 6.2: **Left:** The fraction of the submillimeter contribution to the total luminosity as a function of the core mass. **Right:** The deconvolved size of the MDCs in arcseconds as a function of the core mass.

However, the possible extra thermal support due to the higher temperatures is only marginal as the cores are significantly more massive than the mass that can be supported by isothermal cores at these temperatures. Assuming a core radius of 0.2 pc would require 70 K for virial support in a 30 $M_\odot$ core and up to a 1000 K for a 400 $M_\odot$ core. A way to further investigate this temperature rise is to study the gas kinetic temperature in the cores. This can be done with the NH_3(1,1) and NH_3(2,2) line observations by the KEYSTONE project using the Green Bank telescope (Keown et al., 2019). In the first statistical analysis with the KEYSTONE data of *Herschel* dendogram leaves in several high-mass star forming regions, a correlation between the NH_3 temperature and clump mass was found. However, it was found that this correlation was not very robust. Inspecting the kinetic gas temperature from NH_3 at the location of the cores in Fig. 6.4, a tendency of increasing temperature with core mass is again observed similar to the dust temperature. This tendency is noisy, but seen both for gas and dust. A possible way to investigate whether heating by compact objects gives rise to a higher temperature in the most massive objects, is looking for strong emission of the NH_3(3,3), NH_3(4,4) and NH_3(5,5) lines, which traces warm (> 100 K) NH_3 gas, in the KEYSTONE data.
The core extraction also provides a deconvolved core size for each extracted core. In general, the MDC size is found between 10″-30″, see Fig. 6.2. At a distance of 1.4 kpc for the Cygnus-X region (Rygl et al., 2012) this corresponds to a physical size of 0.068 to 0.2 pc. Fig. 6.2 also shows that there is no clear correlation between the extracted core size and core mass.

Dynamics of the MDCs

To obtain a first idea of the MDC dynamics, the survey with the SEQUOIA receiver on the FCRAO telescope was used which covers ^{13}CO(1-0), C^{18}O(1-0), CS(2-1) and N_2H^+(1-0) (Simon et al., 2006c; Schneider et al., 2006, 2007, 2010), toghether with the KEYSTONE NH_3 data. These surveys have their

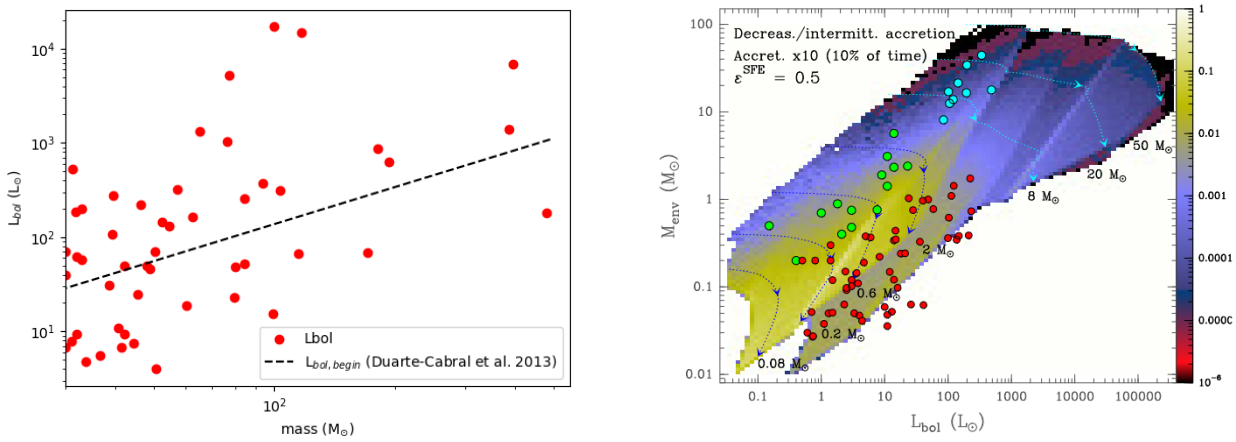

Figure 6.3: **Left:** The bolometric luminosity of the massive dense cores as a function of their mass. The dashed line indicates the initial luminosity of protostellar cores in the evolutionary diagram on the right. **Right:** The evolutionary tracks for low- and high-mass protostars combined with the observational results for class 0 (green) and class I (red) low-mass protostars, and high-mass protostellar fragments in Cygnus-X (blue). This figure was adapted from Duarte-Cabral et al. (2013).

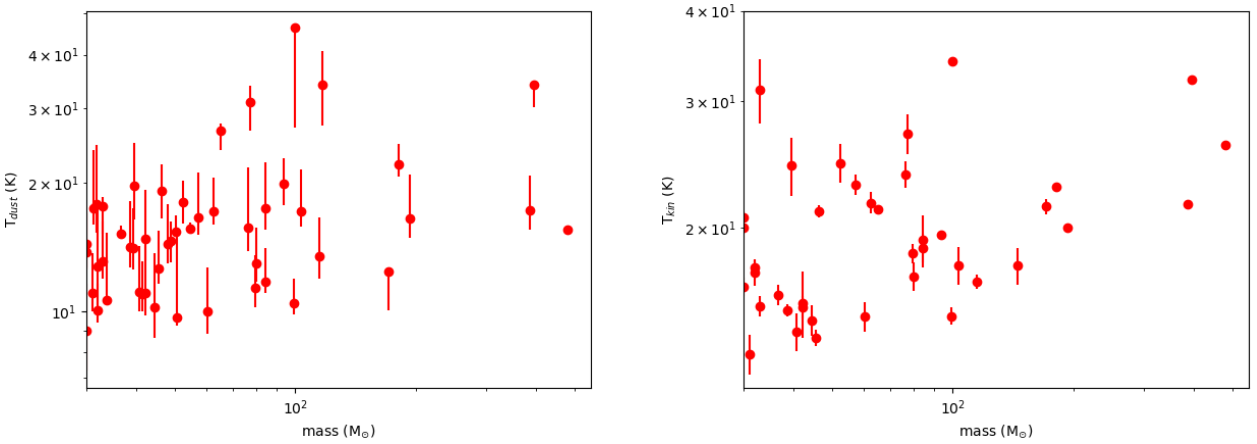

Figure 6.4: **Left:** The dust temperature of the MDCs as a function of the core mass. **Right:** The kinetic temperature obtained from $NH_3(1,1)$ and $NH_3(2,2)$ (Keown et al., 2019) at the location of the MDCs as a function of the core mass.

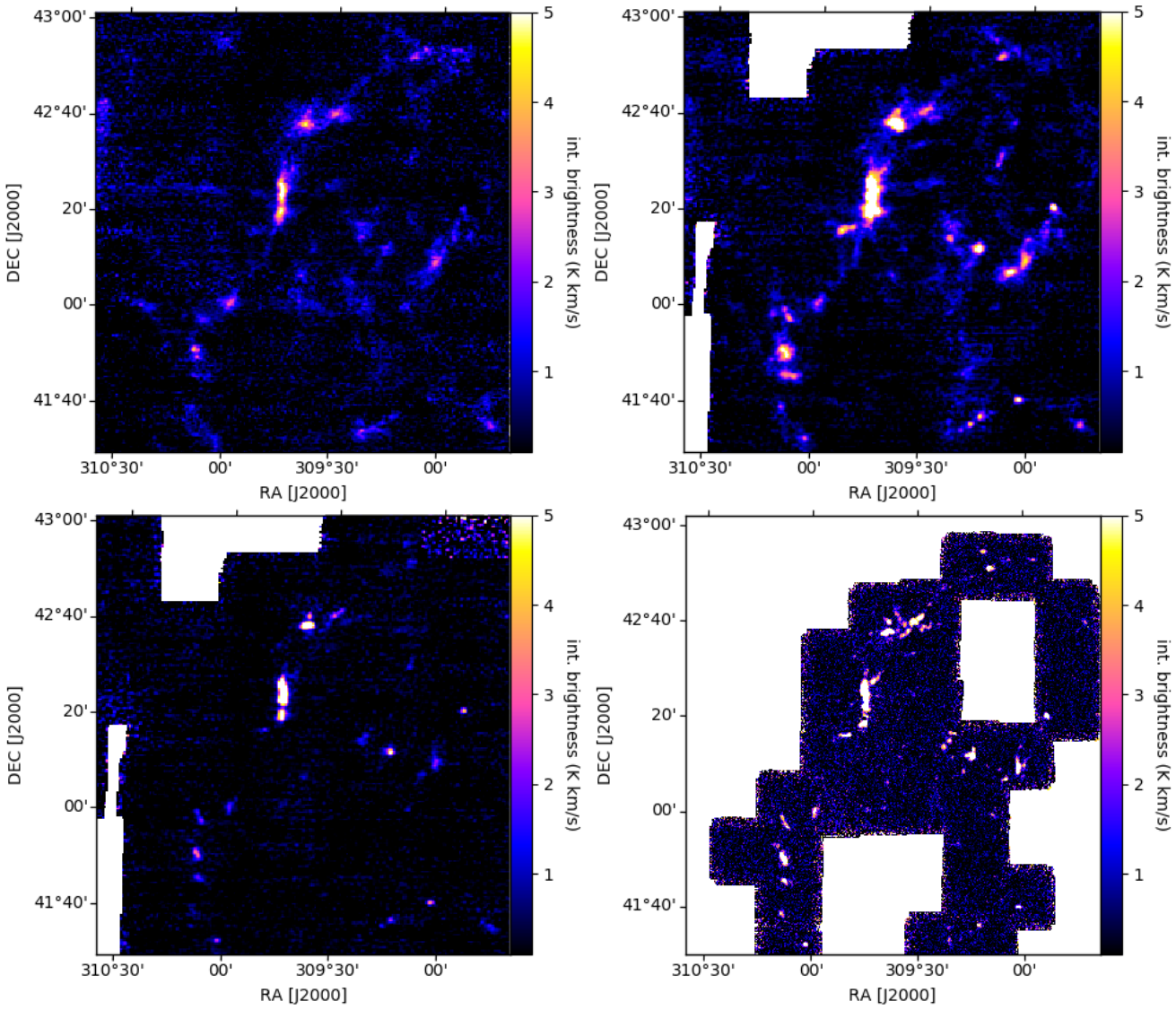

Figure 6.5: **Top left:** The integrated $C^{18}O$(1-0) FCRAO map of the Cygnus-X north region. The brightest filamentary structure is the DR21 ridge. The $C^{18}O$(1-0) emission also traces some extended gas. **Top right:** The same for CS(2-1). **Bottom left:** The same for N_2H^+(1-0). **Bottom right:** The same for NH_3(1,1).

limitations, but they allow a first evaluation of the MDC dynamics at different densities to study the MDC evolution and how this affects high-mass star formation. In particular the spatial resolution is a limiting factor for both surveys. The observations with the FCRAO telescope have a spatial resolution of 45-50″ with a main beam temperature noise rms of $\sim$ 0.4 K within a spectral resolution of 0.1 km s^{-1}. The KEYSTONE observations, have a spatial resolution of 32″ and a spectral resolution of 0.07 km s^{-1}. Within this spectral resolution, the data has a typical noise rms between 0.1 and 0.15 K. Both surveys thus have difficulties to spatially resolve the MDCs. As a result, when studying the dynamics of the MDCs with these lines, it should always be taken into account that it also traces more extended emission than only the gas in the MDCs.
The integrated intensity maps of the different molecular lines are presented in Fig. 6.5. It shows that CS(2-1) and $C^{18}O$(1-0) trace the dense structures and also trace more extended emission. Though CS also experiences depletion (Pagani et al., 2005), it was observed that CS might trace slightly denser gas than $C^{18}O$ (Tafalla et al., 2004) which would explain the detection of CS isotopologues at the center of massive protostellar fragments with high angular resolution observations (e.g. Molet et al., 2019). NH_3 and N_2H^+ on the other hand only trace the dense gas in the star forming filaments as is expected from previous observations (e.g. Ho & Townes, 1983; Tafalla et al., 2002; Caselli et al., 2002). NH_3 in particular highlights the filamentary structure of the dense gas in Fig. 6.5, similar to the results of the recent NH_3 survey of nearby star forming clouds in the Gould Belt (Friesen et al., 2017).

In order to extract the dynamic information from the molecular line emission towards each of the MDCs, it was assumed that the spectrum can be characterised by a single gaussian in all molecular lines. With the current observations, this is the best that can be done. The results presented here are evaluated at the native resolution of the FCRAO and KEYSTONE data which have a slightly different spatial resolution ($\sim$ 45″ and $\sim$ 30″). For the KEYSTONE observations, single gaussian fitting to all the spectra in the map was already performed by Keown et al. (2019) with the *pyspeckit* package (Ginsburg & Mirocha, 2011), providing the NH_3 column density, kinetic temperature, velocity dispersion and line-of-sight velocity. For each MDC, the location in the KEYSTONE map was determined using the Astropy software (Astropy Collaboration et al., 2013, 2018) to get dynamic information from NH_3.
For the FCRAO observations, the $C^{18}O$(1-0) and CS(2-1) line were fitted with a single gaussian providing the linewidth and line-of-sight velocity. The CS(2-1) and $C^{18}O$(1-0) spectra towards six selected MDCs are presented in Fig. 6.6, showing that generally a single gaussian fit should be acceptable. However, in the two most massive cores, inverse P-Cygni self-absorption effects are found for CS(2-1) which makes a gaussian fit less representative. The N_2H^+(1-0) fine-structure was fitted with the CLASS software[1]. Because the Cygnus-X north region has two main velocity components, the fit was done twice. In a first run with an initial guess for the velocity of the -3 km s^{-1}, and in a second run with an initial guess for the velocity of the 10 km s^{-1}. After the two runs, the fit with the best χ^2 was saved for further analysis.

First of all, the detection frequency for each of the molecular lines towards the MDCs is presented in Tab. 6.1 as a function of the minimal mass. It is found that the cores are always detected in all studied lines above 100 $M_\odot$, and that 80 % of the MDCs (above 30 $M_\odot$) are detected in all the studied

[1]https://www.iram.fr/IRAMFR/GILDAS/doc/html/class-html/class.html

transition	no data	30 $M_\odot$	40 $M_\odot$	50 $M_\odot$	60 $M_\odot$	70 $M_\odot$	80 $M_\odot$	90 $M_\odot$	100 $M_\odot$
CS(2-1)	4	95.5 %	94.3 %	96.2 %	100 %	100 %	100 %	100 %	100 %
$C^{18}O$(1-0)	0	89.6 %	91.7 %	92.6 %	100 %	100 %	100 %	100 %	100 %
N_2H^+(1-0)	4	79.5 %	82.9 %	92.3 %	95.5 %	94.7 %	93.3 %	92.3 %	100 %

Table 6.1: The number of MDCs that were not covered for each transition, followed by the detection frequency as a function of the minimal mass of the MDC. At masses above 100 $M_\odot$, each of the lines is always detected.

molecular lines. The fact that CS(2-1) and $C^{18}O$(1-0) trace lower density gas is also reflected in the detection rate. Both transitions are more easily detected in lower mass MDCs than N_2H^+(1-0).
The evolution of the linewidth for the different molecular lines is presented in Fig. 6.7 as a function of the core mass. An increase of the observed linewidth with increasing core mass is found for all lines. The linewidth also significantly depends on the observed molecule. CS(2-1), which appears to trace the most extended emission, generally has the largest linewidth, followed by $C^{18}O$(1-0). This larger linewidth of CS(2-1) might also be affected by opacity broadening since CS(2-1) is generally quite optically thick. N_2H^+(1-0) and NH_3 have the lowest linewidth. Though NH_3 is not smoothed to the same resolution as the FCRAO data, the 20-29 % difference in beamsize should not strongly affect this result. There is thus a clear linewidth change from the transitions that trace more diffuse gas to the transitions that trace the interiour of the MDCs. The slightly larger beamsize of the spectral line observations than the MDC size has to be emphasized but, if the linewidth can be considered as a proxy of an effective turbulent pressure, these observations could indicate that the dense interior (small linewidth) of MDCs is embedded in a higher pressure medium (larger linewidth).
Examining the linewidth evolution for the individual transitions in more detail by fitting a Larson law given by (Larson, 1981)

$$\sigma = a \cdot \mathrm{M}^{\alpha} \tag{6.2}$$

provides further information. σ is the spectral linewidth, and a and α are the prefactor and exponent, respectively. These fitting results are summarized in Tab. 6.2 and confirm the observed trends in Fig. 6.7. It is found that $C^{18}O$(1-0) closely follows the predicted Larson law with basically the same values for α and a. The other tracers have a significantly different prefactor and a higher exponent. This higher exponent results in a more rapid increase of the linewidth as a function of mass. It is found in Tab. 6.2 that NH_3 and N_2H^+ have a very similar exponent and that CS has an exponent between the value for $C^{18}O$ and the values for NH_3 and N_2H^+. As CS is expected to trace gas up to higher densities than $C^{18}O$, this suggests a correlation between the exponent and the density in the MDCs traced by the molecule. These observations first of all suggest that the scaling relation observed with CO might be in part related to depletion at high density, and thus only trace the lower density dynamics ($n_{H_2} < 10^4$ cm^{-3}) of clouds and cores. Because of the significant role of gravity in massive star forming regions, this rapidly increasing linewidth and changing Larson exponent might be the result of an increasing role of gravitational collapse.

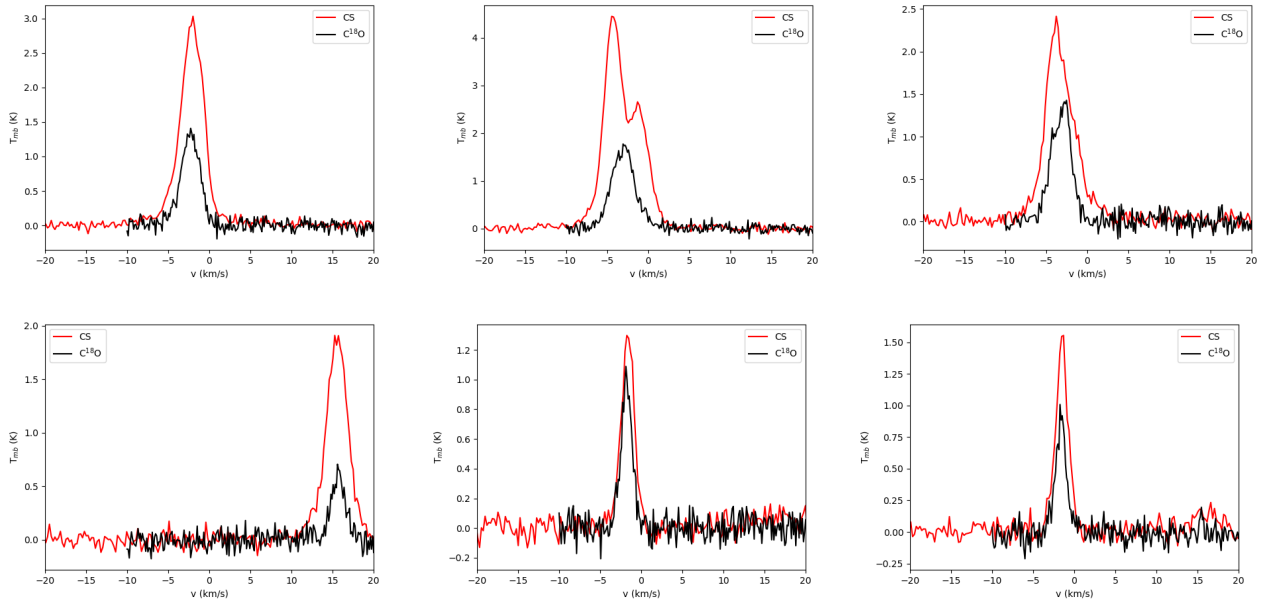

Figure 6.6: The observed CS(2-1) (in black) and $C^{18}O$(1-0) (in red) spectra towards 6 selected MDCs. It demonstrates that in general, fitting a single gaussian can provide a descent fit. However, in the spectra towards the most massive cores (top middle spectrum), there can be self-absorption effects for CS(2-1).

parameters	(Larson, 1981)	CS(2-1)	$C^{18}O$(1-0)	N_2H^+(1-0)	NH_3
a	0.42	0.29 ± 0.004	0.36 ± 0.007	0.15 ± 0.002	0.13 ± 0.003
α	0.20	0.31 ± 0.002	0.21 ± 0.003	0.35 ± 0.003	0.36 ± 0.007

Table 6.2: The two parameters of the Larson law for the evolution of the molecular linewidth as a function of the mass for the considered MDCs in Cygnus-X north. It also presents the values from Larson (1981) based on ^{13}CO observations towards molecular clouds.

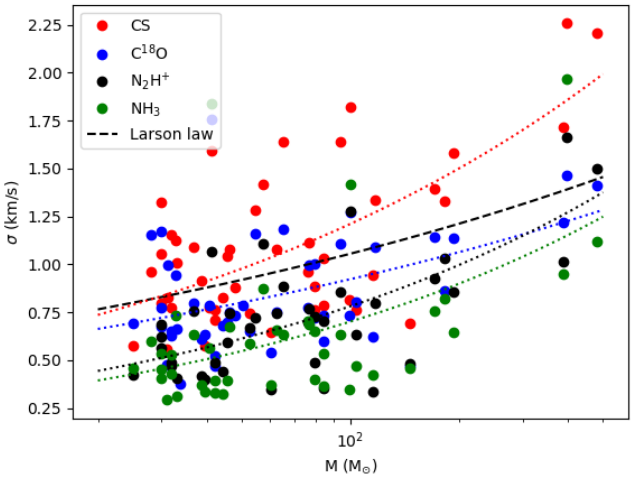

Figure 6.7: The fitted linewidth for CS(2-1), $C^{18}O$(1-0), N_2H^+(1-0) and NH_3 as a function of the core mass. The blacked dashed line gives the evolution of the Larson law (Larson, 1981). The dotted lines show the fit $\sigma \propto M^{\alpha}$ for each molecular line. It is observed that $C^{18}O$(1-0) follows the Larson evolution, while the other lines do not.

6.1.3 Gravitational stability of massive dense cores

A Bonnor-Ebert sphere describes a self-gravitating isothermal core located in a pressurised medium, which is in hydrostatic equilibrium. The density profile in the core then provides support against the self-gravity of the core. In a more general view, turbulent pressure and the magnetic field can also provide support in a core against gravitational collapse and further fragmentation. The Bonnor-Ebert spheres originate from the Lane-Emden equation which describes the hydrostatic equilibrium of a self-gravitating core

$$\frac{1}{r^2}\frac{d}{dr}\left[r^2\frac{d}{dr}\ln(\rho/\rho_0)\right] = -\frac{4\pi G\rho_0}{c_s^2}\exp\left[\ln(\rho/\rho_0)\right] \tag{6.3}$$

with ρ_0 the central density and c_s the isothermal sound speed. A Bonnor-Ebert sphere also assumes that the core is non-singular at its center.
These hydrostatic dense cores have a critical mass, the so-called Bonnor-Ebert mass (M_{BE}). Above this critical mass, the core will experience gravitational collapse. The Bonnor-Ebert mass is given by

$$M_{BE} = 1.18\frac{c_s^4}{G^{3/2}\sqrt{p_0}} = 2.4R_{BE}\frac{c_s^2}{G} \tag{6.4}$$

with p_0 the external pressure and R_{BE} the size of the Bonnor-Ebert core. Taking into account uniform turbulent support in the core, c_s can be replaced with the turbulent linewidth. Since we have the size, mass and information on the thermal and turbulent support of the MDCs in Cygnus-X north, this allows to study whether (some of) the MDCs can be in hydrostatic equilibrium.

In Fig. 6.8 it is shown that the Cygnus-X north cores are significantly more massive than the Bonnor-Ebert masses when taking into account only thermal support at temperatures between 10 and 40 K. Fig. 6.8 also shows that an isothermal temperature of $\sim$ 300 K is required for most MDCs in Cygnus-X north to be possible Bonnor-Ebert spheres, i.e. in equilibrium. With the estimated linewidths for the MDCs in Cygnus-X north, it is possible to study whether isotropic turbulent pressure could result in hydrostatic equilibrium. In Fig. 6.9, the ratio of the Bonnor-Ebert mass over core mass is presented for each core as a function of the mass for the different observed molecular lines. First of all, note that the beamsizes of the molecular line observations are larger than the core sizes. This indicates that the applied molecular linewidth is likely an upper limit for the actual linewidth of the core, since the observations also take into account slightly more extended gas and possibly have more than one velocity component. As it was already noted that the linewidths depend on the molecular line, it comes to no surprise that the results here are also dependent on the line that is considered. However, as NH_3 and N_2H^+ are tracers of the dense interiour of the MDCs it is expected that the results from these lines are representative for the MDCs, while $C^{18}O$ and CS rather trace the gas embedding the MDCs. Inspecting Fig. 6.9 it is observed that N_2H^+ and NH_3 indicate that the core mass for all MDCs with a mass above 30 $M_\odot$ is above the Bonnor-Ebert mass. This suggests that all these cores in Cygnus-X north are not in hydrostatic equilibrium but rather gravitationally collapsing. When considering $C^{18}O$(1-0) and CS(2-1) as accurate tracers of the MDC interiour, this is not entirely true. These lines indicate a higher mass ($\sim$ 70 $M_\odot$) where the MDCs can no longer be in hydrostatic equilibrium.

To conclude, without information from the magnetic field, the MDCs in Cygnus-X appear to be gravitationally unstable. This suggests that the evolution of MDCs both in isolation and in hubs/ridges is driven by gravitational collapse. For increasing mass of the MDCs, the role of gravity becomes increasingly important which could indicate that more massive MDCs are generally located in regions that are increasingly dominated by gravity on large scales and that the mass of MDCs is mainly determined by gravitationally driven accretion. This fits with the observation that the most massive MDCs are predominantly located in the DR21 ridge.
In the previous section, it was proposed that the formation of hubs and ridges in Cygnus-X north was triggered by a GMC collision. From the isolated MDC locations in Fig. 6.1, it was proposed that they might form in a compressed region by feedback from newly formed nearby stars. This suggests that both for clustered and isolated MDCs, external compression can trigger their formation. In the compressed layer, gravity then takes over to form massive stars. The only difference might be that isolated MDC formation is triggered by local compression, such that isolated MDCs might indeed be small filament hubs. However, further studies will have to verify the presence of expanding shells with e.g. [CII]. High resolutions will also be necessary to confirm that these isolated MDCs have small scale filaments and study if they have asymmetric inflow that is predicted by the Inoue et al. (2018) mechanism.

Prospective: Stability in dense cores from low- to high-mass

In the previous section, the first results for the most massive cores in Cygnus-X north were discussed. However, core extraction for an increasing amount of regions covered by *Herschel* with the HOBYS and Gould Belt survey are becoming available. This will allow to study the core stability over an important mass range ($\sim$ 0.1-1000 $M_\odot$) and possibly unveil a different nature of dense cores in high-mass star

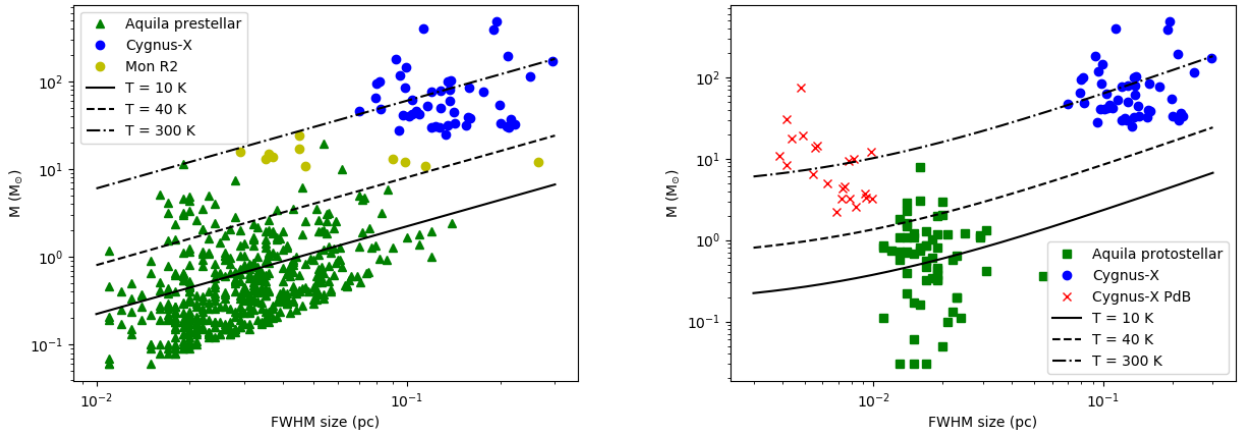

Figure 6.8: **Left:** The mass for the prestellar cores in Aquila (Könyves et al., 2015), the most massive cores in Monoceros R2 (Rayner et al., 2017) and MDCs of Cygnus-X north as a function of their core size. The lines indicate the Bonnor-Ebert mass as a function of the radius for different isothermal core temperatures. **Right**: The same with the protostellar cores from Aquila (Könyves et al., 2015), the fragments observed in the MDCs of Cygnus-X with the Plateau de Bure interferometer (Bontemps et al., 2010b) and the MDCs of Cygnus-X north.

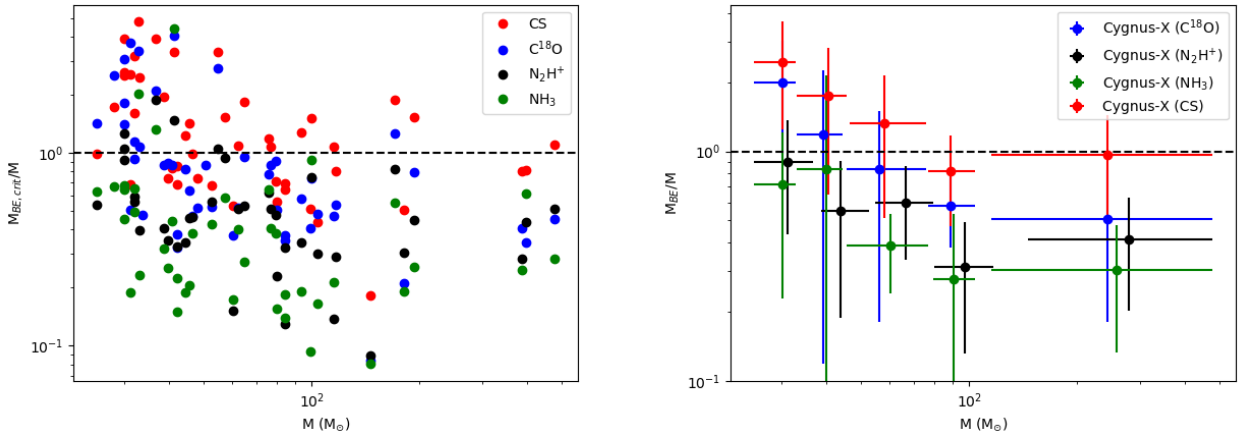

Figure 6.9: **Left:** The ratio of the Bonnor-Ebert mass, calculated using the linewidth of the 4 available molecular transitions, over the core mass as a function of the core mass. **Right:** The same results, but here the ratios are grouped into five mass interval to present the evolution in a clearer way.

forming regions. This can be particularly interesting in the discussion on the origin of the full IMF. For example, is the transition from low- to high-mass star formation a continuous evolution (e.g. gradually increasing role of large-scale gravity for higher-mass stars), or is there a bimodal difference between low- and high-mass star formation where low-mass and high-mass stars each form under specific physical conditions?
Here, a pilot study will be presented, based on the dense cores in Aquila (Könyves et al., 2015) and the MDCs in Cygnus-X north. For the Aquila data, a differentiation will be made between pre- and protostellar cores which is not really possible for the MDCs in Cygnus-X. Fig. 6.8 shows that the prestellar cores in Aquila are generally located on or below the Bonnor-Ebert relation for an isothermal core at 10 K (Könyves et al., 2015). The prestellar cores in Aquila might thus be described by Bonnor-Ebert spheres. Inspecting the protostellar cores in Aquila, presented in Fig. 6.8, it is found that they are generally located between the expected relation for Bonnor-Ebert spheres at 10 and 40 K. This indicates that protostellar cores in Aquila might indeed be gravitationally unstable. However, in comparison with the MDCs in Cygnus-X north, even the protostellar cores in Aquila are still reasonably close to the Bonnor-Ebert relation at 10-20 K.
Between 5 $M_\odot$ and 30 $M_\odot$ there is still a gap in Fig. 6.8 that is not yet covered. However, lower-mass cores in Cygnus-X north will be added later on, as well as cores in other HOBYS regions such as Rosette. Core extraction in these regions is in progress (Bontemps et al., in prep.). At the moment, the most massive cores from Monoceros R2, extracted from HOBYS maps (Rayner et al., 2017), have been added to Fig. 6.8 to have a first look at the gap between the Aquila cores and the MDCs in Cygnus-X north. These Mon R2 cores are generally found above the Bonnor-Ebert relation at 40 K, but more statistics will be necessary to study the transition from low- to high-mass.
Fig. 6.8 also shows the location of the fragments extracted with the Plateau de Bure interferometer towards the most massive MDCs in Cygnus-X north (Bontemps et al., 2010b). This demonstrates that these massive fragments are predominantly located on the 300 K Bonnor-Ebert relation, just as the extracted MDCs from *Herschel* data. This is a possibly interesting observation that could indicate that the properties of massive protostellar fragments are related to the MDCs that host them. However, truly understanding the difference between low- and high-mass star formation will require a more in depth study of all these cores and fragments (Duarte-Cabral et al., 2013).

The comparison between low- and high-mass cores here does not yet take into account the linewidth towards the observed cores, MDCs and fragments. However, the GAS NH_3 survey with the Green Bank Telescope of multiple Gould Belt clouds (Friesen et al., 2017; Kirk et al., 2017; Keown et al., 2017; Redaelli et al., 2017) and the KEYSTONE NH_3 survey of several HOBYS regions should allow to take into account the turbulent linewidth when comparing low- and high-mass cores. Furthermore, a significant amount of $C^{18}O$ maps covering HOBYS and Gould Belt regions are available to extend this analysis with a second molecular line. Simultaneously, the high angular resolution mapping of Cygnus-X north by the MIOPS program using NOEMA can provide information on the linewidth for a large sample of fragments located in the MDCs.

Prospective: Magnetic field observations of MDCs

It was found that none of the MDCs in the Cygnus-X north can be in hydrostatic equilibrium based on the Bonnor-Ebert mass when taking into account thermal and turbulent support. The possible support that has not been taken into account towards the MDCs is the magnetic field as it is currently not constrained by direct observations. However, as the magnetic field in the ISM is highly organised in low- and high-density gas (e.g. Crutcher, 2012; Planck Collaboration et al., 2016b; Hennebelle & Inutsuka, 2019) this does not provide a truely isotropic support to dense cores, which complicates things.
To incorporate the role of the magnetic field in the evolution and support of these MDCs, two observational approaches are straightforward. The magnetic field orientation in the plane of the sky can be mapped with the polarised emission from dust grains. This can be envisioned with the HAWC$^+$ receiver on SOFIA or the new NIKA2 receiver on the IRAM 30m telescope. Using techniques based on the Chandrasekhar-Fermi method (Chandrasekhar & Fermi, 1953; Houde et al., 2009, 2016), it is possible to estimate the magnetic field strength. Furthermore, observations of the magnetic field could also unveil the presence of the hourglass shape associated with gravitational contraction (e.g. Galli & Shu, 1993a,b; Schleuning, 1998; Girart, Rao & Marrone, 2006; Girart et al., 2009; Pattle et al., 2017). Another option is to observe the Zeeman splitting of several molecular lines towards the MDCs which directly provides a measurement of the magnetic field strength along the line of sight (e.g. Crutcher et al., 1993, 2010; Bourke et al., 2001; Falgarone et al., 2008; Pillai et al., 2016). However, the observation of Zeeman splitting remains challenging to date.
These constraints on the magnetic field are important since the gravitational collapse of a region can result in a rapid increase of the magnetic field strength towards the center of the collapse which can prevent further fragmentation and provide additional support to form massive protostellar fragments (e.g. Hennebelle et al., 2011; Peters et al., 2011; Commerçon, Hennebelle & Henning, 2011). The magnetic field observations towards MDCs should thus be combined with observations at high angular resolution towards massive protostellar fragments with e.g. the Submillimeter Array (SMA) (Ching et al., 2017) to understand the possibly crucial role of the magnetic field in surpassing the Jeans fragmentation problem for massive protostellar fragments.

6.2 The impact of accretion on the core mass function

6.2.1 Velocity gradients and mass accretion

In Paper-MC, it was shown that there are organised velocity gradients over the Musca filament crest, similar to what is observed in Fig. 6.10 for DR21 (Schneider et al., 2010). For the Musca filament, it was proposed that the gradient might be related to a mix of inflow and differential filament rotation associated with mass accretion on the crest. If this velocity gradient is purely the result of rotational motion, this can provide supplementary support against collapse (e.g. Recchi, Hacar & Palestini, 2014) and could thus have an impact on the core mass function (CMF) describing the mass distribution of prestellar cores. However, it should be noted in this context that simulations generally suggest that velocity gradients in filaments are rather the result of inflow (Smith et al., 2016; Chen et al., 2020). Since stars form in what used to be prestellar cores, the CMF could provide an explanation for the observed relatively universal stellar mass function (e.g. Salpeter, 1955; Kroupa, 2001; Chabrier, 2003;

Offner et al., 2014). In this scenario, stellar mass is accreted from the gas present in prestellar cores which would make that the process responsible for the CMF is at the origin of the observed IMF (e.g. Padoan & Nordlund, 2002; Hennebelle & Chabrier, 2008; Hopkins, 2012; Hennebelle, Lee & Chabrier, 2019). On the other hand, it is also argued that resemblance between the CMF and IMF is irrelevant, and that the IMF is the result of stochastic accretion in a dynamic environment (Larson, 1978; Zinnecker, 1982; Klessen, Burkert & Bate, 1998; Bonnell et al., 2001b; Bate, Bonnell & Bromm, 2003; Clark, Klessen & Bonnell, 2007). This discussion is also referred to as ′nature′ vs ′nurture′ (Offner et al., 2014).
Since stars form over a large range that covers at least 3 orders of magnitude in mass, the ultimate goal is to arrive at a consistent scenario that explains the formation of stars over the full mass range which is also closely tied to ′nature′ vs ′nurture′. The increasing evidence for the lack of high-mass prestellar cores and several indications for the importance of large-scale dynamics, some of which were presented in the sections above, pushes for a scenario where nurture is important for high-mass star formation. Because there are sufficiently massive prestellar cores towards low-mass star forming regions, the nurture scenario is not imperative for low-mass star formation. However, this does not necessarily imply that there is no nurture for low-mass stars.

6.2.2 Support in a rotating filament

When considering that the velocity gradient is dominantly associated with rotational motion, the filamentary structure is further supported against gravitational instability. Using the study of filamentary rotation from Recchi, Hacar & Palestini (2014), it is possible to investigate this in a bit more detail. As already noted in Paper-MC, the Musca filament is not experiencing uniform rotation which can be the result of local differences in the accretion flow. In this case, the local variation in the accretion flow could help to shape the CMF of the cloud. When studying the impact of rotation on the filament stability, it should be noted that other factors such as temperature gradients can also affect the filament stability (Recchi, Hacar & Palestini, 2013).
Considering an isothermal non-rotating filament, the critical mass for gravitational stability is given by (Ostriker, 1964)

$$\mathrm{M_{crit}} = \frac{2\mathrm{c_s^2}}{G} \tag{6.5}$$

with c_s the thermal sound speed and G the gravitational constant. To study the possible impact of a rotating filament, the calculations in Recchi, Hacar & Palestini (2014) will be used. First of all, it is possible to make a simple estimate of the importance for the rotation compared to gravity. The rotational energy per unit length is given by $\mathrm{T} = \frac{1}{2}\mathrm{M}_{lin}\omega^2\mathrm{R}^2$, where M_{lin} is the mass per unit length, ω the rotation frequency and R the outer radius of the considered rotating filament. With a gravitational energy per unit length $\mathrm{W} = \mathrm{GM}_{lin}^2$ this results in

$$\frac{\mathrm{T}}{\mathrm{W}} = 0.65 \left(\frac{\omega}{6.5 \cdot 10^{-14}}\right)^2 \left(\frac{R}{0.15pc}\right)^2 \left(\frac{M_{lin}}{16.6M_\odot}\right)^{-1} \tag{6.6}$$

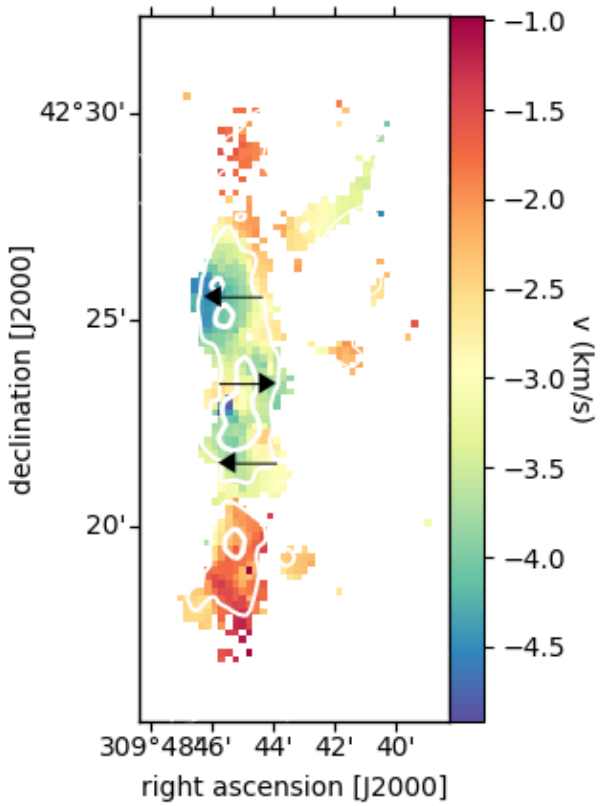

Figure 6.10: The N_2H^+ velocity field of the DR21 ridge, showing alternating velocity gradients (indicated by the arrows) over the ridge.

The input values for the Musca filament crest are $M_{lin} = 4.5\ M_\odot\ pc^{-1}$ within R = 0.05 pc, and a velocity of 0.1 km s^{-1} at R = 0.5 pc, which gives $\omega = 6.4{\cdot}10^{-14}$ Hz. This results in $\frac{T}{W} = 0.26$, suggesting that gravity is significantly more important than rotational energy. This observation that gravity becomes dominant at the filament crest was already pointed out before, and suggests that there probably still is significant mass provision from large scale to small scales even if angular momentum is a significant contributor to the observed gradient.
To study the impact of filament rotation, the normalised frequency is used

$$\Omega = \sqrt{\frac{2}{\pi G \rho_0}}\omega \tag{6.7}$$

with ρ_0 the central density which is calculated from $n_{H_2} = 10^4$ cm^{-3}. Using $\omega = 6.4{\cdot}10^{-14}$ Hz results in $\Omega = 1$ at r = 0.05 pc.
Looking into the tables of Recchi, Hacar & Palestini (2014), this suggests that rotation in the Musca filament crest might affect the stability by more than a factor 2 for $x < 3$, where x is given by $r = Hx$, with H a length scale for the filament given by

$$H = \sqrt{\frac{2kT_0}{\pi G \rho_0 \mu m_H}} \tag{6.8}$$

with T_0 (= 10 K) the central temperature, μ (= 2.33) the mean molecular weight and m_H ($= 1.67{\cdot}10^{-27}$ kg) the hydrogen mass. For Musca this gives H = 0.0304 pc, such that x = 3 corresponds to $r \sim 0.09$ pc. If the observed velocity gradients are indeed related to rotation, it is found that this could affect the observed CMF by a factor 2 or more compared to fragmentation in a non-rotating filament. Taking into account that local variations in the accretion rate might lead to stronger rotation, the accretion inhomogeneities would contribute to shaping the observed core mass functions.

6.2.3 Inflow and the impact on the CMF and IMF

The gravitational energy in the Musca filament crest is significantly larger than the maximal estimated rotational energy. This suggests that in any case there is significant mass inflow in the filament crest. Furthermore, the velocity gradient is strongly associated with large scale inflow. It is thus not unlikely that the observed gradients in the filament are associated with further inflow. Taking into account the orders of magnitude higher mass for DR21, this process will only be more important there. Going a step further for Musca, i.e. working under the assumption that the observed gradients are purely associated with inflow, it is found in Paper-MC that the crossing timescale for the Musca filament is of the order of 0.5-0.7 Myr. This is of the same order and even slightly lower than the obtained lifetime for dense cores during the star formation process (Evans et al., 2009; Brünken et al., 2014). With the significant estimated inflow rate for Musca in Paper-MC, which can replenish the existing mass in the Musca filament within 1 Myr, it is then possible to increase the mass in pre- and protostellar core over their lifetime and even provide mass from large scales to the center of these cores. This first of all implies that pre- and protostellar cores evolve in a dynamic environment and not in isolation, which suggests that the observed prestellar CMF at a specific moment in the cloud evolution is not necessarily reflective of the core mass distribution at the moment that protostellar accretion starts in a core. It

could even imply, though this is more speculative, that the final mass of a star is in part determined by statistical variations in the large scale mass inflow over its protostellar lifetime.

The lack of high-mass prestellar cores automatically points to a nurture scenario for high-mass star formation. For low-mass stars it is in a sense more complicated to differentiate nurture vs nature. Based on the results obtained in this thesis, it is proposed that filaments are dynamical structures that emerge at the location of persistent converging flows. Since stars dominantly form in filaments (Polychroni et al., 2013; Könyves et al., 2015; Marsh et al., 2016), the filamentary structure of the ISM could thus have an effect on the star formation outcome because filaments impose that star formation occurs at the center of continuous large scale inflow. Because of this, both the core mass, as it is the immediate surrounding mass reservoir, and continuous inflow during the core evolution tend to play a role in setting the eventual mass of the forming star(s) in the core. This conclusion that nature and nurture might both play a role in setting the IMF was also put forward, based on a discussion of theoretical calculations and numerical simulations, in the recent review by Offner et al. (2014).

6.2.4 From low- to high-mass star formation

Both for Musca and DR21 it was proposed that dense gas formation was in particular triggered by a large scale collision. In Sec. 5.3.3, the parameters that affect the outcome of this collision were already discussed. Here, it is the goal to discuss on a smaller scale what makes the difference between low- and high-mass star formation once the star forming cloud and dense gas have been formed. In this context, it can be noted that the velocity gradients in Musca filament crest and DR21 ridge are of the order of 2 km s^{-1} pc^{-1} in both clouds. Even though inclination could have an impact, this seems to indicate that the inflow velocity might not be that different, even though gravity seems to drive the evolution of the full DR21 cloud in contrast to Musca. As already discussed, the magnetic field might play an important role in preventing the expected strong gravitational acceleration.

It thus appears that the inflow velocity might not be the key parameter in the differentation between low- and high mass star formation, but rather the density of the inflowing gas which relates back to the compression of the gas. For the DR21 ridge, it was found that the density of the ambient gas near the ridge could be as high as $n_{H_2} = 10^4$ cm^{-3} and even 10^5 cm^{-3} for the inflowing subfilaments. For the Musca, these values are rather of the order of $5{\times}10^2$ to 10^3 cm^{-3}. The density of the region alone can thus make a one to two orders of magnitude difference in the mass provision rate, and thus initiate high-mass star formation. Combining this with e.g. a 2-3 times higher inflow velocity in massive regions, this can easily differentiate low- and high-mass dense cores.
Because of this rapid mass provision to MDCs, they are unstable and can contain protostellar fragments that can form high-mass stars. An open question in this gravitational collapse scenario, is how this collapse and mass provision regulates the evolution of the protostellar fragments. Does the gravitational collapse of the MDCs regulate the mass provision to the subfragments, in a scenario where the MDC is formed first and possibly goes through an extremely short quasi-prestellar stage where it fragments into smaller stuctures? Or do the fragments directly accrete from subfilaments flowing in from the cloud scale with little regard for the presence of the MDC? Large scale mapping at high angular resolution

with NOEMA and ALMA, and magnetic field observations to investigate its potential effect should be able to address this question.

Chapter 7

Conclusion and Perspective

An observational study has been carried out to understand the physical processes responsible for the formation of dense filamentary gas in low- and high-mass star forming regions, and how this can affect the outcome of the star formation process.

First, the Musca filament was identified as an excellent target to study the physics of dense gas formation because of its apparent simple structure and lack of possible contamination. The results for Musca can be summarised as follows:

• The ^{13}CO(3-2)/^{13}CO(2-1) ratio demonstrates high densities ($n_{H_2} \sim 10^4$ cm^{-3}) in the filament, consistent with a cylindrical geometry for the filament.

• The [CII] and [CI] brightnesses show that the Musca cloud is evolving in a weak FUV field (< 1 G_0).

• The ^{12}CO(4-3) observations indicate the presence of a warm and dense gas layer connecting the ambient cloud and dense gas in the Musca filament and strands. This emission can originate from dense gas formation by a low-velocity filament accretion shock.

• [^{13}CO]/[C^{18}O] abundance variations by an order of magnitude are observed in the Musca filament at A_V = 2-3 mag, likely as a result of carbon and oxygen fractionation reactions.

• Transverse velocity gradients are observed over the Musca filament. These gradients are correlated to the local velocity field of the ambient cloud, indicating that the gradients are a mass accretion signature.

• The Musca cloud shows a systematic redshift of dense gas from the HI cloud, associated with the Chamaeleon-Musca complex, to the filament crest.

• It is difficult to reproduce the CO velocity profile of the Musca cloud with the toy model from Shimajiri et al. (2019b), which assumes that inflow is driven by the gravitational potential of the filament while gravitational acceleration is prevented by isotropic turbulence.

Combining all results, it is found that the asymmetric Chamaeleon-Musca and Musca cloud kinematics in HI and CO fit with a scenario where the Musca filament is formed by the intersection of two converging flows. At the intersection of the converging flows, a low-velocity filament accretion shock can play an important role in forming the cold and dense gas of the filament. The converging flow is driven by the bending of the magnetic field, described in Inoue et al. (2018), due to a large scale HI cloud-cloud collision in the Chamaeleon-Musca complex. It is only at a radius of 0.1-0.2 pc from the filament axis that gravity starts driving the evolution of the gas. It is argued that a similar scenario can be valid for the B211/3 filament in Taurus.

To compare dense gas formation in low- and high-mass star forming regions, the kinematics of the DR21 cloud in the Cygnus-X north region are analysed. As for Musca, the DR21 cloud also has velocity gradients over the central ridge associated with inflow (Schneider et al., 2010). The results can be summarised als follows:

• The velocity field of the DR21 cloud suggests an asymmetric accretion scenario similar to the Musca cloud.

• Virial analysis indicates that gravity appears to drive the evolution of the full DR21 cloud on pc scales. This suggests a collision scenario as described in Inoue et al. (2018), followed by large-scale gravitational collapse due to the high density in the compressed cloud.

• Extended SiO emission with a narrow linewidth (FWHM $\sim$ 2-3 km s^{-1}) is observed in the DR21 ridge.

• Bridging of CO gas between two velocity components with Δv $\sim$ 10 km s^{-1} in the line of sight is observed over the full Cygnus-X north region, indicating the interaction or collision of two giant molecular clouds (GMCs).

• The massive star forming hubs, ridges and massive dense cores (MDCs) in Cygnus-X north demonstrate important spatial and velocity substructure in this star forming region, similar to the substructure observed for OB assocations.

• The MDCs ($>$ 30 M$_\odot$) in Cygnus-X north all appear to be gravitationally unstable.

• The Cygnus-X region contains a sufficient amount of dense gas to form stars at a rate of 0.32×10^4 M$_\odot$ Myr^{-1} over the full region.

The Cygnus-X north region is likely forming an association of OB stars similar to OB2, as a result

of a large-scale GMC collision. This collision leads to dense structure formation in the form of hubs, ridges and MDCs which host the formation of OB clusters due to gravitational collapse. An OB association can thus be considered as an unbound collection of OB clusters.
In this scenario where star formation is initiated by a large scale colliding flow, which often already contains molecular gas, the initial density, velocity and magnetic field in the colliding flow will play an important role to determine whether or not a cloud will be able to form high-mass stars or not.

Because the dense star forming gas is located at the convergence of accretion flows, driven by the magnetic field for low-mass stars and by self-gravity for high-mass stars, this continuous inflow can play a significant role in the universal outcome of star formation. In particular for high-mass star formation, the rapid mass provision by the high-density gas in the ambient cloud through gravitational inflow, and the consequent provision of magnetic and kinematic support, during the evolution of the protostellar fragment could be able to form high-mass stars. However, understanding the details of this mechanism requires further high angular resolution studies.

Brief perspective

Several results with regard to the dense gas formation process in the ISM have been put forward in this thesis. This opens a spectrum of possible directions to better understand the star formation process and evolution of the ISM. Existing observational facilities such as SOFIA, APEX, ALMA and NOEMA already allow to explore certain directions. Upcoming facilities, either planned or under construction, such as SPICA, CCAT-prime and SKA will allow to further investigate these ideas with observations in different wavelength ranges and dedicated surveys.

Sensitive mapping of molecular clouds with CO and [CI] using ground-based submm telescopes will be able to follow the large scale gas kinematics in molecular clouds over a vast density range, which can unveil how dense filamentary gas is interacting with the ambient cloud for a variety of star forming clouds. It should also be possible to address whether the observed fibers in dust continuum filaments form in a ′fray & fragment′ or ′fray & gather′ scenario, and thus obtain a better view on the initial conditions of star formation in filaments. Observations with mid- to high-J CO lines can further unveil the role of low-velocity shocks in the formation of dense gas in filamentary structures. One project I am getting involved in is the mapping of selected southern filaments in the ^{12}CO(4-3) line which is one of the important science cases studied within the GEco (Galactic Ecology) project at CCAT-p. Proposed future space missions such as SPICA can then trace the cooling from the diffuse ISM to the dense star forming gas. SPICA could also trace the magnetic field orientation from the ambient cloud into the dense filaments to better understand the mass inflow from large to small scales. In preparation of this big possible step with SPICA, polarisation observations with the NIKA2 receiver on the IRAM 30m telescope and HAWC$^+$ receiver on SOFIA will already provide important new information on the magnetic field evolution in star forming clouds. Combining the large scale kinematics with the resolved magnetic field could also provide a better view on the nature of striations in molecular clouds.

Because the continuous improvements in sensitivity of observations produce increasingly rich datasets, the development of new statistical analysis methods that e.g. describe the self-similarity of the ISM can provide interesting complementary constraints to understand the full evolution of the ISM and extract the maximal amount of information from these rich datasets.

It was proposed in this thesis that the formation of dense star forming gas is directly associated with the molecular cloud formation process. Observations with the Square Kilometre Array (SKA) and its pathfinders (e.g. ASKAP) will be able to provide important information on the evolution from the HI cloud to the dense molecular gas, in particular with HI self-absorption effects. However, in complex regions such as Cygnus-X, HI is extremely difficult to analyse. Therefore, observations of [CII] will be enlightening if the FUV field is sufficiently strong to produce significant [CII] emission. The [CII] line can trace atomic hydrogen, CO-dark molecular hydrogen and the feedback from nearby massive stars, which will provide an interesting view on the different processes governing the evolution and cooling of the diffuse ISM and molecular cloud formation. The FEEDBACK program with SOFIA, in which I participate, is creating large [CII] maps towards active high-mass star forming regions and can provide a significant step in the understanding of the ISM traced by [CII]. These open questions regarding [CII] also revolve around the question if it truly is a good star formation tracer for extragalactic studies.
Finally, for massive stars it becomes increasingly clear that the evolution from large (> 1 pc) to small (≤ 2000 au) scales has to be followed in detail. This requires large programs with a high angular resolution that cover full molecular clouds, such as the MIOPS program to map the Cygnus-X north region with the NOEMA interferometer and the ALMA-IMF program with the ALMA interferometer. These studies to understand the mass provision for massive star forming fragments should ideally cover a variety of cold and warm dense gas tracers to obtain a comprehensive view of the different densities and temperatures in the star formation process.

Chapter 8

Conclusion et Perspective (en français)

Une étude observationelle pour révéler les processus physiques responsables de la formation des structures denses filamentaires qui forment les étoiles de faible et de haute masse, et comment ces processus affectent les propriétés des étoiles formées a été menée.

Premièrement, le filament de Musca a bien été reconnu comme une excellente cible pour étudier la physique de la formation du gaz dense du fait de la simplicité de la région et de l'absence de contamination. Les résultats pour Musca peuvent être résumés ainsi:

• Le rapport ^{13}CO(3-2)/^{13}CO(2-1) montre que la densité dans le filament de Musca est grande ($n_{H_2} > 10^4\,cm^{-3}$) et cohérente avec la géométrie cylindrique d'un filament.

• L'intensité des raies [CII] et [CI] montre que le nuage de Musca ne reçoit qu'un flux UV faible ($< 1\ G_0$).

• La raie ^{13}CO(4-3) montre la présence d'une couche de gaz chaud et dense à l'interface entre le nuage ambient et le filament de Musca. Ce gaz pourrait être chauffé par des chocs à basse vitesse liés à l'accrétion sur le filament.

• Les variations du rapport d'abondance [^{13}CO]/[C^{18}O] d'un ordre de grandeur entre la crête dense du filament et les couches juste autour ont pour origine probable des réactions de fractionation pour le carbone et/ou l'oxygène.

• Des gradients de vitesse transverses à la crêtre du filament sont observés. Ces gradients sont corrélés avec le champ de vitesse du gaz ambiant local ce qui indique que ce sont des signatures d'accrétion.

• Le nuage de Musca montre une tendance d'être de plus en plus décalé vers le rouge depuis les couches de faible densité en HI du complexe Chamaeleon-Musca jusqu'au gaz le plus dense de la crête du filament.

• Il est difficile de reproduire le profil de vitesses CO pour Musca avec le modèle simplifié de Shimajiri et al. (2019b) pour lequel l'accélération est gravitationelle et le freinage est obtenu par une pression turbulente effective qui suppose que toute la largeur des raies représente une micro-turbulence isotrope. Les raies y sont trop étroites.

En combinant l'ensemble des résultats et contraintes, un scénario de formation de Musca se dessine selon lequel l'asymétrie cinématique du complexe Chamaeleon-Musca et de Musca en HI et CO serait le "smoking gun" de la collision de deux nuages HI. Le filament de Musca serait le point de convergence de deux flots principalement guidés par la courbure du champ magnétique derrière le front de choc de la collision comme décrit dans Inoue et al. (2018). La gravité pourrait commencer à ne dominer la convergence et la concentration de matière que dans les derniers 0.1 à 0.2 pc. Ce scénario serait aussi compatible avec les observations de B211 dans le Taureau qui pourrait donc s'être formé aussi de cette façon.

Pour comparer la formation de gaz dense dans les régions de formation d'étoiles de faible et de haute masse, la cinématique du nuage de DR21 dans le Cygne est analysée. Comme pour Musca, DR21 montre des gradients de vitesse transverses le long de son axe qui sont associés à des flots d'accrétion (Schneider et al., 2010). Les résultats obtenus pour DR21 peuvent être résumés ainsi:

• Le champ de vitesse de DR21 montre une asymétrie dans ses flots d'accrétion similaire à ce qui est vu dans Musca.

• Une analyse viriel indique que la gravité y domine néanmoins la cinématique globale sur des échelles de l'ordre de plusieurs pc. Cela suggère qu'une collision de nuages comme dans Inoue et al. (2018) est aussi à l'origine du gaz dense. Comme la vitesse de collision y est plus grande que pour Musca, la compression a été plus forte entrainant un effondrement global.

• Une émission étendue en SiO avec une largeur de raie faible (FWHM $\sim$ 2-3 km s^{-1}) est observée le long du ridge/filament de DR21.

• des ponts en CO avec $\Delta v \sim 10\,\mathrm{km\ s^{-1}}$ sur la ligne de visée entre les deux composantes de vitesse sont observés vers l'ensemble de la région nord du Cygne, indiquant une interaction active entre deux nuages moléculaires géants (GMCs).

• Les hubs, ridges et coeurs denses massifs (MDCs) du Cygne montrent des structures spatiales et en vitesse dans la région qui sont similaires en taille aux sous-structures observées dans les associations OB.

• Les MDCs (M $>$ 30 M$_\odot$) dans le nord du Cygne apparaissent tous instables gravitationellement.

• La région dans le nord du Cygne contient une quantité de gaz dense suffisante pour former des

étoiles à un taux de $0.32 \times 10^4\,\mathrm{M_\odot Myr^{-1}}$.

La région dans le nord du Cygne va probablement former une association OB similaire à Cygnus OB2 comme conséquence de la collision à grande échelle de GMCs. Cette collision entraine la formation de gaz dense sous la forme de hubs, ridges et MDCs qui sont les lieux de formation d'amas d'étoiles dont des étoiles OB massives. Une association OB peut donc être vue comme une collection non liée d'amas OB.
Dans ce scénario de formation stellaire initiée par une collision à grande échelle de nuages qui contiennent déjà du gaz moléculaire, la densité, la vitesse et le champ magnétique de ces nuages initiaux jouent potentiellement un rôle important pour déterminer si la région formera ou pas des étoiles massives.

Parce que la formation du gaz dense est due à la convergence de flots d'accrétions guidés par le champ magnétique pour les étoiles de faible masse et par l'auto-gravité du gaz dense pour les étoiles massives, l'accrétion continue sur les régions denses qui en résulte peut jouer un rôle significatif dans la détermination de la masse des étoiles formées. En particulier pour la formation des étoiles massives, les forts taux d'accrétion concentrés par la gravité à grande échelle pourrait expliquer des apports de masse pendant les phases protostellaires des objets en formation au centre des MDCs, augmentant la masse finale des étoiles. Une confirmation de ces possibles effets nécessite néanmoins des observations à haute résolution angulaire pour suivre précisémment l'histoire de l'accrétion sur les fragments protostellaires.

Brève perspective

Plusieurs résultats sur l'origine du gaz denses du MIS ont été mis en avant dans cette thèse. Cela ouvre des directions multiples d'études pour mieux comprendre les processus de formation des étoiles et de l'évolution du MIS. Les observatoires déjà disponibles tels que SOFIA, APEX, ALMA and NOEMA permettent d'explorer certaines de ces directions. Les futures instruments en projet ou déjà en cours de construction tels que SPICA, CCAT-prime et SKA permettront d'aller encore plus loin sur certains aspects cruciaux.

Des relevés profonds en CO et [CI] avec les télescopes submillimétriques au sol permettront d'étudier encore plus en détail et de façon systématique les nuages moléculaires proches pour une grande gamme de densité et de masse pour confirmer certains des résultats présentés dans cette thèse. Il devrait aussi être possible d'établir si les filaments vus en continuum submillimétrique sont formés par le processus de ′fray & fragment′ ou de ′fray & gather′ et ainsi d'obtenir des meilleures estimations des conditions initiales de la formation des étoiles dans les filaments. Je suis déjà impliqué dans le projet GEco (Galactic Ecology) sur CCAT-p pour cartographier une sélection de filaments proches en ^{12}CO(4-3) qui est une des motivations scientifiques les plus importantes de ce projet. Les futures missions spatiales telles que SPICA pourront étudier les raies de refroidissement du MIS depuis le gaz diffus jusqu'au gaz dense qui forment les étoiles. SPICA cartographiera en même temps la morphologie du champ magnétique avec une résolution spatiale bien meilleure que Planck pour confirmer les scénarii présentés dans cette thèse.

En préparation de SPICA, des observations en polarimétrie avec NIKA2 au télescope de 30m de l'IRAM et avec HAWC+ sur SOFIA permettront déjà d'obtenir d'importantes informations sur l'évolution de l'orientation du champ magnétique dans les nuages moléculaires.
Parce que l'augmentation continue de la sensibilité et de l'efficacité des instruments entraine une augmentation très importante de la richesse et de la quantité de données collectées, le développement de nouveaux outils statistiques, tels que ceux qui pourraient décrire l'auto-similarité et la nature multifractale du MIS est une direction importante à poursuivre pour compléter les analyses plus classiques des observables directes de la physiques du MIS.

Il a été montré dans cette thèse que la formation du gaz dense qui forme les étoiles est directement reliée au processus de formation des nuages moléculaires. Les futures observations avec le Square Kilometre Array (SKA) et avec ses précurseurs tels ASKAP permettront de collecter d'importantes informations sur l'évolution du gaz HI vers le gaz moléculaire, en particulier en interprétant totalement les effets complexes d'auto-absorption de HI vers des nuages comme Musca-Chamaeleon. Pour les régions complexes et massives comme le Cygne, ces étude HI resteront néanmoins extrêmement difficile à analyser. Pour ces régions, les observations du carbone ionisé [CII] seront précieuses pour révéler le gaz caché, non moléculaire. La raie [CII] peut tracer indirectement le gaz atomique, le gaz moléculaire non détecté en CO, mais aussi les effets en rétroaction (feedback) des étoiles massives proches. L'analyse de ces observations riches va certainement nous permettre de mieux nous révéler les processus critiques et le refroidissement du MIS du gaz diffus au gaz dense. Le programme FEEDBACK avec SOFIA (large programme) auquel je participe est déjà en train d'établir des cartes en [CII] vers les régions actives de formation d'étoiles massives dont le Cygne.
Finalement, pour les questions de formation d'étoiles massives, il devient évident que l'évolution depuis les grandes échelles (> 1 pc) jusqu'aux petites échelles (2000 au) doit être comprise en détail. Cela nécessite des grandes programmes à haute résolution spatiale couvrant des régions complètes, tels que MIOPS pour le Cygne avec l'interferomètre NOEMA et ALMA-IMF avec ALMA.

Appendix A

Integrated intensity maps with the IRAM 30m

In Figures A.1, A.2, A.3, A.4 and A.5, maps of the molecular transitions detected with the IRAM 30m telescope, see Tab. 5.1, are displayed. It is found that a variety of molecular transitions are detected, in particular towards the DR21(OH) clump.

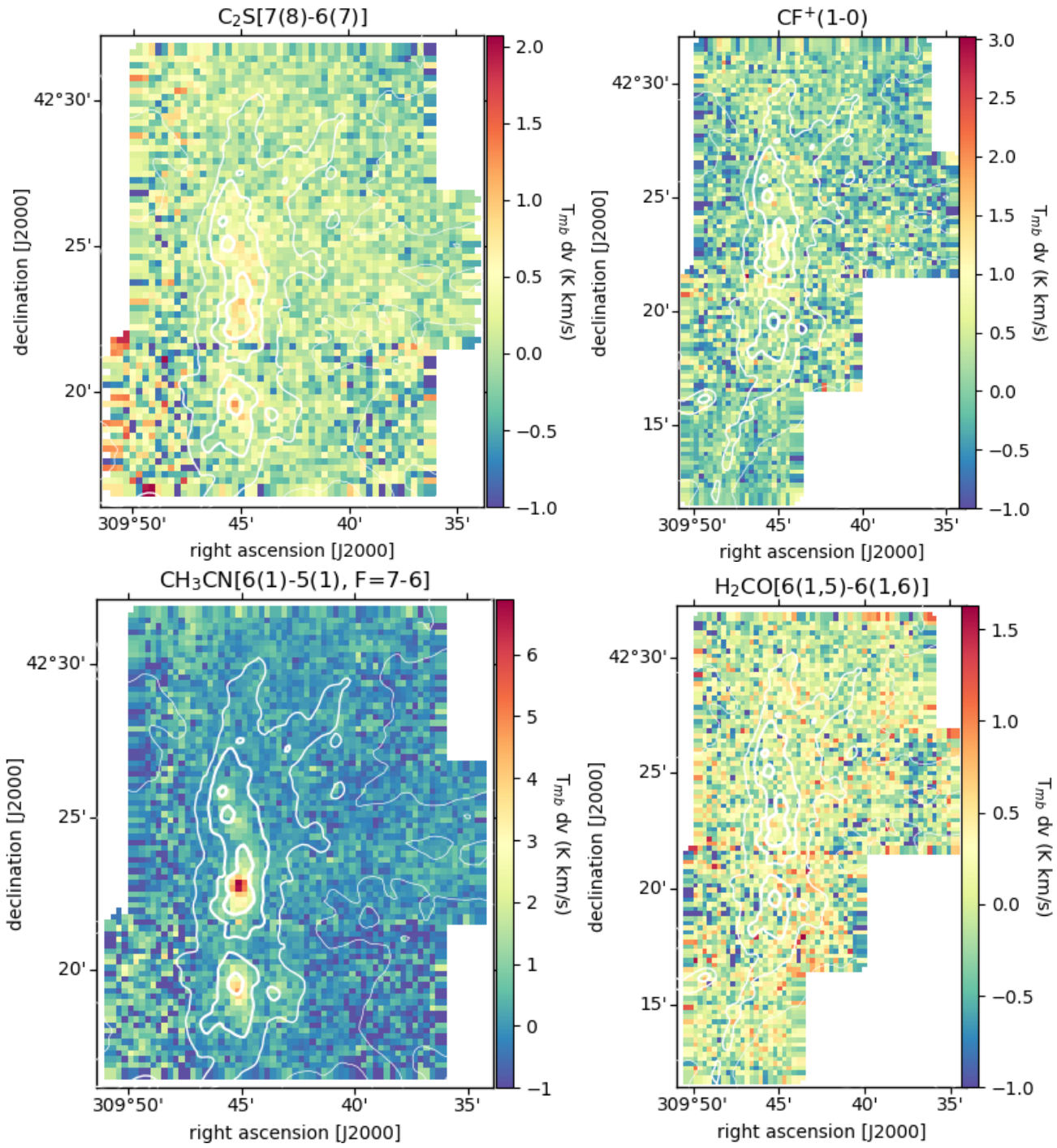

Figure A.1: **Top left**: The integrated intensity map of C_2S[7(8)-6(7)], with *Herschel* column density contours at N_{H_2} = 10^{22}, $3{\cdot}10^{22}$, 10^{23} and $5{\cdot}10^{23}$ cm^{-2}. **Top right**: The same for CF^+(1-0). **Bottom left**: The same for CH_3CN[6(1)-5(1),F=7-6]. **Bottom right**: The same for H_2CO[6(1,5)-6(1,6)].

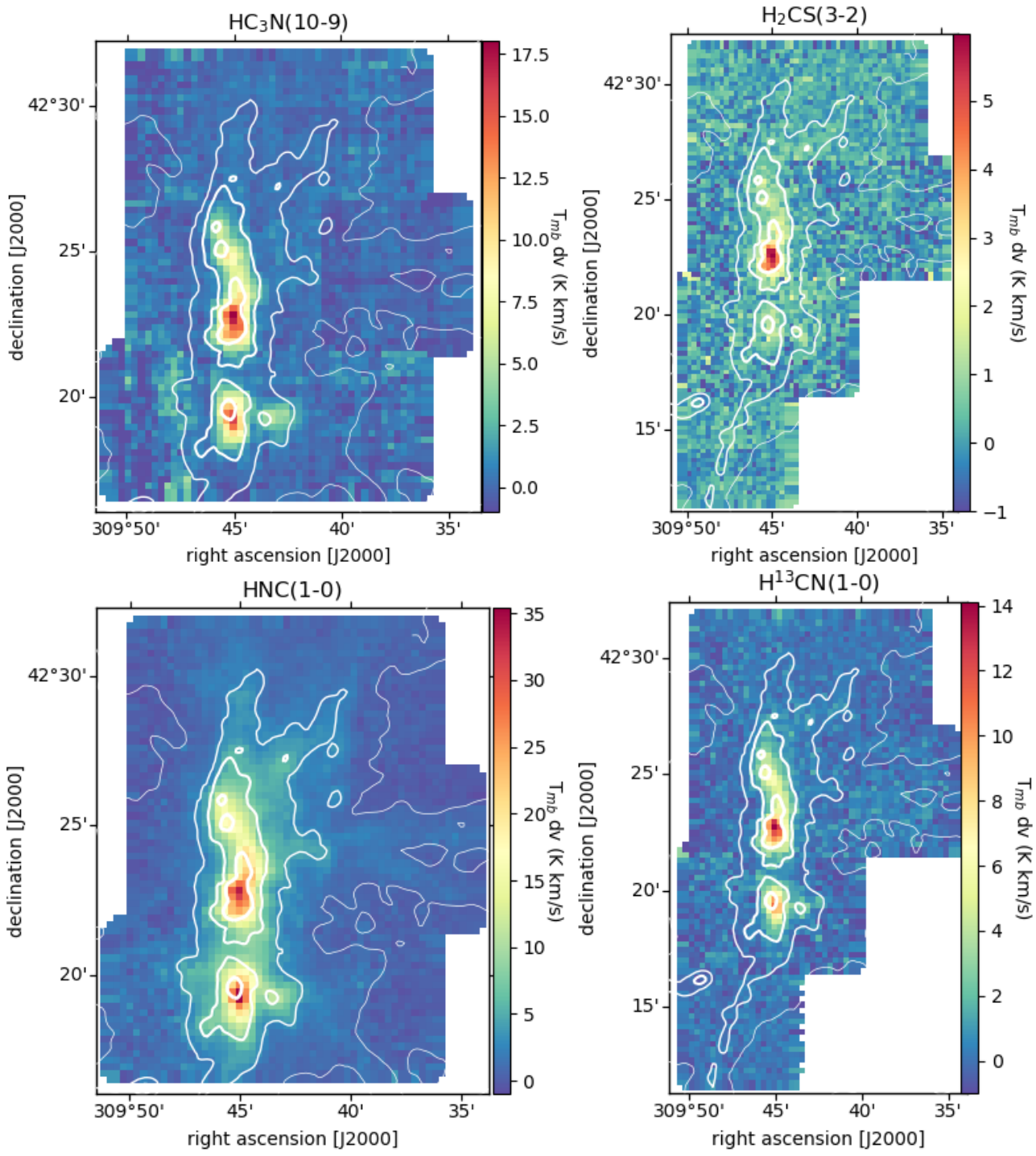

Figure A.2: The same as Fig. A.1 for HC_3N(10-9), H_2CS(3-2), HNC(1-0) and $H^{13}CN$(1-0).

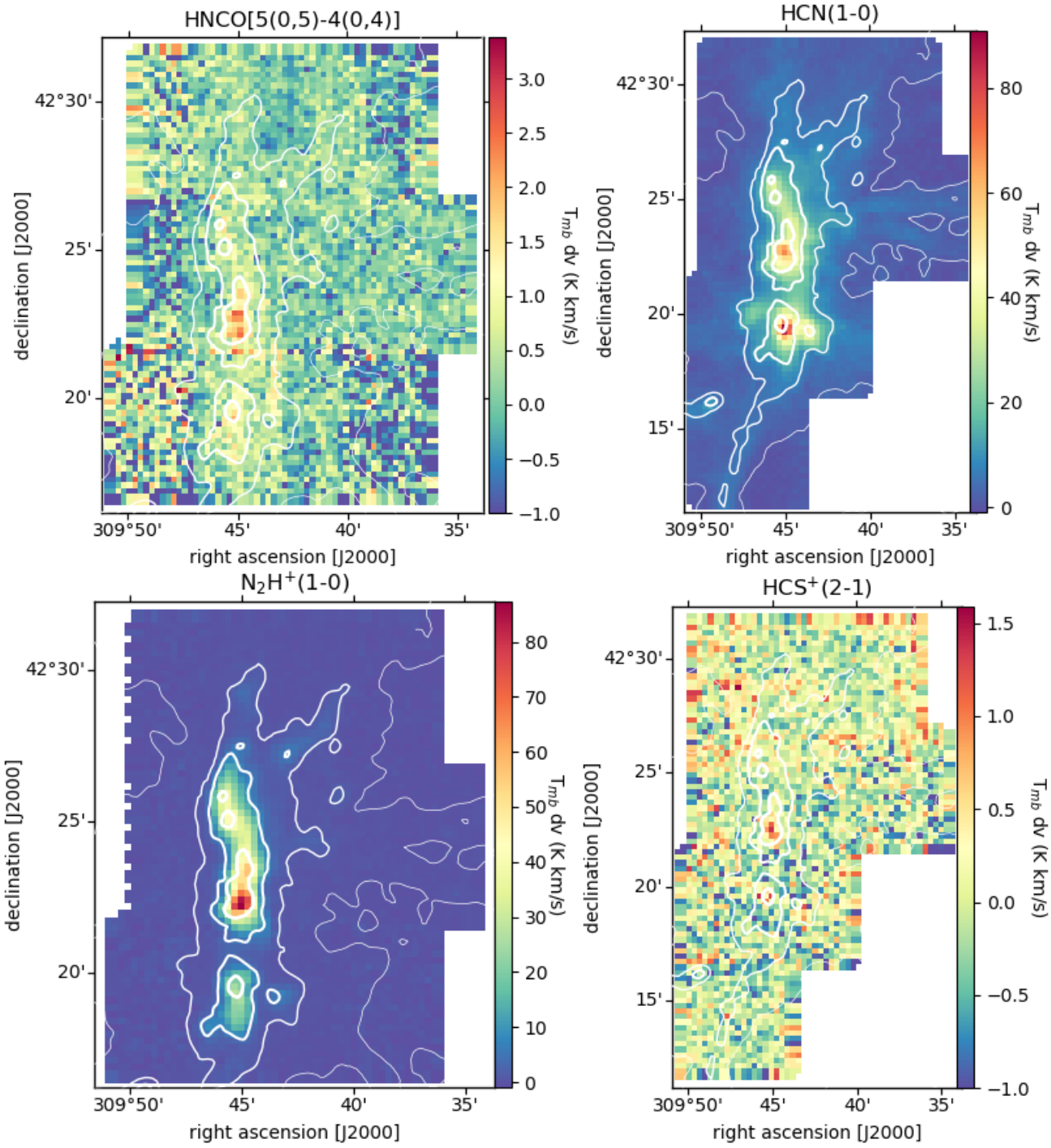

Figure A.3: The same as Fig. A.1 for HNCO[5(0,5)-4(0,4)], HCN(1-0), N_2H^+(1-0) and HCS^+(2-1).

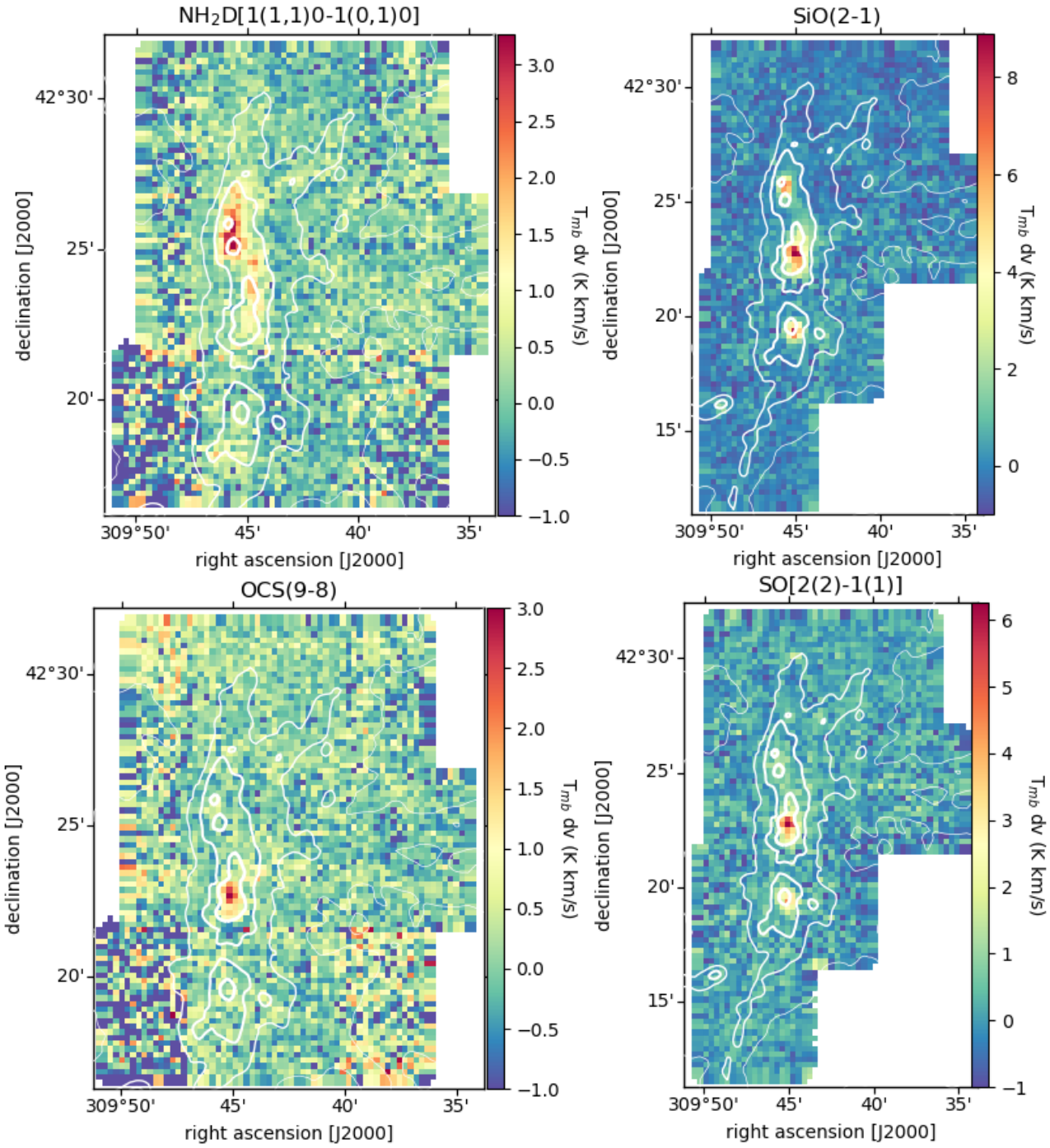

Figure A.4: The same as Fig. A.1 for NH_2D[1(1,1)0-1(0,1)0], SiO(2-1), OCS(9-8) and SO[2(2)-1(1)].

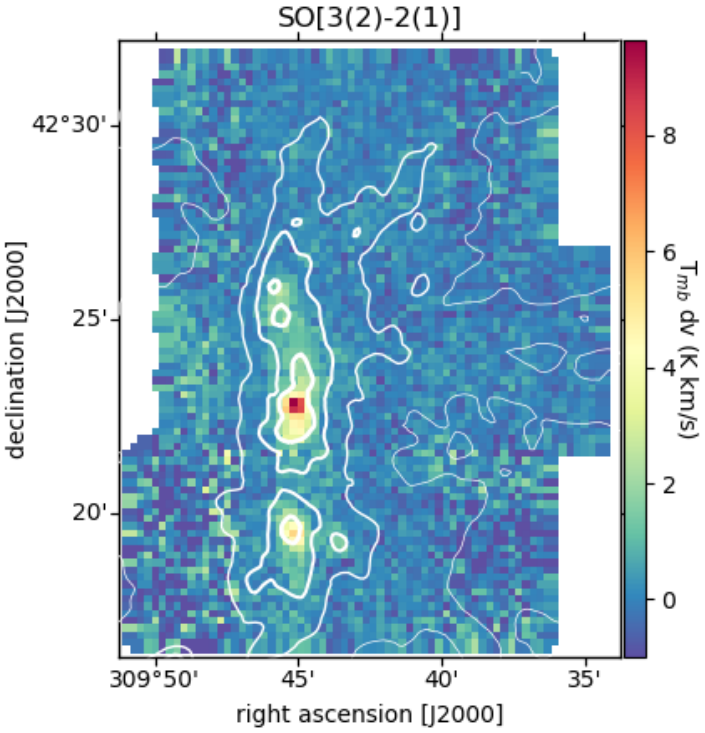

Figure A.5: The same as Fig. A.1 for SO[3(2)-2(1)].

Bibliography

Abreu-Vicente J., Ragan S., Kainulainen J., Henning T., Beuther H., Johnston K., 2016, A&A, 590, A131

Adams F. C., Lada C. J., Shu F. H., 1987, ApJ, 312, 788

Alves J., Lombardi M., Lada C. J., 2007, A&A, 462, L17

Alves J. et al., 2020, Nature, 578, 237

Anathpindika S., 2009, A&A, 504, 437

Anathpindika S. V., 2010, MNRAS, 405, 1431

André P., Arzoumanian D., Könyves V., Shimajiri Y., Palmeirim P., 2019a, A&A, 629, L4

André P., Di Francesco J., Ward-Thompson D., Inutsuka S. I., Pudritz R. E., Pineda J. E., 2014, in Protostars and Planets VI, Beuther H., Klessen R. S., Dullemond C. P., Henning T., eds., p. 27

André P. et al., 2019b, PASA, 36, e029

André P. et al., 2010, A&A, 518, L102

André P., Montmerle T., 1994, ApJ, 420, 837

André P., Ward-Thompson D., Barsony M., 1993, ApJ, 406, 122

Andre P., Ward-Thompson D., Barsony M., 2000, in Protostars and Planets IV, Mannings V., Boss A. P., Russell S. S., eds., p. 59

Araya E. D., Kurtz S., Hofner P., Linz H., 2009, 2009, 698, 1321

Arce H. G., Borkin M. A., Goodman A. A., Pineda J. E., Halle M. W., 2010, ApJ, 715, 1170

Arce H. G., Shepherd D., Gueth F., Lee C. F., Bachiller R., Rosen A., Beuther H., 2007, in Protostars and Planets V, Reipurth B., Jewitt D., Keil K., eds., p. 245

Areal M. B., Paron S., Celis Peña M., Ortega M. E., 2018, A&A, 612, A117

Areal M. B., Paron S., Ortega M. E., Duvidovich L., 2019, PASA, 36, e049

Arneodo A., Bacry E., Muzy J., 1995, Physica A: Statistical Mechanics and its Applications, 213, 232 , proceedings of the Third European Days of Thermodynamics on Inhomogeneous Phases and Pattern Formation

Arnold B., Goodwin S. P., Wright N. J., 2020, MNRAS, 495, 3474

Arzoumanian D. et al., 2011, A&A, 529, L6

Arzoumanian D. et al., 2019, A&A, 621, A42

Arzoumanian D., André P., Peretto N., Könyves V., 2013, A&A, 553, A119

Arzoumanian D., Shimajiri Y., Inutsuka S.-i., Inoue T., Tachihara K., 2018, PASJ, 70, 96

Astropy Collaboration et al., 2018, AJ, 156, 123

Astropy Collaboration et al., 2013, A&A, 558, A33

Auddy S., Basu S., Kudoh T., 2016, ApJ, 831, 46

Audit E., Hennebelle P., 2005, A&A, 433, 1

Bacciotti F., Ray T. P., Mundt R., Eislöffel J., Solf J., 2002, ApJ, 576, 222

Bachiller R., 1996, ARA&A, 34, 111

Balbinot E. et al., 2015, MNRAS, 449, 1129

Ballesteros-Paredes J. et al., 2020, SSRv, 216, 76

Ballesteros-Paredes J., Hartmann L., Vázquez-Semadeni E., 1999, ApJ, 527, 285

Ballesteros-Paredes J., Klessen R. S., Vázquez-Semadeni E., 2003, ApJ, 592, 188

Bally J., 2016, ARA&A, 54, 491

Bally J., Lada C. J., 1983, ApJ, 265, 824

Banerjee R., Vázquez-Semadeni E., Hennebelle P., Klessen R. S., 2009, MNRAS, 398, 1082

Barnard E. E., 1907, ApJ, 25, 218

Barnard E. E., 1919, ApJ, 49, 1

Bate M. R., Bonnell I. A., Bromm V., 2003, MNRAS, 339, 577

Battersby C. et al., 2018, Nature Astronomy, 2, 596

Beckwith S. V. W., Sargent A. I., Chini R. S., Guesten R., 1990, AJ, 99, 924

Beerer I. M. et al., 2010, ApJ, 720, 679

Begum A. et al., 2010, ApJ, 722, 395

Behrend R., Maeder A., 2001, A&A, 373, 190

Belloche A., Müller H. S. P., Menten K. M., Schilke P., Comito C., 2013, A&A, 559, A47

Belloche A., Parise B., Schuller F., André P., Bontemps S., Menten K. M., 2011a, A&A, 535, A2

Belloche A. et al., 2011b, A&A, 527, A145

Benedettini M. et al., 2018, A&A, 619, A52

Bensch F., Stutzki J., Ossenkopf V., 2001, A&A, 366, 636

Bergin E. A., Tafalla M., 2007, ARA&A, 45, 339

Bertoldi F., McKee C. F., 1992, ApJ, 395, 140

Bertram E., Glover S. C. O., Clark P. C., Ragan S. E., Klessen R. S., 2016, MNRAS, 455, 3763

Beuther H. et al., 2015a, A&A, 581, A119

Beuther H. et al., 2013, A&A, 553, A115

Beuther H. et al., 2018, A&A, 617, A100

Beuther H., Ragan S. E., Johnston K., Henning T., Hacar A., Kainulainen J. T., 2015b, A&A, 584, A67

Beuther H. et al., 2014, A&A, 571, A53

Beuther H., Schilke P., Menten K. M., Motte F., Sridharan T. K., Wyrowski F., 2002a, ApJ, 566, 945

Beuther H., Schilke P., Sridharan T. K., Menten K. M., Walmsley C. M., Wyrowski F., 2002b, A&A, 383, 892

Bisbas T. G., Papadopoulos P. P., Viti S., 2015, ApJ, 803, 37

Bisbas T. G. et al., 2018, MNRAS, 478, L54

Bisbas T. G., Tanaka K. E. I., Tan J. C., Wu B., Nakamura F., 2017, ApJ, 850, 23

Black J. H., 1994, in Astronomical Society of the Pacific Conference Series, Vol. 58, The First Symposium on the Infrared Cirrus and Diffuse Interstellar Clouds, Cutri R. M., Latter W. B., eds., p. 355

Blake G. A., Sutton E. C., Masson C. R., Phillips T. G., 1987, ApJ, 315, 621

Bok B. J., 1948, Dimensions and Masses of Dark Nebulae, Vol. 7, p. 53

Bonnell I. A., Bate M. R., 2002, MNRAS, 336, 659

Bonnell I. A., Bate M. R., 2006, MNRAS, 370, 488

Bonnell I. A., Bate M. R., Clarke C. J., Pringle J. E., 1997, MNRAS, 285, 201

Bonnell I. A., Bate M. R., Clarke C. J., Pringle J. E., 2001a, MNRAS, 323, 785

Bonnell I. A., Bate M. R., Zinnecker H., 1998, MNRAS, 298, 93

Bonnell I. A., Clarke C. J., Bate M. R., Pringle J. E., 2001b, MNRAS, 324, 573

Bonnell I. A., Dobbs C. L., Smith R. J., 2013, MNRAS, 430, 1790

Bontemps S. et al., 2001, A&A, 372, 173

Bontemps S. et al., 2010a, A&A, 518, L85

Bontemps S., Andre P., Terebey S., Cabrit S., 1996, A&A, 311, 858

Bontemps S., Motte F., Csengeri T., Schneider N., 2010b, A&A, 524, A18

Boulanger F., Perault M., 1988, ApJ, 330, 964

Bourke T. L., Myers P. C., Robinson G., Hyland A. R., 2001, ApJ, 554, 916

Bresnahan D. et al., 2018, A&A, 615, A125

Brinch C., Hogerheijde M. R., 2010, A&A, 523, A25

Bromm V., Larson R. B., 2004, ARA&A, 42, 79

Bron E., Le Bourlot J., Le Petit F., 2014, A&A, 569, A100

Brünken S. et al., 2014, Nature, 516, 219

Burton W. B., Gordon M. A., Bania T. M., Lockman F. J., 1975, ApJ, 202, 30

Butler M. J., Tan J. C., 2012, ApJ, 754, 5

Cao Y., Qiu K., Zhang Q., Wang Y., Hu B., Liu J., 2019, ApJS, 241, 1

Cappellari M. et al., 2012, Nature, 484, 485

Caselli P., Benson P. J., Myers P. C., Tafalla M., 2002, ApJ, 572, 238

Caselli P., Walmsley C. M., Tafalla M., Dore L., Myers P. C., 1999, ApJL, 523, L165

Chabrier G., 2003, PASP, 115, 763

Chabrier G., 2005, Astrophysics and Space Science Library, Vol. 327, The Initial Mass Function: From Salpeter 1955 to 2005, Corbelli E., Palla F., Zinnecker H., eds., p. 41

Chandrasekhar S., Fermi E., 1953, ApJ, 118, 116

Chapman N. L., Goldsmith P. F., Pineda J. L., Clemens D. P., Li D., Krčo M., 2011, ApJ, 741, 21

Chappell D., Scalo J., 2001, ApJ, 551, 712

Chen C.-Y., Mundy L. G., Ostriker E. C., Storm S., Dhabal A., 2020, arXiv e-prints, arXiv:2004.02898

Ching T.-C., Lai S.-P., Zhang Q., Girart J. M., Qiu K., Liu H. B., 2017, ApJ, 838, 121

Churchwell E. et al., 2009, PASP, 121, 213

Churchwell E. et al., 2006, ApJ, 649, 759

Clark P. C., Glover S. C. O., Ragan S. E., Duarte-Cabral A., 2019, MNRAS, 486, 4622

Clark P. C., Klessen R. S., Bonnell I. A., 2007, MNRAS, 379, 57

Clark S. E., Peek J. E. G., Putman M. E., 2014, ApJ, 789, 82

Clarke S. D., Whitworth A. P., Duarte-Cabral A., Hubber D. A., 2017, MNRAS, 468, 2489

Clarke S. D., Whitworth A. P., Spowage R. L., Duarte-Cabral A., Suri S. T., Jaffa S. E., Walch S., Clark P. C., 2018, MNRAS, 479, 1722

Comerón F., Pasquali A., 2012, A&A, 543, A101

Comerón F., Pasquali A., Figueras F., Torra J., 2008, A&A, 486, 453

Commerçon B., Audit E., Chabrier G., Chièze J. P., 2011, A&A, 530, A13

Commerçon B., Hennebelle P., Henning T., 2011, ApJL, 742, L9

Cox D. P., Smith B. W., 1974, ApJL, 189, L105

Cox N. L. J. et al., 2016, A&A, 590, A110

Crutcher R. M., 2012, ARA&A, 50, 29

Crutcher R. M., Troland T. H., Goodman A. A., Heiles C., Kazes I., Myers P. C., 1993, ApJ, 407, 175

Crutcher R. M., Wandelt B., Heiles C., Falgarone E., Troland T. H., 2010, ApJ, 725, 466

Csengeri T., Bontemps S., Schneider N., Motte F., Dib S., 2011a, A&A, 527, A135

Csengeri T., Bontemps S., Schneider N., Motte F., Gueth F., Hora J. L., 2011b, ApJL, 740, L5

Csengeri T. et al., 2017, A&A, 600, L10

Cyganowski C. J. et al., 2014, ApJL, 796, L2

Cyganowski C. J., Reid M. J., Fish V. L., Ho P. T. P., 2003, ApJ, 596, 344

Dame T. M., Hartmann D., Thaddeus P., 2001, ApJ, 547, 792

de Graauw T. et al., 2010, A&A, 518, L6

de Hoffmann F., Teller E., 1950, Physical Review, 80, 692

Dhabal A., Mundy L. G., Rizzo M. J., Storm S., Teuben P., 2018, ApJ, 853, 169

di Francesco J., Evans, N. J. I., Caselli P., Myers P. C., Shirley Y., Aikawa Y., Tafalla M., 2007, in Protostars and Planets V, Reipurth B., Jewitt D., Keil K., eds., p. 17

Dickel J. R., Dickel H. R., Wilson W. J., 1978, Apj, 223, 840

Dobbs C. L., Bonnell I. A., 2006, MNRAS, 367, 873

Downes D., Rinehart R., 1966, ApJ, 144, 937

Draine B. T., 1978, ApJS, 36, 595

Draine B. T., 1980, ApJ, 241, 1021

Draine B. T., Roberge W. G., Dalgarno A., 1983, ApJ, 264, 485

Duarte-Cabral A., Bontemps S., Motte F., Hennemann M., Schneider N., André P., 2013, A&A, 558, A125

Duarte-Cabral A., Dobbs C. L., 2016, MNRAS, 458, 3667

Duarte-Cabral A., Dobbs C. L., 2017, MNRAS, 470, 4261

Dullemond C. P., Juhasz A., Pohl A., Sereshti F., Shetty R., Peters T., Commercon B., Flock M., 2012, RADMC-3D: A multi-purpose radiative transfer tool

Dunham M. M. et al., 2015, ApJS, 220, 11

Dunham M. M., Crapsi A., Evans, Neal J. I., Bourke T. L., Huard T. L., Myers P. C., Kauffmann J., 2008, ApJS, 179, 249

Dutra C. M., Bica E., 2001, A&A, 376, 434

Egan M. P., Shipman R. F., Price S. D., Carey S. J., Clark F. O., Cohen M., 1998, ApJL, 494, L199

Elia D. et al., 2018, MNRAS, 481, 509

Elmegreen B. G., 2000, ApJ, 530, 277

Elmegreen B. G., Scalo J., 2004, AR&A, 42, 211

Enoch M. L., Evans, Neal J. I., Sargent A. I., Glenn J., Rosolowsky E., Myers P., 2008, ApJ, 684, 1240

Evans, Neal J. I. et al., 2009, ApJS, 181, 321

Falgarone E., Hily-Blant P., Levrier F., 2004, Ap&SS, 292, 89

Falgarone E., Pety J., Hily-Blant P., 2009, A&A, 507, 355

Falgarone E., Phillips T. G., Walker C. K., 1991, ApJ, 378, 186

Falgarone E., Troland T. H., Crutcher R. M., Paubert G., 2008, A&A, 487, 247

Fechtenbaum S., 2015, PhD thesis, University of Bordeaux

Fechtenbaum S., Bontemps S., Schneider N., Csengeri T., Duarte-Cabral A., Herpin F., Lefloch B., 2015, A&A, 574, L4

Federrath C., 2016, MNRAS, 457, 375

Federrath C., Klessen R. S., Schmidt W., 2008, ApJL, 688, L79

Federrath C., Roman-Duval J., Klessen R. S., Schmidt W., Mac Low M. M., 2010, A&A, 512, A81

Fernández-López M. et al., 2014, ApJL, 790, L19

Ferreira J., Dougados C., Cabrit S., 2006, A&A, 453, 785

Ferrière K. M., 2001, Reviews of Modern Physics, 73, 1031

Fiege J. D., Pudritz R. E., 2000, MNRAS, 311, 105

Field G. B., Goldsmith D. W., Habing H. J., 1969, ApJL, 155, L149

Fissel L. M. et al., 2019, ApJ, 878, 110

Fissel L. M. et al., 2016, ApJ, 824, 134

Fitzpatrick E. L., Massa D., 2005, AJ, 129, 1642

Flower D. R., Pineau des Forêts G., 2003, MNRAS, 343, 390

Fogerty E., Carroll-Nellenback J., Frank A., Heitsch F., Pon A., 2017, MNRAS, 470, 2938

Franco G. A. P., 1991, A&A, 251, 581

Franeck A. et al., 2018, MNRAS, 481, 4277

Frank A. et al., 2014, in Protostars and Planets VI, Beuther H., Klessen R. S., Dullemond C. P., Henning T., eds., p. 451

Friesen R. K. et al., 2017, ApJ, 843, 63

Froebrich D., Rowles J., 2010, MNRAS, 406, 1350

Fukui Y., Inoue T., Hayakawa T., Torii K., 2019a, arXiv e-prints, arXiv:1909.08202

Fukui Y. et al., 2019b, ApJ, 886, 14

Furst E., Reich W., Reich P., Reif K., 1990, A&AS, 85, 805

Gaia Collaboration et al., 2018, A&A, 616, A10

Gaia Collaboration et al., 2016, A&A, 595, A1

Galli D., Shu F. H., 1993a, ApJ, 417, 220

Galli D., Shu F. H., 1993b, ApJ, 417, 243

Galván-Madrid R., Zhang Q., Keto E., Ho P. T. P., Zapata L. A., Rodríguez L. F., Pineda J. E., Vázquez-Semadeni E., 2010, ApJ, 725, 17

Gao Y., Solomon P. M., 2004a, ApJS, 152, 63

Gao Y., Solomon P. M., 2004b, ApJ, 606, 271

Garay G., Lizano S., 1999, PAS, 111, 1049

Gazol A., Vázquez-Semadeni E., Kim J., 2005, ApJ, 630, 911

Ginsburg A., Mirocha J., 2011, PySpecKit: Python Spectroscopic Toolkit

Girart J. M., Beltrán M. T., Zhang Q., Rao R., Estalella R., 2009, Science, 324, 1408

Girart J. M., Frau P., Zhang Q., Koch P. M., Qiu K., Tang Y. W., Lai S. P., Ho P. T. P., 2013, ApJ, 772, 69

Girart J. M., Rao R., Marrone D. P., 2006, Science, 313, 812

Girichidis P., Federrath C., Banerjee R., Klessen R. S., 2012, MNRAS, 420, 613

Girichidis P. et al., 2016, MNRAS, 456, 3432

Glassgold A. E., Huggins P. J., Langer W. D., 1985, ApJ, 290, 615

Glover S. C. O., Clark P. C., 2012, MNRAS, 421, 116

Glover S. C. O., Clark P. C., Micic M., Molina F., 2015, MNRAS, 448, 1607

Glover S. C. O., Mac Low M.-M., 2007a, ApJS, 169, 239

Glover S. C. O., Mac Low M.-M., 2007b, ApJ, 659, 1317

Glover S. C. O., Smith R. J., 2016, MNRAS, 462, 3011

Godard B., Pineau des Forêts G., Lesaffre P., Lehmann A., Gusdorf A., Falgarone E., 2019, A&A, 622, A100

Goldsmith P. F., 2001, ApJ, 557, 736

Goldsmith P. F., Heyer M., Narayanan G., Snell R., Li D., Brunt C., 2008, ApJ, 680, 428

Goldsmith P. F., Langer W. D., 1978, ApJ, 222, 881

Goldsmith P. F., Langer W. D., 1999, ApJ, 517, 209

Goldsmith P. F. et al., 2000, ApJL, 539, L123

Gómez G. C., Vázquez-Semadeni E., 2014, ApJ, 791, 124

Gómez G. C., Vázquez-Semadeni E., Zamora-Avilés M., 2018, MNRAS, 480, 2939

Goodman A. A. et al., 2014, ApJ, 797, 53

Greene T. P., Wilking B. A., Andre P., Young E. T., Lada C. J., 1994, ApJ, 434, 614

Grenier I. A., Black J. H., Strong A. W., 2015, ARA&A, 53, 199

Griffin M. J. et al., 2010, A&A, 518, L3

Gueth F., Guilloteau S., 1999, A&A, 343, 571

Güsten R., Nyman L. Å., Schilke P., Menten K., Cesarsky C., Booth R., 2006, A&A, 454, L13

Gutermuth R. A., Megeath S. T., Myers P. C., Allen L. E., Pipher J. L., Fazio G. G., 2009, ApJS, 184, 18

Hacar A., Alves J., Tafalla M., Goicoechea J. R., 2017, A&A, 602, L2

Hacar A., Kainulainen J., Tafalla M., Beuther H., Alves J., 2016, A&A, 587, A97

Hacar A., Tafalla M., Alves J., 2017, A&A, 606, A123

Hacar A., Tafalla M., Forbrich J., Alves J., Meingast S., Grossschedl J., Teixeira P. S., 2018, A&A, 610, A77

Hacar A., Tafalla M., Kauffmann J., Kovács A., 2013, A&A, 554, A55

Harper D. A. et al., 2018, Journal of Astronomical Instrumentation, 7, 1840008

Hartmann D., Burton W. B., 1997, Atlas of Galactic Neutral Hydrogen

Hartmann L., Ballesteros-Paredes J., Bergin E. A., 2001, ApJ, 562, 852

Hartmann L., Ballesteros-Paredes J., Heitsch F., 2012, MNRAS, 420, 1457

Hartmann L., Burkert A., 2007, ApJ, 654, 988

Hatchell J., Fuller G. A., Richer J. S., Harries T. J., Ladd E. F., 2007, A&A, 468, 1009

Haworth T. J., Shima K., Tasker E. J., Fukui Y., Torii K., Dale J. E., Takahira K., Habe A., 2015a, MNRAS, 454, 1634

Haworth T. J. et al., 2015b, MNRAS, 450, 10

Heitsch F., Hartmann L. W., Slyz A. D., Devriendt J. E. G., Burkert A., 2008, ApJ, 674, 316

Heitsch F., Slyz A. D., Devriendt J. E. G., Hartmann L. W., Burkert A., 2006, ApJ, 648, 1052

Hennebelle P., 2013, A&A, 556, A153

Hennebelle P., André P., 2013, A&A, 560, A68

Hennebelle P., Chabrier G., 2008, ApJ, 684, 395

Hennebelle P., Commerçon B., Joos M., Klessen R. S., Krumholz M., Tan J. C., Teyssier R., 2011, A&A, 528, A72

Hennebelle P., Falgarone E., 2012, A&AR, 20, 55

Hennebelle P., Inutsuka S.-i., 2019, Frontiers in Astronomy and Space Sciences, 6, 5

Hennebelle P., Lee Y.-N., Chabrier G., 2019, ApJ, 883, 140

Hennebelle P., Pérault M., 1999, A&A, 351, 309

Hennebelle P., Pérault M., Teyssier D., Ganesh S., 2001, A&A, 365, 598

Hennemann M. et al., 2010, A&A, 518, L84

Hennemann M. et al., 2012, A&A, 543, L3

Henning T., Linz H., Krause O., Ragan S., Beuther H., Launhardt R., Nielbock M., Vasyunina T., 2010, A&A, 518, L95

Henshaw J. D., Caselli P., Fontani F., Jiménez-Serra I., Tan J. C., 2014, MNRAS, 440, 2860

Herbst E., van Dishoeck E. F., 2009, ARA&A, 47, 427

Heyer M., Goldsmith P. F., Yıldız U. A., Snell R. L., Falgarone E., Pineda J. L., 2016, MNRAS, 461, 3918

Heyer M., Gong H., Ostriker E., Brunt C., 2008, ApJ, 680, 420

Heyer M. H., Vrba F. J., Snell R. L., Schloerb F. P., Strom S. E., Goldsmith P. F., Strom K. M., 1987, ApJ, 321, 855

Hill T. et al., 2011, A&A, 533, A94

Ho P. T. P., Townes C. H., 1983, ARA&A, 21, 239

Hogerheijde M. R., van der Tak F. F. S., 2000, A&A, 362, 697

Hollenbach D., McKee C. F., 1989, ApJ, 342, 306

Hollenbach D. J., Tielens A. G. G. M., 1999, Reviews of Modern Physics, 71, 173

Hopkins P. F., 2012, MNRAS, 423, 2037

Hosokawa T., Omukai K., 2009, ApJ, 691, 823

Houde M., Hull C. L. H., Plambeck R. L., Vaillancourt J. E., Hildebrand R. H., 2016, ApJ, 820, 38

Houde M., Vaillancourt J. E., Hildebrand R. H., Chitsazzadeh S., Kirby L., 2009, ApJ, 706, 1504

Howard A. D. P., Whitworth A. P., Marsh K. A., Clarke S. D., Griffin M. J., Smith M. W. L., Lomax O. D., 2019, MNRAS, 489, 962

Immer K., Cyganowski C., Reid M. J., Menten K. M., 2014, A&A, 563, A39

Inoue T., Fukui Y., 2013, ApJL, 774, L31

Inoue T., Hennebelle P., Fukui Y., Matsumoto T., Iwasaki K., Inutsuka S.-i., 2018, PASJ, 70, S53

Inoue T., Inutsuka S.-i., 2012, ApJ, 759, 35

Inutsuka S.-i., 2001, ApJL, 559, L149

Inutsuka S.-i., Inoue T., Iwasaki K., Hosokawa T., 2015, A&A, 580, A49

Inutsuka S.-I., Miyama S. M., 1992, ApJ, 388, 392

Inutsuka S.-i., Miyama S. M., 1997, ApJ, 480, 681

Iwasaki K., Tomida K., Inoue T., Inutsuka S.-i., 2019, ApJ, 873, 6

Jackson J. M., Finn S. C., Chambers E. T., Rathborne J. M., Simon R., 2010, ApJL, 719, L185

Jackson J. M. et al., 2006, ApJS, 163, 145

Jappsen A. K., Klessen R. S., Larson R. B., Li Y., Mac Low M. M., 2005, A&A, 435, 611

Jeans J. H., 1902, Philosophical Transactions of the Royal Society of London Series A, 199, 1

Jiménez-Serra I., Caselli P., Fontani F., Tan J. C., Henshaw J. D., Kainulainen J., Hernand ez A. K., 2014, MNRAS, 439, 1996

Johnstone D., Wilson C. D., Moriarty-Schieven G., Joncas G., Smith G., Gregersen E., Fich M., 2000, ApJ, 545, 327

Kaas A. A. et al., 2004, A&A, 421, 623

Kainulainen J., Beuther H., Henning T., Plume R., 2009, A&A, 508, L35

Kainulainen J., Hacar A., Alves J., Beuther H., Bouy H., Tafalla M., 2016, A&A, 586, A27

Kalberla P. M. W., Kerp J., Haud U., Winkel B., Ben Bekhti N., Flöer L., Lenz D., 2016, ApJ, 821, 117

Kaufman M. J., Neufeld D. A., 1996a, ApJ, 456, 611

Kaufman M. J., Neufeld D. A., 1996b, ApJ, 456, 250

Keene J., Schilke P., Kooi J., Lis D. C., Mehringer D. M., Phillips T. G., 1998, ApJL, 494, L107

Kennel C. F., Blandford R. D., Coppi P., 1989, Journal of Plasma Physics, 42, 299

Kennicutt, Robert C. J., 1998, ApJ, 498, 541

Kennicutt R. C., Evans N. J., 2012, ARA&A, 50, 531

Kenyon S. J., Calvet N., Hartmann L., 1993, ApJ, 414, 676

Kenyon S. J., Hartmann L., 1987, ApJ, 323, 714

Kenyon S. J., Hartmann L., 1995, ApJS, 101, 117

Keown J. et al., 2017, ApJ, 850, 3

Keown J. et al., 2019, ApJ, 884, 4

Keto E., Rybicki G. B., Bergin E. A., Plume R., 2004, ApJ, 613, 355

Khalil A., Joncas G., Nekka F., Kestener P., Arneodo A., 2006, ApJS, 165, 512

Kim C.-G., Ostriker E. C., 2015, ApJ, 802, 99

Kirk H. et al., 2017, ApJ, 846, 144

Kirk H., Myers P. C., Bourke T. L., Gutermuth R. A., Hedden A., Wilson G. W., 2013, ApJ, 766, 115

Kirk J. M., Ward-Thompson D., André P., 2005, MNRAS, 360, 1506

Klein T. et al., 2014, Terahertz Science and Technology, IEEE Transactions on, 4, 588

Klessen R. S., Burkert A., 2000, ApJS, 128, 287

Klessen R. S., Burkert A., Bate M. R., 1998, ApJL, 501, L205

Klessen R. S., Heitsch F., Mac Low M.-M., 2000, ApJ, 535, 887

Klessen R. S., Hennebelle P., 2010, A&A, 520, A17

Koch E. W., Rosolowsky E. W., 2015, MNRAS, 452, 3435

Koch P. M. et al., 2014, ApJ, 797, 99

Kong S., Tan J. C., Caselli P., Fontani F., Liu M., Butler M. J., 2017, ApJ, 834, 193

Könyves V. et al., 2020, A&A, 635, A34

Könyves V. et al., 2015, A&A, 584, A91

Könyves V. et al., 2010, A&A, 518, L106

Koyama H., Inutsuka S.-I., 2000, ApJ, 532, 980

Koyama H., Inutsuka S.-i., 2002, ApJL, 564, L97

Kraemer K. E. et al., 2010, in American Astronomical Society Meeting Abstracts, Vol. 215, American Astronomical Society Meeting Abstracts #215, p. 414.01

Kramer C., Stutzki J., Rohrig R., Corneliussen U., 1998, A&A, 329, 249

Kritsuk A. G., Norman M. L., Wagner R., 2011, ApJL, 727, L20

Kroupa P., 2001, MNRAS, 322, 231

Krumholz M. R., 2014, Physics Reports, 539, 49

Krumholz M. R., Matzner C. D., McKee C. F., 2006, ApJ, 653, 361

Krumholz M. R., McKee C. F., 2005, ApJ, 630, 250

Krumholz M. R., McKee C. F., Bland -Hawthorn J., 2019, ARA&A, 57, 227

Krumholz M. R., McKee C. F., Klein R. I., 2005, ApJL, 618, L33

Krumholz M. R., Thompson T. A., 2012, ApJ, 760, 155

Kuhn M. A., Getman K. V., Feigelson E. D., 2015, ApJ, 802, 60

Kuiper R., Klahr H., Beuther H., Henning T., 2010, ApJ, 722, 1556

Kuiper R., Klahr H., Beuther H., Henning T., 2011, ApJ, 732, 20

Kulkarni S. R., Heiles C., 1987, The Atomic Component, Hollenbach D. J., Thronson Harley A. J., eds., Vol. 134, p. 87

Kurtz S., Cesaroni R., Churchwell E., Hofner P., Walmsley C. M., 2000, in Protostars and Planets IV, Mannings V., Boss A. P., Russell S. S., eds., pp. 299–326

Lada C. J., 1985, ARA&A, 23, 267

Lada C. J., 1987, in IAU Symposium, Vol. 115, Star Forming Regions, Peimbert M., Jugaku J., eds., p. 1

Lada C. J., Lada E. A., 2003, ARA&A, 41, 57

Lada C. J., Lada E. A., Clemens D. P., Bally J., 1994, ApJ, 429, 694

Lada C. J., Lombardi M., Alves J. F., 2010, ApJ, 724, 687

Lada C. J., Wilking B. A., 1984, ApJ, 287, 610

Ladjelate B. et al., 2020, arXiv e-prints, arXiv:2001.11036

Lallement R., Babusiaux C., Vergely J. L., Katz D., Arenou F., Valette B., Hottier C., Capitanio L., 2019, A&A, 625, A135

Lallement R., Vergely J. L., Valette B., Puspitarini L., Eyer L., Casagrande L., 2014, A&A, 561, A91

Langer W. D., Graedel T. E., Frerking M. A., Armentrout P. B., 1984, ApJ, 277, 581

Langer W. D., Penzias A. A., 1990, ApJ, 357, 477

Larson R. B., 1969, MNRAS, 145, 271

Larson R. B., 1978, MNRAS, 184, 69

Larson R. B., 1981, MNRAS, 194, 809

Larson R. B., Starrfield S., 1971, A&A, 13, 190

Larson R. L., Evans, Neal J. I., Green J. D., Yang Y.-L., 2015, ApJ, 806, 70

Larsson B. et al., 2007, A&A, 466, 999

Le Bourlot J., Le Petit F., Pinto C., Roueff E., Roy F., 2012, A&A, 541, A76

Le Duigou J. M., Knödlseder J., 2002, A&A, 392, 869

Le Petit F., Nehmé C., Le Bourlot J., Roueff E., 2006, ApJS, 164, 506

Lee C.-F., Ho P. T. P., Li Z.-Y., Hirano N., Zhang Q., Shang H., 2017, Nature Astronomy, 1, 0152

Lehmann A., Federrath C., Wardle M., 2016, MNRAS, 463, 1026

Lehmann A., Wardle M., 2016, MNRAS, 455, 2066

Lesaffre P., Pineau des Forêts G., Godard B., Guillard P., Boulanger F., Falgarone E., 2013, A&A, 550, A106

Lesaffre P. et al., 2020, MNRAS, 495, 816

Liszt H., Gerin M., Grenier I., 2018, A&A, 617, A54

Liszt H., Gerin M., Grenier I., 2019, A&A, 627, A95

Liszt H. S., 2007, A&A, 476, 291

Liu M., Tan J. C., Cheng Y., Kong S., 2018, ApJ, 862, 105

Lockman F. J., 1989, ApJS, 71, 469

Lohr L. L., 1998, The Journal of Chemical Physics, 108, 8012

Loison J.-C. et al., 2019

Louvet F. et al., 2016a, A&A, 596, A88

Louvet F., Dougados C., Cabrit S., Mardones D., Ménard F., Tabone B., Pinte C., Dent W. R. F., 2018, A&A, 618, A120

Louvet F. et al., 2016b, A&A, 595, A122

Louvet F. et al., 2019, A&A, 622, A99

Low F. J. et al., 1984, ApJL, 278, L19

Luhman K. L., 2008, Chamaeleon, Reipurth B., ed., Vol. 5, p. 169

Luhman K. L., Muench A. A., 2008, ApJ, 684, 654

Lyons J. R., Young E. D., 2005, Nature, 435, 317

Mac Low M.-M., Klessen R. S., 2004, Reviews of Modern Physics, 76, 125

Machaieie D. A., Vilas-Boas J. W., Wuensche C. A., Racca G. A., Myers P. C., Hickel G. R., 2017, ApJ, 836, 19

Malinen J. et al., 2016, MNRAS, 460, 1934

Mangum J. G., Wootten A., Mundy L. G., 1991, ApJ, 378, 576

Mangum J. G., Wootten A., Mundy L. G., 1992, ApJ, 388, 467

Marsh K. A. et al., 2016, MNRAS, 459, 342

Marsh K. A. et al., 2017, MNRAS, 471, 2730

Marston A. P. et al., 2004, ApJS, 154, 333

Masson C. R., Chernin L. M., 1993, ApJ, 414, 230

Masunaga H., Inutsuka S.-i., 2000, ApJ, 531, 350

Masunaga H., Miyama S. M., Inutsuka S.-i., 1998, ApJ, 495, 346

Mattern M., Kainulainen J., Zhang M., Beuther H., 2018a, A&A, 616, A78

Mattern M. et al., 2018b, A&A, 619, A166

Mattila K., Liljeström T., Toriseva M., 1989, in European Southern Observatory Conference and Workshop Proceedings, Vol. 33, European Southern Observatory Conference and Workshop Proceedings, pp. 153–171

Matzner C. D., 2002, ApJ, 566, 302

Maury A. J., André P., Men'shchikov A., Könyves V., Bontemps S., 2011, A&A, 535, A77

McClure-Griffiths N. M., Dickey J. M., Gaensler B. M., Green A. J., Haverkorn M., 2006, ApJ, 652, 1339

McKee C. F., Ostriker E. C., 2007, ARA&A, 45, 565

McKee C. F., Ostriker J. P., 1977, ApJ, 218, 148

McKee C. F., Tan J. C., 2002, Nature, 416, 59

McKee C. F., Tan J. C., 2003, ApJ, 585, 850

Megeath S. T. et al., 2012, AJ, 144, 192

Mel'Nik A. M., Efremov Y. N., 1995, Astronomy Letters, 21, 10

Men'shchikov A. et al., 2010, A&A, 518, L103

Men'shchikov A., André P., Didelon P., Motte F., Hennemann M., Schneider N., 2012, A&A, 542, A81

Miville-Deschênes M. A., Joncas G., Falgarone E., Boulanger F., 2003, A&A, 411, 109

Miville-Deschênes M. A. et al., 2010, A&A, 518, L104

Mizuno A., Yamaguchi R., Tachihara K., Toyoda S., Aoyama H., Yamamoto H., Onishi T., Fukui Y., 2001, PASJ, 53, 1071

Moeckel N., Burkert A., 2015, ApJ, 807, 67

Molet J. et al., 2019, A&A, 626, A132

Molinari S. et al., 2019, MNRAS, 486, 4508

Molinari S., Pezzuto S., Cesaroni R., Brand J., Faustini F., Testi L., 2008, A&A, 481, 345

Molinari S., Schisano E., Faustini F., Pestalozzi M., di Giorgio A. M., Liu S., 2017, CUTEX: CUrvature Thresholding EXtractor

Molinari S. et al., 2010, A&A, 518, L100

Montillaud J. et al., 2019, A&A, 631, A3

Motte F., Andre P., Neri R., 1998, A&A, 336, 150

Motte F., Bontemps S., Louvet F., 2018, ARA&A, 56, 41

Motte F., Bontemps S., Schilke P., Schneider N., Menten K. M., Broguière D., 2007, A&A, 476, 1243

Motte F. et al., 2014, A&A, 571, A32

Motte F. et al., 2018, Nature Astronomy, 2, 478

Motte F. et al., 2010, A&A, 518, L77

Mouschovias T. C., 1976, ApJ, 207, 141

Mouschovias T. C., 1991, ApJ, 373, 169

Mullan D. J., 1971, MNRAS, 153, 145

Murray N., Chang P., 2012, ApJ, 746, 75

Myers P. C., 1998, ApJL, 496, L109

Myers P. C., 2009, ApJ, 700, 1609

Nagai T., Inutsuka S.-i., Miyama S. M., 1998, ApJ, 506, 306

Nakamura F., Hanawa T., Nakano T., 1993, PASJ, 45, 551

Nakano T., 1998, ApJ, 494, 587

Nakano T., Hasegawa T., Morino J.-I., Yamashita T., 2000, ApJ, 534, 976

Nelson R. P., Langer W. D., 1997, ApJ, 482, 796

Nguyen-Lu'o'ng Q. et al., 2013, ApJ, 775, 88

Nony T. et al., 2018, A&A, 618, L5

Nony T. et al., 2020, A&A, 636, A38

Nordh L. et al., 1996, A&A, 315, L185

Ntormousi E., Hennebelle P., André P., Masson J., 2016, A&A, 589, A24

Nutter D., Ward-Thompson D., 2007, MNRAS, 374, 1413

Offner S. S. R., Clark P. C., Hennebelle P., Bastian N., Bate M. R., Hopkins P. F., Moraux E., Whitworth A. P., 2014, in Protostars and Planets VI, Beuther H., Klessen R. S., Dullemond C. P., Henning T., eds., p. 53

Olmi L., Testi L., 2002, A&A, 392, 1053

Olofsson G. et al., 1998, A&A, 339, L81

Onishi T., Mizuno A., Kawamura A., Tachihara K., Fukui Y., 2002, ApJ, 575, 950

Osorio M., Lizano S., D'Alessio P., 1999, ApJ, 525, 808

Ossenkopf V., Krips M., Stutzki J., 2008a, A&A, 485, 917

Ossenkopf V., Krips M., Stutzki J., 2008b, A&A, 485, 719

Ossenkopf V., Mac Low M. M., 2002, A&A, 390, 307

Ossenkopf V., Trojan C., Stutzki J., 2001, A&A, 378, 608

Ossenkopf-Okada V., Stepanov R., 2019, A&A, 621, A5

Osterbrock D. E., Ferland G. J., 2006, Astrophysics of gaseous nebulae and active galactic nuclei

Ostriker J., 1964, ApJ, 140, 1056

Pabst C. et al., 2019, Nature, 565, 618

Padoan P., Federrath C., Chabrier G., Evans, N. J. I., Johnstone D., Jørgensen J. K., McKee C. F., Nordlund Å., 2014, in Protostars and Planets VI, Beuther H., Klessen R. S., Dullemond C. P., Henning T., eds., p. 77

Padoan P., Juvela M., Goodman A. A., Nordlund Å., 2001, ApJ, 553, 227

Padoan P., Nordlund Å., 1999, ApJ, 526, 279

Padoan P., Nordlund Å., 2002, ApJ, 576, 870

Padoan P., Pan L., Juvela M., Haugbølle T., Nordlund Å., 2019, arXiv e-prints, arXiv:1911.04465

Pagani L. et al., 2003, A&A, 402, L77

Pagani L., Pardo J. R., Apponi A. J., Bacmann A., Cabrit S., 2005, A&A, 429, 181

Palau A. et al., 2014, ApJ, 785, 42

Palau A. et al., 2013, ApJ, 762, 120

Palmeirim P. et al., 2013, A&A, 550, A38

Panopoulou G. V., Psaradaki I., Skalidis R., Tassis K., Andrews J. J., 2017, MNRAS, 466, 2529

Panopoulou G. V., Tassis K., Goldsmith P. F., Heyer M. H., 2014, MNRAS, 444, 2507

Park J., Ryu D., 2019, ApJ, 875, 2

Parra R., 2018, Holography ii, advancement report

Pattle K. et al., 2017, ApJ, 846, 122

Pecaut M. J., Mamajek E. E., 2013, ApJS, 208, 9

Perault M. et al., 1996, A&A, 315, L165

Peretto N., André P., Belloche A., 2006, A&A, 445, 979

Peretto N. et al., 2012, A&A, 541, A63

Peretto N., Fuller G. A., 2009, A&A, 505, 405

Peretto N. et al., 2014, A&A, 561, A83

Peretto N. et al., 2013, A&A, 555, A112

Peretto N., Lenfestey C., Fuller G. A., Traficante A., Molinari S., Thompson M. A., Ward-Thompson D., 2016, A&A, 590, A72

Peretto N. et al., 2020, arXiv e-prints, arXiv:2006.05155

Pereyra A., Magalhães A. M., 2004, ApJ, 603, 584

Perryman M. A. C. et al., 1995, A&A, 304, 69

Persi P., Marenzi A. R., Gómez M., Olofsson G., 2003, A&A, 399, 995

Persi P. et al., 2000, A&A, 357, 219

Persi P., Tapia M., Smith H. A., 2006, A&A, 445, 971

Peters T., Banerjee R., Klessen R. S., Mac Low M.-M., 2011, ApJ, 729, 72

Peters T., Klessen R. S., Mac Low M.-M., Banerjee R., 2010, ApJ, 725, 134

Pety J. et al., 2017, A&A, 599, A98

Pilbratt G. L. et al., 2010, A&A, 518, L1

Pillai T., Kauffmann J., Wiesemeyer H., Menten K. M., 2016, A&A, 591, A19

Pillai T., Wyrowski F., Carey S. J., Menten K. M., 2006, A&A, 450, 569

Pineda J. L., Langer W. D., Velusamy T., Goldsmith P. F., 2013, A&A, 554, A103

Planck Collaboration et al., 2016a, A&A, 586, A135

Planck Collaboration et al., 2016b, A&A, 586, A138

Planck Collaboration et al., 2016c, A&A, 586, A136

Planck Collaboration et al., 2015, A&A, 582, A31

Poglitsch A. et al., 2010, A&A, 518, L2

Polychroni D. et al., 2013, ApJL, 777, L33

Pon A., Caselli P., Johnstone D., Kaufman M., Butler M. J., Fontani F., Jiménez-Serra I., Tan J. C., 2015, A&A, 577, A75

Pon A., Johnstone D., Kaufman M. J., 2012, ApJ, 748, 25

Pon A., Johnstone D., Kaufman M. J., Caselli P., Plume R., 2014, MNRAS, 445, 1508

Pon A. et al., 2016, ApJ, 827, 107

Pont O., Turiel A., Yahia H., 2011, in Combinatorial Image Analysis, Aggarwal J. K., Barneva R. P., Brimkov V. E., Koroutchev K. N., Korutcheva E. R., eds., Springer Berlin Heidelberg, Berlin, Heidelberg, pp. 346–357

Pont O., Turiel A., Yahia H., 2013, International Journal of Computer Mathematics, 90, 1693

Pound M. W., Wolfire M. G., 2008, Astronomical Society of the Pacific Conference Series, Vol. 394, The Photo Dissociation Region Toolbox, Argyle R. W., Bunclark P. S., Lewis J. R., eds., p. 654

Pudritz R. E., Kevlahan N. K. R., 2013, Philosophical Transactions of the Royal Society of London Series A, 371, 20120248

Raga A., Cabrit S., 1993, A&A, 278, 267

Ragan S. et al., 2012, A&A, 547, A49

Ragan S. E., Bergin E. A., Gutermuth R. A., 2009, ApJ, 698, 324

Ragan S. E., Bergin E. A., Plume R., Gibson D. L., Wilner D. J., O'Brien S., Hails E., 2006, ApJS, 166, 567

Ragan S. E., Bergin E. A., Wilner D., 2011, ApJ, 736, 163

Ragan S. E., Henning T., Beuther H., Linz H., Zahorecz S., 2015, A&A, 573, A119

Ragan S. E., Henning T., Tackenberg J., Beuther H., Johnston K. G., Kainulainen J., Linz H., 2014, A&A, 568, A73

Rathborne J. M., Jackson J. M., Simon R., 2006, ApJ, 641, 389

Rayner T. S. M. et al., 2017, A&A, 607, A22

Rebull L. M. et al., 2010, ApJS, 186, 259

Recchi S., Hacar A., Palestini A., 2013, A&A, 558, A27

Recchi S., Hacar A., Palestini A., 2014, MNRAS, 444, 1775

Redaelli E. et al., 2017, ApJ, 850, 202

Reich W., Fuerst E., Reich P., Reif K., 1990, A&AS, 85, 633

Reid M. J. et al., 2019, ApJ, 885, 131

Reid M. J. et al., 2014, ApJ, 783, 130

Reid M. J. et al., 2009, ApJ, 700, 137

Reipurth B., Schneider N., 2008, Star Formation and Young Clusters in Cygnus, Reipurth B., ed., Vol. 4, p. 36

Rigby A. J. et al., 2016, MNRAS, 456, 2885

Risacher C. et al., 2018, Journal of Astronomical Instrumentation, 7, 1840014

Robitaille J. F., Joncas G., Miville-Deschênes M. A., 2014, MNRAS, 440, 2726

Robitaille J. F., Motte F., Schneider N., Elia D., Bontemps S., 2019, A&A, 628, A33

Robitaille T. P., 2017, A&A, 600, A11

Robitaille T. P., Whitney B. A., Indebetouw R., Wood K., 2007, ApJS, 169, 328

Roelfsema P. et al., 2012, Society of Photo-Optical Instrumentation Engineers (SPIE) Conference Series, Vol. 8442, The SAFARI imaging spectrometer for the SPICA space observatory, p. 84420R

Roelfsema P. R. et al., 2018, PASA, 35, e030

Röllig M. et al., 2007, A&A, 467, 187

Röllig M., Ossenkopf V., 2013, A&A, 550, A56

Russeil D. et al., 2013, A&A, 554, A42

Ruze J., 1952, Il Nuovo Cimento (1943-1954), 9, 364

Rygl K. L. J. et al., 2012, A&A, 539, A79

Sadaghiani M. et al., 2020, A&A, 635, A2

Salpeter E. E., 1955, ApJ, 121, 161

Scalo J. M., 1987, Theoretical Approaches to Interstellar Turbulence, Hollenbach D. J., Thronson Harley A. J., eds., Vol. 134, p. 349

Schaefer B. E., 2008, AJ, 135, 112

Schilke P., 2018, in Atacama Large-Aperture Submm/mm Telescope (AtLAST), p. 33

Schisano E. et al., 2020, MNRAS, 492, 5420

Schisano E. et al., 2014, ApJ, 791, 27

Schlafly E. F. et al., 2014, ApJ, 786, 29

Schleuning D. A., 1998, ApJ, 493, 811

Schmidt M., 1959, ApJ, 129, 243

Schneider N. et al., 2013, ApJL, 766, L17

Schneider N. et al., 2016a, A&A, 591, A40

Schneider N. et al., 2016b, A&A, 587, A74

Schneider N., Bontemps S., Simon R., Jakob H., Motte F., Miller M., Kramer C., Stutzki J., 2006, A&A, 458, 855

Schneider N. et al., 2011, A&A, 529, A1

Schneider N., Csengeri T., Bontemps S., Motte F., Simon R., Hennebelle P., Federrath C., Klessen R., 2010, A&A, 520, A49

Schneider N. et al., 2012, A&A, 540, L11

Schneider N., Simon R., Bontemps S., Comerón F., Motte F., 2007, A&A, 474, 873

Schöier F. L., van der Tak F. F. S., van Dishoeck E. F., Black J. H., 2005, A&A, 432, 369

Schuller F. et al., 2017, A&A, 601, A124

Schuller F. et al., 2009, A&A, 504, 415

Scoville N. Z., Solomon P. M., 1975, ApJL, 199, L105

Seifried D., Sánchez-Monge Á., Suri S., Walch S., 2017, MNRAS, 467, 4467

Seifried D., Walch S., 2016, MNRAS, 459, L11

Seifried D., Walch S., Weis M., Reissl S., Soler J. D., Klessen R. S., Joshi P. R., 2020, arXiv e-prints, arXiv:2003.00017

She Z.-S., Leveque E., 1994, Phys. Rev. Lett., 72, 336

Shimajiri Y. et al., 2017, A&A, 604, A74

Shimajiri Y., André P., Ntormousi E., Men'shchikov A., Arzoumanian D., Palmeirim P., 2019a, A&A, 632, A83

Shimajiri Y., André P., Palmeirim P., Arzoumanian D., Bracco A., Könyves V., Ntormousi E., Ladjelate B., 2019b, A&A, 623, A16

Shimajiri Y. et al., 2014, A&A, 564, A68

Shirley Y. L., 2015, PASP, 127, 299

Shu F. H., 1977, ApJ, 214, 488

Shu F. H., Adams F. C., Lizano S., 1987, ARA&A, 25, 23

Shull J. M., McKee C. F., 1979, ApJ, 227, 131

Simon M. et al., 2019a, ApJ, 884, 42

Simon R., Jackson J. M., Rathborne J. M., Chambers E. T., 2006a, ApJ, 639, 227

Simon R., Rathborne J. M., Shah R. Y., Jackson J. M., Chambers E. T., 2006b, ApJ, 653, 1325

Simon R. et al., 2019b, BAAS, 51, 367

Simon R., Schneider N., Bontemps S., Brunt C., Motte F., 2006c, in Astronomical Society of the Pacific Conference Series, Vol. 357, The Spitzer Space Telescope: New Views of the Cosmos, Armus L., Reach W. T., eds., p. 153

Skrutskie M. F. et al., 2006, AJ, 131, 1163

Smith D., Adams N. G., 1980, ApJ, 242, 424

Smith R. J., Glover S. C. O., Clark P. C., Klessen R. S., Springel V., 2014, MNRAS, 441, 1628

Smith R. J., Glover S. C. O., Klessen R. S., 2014, MNRAS, 445, 2900

Smith R. J., Glover S. C. O., Klessen R. S., Fuller G. A., 2016, MNRAS, 455, 3640

Smith R. J., Longmore S., Bonnell I., 2009, MNRAS, 400, 1775

Smith R. J. et al., 2020, MNRAS, 492, 1594

Soler J. D. et al., 2017, A&A, 603, A64

Soler J. D., Hennebelle P., 2017, A&A, 607, A2

Soler J. D., Hennebelle P., Martin P. G., Miville-Deschênes M. A., Netterfield C. B., Fissel L. M., 2013, ApJ, 774, 128

Solomon P. M., Rivolo A. R., Barrett J., Yahil A., 1987, ApJ, 319, 730

Spezzi L. et al., 2008, ApJ, 680, 1295

Springel V., 2010a, MNRAS, 401, 791

Springel V., 2010b, ARA&A, 48, 391

Stahler S. W., Palla F., 2005, The Formation of Stars

Stahler S. W., Palla F., Ho P. T. P., 2000, in Protostars and Planets IV, Mannings V., Boss A. P., Russell S. S., eds., pp. 327–352

Stahler S. W., Shu F. H., Taam R. E., 1980, ApJ, 241, 637

Stamatellos D., Whitworth A. P., Bisbas T., Goodwin S., 2007, A&A, 475, 37

Sternberg A., Dalgarno A., 1989, ApJ, 338, 197

Sternberg A., Dalgarno A., 1995, ApJS, 99, 565

Strong A. W., Moskalenko I. V., Ptuskin V. S., 2007, Annual Review of Nuclear and Particle Science, 57, 285

Stutz A. M., Kainulainen J., 2015, A&A, 577, L6

Stutzki J., Bensch F., Heithausen A., Ossenkopf V., Zielinsky M., 1998, A&A, 336, 697

Szűcs L., Glover S. C. O., Klessen R. S., 2014, MNRAS, 445, 4055

Tabone B. et al., 2017, A&A, 607, L6

Tafalla M., Hacar A., 2015, A&A, 574, A104

Tafalla M., Myers P. C., Caselli P., Walmsley C. M., 2004, A&A, 416, 191

Tafalla M., Myers P. C., Caselli P., Walmsley C. M., Comito C., 2002, ApJ, 569, 815

Tan J. C., Kong S., Butler M. J., Caselli P., Fontani F., 2013, ApJ, 779, 96

Tan J. C., Kong S., Zhang Y., Fontani F., Caselli P., Butler M. J., 2016, ApJL, 821, L3

Taylor A. R. et al., 2003, AJ, 125, 3145

Testi L., Sargent A. I., 1998, ApJL, 508, L91

Teyssier D., Hennebelle P., Pérault M., 2002, A&A, 382, 624

Teyssier R., 2015, ARA&A, 53, 325

Tielens A. G. G. M., 2010, The Physics and Chemistry of the Interstellar Medium

Tielens A. G. G. M., Hollenbach D., 1985, ApJ, 291, 722

Tigé J. et al., 2017, A&A, 602, A77

Tomida K., Tomisaka K., Matsumoto T., Hori Y., Okuzumi S., Machida M. N., Saigo K., 2013, ApJ, 763, 6

Torii K. et al., 2011, ApJ, 738, 46

Traficante A., Fuller G. A., Duarte-Cabral A., Elia D., Heyer M. H., Molinari S., Peretto N., Schisano E., 2020, MNRAS, 491, 4310

Traficante A., Fuller G. A., Smith R. J., Billot N., Duarte-Cabral A., Peretto N., Molinari S., Pineda J. E., 2018, MNRAS, 473, 4975

Tremblin P. et al., 2014, A&A, 564, A106

Tremblin P., Schneider N., Minier V., Durand G. A., Urban J., 2012, A&A, 548, A65

Tritsis A., Tassis K., 2016, MNRAS, 462, 3602

Tritsis A., Tassis K., 2018, Science, 360, 635

Tritsis A., Yorke H., Tassis K., 2018, MNRAS, 478, 2056

Turiel A., Pérez-Vicente C. J., Grazzini J., 2006, Journal of Computational Physics, 216, 362

Turiel A., Yahia H., Pérez-Vicente C. J., 2007, Journal of Physics A: Mathematical and Theoretical, 41, 015501

Vacca W. D., Garmany C. D., Shull J. M., 1996, ApJ, 460, 914

Vallée J. P., Fiege J. D., 2006, ApJ, 636, 332

van der Tak F. F. S., Black J. H., Schöier F. L., Jansen D. J., van Dishoeck E. F., 2007, A&A, 468, 627

van Dokkum P. G., Conroy C., 2010, Nature, 468, 940

van Loo S., Falle S. A. E. G., Hartquist T. W., Moore T. J. T., 2007, A&A, 471, 213

Van Loo S., Keto E., Zhang Q., 2014, ApJ, 789, 37

Vaytet N., Audit E., Chabrier G., Commerçon B., Masson J., 2012, A&A, 543, A60

Vaytet N., Chabrier G., Audit E., Commerçon B., Masson J., Ferguson J., Delahaye F., 2013, A&A, 557, A90

Vazquez-Semadeni E., 1994, ApJ, 423, 681

Vázquez-Semadeni E., Banerjee R., Gómez G. C., Hennebelle P., Duffin D., Klessen R. S., 2011, MNRAS, 414, 2511

Vázquez-Semadeni E., Gazol A., Scalo J., 2000, ApJ, 540, 271

Vázquez-Semadeni E., Gómez G. C., Jappsen A. K., Ballesteros-Paredes J., González R. F., Klessen R. S., 2007, ApJ, 657, 870

Vázquez-Semadeni E., Gómez G. C., Jappsen A. K., Ballesteros-Paredes J., Klessen R. S., 2009, ApJ, 707, 1023

Vázquez-Semadeni E., González-Samaniego A., Colín P., 2017, MNRAS, 467, 1313

Vázquez-Semadeni E., Palau A., Ballesteros-Paredes J., Gómez G. C., Zamora-Avilés M., 2019, MNRAS, 490, 3061

Vergely J. L., Valette B., Lallement R., Raimond S., 2010, A&A, 518, A31

Vilas-Boas J. W. S., Myers P. C., Fuller G. A., 1994, ApJ, 433, 96

Visser A. E., Richer J. S., Chandler C. J., 2002, AJ, 124, 2756

Vrba F. J., Coyne G. V., Tapia S., 1981, ApJ, 243, 489

Vrba F. J., Strom S. E., Strom K. M., 1976, AJ, 81, 958

Wakelam V., Herbst E., Selsis F., 2006, A&A, 451, 551

Wakelam V., Ruaud M., Gratier P., Bonnell I. A., 2019, MNRAS, 486, 4198

Walch S. et al., 2015, MNRAS, 454, 238

Wang K., Testi L., Burkert A., Walmsley C. M., Beuther H., Henning T., 2016, ApJS, 226, 9

Wang K., Testi L., Ginsburg A., Walmsley C. M., Molinari S., Schisano E., 2015, MNRAS, 450, 4043

Wang K. et al., 2014, MNRAS, 439, 3275

Wang P., Li Z.-Y., Abel T., Nakamura F., 2010, ApJ, 709, 27

Ward-Thompson D., André P., Crutcher R., Johnstone D., Onishi T., Wilson C., 2007, in Protostars and Planets V, Reipurth B., Jewitt D., Keil K., eds., p. 33

Watson W. D., Anicich V. G., Huntress, W. T. J., 1976, ApJL, 205, L165

Whitney B. A., Hartmann L., 1993, ApJ, 402, 605

Whittet D. C. B., Prusti T., Franco G. A. P., Gerakines P. A., Kilkenny D., Larson K. A., Wesselius P. R., 1997, A&A, 327, 1194

Whitworth A. P., Jaffa S. E., 2018, A&A, 611, A20

Wilking B. A., Lada C. J., Young E. T., 1989, ApJ, 340, 823

Williams G. M., Peretto N., Avison A., Duarte-Cabral A., Fuller G. A., 2018, A&A, 613, A11

Wilson T. L., Rood R., 1994, ARA&A, 32, 191

Winkler K. H. A., Newman M. J., 1980, ApJ, 236, 201

Winter A. J., Clarke C. J., Rosotti G. P., 2019, MNRAS, 485, 1489

Wolfire M. G., Cassinelli J. P., 1987, ApJ, 319, 850

Wolfire M. G., Hollenbach D., McKee C. F., Tielens A. G. G. M., Bakes E. L. O., 1995, ApJ, 443, 152

Wolfire M. G., McKee C. F., Hollenbach D., Tielens A. G. G. M., 2003, ApJ, 587, 278

Woods P. M., Willacy K., 2009, ApJ, 693, 1360

Woody D. P., Scott S. L., Scoville N. Z., Mundy L. G., Sargent A. I., Padin S., Tinney C. G., Wilson C. D., 1989, ApJL, 337, L41

Wright N. J., Bouy H., Drew J. E., Sarro L. M., Bertin E., Cuilland re J.-C., Barrado D., 2016, MNRAS, 460, 2593

Wright N. J., Parker R. J., Goodwin S. P., Drake J. J., 2014, MNRAS, 438, 639

Wu B., Tan J. C., Christie D., Nakamura F., Van Loo S., Collins D., 2017, ApJ, 841, 88

Wu B., Van Loo S., Tan J. C., Bruderer S., 2015, ApJ, 811, 56

Wyrowski F. et al., 2016, A&A, 585, A149

Wyrowski F., Güsten R., Menten K. M., Wiesemeyer H., Klein B., 2012, A&A, 542, L15

Yorke H. W., Bodenheimer P., 1999, ApJ, 525, 330

Yorke H. W., Sonnhalter C., 2002, ApJ, 569, 846

Zamora-Avilés M., Ballesteros-Paredes J., Hartmann L. W., 2017, MNRAS, 472, 647

Zhang Y., Tan J. C., 2018, ApJ, 853, 18

Zhang Y., Tan J. C., Hosokawa T., 2014, ApJ, 788, 166

Zinnecker H., 1982, Annals of the New York Academy of Sciences, 395, 226

Zinnecker H., Yorke H. W., 2007, ARA&A, 45, 481

Zucker C., Battersby C., Goodman A., 2015, ApJ, 815, 23

Zucker C., Battersby C., Goodman A., 2018, ApJ, 864, 153

Zucker C., Speagle J. S., Schlafly E. F., Green G. M., Finkbeiner D. P., Goodman A. A., Alves J., 2019, ApJ, 879, 125

Zuckerman B., Evans, N. J. I., 1974, ApJL, 192, L149